University of Alberta

Measurement, Modelling, and Stochastic Simulation of Concentration Fluctuations in a Shear Flow

by

Trevor Lloyd Hilderman ©

A thesis submitted to the Faculty of Graduate Studies and Research in partial
fulfillment of the requirements for the degree of Doctor of Philosophy

Department of Mechanical Engineering

Edmonton, Alberta
Spring 2004

7

Library and
Archives Canada

Published Heritage
Branch

395 Wellington Street
Ottawa ON K1A 0N4
Canada

Bibliothèque et
Archives Canada

Direction du
Patrimoine de l'édition

395, rue Wellington
Ottawa ON K1A 0N4
Canada

Your file Votre référence
ISBN: 0-612-96277-6
Our file Notre référence
ISBN: 0-612-96277-6

The author has granted a non-exclusive license allowing the Library and Archives Canada to reproduce, loan, distribute or sell copies of this thesis in microform, paper or electronic formats.

The author retains ownership of the copyright in this thesis. Neither the thesis nor substantial extracts from it may be printed or otherwise reproduced without the author's permission.

L'auteur a accordé une licence non exclusive permettant à la Bibliothèque et Archives Canada de reproduire, prêter, distribuer ou vendre des copies de cette thèse sous la forme de microfiche/film, de reproduction sur papier ou sur format électronique.

L'auteur conserve la propriété du droit d'auteur qui protège cette thèse. Ni la thèse ni des extraits substantiels de celle-ci ne doivent être imprimés ou aturement reproduits sans son autorisation.

In compliance with the Canadian Privacy Act some supporting forms may have been removed from this thesis.

While these forms may be included in the document page count, their removal does not represent any loss of content from the thesis.

Conformément à la loi canadienne sur la protection de la vie privée, quelques formulaires secondaires ont été enlevés de cette thèse.

Bien que ces formulaires aient inclus dans la pagination, il n'y aura aucun contenu manquant.

Canada

Abstract

This thesis contains three unpublished papers that develop and validate models for concentration fluctuation statistics in a plume dispersing in the highly sheared flow near the ground in the neutrally-stable atmospheric boundary layer. The models developed are practical, operational models that can be applied to full-scale hazardous outcome prediction. An extensive water channel data set for concentration fluctuations from point source releases in both rough surface boundary layer shear flow and in shear-free grid turbulence are used as a basis for the model development and verification.

A digital linescan camera and laser-induced fluorescence technique is developed for measuring high frequency, high spatial resolution concentration fluctuations at 1024 simultaneous points in a dispersing plume. The large-scale time averaged meandering motions of the plume are directly measured by tracking the plume centroid. The plume spread development with averaging time compares favorably with a modified travel time based power law model for averaging time adjustment while the widely-used 0.2 power law for averaging time effects is demonstrated to be a poor approximation.

An engineering model is developed for the total concentration fluctuation intensity, intermittency factor, and concentration integral time scale for a plume dispersing in a shear flow. The relevant parameter for wind shear effects is found to be the velocity shear normalized by vertical turbulence intensity, plume travel time, and average streamwise velocity. The reference position at which to evaluate the non-dimensional shear is an important factor because both the source position and the receptor position influence the concentration fluctuation statistics.

The overall concentration fluctuation statistics are used to drive a stochastic time series simulation to produce ensembles of realistic exposure events with a clipped lognormal probability distribution of concentration. The accuracy of the stochastic model is verified by favorable comparison with water channel measurements for concentration bursts above a threshold level and gaps below a threshold. A simple time delay technique is developed to produce realistic cross-stream correlations of concentration fluctuations. This greatly enhances the application of the stochastic model as the exposure to an individual and his neighbours can be evaluated simultaneously for the same release event.

Acknowledgements

First, I would like to thank Mom and Dad for their continual support and encouragement throughout my graduate studies.

I would also like to thank my supervisor, Dr. David Wilson, whose role has been both mentor and colleague over the past decade during which we have worked together.

Finally, there are a few other individuals who deserve special thanks for having contributed to the completion of this thesis:

- Darwin Kiel for lending me his LDV to complete my experimental data, giving me a job, and for his patience and flexibility during the final couple years it took me to complete my research.
- Ricky Chong for his assistance in developing the experimental techniques and collecting the majority of the concentration data.
- Kelly Hughes for collecting the grid turbulence data and for invaluable assistance in debugging my work by actually trying to use the information and models in her own research.

Table of Contents

1 Introduction and Overview 1
1.1 Background and Motivation 1
1.2 Basic Plume Parameter Definitions 2
1.3 General Approach to Concentration Fluctuation Problems 4
1.4 Outline of Work 5
1.4.1 Hilderman and Wilson (1999) "Simulating Concentration Fluctuation Time Series with Intermittent Zero Periods and Level Dependent Derivatives" 6
1.4.2 Hilderman et al. (1999) "A Model for Effective Toxic Load from Fluctuating Gas Concentrations" 6
1.4.3 Chapter 2 "Plume Meandering and Averaging Time Effects from High Resolution One-dimensional Concentration Measurements" 7
1.4.4 Chapter 3 "Measurement and Prediction of Wind Shear Distortion of Concentration Fluctuation Statistics" 7
1.4.5 Chapter 4 "Stochastic Modelling of Cross-Stream Correlated Concentration Fluctuations in a Dispersing Plume for Cross-Stream Hazard Evaluation" 8
References 9

2 Plume Meandering and Averaging Time Effects from High Resolution One-dimensional Concentration Measurements 12
2.1 Introduction 12
2.1.1 Scope of Experimental Measurements 14
2.2 Water Channel Scale-Modelling Facility 14
2.2.1 Turbulent Boundary Layer Shear Flow 15
2.2.2 Grid Turbulence 16
2.2.3 Source Configurations 17
2.3 LIF Linescan Measurement Technique 18
2.3.1 Linescan Camera 18
2.3.2 Fluorescein Dye Properties 19
2.3.3 Calibration 21
2.3.4 Data Collection and Analysis 23

2.4 Averaging Time and the Meandering Plume Model of Concentration Fluctuations . . . 25
  2.4.1 Effect of Averaging Time on Plume Spread . . . 25
  2.4.2 Meandering Plume Model . . . 27
  2.4.3 Centreline Fluctuation Intensity as a Function of Averaging Time 29
  2.4.4 Cross-Stream Profiles of Fluctuation Intensity **i** . . . 29
  2.4.5 Cross-Stream Probability Distributions of Centroid Position and Plume Spread . . . 30
  2.4.6 Section Summary . . . 32
2.5 Plume Spread with Averaging Time: Models and Data . . . 33
  2.5.1 Plume Spread Variation with Averaging Time . . . 33
  2.5.2 Plume Meander as a Function of Averaging Time . . . 34
  2.5.3 Improving the Travel Time Power Law Model . . . 35
  2.5.4 Cross-stream Lagrangian Time Scale T_{Lv} . . . 37
  2.5.5 Travel Time t_t Estimates . . . 39
  2.5.6 Testing the TTPL Model for Averaging Time Adjustments to Plume Spread . . . 40
  2.5.7 Plume Spread . . . 40
  2.5.8 Meander . . . 41
2.6 Summary and Conclusions . . . 42
References . . . 45

3 Measurement and Prediction of Wind Shear Distortion of Concentration Fluctuation Statistics **75**
3.1 Introduction . . . 76
3.2 Information Required for a Concentration Fluctuation Model . . . 77
  3.2.1 Time Scale T_{vel} of Turbulence Velocities . . . 78
3.3 Experiment Description . . . 79
  3.3.1 Flow Fields . . . 79
  3.3.2 Tracer Sources . . . 82
  3.3.3 Resolution in the Intermittent Fringes of the Plume . . . 83
3.4 Modelling Wind Shear Effects . . . 84
  3.4.1 No Shear Concentration Fluctuations . . . 84
  3.4.2 Shear Flow Distortion . . . 85
  3.4.3 Non-dimensional Shear **S** . . . 86
  3.4.4 Power Law Model for the Shear Effect . . . 87
  3.4.5 Unsuccessful Models for Wind Shear Effects on Fluctuations . . 87
  3.4.6 Source and Receptor Position Influence on **S** . . . 88
  3.4.7 A Note on Fitting the Constants B_1 through B_4 . . . 89
3.5 The New Operational Model for Wind Shear Effects on Fluctuations . 90
  3.5.1 Fluctuation Intensity i Model . . . 90

3.5.2 Conditional Concentration Fluctuation Intensity i_p and Intermittency Factor γ as a Function of Total Concentration Fluctuation Intensity i 91
3.5.3 Concentration Integral Time Scale T_c Model 92
3.6 Case Study: Application of the Operational Model to Atmospheric Dispersion 96
3.6.1 Case Study: Vertical Velocity Fluctuations w'_{rms} 97
3.6.2 Case Study: Friction Velocity u_* 98
3.6.3 Case Study: Eulerian Integral Time Scale of Velocity T_{vel} . . . 98
3.6.4 Case Study: Setting Minimum Heights for z_{ref} and h_{ref} 99
3.6.5 Case Study: Results - Vertical Profiles in a Neutrally Stable Atmosphere 100
3.6.6 Case Study: Results - Vertical Profiles in Stable and Unstable Atmospheric Conditions 101
3.7 Summary and Conclusions 103
References 107

4 Stochastic Modelling of Cross-Stream Correlated Concentration Fluctuations in a Dispersing Plume for Simultaneous Cross-Stream Hazard Evaluation 132
4.1 Introduction 133
4.2 Concentration Fluctuation Measurements 135
4.2.1 LIF Data 135
4.2.2 Flow Fields 135
4.2.3 Tracer Sources 137
4.3 Probability Distributions of Intermittent Time Series 138
4.3.1 Implementing a Shifted then Clipped Lognormal Distribution 139
4.4 Experimental Validation of the Clipped Lognormal Probability Density 140
4.5 Stochastic Model for Fluctuations 141
4.5.1 Stochastic Differential Equation 142
4.5.2 Fokker-Planck Constraint 142
4.5.3 Functional Relations for a and b 143
4.6 Generating Stochastic Time Series 144
4.6.1 Time Scales of Intermittent and Non-Intermittent Time Series 145
4.6.2 Frequency Spectrum of Experimental Data Compared to the Simulation 145
4.7 Stochastic Model Performance - Burst Duration and Gap Duration Probability Distributions 146
4.8 A Physical Model for Generating Correct Cross-Stream Event Correlation 149
4.8.1 Velocity U for Cross-Stream De-correlation in a Boundary Layer 150
4.8.2 Comparison of Cross-Stream Time Delay De-Correlation with Experimental Data. 151
4.9 Summary and Conclusions 152

References 154

5 Summary and Conclusions **177**
5.1 Complete Toxic Outcome Model 177
5.2 Overview of Thesis Chapters 178
5.3 Future Research 179
References 181

A Water Channel Velocity Profiles **182**
A.1 Shear Flow Boundary Layer 182
A.2 Grid Turbulence 183
References 184

B Linescan Data Summary **196**
B.1 Normalization 196
B.2 Source Types 197
B.3 Horizontal Concentration Profiles 198
B.4 Vertical Concentration Profiles 198
B.5 Additional Data Sets Collected 199
B.6 Data Table Description 199

C Meander Parameters M_{spread} and $M_{\text{intensity}}$ **210**
C.1 Meander Definitions 210
C.2 Measuring Plume Spreads and Meander 211
C.3 Ensemble Averaging 212
C.4 Plots of M_{spread} versus $M_{\text{intensity}}$ 212
References 213

D Averaging Time Effects on i_h and σ_y **222**
References 222

E Cross-Stream Profiles of Concentration Fluctuation Intensity i **231**
References 232

F Cross-Stream Probability Distributions of Centroid Position and Plume Spread **241**
F.1 Centroid Position 241
F.2 Plume Spread 241
References 242

G Travel Time Power Law Averaging Time Model compared to Water Channel Data **275**

H Shear Distortion Model versus Water Channel Data **293**

I Concentration Probability Distributions, and Burst and Gap Duration Distributions 321

List of Figures

1.1 Typical intermittent concentration fluctuation time series that could be observed at a receptor positioned at a fixed point in the dispersing plume . . . 11

2.1 Schematic of linescan measurement experiments . . . 48
2.2 University of Alberta Mechanical Engineering Department water channel schematic . . . 48
2.3 Fluorescein dye sources . . . 49
2.4 Velocity statistics for the rough surface boundary layer shear flow . . 50
2.5 Grid turbulence velocity statistics . . . 51
2.6 Field of view of the linescan camera compared to the width of the laser line . . . 52
2.7 Laminar jet source used for calibration. . . . 52
2.8 Typical raw data used for calibration . . . 53
2.9 Typical calibration constant values for each pixel in the camera . . . 54
2.10 Raw data from tests for effect of the bottom surface . . . 55
2.11 Accuracy of linescan concentration measurement system . . . 56
2.12 Raw fluorescence data and corrected instantaneous concentration profile 57
2.13 Samples of instantaneous plumes and ensemble averages . . . 58
2.14 Samples of typical meander parameters $M_{\text{intensity}}$ and M_{spread} as a function of normalized averaging time $t_{\text{avg}}U_H/H$ . . . 59
2.15 Samples of typical meander parameters $M_{\text{intensity}}$ and M_{spread} at $x/H = 2.5$ downstream of the source as a function of normalized averaging time $t_{\text{avg}}U_H/H$ . . . 60
2.16 Samples of ratios $(i^2_{h,t_{\text{avg}}} + 1)/(i^2_{h,\infty} + 1)$ compared to $\sigma_{y,t_{\text{avg}}}/\sigma_{y,\infty}$ as a function of normalized averaging time $t_{\text{avg}}U_H/H$ . . . 61
2.17 Samples of ratios $(i^2_{h,t_{\text{avg}}} + 1)/(i^2_{h,\infty} + 1)$ compared to $\sigma_{y,t_{\text{avg}}}/\sigma_{y,\infty}$ at $x/H = 2.5$ downstream of the source as a function of normalized averaging time $t_{\text{avg}}U_H/H$ . . . 62
2.18 Samples of typical cross-stream profiles of concentration fluctuation intensity i compared to Equation (2.15) . . . 63
2.19 Samples of typical cross-stream profiles of concentration fluctuation intensity i compared to Equation (2.15) at $x/H = 2.5$ downstream of the source . . . 64

2.20 Cross-stream profiles of concentration fluctuation intensity i compared to Equation (2.15) using three possible meander parameter values . . 65
2.21 Probability density functions of normalized centroid position $p(\overline{y}/\sigma_{y,\infty})$ compared to a Gaussian 66
2.22 Probability density functions of normalized centroid position $p(\overline{y}/\sigma_{y,\infty})$ compared to a Gaussian at $x/H = 2.5$ downstream of the source . . . 67
2.23 Probability density functions of normalized instantaneous plume spread $p(\sigma_{y,ii}/\sigma_{y,\infty})$ compared to a lognormal 68
2.24 Probability density functions of normalized instantaneous plume spread $p(\sigma_{y,ii}/\sigma_{y,\infty})$ compared to a lognormal at $x/H = 2.5$ downstream of the source 69
2.25 Several possible normalized cross-stream Lagrangian time scale values $T_{Lv}U_H/H$ in the boundary layer shear flow 70
2.26 Travel time power law model (TTPL) for plume spread ratio compared with experimental values as a function of normalized averaging time . 71
2.27 Travel time power law model (TTPL) for plume spread ratio compared with experimental values as function of normalized averaging time . . 72
2.28 Travel time power law model (TTPL) for meander $M_{\text{spread}} = \sigma_{y,m}^2/\sigma_{y,i}^2$ compared with experimental values as a function of normalized averaging time and the slope of the 0.2 power law 73
2.29 Travel time power law model (TTPL) for meander $M_{\text{spread}} = \sigma_{y,m}^2/\sigma_{y,i}^2$ compared with experimental values as a function of normalized averaging time $t_{\text{avg}}U_H/H$ and the slope of the 0.2 power law 74

3.1 University of Alberta Mechanical Engineering Department water channel schematic 109
3.2 Fluorescein dye sources 110
3.3 Velocity statistics for the rough surface boundary layer shear flow . . 111
3.4 Grid turbulence velocity statistics 112
3.5 Grid turbulence normalized concentration fluctuation integral time scale T_cU/G and length scale L_c/G profiles for a horizontal jet source on the water channel centreline compared to the no-shear estimate 113
3.6 Grid turbulence concentration fluctuation intensity i profile for a horizontal jet source on the water channel centreline compared to the no-shear model. 113
3.7 Vertical profiles of the fluctuation intensity i compared to the shear model and the no-shear model 114
3.8 Vertical profiles of normalized concentration fluctuation integral time scale T_cU_H/H compared to the shear and no-shear models 115
3.9 Vertical profiles of normalized concentration fluctuation integral length scale L_c/H compared to the shear and no-shear models 116
3.10 Physical example of the effects of shear history from the source and the receptor position 117

3.11 Asymptotic conditional concentration fluctuation intensity $i_{p,\infty}$ deduced from data fit to Equation (3.26) versus universal shear parameter for a range of source conditions and downstream distances including the zero-shear grid turbulence limit 118
3.12 Samples of the best, worst and typical agreement with shear scaling of conditional concentration fluctuation intensity i_p versus total concentration fluctuation intensity i 119
3.13 Samples of the best, worst and typical agreement with shear scaling of intermittency factor γ versus total concentration fluctuation intensity i 120
3.14 Samples of the best, worst and typical agreement of measured cross-stream profiles with pseudo-meandering plume theory of total concentration fluctuation intensity i, conditional concentration fluctuation intensity i_p and intermittency factor γ 121
3.14 Samples of the best, worst and typical agreement of measured cross-stream profiles with pseudo-meandering plume theory of total concentration fluctuation intensity i, conditional concentration fluctuation intensity i_p and intermittency factor γ 122
3.15 The concentration fluctuation integral time scale T_c is approximately constant across the plume as shown in these cross-stream profiles measured near the ground at $(z-d)/H = 0.011$ 123
3.16 Case study samples of concentration fluctuation integral time scale ratios $T_{c,\text{shear}}/T_{c,\text{no-shear}}$ computed with the shear model Equation (3.32) for a neutrally stable atmosphere (high wind low heat flux) 124
3.17 Case study samples of concentration fluctuation intensity i for $i_h^2 = 0.1$ computed with the shear model Equation (3.23) for a neutrally stable atmosphere (high wind low heat flux) 125
3.18 Case study samples of concentration fluctuation intensity i for $i_h^2 = 10$ computed with the shear model Equation (3.23) for a neutrally stable atmosphere (high wind low heat flux 126
3.19 Case study samples of conditional concentration fluctuation intensity i_p for $i_h^2 = 0.1$ computed with the shear model in Equations (3.26) and (3.27) for a neutrally stable atmosphere (high wind low heat flux) . . 127
3.20 Case study samples of conditional concentration fluctuation intensity i_p for $i_h^2 = 10$ computed with the shear model in Equations (3.26) and (3.27) for a neutrally stable atmosphere (high wind low heat flux) . . 128
3.21 Case study samples of intermittency factor γ for $i_h^2 = 0.1$ computed from the i and i_p values given in Figures 3.17 and 3.19 using the definition in Equation (3.3) for a neutrally stable atmosphere (high wind low heat flux) 129
3.22 Case study samples of intermittency factor γ for $i_h^2 = 10$ computed from the i and i_p values given in Figures 3.18 and 3.20 using the definition in Equation (3.3) for a neutrally stable atmosphere (high wind low heat flux) 130

3.23 Estimated concentration fluctuation integral time scale in full-scale atmospheric conditions calculated with Equation (3.32) for stability classes A (very unstable, light wind, sunny clear day), D (neutrally stable, strong wind, low heat flux), and F (very stable, light wind, clear night sky) 131

4.1 Typical intermittent concentration fluctuation time series that could be observed at a receptor positioned at a fixed point in the dispersing plume 156
4.2 University of Alberta Mechanical Engineering Department water channel schematic 157
4.3 Fluorescein dye sources 158
4.4 Physical model for interpreting the pdf of negative concentrations as intermittent periods of clean air (zero concentration) 159
4.5 Three step shifting and clipping procedure used to produce an intermittent time series from a non-intermittent stochastic simulation. . . 160
4.6 Normalized concentration probability density functions $p(c/C_p)$ of the linescan data compared to the clipped lognormal generated by the stochastic model 161
4.7 Normalized concentration probability density functions $p(C/C_p)$ of the linescan data compared to the clipped lognormal generated by the stochastic model 162
4.8 Exceedance probability functions $E(c/C_p)$ of the linescan data compared to the clipped lognormal generated by the stochastic model . . 163
4.9 Exceedance probability functions $E(c/C_p)$ of the linescan data compared to the clipped lognormal generated by the stochastic model . . 164
4.10 Typical normalized spectral density of the water channel linescan LIF data compared to the stochastic simulation 165
4.11 Time series example of bursts above and gaps below a threshold level in a concentration time series. 166
4.12 Probability distributions of bursts above $c/C_p = 0$ and $c/C_p = 2$ for a ground level horizontal jet and a ground level receptor position 167
4.13 Probability distributions of gaps below $c/C_p = 0$ and $c/C_p = 2$ for a ground level horizontal jet and a ground level receptor position 168
4.14 Probability distributions of bursts above $c/C_p = 0$ and $c/C_p = 1$ for a large ground level source and a ground level receptor position 169
4.15 Probability distributions of gaps below $c/C_p = 0$ and $c/C_p = 1$ for a large ground level source and a ground level receptor position 170
4.16 Probability distributions of bursts above $c/C_p = 0$ and $c/C_p = 10$ for an elevated iso-kinetic horizontal jet source in shear flow 171
4.17 Probability distributions of gaps below $c/C_p = 0$ and $c/C_p = 10$ for an elevated iso-kinetic horizontal jet source in shear flow 172

4.18 Cross-stream total concentration correlation coefficients for ground level sources and ground level receptors $(z-d)/H = 0.011$ in a boundary layer shear flow compared to the stochastic simulation 173
4.19 Cross-stream total concentration correlation coefficients for elevated sources with the receptor at source height compared to the stochastic simulation 174
4.20 Cross-stream total concentration correlation coefficients for ground level sources with elevated receptor positions $(z-d)/H = 0.12$ in a boundary layer shear flow compared to the stochastic simulation . . 175
4.21 Cross-stream total concentration correlation coefficients for an elevated iso-kinetic jet source at $(h-d)/H = 0.12$ in shear flow with the receptor at ground level $(z-d)/H = 0.011$ compared to the stochastic simulation. 176

A.1 (a) Square bar array. All square bars of 19mm (nominal 3/4") stainless steel hollow square tubes. (b) Trip fence made from 16 gauge stainless steel sheet metal. All dimensions are in mm. 185
A.2 Shear flow boundary layer cross-stream velocity profile of mean streamwise velocity U. 186
A.3 Shear flow boundary layer cross-stream profiles $\overline{uw}$ Reynolds stress. . 186
A.4 Shear flow boundary layer cross-stream profiles of rms streamwise velocity fluctuation, u'_{rms}. 187
A.5 Shear flow boundary layer cross-stream profiles of rms vertical velocity fluctuation, w'_{rms}. 187
A.6 Shear flow boundary layer vertical profiles of the mean velocity U on linear scales. 188
A.7 Shear flow boundary layer vertical profiles of the mean velocity U on semi-logarithmic scales. 188
A.8 Shear flow boundary layer vertical profiles of the rms fluctuating velocity components u'_{rms}, v'_{rms}, and w'_{rms}. 189
A.9 Shear flow boundary layer vertical profile of rms vertical fluctuating velocity component w'_{rms} fit with an approximating function. 189
A.10 Shear flow boundary layer vertical profiles of the Reynolds stresses $\overline{uv}$ 190
A.11 Shear flow boundary layer vertical profiles of the Reynolds stresses $\overline{uw}$. 190
A.12 Shear flow boundary layer vertical profiles of the Eulerian velocity fluctuation timescales. 191
A.13 Shear flow boundary layer vertical profiles of the Eulerian velocity fluctuation timescales fit with an approximating function. 191
A.14 Grid turbulence horizontal profile of streamwise velocity U 192
A.15 Grid turbulence vertical profile of streamwise velocity U. 192
A.16 Grid turbulence horizontal profile of the streamwise rms velocity fluctuation u'_{rms} 193

A.17 Grid turbulence horizontal profile of the vertical rms velocity fluctuation w'_{rms} 193
A.18 Grid turbulence vertical profile of the streamwise rms velocity fluctuation u'_{rms} 194
A.19 Grid turbulence vertical profile of the vertical rms velocity fluctuation w'_{rms} 194
A.20 Grid turbulence intensity decay with downstream distance along the centreline of the channel. 195
A.21 Grid turbulence Eulerian integral timescales of velocity fluctuations in the streamwise T_u and vertical T_w directions along the centreline of the channel. 195

B.1 Fluorescein dye sources 202

C.1 Meander parameter $M_{\mathrm{intensity}}$ and M_{spread} values for the iso-kinetic horizontal jet source in grid turbulence 214
C.2 Meander parameter $M_{\mathrm{intensity}}$ and M_{spread} values for the large ground level source at a flow rate $Q = 1.47$ ml/s 215
C.3 Meander parameter $M_{\mathrm{intensity}}$ and M_{spread} values for the small ground level vertical jet source at a flow rate $Q = 1.47$ ml/s 216
C.4 Meander parameter $M_{\mathrm{intensity}}$ and M_{spread} values for the small ground level vertical jet source at a flow rate $Q = 0.73$ ml/s 217
C.5 Meander parameter $M_{\mathrm{intensity}}$ and M_{spread} values for the horizontal jet source at $h = 7$ mm at a flow rate $Q = 1.47$ ml/s 218
C.6 Meander parameter $M_{\mathrm{intensity}}$ and M_{spread} values for the horizontal jet source at $h = 7$ mm at a flow rate $Q = 0.73$ ml/s 219
C.7 Meander parameter $M_{\mathrm{intensity}}$ and M_{spread} values for the horizontal jet source at $h = 25$ mm at a flow rate $Q = 1.47$ ml/s 220
C.8 Meander parameter $M_{\mathrm{intensity}}$ and M_{spread} values for the horizontal jet source at $h = 50$ mm at a flow rate $Q = 1.47$ ml/s 221

D.1 Ratios of plume centreline fluctuation intensity $(i^2_{h,t_{\mathrm{avg}}} + 1)/(i^2_{h,\infty} + 1)$ compared to the plume spread ratio $\sigma_{y,t_{\mathrm{avg}}}/\sigma_{y,\infty}$ as a function of averaging time t_{avg} for the iso-kinetic horizontal jet source in grid turbulence. 223
D.2 Ratios of plume centreline fluctuation intensity $(i^2_{h,t_{\mathrm{avg}}} + 1)/(i^2_{h,\infty} + 1)$ compared to the plume spread ratio $\sigma_{y,t_{\mathrm{avg}}}/\sigma_{y,\infty}$ as a function of averaging time t_{avg} for the large ground level source with a flow rate $Q = 1.47$ ml/s in the boundary layer shear flow. 224
D.3 Ratios of plume centreline fluctuation intensity $(i^2_{h,t_{\mathrm{avg}}} + 1)/(i^2_{h,\infty} + 1)$ compared to the plume spread ratio $\sigma_{y,t_{\mathrm{avg}}}/\sigma_{y,\infty}$ as a function of averaging time t_{avg} for the small ground level vertical jet source at a flow rate $Q = 1.47$ ml/s in the boundary layer shear flow. 225

D.4 Ratios of plume centreline fluctuation intensity $(i^2_{h,t_{\mathrm{avg}}} + 1)/(i^2_{h,\infty} + 1)$ compared to the plume spread ratio $\sigma_{y,t_{\mathrm{avg}}}/\sigma_{y,\infty}$ as a function of averaging time t_{avg} for the small ground level vertical jet source at a flow rate $Q = 0.73$ ml/s in the boundary layer shear flow. 226
D.5 Ratios of plume centreline fluctuation intensity $(i^2_{h,t_{\mathrm{avg}}} + 1)/(i^2_{h,\infty} + 1)$ compared to the plume spread ratio $\sigma_{y,t_{\mathrm{avg}}}/\sigma_{y,\infty}$ as a function of averaging time t_{avg} for the horizontal jet source at $h = 7$ mm at a flow rate $Q = 1.47$ ml/s in the boundary layer shear flow. 227
D.6 Ratios of plume centreline fluctuation intensity $(i^2_{h,t_{\mathrm{avg}}} + 1)/(i^2_{h,\infty} + 1)$ compared to the plume spread ratio $\sigma_{y,t_{\mathrm{avg}}}/\sigma_{y,\infty}$ as a function of averaging time t_{avg} for the horizontal jet source at $h = 7$ mm at a flow rate $Q = 0.73$ ml/s in the boundary layer shear flow. 228
D.7 Ratios of plume centreline fluctuation intensity $(i^2_{h,t_{\mathrm{avg}}} + 1)/(i^2_{h,\infty} + 1)$ compared to the plume spread ratio $\sigma_{y,t_{\mathrm{avg}}}/\sigma_{y,\infty}$ as a function of averaging time t_{avg} for the horizontal jet source at $h = 25$ mm at a flow rate $Q = 1.47$ ml/s in the boundary layer shear flow. 229
D.8 Ratios of plume centreline fluctuation intensity $(i^2_{h,t_{\mathrm{avg}}} + 1)/(i^2_{h,\infty} + 1)$ compared to the plume spread ratio $\sigma_{y,t_{\mathrm{avg}}}/\sigma_{y,\infty}$ as a function of averaging time t_{avg} for the horizontal jet source at $h = 50$ mm at a flow rate $Q = 1.47$ ml/s in the boundary layer shear flow. 230

E.1 Cross-stream profiles of concentration fluctuation intensity i compared to equation (E.2) for the iso-kinetic horizontal jet source in grid turbulence 233
E.2 Cross-stream profiles of concentration fluctuation intensity i compared to equation (E.2) for the large ground level source at a flow rate $Q = 1.47$ ml/s in the boundary layer shear flow 234
E.3 Cross-stream profiles of concentration fluctuation intensity i compared to equation (E.2) for the small ground level vertical jet source at a flow rate $Q = 1.47$ ml/s in the boundary layer shear flow 235
E.4 Cross-stream profiles of concentration fluctuation intensity i compared to equation (E.2) for the small ground level vertical jet source at a flow rate $Q = 0.73$ ml/s in the boundary layer shear flow 236
E.5 Cross-stream profiles of concentration fluctuation intensity i compared to equation (E.2) for the horizontal jet source at $h = 7$ mm at a flow rate $Q = 1.47$ ml/s in the boundary layer shear flow 237
E.6 Cross-stream profiles of concentration fluctuation intensity i compared to equation (E.2) for the horizontal jet source at $h = 7$ mm at a flow rate $Q = 0.73$ ml/s in the boundary layer shear flow 238
E.7 Cross-stream profiles of concentration fluctuation intensity i compared to equation (E.2) for the horizontal jet source at $h = 25$ mm at a flow rate $Q = 1.47$ ml/s in the boundary layer shear flow 239

E.8 Cross-stream profiles of concentration fluctuation intensity i compared to equation (E.2) for the horizontal jet source at $h = 25$ mm at a flow rate $Q = 1.47$ ml/s in the boundary layer shear flow 240

F.1 Probability density functions of centroid position $\overline{y}$ compared to a Gaussian for the iso-kinetic horizontal jet source in grid turbulence . 243
F.2 Probability density functions of centroid position $\overline{y}$ compared to a Gaussian for the iso-kinetic horizontal jet source in grid turbulence . 244
F.3 Probability density functions of centroid position $\overline{y}$ compared to a Gaussian for the large ground level source with a flow rate $Q = 1.47$ ml/s plotted on linear scales 245
F.4 Probability density functions of centroid position $\overline{y}$ compared to a Gaussian for the large ground level source with a flow rate $Q = 1.47$ ml/s plotted on linear-log scales 246
F.5 Probability density functions of centroid position $\overline{y}$ compared to a Gaussian for the small ground level vertical jet source at a flow rate $Q = 1.47$ ml/s plotted on linear scales 247
F.6 Probability density functions of centroid position $\overline{y}$ compared to a Gaussian for the small ground level vertical jet source at a flow rate $Q = 1.47$ ml/s plotted on log-linear scales 248
F.7 Probability density functions of centroid position $\overline{y}$ compared to a Gaussian for the small ground level vertical jet source at a flow rate $Q = 0.73$ ml/s plotted on linear scales 249
F.8 Probability density functions of centroid position $\overline{y}$ compared to a Gaussian for the small ground level vertical jet source at a flow rate $Q = 1.47$ ml/s plotted on log-linear scales 250
F.9 Probability density functions of centroid position $\overline{y}$ compared to a Gaussian for the horizontal jet source at $h = 7$ mm at a flow rate $Q = 1.47$ ml/s plotted on linear scales 251
F.10 Probability density functions of centroid position $\overline{y}$ compared to a Gaussian for the horizontal jet source at $h = 7$ mm at a flow rate $Q = 1.47$ ml/s plotted on log-linear scales 252
F.11 Probability density functions of centroid position $\overline{y}$ compared to a Gaussian for the horizontal jet source at $h = 7$ mm at a flow rate $Q = 0.73$ ml/s plotted on linear scales 253
F.12 Probability density functions of centroid position $\overline{y}$ compared to a Gaussian for the horizontal jet source at $h = 7$ mm at a flow rate $Q = 0.73$ ml/s plotted on log-linear scales 254
F.13 Probability density functions of centroid position $\overline{y}$ compared to a Gaussian for the horizontal jet source at $h = 25$ mm at a flow rate $Q = 1.47$ ml/s plotted on linear scales 255

F.14 Probability density functions of centroid position $\overline{y}$ compared to a Gaussian for the horizontal jet source at $h = 25$ mm at a flow rate $Q = 1.47$ ml/s plotted on log-linear scales 256
F.15 Probability density functions of centroid position $\overline{y}$ compared to a Gaussian for the horizontal jet source at $h = 50$ mm at a flow rate $Q = 1.47$ ml/s plotted on linear scales 257
F.16 Probability density functions of centroid position $\overline{y}$ compared to a Gaussian for the horizontal jet source at $h = 50$ mm at a flow rate $Q = 1.47$ ml/s plotted on log-linear scales 258
F.17 Probability density functions of plume spread σ_y compared to a clipped lognormal for the iso-kinetic horizontal jet source in grid turbulence plotted on linear scales. 259
F.18 Probability density functions of plume spread σ_y compared to a clipped lognormal for the iso-kinetic horizontal jet source in grid turbulence plotted on logarithmic scales. 260
F.19 Probability density functions of plume spread σ_y compared to a lognormal for the large ground level source at a flow rate $Q = 1.47$ ml/s plotted on linear scales. 261
F.20 Probability density functions of plume spread σ_y compared to a lognormal for the large ground level source at a flow rate $Q = 1.47$ ml/s plotted on logarithmic scales. 262
F.21 Probability density functions of plume spread σ_y compared to a lognormal for the small ground level vertical jet source at a flow rate $Q = 1.47$ ml/s plotted on linear scales. 263
F.22 Probability density functions of plume spread σ_y compared to a lognormal for the small ground level vertical jet source at a flow rate $Q = 1.47$ ml/s plotted on logarithmic scales. 264
F.23 Probability density functions of plume spread σ_y compared to a lognormal for the small ground level vertical jet source at a flow rate $Q = 0.73$ ml/s plotted on linear scales. 265
F.24 Probability density functions of plume spread σ_y compared to a lognormal for the small ground level vertical jet source at a flow rate $Q = 0.73$ ml/s plotted on logarithmic scales. 266
F.25 Probability density functions of plume spread σ_y compared to a lognormal for the horizontal jet source at $h = 7$ mm at a flow rate $Q = 1.47$ ml/s plotted on linear scales. 267
F.26 Probability density functions of plume spread σ_y compared to a lognormal for the horizontal jet source at $h = 7$ mm at a flow rate $Q = 1.47$ ml/s plotted on logarithmic scales. 268
F.27 Probability density functions of plume spread σ_y compared to a lognormal for the horizontal jet source at $h = 7$ mm at a flow rate $Q = 0.73$ ml/s plotted on linear scales. 269

F.28 Probability density functions of plume spread σ_y compared to a log-normal for the horizontal jet source at h = 7 mm at a flow rate $Q = 0.73$ ml/s plotted on logarithmic scales. 270
F.29 Probability density functions of plume spread σ_y compared to a log-normal for the horizontal jet source at h = 25 mm at a flow rate $Q = 1.47$ ml/s plotted on linear scales. 271
F.30 Probability density functions of plume spread σ_y compared to a log-normal for the horizontal jet source at h = 25 mm at a flow rate $Q = 0.73$ ml/s plotted on linear scales. 272
F.31 Probability density functions of plume spread σ_y compared to a log-normal for the horizontal jet source at h = 50 mm at a flow rate $Q = 1.47$ ml/s plotted on linear scales. 273
F.32 Probability density functions of plume spread σ_y compared to a log-normal for the horizontal jet source at h = 50 mm at a flow rate $Q = 1.47$ ml/s plotted on logarithmic scales. 274

G.1 Measured meander M_{spread} compared to TTPL model and 0.2 power law for the iso-kinetic horizontal jet source in grid turbulence 277
G.2 Measured meander M_{spread} compared to TTPL model and 0.2 power law for the large ground level source, flow rate $Q = 1.47$ ml/s 278
G.3 Measured meander M_{spread} compared to TTPL model and 0.2 power law for the small ground level vertical jet, flow rate $Q = 1.47$ ml/s . . 279
G.4 Measured meander M_{spread} compared to TTPL model and 0.2 power law for the small ground level vertical jet, flow rate $Q = 0.73$ ml/s . . 280
G.5 Measured meander M_{spread} compared to TTPL model and 0.2 power law for the horizontal jet at $h = 7$ mm, flow rate $Q = 1.47$ ml/s . . . 281
G.6 Measured meander M_{spread} compared to TTPL model and 0.2 power law for the horizontal jet at $h = 7$ mm, flow rate $Q = 1.47$ ml/s . . . 282
G.7 Measured meander M_{spread} compared to TTPL model and 0.2 power law for the horizontal jet at $h = 25$ mm, flow rate $Q = 1.47$ ml/s . . . 283
G.8 Measured meander M_{spread} compared to TTPL model and 0.2 power law for the horizontal jet at $h = 50$ mm, flow rate $Q = 1.47$ ml/s . . . 284
G.9 Measured plume spread ratio $\sigma_{y,t_{\text{avg}}}/\sigma_{y,t_{\text{avg}\to\infty}}$ compared to TTPL model and 0.2 power law for the iso-kinetic horizontal jet source in grid turbulence 285
G.10 Measured plume spread ratio $\sigma_{y,t_{\text{avg}}}/\sigma_{y,t_{\text{avg}\to\infty}}$ compared to TTPL model and 0.2 power law for the large ground level source, flow rate $Q = 1.47$ ml/s 286
G.11 Measured plume spread ratio $\sigma_{y,t_{\text{avg}}}/\sigma_{y,t_{\text{avg}\to\infty}}$ compared to TTPL model and 0.2 power law for the small ground level vertical jet source, flow rate $Q = 1.47$ ml/s 287

G.12 Measured plume spread ratio $\sigma_{y,t_{\mathrm{avg}}}/\sigma_{y,t_{\mathrm{avg}\to\infty}}$ compared to TTPL model and 0.2 power law for the small ground level vertical jet source, flow rate $Q = 0.73$ ml/s . . . 288
G.13 Measured plume spread ratio $\sigma_{y,t_{\mathrm{avg}}}/\sigma_{y,t_{\mathrm{avg}\to\infty}}$ compared to TTPL model and 0.2 power law for the horizontal jet source at $h = 6$ mm, flow rate $Q = 1.47$ ml/s . . . 289
G.14 Measured plume spread ratio $\sigma_{y,t_{\mathrm{avg}}}/\sigma_{y,t_{\mathrm{avg}\to\infty}}$ compared to TTPL model and 0.2 power law for the horizontal jet source at $h = 6$ mm, flow rate $Q = 1.47$ ml/s . . . 290
G.15 Measured plume spread ratio $\sigma_{y,t_{\mathrm{avg}}}/\sigma_{y,t_{\mathrm{avg}\to\infty}}$ compared to TTPL model and 0.2 power law for the horizontal jet source at $h = 25$ mm, flow rate $Q = 1.47$ ml/s . . . 291
G.16 Measured plume spread ratio $\sigma_{y,t_{\mathrm{avg}}}/\sigma_{y,t_{\mathrm{avg}\to\infty}}$ compared to TTPL model and 0.2 power law for the horizontal jet source at $h = 50$ mm, flow rate $Q = 1.47$ ml/s . . . 292

H.1 Vertical profiles of the fluctuation intensity i compared to the shear model and the no shear model for the vertical ground level jet source 294
H.2 Vertical profiles of the fluctuation intensity i compared to the shear model and the no shear model for the horizontal ground level jet source $h = 7$ mm . . . 295
H.3 Vertical profiles of the fluctuation intensity i compared to the shear model and the no shear model for the horizontal elevated jet source $h = 50$ mm . . . 296
H.4 Vertical profiles of the concentration fluctuation integral time scale T_c and length scale L_c for the small ground level vertical jet source at a flow rate of 1.47 ml/s compared to the shear model and the no shear model . . . 297
H.5 Vertical profiles of the concentration fluctuation integral time scale T_c and length scale L_c for the small ground level vertical jet source at a flow rate of 0.73 ml/s compared to the shear model and the no shear model . . . 298
H.6 Vertical profiles of the concentration fluctuation integral time scale T_c and length scale L_c for the horizontal jet source at $h = 7$ mm at a flow rate of 1.47 ml/s compared to the shear model and the no shear model 299
H.7 Vertical profiles of the concentration fluctuation integral time scale T_c and length scale L_c for the horizontal jet source at $h = 7$ mm at a flow rate of 0.73 ml/s compared to the shear model and the no shear model 300
H.8 Vertical profiles of the concentration fluctuation integral time scale T_c and length scale L_c for the horizontal jet source at $h = 7$ mm at a flow rate of 1.47 ml/s compared to the shear model and the no shear model 301

H.9 Vertical profiles of the concentration fluctuation integral time scale T_c and length scale L_c for the horizontal jet source at $h = 7$ mm at a flow rate of 0.73 ml/s compared to the shear model and the no shear model 302
H.10 Conditional concentration fluctuation intensity i_p versus total concentration fluctuation intensity i for the elevated horizontal jet source $h = 25$ mm 303
H.11 Intermittency factor γ versus total concentration fluctuation intensity i for the elevated horizontal jet source $h = 25$ mm 304
H.12 Conditional concentration fluctuation intensity i_p versus total concentration fluctuation intensity i for the elevated horizontal jet source $h = 50$ mm 305
H.13 Intermittency factor γ versus total concentration fluctuation intensity i for the elevated horizontal jet source $h = 50$ mm 306
H.14 Conditional concentration fluctuation intensity i_p versus total concentration fluctuation intensity i for the large ground level source 307
H.15 Intermittency factor γ versus total concentration fluctuation intensity i for the large ground level source 308
H.16 Measured and pseudo-meandering plume theory cross-stream profiles of total concentration fluctuation intensity i, conditional concentration fluctuation intensity i_p, and intermittency factor γ for the ground level horizontal jet source $h = 7$ mm at $x = 500$ mm downstream 309
H.17 Measured and pseudo-meandering plume theory cross-stream profiles of total concentration fluctuation intensity i, conditional concentration fluctuation intensity i_p, and intermittency factor γ for the ground level horizontal jet source $h = 7$ mm at $x = 1000$ mm downstream 310
H.18 Measured and pseudo-meandering plume theory cross-stream profiles of total concentration fluctuation intensity i, conditional concentration fluctuation intensity i_p, and intermittency factor γ for the ground level horizontal jet source $h = 7$ mm at $x = 1500$ mm downstream 311
H.19 Measured and pseudo-meandering plume theory cross-stream profiles of total concentration fluctuation intensity i, conditional concentration fluctuation intensity i_p, and intermittency factor γ for the elevated horizontal jet source $h = 25$ mm at $x = 500$ mm downstream 312
H.20 Measured and pseudo-meandering plume theory cross-stream profiles of total concentration fluctuation intensity i, conditional concentration fluctuation intensity i_p, and intermittency factor γ for the elevated horizontal jet source $h = 25$ mm at $x = 1000$ mm downstream 313
H.21 Measured and pseudo-meandering plume theory cross-stream profiles of total concentration fluctuation intensity i, conditional concentration fluctuation intensity i_p, and intermittency factor γ for the elevated horizontal jet source $h = 25$ mm at $x = 1500$ mm downstream 314

H.22 Measured and pseudo-meandering plume theory cross-stream profiles of total concentration fluctuation intensity i, conditional concentration fluctuation intensity i_p, and intermittency factor γ for the elevated horizontal jet source $h = 50$ mm at $x = 500$ mm downstream 315
H.23 Measured and pseudo-meandering plume theory cross-stream profiles of total concentration fluctuation intensity i, conditional concentration fluctuation intensity i_p, and intermittency factor γ for the elevated horizontal jet source $h = 50$ mm at $x = 1000$ mm downstream 316
H.24 Measured and pseudo-meandering plume theory cross-stream profiles of total concentration fluctuation intensity i, conditional concentration fluctuation intensity i_p, and intermittency factor γ for the elevated horizontal jet source $h = 50$ mm at $x = 1500$ mm downstream 317
H.25 Measured and pseudo-meandering plume theory cross-stream profiles of total concentration fluctuation intensity i, conditional concentration fluctuation intensity i_p, and intermittency factor γ for the large ground level source at $x = 500$ mm downstream 318
H.26 Measured and pseudo-meandering plume theory cross-stream profiles of total concentration fluctuation intensity i, conditional concentration fluctuation intensity i_p, and intermittency factor γ for the large ground level source at $x = 1000$ mm downstream 319
H.27 Measured and pseudo-meandering plume theory cross-stream profiles of total concentration fluctuation intensity i, conditional concentration fluctuation intensity i_p, and intermittency factor γ for the large ground level source at $x = 1500$ mm downstream 320

I.1 Normalized concentration probability distributions for the horizontal iso-kinetic jet in grid turbulence, $h = 200$ mm (channel centreline),$x = 1000$ mm, measured at $z = 200$ mm compared to the clipped lognormal generated by the stochastic model 322
I.2 Normalized concentration probability distributions for the horizontal iso-kinetic jet in shear flow, $h = 50$ mm, $x = 500$ mm, measured at $z = 50$ mm compared to the clipped lognormal generated by the stochastic model 323
I.3 Normalized concentration probability distributions for the horizontal iso-kinetic jet in shear flow, $h = 50$ mm, $x = 1000$ mm, measured at $z = 50$ mm compared to the clipped lognormal generated by the stochastic model 324
I.4 Normalized concentration probability distributions for the horizontal iso-kinetic jet in shear flow, $h = 50$ mm, $x = 1500$ mm, measured at $z = 50$ mm compared to the clipped lognormal generated by the stochastic model 325

I.5 Normalized concentration probability distributions for the ground level horizontal jet in shear flow, $h = 7$ mm, $x = 500$ mm, measured at $z =$ 6 mm compared to the clipped lognormal generated by the stochastic model 326
I.6 Normalized concentration probability distributions for the ground level horizontal jet in shear flow, $h = 7$ mm, $x = 1000$ mm, measured at $z = 6$ mm compared to the clipped lognormal generated by the stochastic model 327
I.7 Normalized concentration probability distributions for the ground level horizontal jet in shear flow, $h = 7$ mm, $x = 1500$ mm, measured at $z = 6$ mm compared to the clipped lognormal generated by the stochastic model 328
I.8 Normalized concentration probability distributions for the large ground level source in shear flow, $x = 500$ mm, measured at $z = 6$ mm compared to the clipped lognormal generated by the stochastic model . . 329
I.9 Normalized concentration probability distributions for the large ground level source in shear flow, $x = 1000$ mm, measured at $z = 6$ mm compared to the clipped lognormal generated by the stochastic model 330
I.10 Normalized concentration probability distributions for the large ground level source in shear flow, $x = 1500$ mm, measured at $z = 6$ mm compared to the clipped lognormal generated by the stochastic model 331
I.11 Burst duration probability distributions for the horizontal iso-kinetic jet in shear flow, $h = 50$ mm, $x = 1000$ mm, measured at $z = 50$ mm, $y/\sigma_y = 0$ compared to stochastic simulation results for bursts above $(c/C_p) = 0$ and $(c/C_p) = 2$ 332
I.12 Gap duration probability distributions for the horizontal iso-kinetic jet in shear flow, $h = 50$ mm, $x = 1000$ mm, measured at $z = 50$ mm, $y/\sigma_y = 0$ compared to stochastic simulation results for gaps below $(c/C_p) = 0$ and $(c/C_p) = 2$ 333
I.13 Burst duration probability distributions for the horizontal iso-kinetic jet in shear flow, $h = 50$ mm, $x = 1000$ mm, measured at $z = 50$ mm, $y/\sigma_y = 0$ compared to stochastic simulation results for bursts above $(c/C_p) = 5$ and $(c/C_p) = 10$ 334
I.14 Gap duration probability distributions for the horizontal iso-kinetic jet in shear flow, $h = 50$ mm, $x = 1000$ mm, measured at $z = 50$ mm, $y/\sigma_y = 0$ compared to stochastic simulation results for gaps below $(c/C_p) = 5$ and $(c/C_p) = 10$ 335
I.15 Burst duration probability distributions for the horizontal iso-kinetic jet in shear flow, $h = 50$ mm, $x = 1000$ mm, measured at $z = 50$ mm, $y/\sigma_y = 2$ compared to stochastic simulation results for bursts above $(c/C_p) = 0$ and $(c/C_p) = 2$ 336

I.16 Gap duration probability distributions for the horizontal iso-kinetic jet in shear flow, $h = 50$ mm, $x = 1000$ mm, measured at $z = 50$ mm, $y/\sigma_y = 2$ compared to stochastic simulation results for gaps below $(c/C_p) = 0$ and $(c/C_p) = 2$ 337
I.17 Burst duration probability distributions for the horizontal iso-kinetic jet in shear flow, $h = 50$ mm, $x = 1000$ mm, measured at $z = 50$ mm, $y/\sigma_y = 2$ compared to stochastic simulation results for bursts above $(c/C_p) = 5$ and $(c/C_p) = 10$ 338
I.18 Gap duration probability distributions for the horizontal iso-kinetic jet in shear flow, $h = 50$ mm, $x = 1000$ mm, measured at $z = 50$ mm, $y/\sigma_y = 2$ compared to stochastic simulation results for gaps below $(c/C_p) = 5$ and $(c/C_p) = 10$ 339
I.19 Burst duration probability distributions for the ground level horizontal jet in shear flow, $h = 7$ mm, $x = 1000$ mm, measured at $z = 6$ mm, $y/\sigma_y = 0$ compared to stochastic simulation results for bursts above $(c/C_p) = 0$ and $(c/C_p) = 0.5$ 340
I.20 Gap duration probability distributions for the ground level horizontal jet in shear flow, $h = 7$ mm, $x = 1000$ mm, measured at $z = 6$ mm, $y/\sigma_y = 0$ compared to stochastic simulation results for gaps below $(c/C_p) = 0$ and $(c/C_p) = 0.5$ 341
I.21 Burst duration probability distributions for the ground level horizontal jet in shear flow, $h = 7$ mm, $x = 1000$ mm, measured at $z = 6$ mm, $y/\sigma_y = 0$ compared to stochastic simulation results for bursts above $(c/C_p) = 1$ and $(c/C_p) = 2$ 342
I.22 Gap duration probability distributions for the ground level horizontal jet in shear flow, $h = 7$ mm, $x = 1000$ mm, measured at $z = 6$ mm, $y/\sigma_y = 0$ compared to stochastic simulation results for gaps below $(c/C_p) = 1$ and $(c/C_p) = 2$ 343
I.23 Burst duration probability distributions for the ground level horizontal jet in shear flow, $h = 7$ mm, $x = 1000$ mm, measured at $z = 6$ mm, $y/\sigma_y = 3$ compared to stochastic simulation results for bursts above $(c/C_p) = 0$ and $(c/C_p) = 0.5$ 344
I.24 Gap duration probability distributions for the ground level horizontal jet in shear flow, $h = 7$ mm, $x = 1000$ mm, measured at $z = 6$ mm, $y/\sigma_y = 3$ compared to stochastic simulation results for gaps below $(c/C_p) = 0$ and $(c/C_p) = 0.5$ 345
I.25 Burst duration probability distributions for the ground level horizontal jet in shear flow, $h = 7$ mm, $x = 1000$ mm, measured at $z = 6$ mm, $y/\sigma_y = 3$ compared to stochastic simulation results for bursts above $(c/C_p) = 1$ and $(c/C_p) = 2$ 346

I.26 Gap duration probability distributions for the ground level horizontal jet in shear flow, $h = 7$ mm, $x = 1000$ mm, measured at $z = 6$ mm, $y/\sigma_y = 3$ compared to stochastic simulation results for gaps below $(c/C_p) = 1$ and $(c/C_p) = 2$ 347
I.27 Burst duration probability distributions for the large ground level source in shear flow, $h = 7$ mm, $x = 1000$ mm, measured at $z = 6$ mm, $y/\sigma_y = 0$ compared to stochastic simulation results for bursts above $(c/C_p) = 0.5$ and $(c/C_p) = 2$ 348
I.28 Gap duration probability distributions for the large ground level source in shear flow, $h = 7$ mm, $x = 1000$ mm, measured at $z = 6$ mm, $y/\sigma_y = 0$ compared to stochastic simulation results for gaps below $(c/C_p) = 0.5$ and $(c/C_p) = 2$ 349
I.29 Burst duration probability distributions for the large ground level source in shear flow, $h = 7$ mm, $x = 1000$ mm, measured at $z = 6$ mm, $y/\sigma_y = 3$ compared to stochastic simulation results for bursts above $(c/C_p) = 0$ and $(c/C_p) = 1$ 350
I.30 Gap duration probability distributions for the large ground level source in shear flow, $h = 7$ mm, $x = 1000$ mm, measured at $z = 6$ mm, $y/\sigma_y = 3$ compared to stochastic simulation results for gaps below $(c/C_p) = 0$ and $(c/C_p) = 1$ 351

List of Tables

B.1 Streamwise, x-direction position normalization. 201
B.2 Vertical, z-direction position normalization. 201
B.3 Horizontal linescan data subset used for analysis. Horizontal jet source in grid turbulence, large ground level source in shear flow and small ground level vertical jet in shear flow. 203
B.4 Horizontal linescan data subset used for analysis. Horizontal jet source in shear flow at $h = 7$ mm, $h = 25$ mm and $h = 50$ mm. 204
B.5 Vertical linescan data set used for analysis. Small ground level vertical jet, horizontal jet source at $h = 7$ mm and $h = 50$ mm. 205
B.6 Horizontal linescan measurement for the horizontal iso-kinetic jet in grid turbulence. 206
B.7 Horizontal linescan measurement for the large ground level source in shear flow at the high flow rate. 206
B.8 Horizontal linescan measurement for the small ground level vertical jet source in shear flow at the high flow rate. 207
B.9 Horizontal linescan measurement for the small ground level vertical jet source in shear flow at the low flow rate. 207
B.10 Horizontal linescan measurement for the horizontal jet source $h =$ 7 mm in shear flow at the high flow rate. 208
B.11 Horizontal linescan measurement for the horizontal jet source $h =$ 7 mm in shear flow at the low flow rate. 208
B.12 Horizontal linescan measurement for the horizontal elevated source $h =$ 25 mm in shear flow at the high flow rate. 209
B.13 Horizontal linescan measurement for the horizontal iso-kinetic elevated source $h = 50$ mm in shear flow at the high flow rate. 209

List of Symbols

A	attenuation correction factor
A	fraction of available light collected by lens
$a(c,t)$	deterministic term in the stochastic differential equation for the time derivative of concentration, units of concentration/time
a_0,a_1,a_2	coefficients for fluorescence calibration curve
$b(c,t)$	random forcing function term in the stochastic differential equation for the time derivative of concentration, units of concentration/$\sqrt{\text{time}}$
B_0	empirical source size adjustment for low velocity releases
B_1,B_2,B_3,B_4	temporary variables for constants in shear model calculations.
B_{Lv}	Lagrangian-Eulerian cross-stream time scale adjustment constant
C	total mean concentration including the zero concentration periods (kg/m^3)
c	instantaneous concentration, $c = C + c'$ (kg/m^3)
c'	instantaneous concentration fluctuation from mean (kg/m^3)
c'_{rms}	standard deviation (root mean square) concentration fluctuation from mean (kg/m^3)
$\tilde{c}$	positive and negative concentration values produced after shifting c_+ concentration by c_{base}, $\tilde{c} = c_+ - c_{base}$ (kg/m^3)
c_+	pseudo-concentration coordinates used for stochastic simulation, it can have only positive values (kg/m^3)
c_{50+}	median (50th percentile) pseudo-concentration (kg/m^3)
c_{50}	median (50th percentile) concentration (kg/m^3)
c_{base}	concentration shift required to produce the intermittency from the pseudo-concentration c_+ simulated time series (kg/m^3)

C_p	conditional mean concentration (in-plume, not including zero concentration intermittent periods) (kg/m^3)
c'_p	standard deviation of the conditional (in-plume) concentration about the conditional mean C_p, excludes the zero concentration intermittent periods (kg/m^3)
D	molecular diffusivity (m^2/s)
d	displacement height in log-law boundary layer (m)
d_s	source diameter (m)
E_c	concentration power spectral density (kg^2 / m^6· s)
$E_p(c)$	conditional (in-plume) exceedance probability of observing a concentration greater than c
f	frequency, (Hz)
G	centre to centre mesh spacing on grid used to generate turbulence (m)
H	mixing layer depth (m)
h	source height (m)
Δh	plume rise height (m)
h_{ref}	reference height at which to evaluate source position non-dimensional shear S (m)
I	light intensity measured by camera (digital counts)
i	fluctuation intensity c'_{rms}/C including zero concentration intermittent periods
I_0	background intensity measured by camera (digital counts)
$i_{\text{no-shear}}$	concentration fluctuation intensity under no-shear conditions.
i_{shear}	concentration fluctuation intensity with shear effects included.
I_e	fluorescence excitation light intensity (W/m^2)
I_f	fluorescence emission light intensity (W/m^2)
$i_{h,\text{ref}}$	source centreline concentration fluctuation intensity at a reference averaging time t_{ref}
i_h	source centreline concentration fluctuation intensity.

I_{in}	input light intensity to experiment (W/m^2)
i_p	conditional (in-plume) fluctuation intensity $c'_{p,\text{rms}}/C_p$ excluding zero concentration intermittent periods
$i_{p,\infty}$	asymptotic value for i_p as $i \to \infty$.
K_{line}	laser line position correction factor
ℓ	Eulerian large eddy length scale (m)
L	length of fluorescence sampling volume (m)
L_*	Monin-Obukhov length (m)
L_c	concentration integral length scale (m)
$L_{c,\text{no-shear}}$	concentration integral length scale under no-shear conditions (m)
$L_{c,\text{shear}}$	concentration integral length scale with shear effects included (m).
$M_{\text{intensity}}$	pseudo-meander parameter, includes internal plume fluctuation in addition to meandering
M_{spread}	meander parameter based on plume spreads $\sigma^2_{y,m}/\sigma^2_{y,i}$
N	Gaussian random number with zero mean and unity variance
n	toxic load exponent in $L = c^n t$.
$p(\overline{y})$	probability density function of centroid position (1/m)
$p(\sigma_{y,ii})$	probability density function of instantaneous plume spread (1/m)
$p(c)$	probability density function (pdf) of concentration
$P(c)$	conditional (in-plume) cumulative probability, probability of observing a concentration less than c
r_1	empirical parameter in the travel time power law model for averaging time adjustment
R_p	radius of top-hat plume (m)
$R_{y_1 y_2}$	correlation coefficient between concentration at cross-stream position y_1 and y_2
R_s	source radius (m)
S	non-dimensional shear parameter.

Sc	Schmidt number, ratio of kinematic viscosity to molecular diffusivity (ν/D)
$S_{h_{\mathrm{ref}}}$	non-dimensional shear parameter evaluated at source reference height h_{ref}
$S_{z_{\mathrm{ref}}}$	non-dimensional shear parameter evaluated at receptor reference height z_{ref}
t	time (s)
t_{avg}	averaging time (s)
T_{c+}	Eulerian integral time scale of the pseudo-concentration fluctuations (s)
$T_{c,\mathrm{no\text{-}shear}}$	concentration fluctuation integral time scale under no-shear conditions (s)
$T_{c,\mathrm{shear}}$	concentration fluctuation integral time scale with shear effects included (s)
T_c	Eulerian integral time scale of concentration fluctuations (s)
t_{delay}	delay time necessary to produce corrected cross-stream correlation (s)
T_{Lv}	cross-stream Lagrangian time scale of velocity (s)
t_t	travel time (s)
T_u,T_v,T_w	along-wind (x-direction), cross-wind (y-direction), and vertical (z-direction) integral time scales of velocity fluctuation (s)
T_{vel}	overall velocity integral time scale (s)
U,V,W	along-wind (along -wind (x-direction), cross-wind (y-direction), and vertical (z-direction) mean velocities (m/s)
u,v,w	along-wind (x-direction), cross-wind (y-direction), and vertical (z-direction) instantaneous velocities (m/s)
u',v',w'	along -wind (x-direction), cross-wind (y-direction), and vertical (z-direction) instanteous velocity fluctuations (m/s)
u'_{rms},v'_{rms},w'_{rms}	along-wind (x-direction), cross-wind (y-direction), and vertical (z-direction) root-mean square velocity fluctuation (m/s)
u_*	boundary layer friction velocity (m/s)
$U_{\mathrm{no\text{-}shear}}$	streamwise no-shear mean flow velocity. In a boundary layer this is the velocity at the top of the mixing layer U_H (m/s)
U_a	advection velocity (m/s)

U_H	velocity at the top of the mixed layer (m/s)
$U_{z_{\mathrm{ref}}}$	streamwise flow velocity at the receptor reference position z_{ref} (m/s)
w_*	convective scaling velocity (m/s)
x,y,z	downwind, cross-wind, and vertical distance from source (m)
$\overline{y}$	cross-stream centroid position (m)
z	height above ground level
z_0	surface roughness length in log-law boundary layer (m)
z_{ref}	reference height at which to evaluate receptor position non-dimensional shear S (m)
z_a	height at which to measure plume advection velocity (m)

Greek Symbols

β_e	vertical entrainment coefficient
ε	fluorescence extinction coefficient (l/mg·mm)
ϵ	turbulent energy dissipation (m^2/s^3)
ϵ_u,ϵ_v,ϵ_w	along-wind (x-direction), cross-wind (y-direction), and vertical (z-direction) components of turbulent energy dissipation (m^2/s^3)
γ	intermittency factor, probability of non-zero concentration
γ_+	intermittency factor of the pseudo-concentration time series, always equal to 1.0
κ	von Karman constant = 0.4
λ_e	fluorescence excitation wavelength (nm)
λ_f	peak fluorescence emission wavelength (nm)
Λ_g	lateral integral length scale (m)
ν	kinematic viscosity (m^2/s)
Ψ	non-dimensional function of L_* and height z for calculating u_*
σ_0	effective source size (m)
σ_{l+}	log standard deviation of pseudo-concentration lognormal pdf

σ_x	along-wind (streamwise) plume spread (m)
σ_y	cross-wind plume spread (m)
$\sigma_{y,ii,50}$	median non-intermittent instantaneous plume parameter for clipped lognormal intermittent pdf $p(\sigma_{y,i})$ of instantaneous plume spread (m)
$\sigma_{y,ii,\mathrm{base}}$	shift parameter for clipped lognormal intermittent pdf $p(\sigma_{y,i})$ of instantaneous plume spread (m)
$\sigma_{y,\mathrm{ref}}$	cross-wind plume spread at a reference averaging time t_{ref} (m)
$\sigma_{y,ii}$	cross-wind instantaneous plume spread (m)
$\sigma_{y,i}$	cross-wind ensemble averaged instantaneous plume spread = $\langle\sigma_{y,ii}\rangle$ (m)
$\sigma_{y,m}$	cross-wind plume spread due to meandering (m)
σ_z	vertical plume spread (m)
Υ_s	density weighted velocity ratio
φ	fluorescence quantum yield
$d\zeta$	Gaussian random number in the stochastic differential equation, has a zero mean and variance dt with the units $\sqrt{\mathrm{time}}$

Chapter 1

Introduction and Overview

1.1 Background and Motivation

This thesis is a continuation of work in my MSc thesis, Hilderman (1997) "Stochastic Simulation of Concentration Fluctuations for an Effective Toxic Load Model". The objective is to find a practical physical and engineering model of scalar concentration fluctuations in a plume dispersing in a turbulent shear flow. More specifically, I am concerned with accidental releases of hazardous material into the atmosphere that cause acute toxic responses, odour annoyance, flammability dangers, or other short-term hazardous effects on-site in the occupational exposure setting or off-site where the general public can be exposed.

The key issue is that the random nature of turbulent dispersion causes the instantaneous concentration of a contaminant at any point in a dispersing plume to vary widely over a range from zero to 20 times the mean concentration or greater. Figure 1.1 shows two examples of typical time series of concentration. The hazardous effects of a release, such as acute toxicity, are non-linearly dependent on the instantaneous or short-term average concentrations. For example, a widely-used model for acute toxicity is toxic load

$$L = c^n t \tag{1.1}$$

where L is the toxic load, c is the exposure concentration, t is the exposure duration, and n is the toxic load exponent which ranges between 1.0 to 5.0 depending on the chemical, see, for example, ten Berge et al. (1986); CCPS (1989); AEGL (2000); Rogers (1990). Most chemicals have n values between 2.0 and 3.0. Adverse effects, such as fatality, occur when the exposure toxic load exceeds some threshold level. With this type of non-linearity, the peak concentration fluctuations are much more important than the mean concentration. A simple mean concentration estimate does not provide sufficient information to evaluate the hazard.

The overall goal of this PhD thesis research has been to develop the tools to enable complete atmospheric dispersion modelling from the source to the eventual outcome of the hazardous release. I was heavily involved in the Natural Sciences and

Engineering Research Council of Canada (NSERC) Strategic Project (1998-2002) "Outcome-Based Risk Scaling and Uncertainty Factors for Toxic Gas Releases" in cooperation with the Alberta Energy and Utilities Board, Imperial Oil Ltd., and Shell Canada Ltd. to develop and apply a prototype of a complete outcome-based model to develop guidelines for assessing toxic pipeline and gas well releases (see Wilson (2002) for the final report on the project).

As a result of this project, the basic prototype computer-based toxic fatality outcome model, EVENTSIM, was developed. My PhD research draws on lessons learned from EVENTSIM, and produced a significantly improved model EVENTSIM2 along with extensive experimental validation of the new concentration fluctuation model. At present, EVENTSIM2 is operational, but very user-hostile and unsuitable for application outside of the research environment. Some of my concentration fluctuation modelling contributions to EVENTSIM2 are discussed in this thesis, but the complete computer-based EVENTSIM2 model itself is not included.

1.2 Basic Plume Parameter Definitions

Throughout the thesis, a general understanding of common plume dispersion parameters will be assumed so a few basic definitions are given here to assist those who are unfamiliar with the terminology.

- **Fluctuation Intensity** i: The fluctuation intensity i, is

  $$i = \sqrt{\frac{\overline{c'^2}}{C^2}} \tag{1.2}$$

  where $\overline{c'^2}$ is the variance of the concentration and $\sqrt{\overline{c'^2}} = c'_{\mathrm{rms}}$ which is the standard deviation or root mean square fluctuation. (The convention used is $c = C + c'$ where c is the instantaneous concentration and c' is the fluctuation from the mean C).

- **Conditional (in-plume) Fluctuation Intensity** i_p: The conditional fluctuation intensity i_p is calculated by excluding the zero concentration intermittent periods.

  $$i_p = \sqrt{\frac{\overline{c_p'^2}}{C_p^2}} \tag{1.3}$$

  where $\overline{c_p'^2}$ is the conditional concentration variance and C_p is the conditional mean concentration.

- **Intermittency Factor** γ: The intermittency factor γ is the probability of the concentration being greater than zero (i.e. the fraction of time during which there is measurable non-zero concentration.) The total and conditional fluctuation intensities are related to the intermittency factor by the definition, see Wilson et al. (1985, Equation (8)),

$$\gamma = \frac{1 + i_p^2}{1 + i^2} \tag{1.4}$$

- **coordinate system** x, y, z: The x coordinate measures downstream (or downwind) distances, y is the cross-stream direction, and z is the vertical direction with zero at the ground and positive upward.

- **plume centroids** $\overline{y}$, $\overline{z}$: The cross-stream centroid $\overline{y}$ and vertical centroid $\overline{z}$ are the concentration weighted centres of the plume measured across a profile in the y or z direction respectively. For a continuous cross-stream distribution, for example

$$\overline{y} = \frac{\int_{-\infty}^{\infty} y c(y)\,\mathrm{d}y}{\int_{-\infty}^{\infty} c(y)\,\mathrm{d}y} \tag{1.5}$$

  where $c(y)$ is the function describing the cross-stream distribution of concentration in the plume

- **plume spreads** σ_y, σ_z: The plume spread is the standard deviation of the spatial distribution of concentration in the cross-stream direction, σ_y or the vertical direction σ_z. For a continuous cross-stream distribution:

$$\sigma_y^2 = \frac{\int_{-\infty}^{\infty} (y - \overline{y})^2 c(y)\,\mathrm{d}y}{\int_{-\infty}^{\infty} c(y)\,\mathrm{d}y} \tag{1.6}$$

- **instantaneous plume spread** $\sigma_{y,i}$, $\sigma_{z,i}$: Instantaneous plume spreads are simply the plume spread of the instantaneous ensemble average plume calculated by aligning each of the instantaneous plume centroids $\overline{y}_i$ in the ensemble and then determining the average concentration distribution across the plume.

- **plume meander**: Turbulent eddies of equal size or larger than the plume cause the entire plume to be pushed in one direction or another. This large scale motion is distinctly different than the smaller scale turbulent mixing that involves only small pieces of the plume cross-section at any one time. One way to measure the plume meander is to consider the spatial distribution of the instantaneous centroid position of the plume over an appropriate duration t_{avg}. The meandering component of plume spread $\sigma_{y,M}$ is

$$\sigma_{y,M}^2 = \int_0^{t_{\mathrm{avg}}} (\overline{y}_i - \overline{y}_{t_{\mathrm{avg}}})^2 p(\overline{y}_i)\,\mathrm{d}\overline{y}_i \tag{1.7}$$

  where $p(\overline{y}_i)$ is the probability distribution function describing the instantaneous centroid position. The meander parameter M is the ratio of meandering spread to instantaneous spread $\sigma_{y.M}/\sigma_{y,i}$

Other plume parameters will be defined where necessary in the body chapters and appendices.

1.3 General Approach to Concentration Fluctuation Problems

There are two fundamentally different ways to evaluate hazards caused by intermittent fluctuating concentration exposures:

1. **Consider only overall statistics of the release.** The most easily predicted statistic is the mean exposure concentration. From this mean concentration, fluctuation effects can be taken into account by approaches ranging from a simple safety factor or peak to mean ratio estimate to the prediction of the probability distribution and higher order moments of concentration. A toxic exposure human outcome model is then applied to this statistical description of the concentration fluctuations to determine the eventual outcome.

2. **Simulate physically realistic time series of concentration fluctuations.** An ensemble of these simulated events will automatically include the mean concentration, higher order moments and all important features, such as time correlations and peak concentrations. With these simulated time series, complex and realistic human exposure outcome effects models can be applied directly to each member of the ensemble of repeated events to assess health effects and the event-to-event variability.

The first approach is the simplest. There is a vast array of dispersion models available to predict long-term (i.e. several minute to several hour) average concentrations. There are considerably fewer methods to predict higher order moments of concentration or accurate peak to mean ratios. This use of overall summary statistics also requires hazardous effects models to be relatively simple because only a few statistical parameters can be included. Methods that follow this first approach to modelling concentration fluctuations end up trying to fit the outcome models to the few parameters that they have available.

The second approach, developed in this thesis, is to take basic statistical information about the concentration fluctuations in a dispersing plume and generate realistic stochastic time series of concentration fluctuations that have these overall statistics. With these computer-generated time series, complex hazardous effects models can be applied and the real exposure problem can be examined directly.

Instead of forcing the outcome model to fit a limited set of predetermined statistics, we let the time series of concentration and the hazardous effects model determine the important variables. By predicting the outcome from an ensemble of realistic random concentration time series we can determine whether the important variable is the mean, the variance, the 90th percentile concentration, the number of times a threshold is exceeded per event, the duration of exposure above a particular threshold coupled with the time spent below a threshold where there is recovery from the previous exposure, or any other possible combination of parameters. *In short, a-priori assumptions about how exposure concentration fluctuations are related to the* *outcome are minimized. The important parameters are determined from those which are actually observed to influence the outcome.*

Direct event simulation techniques also provide the powerful and useful ability to predict event-to-event variability. Although each event in a simulated ensemble is constrained to the same mean values, the time correlation parameter in the model ensures that the simulated time series reaches statistically stationary conditions in the same way as the full-scale atmosphere. In other words, large ensemble averages of events converge to the correct mean values, but the event-to-event variability is also realistically simulated. This approximates the natural variability observed in the full-scale atmosphere caused by turbulence time scales that are comparable to event durations. Natural variability produces surprisingly large differences in outcomes predicted under atmospheric conditions that are identical in their mean values, but have underlying turbulent variations. Direct event simulation allows planners and regulators to refine the meaning of "worst reasonable case" when setting up exclusion zones and planning for emergency response.

Others have also begun to recognize this need for concentration fluctuation time series in addition to overall statistics. Venkatram (2002) used a very simple time series model with randomly spaced zero and peak concentration periods to examine the effects of averaging time. Yamartino et al. (1996) and Yamartino and Strimaitis (2000) have developed the sophisticated Kinematic-Simulation-Particle (KSP) dispersion model for the German EPA. This computationally-intensive model attempts to predict second-by-second concentration fluctuations. However, the published material for KSP limits its validation to some peak concentrations and a few probability distributions compared with experimental data. A lack of detailed experimental data has limited their ability to test this part of the KSP model.

1.4 Outline of Work

Both my MSc thesis and this PhD thesis are written as a series of papers. Two chapters of my MSc have already been published in refereed journals and my PhD papers will be submitted in the near future. A brief description of the MSc based papers and the three PhD chapters is given in the following subsections. Note that each of the PhD Chapters 2 through 4 is intended to be a complete stand-alone paper, so there is some repetition of content, particularly the experimental descriptions.

The Appendices at the end of the thesis contain supplemental information and are designed primarily for future students in this area of study. This material is not critical to understanding the work in Chapters 2 through 4. However, the appendices do provide many additional plots comparing experimental measurements with theoretical lines for source types and downstream positions that were not covered directly in the body chapters. The reader is encouraged to refer to the appendices if there are any doubts about the conclusions drawn from the few selected graphs presented in the body chapters.

1.4.1 Hilderman and Wilson (1999) "Simulating Concentration Fluctuation Time Series with Intermittent Zero Periods and Level Dependent Derivatives"

This paper was based on Chapter 2 of my MSc thesis and presented a stochastic model for generating realistic intermittent concentration fluctuation time series as a first order Markov process. This model was an extension and improvement of the non-intermittent upcrossing rate model of Du et al. (1999). The stochastically generated time series compared very favorably to water channel dispersion data collected by Wilson et al. (1991) using salinity probes. This was also the first publication of the clipped lognormal probability distribution for describing intermittent concentration fluctuations. Some details of the stochastic model have also been presented in the conference paper Hilderman et al. (1997b) with a small extension to these results presented in the conference paper Wilson and Hilderman (1998).

Although the Hilderman and Wilson (1999) paper proved that the concept of stochastic time series simulation was viable, it did not provide any method of determining the correct input statistics to drive the stochastic model (i.e. the intermittency factor, fluctuation intensity, and fluctuation integral time scale). The data set tested did not include measurements in the highly sheared flow near a rough surface that would be typical of a full-scale atmospheric exposure.

1.4.2 Hilderman et al. (1999) "A Model for Effective Toxic Load from Fluctuating Gas Concentrations"

Based on Chapter 3 of my MSc thesis, this paper developed a modified toxic load model with an uptake time constant, a recovery time constant, and a saturation level. A case study was completed for hydrogen sulphide releases using the best estimated values for uptake and recovery time constants that could be derived from the toxicological literature. Exposure concentration time series were simulated using the methods of Hilderman and Wilson (1999). The case study results showed that the effective toxic load model provided realistic estimates of population fatalities when compared with the standard occupational exposure limits. Fatality estimates using the simple mean concentration toxic load and ignoring fluctuations did not produce realistic results.

Some of this toxicity work was also presented in a conference paper Hilderman et al. (1997a). An examination of uncertainty factors and proposed hydrogen sulphide exposure limits was presented in a poster by Hilderman et al. (2000).

1.4.3 Chapter 2 "Plume Meandering and Averaging Time Effects from High Resolution One-dimensional Concentration Measurements"

This paper documents the development of the linescan laser-induced fluorescence (LIF) technique for high temporal and spatial resolution measurements of concentration fluctuations in a water channel. This non-intrusive optical technique allowed measurement of 1024 simultaneous data points along a laser beam used to illuminate fluorescent dye dispersing in a water channel.

The water channel was configured to produce both a rough surface boundary layer shear flow and a shear-free grid generated turbulent flow. Near surface measurements in the shear flow were of the most interest because nearly all human exposures occur near the ground in the atmospheric boundary layer. The grid turbulence data provides an interesting no-shear reference to test the robustness of concentration fluctuation models in the limit of zero vertical velocity shear.

With the large number of simultaneous data points and high spatial and temporal resolution of the data, the centroid of the plume is tracked and time averaged to allow detailed examination of averaging time relationships. In addition, the probability distribution of instantaneous centroid position is examined along with the probability distribution of instantaneous plume spread. There are currently no other experimental methods that can provide these detailed near-instantaneous concentration profile measurements in a dispersing plume.

The LIF data set is used to verify the applicability of the pseudo-meandering plume model for concentration fluctuations developed by Wilson (1995) and to test a modified travel time power law model (TTPL) for averaging time effects on plume spread. The TTPL proves to be a better model for averaging time effects than the widely used 0.2 power law adjustment (see, for example Hanna et al. (1996))

1.4.4 Chapter 3 "Measurement and Prediction of Wind Shear Distortion of Concentration Fluctuation Statistics"

Vertical linescan LIF profiles through dispersing plumes are used to examine the effect of wind shear distortion of concentration fluctuation statistics near the ground. This is a critical issue as virtually all important full-scale atmospheric exposures occur in near-surface sheared flow. These statistical parameters are necessary as inputs to the stochastic model described in Hilderman and Wilson (1999) and in Chapter 4.

The most challenging aspect of the model development was to find a single physically realistic model that included the effects of receptor position and a changing release height. The experimental data showed that there were significant differences between a release high above the ground, initially dispersing in no-shear flow and descending to the ground; and a ground level release that experiences a wide range of wind shear over the plume height.

An operational engineering model for shear distortion of fluctuation intensities, intermittency factors, and time scales is developed. The important variable in the model is the wind shear normalized by the vertical component of turbulent velocity fluctuation, travel time, and flow velocity at both the source and receptor positions. The model fits well with the experimental data, and in the limit of no-shear describes the grid turbulence case.

Recommendations are made to allow direct application of the proposed shear distortion model to real atmospheric dispersion problems where the available flow field information may be limited. A case study of a plume in a neutrally stable full-scale atmosphere is used to verify the robustness and realism of the model over a wide range of conditions. The case study shows large shear-induced variations in fluctuation intensity and intermittency in vertical profiles through any plume.

1.4.5 Chapter 4 "Stochastic Modelling of Cross-Stream Correlated Concentration Fluctuations in a Dispersing Plume for Cross-Stream Hazard Evaluation"

This paper is an update and extension to the original stochastic model paper Hilderman and Wilson (1999). With the new LIF shear flow data set, the clipped lognormal probability distribution, first proposed by Hilderman and Wilson (1999), was demonstrated to be an excellent fit to intermittent concentration fluctuations even in the highly sheared flow near the ground.

With the basic specifications of the stochastic model confirmed, higher order statistics of burst and gap length were investigated as a measure of the model performance. A burst is a series of consecutive concentration samples that exceed a threshold level and a gap is a series of consecutive concentration samples below a threshold level. Burst and gap periods can be important for hazardous release effects that depend on exceeding a threshold for a minimum amount of time, or for considering recovery during the low concentration time periods. These types of statistics are difficult to predict analytically, but can be easily extracted from a stochastic simulation time series. The stochastic model provides a close match to the distribution of gaps and bursts observed in the water channel data.

The scope of the stochastic model is expanded by considering the cross-stream correlation between points in the plume. The pseudo-random number generator driving the stochastic model allows highly correlated fluctuation time series to be simulated and then de-correlated with a simple time delay. This de-correlation method is confirmed by comparison with the water channel data.

References

AEGL (2000), PUBLIC DRAFT: Acute Exposure Guideline Levels (AEGLs) for Hydrogen Sulfide, Public Draft report from the National Advisory Committee to develop Acute Exposure Guideline Levels (AEGLs).

CCPS (1989), *Guidelines for Chemical Process Quantitative Risk Analysis*, Center for Chemical Process Safety of the American Institute of Chemical Engineers.

Du, S., Wilson, D. J., and Yee, E. (1999), A Stochastic Time Series Model for Threshold Crossing Statistics of Concentration Fluctuations in Non-Intermittent Plumes, *Boundary-Layer Meteorology*, 92:229–241.

Hanna, S. R., Drivas, P. J., and Chang, J. J. (1996), *Guidelines for Use of Vapor Cloud Dispersion Models*, Center for Chemical Process Safety of the American Institute of Chemical Engineers, New York, NY, second edition.

Hilderman, T. L. (1997), Stochastic Simulation of Concentration Fluctuations for an Effective Toxic Load Model, Master's thesis, University of Alberta.

Hilderman, T. L., Hrudey, S. E., and Wilson, D. J. (1999), A Model for Effective Toxic Load from Fluctuating Gas Concentrations, *Journal of Hazardous Materials A*, 64:115–134.

Hilderman, T. L. and Wilson, D. J. (1999), Simulating Concentration Fluctuation Time Series with Intermittent Zero Periods and Level Dependent Derivatives, *Boundary-Layer Meteorology*, 91:451–482.

Hilderman, T. L., Wilson, D. J., and Hrudey, S. E. (1997a), The Effect of Uptake and Recovery Rates on the Toxic Load Predicted from Toxic Gas Exposure Concentration Fluctuations, In *International Society of Exposure Analysis (ISEA) Annual Meeting, Research Triangle Park, NC - November 2-5, 1997.*

Hilderman, T. L., Wilson, D. J., and Hrudey, S. E. (1997b), Modeling Zero Concentration Intermittent Periods in Toxic Gas Risk Assessment, In *Presented at the Society for Risk Analysis Annual Meeting, Washington, D.C. - December 8 - 10, 1997.*

Hilderman, T. L., Wilson, D. J., and Hrudey, S. E. (2000), Application of Inter- and Intra-Species Uncertainty Factors to Rat Fatality Data Used in the Hydrogen Sulfide AEGL-3 Levels, In *API Hydrogen Sulfide Health Research and Risk Assessment Symposium, October 31 - November 2, 2000, Chapel Hill, NC*, poster presentation with 14 page handout.

Rogers, R. E. (1990), Toxicological Justification of the Triple Shifted Rijnmond Equation, Technical report, Alberta Energy Resources Conservation Board, Appendix B, Volume 7 of the Risk Approach: An Approach for Estimating Risk to Public Safety from Uncontrolled Sour Gas Releases.

ten Berge, W. F., Zwart, A., and Appelman, L. M. (1986), Concentration-time mortality response relationship of irritant and systemically acting vapours and gases, *Journal of Hazardous Materials*, 13:301–309.

Venkatram, A. (2002), Accounting for averaging time in air pollution modeling, *Atmospheric Environment*, 36:2165–2170.

Wilson, D. J. (1995), *Concentration Fluctuations and Averaging Time in Vapor Clouds*, Center for Chemical Process Safety of the American Institute of Chemical Engineers, New York, NY.

Wilson, D. J. (2002), Outcome-Based Risk Scaling and Uncertainty Factors for Toxic Gas Releases, Technical report, University of Alberta, Final Report for NSERC Strategic Project 215980-1998.

Wilson, D. J. and Hilderman, T. L. (1998), Stochastic Reconstruction of Intermittent Zero Concentration Periods in Plumes for Accidental Toxic and Flammable Releases, In *Proceedings, 23rd NATO/CCMS International Technical Meeting on Air Pollution and its Application, September 28 - October 2, 1998 Varna, Bulgaria*.

Wilson, D. J., Robins, A. G., and Fackrell, J. E. (1985), Intermittency and Conditionally-Averaged Concentration Fluctuation Statistics in Plumes, *Atmospheric Environment*, 19:1053–1064.

Wilson, D. J., Zelt, B. W., and Pittman, W. E. (1991), Statistics of Turbulent Fluctuation of Scalars in a Water Channel, Technical report, Department of Mechanical Engineering, University of Alberta, Edmonton, Alberta.

Yamartino, R. and Strimaitis, D. (2000), Results of and Extensive Evaluation of the Kinematic Simulatioln Particle Model Using Tracer and Wind Tunnel Experiments, In *11th joint AMS/AWMA Conference on the Applications of Air Pollution Meteorology, Long Beach, CA, January 9-14,2000*.

Yamartino, R. J., Strimaitis, D. G., Scire, J. S., Insley, E. M., and Spitzak, M. J. (1996), Final Report on the Phase I Development of the Kinematic Simulation Particle (KSP) Atmospheric Dispersion Model, Technical report, Institut fuer Meteorologie, Freie Universitaet Berlin, Carl-Heinrich-Becker Weg 6-10, D-12165 Berlin, Germany and Umweltbundesamt, Document No. 1274-3.

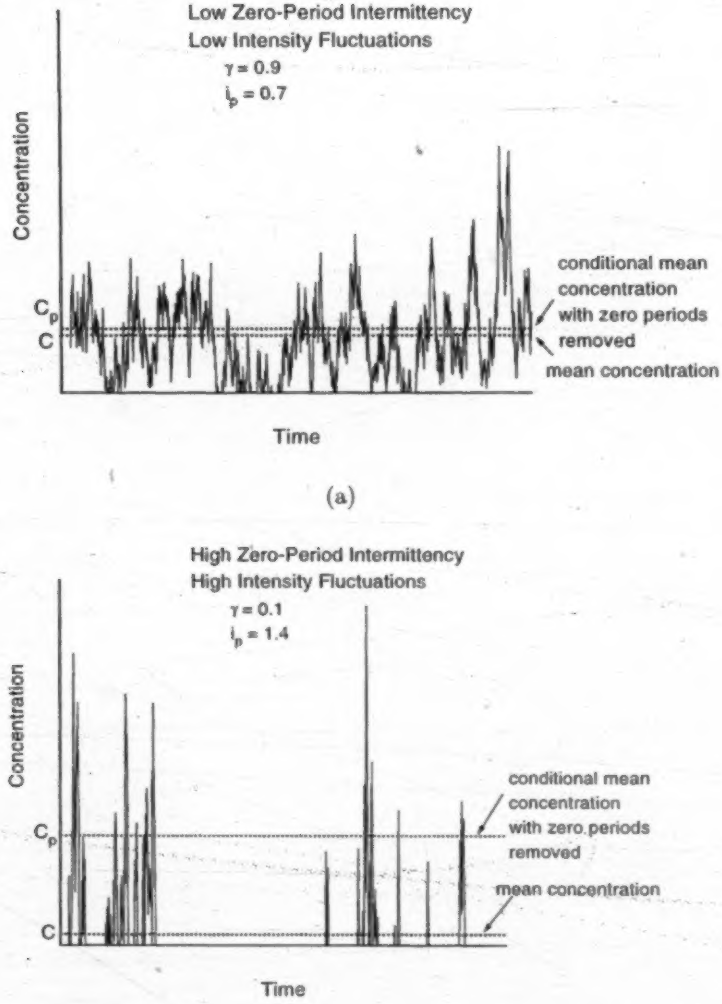

(a)

(b)

Figure 1.1: Typical intermittent concentration fluctuation time series that could be observed at a receptor positioned at a fixed point in the dispersing plume. (a) low intermittency ($\gamma = 0.9$), low fluctuation intensity ($i_p = 0.7$) (b) high intermittency ($\gamma = 0.1$), high fluctuation intensity ($i_p = 1.4$). The total mean concentration C and conditional (in-plume) mean concentration C_p which excludes the zeroes are shown as horizontal lines. The peak concentrations can be $20C$ or more.

Chapter 2

Plume Meandering and Averaging Time Effects from High Resolution One-dimensional Concentration Measurements

Abstract

Linescan laser induced fluorescence (LIF) concentration measurement techniques were developed and then used to acquire high spatial resolution, high frequency measurements of fluorescein dye plumes dispersing in a water channel. A novel calibration technique was developed to produce individual calibration curves for each pixel in the linescan camera CCD array of 1024 pixels. Post-processing of the collected data removed time dependent background dye levels and corrected for attenuation across the laser beam to produce accurate measurements over long sample times in both a rough surface boundary layer shear flow and shear free grid-generated turbulent flow.

The data collected was used to verify the applicability and modify a pseudo-meandering plume concentration fluctuation model originally developed by Wilson (1995). The large-scale time averaged meandering motions of the plume were directly measured by tracking the plume centroid in the cross-stream direction. The time averaged meander and plume spread development with averaging time compared favorably with a modified travel time based power law model for averaging time adjustment. The widely-used 0.2 power law averaging time adjustment was demonstrated to be a poor approximation of the time averaging effects observed in a dispersing plume.

2.1 Introduction

Development of the linescan laser-induced fluorescence (LIF) experimental technique was motivated by the desire to measure high frequency scalar concentration fluctuations simultaneously across a range of measurement positions in a water channel. Concentration fluctuations are important for a wide range of practical dispersion problems ranging from atmospheric releases of toxic materials, where effects are typically non-linearly proportional to instantaneous exposure concentration (e.g. Hilderman et al. (1999)) to chemical reactions between two mixing materials where the reaction rates and products formed may be dependent on concentration levels.

The information in this study can be considered from two points of view. Firstly, it is a water channel study of the effects of averaging time on the dispersion of a high Schmidt number (low molecular diffusivity) plume in a shear flow. Secondly, it is a scale model study of the atmospheric dispersion of a small momentum jet source in neutral stability. This work was done with the ultimate goal of developing a complete atmospheric dispersion model which includes the effects of concentration fluctuations.

The basic experimental configuration is illustrated in Figure 2.1. A linescan camera is aligned with a laser beam which illuminates a line of fluorescent dye within a dispersing plume in the water channel. Optical techniques, in general, are one of the few cost-effective and non-intrusive ways to make simultaneous measurements at many different points. Other methods of measuring concentration fluctuations such as conductivity probes, thermocouples, or flame ionization detectors (in gas flows) can provide high sampling rates under the right conditions, but all of these methods are intrusive and are usually limited to a few simultaneous measurement points. LIDAR measurement (for example, Jørgensen and Mikkelsen (1993)), is a large scale optical concentration measurement technique that produces similar results to the laboratory scale LIF measurements, but measures time delayed back-scatter from dispersing particles instead of fluorescence. The advantages of a laboratory scale experiment such as LIF are that the flow conditions can be easily controlled by the experimenter and long samples of statistically stationary turbulent dispersion are possible.

LIF has been widely used for both qualitative and quantitative fluid mechanics measurements for more than 25 years. Some examples that are similar to the present study are Distellhoff and Marquis (1998) who made linescan measurements in a stirred tanks and Koochesfahani and Dimotakis (1985, 1986), who made linescan measurements across a plane shear layer. Other recent examples of LIF development are Crimaldi (1997); Crimaldi and Koseff (2001); Crimaldi et al. (2002) who present low frame rate (2 to 8 Hz) area scan measurements and single point high frequency (1000Hz) measurements in plumes dispersing in a water channel. In the present study, LIF measurements were made at 1024 points across the entire cross-stream extent of the water channel at rates of 500 samples per second for durations of 500 seconds. The measurement techniques presented in this study are a significant improvement over previous linescan LIF and cover a range of spatial and temporal resolution between the extremes of Crimaldi's LIF methods.

For comparison, in the neutral atmosphere with a 400 m mixing height H, the water channel is approximately a 1:1000 scale model. With a typical full-scale wind speed of 3 m/s at 10 m above the ground compared to the water channel velocity of 100 mm/s at 10 mm above the ground the time scale of the water channel is 1:30

of the full scale. The total sample time of 500 seconds at 500 samples/second is approximately equivalent to 15,000 seconds $\simeq$ 4 hours at a rate of 16 samples per second in full scale.

2.1.1 Scope of Experimental Measurements

Numerous samples in both a shear flow boundary layer and a shear-free grid turbulence flow with a variety of source types were tested. With the LIF data, a number of concentration fluctuation statistics and averaging time effects will be examined in detail and compared to a pseudo-meandering plume model for concentration fluctuations developed by Wilson (1995) from the meandering plume moments derived by Sawford and Stapountzis (1986). Modifications to this model will be recommended based on the new data. The following statistics and dispersion parameters will be examined.

- Averaging time effects on plume meander M and concentration fluctuation intensity i
- Cross-stream profiles of concentration fluctuation intensity i.
- Cross-stream probability distributions of instantaneous plume centroid position $\overline{y}$ and instantaneous plume spread $\sigma_{y,i}$
- The effect of averaging time on plume meander M and plume spread σ_y as compared to a travel time power law model of averaging time effects and the typical 0.2 power law adjustment for averaging time.

2.2 Water Channel Scale-Modelling Facility

The recirculating water channel in the Mechanical Engineering Department at the University of Alberta has a test section 5240mm long by 680mm wide by 470mm deep with glass sides and bottom for complete optical access to the entire test section. Figure 2.2 shows the configuration of the channel. The total volume is approximately 5000 litres, allowing long averaging times without excessive accumulation of background tracer concentration. A pair of centrifugal pumps drives the flow into the bottom half of the inlet plenum where it is turned through 180° by two sets of turning vanes and passed through a flow straightener and a contraction down to the width of the test section. For these experiments, the channel was run with a water depth of 400mm using throttling valves on the pump inlet lines and a weir gate in the outlet plenum to set the average flow rate and depth. Three different tracer sources, shown in Figure 2.3, will be discussed in more detail in Section 2.2.3

2.2.1 Turbulent Boundary Layer Shear Flow

For most experiments, the channel was configured as in Figure 2.2 to produce a well-developed rough surface turbulent boundary layer flow similar to what would be observed in the atmosphere under neutrally stable conditions. The rough bottom surface was made of nominal 1/2" x 18 gauge raised surface stainless steel expanded metal fastened to 6mm thick acrylic panels. The expanded metal had diamond shaped openings approximately 11 mm wide in the flow direction and 24 mm wide in the cross-stream direction. The raised surface extended about 4 mm above the acrylic panels. Boundary-layer development was accelerated by additional flow conditioning elements placed at the inlet of the channel test section. An array of 4 horizontal and 4 vertical 19 mm (nominal 3/4") stainless steel square bars and a 70 mm high trip fence with 40 mm high by 60 mm wide triangular "teeth" were used to redistribute the flow and generate some mid to large scale turbulence.

A two-component TSI Inc. Laser Doppler Velocimeter (LDV) system was used to make measurements of the velocity profiles in the channel and fine tune the positions of the square bar and trip fence conditioning elements. The cross-stream uniformity of the mean streamwise velocity U was ±5% across the channel.

Figure 2.4(a) shows a typical vertical profile of the mean streamwise velocity U measured at 3000 mm downstream from the inlet of the channel ($x/H = 7.5$). The log-law fit to the profile is

$$U = \frac{u_*}{\kappa} \ln\left(\frac{z-d}{z_0}\right) \tag{2.1}$$

where $u_* = 14$ mm/s is the friction velocity, $\kappa = 0.4$ is the Von Karman constant, $d = 1.7$ mm is the zero-plane displacement height, and $z_0 = 0.52$ mm is the roughness height. The zero-plane displacement d is a virtual position necessary to fit the log-law and is a function of the real roughness height and density of the roughness elements.

The log-law mixing layer depth $H = 400$ mm was the entire depth of the channel and the velocity at H was $U_H = 232$ mm/s which was used as a normalizing factor in the plots. Figure 2.4(b) shows vertical profiles of the rms fluctuating velocity components, u'_{rms}, v'_{rms}, and w'_{rms} normalized by U_H. Figure 2.4(c) shows vertical profiles of the Eulerian integral timescale of velocity fluctuations for all three coordinate directions, T_u, T_v, and T_w normalized by $H/U_H = 1.7$ seconds.

Figure 2.4(d)shows the vertical profile of the $\overline{uw}$ Reynolds stress. This linear profile indicates fully-developed channel flow rather than the constant stress layer near the surface that might be expected in a zero-pressure gradient boundary layer shear flow in the atmosphere. However, this should still be a reasonable approximation of a rough-surface neutrally stable atmospheric boundary-layer.

Appendix A has all of the graphs shown here in measured units of mm without the normalization by U_H and H, as well as additional detailed profiles of other measured velocity statistics for the shear flow.

2.2.2 Grid Turbulence

For comparison purposes, plume dispersion measurements were also made in a shear free grid-generated turbulent flow. The grid was made of flat stainless steel bars 19.2 mm wide by 5 mm thick with a centre to centre spacing of $G = 76.2$ mm and a total open area of 56%. The bars were standard stainless steel rolled stock with slightly rounded edges rather than sharply machined edges. The grid was positioned at $x/G = 4.3$ from the channel inlet and the flow was run 405 mm deep with a $U = 200$ mm/s average flow velocity.

The cross stream variation of the mean streamwise velocity U was at most ±5% if the wall boundary layers were neglected. The vertical fluctuations w'_{rms} were approximately 95% of the streamwise fluctuations u'_{rms} indicating some slight anisotropy in the flow. As expected for grid turbulence, the turbulence intensity decays with downstream distance as shown in Figure 2.5(a). The power law curve plotted on the figure is the best fit to the power law decay of grid turbulence using Saffman's invariant (Hinze, 1975, pp. 217 and 265-267).

As documented by Hinze, Saffman's invariant arises from the hypothesis that the mechanism producing the turbulence can only produce a finite total linear momentum even if the flow field increases in size. This limit on momentum in grid turbulence occurs when the turbulent fluctuation directions become uncorrelated for large separations and the x-momentum will go to zero. The volume with correlated turbulent motions is proportional to the lateral integral length scale Λ_g^3 and the momentum is proportional to $\overline{u^2}$ so the product $\overline{u^2}\Lambda_g^3$ = constant, see Hinze (1975, Equation (3-183)). From this and the assumption that turbulence intensity u'_{rms}/U decays according to a simple power law with time leads to the power law exponent of -0.6 for u'_{rms}/U and the corresponding power of 0.4 for integral scales. Hinze (1975, Equations (3-184) and (3-186)) gives these relationships in terms of travel time t_t, but for the purposes of this study they are reformulated as functions of normalized downstream distance $x/G = Ut_t/G$. The decay of grid turbulence intensity is

$$\frac{u'_{\text{rms}}}{U} = 0.3\left(\frac{x}{G} - 2.3\right)^{-0.6} \tag{2.2}$$

with the constants 0.3 and 2.3 fit to the present data. The dye source was placed at $x/G = 23.6$ where the turbulence intensity was about 5% and decayed to about 3% at the farthest downstream measurement position $x/G = 43.3$.

The normalized Eulerian time scale of velocity fluctuations for the streamwise component is about $T_uU/G = 0.4$ and for the vertical component $T_wU/G = 0.2$ as shown in Figure 2.5(b). The two curves on this plot are the theoretical streamwise time scale calculated using the grid power law decay as fit in Equation (2.2).

$$\frac{T_uU}{G} = 0.05\left(\frac{x}{G} - 2.3\right)^{0.4} \tag{2.3}$$

The curve for the vertical time scale T_w is one half of that given in Equation (2.3). The fit to theory with the exponent of 0.4 set by Saffman's invariant was not as good as for the turbulence intensity decay curve, but the general shape is correct and the ratio between the streamwise and vertical scales is almost exactly the expected factor of 2.0 that would occur in homogeneous isotropic turbulence. Some errors might be expected because the integral scale is difficult to measure as is apparent in the larger scatter as compared to the turbulence intensity data.

2.2.3 Source Configurations

Three different dye sources were used. The basic configurations are illustrated in Figure 2.3 and the detailed specifications are discussed below.

1. **Horizontal Jet** 4.3 mm OD and 3.25 mm ID stainless steel tube, 38 mm long suspended from above the channel by a streamlined support. In normalized units the source diameter $d_s \approx 6z_0 \approx 0.008H$ in the shear flow and $d_s \approx 0.04G$ in grid turbulence. In grid turbulence, the source was placed in the centre of the channel at $z = 200$ mm $= 2.6G$ above the channel bottom, and in the shear flow the source was placed at height h between 7 and 50 mm ($(h-d)/H = 0.013$ to 0.12 or $(h-d)/z_0 = 10$ to 93) above the surface depending on the experiment. The source flow rate was iso-kinetic in grid turbulence and for $(h-d)/H = 0.12$ above the ground in the shear flow. With the small diameter and low flow rates the jets from the source were laminar ($\mathrm{Re} = U_{\mathrm{source}} d_s/\nu \approx 600$).

2. **Vertical Jet at Ground Level** 3.25 mm ID flush with ground ($d_s \approx 6z_0 \approx 0.008H$). To prevent dye from becoming trapped in the roughness elements the expanded metal was removed from an area 25 mm on either side and 100 mm downstream of the source. The source flow rate was the same as for the horizontal jets and produced a laminar jet with a mean velocity equal to the cross flow velocity at $(z-d)/H = 0.12$, $\mathrm{Re} \approx 600$.

3. **Large Ground Level Source** 11 mm ID flush with ground. ($d_s \approx 21z_0 \approx 0.028H$). As with the vertical ground level jet the expanded metal was trimmed away 25 mm on either side and 100 mm downstream of the source. The source flow rate was the same as the other two source ($\mathrm{Re} \approx 175$ based on source diameter).

The sources were placed 2750 mm ($x/H = 6.9$) downstream of the channel inlet in the shear flow and 1800 mm ($x/G = 23.6$) downstream of the grid in the no-shear experiments.

For the elevated sources and grid turbulence measurements the average source flow rates were iso-kinetic with the surrounding flow. The vertical ground level sources had very low momentum with insignificant plume rise. At 1:1000 scale the full-scale equivalent source sizes were 3 to 11 m at the source and effectively 2 to 3 times larger than this after entraining sufficient fluid to take on the turbulent structure of the flow field. Measurements were taken at $x/d_s > 150$ for the jet sources and $x/d_s > 50$ for the large ground level source. At this downwind point the dilution was at least 100:1 which allowed the tracer-marked fluid to take on the turbulent structure of the cross flow. There was little measurable effect of source size or release rate. Appendix B lists all of the parameters of the data sets that were collected and used in this study.

2.3 LIF Linescan Measurement Technique

2.3.1 Linescan Camera

All LIF data in this study were measured with a Dalsa model CLC6-2048T monochrome CCD linescan camera. The camera has a single row of 2048 pixels with a wide dynamic range and an onboard 12-bit (4096 gray level) analog to digital converter. A wide angle 28mm Nikon f2.8 camera lens was used for all experiments to give the necessary field of view.

The output was collected with a National Instruments PCI-1424 digital image acquisition card and stored on a computer using a custom National Instruments Labview data acquisition program. The camera was capable of data output rates of up to 10 MHz or 4800 lines/second, but in the current experiments 500 lines/second data rates were sufficient to capture all of the concentration fluctuations of interest.

The gain and offset for each pixel in the camera were not adjustable. The typical offset was between 400 and 500 digital counts and varied from pixel to pixel. The standard deviation of the background noise was between 1.25 and 1.7 digital counts for each pixel. To improve the light sensitivity of the CCD sensor, the output of pairs of adjacent pixels could be binned together to produce an effective image of 1024 pixels with double the light collecting area. Binning was used in all experiments.

This model of Dalsa linescan camera has an unique feature that makes it particularly suitable for these types of LIF measurements. The light sensitive elements on the CCD sensor are rectangular with an aspect ratio of 38:1 (each element is 13 μm wide by 500 μm long). As shown in Figure 2.6, this makes the alignment of the camera with the laser beam relatively easy. CCD pixels are photon collectors and one part of the CCD pixel has the same sensitivity as any other part of the same pixel. The laser line just has to be somewhere in the field of view of the pixel to produce the correct reading. In a typical experiment with the camera about 700 mm away from the laser line and with binning enabled, each of the 1024 effective pixels sees an area approximately 0.5 mm by 10 mm. It is relatively easy to align the camera so that the laser beam is within that 10 mm wide area at all positions across the channel. The effective spatial resolution of the measurement was then defined by the field of view of the pixel in one direction (approximately 0.5 mm per pixel) and the width of the laser beam in the other direction (approximately 1 mm).

2.3.2 Fluorescein Dye Properties

There are a wide variety of fluorescent dyes suitable for LIF, including some very specialized and very expensive dyes with carefully controlled absorption and emission properties; see Guilbault (1973) and Molecular Probes Inc. (2002) for some of the possibilities. Studies have been done to determine the "best" dye for a given experimental situation, see Arcoumanis et al. (1990); but like most experimental techniques, accurate results can be achieved only by careful calibration and consideration of all of the relevant dye properties regardless of which dye is used.

In this study, fluorescent dye tracer solutions were made by dissolving disodium fluorescein salt ($C_{20}H_{10}Na_2O_5$) in water. Disodium fluorescein is readily available, inexpensive and non-toxic. The molecular diffusivity of fluorescein is 5.2×10^{-6} cm^2/s. The Schmidt number, $\mathrm{Sc} = \nu/D$, for fluorescein in water is approximately $\mathrm{Sc} = 1930$ when the kinematic viscosity of water is 1×10^{-6} m^2/s at 20 °C. This is the major scaling mismatch for modelling gas diffusion in the atmosphere where $Sc \simeq 1$. For modelling aerosols or particles dispersing in the atmosphere $Sc \rightarrow \infty$ and the mismatch is less important.

Argon-ion lasers, used to excite the dye, produce peak power at 488 nm and 514.5 nm wavelengths which are compatible with the peak of the excitation spectrum for fluorescein at $\lambda_e \approx 490$ nm and the fluorescence peak at $\lambda_f \approx 515$ nm, see Walker (1987) and Guilbault (1973, chap. 5). A number 16 Kodak Wratten gel-type filter was used on the linescan camera to remove most of the excitation wavelengths produced by the laser, but pass the longer fluorescence wavelengths produced by the excited dye.

As discussed by Walker (1987) there is approximately a 5 ns delay between the absorption and emission of light energy by the fluorescein molecules. This delay time is long enough for the molecules to spin randomly due to Brownian motion so that the direction of the emitted fluorescence light is independent of the direction of the excitation light. Therefore, illumination can be from any convenient direction and measurements can be made from any other direction. Typically, the camera was positioned perpendicular to the laser beam as shown in Figure 2.1.

Attenuation

For linescan measurements, the dye was illuminated with a single laser beam from one side of the channel. As molecules of dye in the beam path absorbed light energy from the incoming beam there was less energy available to cause fluorescence in the remaining molecules. Following Walker (1987), for a beam path $\mathrm{d}z$, the absorption is

$$\mathrm{d}I_e(z) = -\varepsilon C(z) I_e(z) \mathrm{d}z \tag{2.4}$$

where I_e is the intensity of the excitation beam at a point z along the beam path, C is the concentration at a point z, and ε is the extinction coefficient of the dye.

Only attenuation along the excitation path needed to be considered because the effective extinction coefficient at the fluorescence wavelength λ_f is much smaller than at the excitation wavelength λ_e. This property was confirmed by simple measurements of fluorescence intensity through different depths of dye solution. There was no measurable difference in the intensity measured by the camera for transmission through 0 to 300 mm of dye solution. The fluorescence intensity at the detector is:

$$I_f(z) = I_e(z) A \varphi \varepsilon L C(z) \tag{2.5}$$

where φ is the quantum yield of the fluorescence, L is the length of the sampling volume along the incident beam and A is the fraction of the available light collected.

Integrating Equation (2.4), substituting for I_e in Equation (2.5), and assuming a straight beam path produces an equation for beam intensity at any point b along the beam with arbitrarily varying concentration and an input light intensity I_{in}.

$$I_f(b) = I_{\text{in}} A \varphi \varepsilon L C(b) \exp(-\varepsilon \int_0^b C \, \mathrm{d}z) \tag{2.6}$$

At very low concentrations, the integral in the exponential term goes to zero and the attenuation can be neglected. For the present study, the source concentrations were typically 10 to 100 mg/l and the total path length through the dye was approximately 500 mm. Attenuation was significant and had to be taken into account.

Sensitivity to External Conditions

As documented by Walker (1987) and Karasso (1994) the fluorescence intensity is strongly sensitive to pH of the solution and very weakly sensitive to temperature. The pH effect was automatically included in the calibration by using fresh water, from the domestic building supply, in the channel each day and using this same water to mix calibration solutions. The temperature effect was ignored because it is only 0.3% per K and there was little change in the water temperature over each set of measurements.

Photobleaching

Photobleaching is the decrease in fluorescent intensity over time when a fluorescent material is exposed to light. Over a long period of time (i.e. several days to weeks) even ambient room lighting has been observed to bleach low concentrations (< 0.1 mg/l) of fluorescein dye. With laser beam illumination, bleaching can be seen with the naked eye after exposures of several seconds in stagnant solutions where the fluid in the beam path is not constantly refreshed. In the literature there are several studies which have attempted to quantify this photobleaching effect, but there has been little agreement between experiments.

For example, Crimaldi (1997) tested for photobleaching during simultaneous LIF and LDA (laser - Doppler anemometer) measurements and Saylor (1995) performed small scale tests with a tightly focused 1 watt laser in a small sample bottle. In both cases, photobleaching was observed on relatively short timescales of 10's of milliseconds. However, in both of these studies the measuring volume cross section diameter was of the order of 20 to 30 μm with tightly focussed laser beams resulting in very high light intensities in the measurement volume.

In the present study, the light intensities were much lower with the cross section diameter of the measurement volume on the order of 1 mm and laser intensities of about 100 mW. At these lower intensities, photobleaching was observed only in stagnant solutions. Any small fluid motion was sufficient to refresh the measurement volume with new dye molecules and maintain the fluorescence intensity. In the plume measurements, the dye in the measurement volume was constantly refreshed by new dye from the source so photobleaching was not a concern.

2.3.3 Calibration

There are several unknown, but presumed constant factors that must be taken into account when trying making quantitative measurements:

- dye properties from Equation (2.6)
- individual camera pixel gain and offsets
- input light intensity
- reflection and/or absorption by the glass walls of the channel
- absorption of light by the water
- water pH

These factors may also change from day to day. Because there are no absolute standards easily available to calibrate the camera and the dye fluorescence independently, the best solution was to do an in-situ calibration and account for all of the unknowns at once.

After several attempts, the best results were achieved by calibrating each pixel of the camera individually using a small laminar jet source placed immediately in front of the laser line as shown in Figure 2.7. This small jet was slid across the laser line in the field of view of the camera to expose each pixel of the camera to a known concentration of dye with effectively zero attenuation. Although the jet added some additional background dye concentration into the channel, it was a very small amount for the low concentration and short duration of the calibrations and could be safely ignored. A similar calibration jet was used by Crimaldi (1997) for a single point LIF probe.

For the current study, calibration measurements were made at 5 concentrations from 0 (the background intensity measured by the camera with no dye in the channel) up to 0.1 mg/l which produced about 4000 digital counts near the centre pixels of the camera. The zero concentration level was measured by averaging 20 seconds of data. The non-zero concentration calibration points were determined by taking a 1 to 2 minute data set during which the jet traversed the entire field of view of the camera. The 10 highest readings for each pixel were selected and averaged to determine the calibration intensity. It was assumed that the highest readings for each pixel occurred when the jet was present at that pixel. Figure 2.8 shows a typical set of calibration data.

Walker (1987) stated that the fluorescence intensity to concentration relationship should be approximately linear, but the best fit for the present study was found with a second order polynomial. This equation empirically accounts for non-linearities in the dye response at high concentrations. For each pixel, the response curve is

$$C = a_0 + a_1 I + a_2 I^2 \tag{2.7}$$

where a_0, a_1, and a_2 are calibration constants, I is the measured intensity in digital counts, and C is the concentration in mg/l.

The zero dye background intensity measurement, I_0 can be obtained very accurately by using a 20 second sample time to average out all of the background noise fluctuations. Because this was the best calibration point, the calibration curve was forced through the point at zero concentration and I_0. Equation (2.7) then becomes

$$C = a_1(I - I_0) + a_2(I - I_0)^2 \tag{2.8}$$

At $I = I_0$, the concentration should be zero, so $a_0 = 0$. The remaining constants were fit using least squares regression. Figure 2.9 shows some typical calibration constant values and the calibration curve for a pixel near the centre of the camera.

Attenuation Measurements

Several tests were performed to confirm the literature values of the attenuation constant ε by filling a glass walled fish tank with a known concentration of dye, making a 20 second measurement, and then averaging to find the intensity for each pixel. These intensity values were then converted to concentration measurements using the calibration procedure from section 2.3.3 which effectively removed the pixel-to-pixel variation from the measurement. The measured attenuation constant was $\varepsilon = 0.023$ l/mg·mm as compared to Walker (1987) who measured 0.0226 l/mg·mm.

During the attenuation testing, the clarity of the water proved to be a confounding factor. Residual titanium dioxide LDV seed particles in the channel water caused changes in the beam attenuation from day to day. The solution was to thoroughly clean the channel to eliminate the particles before proceeding with LIF tests. Fortunately, the water supply at the University of Alberta in Edmonton was sufficiently clean that additional filtering was not required. This experimenter has been involved in LIF measurements in another Canadian city where the supply water used to fill the experiment caused more than a 50% loss of laser intensity even before any dye was added. Under these extreme conditions additional water filtration was necessary.

The method of calibration discussed in Section 2.3.3 effectively accounts for all of the unknown constants in Equation (2.6). For the purposes of attenuation correction in the measured plume data, the only important factor is the relative change in intensity from pixel to pixel as light is absorbed by the dye. From Equation (2.6) the ratio of input light intensity at pixel k relative to the incoming light intensity before any attenuation I_{in} gives the attenuation correction factor A

$$A = \frac{I_k}{I_0} = \prod_{j=0}^{k-1} \exp\left(-\varepsilon\, c_j\, \Delta y\right) \tag{2.9}$$

where I_k is the input light intensity at pixel k, c_j is the concentration at pixel j and Δy is the effective pixel width. At the first pixel location $A = 1$ and it decreases exponentially as a function of the concentration at each subsequent pixel.

Surface Reflection Effects

There was some concern that the expanded metal roughness on the bottom of the channel would reflect light and distort the data. This was especially problematic because of the desire to make measurements very close to the rough surface. The solution was to paint the roughness with flat black paint. To confirm this solution, some test pieces were placed in the channel to see if they caused any measurable effect. The test configurations were a piece of painted stainless steel expanded metal boundary layer roughness over a black piece of plastic, painted roughness over clear plastic and painted roughness over a bare piece of aluminum. Figure 2.10 shows the results of a number of these tests done at several vertical locations. There is no evidence of the roughness over the black plastic or the roughness over the clear plastic, but the roughness over the aluminum sheet produces reflections that clearly interfere with accurate measurements. Flat black roughness over flat black painted plastic was used for all data collection.

Overall Accuracy

Using all of the above measurement and calibration techniques, the overall accuracy was checked by injecting known concentrations of dye with the calibration source and measuring the concentration across the field of view of the camera. The result is shown in Figure 2.11. As expected, the accuracy is poor at very low concentrations where random camera electrical noise is of similar magnitude to the signal. Overall, the accuracy of the measurement was about 5% for the measured plume concentrations.

2.3.4 Data Collection and Analysis

Each linescan measurement was 500 seconds long at a data rate of 500 lines/second and produced 500 megabytes of data for the 12 bit range of 1024 binned pixels. The basic collection procedure was:

1. collect 10 seconds of data with the source off to be used to calculate the background level at the start of the data collection.

2. turn on the dye source
3. collect 500 seconds of linescan data with the source on
4. turn off the dye source
5. collect 10 seconds of data to calculate the background level at the end of the data collection.

Calculating Concentration

For each line of data, several corrections were made to account for effects such as the change in position of the measurement location as compared to the calibration position, the attenuation of the laser light through the dye, and the background dye level building up in the channel. The procedure was as follows:

1. The camera was fixed in position, so as the laser line was moved to different z positions the effective spatial resolution of the pixels and the intensity measured at the camera changed. Fluorescein emits light equally in all directions so the intensity at any distance from the laser line follows an inverse square law. As the line gets closer to the camera the effective field of view of the camera decreases and the measured fluorescence intensity will be directly proportional to the effective field of view. The correction factor K_{line}:

$$K_{\text{line}} = \frac{w_{\text{cal}}}{w_{\text{line}}} \left(\frac{h_{\text{cam}} - z_{\text{line}}}{h_{\text{cam}} - z_{\text{cal}}} \right) \tag{2.10}$$

   where w_{cal} is the pixel width in mm for the calibration, w_{line} is the pixel width for the line being measured, z_{cal} is the calibration height in mm, z_{line} is the line height in mm, and h_{cam} is the effective camera height in mm.

2. Attenuation at each pixel was corrected by marching through the data pixel by pixel working in the direction of laser beam propagation using Equation (2.9) to find A.
3. Concentration based on the corrected fluorescence intensity was calculated using the constants determined for the calibration Equation (2.8)
4. The background concentration was subtracted from the measured concentration for each line of data collected. The current background level was calculated by a linear interpolation of the background images collected before and after each experiment.

The result of this four-step process was a concentration measurement for each pixel for each line of data collected. Figure 2.12 shows a typical cross-stream fluorescence intensity measurement and the resulting concentration profile after the above calculations and corrections. In Figure 2.12(a) it appears that the signal is noisy with about a ±25 digital count range from pixel to pixel, but this is simply a consistent variation in offset and response between pixels. After applying the calibration for each individual pixel, this pixel to pixel variation is eliminated and the result is a much cleaner signal as shown in Figure 2.12(b).

Further Data Analysis

All subsequent analysis was performed on the concentration files using custom software written by the author. This analysis included operations such as calculating time averaged and ensemble averaged centroids, plume spreads, concentrations and any other statistics that were required.

2.4 Averaging Time and the Meandering Plume Model of Concentration Fluctuations

Using the data collected with the linescan LIF technique it will be shown that the meandering Gaussian plume model first proposed by Gifford (1959) and generalized by Sawford and Stapountzis (1986) is a useful tool for predicting concentration fluctuation statistics in a dispersing plume. The models presented are based on the operational model described in Wilson (1995) with some modifications and further development. The effect of wind shear distortion of concentration fluctuations near the ground will be specifically addressed in a companion paper in Chapter 3.

2.4.1 Effect of Averaging Time on Plume Spread

Averaging time t_{avg} is simply the time interval over which any variable of interest is averaged to produce a mean value. Sampling time t_{sample} is the time interval over which a variable of interest is actually measured. It is obvious that the averaging time can never be longer than the total available sampling time (i.e. $t_{\text{avg}} \leq t_{\text{sample}}$) Pasquill and Smith (1983, pp. 12-19) and Wilson (1995) use these same definitions. The definitions seem clear enough, but the two terms are often used interchangeably and there can be confusion when discussing the effects of averaging time or sampling time on various dispersion parameters.

Plume dispersion is a complex, highly variable process with material moving in three dimensions in a turbulent flow field. Even in the laboratory, where the flow is confined by the walls of a wind tunnel or water channel, plumes still meander back and forth and have a clearly defined axis only in a large ensemble average or in a long time average of instantaneous samples.

Plume spreads and mean concentrations are usually computed for a specific averaging time, t_{avg}. As t_{avg} increases, the centroid of the *instantaneous* plume has more opportunity to meander away from the axis of the plume (i.e. more opportunity to the sample the extremes of the probability distribution describing its position). The time-averaged total plume spread increases as t_{avg} increases. The only reliable way to measure these values is to take a large ensemble of samples of length t_{avg}. The unsteady nature of the full-scale atmosphere precludes obtaining more than a few sample points in an ensemble and as a result there are large variabilities in full-scale spreads and concentrations.

Consider instantaneous measurements of a plume where $t_{\text{avg}} \rightarrow 0$. At a fixed downwind distance from the source, instantaneous snapshots of the plume will show it meandering from side to side as well as vertically about some ensemble mean position. A single instantaneous sample of length $t_{\text{avg}} \rightarrow 0$ will reveal very little useful information about the overall plume properties so the usual approach is to take an ensemble of these short samples to determine any plume statistics.

The only practical method of determining any statistic of a dispersing plume requires the assumption that it is a stationary and ergodic process. Stationary because all the statistics are assumed to come from a process that has the same mean, variance, etc. at all times. Ergodic because it is assumed that any sample taken or ensemble used has captured all the variation in the process and that any other sample or ensemble of the same size will give exactly the same result. Arguably, the full-scale atmosphere and most measurements of it do not satisfy these conditions, but almost without exception dispersion is modelled as if it were stationary and ergodic over the sampling time of interest. With this assumption, any plume property measured relative to a reference point fixed to the ground, such as the ensemble average mean concentration, plume spread, concentration variance, or any other plume statistic will be constant regardless of the averaging time interval. A large ensemble of short time interval measurements or an ensemble of long time interval measurements will both give the same results.

The only way produce a variation with averaging time in a stationary dispersion process is to follow the plume motion in a time averaged way. The most logical approximation of overall plume movement is to follow the plume centroid. To follow the plume centroid averaged over a time interval t_{avg} requires us to take samples of the plume each of length $t_{\text{sample}} = t_{\text{avg}}$. Then, line up all of the centroids of these samples to create the ensemble before computing the plume statistics. With this approach, as t_{avg} increases the plume will effectively appear to be wider because more of the slow large scale meandering of the instantaneous plume samples will be included. As $t_{\text{avg}} \rightarrow \infty$, or more accurately as t_{avg} becomes much larger than the largest scales of turbulent motion, all of the plume parameters will reach the asymptotic value equal to the fixed to the ground reference frame value.

Figure 2.13 shows graphically the difference between averaging in a fixed frame of reference versus following the plume centroid. On the left side of the figure the reference frame is fixed to the ground giving a Eulerian or $t_{\text{avg}} \rightarrow \infty$ average of the plume. On the right side of Figure 2.13 is the instantaneous relative dispersion with each instantaneous centroid shifted to a common baseline. This set of instantaneous profiles is the $t_{\text{avg}} \rightarrow 0$ case.

Confusion can arise because the convention in dispersion literature seems to use the term *averaging time* and assume that everyone understands that it is really a *sampling time* if we are discussing concentration fluctuation parameters (or velocity fluctuation parameters for that matter). For the remainder of this paper, in an attempt to follow convention and minimize further confusion, only the term averaging time t_{avg} will be used, even when describing *instantaneous* concentration fluctuations measured over an sampling interval of length t_{avg}.

The linescan LIF measurement technique allows the plume centroid to be tracked in the cross-stream y coordinate direction, but not simultaneously in the vertical z direction. All plume statistics in this study were calculated by following the centroid of the plume in the cross-stream direction as it meanders from side to side.

2.4.2 Meandering Plume Model

The meandering plume model first proposed by Gifford (1959) leads to closed form solutions for concentration fluctuation parameters such as those given in Wilson (1995). Gifford's idea was to model a dispersing plume as a narrow instantaneous Gaussian plume with spread $\sigma_{y,i}$ and no internal concentration fluctuations, which is meandered by larger scale eddies in the flow to produce a wider time-averaged Gaussian plume. If we consider just one-dimensional meandering, in the y-direction, then the total plume spread, σ_y is the sum of the spread of the instantaneous plume, $\sigma_{y,i}$ and the spread caused by the meandering of this instantaneous plume, $\sigma_{y,M}$

$$\sigma_y^2 = \sigma_{y,i}^2 + \sigma_{y,M}^2 \tag{2.11}$$

Plume spreads σ_y are the standard deviation of concentration across the plume. Most plume spreads are calculated from large ensembles of data or long time samples. For example, the instantaneous plume spread $\sigma_{y,i}$ is calculated by following the centroid of the plume for each sample, calculating the ensemble average instantaneous plume and determining the spread of that ensemble average as shown in Figure 2.13. Similarly, the total plume spread σ_y for a given averaging time is calculated by taking an ensemble of samples of length t_{avg}, lining up the centroids of each member of the ensemble and computing the spread of that ensemble average distribution of concentration.

The meander parameter M_{spread} is defined as the ratio of the squares of the meandering spread to the instantaneous spread.

$$M_{\text{spread}} = \frac{\sigma_{y,M}^2}{\sigma_{y,i}^2} \tag{2.12}$$

The subscript "spread" is necessary because there is another meander parameter, $M_{\text{intensity}}$ which is the meander required to produce the correct concentration fluctuations in the plume. As evident in Figure 2.13, plumes are not smooth fluctuation-free Gaussian distributions as implied by Gifford's original model. The real concentration fluctuations at any point are a result of a range of scales of mixing from large scale meandering down to the smaller internal mixing scales of the plume down to the dissipation scales. Yee et al. (1994) extended the meandering plume model by explicitly including internal fluctuations in the instantaneous plume. Wilson (1995) implicitly included the internal instantaneous fluctuations by defining a pseudo-meander $M_{\text{intensity}}$ to account for the increased fluctuation intensity. Instead of measuring meandering directly using the ratio of spreads as in Equation (2.12), the pseudo-meander $M_{\text{intensity}}$ is the meander necessary to produce the fluctuation level that is observed. This is discussed in Wilson (1995) and Bara et al. (1992) working from the Sawford and Stapountzis (1986) meandering plume formulation for two dimensional meandering and the result is

$$M_{\text{intensity}} = i_h^2 + (i_h^4 + i_h^2)^{0.5} \tag{2.13}$$

where i_h is the fluctuation intensity on the plume horizontal and vertical centreline.

The linescan LIF measurement technique allows the one-dimensional, y-direction, meandering to be investigated because the entire cross-wind extent of the plume is sampled at 1024 points simultaneously at a high enough data rate (500 samples per second) that $\sigma_{y,i}$ can be measured directly. The high frequency data can be time averaged to determine σ_y, and the centroid movement can be tracked to measure $\sigma_{y,M}$ and thus M_{spread} calculated using Equation (2.12). The high frequency measurements also allow pseudo-meander $M_{\text{intensity}}$ to be determined by measuring the concentration fluctuation intensity i_h on the time averaged plume centreline at the effective source height h, which includes any jet momentum rise, and applying Equation (2.13).

Figures 2.14 and 2.15 are some typical M_{spread} and $M_{\text{intensity}}$ values from the water channel data set. In grid turbulence, Figure 2.14(a), $M_{\text{intensity}}$ is typically an order of magnitude greater than the real meander of the plume centroid M_{spread}. In the shear flow cases, Figures 2.14(b) and 2.15, the differences are less pronounced, but $M_{\text{intensity}}$ is still typically a factor or 2 to 10 greater than the actual meander ratio M_{spread}. This is not unexpected because the large scale slow meandering is suppressed by the side walls of the channel, allowing the rapid fluctuations in the instantaneous plume to dominate in laboratory simulations. Appendix C has additional plots of meander parameters from all of the sources and positions that were tested and the same trends are evident.

In the water channel, plume meandering ceases at long averaging times as expected for a statistically stationary ergodic process. For $t_{\text{avg}}U/G > 10$ in grid turbulence and $t_{\text{avg}}U_H/H > 10$ in shear flow (i.e. $t_{\text{avg}} \simeq 5$ to 10 seconds) meandering has effectively stopped because the limited size of the water channel restricts the meandering of the plume. The levelling off of the statistics also indicates that the 500 second sample times for the water channel data were sufficient to capture all of the t_{avg} effects. As t_{avg} gets longer, the number of effective samples that can be obtained from a single 500 second measurement decreases. Regardless of the real behaviour of the plume we would expect all the statistics to level off as t_{avg} gets large because of the shrinking sample size. The fact that this levelling happens at 5 to 10 seconds and not at 100 to 500 seconds indicates that 500 second samples were long enough to capture statistically meaningful t_{avg} effects.

The differences between the actual and pseudo-meander ratios indicate that the restricted plumes in the water channel have a great deal of internal concentration fluctuation and large scale meander contributes only a small part to the overall concentration fluctuation level. The $M_{\text{intensity}}$ necessary to produce the measured fluctuations is not directly related to the real large scale meandering of the plume centroid given by M_{spread}. Although this implies that a meandering plume is not a good physical model for the dispersion process, substituting the pseudo-meander $M_{\text{intensity}}$ for the real meander M_{spread} will be shown to produce a very robust and accurate model for engineering estimates of the spatial distribution of concentration fluctuations. The other implication is that predicting M_{spread} may not be particularly useful for plume modelling purposes.

2.4.3 Centreline Fluctuation Intensity as a Function of Averaging Time

One of the key relationships in the Wilson (1995) meandering plume model is that the centreline fluctuation intensity i_h can be adjusted for averaging time based on the changes in plume spread σ_y with t_{avg}. Wilson (1995, Equation (6.9))

$$\frac{i^2_{h,t_{\text{avg}}} + 1}{i^2_{h,\text{ref}} + 1} \simeq \frac{\sigma_{y,t_{\text{avg}}}}{\sigma_{y,\text{ref}}} \tag{2.14}$$

This relationship requires that $i_{h,\text{ref}}$ and $\sigma_{y,\text{ref}}$ at some reference averaging time are known.

The water channel data was used to test this relationship. The results are shown in Figures 2.16 and 2.17 with a reference time of $t_{\text{avg}} \to \infty$ taken as the 500 second total measurement time. The correspondence between i^2_h and σ_y is not perfect, but is generally within about 10% and all of the trends are correct. This is an important result because Equation (2.14) is essential to scaling water channel simulations to the longer averaging times of the full-scale atmosphere. Appendix D has additional plots for the other sources and positions that were measured.

2.4.4 Cross-Stream Profiles of Fluctuation Intensity i

Another relationship from the Wilson (1995) operational model that can be tested with the linescan data set is the off-axis fluctuation intensity values, Wilson (1995, equation (6.8))

$$i^2 + 1 = (i^2_h + 1)\left[\exp\left(\frac{(z-h)^2}{2\sigma_z^2} + \frac{y^2}{2\sigma_y^2}\right)\right]^{\frac{2M_{\text{intensity}}}{1+2M_{\text{intensity}}}} \tag{2.15}$$

where i_h is the plume centreline fluctuation intensity, h is the source height, z is the measurement height, σ_y and σ_z are the plume spreads, y is the cross-stream position and $M_{\text{intensity}}$ is the pseudo-meander parameter for fluctuation intensity given by Equation (2.13).

It is already known that the shear flow will greatly distort this profile near the ground, but for the moment we can avoid having to deal with this issue by using the measured $i_{y=0}$ value on the cross-stream centreline of the plume at each vertical position instead of i_h. Figures 2.18 and 2.19 show some typical cross stream profiles compared to Equation (2.15). Appendix E contains a more complete set of plots of cross-stream fluctuation intensity for other sources and measurement positions. The fit is very good, especially for the grid turbulence, which is more spatially homogeneous and has no mean velocity shear. In the shear flow cases and far off the centreline at 3 to 4 σ_y, the fit is not quite as good, but at this point it is possible that the walls of the water channel are having an effect. This is a smaller problem in grid turbulence because the plumes are very narrow and less influenced by the side walls of the channel.

The best agreement between theory and experiment is obtained when the pseudo-meander $M_{\text{intensity},z}$ is calculated using Equation (2.13) with i taken at the measurement height z on the plume centreline $y = 0$, rather than using $M_{\text{intensity},h}$ calculated from the source height fluctuation intensity i_h. As an example, Figure 2.20 compares the cross stream intensity profiles for the $x/H = 2.5$, $(z-d)/H = 0.011$ case for the horizontal elevated jet at $(h-d)/H = 0.12$, with $M_{\text{intensity,z}}$, $M_{\text{intensity,h}}$ and M_{spread}. The best fit is with the pseudo-meander $M_{\text{intensity,z}}$ calculated at the local height of each cross-stream profile to minimize the shear distortion effects. The success of the local pseudo-meander suggests that wind shear distortion of concentration fluctuations is a localized height dependent effect.

2.4.5 Cross-Stream Probability Distributions of Centroid Position and Plume Spread

The detailed data sets obtained from the linescan LIF enable direct measurement of many interesting properties of plume dispersion which are very difficult or impossible to measure with other experimental techniques. Two parameters that may be useful to future development of meandering plume dispersion and concentration fluctuation models are the probability distribution of the position of the instantaneous plume centroid $\overline{y}$ and the probability distribution of instantaneous plume spread $\sigma_{y,ii}$. (The double subscript ii is necessary because $\sigma_{y,i}$ is defined as the ensemble average instantaneous plume spread $\langle\sigma_{y,ii}\rangle$) The centroid position and instantaneous spread size will be normalized by the total plume spread $\sigma_{y,\infty}$ which is the 500 second average plume spread in the water channel.

At each downstream position, the time-varying location of the plume centroid is a function of the larger scale eddies that have meandered the entire plume during its time of travel. The centroid moves as a random additive process that should produce a Gaussian distribution. Figures 2.21 and 2.22 are some samples of the centroid position $\overline{y}/\sigma_{y,\infty}$ probability distributions. The Gaussian curves plotted with the data have the same mean (defined as $\overline{y}/\sigma_{y,\infty} = 0$ on the plots) and centroid standard deviations as the data. The standard deviation of the centroid is equal to the meandering plume spread $\sigma_{y,M}$ from Equation (2.11). Other source types show similar correspondence between the plume centroid position and a Gaussian distribution as shown in the additional plots in Appendix F.

Instantaneous plume spread $\sigma_{y,ii}$ is highly variable and has a probability distribution of its own. This variability is caused by the random dilution and spreading of the plume and also by plume meandering perpendicular to the linescan measurement. Dilution is a random multiplicative process so a lognormal distribution might is expected for plume spread.

Comparing measurements of instantaneous spread to a lognormal is complicated by the fact that in grid turbulence there are significant periods of time during which no part of the plume is in the measurement beam, even when the measurement location is on the vertical plume centreline. The intermittency factor γ_{line} is the fraction of time during which there is a measurable plume somewhere in the measurement volume. Even on the centreline of the plume, γ_{line} ranges from 87% at $x/G = 6.6$ from the source to 95% at $x/G = 19.7$. For the boundary layer shear flow some part of plume is present for 100% of the time at all positions $(z-d)/H < 0.12$ so $\gamma_{\text{line}} = 1.0$ for all of the shear flow cases.

Figures 2.23 and 2.24 show some samples of the distributions of measured normalized instantaneous plume spreads $\sigma_{y,ii}/\sigma_{y,\infty}$ compared to a clipped lognormal (for $\gamma_{\text{line}} < 1$) or lognormal distribution for all other cases. The clipped lognormal was first used for modelling intermittent Eulerian concentration level probability distributions by Hilderman and Wilson (1999). In its application here to the instantaneous plume spread $\sigma_{y,ii}$ the pdf is

$$p(\sigma_{y,ii}) = \frac{1}{\sqrt{2\pi}\sigma_{y,ii,l}\left(\sigma_{y,ii} + \sigma_{y,ii,\text{base}}\right)} \exp\left(-\frac{\ln^2\left(\frac{\sigma_{y,ii}+\sigma_{y,ii,\text{base}}}{\sigma_{y,ii,50}}\right)}{2\sigma^2_{y,ii,l}}\right) \tag{2.16}$$

where $\sigma_{y,ii,l}$ is the log standard deviation of the plume spread, $\sigma_{y,ii,\text{base}}$ is the shift of the distribution needed to generate the correct plume intermittency, and $\sigma_{y,ii,50}$ is the median of the unclipped lognormal distribution. Essentially, this is just a lognormal distribution shifted to the left by $\sigma_{y,ii,\text{base}}$. All values less than 0 are clipped off and replaced with a delta function at zero that represents the intermittent periods where there is no measurable plume anywhere along the measurement line. The $\sigma_{y,ii,l}$ and $\sigma_{y,ii,\text{base}}$ values are chosen so that after clipping the remaining distribution has the correct mean and variance. Hilderman and Wilson (1999) give additional details on the calculations required to compute $\sigma_{y,ii,l}$ and $\sigma_{y,ii,\text{base}}$. For the non-intermittent case $\sigma_{y,ii,\text{base}} = 0$ and (2.16) reduces to the lognormal. Appendix F has additional plots of the plume spread data fit to the lognormal and clipped lognormal.

The clipped lognormal is a remarkably good fit to instantaneous plume spread distributions. The only discrepancies are for the extremely small plume spreads where $\sigma_{y,ii} \rightarrow 0$ such as in the grid turbulence case. These errors are not surprising as the camera pixel resolution limits the ability to measure very small plume spreads. To date, there has been no theoretical basis developed for the clipped lognormal. A simple physical explanation is that dilution/spread is a naturally multiplicative process so a lognormal might be expected. A clipped lognormal implies that even zero periods are part of this same multiplicative process.

2.4.6 Section Summary

In this section the basics of averaging time and the meandering plume model were presented and models of the concentration fluctuation intensity developed in Wilson (1995) were tested against the water channel experimental data. The key observations are listed below. The engineering design and physical modelling implications of these observations will be discussed the conclusions section.

- Averaging time effects on a dispersing plume can only be accurately measured in a Lagrangian frame of reference that follows the plume movement.

- The concentration fluctuations in the plume change with averaging time in parallel with the changes in the time averaged plume spread.

- The meander parameter based on the large scale meandering of the plume M_{spread} is much less than the pseudo-meander $M_{\text{intensity}}$ required to explain all of the concentration fluctuation measured in a dispersing plume. The large scale meandering of the plume only contributes a small part to the overall concentration fluctuation level the remainder is due to internal plume variability.

- Despite the above conclusion, the meandering plume model remains a useful tool to predict concentration fluctuations. Using $M_{\text{intensity}}$ evaluated at the local profile height above the ground for cross-stream variation in fluctuation intensity i produced very good agreement with the water channel data.

- The instantaneous centroid of the plume meanders in the cross-stream direction in a random additive process that produces a Gaussian distribution for the centroid position.

- The instantaneous plume spread has a probability distribution that is well described by a lognormal in the case where $\gamma_{\text{line}} = 1$ or clipped lognormal for $\gamma_{\text{line}} < 1$ when the plume meanders entirely outside of the measurement volume for significant periods of time.

2.5 Plume Spread with Averaging Time: Models and Data

2.5.1 Plume Spread Variation with Averaging Time

As the averaging time interval increases, the instantaneous plume will meander more and total plume spreads will increase while the plume centreline average concentration decreases. In Figure 2.13 the left side of the figure is the ensemble averaged plume for $t_{\text{avg}} \rightarrow \infty$ while the right hand side is the ensemble averaged plume for $t_{\text{avg}} \rightarrow 0$. The shorter time average filters out the larger scale motions of the plume causing a reduced plume spread.

One widely used method of accounting for time average effects is to adjust plume spreads $\sigma_{y,t_{\text{avg}}}$ for an averaging time t_{avg} relative to some reference averaging time t_{ref} for which the spread $\sigma_{y,t_{\text{ref}}}$ is known. The typical power law model is (Hanna et al. (1996, Equation (6.1)))

$$\frac{\sigma_{y,t_{\text{avg}}}}{\sigma_{y,t_{\text{ref}}}} = \left(\frac{t_{\text{avg}}}{t_{\text{ref}}}\right)^{0.2} \tag{2.17}$$

Gifford (1982, 1984) proposed a random force model to describe crosswind plume spread at all stages of the dispersion by adapting the Langevin random force diffusion equation. Wilson (1995) developed a travel time power law model for averaging time effects inspired by the Gifford random force model. Wilson's model considers source size and averaging time as equivalent to a change in the effective travel time of the plume. The constants in the power law were chosen to produce results that approximated Gifford's solution to the Langevin equation, see Wilson (1995, Chap. 3 and Appendix A). From Wilson (1995, Equation (3.12)):

$$\frac{\sigma_{y,t_{\text{avg}}}}{\sigma_{y,t_{\text{ref}}}} = \left(\frac{3\phi_0^2\left(\frac{T_{Lv}}{t_t}\right)^2 + \frac{t_t}{T_{Lv}} + r_1\frac{t_{\text{avg}}}{T_{Lv}}}{3\phi_0^2\left(\frac{T_{Lv}}{t_t}\right)^2 + \frac{t_t}{T_{Lv}} + r_1\frac{t_{\text{ref}}}{T_{Lv}}}\right)^{0.5} \tag{2.18}$$

where t_t is the plume travel time, t_{avg} is the averaging time, t_{ref} is the reference averaging time, and T_{Lv} is the cross-stream (y-direction) Lagrangian integral velocity fluctuation time scale. The source size parameter ϕ_0 is the non-dimensional source size from Wilson (1995, Equation (3.13))

$$\phi_0 = \frac{\sigma_0}{\sqrt{2}v'_{\text{rms}}T_{Lv}} \tag{2.19}$$

where σ_0 is the source size, and v'_{rms} is the cross-stream rms velocity fluctuation. The empirical parameter r_1 from Wilson (1995, equation (3.14))

$$r_1 = \frac{1}{2\left(1 + 0.6\dfrac{t_t}{T_{LV}} + 0.3\dfrac{t_{\text{avg}}}{T_{LV}}\right)} \tag{2.20}$$

An alternative form for r_1 will be proposed in the present study. The effective initial source size σ_o is (Wilson et al., 1998, Equations (A.31) and (A.32))

$$\frac{\sigma_o^2}{R_s^2} = \frac{\Upsilon_s}{2} + \frac{\beta_e^2}{2}\left(\frac{\Delta h}{R_s}\right)^2 + 4B_o^2 \tag{2.21}$$

where R_s is the source radius, Δh is the plume rise, and β_e is

$$\beta_e = 0.6\left(\frac{1 + 0.015\Upsilon_s^2}{1 + 0.04\Upsilon_s^2}\right) \tag{2.22}$$

Υ_s is the density weighted velocity ratio given by (Wilson et al., 1998, Equation (A.21))

$$\Upsilon_s = \left(\frac{\rho_s}{\rho_a}\right)^{0.5}\frac{W_s}{U} \tag{2.23}$$

where ρ_s is the source density, ρ_a is the ambient fluid density, W_s is the vertical velocity component of the source, and U is the average flow velocity. The empirical source size constant B_0 accounts for source size of low velocity releases with no plume rise and Wilson et al. (1998) found $B_0 = 0.5$ based on water channel plumes.

2.5.2 Plume Meander as a Function of Averaging Time

The travel time power law model of Wilson (1995) given by Equations (2.18) through (2.23) can also be used to predict the meander parameter M_{spread} as a function of averaging time. Using the definition of M_{spread} from (2.12) and the meandering spread from (2.11)

$$M_{\text{spread}} = \left(\frac{\sigma_{y,t_{\text{avg}}}}{\sigma_{y,i}}\right)^2 - 1 \tag{2.24}$$

In (2.18) let $\sigma_{y,\text{ref}} = \sigma_{y,t_{\text{avg}}\to 0} = \sigma_{y,i}$ and combine with (2.24)

$$M_{\text{spread}} = \left(\frac{3\phi_0^2\left(\dfrac{T_{Lv}}{t_t}\right)^2 + \dfrac{t_t}{T_{Lv}} + r_1\dfrac{t_{\text{avg}}}{T_{Lv}}}{3\phi_0^2\left(\dfrac{T_{Lv}}{t_t}\right)^2 + \dfrac{t_t}{T_{Lv}}}\right) - 1 \tag{2.25}$$

As discussed in Section 2.4 knowing M_{spread} is of limited use in predicting concentration fluctuations. However, it is useful for verifying the accuracy of the fit between the travel time power law model and Gifford's original random force model because meander is a much more sensitive indicator of the power law fit than the plume spread.

2.5.3 Improving the Travel Time Power Law Model

An improved fit between the Gifford random force model and the travel time power law model can be made by adjusting the coefficient r_1 from Equation (2.20). An improved empirical fit for the parameter r_1 is

$$r_1 = \frac{1 + 0.2\left(\dfrac{t_t}{T_{Lv}}\right)^{1.5}}{2\left(1 + 0.2\dfrac{t_{\text{avg}}}{T_{Lv}}\right)\left(1 + 0.5\left(\dfrac{t_t}{T_{Lv}}\right)^{1.5}\right)} \tag{2.26}$$

This form of r_1 is less sensitive to changes in travel time than Equation (2.20) and behaves correctly in the limits of t_{avg} and t_t. With this new equation for r_1, the travel time power law model matches Gifford's predictions of meander within approximately ±20% over any reasonable choice of travel time, sample time and source size. The travel time power law model in Equation (2.18) with the new r_1 value from Equation (2.26) will be referred to as the TTPL model.

TTPL Behaviour for Long Travel Times $t_t \gg T_{Lv}$

To check the behaviour of the modified r_1 coefficient, consider the case of a point source, $\sigma_0 \to 0$ and compare the spread at $t_{\text{avg}} \to \infty$ to the instantaneous spread at $t_{\text{avg}} \to 0$. From Equation (2.18) squaring both sides

$$\frac{\sigma^2_{y,\infty}}{\sigma^2_{y,i}} = \left(\frac{\dfrac{t_t}{T_{Lv}} + r_1\dfrac{t_{\text{avg}}}{T_{Lv}}}{\dfrac{t_t}{T_{Lv}}}\right) \tag{2.27}$$

In the limit of long travel time $t_t \gg T_{Lv}$ the modified r_1 goes to 0.1 and the ratio $\sigma^2_{y,t_{avg}}/\sigma^2_{y,i}$ is very weakly dependent on t_{avg}. When $t_t > t_{\text{avg}}$ then, as expected, averaging time will have almost no effect. At large t_t the plume has travelled far downstream and the instantaneous spread is so large that there are no eddies larger than the instantaneous plume to cause meandering.

TTPL Behaviour for Short Travel Times $t_t \ll T_{Lv}$

In the limit of short travel times $t_t \ll T_{Lv}$ it is expected that

$$\sigma_y \simeq v'_{\text{rms}} t_t \tag{2.28}$$

This relationship for short plume travel times is from Taylor (1921) with derivations reproduced in most textbooks that discuss turbulent diffusion.

The instantaneous plume spread $\sigma_{y,i}$ can be estimated from the simple differential equation

$$\frac{\mathrm{d}\sigma_{y,i}}{\mathrm{d}t_t} \approx v'_{\mathrm{rms},i} \tag{2.29}$$

The instantaneous measurement $v'_{\mathrm{rms},i}$ is somewhat less than the total v'_{rms} of the flow because scales larger than the plume size are effectively filtered out. Referring back to the discussion in Section 2.4.1, following the centroid of the instantaneous plume is necessary to measure $\sigma_{y,i} = \sigma_{y,t_{\mathrm{avg}}\to 0}$ and filters out any v'_{rms} greater than the size of the plume. Using relationship for turbulent dissipation ε and the fact that the energy transfer rate from small scales to large in the inertial subrange is equal to ϵ

$$\epsilon \propto \frac{v'^{\,3}_{\mathrm{rms}}}{\ell} = \frac{v'^{\,3}_{\mathrm{rms},i}}{R_p} \tag{2.30}$$

where ℓ is the Eulerian large eddy scale and a logical corresponding length scale for $v'_{\mathrm{rms},i}$ is $R_p = \sqrt{2}\sigma_{y,i}$, the radius of the equivalent top hat plume profile. Solving for $v'_{\mathrm{rms},i}$

$$v'_{\mathrm{rms},i} = v'_{\mathrm{rms}} \left(\frac{\sqrt{2}\sigma_{y,i}}{\ell}\right)^{1/3} \tag{2.31}$$

Putting Equation (2.31) into (2.29) and then integrating

$$\begin{aligned}
\int \sigma_{y,i}^{-1/3}\mathrm{d}\sigma_{y,i} &= \int v'_{\mathrm{rms}} \left(\frac{\sqrt{2}}{\ell}\right)^{1/3} \mathrm{d}t_t \\
\frac{3}{2}\sigma_{y,i}^{2/3} &= v'_{\mathrm{rms}} t \left(\frac{\sqrt{2}}{\ell}\right)^{1/3} \\
\sigma_{y,i} &= \left(\frac{2}{3}\right)^{3/2} (\sqrt{2})^{1/2} \frac{v'^{\,3/2}_{\mathrm{rms}} t^{3/2}}{\ell^{1/2}}
\end{aligned} \tag{2.32}$$

The Lagrangian time scale is related to the Eulerian length scale ℓ and the velocity scale v'_{rms} by

$$T_{Lv} \propto \frac{\ell}{v'_{\mathrm{rms}}} \tag{2.33}$$

with a constant of proportionality of order 1. Putting Equation (2.33) into (2.32) then

$$\sigma_{y,i} \simeq 0.6 \frac{v'_{\mathrm{rms}} t_t^{3/2}}{T_{Lv}^{1/2}} \tag{2.34}$$

Pasquill and Smith (1983, p. 122) give a similar solution for $\sigma_{y,i}$ derived by a different method employing correlation functions of velocity. Their lead constant is 0.82 instead of 0.6. Wilson (1995, Appendix A) suggests the constant is in the range of 0.6 ± 0.2.

Close to the source where $t_t \ll T_{Lv}$, r_1 is

$$r_1 = \frac{1}{0.4\dfrac{t_{\text{avg}}}{T_{Lv}}} \tag{2.35}$$

and with Equation (2.27)

$$\frac{\sigma^2_{y,\infty}}{\sigma^2_{y,i}} = 1 + \frac{1}{0.4}\left(\frac{T_{Lv}}{t_t}\right) \tag{2.36}$$

Putting Equation (2.34) into (2.36) and noting that the second term in (2.36) dominates for short travel times

$$\sigma^2_{y,\infty} = \frac{0.6^2}{0.4}\left(\frac{v'^2_{\text{rms}}t_t^3}{T_{Lv}}\right)\left(\frac{T_{Lv}}{t_t}\right) \tag{2.37}$$

$$\simeq v'^2_{\text{rms}}t_t^2 \tag{2.38}$$

which is equivalent to Equation (2.28).

2.5.4 Cross-stream Lagrangian Time Scale T_{Lv}

The cross-stream Lagrangian turbulence time scale, T_{Lv}, is an important parameter for the proposed TTPL travel time power law averaging time adjustment. Unfortunately, it is extremely difficult to make direct measurements of T_{Lv}. Typically, the Lagrangian time scale is inferred from Eulerian measurements. McComb (1990, pp. 444-447) gives an overview of some of the models proposed for calculating the Lagrangian timescale from Eulerian measurements. Pasquill and Smith (1983) cite a few examples related to the atmospheric dispersion problem. The basic hypothesis is that the Lagrangian and Eulerian correlation functions (or spectra) have similar shapes but different scales. It is also generally found that the proportionality between Eulerian and Lagrangian scales is a function of the turbulence intensity at the position of interest. The idea of proportionality is generally attributed to Hay and Pasquill (1960) with further analysis by Wandel and Kofoed-Hansen (1962) and Lee and Stone (1984). The basic functional form is:

$$T_{Lv} = B_{Lv}\frac{T_v U}{v'_{\text{rms}}} \tag{2.39}$$

where B_{Lv} is a constant whose value seems to be in the range of 0.4 to 0.8. Wilson (1995, Appendix C) recommends $B_{Lv} = 0.6$ for use in dispersion modelling.

There is also a range of T_v, U and v'_{rms} values to use in this calculation. The choices include; using only local values at the measurement location, using some average values that are representative of the average velocities and timescales experienced by the plume as it is convected downstream, or using some combination of the two with the free stream velocity U and the local Eulerian timescale T_v and cross-stream velocity fluctuation v'_{rms}.

The local velocity components and Eulerian timescales can be determined from Figures 2.4(b) and 2.4(c) for the shear flow and Figures 2.5(a) and 2.5(b) for the grid turbulence. The average advection velocity U_a of the plume is, from Wilson (1981, Equation (14)), the velocity measured at height

$$z_a = h + 0.17\sigma_z \tag{2.40}$$

where h is the height of the source and σ_z is the vertical spread.

For example, Figure 2.25 shows the normalized cross-stream Lagrangian time scale $T_{Lv}U_H/H$ for the shear flow calculated using $B_{Lv} = 0.6$ and either local or advection height values for T_v, v'_{rms} and U in Equation (2.39). Based on these results and similar calculations for grid turbulence the T_{Lv} was estimated as

Shear Flow $0.5\mathrm{s} < T_{Lv} < 1.9\mathrm{s}$ or in normalized terms $0.29 < T_{Lv}U_H/H < 1.10$

Grid Turbulence $0.8\ \mathrm{s} < T_{Lv} < 1.8\ \mathrm{s}$ or in normalized terms $2.1 < T_{Lv}U/G < 4.7$

where H is the log-law mixing layer thickness and G is the grid mesh spacing. It is expected that there will be slight changes in T_{Lv} with downstream distance as the grid turbulence decays, but given the other uncertainties these changes are insignificant. There are few compelling reasons to choose one T_{Lv} value over another so the geometric mean (the most probable value of a lognormal distribution of scales) of the values given above will be used for all further calculations. In the shear flow $T_{Lv}U_H/H = 0.58$ and in grid turbulence $T_{Lv}U/G = 3.1$.

Despite the possibility of variation in T_{Lv} with height z in shear flow as indicated by two of the curves in Figure 2.25, only a single T_{Lv} value was chosen to represent the entire boundary layer with a bias towards the lower part $(z - d)/H < 0.4$ where the majority of the tracer plume was concentrated. Over this height range even the worst case T_{Lv} model in Figure 2.25 varies by less than a factor of 4 from the smallest to largest estimated T_{Lv}.

The literature provides little guidance about Lagrangian time scales in non-uniform flows. The variation in the Lagrangian-Eulerian scale ratios cited in McComb (1990) covers an order of magnitude even in a uniform flow field. Atmospheric examples cited in Pasquill and Smith (1983) are somewhat vague about the exact vertical position considered. Gifford (1984) suggests many full-scale estimates for T_{Lv} are too small because of practical limitations on sampling time and Barr and Gifford (1987) estimate the full-scale $T_{Lv} \approx 10,000$ seconds as sampling time goes to infinity. More recently, Koeltzsch (1999) and Massman and Weil (1999) let the Lagrangian scale vary with z in a boundary layer. Koeltzsch (1999) also lets the Lagrangian-Eulerian scale ratio vary with z.

This also calls into question the wisdom of normalizing with velocity U_H and mixing layer depth H. I suspect that cross-stream scales are more likely to be a function of channel width rather than the mixing layer depth because the width is critical in determining the upper limit on plume meandering and averaging time. As Barr and Gifford (1987) note limited averaging time of measurements filters out lower frequency contributions and produces shorter Lagrangian time scales.

It is impossible to resolve all these issues in the present study with the present experimental data, so the practical approach was to assume a single cross stream Lagrangian time scale and prevent this study from degenerating into a curve fitting exercise. The primary objective is to determine whether the TTPL model is a reasonable approach for estimating averaging time effects. A reasonable estimate of T_{Lv} is necessary, but errors of less than an order of magnitude should not compromise this effort. The normalization with mixing layer depth and velocity is appropriate for scaling to other similarly confined laboratory flows, but any full-scale application may require a different estimate of T_{Lv}. The normalization factors U_H and H cancel out in the TTPL model where only ratios of travel times and averaging time to the Lagrangian time scale are used.

2.5.5 Travel Time t_t Estimates

There is some uncertainty in the travel time of the plume because the vertical plume spread σ_z increases with t_t and in a boundary layer the plume samples a range of different velocities $U(z)$ over its vertical extent. It is not immediately obvious which velocity sampled by the plume should be used to calculate the ensemble averaged travel time. The water channel experiments consistently produce cross-stream plume spreads σ_y that decrease with height z indicating that the travel time at large z is shorter than the travel time at small z. This implies that the local flow velocity at the measurement height z should be be used to determine the travel time. Using the local flow velocity $U(z)$ the travel times are given below:

Shear Flow for $x/H = 2.5$ downstream of the source

- $t_tU_H/H = 7.8$ at $(z-d)/H = 0.011$ which is the lowest measurement point in the shear flow (6 mm above the bottom of the channel) where the velocity shear $\mathrm{d}U/\mathrm{d}z$ is large.

- $t_tU_H/H = 4.4$ at $(z-d)/H = 0.058$, a mid height position (25 mm above the bottom of the channel) between the high shear and the low shear measurement positions.

- $t_tU_H/H = 3.8$ at $(z-d)/H = 0.12$ which is the vertical position of the elevated source (50 mm above the bottom of the channel), the highest vertical position considered in this study, and a positions with relatively little shear.

Grid Turbulence for $x/G = 13.1$ downstream, $t_t U/G = 13.1$ at all z positions because the velocity profile is uniform with z.

At the same heights, travel times to other downstream distances are linearly proportional to the times given above.

2.5.6 Testing the TTPL Model for Averaging Time Adjustments to Plume Spread

To examine the applicability of the TTPL model, both the plume spread σ_y variation and the meander parameter M_{spread} variation with t_{avg} will be considered.

Four source types and flow conditions are presented as examples to cover the wide range of conditions tested.

1. Iso-kinetic horizontal jet source in grid turbulence, measured on vertical source centreline.

2. Large ground level source in shear flow, measured at ground level just above the roughness at $(z-d)/H = 0.011$.

3. Iso-kinetic horizontal jet source at $(h-d)/H = 0.12$ in shear flow, measured at source height $(z-d)/H = 0.12$.

4. Horizontal ground level jet source at $(h-d)/H = 0.013$ in shear flow, measured at ground level just above the roughness at $(z-d)/H = 0.011$. The flow rate of this source is the same as the flow rate of the iso-kinetic horizontal jet source.

Results from the other source configurations and measurement positions can be seen in Appendix G.

2.5.7 Plume Spread

Figures 2.26 and 2.27 show the plume spread ratios $\sigma_{y,t_{\text{avg}}}/\sigma_{y,\infty}$ for the data and the TTPL model Equation (2.18) with a reference averaging time of $t_{\text{ref}} \to \infty$ and the r_1 value from Equation (2.26). The 0.2 power law from Equation (2.17) is also shown for comparison. There are no empirical constants used to fit the TTPL model to the water channel data. The r_1 parameter is fit to Gifford's analytical solution of the random force model and the Lagrangian time scale T_{Lv} was determined as discussed in the previous section.

For the shear flow, the shape and the trends of the TTPL model are approximately correct. The worst fits are for positions close to the source ($x/G = 6.6$ in grid turbulence and $x/H = 1.25$ in shear flow). These points have short normalized averaging times where the plume spread ratio for the TTPL model is about 15% too high. In grid turbulence, the data shows a very rapid change in plume spread between $t_{\text{avg}}U/G = 0.1$ and 20 that is not accurately reflected in the TTPL model.

More importantly, the TTPL model predicts differences with downstream distance in grid turbulence that are not evident in the data.

It is odd that the grid turbulence fit is the poorest because it is by far the simplest, most idealized flow. Gifford's original random force model and the TTPL model have no terms that account explicitly for shear effects, yet the best fit of theory to experiment is in the shear flow. There may be some interesting physics that cause this effect, but the current data set is insufficient to provide any enlightenment on this subject. In terms of atmospheric dispersion modelling, the shear flow case is the most important and grid turbulence is only a curiosity, so based on the present experimental evidence the TTPL model is the best available method for predicting plume spread changes with averaging time.

In all cases, the TTPL model fits the data much better than the 0.2 power law over a range of averaging times covering 4 orders of magnitude. The fit between TTPL and the data could be improved by altering the cross stream Lagrangian time scale T_{Lv}, but there is little justification for doing this based on available information. Lagrangian scales are extremely difficult to measure or predict so this will always be a limitation on the accuracy of the TTPL model.

2.5.8 Meander

Figure 2.28 and 2.29 show the measured meander M_{spread}, compared to the meander predicted by the TTPL model from Equations (2.25) with r_1 from Equation (2.26). As stated earlier, the M_{spread} value may be interesting but it has little practical application for dispersion and concentration fluctuation modelling.

The basic shape of the TTPL model is well-supported by the meander data as well as the spread data, but the absolute numerical prediction of M_{spread} is poor. The meander prediction is as much as a factor of 5 different for the shear flow cases and as much as 2 orders of magnitude underestimated in grid turbulence. The general shape of meander M_{spread} from the TTPL is a power law with a slope of approximately 1.0 at small averaging times levelling off to a steady value as averaging time becomes large. The meander values are under-predicted by up to an order of magnitude at large averaging times. At small averaging times, meander is under-predicted for elevated measurement positions and over-predicted for ground level measurements.

The 0.2 power law from Equation (2.17) is also represented in Figures 2.28 and 2.29. Calculating the meander from the power law presents some difficulties because using $\sigma_{y,i}$ as $\sigma_{y,\text{ref}}$ means that the reference time is $t_{\text{ref}} = 0$. Equation (2.17) can be reformulated in terms of the meander at some reference time as

$$M_{\text{spread}} = \left(\frac{t}{t_{\text{ref}}}\right)^{0.4} (1 + M_{\text{spread,ref}}) - 1 \tag{2.41}$$

but this equation causes the meander to increase rapidly for times slightly greater than t_{ref} and then level off to a 0.4 power law form. (Note that the 0.4 power law is a direct result of the 0.2 power law for plume spread adjustments as applied to

M_{spread} which is a ratio of the squares of plume spreads.) At times less than t_{ref} it gives a negative meander. Even when these problems are ignored, the 0.2 power law averaging time slope shown in Figures 2.28 and 2.29 matches the data only over a small range.

2.6 Summary and Conclusions

As stated in the introduction, this study can be considered as both a water channel study of a dispersion of a high Schmidt number (low molecular diffusivity) tracer and as a small-scale model of dispersion in a neutrally stable full-scale atmosphere. The ultimate goal is to apply this information to a model for full-scale atmospheric dispersion and concentration fluctuations. The conclusions will be made in terms of these perspectives.

The linescan LIF measurement technique developed in this study enabled the collection of detailed one-dimensional measurements of fluorescent dye plumes dispersing in a water channel. Measurements of concentrations were made at a rate of 500 Hz simultaneously at 1024 points across the plume with total sample times of 500 seconds. The measuring volume for each point was approximately 0.5 mm by 1 mm. This high temporal and spatial resolution allows concentration fluctuation parameters and short time average $t_{\text{avg}} \rightarrow 0$ properties of the plume to be measured directly. The plume centroid can be tracked in one dimension to eliminate meandering.

As a model of the full-scale atmosphere, the water channel is geometrically a 1:1000 scale model of a neutral boundary layer with a depth of 400 m. The equivalent measurement volume is on the order of 1 m in full scale. Using a full-scale wind speed of 3 m/s at 10 m above the ground, time in the water channel scales approximate 1:30 which means the full-scale equivalent sampling rate is 16 Hz with a total measurement time of about 4 hours.

Data collected from a variety of sources in both a shear flow boundary layer and shear free grid turbulence were used to verify the applicability of a pseudo-meandering plume based concentration fluctuation model proposed by Wilson (1995) and an improved travel time power law model (TTPL) for averaging time adjustment. The models were then tested against the water channel data. Based on this data set the following conclusions can be made.

- Averaging time effects on a dispersing plume can only be accurately measured by tracking the plume centroid and comparing ensembles of plumes with the time averaged centroid positions aligned. This requires a measurement technique, such as the linescan LIF technique in the water channel, that can measure enough simultaneous points to allow determination of the centroid position. For wind tunnel or full-scale measurements, averaging time effects may have to be estimated from much sparser data sets.

- The concentration fluctuation intensity i in the plume changes with averaging time in parallel with the changes in the time averaged plume spread $\sigma_{y,t_{\text{avg}}}$. This simplifies the modelling of concentration fluctuations because gross plume parameters such as spreads are generally easier to model than high frequency concentration fluctuations.

- The meander parameter based on the large scale meandering of the plume M_{spread} is much less than the concentration fluctuation intensity based pseudo-meander $M_{\text{intensity}}$ required to account for all of the fluctuations measured in the water channel plumes. This implies that most of the concentration fluctuation is caused by internal plume structures.
- Despite the above conclusion, the meandering plume model remains a useful tool to predict concentration fluctuations. Using pseudo-meander $M_{\text{intensity}}$ in the model for cross-stream variation in fluctuation intensity i produces excellent results compared with the water channel data.
- The instantaneous centroid $\overline{y}$ of the plume meanders in the cross-stream direction in a random additive process that produces a Gaussian distribution for the centroid position. There is no immediate application for this information, but it is an interesting result that demonstrates that meandering is a simple Gaussian process which may be useful for future modellers.
- The instantaneous plume spread $\sigma_{y,ii}$ has a probability distribution that is well described by a clipped lognormal. In grid turbulence there are significant periods of time during which the plume meanders entirely outside of the measurement volume and the clipped lognormal distribution accounts for this. In the shear flow cases that were measured, the clipped lognormal reduced to a standard lognormal distribution because the vertical meander was small and there was always measurable dye in the measurement volume. The application for this information is not immediately apparent, but it does confirm that the clipped lognormal probability distribution is a good fit for the random multiplicative dilution processes in a plume. The fact that clipping the distribution produces good results indicates that the intermittent periods are an essential part of the dilution process and are characterized by the part of the distribution that is clipped.
- The travel time power law (TTPL) model for averaging time adjustment of plume spread σ_y with the improved empirical parameter r_1 describes the effect of averaging time on plume spread and meander much better than the commonly used 0.2 power law. The limiting factor is the ability to estimate the cross-stream Lagrangian time scale T_{Lv}. This will continue to be an issue in both laboratory scale and full-scale conditions and warrants additional research. However, as demonstrated in this study even relatively uncertain estimates of T_{Lv} provide reasonable answers for averaging time adjustment and the accuracy will only improve with better T_{Lv} estimates.

- Plume meander M_{spread} can be modelled with the TTPL, but with less accuracy than the plume spread. M_{spread} is not very useful for further calculations because it does not account for any of the concentration fluctuations inside the plume.

- One limitation of the water channel data is that the flow is confined and the extent of plume meandering is restricted by the size of the experiment. This limits the largest scales that can be simulated, and hence very long time averages cannot be simulated. However, in terms of the ratio of travel times and averaging time to Lagrangian scales, the water channel results are very comparable to full scale. The laboratory averaging times range from 0.001 T_{Lv} to 10 T_{Lv} (from instantaneous measurement up to about 10 seconds of averaging time). Scaled up to the full scale atmosphere with a typical T_{Lv} of $1,000$ to $10,000$ s (Wilson (1995)) this equates to averaging times of 1 second to 10 hours. In this respect the water channel is almost a perfectly scaled down version of the full-scale atmosphere. Over this realistic range, the experimental evidence suggests that the TTPL model and the corresponding meandering plume relationships for concentration fluctuations are much more accurate that the standard 0.2 power law averaging time adjustment.

- Another limitation of the present data set is that all of the source sizes tested were effectively small area source in comparison with the turbulent scales in the channel. Source size had no measurable effect on any of the experiments. Further investigation with a larger range of source sizes and a range of measurement positions closer to the source would provide more insight into the role of the source size term in the TTPL model for averaging time.

—

References

Arcoumanis, C., McGuirk, J., and Palma, J. (1990), On the use of fluorescent dyes for concentration measurements in water flows, *Experiments in Fluids*, 10:177–180.

Bara, B. M., Wilson, D. J., and Zelt, B. W. (1992), Concentration Fluctuation Profiles from a Water Channel Simulation of a Ground-Level Release, *Atmospheric Environment*, 26A(6):1053–1062.

Barr, S. and Gifford, F. (1987), The Random Force Theory Applied to Regional Scale Tropospheric Diffusion, *Atmospheric Environment*, 21:1737–1741.

Crimaldi, J. (1997), The effect of photobleaching and velocity fluctuations on single-point LIF measurements, *Experiments in Fluids*, 23:325–330.

Crimaldi, J. P. and Koseff, J. R. (2001), The structure of passive scalar plumes in turbulent boundary layers, In *Proceedings of the 2nd International Symposium on Turbulence and Shear Flow Phenomena, vol. I*, pages 115–120, Stockholm, Sweden, June 27-29.

Crimaldi, J. P., Wiley, M. B., and Koseff, J. R. (2002), The relationship between mean and instantaneous structure in turbulent passive scalar plumes, *Journal of Turbulence*, 3(014).

Distellhoff, M. F. W. and Marquis, A. J. (1998), An LIF line scan system for the measurement of scalar concentration in a continuously operated stirred tank, *Experiments in Fluids*, 25:77–88.

Gifford, F. (1959), Statistical Properties of a Fluctuating Plume Dispersion Model, In *Proceedings of Symposium on Atmospheric Diffusion and Air Pollution*, pages 117–137, New York. Academic Press.

Gifford, F. (1982), Horizontal Diffusion in the Atmosphere: A Lagrangian-Dynamical Theory, *Atmospheric Environment*, 16(3):505–512.

Gifford, F. (1984), The Random Force Theory: Application to Meso- and Large-Scale Atmospheric Diffusion, *Boundary-Layer Meteorology*, 30:159–175.

Guilbault, G. G. (1973), *Practical Fluorescence: Theory, Methods and Techniques*, Marcel Dekker Inc., New York.

Hanna, S. R., Drivas, P. J., and Chang, J. J. (1996), *Guidelines for Use of Vapor Cloud Dispersion Models*, Center for Chemical Process Safety of the American Institute of Chemical Engineers, New York, NY, second edition.

Hay, J. S. and Pasquill, F. (1960), Diffusion from a Continuous Source in Relation to the Spectrum and Scale of Turbulence, *Advances in Geophysics*, 6:345–365.

Hilderman, T. L., Hrudey, S. E., and Wilson, D. J. (1999), A Model for Effective Toxic Load from Fluctuating Gas Concentrations, *Journal of Hazardous Materials A*, 64:115–134.

Hilderman, T. L. and Wilson, D. J. (1999), Simulating Concentration Fluctuation Time Series with Intermittent Zero Periods and Level Dependent Derivatives, *Boundary-Layer Meteorology*, 91:451–482.

Hinze, J. (1975), *Turbulence*, McGraw-Hill, second edition.

Jørgensen, H. E. and Mikkelsen, T. (1993), LIDAR Measurements of Plume Statistics, *Boundary-Layer Meteorology*, 62:361–378.

Karasso, P. S. (1994), *Experiments on Mixing and Reaction in Plane and Curved Turbulent Shear Layers*, PhD thesis, Stanford University.

Koeltzsch, K. (1999), On the relationship between the Lagrangian and Eulerian time scale, *Atmospheric Environment*, 33:117–128.

Koochesfahani, M. M. and Dimotakis, P. E. (1985), Laser-Induced Fluorescence Measurements of Mixed Fluid Concentration in a Liquid Plane Shear Layer, *AIAA Journal*, 23(11):1700–1707.

Koochesfahani, M. M. and Dimotakis, P. E. (1986), Mixing and chemical reactions in a turbulent liquid mixing layer, *Journal of Fluid Mechanics*, 170:83–112.

Lee, J. T. and Stone, G. L. (1984), Eulerian-Lagrangian Relationships in Monte Carlo Simulations of Turbulent Diffusion, *Atmospheric Environment*, 17(12):2483–2487.

Massman, W. and Weil, J. (1999), An Analytical One-Dimensional Second-Order Closure Model of Turbulence Statistics and the Lagrangian Time Scale Within and Above Plant Canopies of Arbitrary Structure, *Boundary-Layer Meteorology*, 91:81–107.

McComb, W. (1990), *The Physics of Fluid Turbulence*, Oxford University Press.

Molecular Probes Inc. (2002), Handbook of Fluorescent Probes and Research Products, Web Edition, continuously updated at http://www.probes.com/handbook/.

Pasquill, F. and Smith, F. (1983), *Atmospheric Diffusion*, John Wiley and Sons, third edition.

Sawford, B. L. and Stapountzis, H. (1986), Concentration Fluctuations According to Fluctuating Plume Models in One and Two Dimensions, *Boundary-Layer Meteorology*, 37:89–105.

Saylor, J. (1995), Photobleaching of disodium fluorescein in water, *Experiments in Fluids*, 18:445–447.

Taylor, G. (1921), Diffusion by Continuous Movements, *Proceedings of the London Mathematical Society*, 20:196–212.

Walker, D. A. (1987), A fluorescence technique for measurement of concentration in mixing liquids, *Journal of Physics E, Journal of Scientific Instruments*, 20:217–224.

Wandel, C. F. and Kofoed-Hansen, O. (1962), On the Eulerian-Lagrangian Transform in the Statistical Theory of Turbulence, *Journal of Geophysical Research*, 67(8):3089–3093.

Wilson, D. (1981), Along-Wind Diffusion of Source Transients, *Atmospheric Environment*, 15:489–495.

Wilson, D., Fabris, I., Chen, J., and Ackerman, M. (1998), Adjacent Building Effects of Laboratory Fume Hood Exhaust Stack Design, Technical report, University of Alberta, Final Report ASHRAE Research Project 897.

Wilson, D. J. (1995), *Concentration Fluctuations and Averaging Time in Vapor Clouds*, Center for Chemical Process Safety of the American Institute of Chemical Engineers, New York, NY.

Yee, E., Chan, R., Kosteniuk, P., Chandler, G., Biltoft, C., and Bowers, J. (1994), Incorporation of Internal Fluctuations in a Meandering Plume Model of Concentration Fluctuations, *Boundary-Layer Meteorology*, 67:11–39.

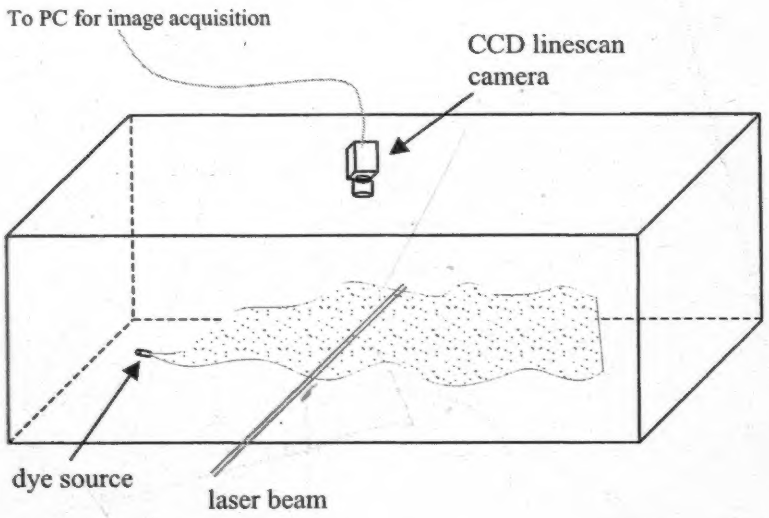
To PC for image acquisition
CCD linescan camera
dye source
laser beam

Figure 2.1: Schematic of linescan measurement experiments. Typical configuration for measuring cross-stream profiles of concentration.

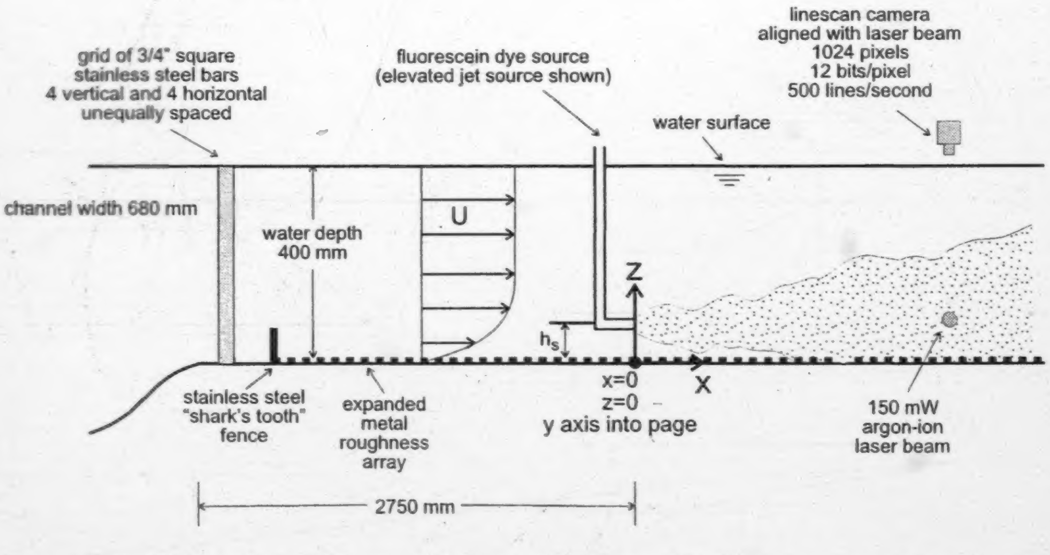
grid of 3/4" square stainless steel bars 4 vertical and 4 horizontal unequally spaced
fluorescein dye source (elevated jet source shown)
linescan camera aligned with laser beam 1024 pixels 12 bits/pixel 500 lines/second
water surface
channel width 680 mm
water depth 400 mm
U
Z
h_s
x=0
z=0
y axis into page
X
stainless steel "shark's tooth" fence
expanded metal roughness array
150 mW argon-ion laser beam
2750 mm

Figure 2.2: University of Alberta Mechanical Engineering Department water channel schematic. The recirculation piping, downstream weir gate, and inlet plenum flow straighteners are not shown. Coordinate system origin is at ground level on the channel centreline at the downstream location of the tracer source. Laser beam diameter is approximately 1 mm and projects into the page.

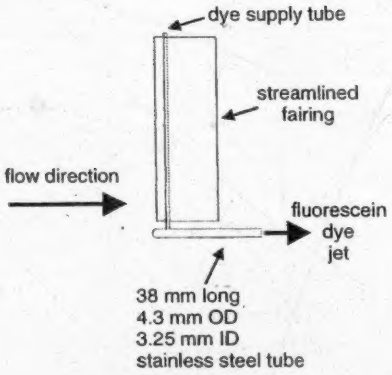
dye supply tube
streamlined fairing
flow direction
fluorescein dye jet
38 mm long
4.3 mm OD
3.25 mm ID
stainless steel tube

Horizontal Jet Source - Side View

(a)

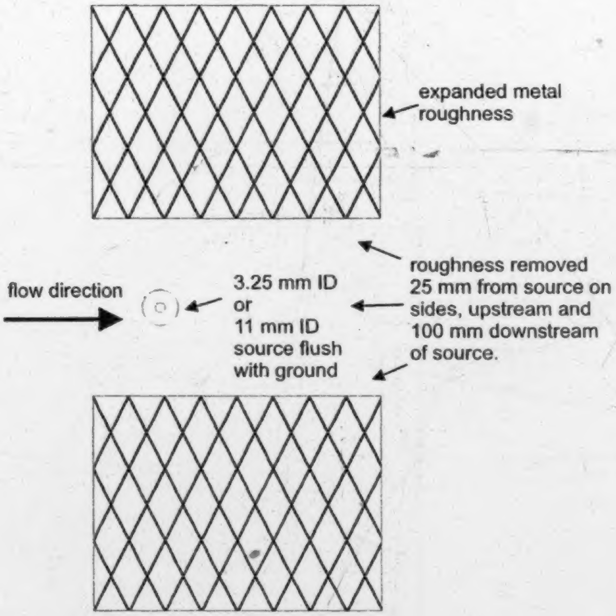
expanded metal roughness
flow direction
3.25 mm ID
or
11 mm ID
source flush
with ground
roughness removed
25 mm from source on
sides, upstream and
100 mm downstream
of source.

Ground Level Sources - Top View

(b)

Figure 2.3: Fluorescein dye sources: (a) Side view of elevated horizontal jet sources. Source was suspended from above the channel. (b) Top view of ground level sources. Expanded metal roughness was removed from the immediate area of the source and dye supply lines were underneath the acrylic panel below the roughness. The large (11 mm ID) ground level source was changed to the small ground level source by inserting a plug with a 3.25 mm ID hole for the small source.

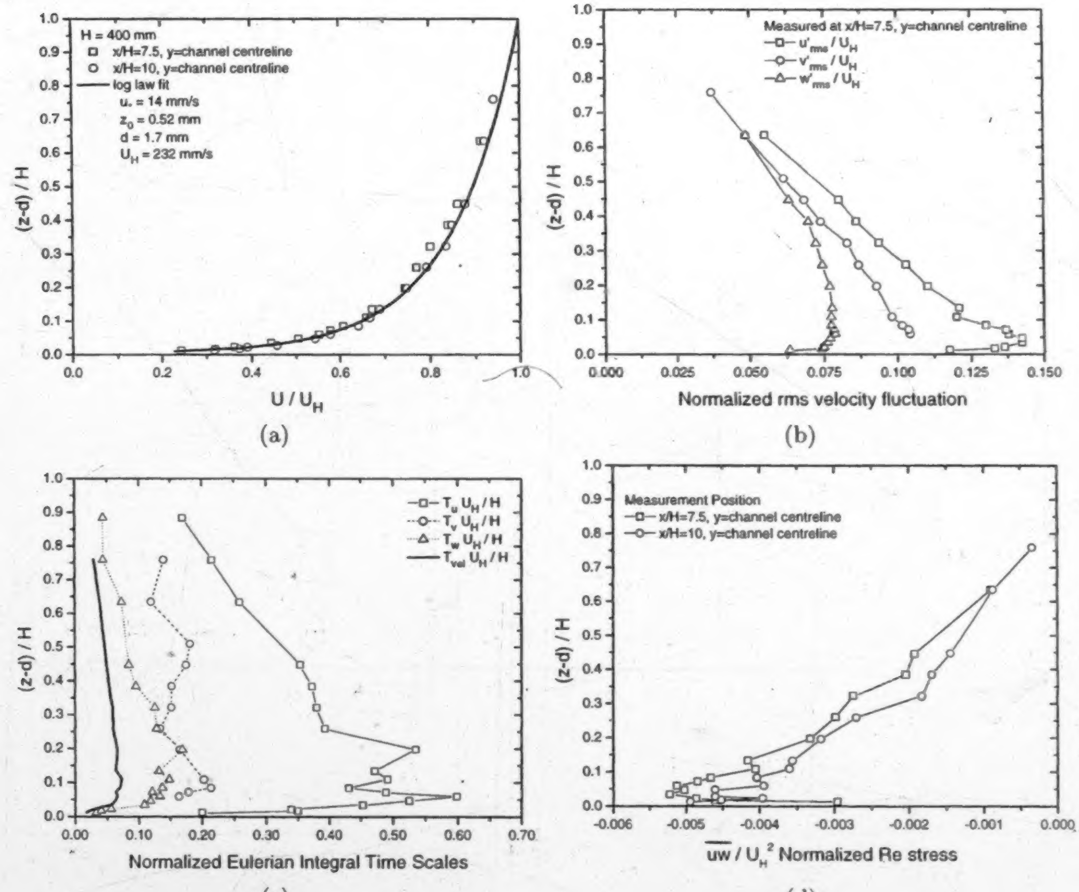

(a) (b) (c) (d)

Figure 2.4: Velocity statistics for the rough surface boundary layer shear flow. measured at 3000 mm ($x/H = 7.5$) downstream from the water channel inlet. (a) Normalized vertical profiles of the mean streamwise velocity U/U_H. (b) Normalized vertical profiles of the rms fluctuating velocity components u'_{rms}/U_H, v'_{rms}/U_H, and w'_{rms}/U_H. (c) Vertical profiles of the normalized Eulerian velocity fluctuation timescales, T_uU_H/H, T_vU_H/H, T_wU_H/H and $T_{\text{vel}}U_H/H$. (d) Vertical profiles of the normalized Reynolds stresses $\overline{uw}/U_H^2$

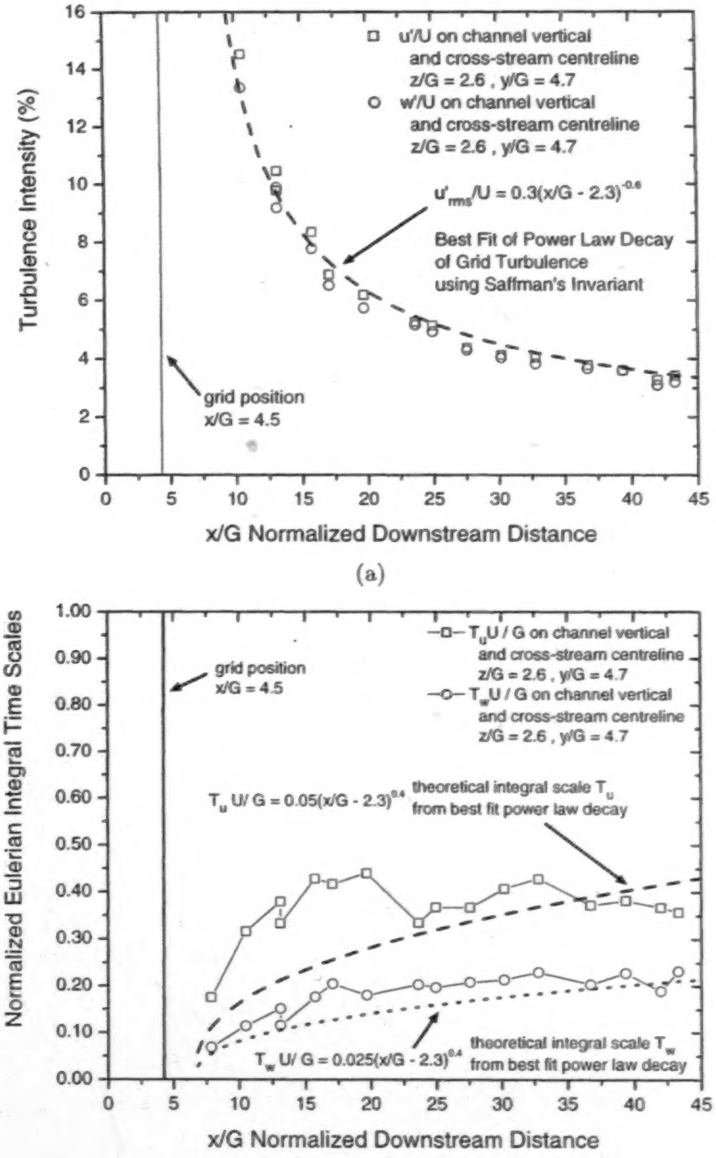

(a)

(b)

Figure 2.5: Grid turbulence velocity statistics. (a) Turbulence intensity decay with normalized downstream distance x/G along the centreline of the channel. Best fit power law decay of turbulence intensity based on Saffman's invariant. (b) Normalized Eulerian integral timescales of velocity fluctuation in the streamwise $T_u U/G$ and vertical $T_w U/G$ directions along the centreline of the channel compared to $T_u U/G$ calculated using the best fit power law decay of grid turbulence based on Saffman's invariant.

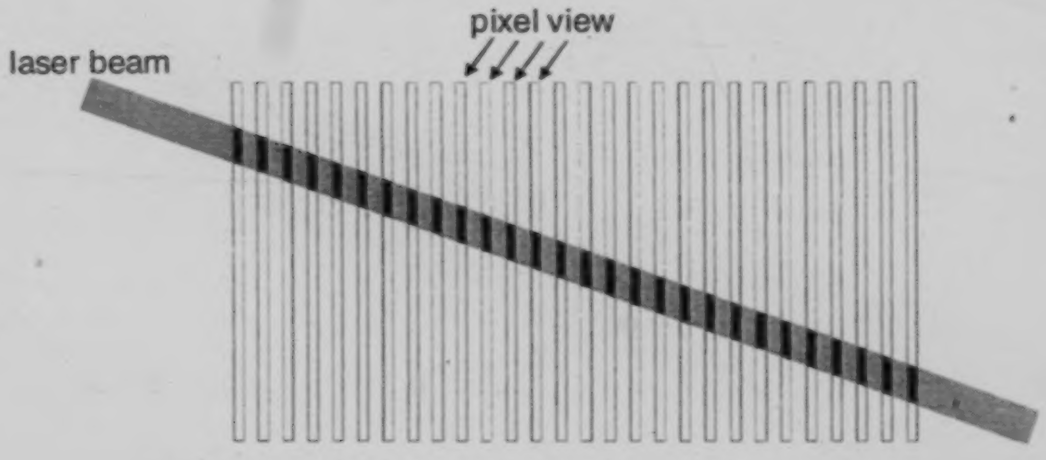
pixel view
laser beam

Figure 2.6: Field of view of the linescan camera compared to the width of the laser line. The Dalsa CLC6-2048T linescan camera pixels have an aspect ratio of 38:1.

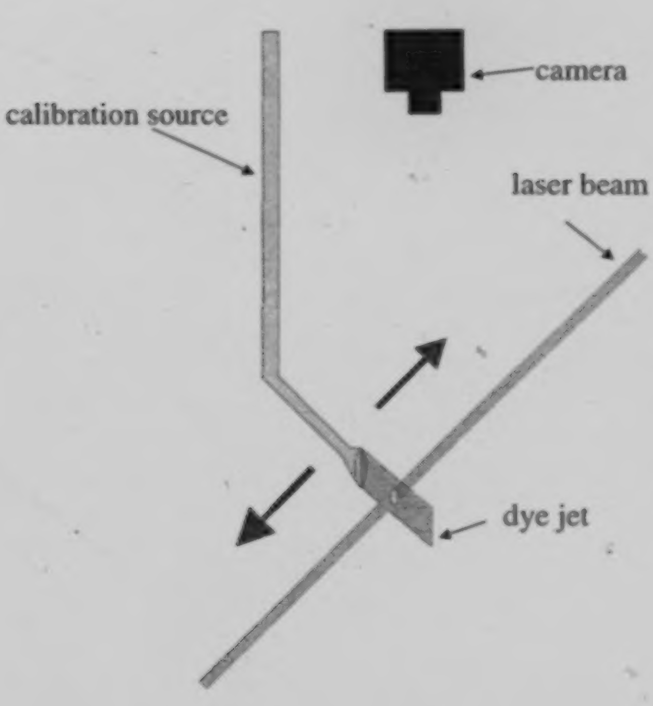
camera
calibration source
laser beam
dye jet

Figure 2.7: Laminar jet source used for calibration.

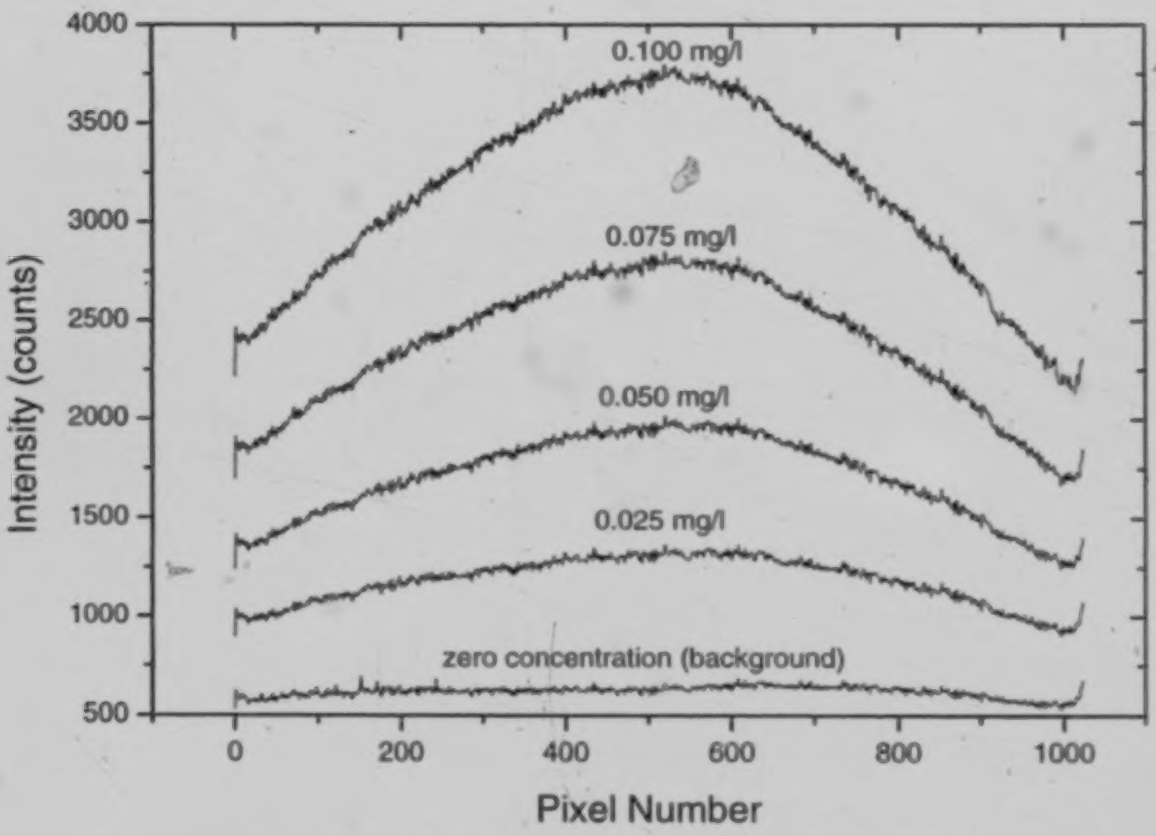

Figure 2.8: Typical raw data used for calibration. Zero concentration is the mean of 20 seconds of data, while the non-zero concentration values are the averages of the 10 highest values measured at each pixel using the laminar jet source in Figure 2.7.

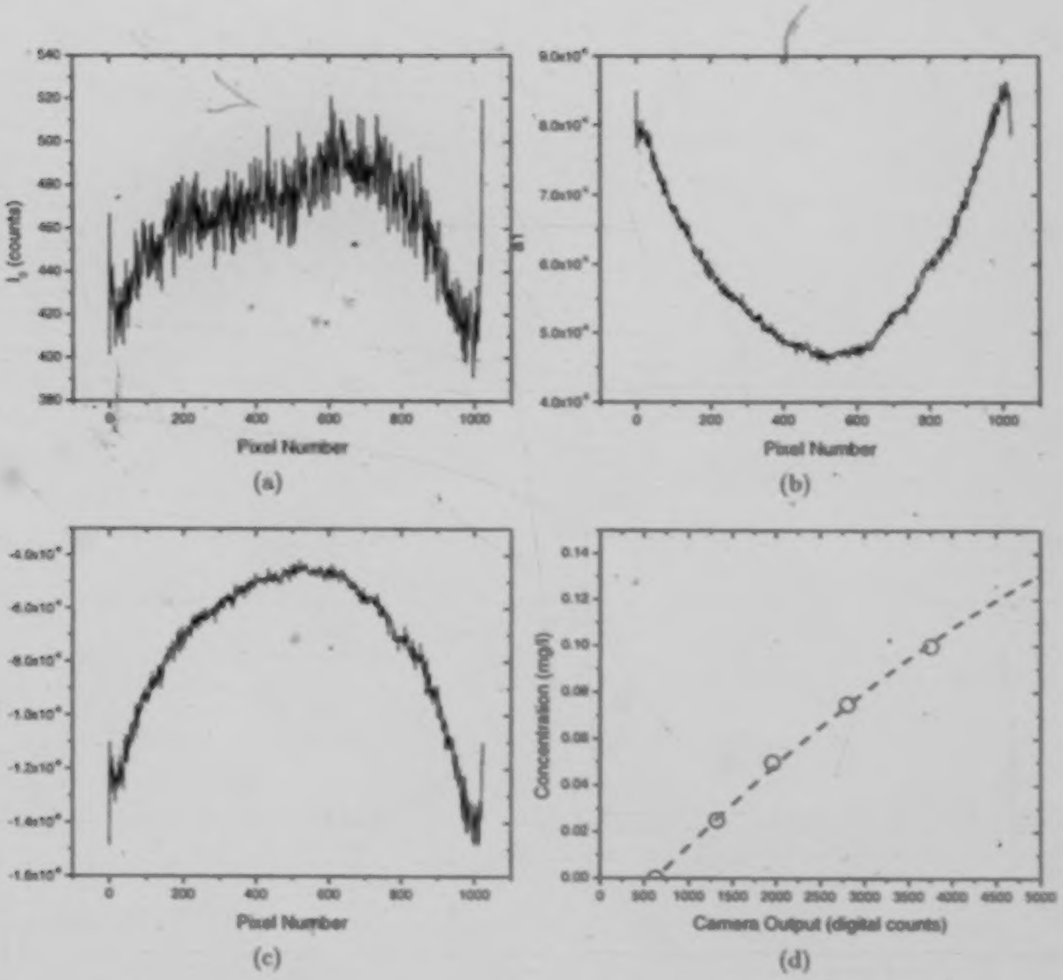

(a)
(b)
(c)
(d)

Figure 2.9: Typical calibration constant values for each pixel in the camera. (a) is the zero concentration intensity reading I_0, (b) is the a_1 value, (c) is the a_2 value, and (d) is a typical calibration curve for a pixel near the centre of the camera.

8

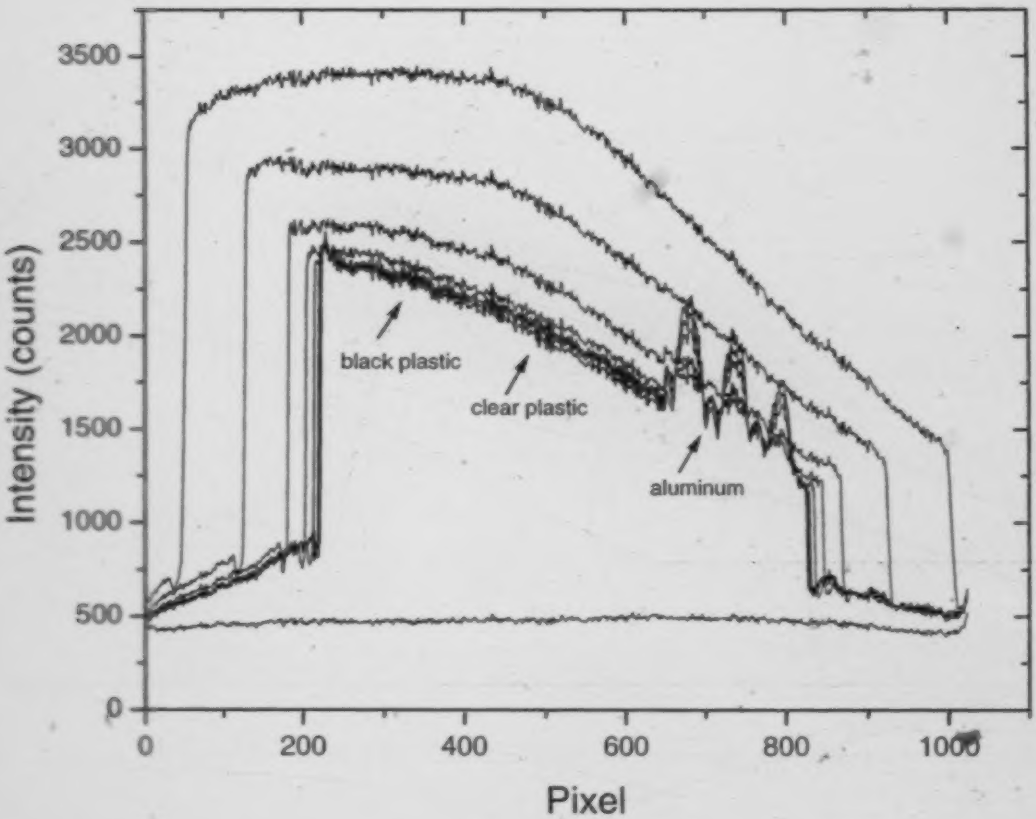

Figure 2.10: Raw data from tests for effect of the bottom surface. Each line is at a different height above the bottom of the channel. All roughness was painted flat black. There is no effect from the roughness over either black painted plastic or even clear plastic. The highly reflective aluminum can be seen at the lower level locations starting at about pixel 600.

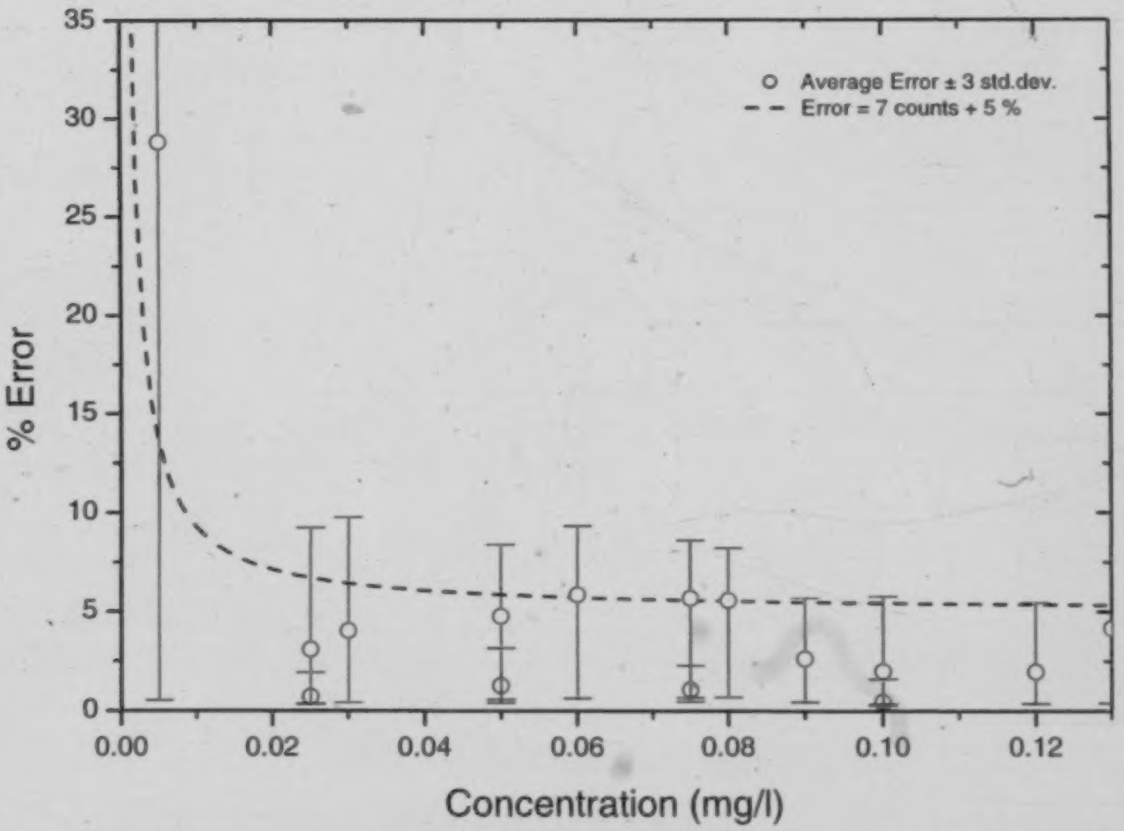

Figure 2.11: Accuracy of linescan concentration measurement system. Data points and error bars are mean errors ±3 standard deviations. Dotted line is 5% error with 7 digital counts added to simulate the error caused by electrical noise in the camera.

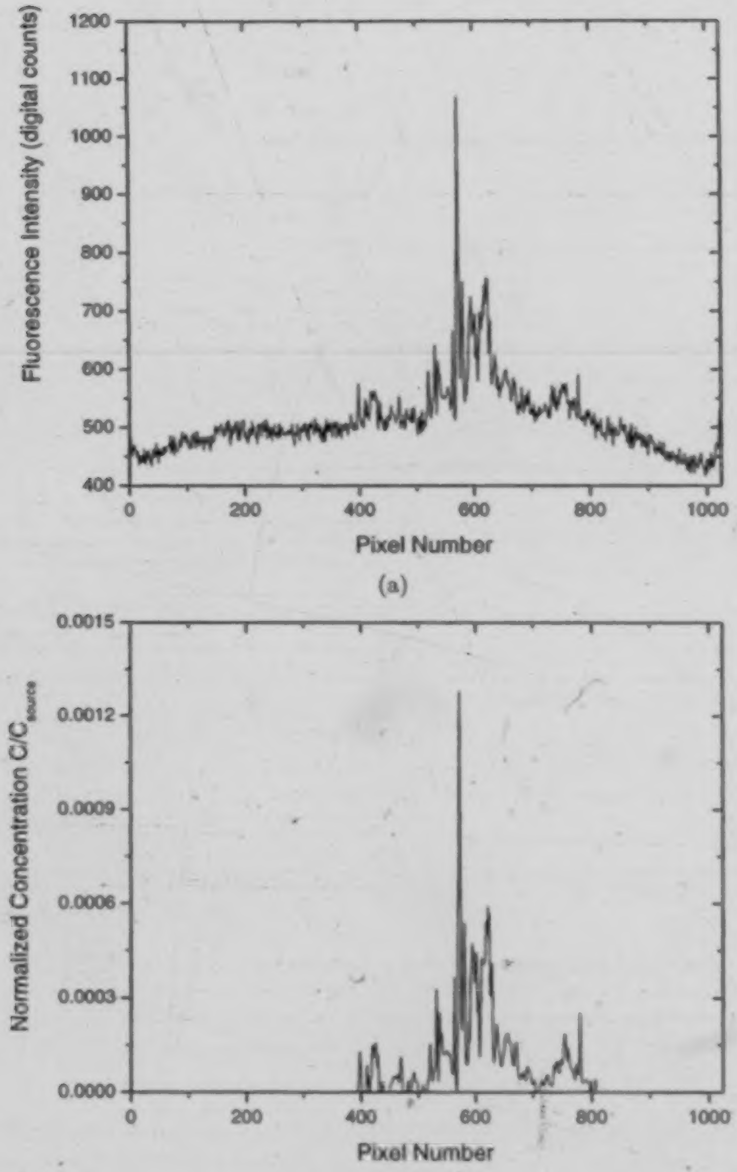

(a)

(b)

Figure 2.12: (a) Typical raw fluorescence data output for a single line (1/500 second). (b) After subtracting the background, correcting for attenuation, and applying the calibration equation, the result is an instantaneous concentration profile across the plume.

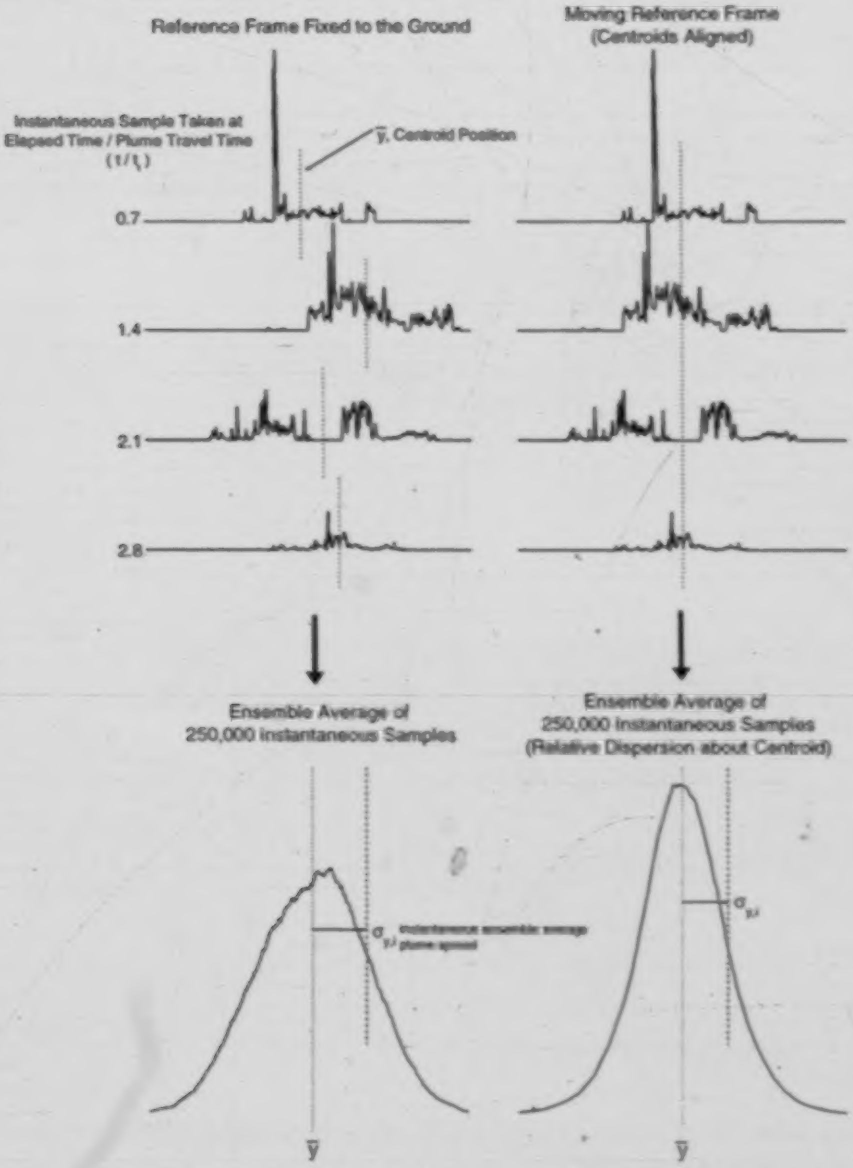

Figure 2.13: Samples of instantaneous plumes and ensemble averages. On the left, the reference frame is fixed to the ground and on the right the instantaneous centroids of each sample are aligned. Following the centroid removes the larger scale meander of the plume, reduces the plume spread and increases the centreline average concentration.

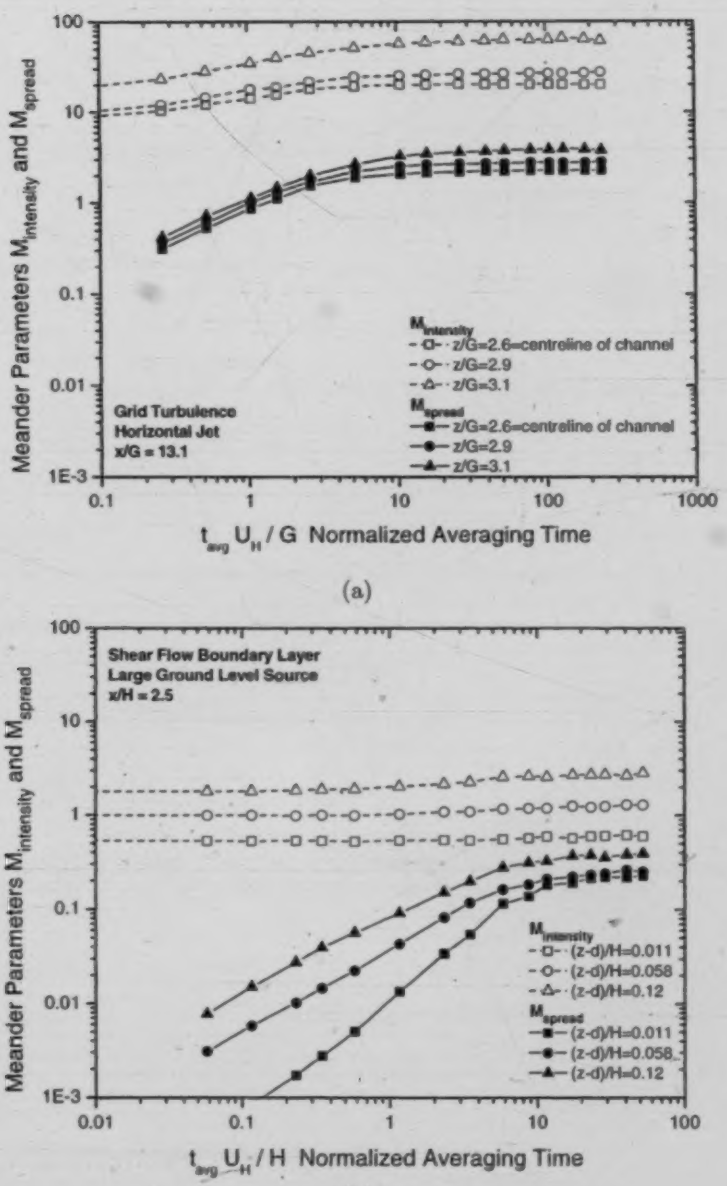

Figure 2.14: Samples of typical meander parameters $M_{\text{intensity}}$ and M_{spread} as a function of normalized averaging time $t_{\text{avg}}U_H/H$. (a) $x/G = 13.1$ downstream of the iso-kinetic jet source in grid turbulence (b) $x/H = 2.5$ downstream of the large ground level source in boundary layer shear flow.

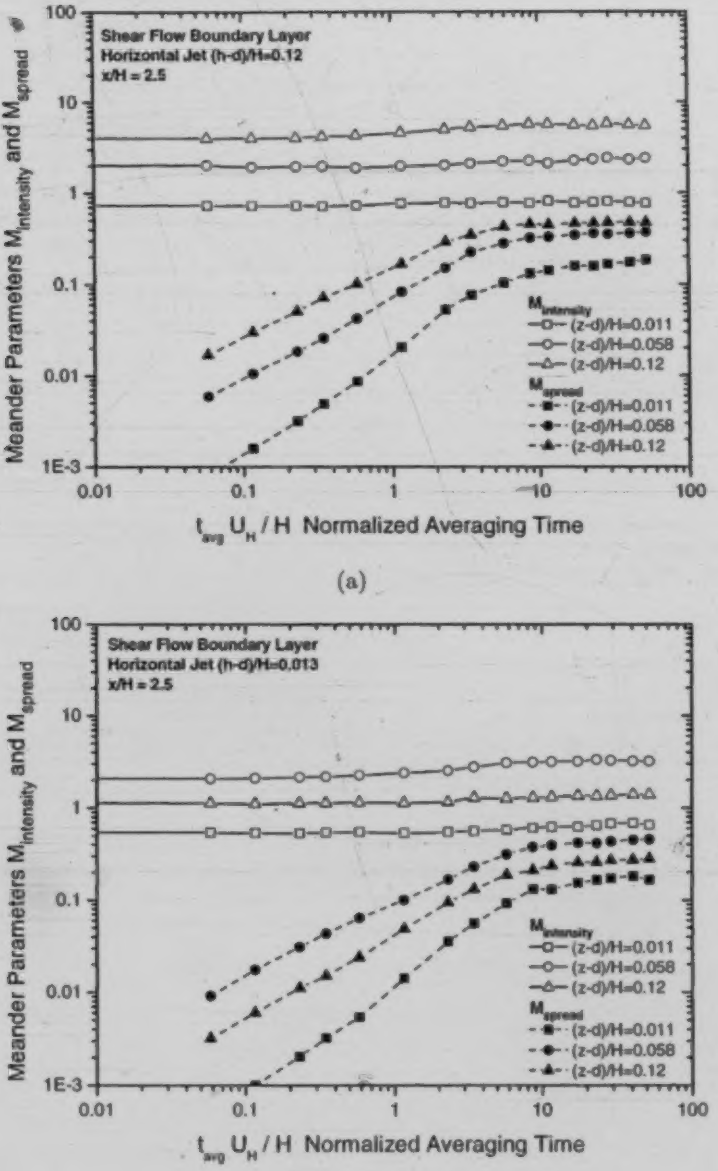

(a)

(b)

Figure 2.15: Samples of typical meander parameters $M_{\text{intensity}}$ and M_{spread} at $x/H = 2.5$ downstream of the source as a function of normalized averaging time $t_{\text{avg}}U_H/H$. (a) iso-kinetic horizontal jet $(h-d)/H = 0.12$ above the ground in shear flow (b) horizontal jet at ground level, $(h-d)/H = 0.013$ in shear flow.

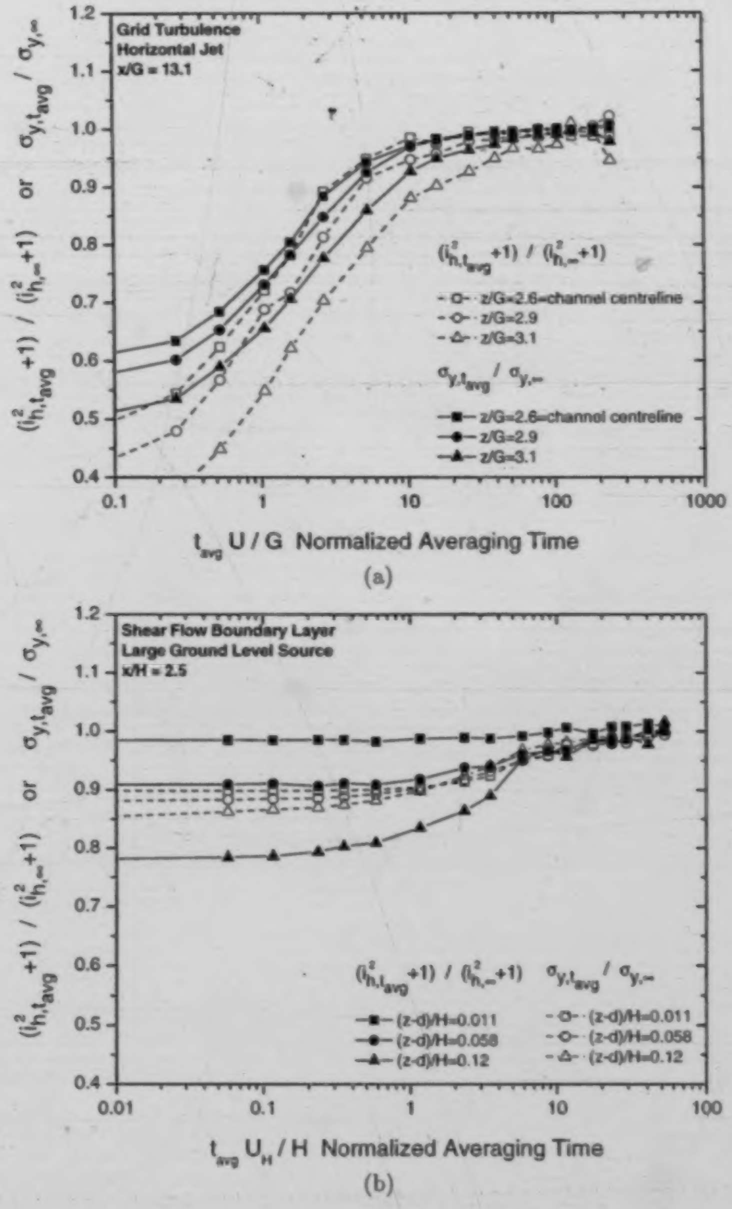

Figure 2.16: Samples of ratios $(i^2_{h,t_{avg}}+1)/(i^2_{h,\infty}+1)$ compared to $\sigma_{y,t_{avg}}/\sigma_{y,\infty}$ as a function of normalized averaging time $t_{avg}U_H/H$. (a) $x/G = 13.1$ downstream of the iso-kinetic jet source in grid turbulence (b) $x/H = 2.5$ downstream of the large ground level source in boundary layer shear flow.

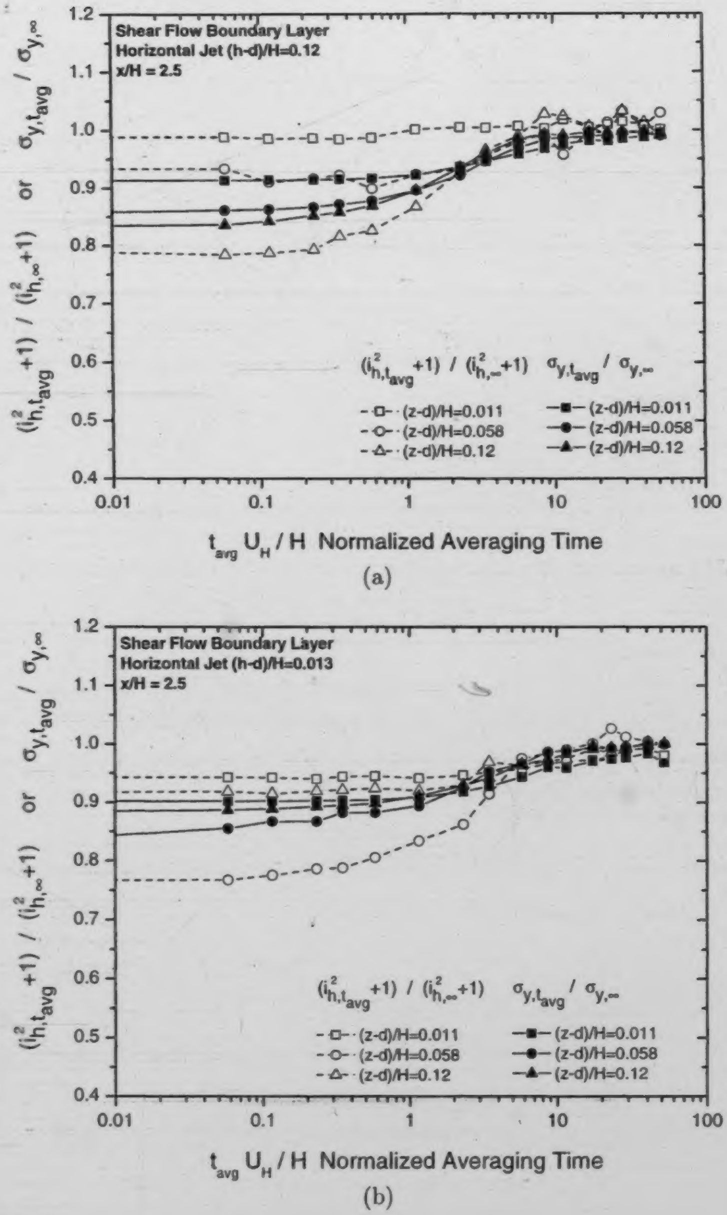

Figure 2.17: Samples of ratios $(i^2_{h,t_{\mathrm{avg}}}+1)/(i^2_{h,\infty}+1)$ compared to $\sigma_{y,t_{\mathrm{avg}}}/\sigma_{y,\infty}$ at $x/H = 2.5$ downstream of the source as a function of normalized averaging time $t_{\mathrm{avg}}U_H/H$. (a) iso-kinetic horizontal jet $(h-d)/H = 0.12$ above the ground in shear flow (b) horizontal jet at ground level, $(h-d)/H = 0.013$ in shear flow.

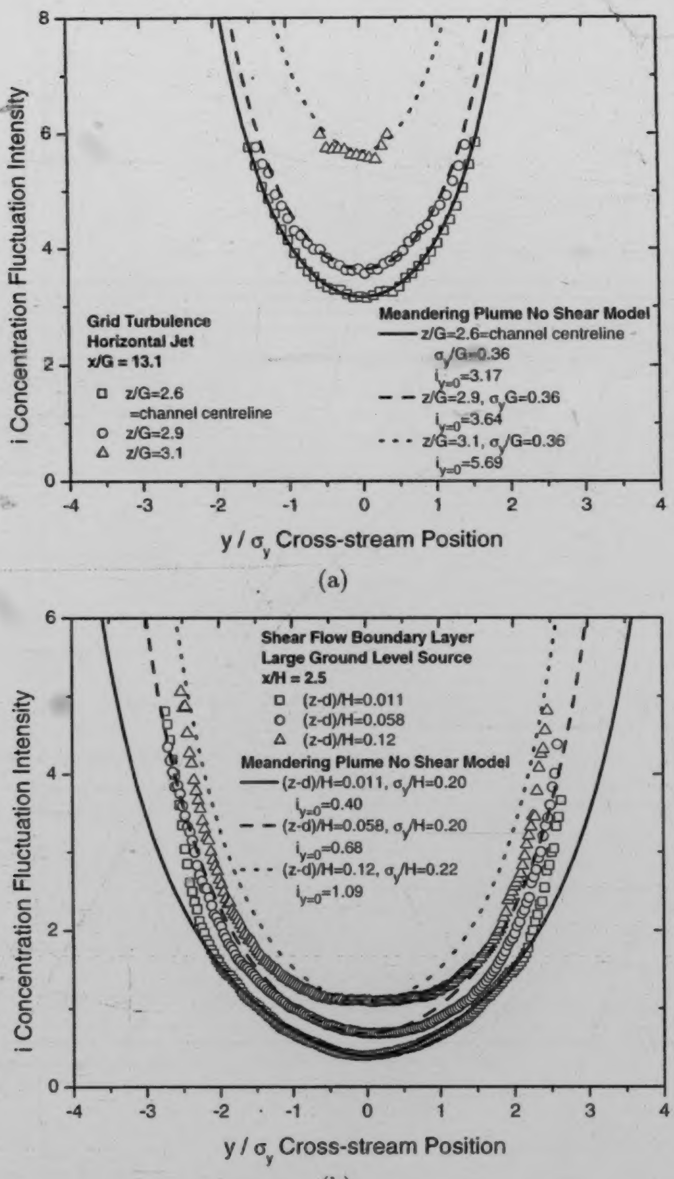

(a)

(b)

Figure 2.18: Samples of typical cross-stream profiles of concentration fluctuation intensity i compared to Equation (2.15) (a) $x/G = 13.1$ downstream of the iso-kinetic jet source in grid turbulence (b) $x/H = 2.5$ downstream of the large ground level source in boundary layer shear flow.

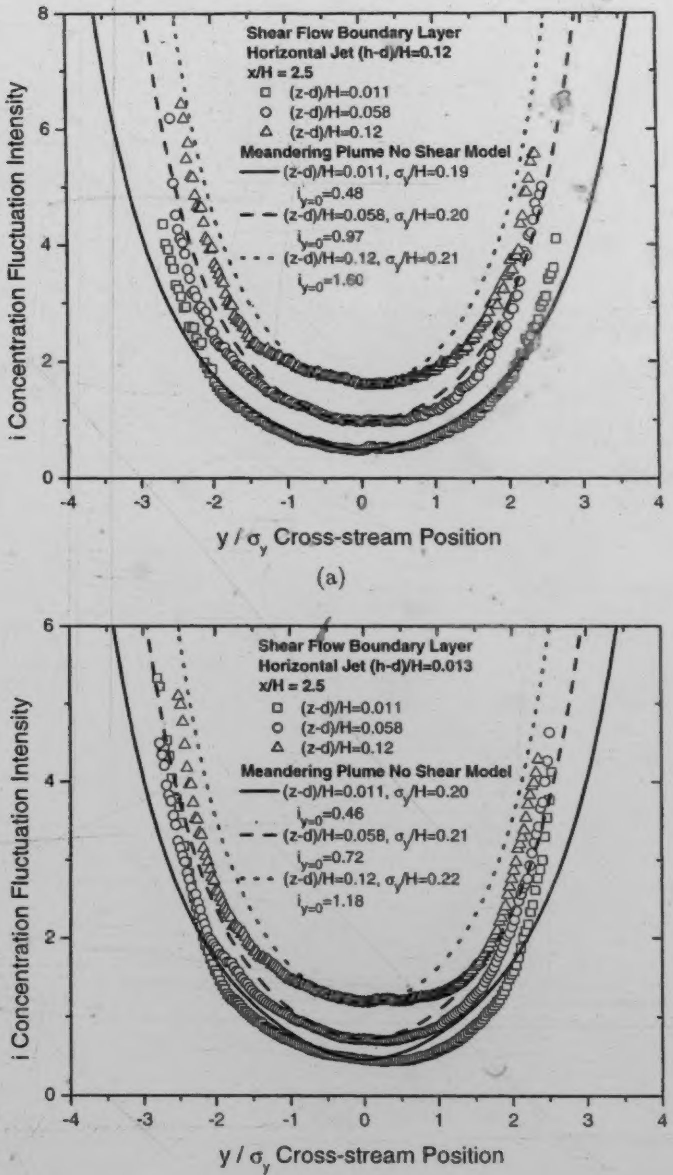

(a)

(b)

Figure 2.19: Samples of typical cross-stream profiles of concentration fluctuation intensity i compared to Equation (2.15) at $x/H = 2.5$ downstream of the source (a) iso-kinetic horizontal jet $(h-d)/H = 0.12$ above the ground in shear flow (b) horizontal jet at ground level, $(h-d)/H = 0.013$ in shear flow.

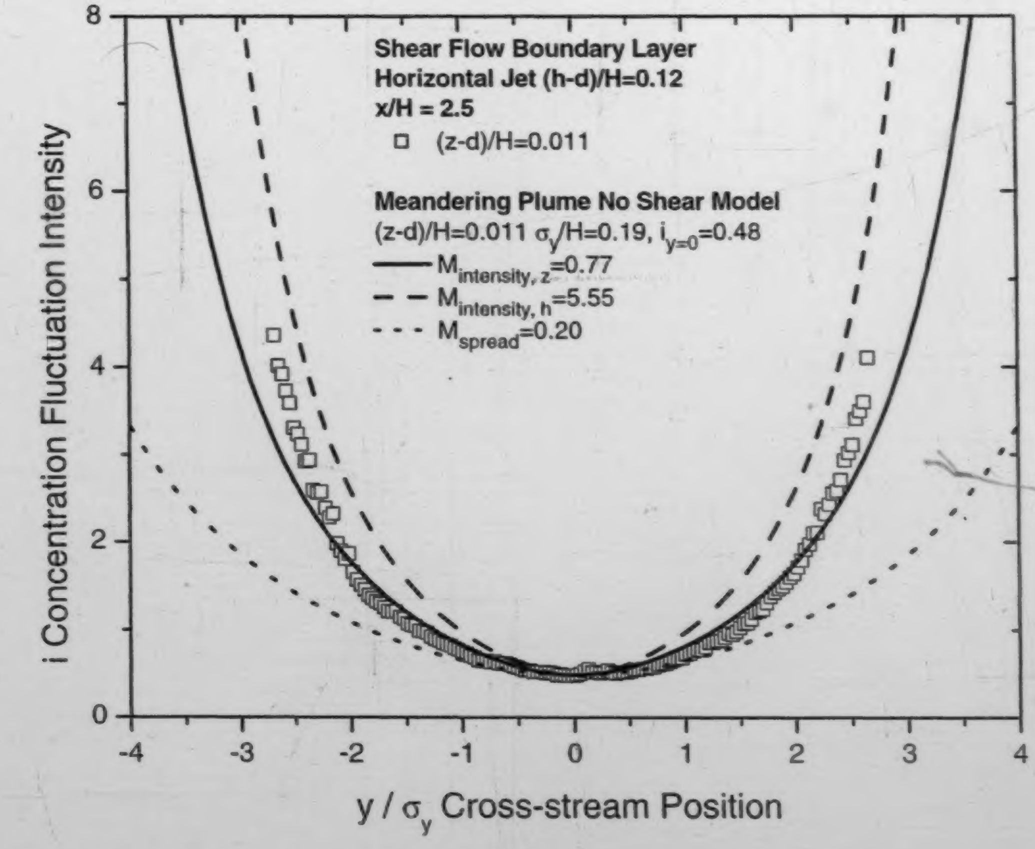

Figure 2.20: Cross-stream profiles of concentration fluctuation intensity i compared to Equation (2.15) using three possible meander parameter values $M_{\text{intensity},z}$ from $i_{y=0}$, $M_{\text{intensity},h}$ from i_h and M_{spread} from the plume spread ratio $\sigma_{y,m}/\sigma_{y_i}$.

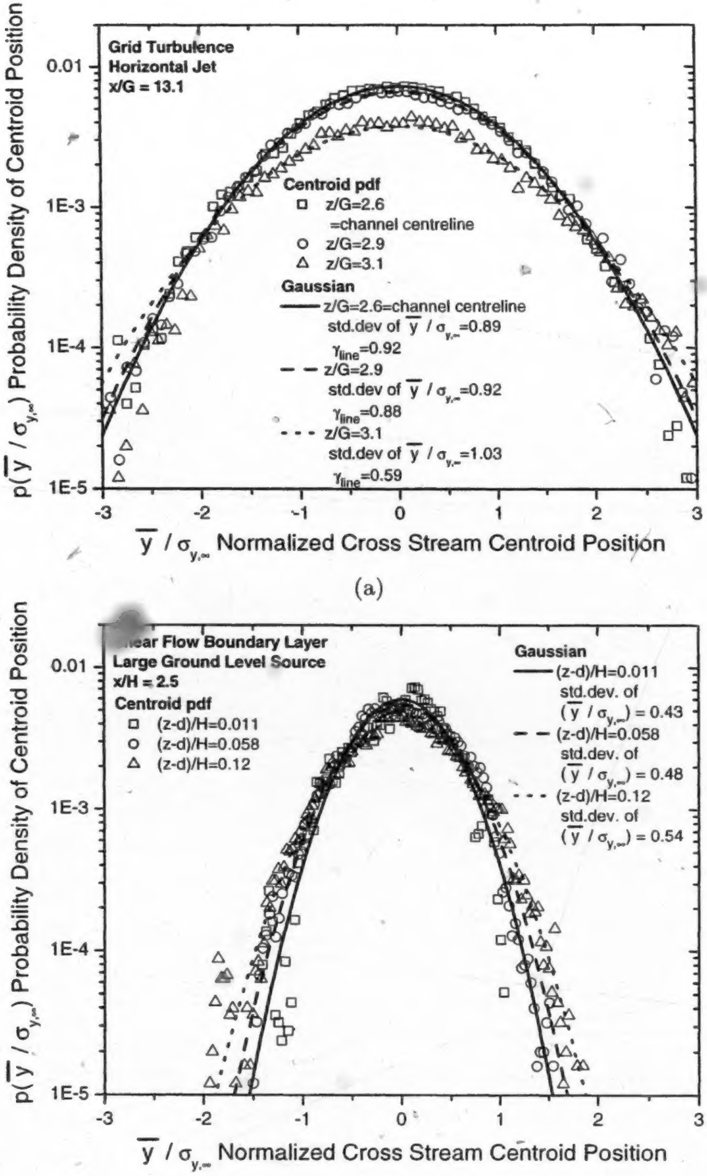

(a)

(b)

Figure 2.21: Probability density functions of normalized centroid position $p(\overline{y}/\sigma_{y,\infty})$ compared to a Gaussian. (a) $x/G = 13.1$ downstream of the iso-kinetic jet source in grid turbulence (b) $x/H = 2.5$ downstream of the large ground level source in boundary layer shear flow.

7

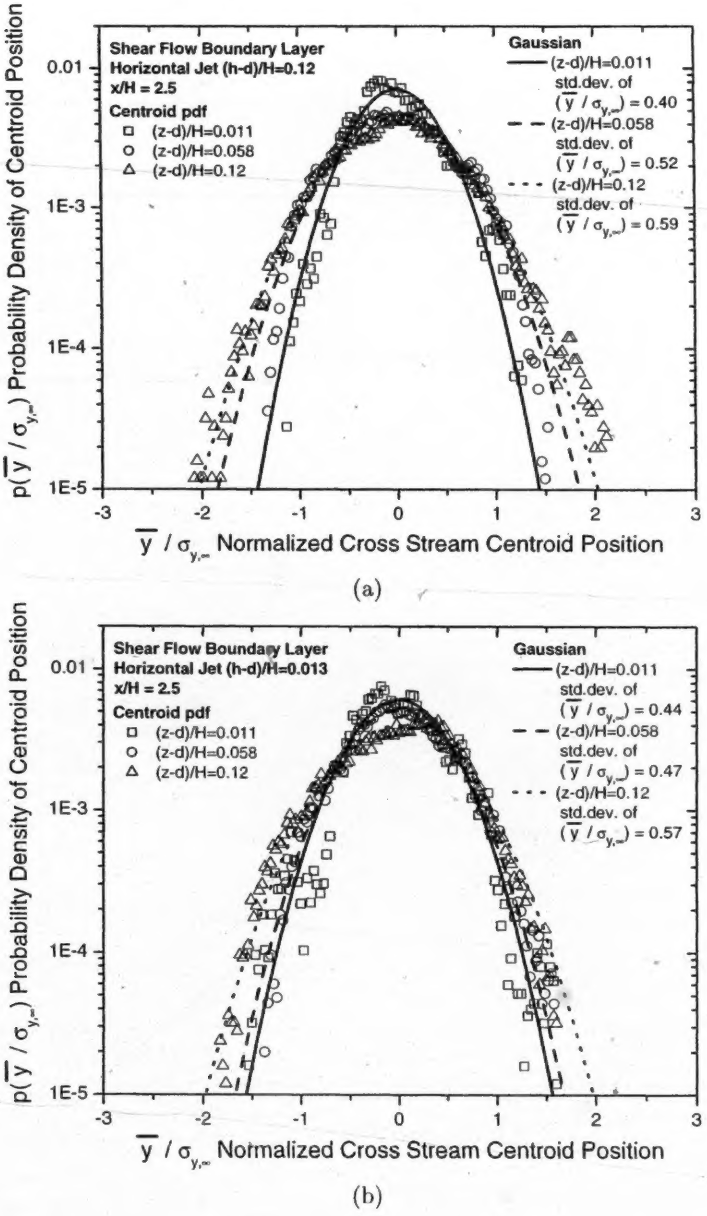

(a)

(b)

Figure 2.22: Probability density functions of normalized centroid position $p(\overline{y}/\sigma_{y,\infty})$ compared to a Gaussian at $x/H = 2.5$ downstream of the source (a) iso-kinetic horizontal jet $(h-d)/H = 0.12$ above the ground in shear flow (b) horizontal jet at ground level, $(h-d)/H = 0.013$ in shear flow.

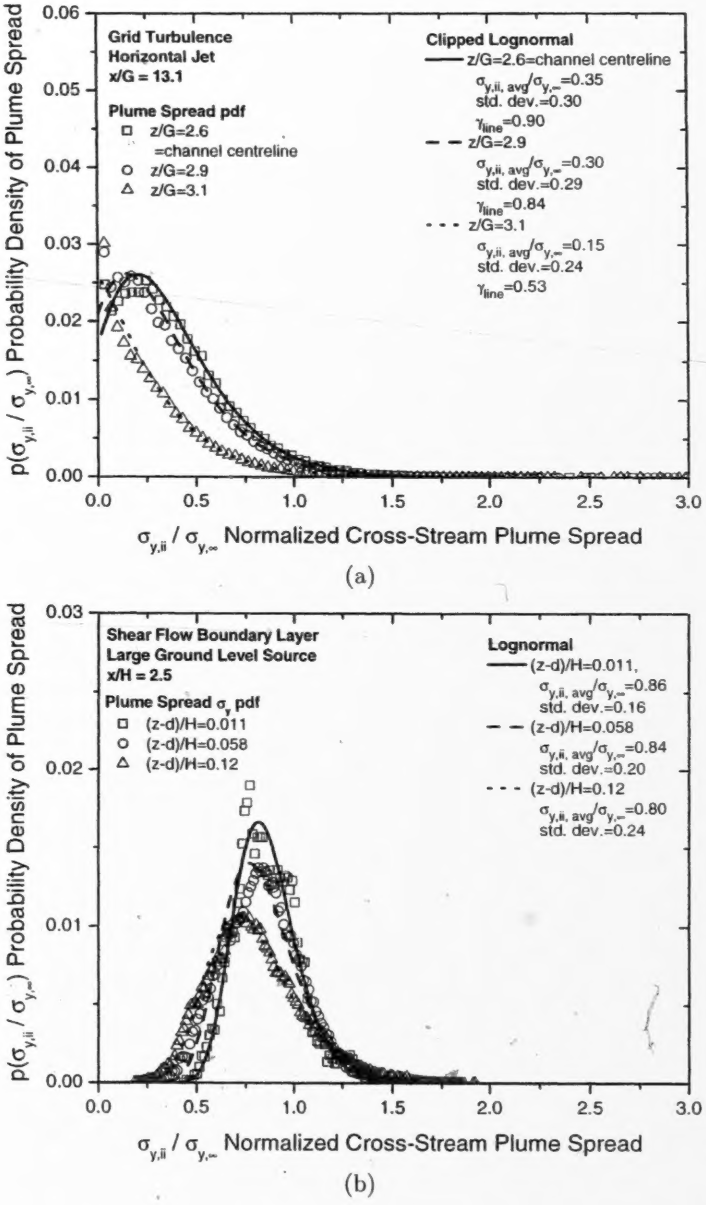

Figure 2.23: Probability density functions of normalized instantaneous plume spread $p(\sigma_{y,ii}/\sigma_{y,\infty})$ compared to a lognormal. (a) $x/G = 13.1$ downstream of the iso-kinetic jet source in grid turbulence (b) $x/H = 2.5$ downstream of the large ground level source in boundary layer shear flow.

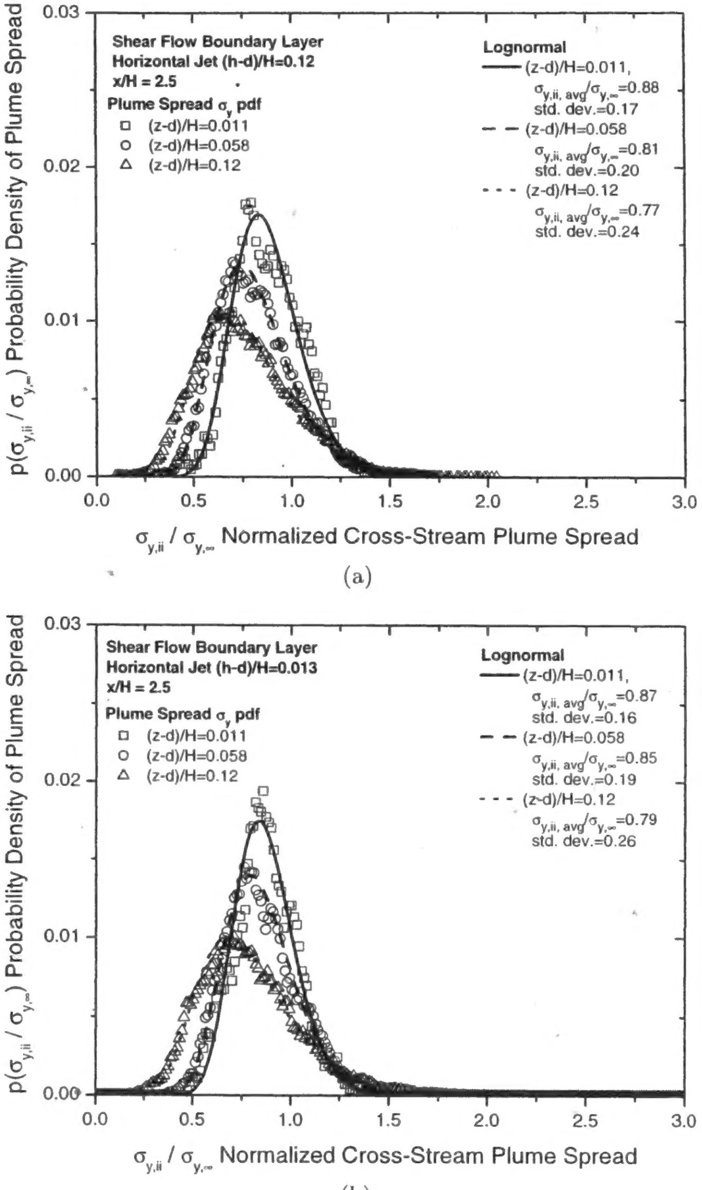

(a)

(b)

Figure 2.24: Probability density functions of normalized instantaneous plume spread $p(\sigma_{y,ii}/\sigma_{y,\infty})$ compared to a lognormal at $x/H = 2.5$ downstream of the source (a) isokinetic horizontal jet $(h-d)/H = 0.12$ above the ground in shear flow (b) horizontal jet at ground level, $(h-d)/H = 0.013$ in shear flow.

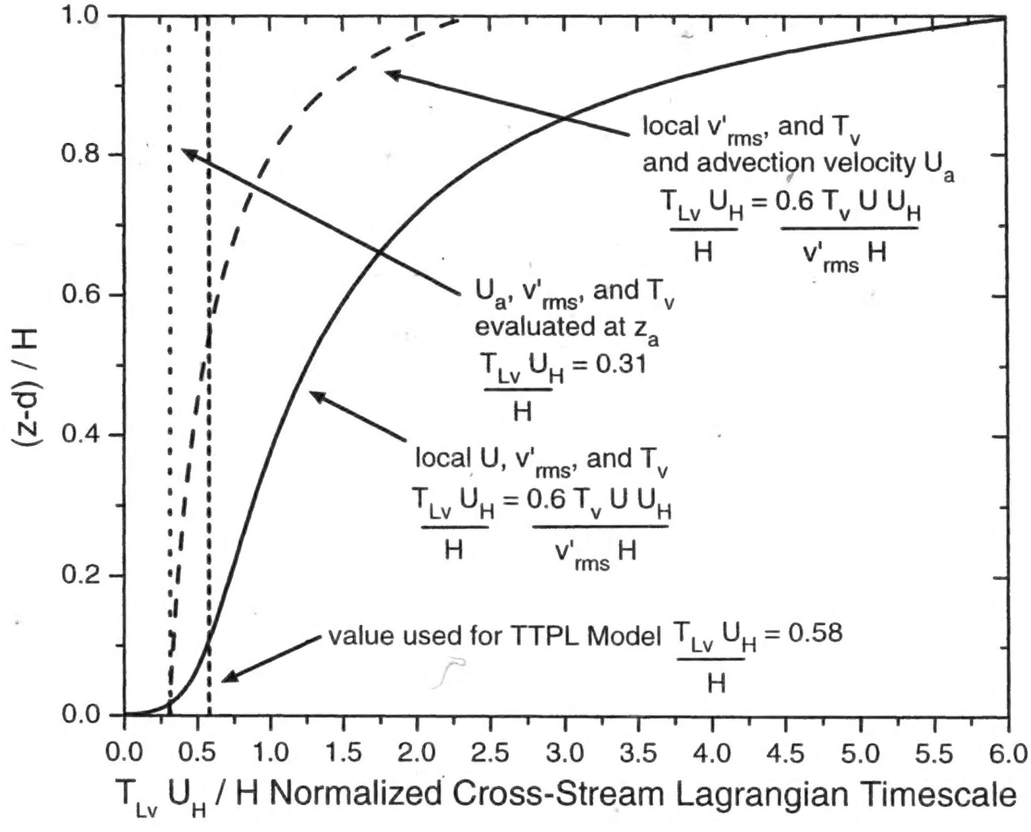

Figure 2.25: Several possible normalized cross-stream Lagrangian time scale values $T_{Lv}U_H/H$ in the boundary layer shear flow calculated for combinations of local or advection height z_a values for Eulerian integral time scale T_v, v'_{rms} and U. The value used in the TTPL model was $T_{Lv}U_H/H = 0.58$.

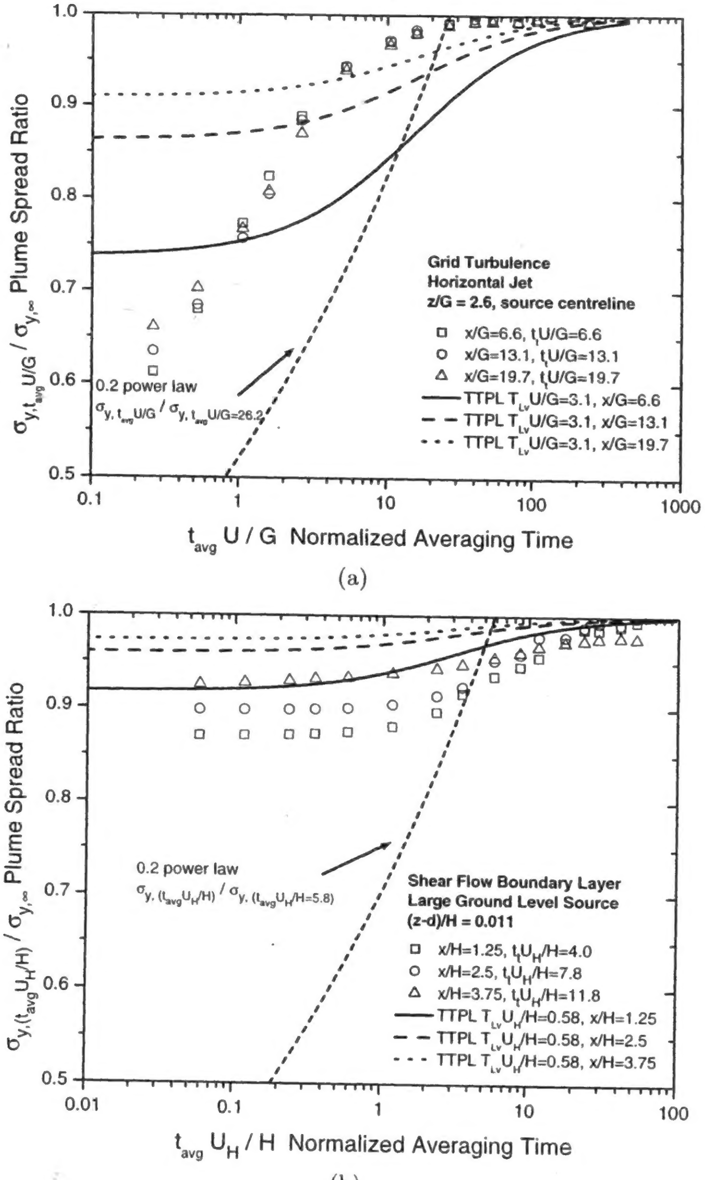

(a)

(b)

Figure 2.26: Travel time power law model (TTPL) for plume spread ratio compared with experimental values as a function of normalized averaging time. (a) $\sigma_{y,(t_{\text{avg}}U/G)}/\sigma_{y,\infty}$ as function of $t_{\text{avg}}U/G$ for the iso-kinetic jet source in grid turbulence measured on the jet centreline at downstream positions $x/G = 6.9$, 13.1, 19.7. The 0.2 power law is fit with $\sigma_{y,(t_{\text{avg}}U/G)}/\sigma_{y,(t_{\text{avg}}U/G=26.2)} = 1.0$ (b) $\sigma_{y,(t_{\text{avg}}U_H/H)}/\sigma_{y,\infty}$ as function of $t_{\text{avg}}U_H/H$ for the large ground level source in shear flow measured at ground level $(z-d)/H = 0.011$ and downstream positions $x/H = 1.25$, 2.5, 3.75. The 0.2 power law is fit with $\sigma_{y,(t_{\text{avg}}U_H/H)}/\sigma_{y,(t_{\text{avg}}U_H/H=0.35)} = 1.0$.

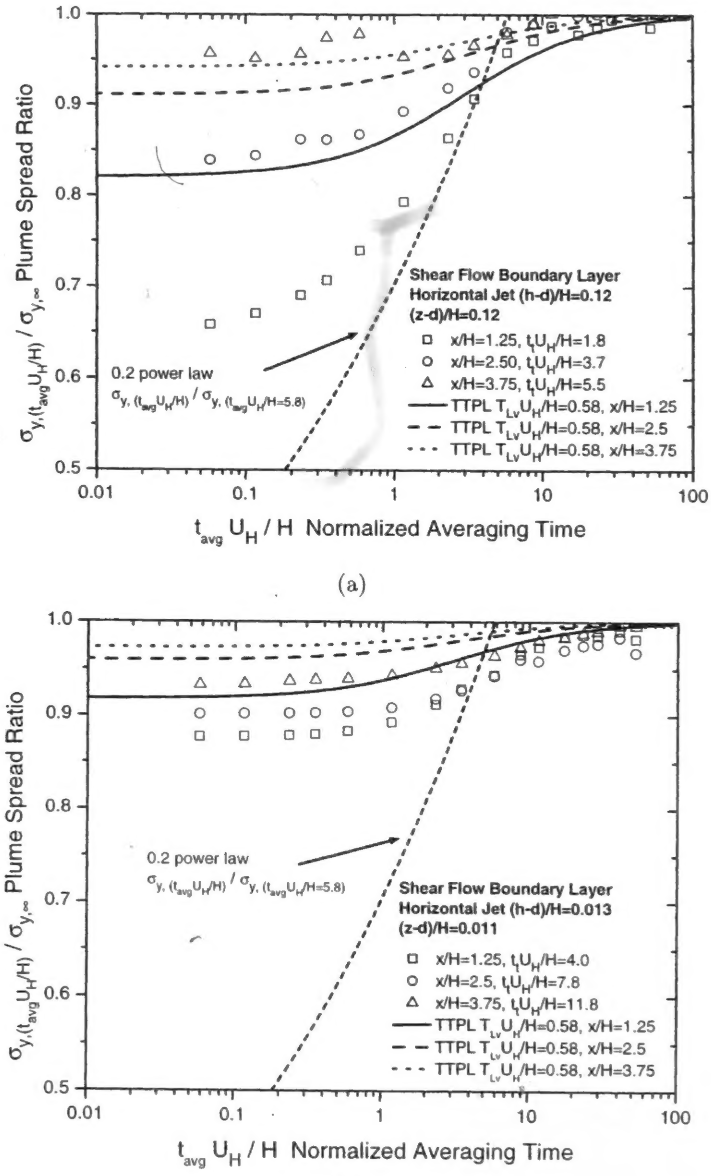

Figure 2.27: Travel time power law model (TTPL) for plume spread ratio $\sigma_{y,(t_{\mathrm{avg}}U_H/H)}/\sigma_{y,\infty}$ compared with experimental values as function of normalized averaging time $t_{\mathrm{avg}}U_H/H$. The 0.2 power law is fit with $\sigma_{y,(t_{\mathrm{avg}}U_H/H)}/\sigma_{y,(t_{\mathrm{avg}}U_H/H=0.35)} = 1.0$ (a) elevated iso-kinetic jet source in shear flow $(h-d)/H = 0.12$, measured at source height and downstream positions $x/H = 1.25,\ 2.5,\ 3.75$ (b) horizontal jet at ground level, $(h-d)/H = 0.013$ in a shear flow, measured at ground level $(z-d)/H = 0.011$ and downstream positions $x/H = 1.25,\ 2.5,\ 3.75$.

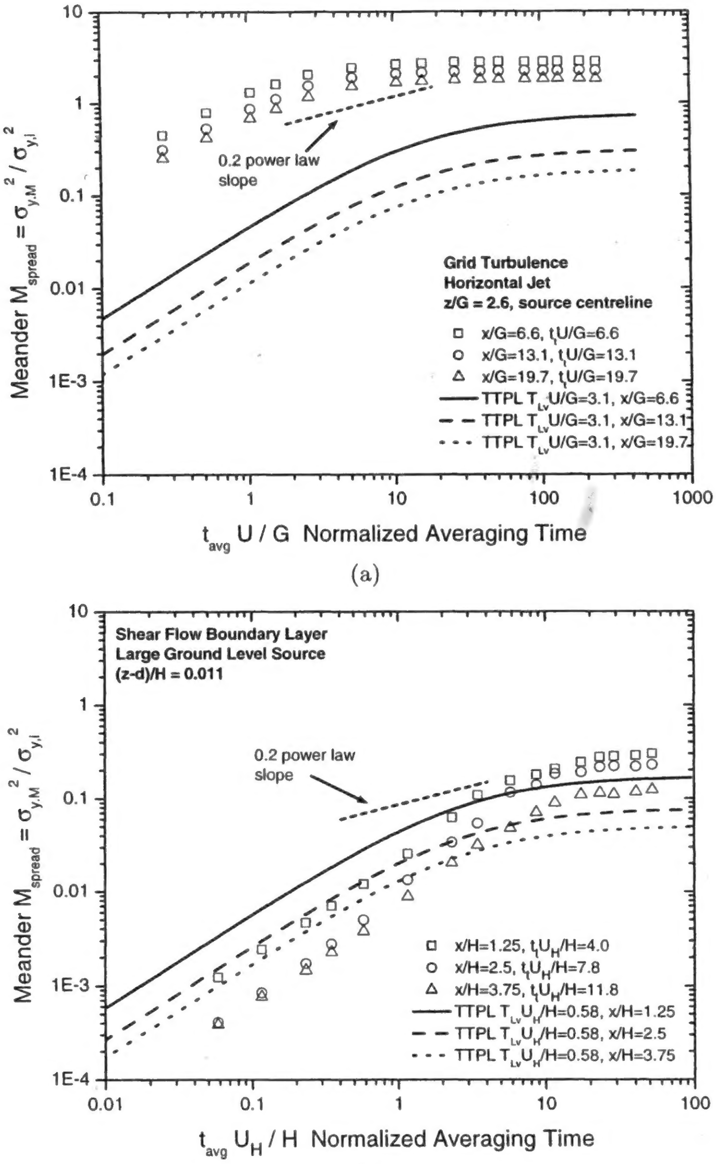

(a)

(b)

Figure 2.28: Travel time power law model (TTPL) for meander $M_{\text{spread}} = \sigma^2_{y,m}/\sigma^2_{y,i}$ compared with experimental values as a function of normalized averaging time and the slope of the 0.2 power law. (a) normalized averaging time $t_{\text{avg}}U/G$ for the iso-kinetic jet source in grid turbulence measured on the jet centreline at downstream positions x/G = 6.9, 13.1, 19.7. (b) normalized averaging time $t_{\text{avg}}U_H/H$ for the large ground level source in shear flow measured at ground level $(z-d)/H = 0.011$ and downstream positions x/H = 1.25, 2.5, 3.75.

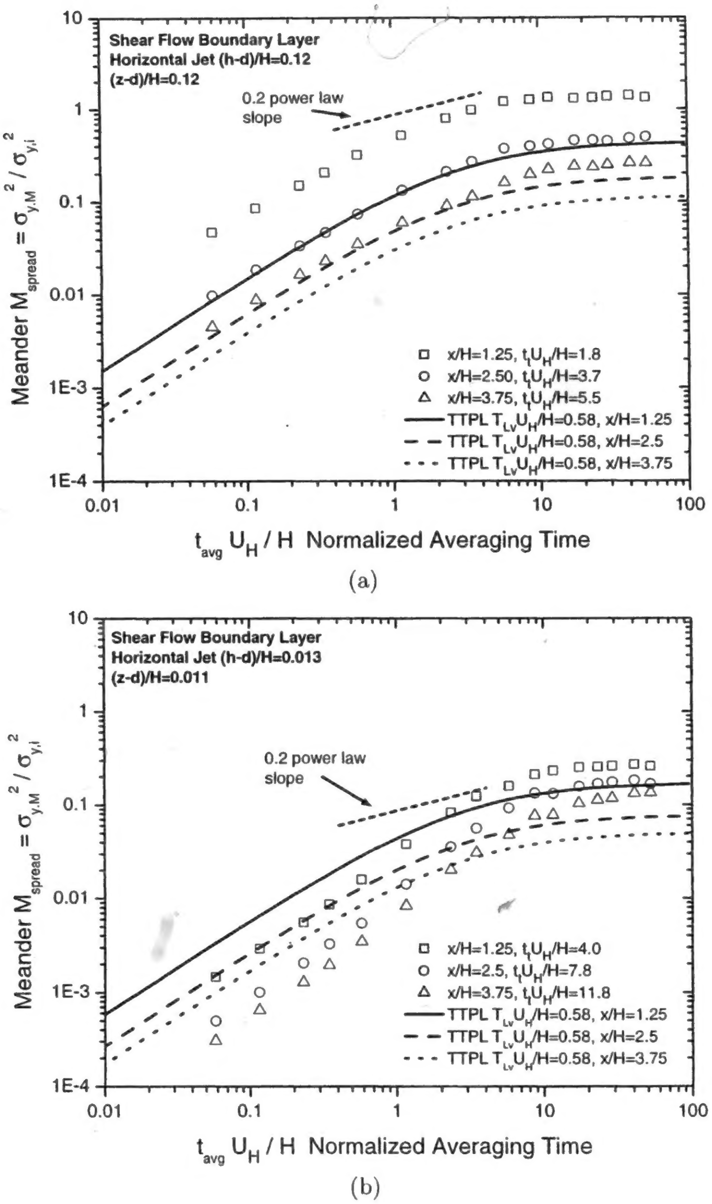

Figure 2.29: Travel time power law model (TTPL) for meander $M_{\text{spread}} = \sigma_{y,m}^2/\sigma_{y,i}^2$ compared with experimental values as a function of normalized averaging time $t_{\text{avg}}U_H/H$ and the slope of the 0.2 power law. (a) elevated iso-kinetic jet source in shear flow $(h-d)/H = 0.12$, measured at source height and downstream positions $x/H = 1.25$, 2.5, 3.75 (b) horizontal jet at ground level, $(h-d)/H = 0.013$ in a shear flow, measured at ground level $(z-d)/H = 0.011$ and downstream positions $x/H = 1.25$, 2.5, 3.75.

Chapter 3

Measurement and Prediction of Wind Shear Distortion of Concentration Fluctuation Statistics

Abstract

The objective of this study is to develop an engineering model for the concentration fluctuation intensity, intermittency factor, and integral time scale for a plume dispersing in a well-developed rough surface boundary layer shear flow. The model is based on experimental data measured with a linescan laser-induced fluorescence technique in a water channel. The concentration fluctuations discussed are high frequency near instantaneous measurements sampled over long total times to ensure convergence of all statistical values.

The relevant parameter for wind shear effects is found to be the velocity shear normalized by vertical turbulence intensity, plume travel time, and local wind speed. The reference position at which to evaluate the non-dimensional shear is an important factor because both the source position and the receptor position influence the concentration fluctuations.

These concentration fluctuation models are intended to be applied with limited information about the surrounding flow field, which is typical of information available for full-scale atmospheric dispersion predictions. It is assumed that a minimal set of parameters is known: atmospheric stability, surface roughness, vertical velocity profile, and plume spreads. In addition, the proposed models require a no-shear estimate of the concentration fluctuation intensity from which the shear flow fluctuation intensity is determined as a function of the non-dimensional shear parameter. The integral time scale of concentration fluctuation is found to be a function of the non-dimensional shear and the velocity fluctuation time scale. The conditional fluctuation intensity (excluding intermittent zero concentrations) is modelled as a function of the

total fluctuation intensity with an asymptote as the total fluctuation intensity gets very large.

3.1 Introduction

The objective of this study is to develop an engineering model for the intensity i, intermittency factor γ and integral time scale T_c of concentration fluctuations in a well-developed rough surface boundary layer shear flow. These descriptive statistics are necessary as inputs to the stochastic concentration time series model described in Hilderman and Wilson (1999). In all cases, the concentration fluctuations discussed here are very high frequency near instantaneous measurements sampled over total times long enough to ensure convergence of all statistical values. The motivation for considering the near surface boundary layer is that in almost any realistic full-scale atmospheric scenario, receptors are exposed to the dispersing plume in the highly sheared flow near the ground where there are large differences in plume statistics compared to dispersion in more homogeneous turbulence well above the ground.

Many laboratory and full-scale experiments have collected concentration fluctuation data, but much of it is horizontal profiles measured at some elevated position and typically at the source height. In order to measure the effect of shear it is important to have good resolution through the vertical extent of the boundary layer. Some past experimental measurements of vertical profiles are the wind tunnel studies of Fackrell and Robins (1982), water channel studies of Bara et al. (1992), and atmospheric studies of Mylne (1993) and Yee et al. (1995). The measurements used in this study were taken with the linescan laser-induced fluorescence (LIF) technique described in Chapter 2 and have much better spatial and temporal resolution than these older experiments.

Hanna (1984) reviews seven categories of models for concentration fluctuations ranging from empirical Gaussian approaches, to eddy diffusivity models, to advanced numerical methods. Application of such models to concentration fluctuation statistics in a shear flow has been severely limited because of a lack of case-specific information on the scalar fluctuation statistics needed to drive these models. The shear effects models presented here can be used with any dispersion model that predicts the no-shear concentration fluctuation statistics.

The most challenging aspect of the model development was to find a single physically realistic model that included the effects of receptor position and a changing release height. The experimental data showed that there were significant differences between a release high above the ground, initially dispersing in no-shear flow and descending to the ground; and a ground level release that experiences a wide range of wind shear over the plume height. A case study of the resulting model will show large shear-induced variations in fluctuation intensity and intermittency in vertical profiles through any plume.

3.2 Information Required for a Concentration Fluctuation Model

At a minimum, the following parameters are required to adequately describe concentration fluctuations:

- **Mean Concentration** C: The mean concentration can be obtained from one of the innumerable dispersion models available. It will be assumed that the mean concentration is known.

- **Fluctuation Intensity** i: The fluctuation intensity i, is

$$i = \sqrt{\frac{\overline{c'^2}}{C^2}} \tag{3.1}$$

  where $\overline{c'^2}$ is the variance of the concentration and $\sqrt{\overline{c'^2}} = c'_{\text{rms}}$ which is the standard deviation or root mean square fluctuation. (The convention used is $c = C + c'$ where c is the instantaneous concentration and c' is the fluctuation from the mean C).

- **Conditional (in-plume) Fluctuation Intensity** i_p: The conditional fluctuation intensity i_p is calculated by excluding the zero concentration intermittent periods.

$$i_p = \sqrt{\frac{\overline{c_p'^2}}{C_p^2}} \tag{3.2}$$

  where $\overline{c_p'^2}$ is the conditional concentration variance and C_p is the conditional mean concentration.

- **Intermittency Factor** γ: The intermittency factor γ is the probability of the concentration being greater than zero (i.e. the fraction of time during which there is measurable non-zero concentration.) The total and conditional fluctuation intensities are related to the intermittency factor by the definition, see Wilson et al. (1985, Equation (8))

$$\gamma = \frac{1 + i_p^2}{1 + i^2} \tag{3.3}$$

- **Integral Time Scale of Concentration Fluctuation** T_c, and **Integral Length Scale of Concentration Fluctuation** L_c: The integral time scale T_c is defined as the area under the auto-correlation curve for the concentration time series and is an indication of the average time scale of concentration fluctuations occur and the time over which the concentration remains correlated. Using a frozen turbulence assumption the integral length scale $L_c = T_c U$ where U is the local mean velocity. Following Hinze (1975, pp. 62-65), the time scale can be calculated from a time series of data by computing the one-dimensional power spectrum. The zero frequency intercept $E_c(0)$ is found by extrapolation and applied to the definition:

$$T_c = \frac{E_c(0)}{4\overline{c'^2}} \tag{3.4}$$

- **Wind Shear** A vertical velocity profile of the streamwise component U and the shear profile $\partial U/\partial z$ are assumed to be known. Other parameters of the flow such as a friction velocity u_* or an integral time scale T_{vel} may also be required.

In this study, models will be developed for T_c, L_c, i, i_p and γ in a shear flow boundary layer.

3.2.1 Time Scale T_{vel} of Turbulence Velocities

Although each component of velocity (u, v, and w) is measured individually, and an integral time scale of each component can be computed separately, it can be argued that for scalar fluctuations only a combined time scale of the three components is important. Regardless of what direction the flow is moving, all that can be measured is a change in concentration at a point. A simple addition or average of the 3 component time scales will not give the correct result because the longest time scale will dominate. It is expected that the shortest time scale and the smallest eddies will dominate the process because any movement of fluid can cause a change in concentration measured at a point.

The scalar turbulent energy dissipation ϵ is calculated as a simple sum of the 3 components of dissipation

$$\epsilon = \epsilon_u + \epsilon_v + \epsilon_w \tag{3.5}$$

Assuming a parallel relationship between concentration fluctuations and dissipation and given that $\epsilon \propto$ velocity variance/time scale, it is expected that velocity time scales should add as inverses so that

$$\frac{1}{T_{\text{vel}}} = \frac{1}{T_u} + \frac{1}{T_v} + \frac{1}{T_w} \tag{3.6}$$

where T_{vel} is the overall effective scalar velocity time scale, and T_u, T_v, and T_w are the integral velocity time scales for each component. Strictly speaking, Equation (3.6) is only true in isotropic turbulence where the variances are the same in all directions. However, with this inverse time scale relationship it is the smallest time scale that dominates so Equation (3.6) will be used as a simple approximation to deal with non-isotropic time scales.

Another way to visualize the relationship in Equation (3.6) is as a sum of probabilities. In a given time interval the probability of some turbulent motion causing a change in the observed concentration at a point is inversely proportional to the integral timescale. The three directions are assumed to be independent, so the total probability of some turbulent motion happening over a given length of time is the sum of the three component probabilities. The shorter the time scale, the higher the probability it will cause a fluctuation which in turn increases the total probability of some change in concentration and decreases the time scale T_{vel}.

3.3 Experiment Description

All of the measurements used in this study were obtained with linescan laser-induced fluorescence (LIF) optical measurement techniques in the recirculating water channel in the Mechanical Engineering Department at the University of Alberta. Disodium fluorescein ($C_{20}H_{10}Na_2O_5$) dye solutions were injected into either a rough surface boundary-layer shear flow or a shear-free grid turbulent flow in the 5240 mm long by 680 mm wide by 470 mm deep test section of the channel. High spatial and temporal resolution concentration measurements were made with a Dalsa model CLC6-2048T 12-bit gray-scale CCD linescan camera along a line illuminated by an argon-ion laser. Each of the 1024 pixels had a measurement volume of approximately 0.5mm x 1mm x 1mm and was sampled at 500 samples per second for a total of 500 seconds per sample.

Figure 3.1 is a schematic of the water channel. The experimental technique and apparatus are discussed in more detail in Chapter 2. Figure 3.1 shows a laser line entering the channel from the side with the camera on top of the channel to produce a horizontal profile of concentration, but the most important shear flow data were produced by swapping the positions of the laser line and the camera and measuring vertical profiles through the dispersing plume. Three different source types, shown in Figure 3.2, will be discussed in more detail in Section 3.3.2

For comparison with full-scale atmospheric measurements, 1.0 second in the water channel is roughly equivalent to 1.0 minute in the atmosphere which means the total sample time was approximately 500 minutes $\approx$ 8 hours at a sample rate of 8 samples per second at 1024 simultaneous points across the plume. It is very difficult to do such long statistically stationary and detailed samples in the atmosphere.

3.3.1 Flow Fields

Rough Surface Turbulent Boundary Layer Shear Flow

For most experiments, the channel was configured as in Figure 3.1 to produce a well-developed rough surface turbulent boundary layer flow similar to what would be observed in the atmosphere under neutrally stable conditions. The rough bottom surface was made of nominal 1/2" x 18 gauge raised surface stainless steel expanded metal fastened to 6 mm thick acrylic panels. The expanded metal had diamond shaped openings approximately 11 mm wide in the flow direction and 24 mm wide in the cross-stream direction. The raised surface extended 4 mm above the acrylic panels. Boundary-layer development was accelerated by additional flow conditioning elements placed at the inlet of the channel test section. An array of 4 horizontal and 4 vertical 19 mm (nominal 3/4") stainless steel square bars and a 70 mm high trip fence with 40 mm high by 60 mm wide triangular "teeth" were used to redistribute the flow and generate some mid to large scale turbulence.

A two-component TSI Inc. Laser Doppler Velocimeter (LDV) system was used to make measurements of the velocity profiles in the channel and fine tune the positions of the square bar and trip fence conditioning elements. The cross-stream uniformity of the mean streamwise velocity U was ±5% across the channel.

Figure 3.3(a) shows a typical vertical profile of the mean streamwise velocity U measured at 3000 mm downstream of the channel inlet ($x/H = 7.5$). The log-law fit to the profile is

$$U = \frac{u_*}{\kappa} \ln\left(\frac{z-d}{z_0}\right) \tag{3.7}$$

where $u_* = 14$ mm/s is the friction velocity, $\kappa = 0.4$ is the Von Karman constant, $d = 1.7$ mm is the zero-plane displacement height, and $z_0 = 0.52$ mm is the roughness height. All z coordinates are measured from the bottom of the roughness (i.e. the top of the expanded metal is at $z = 4$ mm.) The zero-plane displacement d is a virtual position necessary to fit the log law and is a function of the real roughness height and density of the roughness elements.

The log-law mixing layer depth $H = 400$ mm $= 769z_0$ was the entire depth of the channel. Velocity at H was $U_H = 232$ mm/s which was used as a normalizing factor in the plots.

The shear is the partial derivative of Equation (3.7) with respect to z

$$\frac{\partial U}{\partial z} = \frac{u_*}{\kappa\,(z-d)} \tag{3.8}$$

In the log-law profile the velocity goes to zero at $(z-d) = z_0$ at which point there is still a finite velocity gradient $u_*/\kappa z_0$. These profiles should only be used down to the zero velocity point $z_{\text{min}} = z_0 + d \approx 2.2$ mm. In the water channel the lowest point at which measurement were taken was $z = 6$ mm, well above z_{min}.

Some other important velocity statistics are the velocity fluctuations u'_{rms}, v'_{rms} and w'_{rms} shown in Figure 3.3(b) normalized by U_H. The vertical fluctuations were fit with a simple function $w'_{\text{rms}} = (1 - \exp(-0.03(z+42)))(23 - 0.04(z+42))$ which was used in the modelling process to interpolate w'_{rms} values from the data points.

Figure 3.3(c) shows vertical profiles of the Eulerian integral timescale of velocity fluctuations for all three coordinate directions, T_u, T_v, and T_w normalized by $H/U_H =$ 1.7 seconds. The total velocity time scale T_{vel} calculated using Equation (3.6) is the thick solid line in Figure 3.3(c).

Figure 3.3(d)shows the vertical profile of the $\overline{uw}$ Reynolds stress. This linear profile indicates fully-developed channel flow rather than the constant stress layer near the surface that might be expected in a zero-pressure gradient boundary layer shear flow in the atmosphere. However, this should still be a reasonable approximation of a rough-surface neutrally stable atmospheric boundary-layer.

Appendix A has the graphs shown here in measured units of mm without the normalization by U_H and H, as well as additional detailed profiles of velocity statistics for the shear flow.

Grid Turbulence as a Zero Shear Reference

For comparison purposes, plume dispersion measurements were also made in a shear free grid-generated turbulent flow. The grid was made of flat stainless steel bars 19.2 mm wide by 5 mm thick with a centre to centre spacing of $G = 76.2$ mm and a total open area of 56%. The bars were standard stainless steel rolled stock with slightly rounded edges rather than sharply machined edges. The grid was positioned at $x/G = 4.3$ from the channel inlet and the flow was run 405 mm deep with a $U = 200$ mm/s average flow rate.

The cross-stream variation of the mean streamwise velocity U was at most ±5% if the wall boundary layers were neglected. The vertical fluctuations w'_{rms} were approximately 95% of the streamwise fluctuations u'_{rms} indicating some slight anisotropy in the flow. As expected for grid turbulence, the turbulence intensity decays with downstream distance as shown in Figure 3.4(a). The power law curve plotted on the figure is the best fit to the power law decay of grid turbulence using Saffman's invariant (Hinze, 1975, pp. 217 and 265-267).

As documented by Hinze, Saffman's invariant arises from the hypothesis that the mechanism producing the turbulence can only produce a finite total linear momentum even if the flow field increases in size. This limit on momentum in grid turbulence occurs when the turbulent fluctuation directions become uncorrelated for large separations and the x-momentum will go to zero. The volume with correlated turbulent motions is proportional to the lateral integral length scale Λ_g^3 and the momentum is proportional to $\overline{u^2}$ so the product $\overline{u^2}\Lambda_g^3 =$ constant, see Hinze (1975, Equation (3-183)). From this and the assumption that turbulence intensity u'_{rms}/U decays according to a simple power law with time leads to the power law exponent of -0.6 for u'_{rms}/U and the corresponding power of 0.4 for integral scales. Hinze (1975, Equations (3-184) and (3-186)) gives these relationships in terms of travel time t_t, but for the purposes of this study they are reformulated as functions of normalized downstream distance $x/G = Ut_t/G$. The decay of grid turbulence intensity is

$$\frac{u'_{\text{rms}}}{U} = 0.3\left(\frac{x}{G} - 2.3\right)^{-0.6} \tag{3.9}$$

with the constants 0.3 and 2.3 fit to the present data. The dye source was placed at $x/G = 23.6$ where the turbulence intensity was about 5% and decayed to about 3% at the farthest downstream measurement position $x/G = 43.3$.

The normalized Eulerian time scale of velocity fluctuations for the streamwise component was about $T_u U/G = 0.4$ and for the vertical component $T_w U/G = 0.2$ as shown in Figure 3.4(b). The two curves on this plot are the theoretical streamwise time scale calculated using the grid power law decay as fit in Equation (3.9).

$$\frac{T_u U}{G} = 0.05 \left(\frac{x}{G} - 2.3 \right)^{0.4} \tag{3.10}$$

The theoretical curve for the vertical time scale T_w is one half of that given in Equation (3.10). The fit to theory with the exponent of 0.4 set by Saffman's invariant was not as good as for the turbulence intensity decay curve, but the general shape is correct and the ratio between the streamwise and vertical scales is almost exactly the expected factor of 2.0 that would occur in homogeneous isotropic turbulence. Some errors might be expected because the integral scale is difficult to measure as is apparent in the larger scatter as compared to the turbulence intensity data.

For this study the velocity fluctuation integral time scales were taken as the average values in normalized terms $T_u U/G = 0.39$, $T_v U/G = T_w U/G = 0.21$, and $T_{\text{vel}} U/G = 0.084$

3.3.2 Tracer Sources

Three different dye sources were used as shown in Figure 3.2:

1. **Horizontal Jet** 4.3 mm OD and 3.25 mm ID stainless steel tube, 38 mm long suspended from above the channel by a streamlined support. In normalized units the source diameter $d_s \approx 6z_0 \approx 0.008H$ in the shear flow and $d_s \approx 0.04G$ in grid turbulence. In grid turbulence, the source was placed in the centre of the channel at $z = 200$ mm $= 2.6G$ above the channel bottom, and in the shear flow the source was placed at height h between 7 and 50 mm ($(h - d)/H = 0.013$ to 0.12 or $(h - d)/z_0 = 10$ to 93) above the surface depending on the experiment. The source flow rate was iso-kinetic in grid turbulence and for $(h - d)/H = 0.12$ above the ground in the shear flow. With the small diameter and low flow rates the jets from the source were laminar ($\text{Re} = U_{\text{source}} d_s/\nu \approx 600$).

2. **Vertical Jet at Ground Level** 3.25 mm ID flush with ground ($d_s \approx 6z_0 \approx 0.008H$). To prevent dye from becoming trapped in the roughness elements the expanded metal was removed from an area 25 mm on either side and 100 mm downstream of the source. The source flow rate was the same as for the horizontal jets and produced a laminar jet with a mean velocity equal to the cross flow velocity at $(z - d)/H = 0.12$, $\text{Re} \approx 600$.

3. **Large Ground Level Source** 11 mm ID flush with ground. ($d_s \approx 21z_0 \approx 0.028H$). As with the vertical ground level jet the expanded metal was trimmed away 25 mm on either side and 100 mm downstream of the source. The source

flow rate was the same as the other 2 source (Re $\approx$ 175 based on source diameter).

The sources were placed 2750 mm ($x/H = 6.9$) downstream of the channel inlet in the shear flow and 1800 mm ($x/G = 23.6$) downstream of the grid in the no-shear experiments.

For the elevated sources and grid turbulence measurements the average source flow rates were iso-kinetic with the surrounding flow. The vertical ground level sources had very low momentum with insignificant plume rise. If modelled at 1:1000 scale the full-scale equivalent source sizes were 3 to 11 m at the source and effectively 2 to 3 times larger than this after entraining sufficient fluid to take on the turbulent structure of the flow field. Measurements were taken at $x/d_s > 150$ for the jet sources and $x/d_s > 50$ for the large ground level source. At this downwind point the dilution was at least 100:1 which allowed the tracer-marked fluid to take on the turbulent structure of the cross flow. There was little measurable effect of source size or release rate. Appendix B lists all of the parameters of the data sets that were collected and used in this study.

3.3.3 Resolution in the Intermittent Fringes of the Plume

Accurate measurement of concentration fluctuation statistics in the outer edges of the plume was limited by the total measurement time. See Pasquill and Smith (1983, pp. 24-29 and Fig. 2.2) for discussion of sampling time effects on variance. In the laboratory, flow fields and dispersing plumes can be made statistically stationary and sampled for relatively long periods of time, but there are still practical limitations. In the present experiments, samples were collected for 500 seconds at each measurement position at 500 samples per second for a total of 250,000 samples per pixel. This is sufficient to resolve profiles of mean concentration, variance etc. out to y or $(z-h) \approx 2-3\sigma$. As intermittency factor γ gets small in the outer fringes of the plume, the small number of non-zero concentration samples limits our ability to measure variances accurately, and also all of the associated statistics such as fluctuation intensities, and time scales. As γ decreases, the effective non-zero sample size decreases and the measured variance, especially the in-plume conditional variance, decreases. In the extreme case where there is only one non-zero measurement during the entire sample time, the conditional variance will be zero, a severe underestimate of the actual value. In all cases discussed here, data sets were restricted to cases where $\gamma \geq 0.1$ to assure sufficiently long non-zero time series. At $\gamma = 0.1$, there are only 50 seconds out of 500 that have useful data or about 200 non-zero integral time scales out of a total 2000 concentration integral time scales of data.

3.4 Modelling Wind Shear Effects

The objective was to develop a practical operational model for distortion of concentration fluctuation statistics in a shear flow that can be applied to existing regulatory dispersion models. An operational model is distinctly different from a research model which may require input parameters not readily available outside the laboratory. The operational concentration fluctuation model given in Wilson (1995, chap.10) was used as a starting point. It does account for some of the effects of shear flow in the empirical equation used to predict the centreline source-height fluctuation reference level i_h, but it does not include shear effects on off-axis fluctuation intensities. Wilson (1995) also predicts that T_c increases quite rapidly with downstream distance and plume size, while the new data presented here suggests that there is an evolution of integral scale, but it is dependent only on local shear and travel time.

In the following sections, models will be developed using vertical profiles of concentration fluctuation statistics in a boundary layer. For each of two downstream positions ($x/H = 1.25$ and $x/H = 3.75$) six vertical profiles were measured. Three source types, the small vertical ground level jet, the horizontal jet at a high elevated position $(z-d)/H = 0.12$ and the horizontal jet near the ground at $(z-d)/H = 0.013$ were used with tracer flow rates of 0.7 and 1.5 ml/s. The higher flow rate was selected to produce an iso-kinetic horizontal jet at $(z-d)/H = 0.12$. All 12 profiles were used to fit the model, but only 4 cases will be shown in the figures because there was no significant difference between the two ground level sources or the two source flow rates. The cases shown are the elevated horizontal jet at the high flow rate and the ground level vertical jet at the high flow rate. A complete set of plots for all of the source and flow rates is included in Appendix H. A combination of least squares curve fitting techniques and engineering judgement was used for the curve fits. If necessary, the fits were biased to produce better results near the ground where real receptors (e.g. people) are likely to be located.

3.4.1 No Shear Concentration Fluctuations

The limiting case where shear goes to zero was measured in the grid generated turbulent flow. A robust boundary layer model will reduce to this case as shear approaches zero where $z \gg z_0$. Figures 3.5 and 3.6 show integral time scale $T_c U/G$, length scale L_c/G and concentration fluctuation intensity i statistics in the shear-free grid flow with an iso-kinetic horizontal jet source placed on the centreline of the channel.

In Figure 3.5 the integral time scale $T_c U/G$ is approximately constant across the plume and with downstream distance. Contrary to Wilson's (1995) recommended equation, the time scale did not increase with downstream distance x or plume size σ_y or σ_z. Based on the grid turbulence experiments, in the absence of wind shear, with $\mathrm{d}U/\mathrm{d}z = 0$

$$T_c \simeq 0.8 T_{\mathrm{vel}} \tag{3.11}$$

$T_{\mathrm{vel}}U/G = 0.084$ so $T_cU/G = 0.066$ as shown in the plot. It will be assumed for the new model that the turbulence is "frozen" into the mean flow so that the normalized integral length scale in grid turbulence is exactly the same as the normalized integral time scale, $L_c/G = T_cU/G = 0.066$.

Figure 3.6 shows the fluctuation intensity i measured at $x/G = 6.6$ to 19.7 downstream. The lines are Wilson (1995, Equation (6.8)) for shear free conditions

$$i^2 + 1 = (i_h^2 + 1)\left[\exp\left(\frac{(z-h)^2}{2\sigma_z^2} + \frac{y^2}{2\sigma_y^2}\right)\right]^{\frac{2M_{\mathrm{intensity}}}{1+2M_{\mathrm{intensity}}}} \tag{3.12}$$

where i_h^2 is the fluctuation intensity squared at the source height h on the cross-stream centreline of plume (i.e. at $y = 0$) and $M_{\mathrm{intensity}}$ is the 2-dimensional pseudo-meander parameter defined in Wilson (1995, equation (6.10)) which was developed from Sawford and Stapountzis (1986)

$$M_{\mathrm{intensity}} = i_h^2 + (i_h^4 + i_h^2)^{1/2} \tag{3.13}$$

In a no-shear flow, the simple pseudo-meandering plume model works exceptionally well. As will be shown, and as expected, shear distorts the concentration fluctuations near the ground and significant modifications to the pseudo-meandering plume model are needed.

3.4.2 Shear Flow Distortion

The central hypothesis is that the most important parameter for vertical variation of concentration fluctuation variance, intermittency, and time scale in a boundary layer is the non-dimensional shear. In contrast, the vertical mean concentration profile is usually modelled without reference to shear by assuming a zero-mass flux at the ground and a uniform wind without shear. It is acceptable to ignore shear for mean concentration because the mean is strictly a mass conservation calculation and unaffected by local changes in scale or higher order moments. There is no comparable conservation rule for higher order moments or fluctuation scales. In fact, dissipation guarantees that turbulent fluctuations are not conserved, so shear effects must be taken into account in some other manner.

The shear $\partial U/\partial z$ has the units of 1/time so an appropriate time scale, T_S, is required to non-dimensionalize. Using a frozen turbulence assumption, the time scale T_S can be reformulated as a length scale L_S divided by a velocity U. The non-dimensional shear S at height z

$$S = T_S\left(\frac{\partial U}{\partial z}\right) = \frac{L_S}{U}\left(\frac{\partial U}{\partial z}\right) \tag{3.14}$$

Figures 3.7, 3.8, and 3.9 are the concentration fluctuation data in shear flow along with the models for shear and no-shear cases that will be discussed later. From these plots a few important points should be noted:

- Local effects of shear are important, especially very close to the ground. This is evident in the similarity of the profiles as they approach the ground.

- The source position has a substantial effect on the profiles even at more than $x/H = 3.75$ downstream in the shear flow.

- There appears to be slow evolution with downstream distance (i.e. plume size). However, based on the grid turbulence results discussed in Section 3.4.1 this downstream evolution is really caused by the shear history of the plume, not its position or size.

- The normalized length scales L_c/H are more constant with height than the time scales $T_c U_H/H$. Coupled with the frozen turbulence assumption this indicates that the wind shear and the local advection velocity past a fixed receptor both contribute to the observed variation of time scale with height above ground. In contrast, the length scale is affected mainly by wind shear and not the advection velocity. This observation will be exploited by modelling the effect of wind shear on the length scale L_c rather than time scale T_c

3.4.3 Non-dimensional Shear S

Assuming that shear has no effect on cross-stream components, the relevant time and length scales T_S and L_S in Equation (3.14) must be scales of vertical dispersion and not cross-stream dispersion. A logical guess for a vertical scale is the vertical plume spread σ_z, but this is not a local height scale and there is little variation in σ_z between different source types. A closely related length scale is $w'_{\mathrm{rms}} t_t \propto \sigma_z$ where w'_{rms} is the rms vertical velocity fluctuation and t_t is the travel time at the vertical position of interest. In physical terms, a receptor $w'_{\mathrm{rms}} t_t$ can be used to account for the receptor vertical position shear effects that will vary with travel time. A source based $w'_{\mathrm{rms}} t_t$ can provide a source influence term.

Figure 3.10 is an illustration of the physical model implied by measuring S at the source position and at the ground level receptor position. A global plume scale such as σ_z cannot capture these differences between source and receptor positions. Using these observations and ideas a non-dimensional shear term

$$S = \frac{w'_{\mathrm{rms}} t_t}{U} \left(\frac{\partial U}{\partial z} \right) \tag{3.15}$$

was chosen as the independent flow variable. In the water channel flow w'_{rms} is nearly a constant through the lower part of the boundary layer. If w'_{rms} cannot be measured it is usually determined as a function of the shear velocity u_*. Near the ground in neutrally stable conditions $w'_{\mathrm{rms}} \approx 1.3 u_*$ (see Kerschgens et al. (2000) and Section

3.6.1 for additional discussion). The shear term S can be rewritten in terms of u_* as

$$S = \frac{1.3u_* t_t}{U}\left(\frac{\partial U}{\partial z}\right) \tag{3.16}$$

The factor of 1.3 indicates that the model was really determined in terms of the vertical velocity fluctuation component $w'_{\rm rms}$, but that u_* is much more convenient for calculations in a shear flow. Equation (3.16) and u_* will be used for all calculations rather than applying Equation (3.15) and the curve fit of the measured $w'_{\rm rms}$ profile.

3.4.4 Power Law Model for the Shear Effect

Using the pseudo-meandering plume model, profiles of mean concentration and total second order moments (mean squared plus variance) are both approximately Gaussian with different spreads for the mean and total second moments. These Gaussian profiles also agree well with the data. For a ground level measurement a reflected Gaussian is a better model for the mean concentration. The point of this discussion is that some sort of squared exponential type of profile is expected for many of the concentration statistics. However, exponentials are notoriously difficult to fit because they are very sensitive to small changes in the exponent. Over a fairly wide range, a power law can approximate an exponential and it is a power law that will be applied to the data in the present study.

An additional restriction on a shear effects model is that in a no-shear flow like grid turbulence, or at a vertical position well away from the influence of the wall $z \gg z_0$, any relationship derived should reduce to the no-shear case. The universal shear function proposed is the simplest power law form:

$$\frac{\text{shear statistic}}{\text{no-shear statistic}} = (1 + B_1 S)^{B_2} \tag{3.17}$$

It is possible that the constants B_1 and B_2 in Equation (3.17) are functions of other variables such as source size d_s, roughness z_0 etc. The present data set did not encompass a comprehensive range of source types and flow conditions to test these dependencies thoroughly. However, for the fairly wide range of variables that were tested, only the local receptor and source position S values were needed to correlate the results, and no obvious dependence on source size or jet momentum was evident.

3.4.5 Unsuccessful Models for Wind Shear Effects on Fluctuations

Although the previous section presents a logical approach to the final model, several less successful ideas were tried.

One idea was a spectral similarity approach. It was hypothesized that dissipation of concentration fluctuations by shear only affected the small scale fluctuations, leaving the larger scales relatively unchanged. As the variance, integral time scale and spectral energy are all directly related (see Equation (3.4)) it was hoped that this would lead to some sort of closure. However, the data showed $E_c(0)$ varies with vertical position as do the variance $\overline{c'^2}$ and the integral time scale T_c. As Warhaft (2000) notes large and small scale scalar fluctuations seem to be coupled and probably should not be separated. My experience indicates that this is good advice.

Another hypothesis considered was that the entire shear history of the plume would influence the fluctuations. The non-dimensional shear is a time multiplied by the velocity shear, so some sort of "memory" time or shear history might be important to the concentration fluctuation statistics. Some brief attempts were made to use a Lagrangian particle tracking model to compute the shear history of the plume, but this proved too cumbersome for an engineering model and, fortunately, the average of source height and receptor height shear effects appeared to be much more important than the entire shear history.

3.4.6 Source and Receptor Position Influence on S

As shown in Figures 3.7 through 3.9, there are strong local receptor location effects, but also a strong influence of the source release position that persists with downstream distance. Therefore, two logical places to measure the non-dimensional shear S are at the receptor position of interest z and the source height h.

In Wilson (1981), the approach for computing advection velocities and along-wind dispersion in a shear flow was to calculate an effective height at which to evaluate these parameters. The effective height was found to be a function of the source height plus some fraction of the vertical plume spread σ_z. For example, the effective advection velocity is U_a measured at $z = h + 0.17\sigma_z$ for a ground level source (Wilson, 1981, Equation (12)). A similar sort of adjustment was anticipated for the appropriate height at which to evaluate the shear. An offset of some small fraction of σ_z also prevents $S \rightarrow \infty$ as $U \rightarrow 0$ at $z - d = z_0$ for a log-law profile (see Equation (3.7) and Figure 3.3(a)) The reference position for the receptor will be

$$z_{\text{ref}} = z + B_3\sigma_z \tag{3.18}$$

and the reference position for the source will be

$$h_{\text{ref}} = h + B_4\sigma_z \tag{3.19}$$

where the constants B_3 and B_4 are likely to be less than 1. Any variations in source size are automatically included in the modelled or measured σ_z.

A physical explanation for the combined shear effect of the source and the local position is shown in Figure 3.10. The source supplies the tracer material and projects a downstream zone of influence. This is the effect captured by using h_{ref} in Equation (3.17). All material must come from the source so it is clear that the source position must have an influence on the amount of shear distortion of the plume. Similarly, the receptor position z_{ref} projects an upstream zone of sensitivity. A particle of fluid directly above the receptor has a near zero probability of passing through the receptor position, but as we examine positions farther upstream it becomes more likely that material from anywhere in the plume could eventually pass through the receptor position. The overlap between these two regions is the relevant value for any receptor position of interest.

3.4.7 A Note on Fitting the Constants B_1 through B_4

There is no single best-fit set of constants for any of the concentration fluctuation statistics. The flexibility of the power law model in Equation (3.17) and the limitations of the data set allow the power B_2 to be changed and the other constants B_1, B_3 and B_4 in Equations (3.17), (3.18) and (3.19) can be adjusted to give approximately the same goodness-of-fit for a number of different combinations of constants. The data sets presently available are insufficient to support the selection of different constants for each concentration fluctuation statistic, so it was decided to make the constants as universal as possible.

The following choices were made as a compromise to provide a robust, physically realistic fit with the correct trends for all of the variables that were tested. The constant $B_1 = 5$ in the shear function Equation (3.17). The power B_2 was allowed to change for each type of statistic (i.e. i, T_c, or i_p).

$$\frac{\text{shear statistic}}{\text{no-shear statistic}} = (1 + 5S)^{B_2} \tag{3.20}$$

The shear function Equation (3.20) taken to the power B_2 is a simple multiplicative correction factor between no-shear dispersion statistics and the shear distorted values of those statistics.

In Equations (3.18) and (3.19) $B_3 = B_4 = 0.1$

$$z_{\text{ref}} = z + 0.1\sigma_z \tag{3.21}$$

$$h_{\text{ref}} = h + 0.1\sigma_z \tag{3.22}$$

Making B_3 and B_4 larger than 0.15 produced very poor fits because as the effective height increased there was insufficient shear effect near the ground. Similarly, making B_3 and B_4 less than 0.075 caused too much shear effect to be included. With Equations (3.20) through (3.22) the models for i, i_p, γ and T_c typically were within ±20% of the experimental values.

3.5 The New Operational Model for Wind Shear Effects on Fluctuations

3.5.1 Fluctuation Intensity i Model

The fluctuation intensity for all positions across the plume is a function of the plume source height and cross-stream centreline fluctuation intensity i_h. Under no-shear conditions, the model of Wilson (1995) given in Equation (3.12) accurately predicts changes in $i_{\text{no-shear}}$ through the entire plume in both the cross-stream (y) and vertical (z) directions as demonstrated by tests in grid turbulence as shown in Figure 3.6. However, there are no good models to predict the plume centreline fluctuation intensity i_h for no-shear conditions that are appropriately equivalent to the shear flow cases of interest. In the water channel shear flow, the fluctuation intensity measurements automatically include shear effects. Similarly, most atmospheric dispersion models of fluctuation intensity (see, for example, Wilson (1995, equation (6.3))) are based on measurements in a shear flow. In summary, source height shear effects are inextricably included in both experimental measurements and models for i_h. To account for this automatic inclusion of source height shear, the shear distortion of fluctuation intensity is modelled as only a function of the receptor reference shear $S_{z_{\text{ref}}}$

$$\frac{i_{\text{shear}}}{i_{\text{no-shear}}} = \frac{1}{\left(1 + 5S_{z_{\text{ref}}}\right)^{1/3}} \tag{3.23}$$

where $S_{z_{\text{ref}}}$ is the non-dimensional shear S from Equation (3.20) evaluated at z_{ref} from Equation (3.18).

Figure 3.7 shows the measured data from the water channel versus the shear effect model of Equation (3.23) and the no-shear model of Equation (3.12). There is a significant difference between the shear and no-shear models which is as much as an order of magnitude near the ground. Without shear, Equation (3.23) reduces to the no-shear case. Clearly, wind shear has a strong influence on concentration fluctuation intensity and must be taken into account. The worst fit of the model to the data is still within a factor of 2.0 at the furthest downstream location for the elevated source. Where there is error, the shear model tends to overestimate the fluctuation intensity near the ground which will produce larger peak concentrations and hence conservative errors that overestimate adverse effects of an exposure.

Averaging Time Effects on i

All of the values discussed here were derived for the long averaging time case using the entire 500 second long data sets. The effective maximum averaging time based on plume meandering in the water channel is restricted by the size of the test section to approximately 10 seconds, see Chapter 2 for details. Changes in averaging time will have an effect on the plume spread and fluctuation intensities, but these effects can be taken into account by adjusting the no-shear estimates of concentration fluctuation intensity on the source centreline i_h as discussed in Chapter 2. Averaging time adjustments to the fluctuation intensity i_h can be made using Wilson's (1995, Equation (6.9)) pseudo-meandering plume relationship relating fluctuation intensity and averaging time effects on plume spread σ_y

$$\frac{i_h^2 + 1}{i_{h,\text{ref}}^2 + 1} \simeq \frac{\sigma_y}{\sigma_{y.\text{ref}}} \tag{3.24}$$

where $\sigma_{y.\text{ref}}$ and $i_{h,\text{ref}}$ are the plume spread and fluctuation intensity at some reference averaging time t_{ref}.

3.5.2 Conditional Concentration Fluctuation Intensity i_p and Intermittency Factor γ as a Function of Total Concentration Fluctuation Intensity i

The remaining two parameters to complete the description of the second order concentration fluctuation statistics are i_p, the conditional in-plume concentration fluctuation intensity, and the intermittency factor γ. Wilson et al. (1985) recognized that i_p is a better candidate for modelling than γ because it does not vary much across the plume. The statistics i_p, γ and i are related by the exact relationship by Wilson et al. (1985, Equation (8)) which is given in Equation (3.3). The original idea of a relationship between the total and conditional fluctuation intensity was given in Wilson (1995, equation (5.7)) which came from modelling work by Wilson and Zelt (1990). This empirical relationship was

$$i_p^2 = \frac{2i^2}{2 + i^2} \tag{3.25}$$

Combining Equation (3.25) with the definition in Equation (3.3) allows any of the three statistics i, i_p and γ to be determined. With the additional data collected in the present study it became apparent that Equation (3.25) was not as universal as originally thought. A first examination of the data led to a modified model suggested by Wilson (2002)

$$i_p = \frac{i}{\left(1 + \left(\frac{i}{i_{p,\infty}}\right)^q\right)^{1/q}} \tag{3.26}$$

Any value of q will meet the asymptotic requirements that i_p = constant as $i \to \infty$ and $i_p = i$ as $i \to 0$. The exponent $q = 3$ was found empirically from the present data and $i_{p,\infty}$ was set to 1.4 based on an initial survey of the data. However, using all of the horizontal linescan LIF profiles of concentration fluctuation statistics discussed in Chapter 2 it became clear that $i_{p,\infty}$ was a function of the non-dimensional shear. Applying the shear function, Equation (3.20), it was found that

$$i_{p,\infty} = \frac{1.9}{(1 + 5S_{\text{avg}})^{1/6}} \tag{3.27}$$

Figure 3.11 is $i_{p,\infty}$ for a variety of source and downstream positions with Equation (3.27) plotted as the solid line. Over a range of about 2 orders of magnitude in $(1+5S_{\text{avg}})$ and approximately an order of magnitude in $i_{p,\infty}$ Equation (3.27) captures the trend of the the asymptotic high intermittency ($\gamma \rightarrow 0$) limit of the conditional intensity i_p typically within a factor of 1.2 of the measured value. Figures 3.12 and 3.13 show some samples of the best, worst and typical agreement for i_p versus i and γ versus i respectively. Figure 3.14 shows samples of the cross-stream profiles of i, i_p and γ. Appendix H has a complete set of plots for all the data examined. In Figures 3.12 to 3.14, as fluctuation intensity i gets very large the scatter increases, and the fit is poorer. This scatter is expected because the large i values are the highly intermittent fringes of the plume where the intermittency factor γ approaches zero and the small number of non-zero concentration data points increases the uncertainty in the measured conditional fluctuation intensity i_p. In the worst agreement cases, Figures 3.12(b), 3.13(b), and 3.14(b), γ and i_p are under-predicted. If the mean concentration C is accurately predicted, then some of these errors should cancel out. If C is correct and the predicted γ is too small, then the conditional mean concentration C_p will be over-predicted. Although i_p will be too small, the predicted average non-zero concentration value C_p will be higher which should compensate for some of the error. Much more data would be required to resolve and justify a more complicated model.

3.5.3 Concentration Integral Time Scale T_c Model

It was assumed that the concentration fluctuation integral time scale T_c does not vary across the plume in the y direction and that T_c does not change with averaging time. These assumptions will be discussed in more detail at the end of this section.

With the above assumptions, only the vertical z direction changes in the time scale will be modelled. The time scale is more conveniently modelled as a length scale because the length scales are more consistent with height. Using a frozen turbulence approach

$$L_c = T_c U \tag{3.28}$$

The ratio of the $L_{c,\text{shear}}$ and $L_{c,\text{no-shear}}$

$$\frac{L_{c,\text{shear}}}{L_{c,\text{no-shear}}} = \left(1 + 5S_{\text{avg}}\right)^{1/3} \tag{3.29}$$

where S_{avg} is the average of the non-dimensional shear at the receptor and at the source.

$$S_{\text{avg}} = \frac{S_{z_{\text{ref}}} + S_{h_{\text{ref}}}}{2} \tag{3.30}$$

As shown in Figure 3.10, both the source and the receptor position are important. Unlike the source effect included implicitly in the calculation of the source height fluctuation intensity, the non-dimensional shear at the source height $S_{h_{\text{ref}}}$ must be explicitly included in the time scale estimate. There are myriad other possible weightings of $S_{z_{\text{ref}}}$ and $S_{h_{\text{ref}}}$, for example Gaussian weighting or Lagrangian particle tracking weighting, but the simple arithmetic averaging in Equation (3.30) seems to work well.

The no-shear length scale is estimated using the relationship observed in grid turbulence that T_c is approximately 80% of the velocity time scale. The velocity time scale T_{vel} is calculated in Equation (3.6) from the three velocity components

$$L_{c,\text{no-shear}} = 0.8T_{\text{vel}}U_{\text{no-shear}} = T_{c,\text{no-shear}}U_{\text{no-shear}} \tag{3.31}$$

where $U_{\text{no-shear}}$ is the no-shear velocity. In a boundary layer $U_{\text{no-shear}}$ is the velocity at the top of the log-law mixing layer U_H. In the water channel boundary layer shear flow $L_{c,\text{no-shear}}/H \simeq 0.025$ and in the grid turbulence $L_{c,\text{no-shear}}/G \simeq 0.066$.

Reformatting Equation (3.29) in terms of the time scale using Equation (3.31)

$$\frac{T_{c,\text{shear}}}{T_{c,\text{no-shear}}} = \frac{U_{\text{no-shear}}}{U_{z_{\text{ref}}}}\left(1 + 5S_{\text{avg}}\right)^{1/3} \tag{3.32}$$

Note that the effect of the local advection velocity of the frozen turbulence $U_{z_{\text{ref}}}$ appears explicitly because the length scale, rather than the time scale, has been adjusted for wind shear. Figure 3.8 is a comparison of the water channel data with Equation (3.32). Shear near the ground increases T_c by a factor of 6 to 8.

Justification for Cross-Stream T_c = Constant

An important modelling assumption is that the concentration integral time scale T_c is constant in the cross-stream direction. However, the plots of cross-stream profiles shown in Figure 3.15 for cross-stream ground level measurements in shear flow, and Figure 3.5 for grid turbulence, indicate that the range of T_c is approximately ±20%. There is a trend of shorter time scales in the centre of the plume and longer time scales in the edges with a peak between 1 to 2 σ_y. This trend is especially evident for elevated sources. There are several possible reasons for errors to occur or trends to develop:

- The integral time scale is defined as the area under the autocorrelation function. It is a type of average large scale that describes the time over which concentration values remain correlated. Because T_c is a representative measure of the larger concentration scales, it requires long sample times and large samples to measure accurately. As discussed in Section 3.3.3, to minimize this sampling problem, all statistics were only calculated for points with $\gamma > 0.1$, but it is unclear if this was sufficient to prevent an adverse effect on the time scale calculations. However, other concentration fluctuation statistics do not seem grossly distorted by the intermittency factor changes.

- Other than effective sample size issues, the Appendix to this chapter shows that the inclusion of intermittent periods in a time series does not affect the time scale.
- The method for calculating the integral time scale is given by Equation (3.4) in Section 3.2 in which the one-dimensional power spectral density of the concentration data, E_c, was extrapolated to zero frequency. In my experience, extrapolation of the one-dimensional power spectrum has proved to be a reliable, consistent method of measuring time scales for both concentration and velocity statistics. It gives excellent results for stochastically simulated time series where the time scale and spectral shape is known, but the accuracy is less certain for experimental data where the spectral functions have much more scatter.
- The literature continues to debate the best method for calculating time scales and power spectra. One recent example of this is Hogrefe et al. (2003) who examine four methods of spectrally decomposing time series of atmospheric variables. They conclude that no single method performs well in all circumstances and that a great deal of care must be used in matching characteristics of analysis techniques to the objectives of the analysis. Many spectral analysis papers have these type of conclusions and there seems to be more art than science in the choice of technique. This corresponds well with the observation in Section 3.4.5 that variances, time scales, and spectra seem to be coupled and it is not clear how to disentangle them.
- It is also possible that the trend is a real physical effect. For example, large scale highly correlated movements of fluid are required to transport tracer material over large cross-stream distances from the plume centroid, so on average the concentration scales may be larger in the fringes of the plume.
- None of these factors explain why there is a difference in the T_c trends for ground level sources or why the vertical profiles of T_c in Figure 3.8 do not exhibit the same trends. At vertical well-elevated positions the shear should be very small and the plume should have similar characteristics to the off-centreline cross-stream positions.

With this background of uncertainty, a 20% variation in T_c for the experimental data is not surprising. The fact that there is a trend, rather than simply 20% scatter, is more disturbing, but it is entirely possible that it is a result of a undetected systematic bias in calculation that becomes evident as the zero-period intermittency increases and γ decreases. I have no doubt some "tuning" of the spectral analysis could remove some of this trend, but it is difficult to justify these sort of manipulations.

Based on this discussion and the fact that the variation is only 20% compared to the order of magnitude effects of shear, I am comfortable with the current assumption of a constant cross-stream T_c. However, it is a topic worthy of further investigation in the future.

Averaging Time Effects on T_c

Equation (3.6) leads to the surprising prediction that the velocity integral time scale T_{vel} and therefore the fluctuation concentration fluctuation time scale T_c do not change much with the averaging time over which concentration fluctuation statistics are sampled. This very weak dependence of the T_c model on t_{avg} occurs because the smallest time scale of turbulent motion will dominate T_{vel} in Equation (3.6). As Hanna et al. (1996) state, vertical dispersion is caused by turbulent fluctuations that have much smaller time scales than those that cause cross-stream dispersion so σ_z does not change as a function of averaging time. So, the smallest turbulent motion scales are then the vertical motions, which do not change with averaging time so T_{vel} and T_c should also remain unaffected by changes in averaging time.

A constant T_c may seem physically counterintuitive, but consider a narrow plume meandering over a measurement position. As averaging time increases it is expected that the effective plume width gets larger, the intermittency factor γ decreases, fluctuation intensity i increases and mean concentration C decreases due to the increased meandering. Increased meandering means that sometimes the plume will be directly over the receptor and other times it will be off to one side or the other. However, when the plume is directly over the receptor, concentration fluctuations will look exactly the same as fluctuations for a shorter time average case. Concentration fluctuations are not expected to slow down or become more time-correlated just because t_{avg} increases, so T_c should not change with t_{avg}. The overall fluctuation statistics will change and the bursts of concentration will be less frequent, but when those bursts occur they should be correlated in time and happening at approximately the same rate as for a shorter time average case.

With the present data set it is impossible to verify this assumption of T_c invariance with averaging time. As discussed in Chapter 2 the LIF measurements allow the centroid of the plume to be tracked in time to allow some adjustment for time averaged fluctuation statistics, but to date this has not proven useful for time scale calculations. Shifting plume centroids seems to introduce too much high frequency distortion to the correlation function. These distortions are not a problem for simpler statistics such as means, variances, and plume spreads, but they do affect the time-correlation between points. The simpler alternative of sampling smaller blocks of time suffers from the problem of severely reducing the size of the data set which also prevents accurate time scale estimation.

3.6 Case Study: Application of the Operational Model to Atmospheric Dispersion

In an ideal world, a complete description of the flow field and all of the relevant turbulence statistics and scales would be available for dispersion modelling. In a close to ideal world, such as the laboratory, good measurements of most of the turbulence parameters are available. In the real world of dispersion modelling in a non-stationary full-scale atmosphere, usually all that is available are parameterizations for the atmospheric conditions.

For a case study of applying the new operational model to the full-scale atmosphere, it is assumed the mean velocity profile U as a function of z is known and shear $\partial U/\partial z$ is also known. For the concentration fluctuation statistics models discussed in the previous sections the other two important parameters are:

- the vertical velocity fluctuation component w'_{rms} as a function of z. This is needed to calculate the non-dimensional shear, S, in Equation (3.15).
- the no-shear Eulerian integral time scale of velocity T_{vel} needed in Equation (3.31) to calculate the no-shear scale of concentration $T_{c,\text{no-shear}}$ in the T_c time scale model Equation (3.32).

The recommendations for an applied model are heavily biased by the experimental data to dispersion of a high Schmidt number (i.e. low molecular diffusivity), neutrally buoyant tracer in the neutrally stable atmosphere. It is expected that the fluorescein dye in water is a good approximation for aerosol or particle dispersion in a Pasquill-Gifford class D neutrally stable (high wind, low heat flux) atmosphere, but possibly less reliable for other conditions.

The author's personal experience with other water channel data compared to full-scale atmospheric data suggests that the Schmidt number issue is not very important. Concentration fluctuation parameters such as variances and fluctuation intensities seem to match well between water channel data (with Sc $\simeq$ 2000) and atmospheric tracer studies with gases (Sc $\simeq$ 1). Chatwin and Sullivan (1990) made a similar observation when comparing a variety of dispersion experiments with heat, smoke, or hydrocarbons as tracers. Additional indirect support for insignificance of the Schmidt number mismatch is given by Hilderman and Wilson (1999) and in Chapter 4 where a stochastic model is used to generate simulated concentration fluctuation spectra that are a much closer match to low Schmidt number dispersion in the atmosphere than the high Schmidt number water channel data, but the difference produces minimal adverse effects.

Atmospheric stability effects are an unknown factor as there are no measurements available for unstable or stable conditions that are comparable to detailed neutral stability linescan LIF data sets. The assumption made for the case study is that concentration fluctuations for unstable and stable atmospheric conditions are similar to those in neutral stability. The stability will affect the estimation of parameters such as the no-shear time scale $T_{c,\text{no-shear}}$, the vertical velocity fluctuations w'_{rms}, and the plume spreads σ_y and σ_z but the behaviour of the concentration fluctuations with respect to these parameters is assumed to be the same.

3.6.1 Case Study: Vertical Velocity Fluctuations w'_{rms}

Based on a review of the literature, the standard parameterizations for turbulent velocity components are functions of the friction velocity u_*, the height above the ground z and some stability parameter, typically the Monin-Obukhov length L_*. A recent summary of the literature on this subject is Kerschgens et al. (2000, equation (4.1)), who recommend for neutral to unstable conditions

$$w'_{\text{rms}} = \left\{ \left(1.3u_* \exp\left(-\frac{z}{H}\right)\right)^3 + \left[1.3\left(\frac{z}{H}\right)^{1/3}\left(1-0.8\left(\frac{z}{H}\right)\right)w_*\right]^3 \right\}^{1/3} \tag{3.33}$$

and for stable conditions

$$w'_{\text{rms}} = 1.3u_* \exp\left(-\frac{z}{H}\right) \tag{3.34}$$

The stability parameter L_* is the Monin-Obukhov length defined as

$$L_* = -\frac{u_*^3 C_p \rho T}{\kappa g H_0} \tag{3.35}$$

where C_p is the heat capacity, ρ is the density, T is the temperature, g is the gravitational acceleration, and H_0 is the surface heat flux. H is the mixing height which can be calculated from Kerschgens et al. (2000, equation (4.3))

$$H = 0.7\left(\frac{u_* L_*}{1.11 \times 10^{-4}\text{s}^{-1}}\right)^{0.5} \tag{3.36}$$

with a maximum H of 1100 m, a minimum of $H = 250$ m for neutral to stable conditions and a constant $H = 1100$ m for unstable conditions. The convective scaling velocity w_* is

$$w_* = u_*\left(-\frac{H}{\kappa L_*}\right)^{1/3} \tag{3.37}$$

with von Karman constant $\kappa = 0.4$. The u_*^3 in Equation (3.35) may be alarming, given the likely uncertainties in estimates of u_*, but when it is plugged into the convective scaling velocity Equation (3.37) it cancels out leaving w'_{rms} at worst linearly dependent on u_*. Near the ground $z \ll H$ both Equations (3.33) and (3.34) tend to reduce to approximately $w'_{\text{rms}} = 1.3u_*$.

3.6.2 Case Study: Friction Velocity u_*

Estimates of w'_{rms} require an estimate of the friction velocity u_*. Using the recommendations of van Ulden and Holtslag (1985)

$$u_* = \frac{\kappa U_{\mathrm{met}}}{\ln\left(\frac{z_{\mathrm{met}}}{z_0}\right) - \Psi\left(\frac{z_{\mathrm{met}}}{L}\right) + \Psi\left(\frac{z_0}{L}\right)} \tag{3.38}$$

where $\kappa = 0.4$ is the von Karman constant, z_{met} is the reference height at which the velocity U_{met} is known, z_0 is the surface roughness, and L is the Monin-Obukhov length. Typically the reference velocity U_{met} is the meteorological measurement of wind speed at the standard height of $z_{\mathrm{met}} = 10$ m. The function Ψ for unstable conditions (i.e. Pasquill-Gifford classes A through C) is from van Ulden and Holtslag (1985)

$$\Psi = \left(1 - 16\frac{z}{L}\right)^{1/4} - 1 \tag{3.39}$$

and for stable conditions (i.e. classes E and F)

$$\Psi = -17\left(1 - \exp\left(\frac{-0.29z}{L}\right)\right)^{1/4} - 1 \tag{3.40}$$

For neutral conditions (class D) Equations (3.39) and (3.40) both reduce to

$$\Psi = 0 \tag{3.41}$$

3.6.3 Case Study: Eulerian Integral Time Scale of Velocity T_{vel}

The available data for Eulerian integral time scales in atmospheric boundary layers is limited and there is even more scatter in the estimates for the time scales than for the turbulent velocity components. Counihan (1975) presented a comprehensive review of the ranges of various turbulence parameters in the adiabatic (neutrally stable, high wind speed, low heat flux) boundary layer and concluded that the stream-wise integral length scale of turbulence $L_u \propto z$ up to about 1/3 of the boundary layer depth H after which it decreases. He also found that the length scales of the other components $L_v \approx 0.3$ to $0.4L_u$ and $L_w \approx 0.5$ to $0.6L_u$ in the lower part of the boundary layer and $L_v = L_w = 0.5L_u$ at elevated locations well above ground level. Other literature tends to also find or assume that well above the ground $L_v \approx L_w$. In the present study, it was observed that $T_v \approx 0.5T_u$ and $T_w \approx 0.3T_u$ in the shear flow while $T_v = T_w \approx 0.5T_u$ in grid turbulence.

If specific information or measurements of velocity time scales are available for the dispersion conditions modelled, they should be used. However, in the absence of other estimates, an approximation based on the previous paragraph, is that the no-shear streamwise integral length scale $L_{u,\text{no-shear}}$ is approximately 1/2 of the maximum L_u expected at 1/3 H so that

$$L_{u,\text{no-shear}} \approx \frac{H}{6} \tag{3.42}$$

Given that the smallest scale will tend to dominate the velocity time scale calculation in Equation (3.6) it is proposed that in the absence of better information, a reasonable estimate for the no-shear timescale is

$$T_{\text{vel, no-shear}} \approx T_u/5 \tag{3.43}$$

and with the frozen turbulence assumption

$$T_{\text{vel, no-shear}} = \frac{L_{u,\text{no-shear}}}{U_{\text{no-shear}}} \tag{3.44}$$

The recommended estimate for the no-shear time scale is obtained by combining Equations (3.42) to (3.44) with the relationship between the $T_{c,\text{no-shear}}$ and T_{vel} in Equation (3.31)

$$T_{c,\text{no-shear}} \approx \frac{H}{40U_{\text{no-shear}}} \tag{3.45}$$

Using the measurements from this study with $H \approx 400$ mm, $U_{\text{no-shear}} \approx 232$ mm/s then $T_{c,\text{no-shear}} \approx 0.04$ s and $L_{c,\text{no-shear}} \approx 10$ mm which agrees with the value actually found in the fit for the experimental data in Section 3.5.3.

As another test of this approach, consider the full-scale atmospheric concentration fluctuation experiments of Yee et al. (1995). Assume that $H \approx 600$ m (Counihan, 1975), and from Yee et al. (1995) $U_{\text{no-shear}} \approx 5$ m/s based on the flow velocity near the ground adjusted for height H. Then $T_{c,\text{no-shear}} \approx 3$ s and $L_{c,\text{no-shear}} \approx 15$ m. With a velocity profile similar to the one measured in the water channel it is expected that the ground level time scale is about 8 times the no-shear value so $T_c \approx 25$ s and $L_c \approx 125$ m. This is well within the range of values measured by Yee et al. (1995).

3.6.4 Case Study: Setting Minimum Heights for z_{ref} and h_{ref}

Close to the source where σ_z is very small, z_{ref} and h_{ref} can become very small and the effective shear S_{avg} becomes unrealistically large. To prevent this problem it is recommended that z_{ref} and h_{ref} should be no less than $5z_0$ at any receptor position. The physical argument to support this is that near the ground there is likely some spatial averaging due to mixing around the roughness elements. Whether the constant should be 5 or some other number of order one will have to be decided with further testing of near source concentration fluctuations. A more practical recommendation for the full-scale atmosphere is that the minimum z height is 2 m; approximately the height of the breathing zone if we are considering human exposures.

In the experimental data set, the lowest measurement positions were above $z =$ 4 mm which was the height of the expanded metal roughness elements. The roughness length z_0 was 0.52 mm and the displacement height d of the log-law was 1.7 mm. No measurements could be taken below about $3(z_0 + d)$. Assuming a full-scale atmospheric roughness length $z_0 = 0.1$ m (a moderate roughness length between a grassy plain at $z_0 = 0.01$ m and an urban environment of $z_0 = 1$ m) then the water channel is geometrically 1:200 scale. No measurements were taken below about 6 mm in the water channel which corresponds to 1.2 m in full-scale. This puts us within range of the recommended 2 m full-scale lower limit on z position.

3.6.5 Case Study: Results - Vertical Profiles in a Neutrally Stable Atmosphere

To demonstrate the trends produced by the models of Section 3.5 a sample case is shown in Figures 3.16 through 3.22 using the restrictions and parameterizations specified in sections 3.6.1 through 3.6.4 with the following additional conditions:

- neutrally stable conditions - class D
- rough surface boundary layer flow equivalent to $z_0 = 1.0$ m in the atmosphere
- sources at 0.1H and ground level where H is the boundary layer thickness.
- log-law velocity profile with $u_* = 0.1U_H$
- vertical plume spread $\sigma_z = 0.5x^{0.7}$ (from Wilson (1994) based on Pasquill and Smith (1983))
- four downstream positions where $\sigma_z/H = 0.01, 0.03, 0.1, 0.3$ which is at $x/H =$ 0.05, 0.23, 1.3, 6.3 respectively for the plume spread function given above.
- two source height fluctuation intensities $i_h^2 = 0.1$ and 10 which covers the range of likely values.
- All length variables (x, z, σ_z etc.) are normalized by the boundary layer depth H.
- Only the cross-stream centreline ($y = 0$) values are plotted.

The results of this case study simulation are shown in Figures 3.16 through 3.22.

- Figure 3.16 shows time scale ratios $T_{c,\text{shear}}/T_{c,\text{no-shear}}$ using Equation (3.32). It is interesting to note that as the plume spread increases with downstream distance the ratio actually decreases very near the ground at z less than $0.005H$. Based on the model derived in section 3.5.3 this is exactly what would be expected. As the plume gets larger there is more influence of conditions above the ground where the velocities are higher and the time scales are shorter. This decreasing time scale ratio near the ground also follows from model assumption that the smallest velocity scales will govern the fluctuation time scale T_c and downstream distance, plume size and intermittency have little effect on T_c.

  In practical terms, $0.005H$ is very small, typically about 2 m or less in the atmosphere. Under these conditions the recommendation of section 3.6.4 for small z locations should apply and statistics that represent near surface conditions in the shear layer should be taken at about $z = 2$ m. Further experiments are required to resolve this issue with any more accuracy.

- Figures 3.17 and 3.18 show the fluctuation intensity i calculated using Equations (3.23) with Equation (3.12) and (3.13) for the elevated and ground level sources with source centreline no-shear fluctuation intensities $i_h^2 = 0.1, 10$. The only effect that changing i_h^2 has is to shift the curves to the right or left, as expected. The fluctuation intensity is almost a symmetrical parabola around the source height for the elevated source until the plume gets large and the ground starts to have an influence.

- Figures 3.19 and 3.20 show the conditional fluctuation intensity i_p from Equations (3.26) and (3.27). The behaviour is similar to that of i with the restriction that i_p reaches a maximum of $i_{p,\infty}$ at the higher elevations

- Figures 3.21 and 3.22 show the intermittency factors γ corresponding to the i and i_p plots of Figures 3.17 through 3.20 using Equation (3.3). As expected for the ground level source, wind shear smears out the plume and removes all the pockets of zero concentration, forcing γ to 1.0 near the ground. In contrast, in the highly intermittent fringes of the elevated plume, γ is near zero until the plume begins to interact with the ground.

Overall the model has reasonable behaviours and does not have any discontinuities or unrealistic limits, so it should prove useful for engineering modelling of concentration fluctuations in dispersing plumes.

3.6.6 Case Study: Results - Vertical Profiles in Stable and Unstable Atmospheric Conditions

The previous case study examples were for dispersion in a neutrally stable class D atmosphere. In other atmospheric stability conditions, such as the very unstable convectively driven of Pasquill-Gifford class A conditions to the very stable ground based inversion conditions of Paquill-Gifford class F, turbulence characteristics and vertical velocity profiles can be considerably different. The available concentration fluctuation data for unstable and stable dispersion conditions is limited to a few points in a few experiments, so it is difficult to draw many conclusions. For example, Mylne (1992) and Mylne and Mason (1991) discuss some full-scale measurements of concentration fluctuations in conditions ranging from slightly convective to neutral to stable and note that fluctuation statistics and spectra are qualitatively similar in all stabilities, but differ quantitatively. Mole and Jones (1994) make similar observations. Quantitative differences will also occur with the shear effects model developed in this study due to differences in velocity profiles, vertical velocity fluctuations, vertical spreads and travel times in the different stability conditions.

The shapes of the intermittency γ, fluctuation intensity i and conditional fluctuation intensity i_p profiles will be qualitatively similar to those in Figures 3.17 to 3.22 with some shifting in magnitudes caused by changes in the input parameters, so there is little point in producing additional plots for these other stabilities. The concentration fluctuation time scale T_c can be examined in a little more detail to determine if its behaviour seems realistic. Figure 3.23(a) shows the downstream change in T_c predicted for small ground level source with a receptor at $z = 2$ m above the ground and Figure 3.23(b) shows the predicted change in T_c with receptor height z at a position $x = 1000$ m downstream of the source. These time scales were calculated using the same $U_{\text{met}} = 3$ m/s wind speed at $z_{\text{met}} = 10$ m for all stability classes with $z_0 = 0.1$ m and power law velocity profiles

$$\frac{U}{U_{\text{met}}} = \left(\frac{z}{z_{\text{met}}}\right)^p \tag{3.46}$$

where the power p from Irwin (1979), is 0.08 for class A, 0.16 for class D, and 0.54 for class F. Mixed layer depths H, vertical fluctuations w'_{rms} and the no-shear time scale $T_{c,\text{no-shear}}$ were computed using the recommendations in Section 3.6.

- Class A time scales are the longest at all positions because the convective motions produce deep mixed layers with corresponding large scales of vertical mixing.

- Class F scales are the next longest, near the ground. In stable conditions, the small vertical spreads σ_z produce small plumes that spend most of their travel time near the ground where shear has a large effect, local wind speeds are low, and travel times are long leading to a large non-dimensional shear S_{avg}. There are quite large changes in T_c with vertical position as shown in Figure 3.23(b) so the uncertainty in the estimated class F time scales is expected to be higher than for class A or D. At downstream distances greater than a few kilometres, the class F time scale begins to decreases as the majority of the plume spreads outside the near ground region and samples the predicted shorter time scale effects farther above the ground.

- Class D has moderate shear effects and moderate plume spreads that together produce somewhat shorter time scales near the ground. The differences in T_c between the three classes only about 20%.

It is difficult to determine whether these results are realistic or not because of the lack of comparison data. Mylne (1992) measured $T_c = 21.4$ s in a stable atmosphere with a wind speed of 0.92 m/s at 2 m above the ground and $x = 100$ m downstream and $T_c = 1.8$ s in neutral conditions with $U = 5.7$ m/s at 2 m above the ground. The predictions in Figure 3.23 are of the same order of magnitude as these measurements.

In the absence of better information, it is recommended that all atmospheric stabilities be treated in the same manner. As stability changes, the mechanisms producing the measured turbulence change from convective buoyancy driven motions in unstable air, to mechanically generated turbulence in neutral conditions, to the suppression of turbulent mixing as stability increases due to buoyancy forces in an inversion layer. These changing properties are hopefully accounted for implicitly within the empirical meteorological models for u_*, w'_{rms}, plume spreads σ_y and σ_z, velocity $U(z)$, and shear profile $\partial U/\partial z$. There still may be further adjustments necessary that will be require additional research and more detailed measurements in other stability conditions.

3.7 Summary and Conclusions

An operational engineering model for concentration fluctuations in a rough surface boundary layer shear flow has been developed using high spatial and temporal resolution data collected using linescan LIF techniques in a neutrally stable scale model shear flow in a water channel. The model for the effect of wind shear requires input parameters generated by other dispersion models:

- mean concentration, C
- vertical velocity profile U and shear profile $\partial U/\partial z$
- vertical rms velocity fluctuation w'_{rms}.
- no-shear prediction of the fluctuation intensity i
- vertical plume spread σ_z
- no-shear concentration fluctuation time scale $T_{c,\text{no-shear}}$.

Direct measurements of these parameters were available for the linescan LIF data used to develop the shear distortion models.

The shear distortion model equations are summarized here for convenience, with their original equation numbers. The non-dimensional shear is

$$S = \frac{w'_{\mathrm{rms}} t_t}{U} \left(\frac{\partial U}{\partial z} \right) \tag{3.15}$$

where $t_t = x/U$ is the local travel time evaluated at either

$$z_{\mathrm{ref}} = z + 0.1\sigma_z \tag{3.21}$$

or

$$h_{\mathrm{ref}} = h + 0.1\sigma_z \tag{3.22}$$

The fluctuation intensity i is calculated from a no-shear estimate of the fluctuation intensity and the relationship

$$\frac{i_{\mathrm{shear}}}{i_{\text{no-shear}}} = \frac{1}{(1 + 5S_{z_{\mathrm{ref}}}))^{1/3}} \tag{3.23}$$

The source position shear effects are implicitly included in the water channel data and in most models of source centreline fluctuation intensity so only the receptor position shear $S_{z_{\mathrm{ref}}}$ is included in Equation (3.23). The concentration fluctuation integral time scale

$$\frac{T_{c,\mathrm{shear}}}{T_{c,\text{no-shear}}} = \frac{U_{\text{no-shear}}}{U_{z_{ref}}}\left(1 + 5S_{\mathrm{avg}}\right)^{1/3} \tag{3.32}$$

where S_{avg} includes both the receptor and source effects

$$S_{\mathrm{avg}} = \frac{S_{z_{\mathrm{ref}}} + S_{h_{\mathrm{ref}}}}{2} \tag{3.30}$$

The no-shear time scale is calculated from the velocity fluctuation timescales

$$T_{c,\text{no-shear}} = 0.8T_{\mathrm{vel}} \tag{3.31}$$

with T_{vel} as the relevant velocity time scale

$$\frac{1}{T_{\mathrm{vel}}} = \frac{1}{T_u} + \frac{1}{T_v} + \frac{1}{T_w} \tag{3.6}$$

where T_u, T_v and T_w are velocity fluctuation time scales of the three velocity components. The conditional (in-plume) fluctuation intensity is

$$i_p = \frac{i}{\left(1 + \left(\frac{i}{i_{p,\infty}}\right)^3\right)^{1/3}} \tag{3.26}$$

where the asymptotic value for $i_{p,\infty}$ when i is very large is

$$i_{p,\infty} = \frac{1.9}{(1 + 5S_{\mathrm{avg}})^{1/6}} \tag{3.27}$$

The intermittency factor can be calculated from the conditional and total fluctuation intensities using the definition

$$\gamma = \frac{1 + i_p^2}{1 + i^2} \tag{3.3}$$

The end result is a complete model for the second moment conditional and total concentration fluctuation statistics that can be easily applied to almost any existing dispersion model. The input requirements can be satisfied by a variety of models available in the literature or those discussed in the previous sections.

Recommendations were made in Section 3.6 for using models from the literature to predict w'_{rms}, and $T_{c,\text{no-shear}}$ for full scale conditions in the absence of the more detailed information available in laboratory studies. A computational case study example of the application of this shear distortion model to a full-scale release was presented to demonstrate that the models are robust over the entire range of full-scale conditions and produce plausible results.

As with any new model, additional data would help to clarify some of the model coefficients and improve the applicability to other release scenarios. In particular, some near source and near ground full-scale measurements in different atmospheric stabilities would be very useful.

Appendix: Intermittency Effects on Integral Time Scale T_c

In the cross-stream direction, time scales and length scales of concentration are approximately constant across the plume, as shown in Figure 3.15 for ground level measurements in shear flow, and Figure 3.5 for grid turbulence. Elevated measurement positions in shear flow show similar trends. It is interesting and somewhat counter-intuitive that the time scales do not change much even as the intermittency factor γ rapidly decreases as y/σ_y increases. At $2\sigma_y$, γ can be as low as 10%, yet the time scale remains about the same. The physical reason for this welcome invariance of the concentration fluctuation integral time scale T_c with plume intermittency can be demonstrated by considering the definition of T_c as the area under the autocorrelation function $R_c(t)$

$$T_c = \int_{-\infty}^{\infty} R_c(t) \mathrm{d}t \tag{3.47}$$

The autocorrelation for a time delay τ is defined as

$$R_c(\tau) = \frac{\overline{c(t)c(t+\tau)}}{\overline{c^2}} \tag{3.48}$$

where $\overline{c^2}$ is the second moment of concentration. Consider a time series with second moment $\overline{c^2}$ and $\gamma = 1.0$ and add intermittent periods so $\gamma < 1.0$. The new second moment $\overline{c^2}_{\text{intermittent}} = \gamma\overline{c^2}$. Similarly, consider the definition of the time average in the numerator of Equation (3.48) for a non-intermittent time series

$$\overline{c(t)c(t+\tau)} = \frac{1}{T}\int_0^T c(t)c(t+\tau)\mathrm{d}t \tag{3.49}$$

and adding intermittent periods

$$\begin{aligned}\overline{c(t)c(t+\tau)}_{\text{intermittent}} &= \frac{\gamma}{T}\int_0^T c(t)c(t+\tau)\mathrm{d}t \\ &= \gamma\overline{c(t)c(t+\tau)}\end{aligned} \tag{3.50}$$

For a fraction of time $1-\gamma$ the concentration will be zero, so $c(t)c(t+\tau)$ only has non-zero values for a fraction γ of the total duration T. Now putting the definitions for the intermittent values into the definition of the correlation function from Equation (3.48)

$$\begin{aligned}R_{\text{cintermittent}}(\tau) &= \frac{\gamma\overline{c(t)c(t+\tau)}}{\gamma\overline{c^2}} \\ &= \frac{\overline{c(t)c(t+\tau)}}{\overline{c^2}} \\ &= R_c(\tau)\end{aligned} \tag{3.51}$$

which shows that the time scale of concentration fluctuation T_c should not change with intermittency factor γ. The key assumption necessary for this to work is that the non-zero concentration fluctuations have the same normalized spectra, independent of the intermittency. This assumption is supported by both grid turbulence and shear flow data.

References

Bara, B. M., Wilson, D. J., and Zelt, B. W. (1992), Concentration Fluctuation Profiles from a Water Channel Simulation of a Ground-Level Release, *Atmospheric Environment*, 26A(6):1053–1062.

Chatwin, P. C. and Sullivan, P. J. (1990), A Simple and Unifying Physical Interpretation of Scalar Fluctuation Measurements from Many Turbulent Shear Flows, *Journal of Fluid Mechanics*, 212:533–556.

Counihan, J. (1975), Adiabatic Atmospheric Boundary Layers: A Review and Analysis of Data from the Period 1880-1972, *Atmospheric Environment*, 9:871–905.

Fackrell, J. E. and Robins, A. G. (1982), Concentration Fluctuations and Fluxes in Plumes from Point Sources in a Turbulent Boundary Layer, *Journal of Fluid Mechanics*, 117:1–26.

Hanna, S. R. (1984), Concentration Fluctuations in a Smoke Plume, *Atmospheric Environment*, 18(6):1091–1106.

Hanna, S. R., Drivas, P. J., and Chang, J. J. (1996), *Guidelines for Use of Vapor Cloud Dispersion Models*, Center for Chemical Process Safety of the American Institute of Chemical Engineers, New York, NY, second edition.

Hilderman, T. L. and Wilson, D. J. (1999), Simulating Concentration Fluctuation Time Series with Intermittent Zero Periods and Level Dependent Derivatives, *Boundary-Layer Meteorology*, 91:451–482.

Hinze, J. (1975), *Turbulence*, McGraw-Hill, second edition.

Hogrefe, C., Vempaty, S., Rao, S. T., and Porter, P. S. (2003), A comparison of four techniques for separating different time scales in atmospheric variables, *Atmospheric Environment*, 37:313–325.

Irwin, J. S. (1979), A Theoretical Variation of the Wind Profile Power-Law Exponent as a Function of Surface Roughness and Stability, *Atmospheric Environment*, 13:191–194.

Kerschgens, M. J., Nolle, C., and Martens, R. (2000), Comments on turbulence parameters for the calculation of dispersion in the atmospheric boundary layer, *Meteorologische Zeitschrift*, 9(3):155–163.

Mole, N. and Jones, C. (1994), Concentration Fluctuation Data from Dispersion Experiments Carried out in Stable and Unstable Conditions, *Boundary-Layer Meteorology*, 67:41–74.

Mylne, K. R. (1992), Concentration Fluctuation Measurements in a Plume Dispersing in a Stable Surface Layer, *Boundary-Layer Meteorology*, 60:15–48.

Mylne, K. R. (1993), The Vertical Profile of Concentration Fluctuations in Near-Surface Plumes, *Boundary-Layer Meteorology*, 65:111–136.

Mylne, K. R. and Mason, P. (1991), Concentration fluctuation measurements in a dispersing plume at a range of up to 1000 m, *Quarterly Journal of the Royal Meteorological Society*, 117:177–206.

Pasquill, F. and Smith, F. (1983), *Atmospheric Diffusion*, John Wiley and Sons, third edition.

Sawford, B. L. and Stapountzis, H. (1986), Concentration Fluctuations According to Fluctuating Plume Models in One and Two Dimensions, *Boundary-Layer Meteorology*, 37:89–105.

van Ulden, A. P. and Holtslag, A. A. M. (1985), Estimation of Atmospheric Boundary Layer Parameters for Diffusion Applications, *Journal of Climate and Applied Meteorology*, 24:1196–1207.

Warhaft, Z. (2000), Passive Scalars in Turbulent Flows, *Annual Review of Fluid Mechanics*, 32:203–240.

Wilson, D. (1981), Along-Wind Diffusion of Source Transients, *Atmospheric Environment*, 15:489–495.

Wilson, D. (1994), Predicting Pollutant Concentrations in the Atmosphere, Department of Mechanical Engineering, University of Alberta.

Wilson, D. J. (1995), *Concentration Fluctuations and Averaging Time in Vapor Clouds*, Center for Chemical Process Safety of the American Institute of Chemical Engineers, New York, NY.

Wilson, D. J. (2002), Outcome-Based Risk Scaling and Uncertainty Factors for Toxic Gas Releases, Technical report, University of Alberta, Final Report for NSERC Strategic Project 215980-1998.

Wilson, D. J., Robins, A. G., and Fackrell, J. E. (1985), Intermittency and Conditionally-Averaged Concentration Fluctuation Statistics in Plumes, *Atmospheric Environment*, 19:1053–1064.

Wilson, D. J. and Zelt, B. W. (1990), Technical Basis for EXPOSURE-1 and SHELTER-1 Models for Predicting Outdoor and Indoor Exposure Hazards from Toxic Gas Releases, Engineering report 72, University of Alberta Department of Mechanical Engineering.

Yee, E., Chan, R., Kosteniuk, P., Chandler, G., Biltoft, C., and Bowers, J. (1995), The Vertical Structure of Concentration Fluctuation Statistics in Plumes Dispersing in the Atmospheric Surface Layer, *Boundary-Layer Meteorology*, 76:41–67.

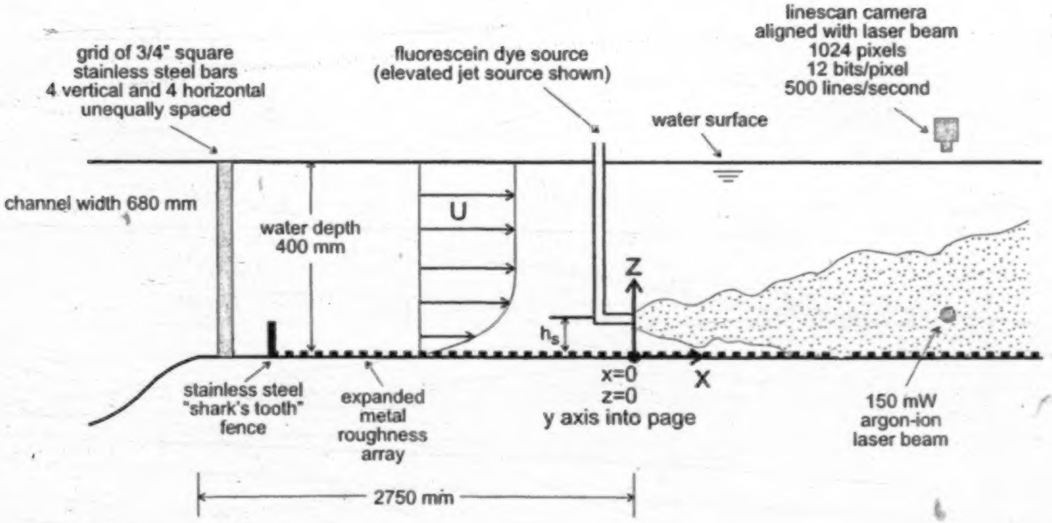
grid of 3/4" square
stainless steel bars
4 vertical and 4 horizontal
unequally spaced
fluorescein dye source
(elevated jet source shown)
linescan camera
aligned with laser beam
1024 pixels
12 bits/pixel
500 lines/second
water surface
channel width 680 mm
water depth
400 mm
U
Z
h_s
x=0
z=0
y axis into page
X
stainless steel
"shark's tooth"
fence
expanded
metal
roughness
array
150 mW
argon-ion
laser beam
2750 mm

Figure 3.1: University of Alberta Mechanical Engineering Department water channel schematic. The recirculation piping, downstream weir gate, and inlet plenum flow straighteners are not shown. Coordinate system origin is at ground level on the channel centreline at the downstream location of the tracer source. Laser beam diameter is approximately 1 mm and projects into the page.

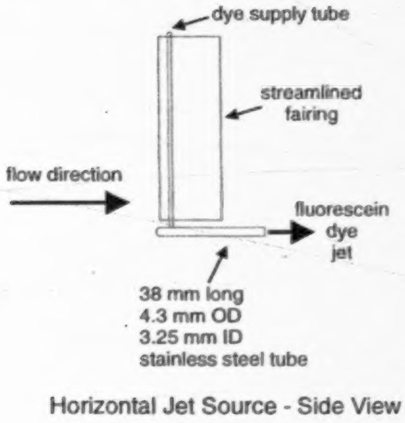
dye supply tube
streamlined fairing
flow direction
fluorescein dye jet
38 mm long
4.3 mm OD
3.25 mm ID
stainless steel tube
Horizontal Jet Source - Side View

(a)

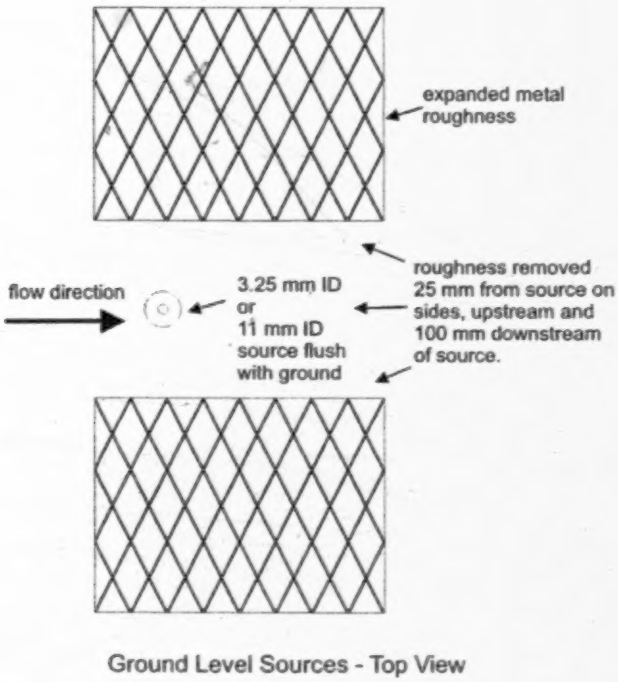
expanded metal roughness
flow direction
3.25 mm ID
or
11 mm ID
source flush
with ground
roughness removed
25 mm from source on
sides, upstream and
100 mm downstream
of source.
Ground Level Sources - Top View

(b)

Figure 3.2: Fluorescein dye sources. (a) Side view of elevated horizontal jet sources. Source was suspended from above the channel. (b) Top view of ground level sources. Expanded metal roughness was removed from the immediate area of the source and dye supply lines were underneath the acrylic panel below the roughness. The large (11 mm ID) ground level source was changed to the small ground level source by inserting a plug with a 3.25 mm ID hole for the small source.

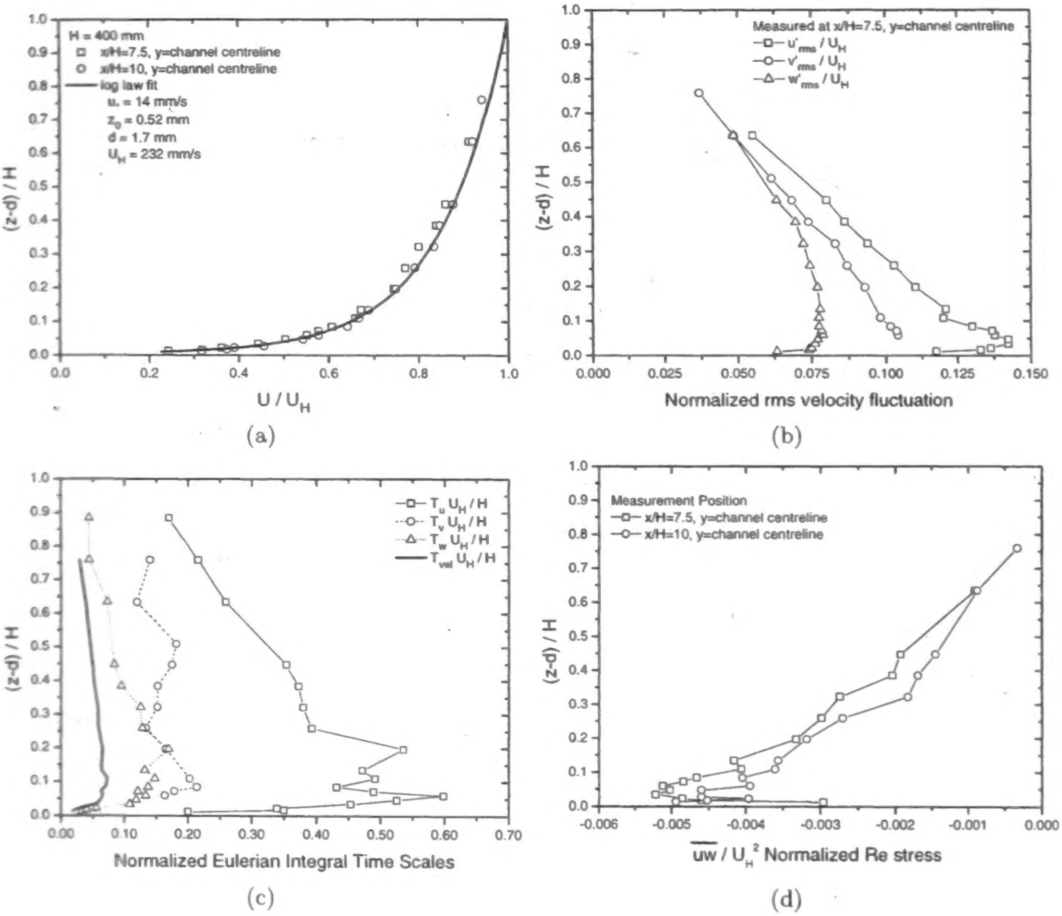

(a) (b)

(c) (d)

Figure 3.3: Velocity statistics for the rough surface boundary layer shear flow measured at 3000 mm ($x/H = 7.5$) downstream from the water channel inlet. (a) Normalized vertical profiles of the mean streamwise velocity U/U_H. (b) Normalized vertical profiles of the rms fluctuating velocity components u'_{rms}/U_H, v'_{rms}/U_H, and w'_{rms}/U_H. (c) Vertical profiles of the normalized Eulerian velocity fluctuation timescales, $T_u U_H/H$, $T_v U_H/H$, $T_w U_H/H$ and $T_{\text{vel}} U_H/H$. (d) Vertical profiles of the normalized Reynolds stresses $\overline{uw}/U_H^2$

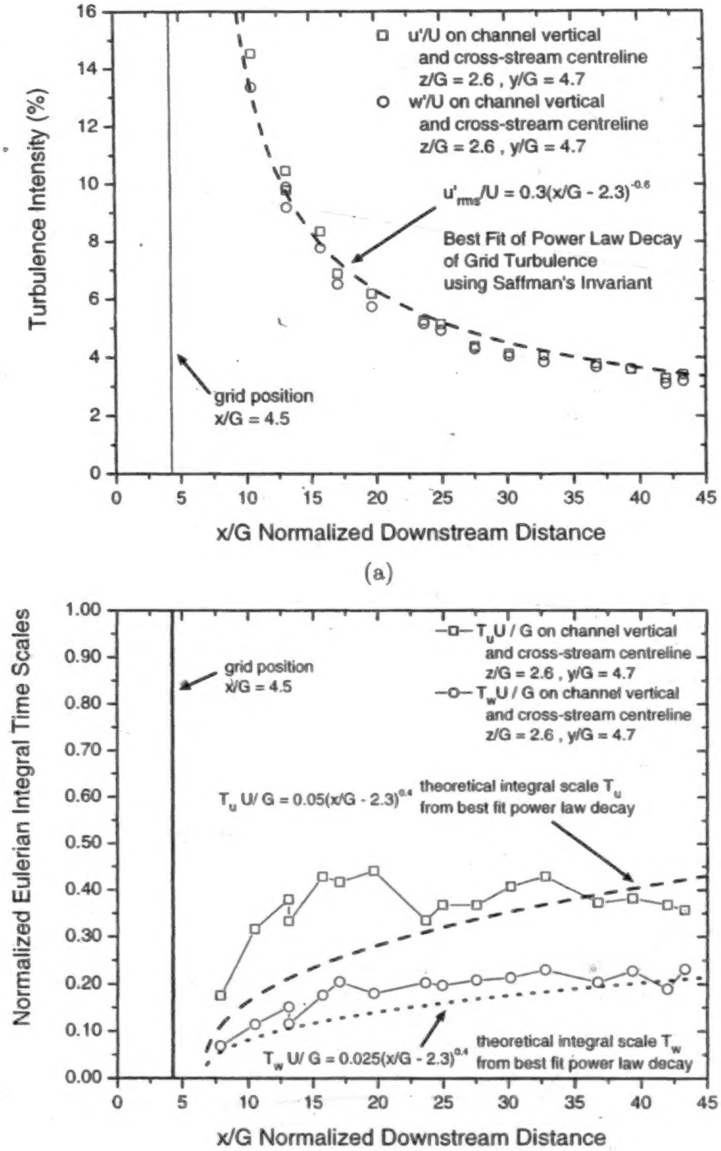

(a)

(b)

Figure 3.4: Grid turbulence velocity statistics. (a) Turbulence intensity decay with normalized downstream distance x/G along the centreline of the channel. Best fit power law decay of turbulence intensity based on Saffman's invariant. (b) Normalized Eulerian integral timescales of velocity fluctuation in the streamwise T_uU/G and vertical T_wU/G directions along the centreline of the channel compared to T_uU/G calculated using the best fit power law decay of grid turbulence based on Saffman's invariant.

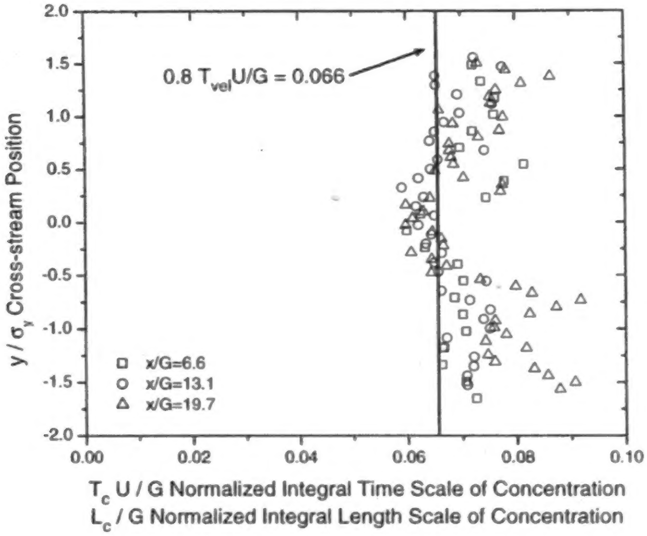

Figure 3.5: Grid turbulence normalized concentration fluctuation integral time scale T_cU/G and length scale L_c/G profiles for a horizontal jet source on the water channel centreline compared to the no-shear estimate. The normalizing velocity U is the local flow velocity so the normalized time and length scales are exactly the same.

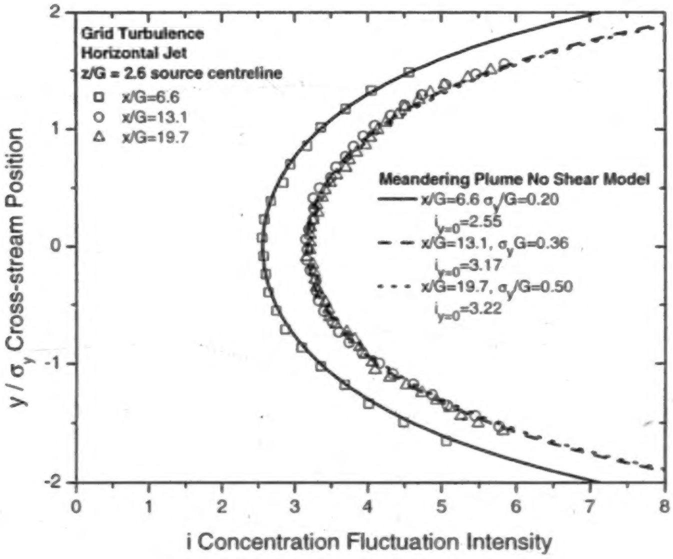

Figure 3.6: Grid turbulence concentration fluctuation intensity i profile for a horizontal jet source on the water channel centreline compared to the no-shear model.

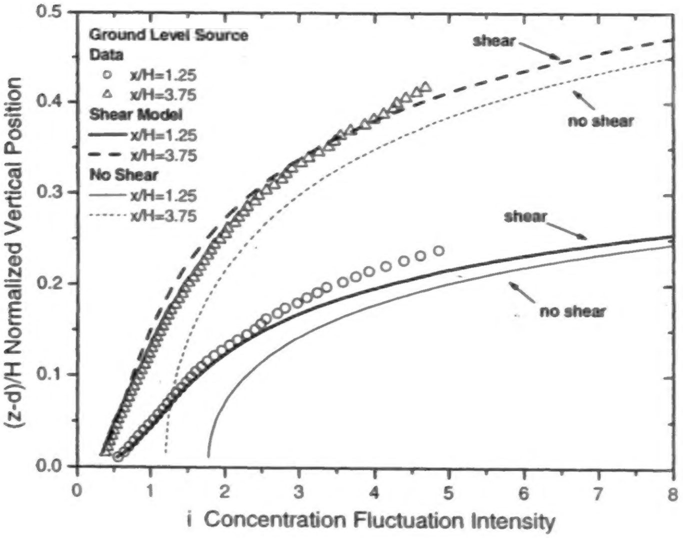

(a)

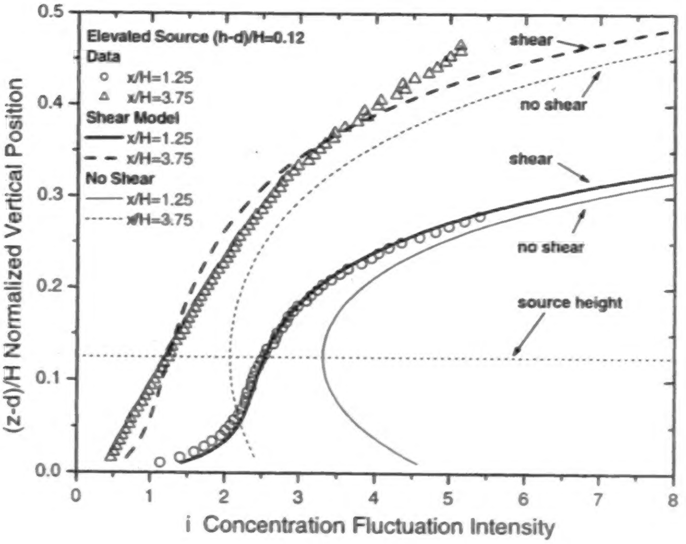

(b)

Figure 3.7: Vertical profiles of the fluctuation intensity i compared to the shear model and the no-shear model. (a) ground level source (b) elevated horizontal iso-kinetic jet source $(h-d)/H = 0.12$.

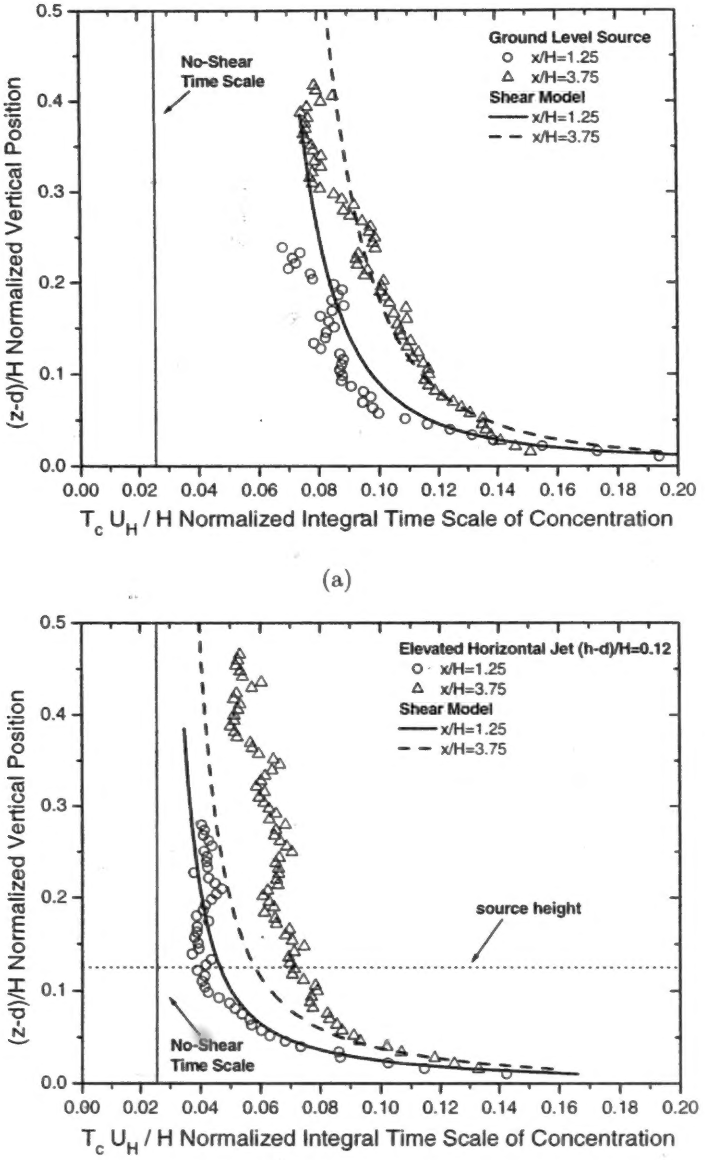

(a)

(b)

Figure 3.8: Vertical profiles of the normalized concentration fluctuation integral time scale $T_c U_H / H$ compared to the shear model and the no-shear model. (a) ground level source (b) elevated horizontal iso-kinetic jet source $(h-d)/H = 0.12$.

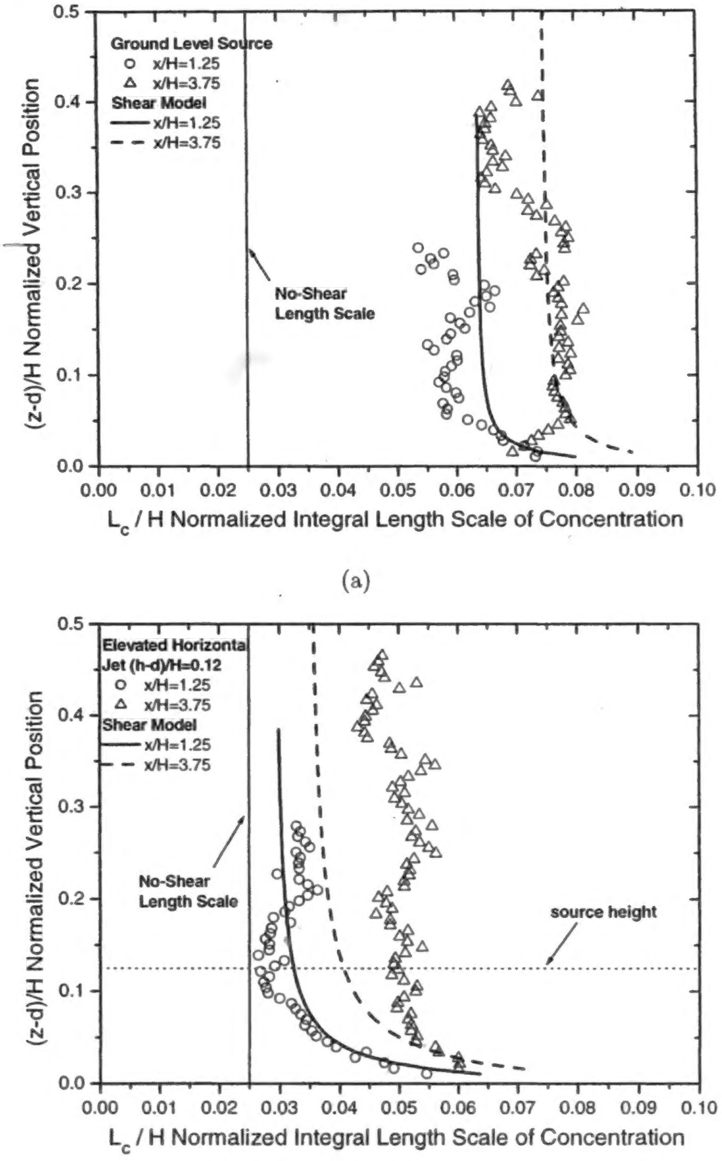

(a)

(b)

Figure 3.9: Vertical profiles of the normalized concentration fluctuation integral length scale L_c/H compared to the shear model and the no-shear model. (a) ground level source (b) elevated horizontal jet source $(h-d)/H = 0.12$.

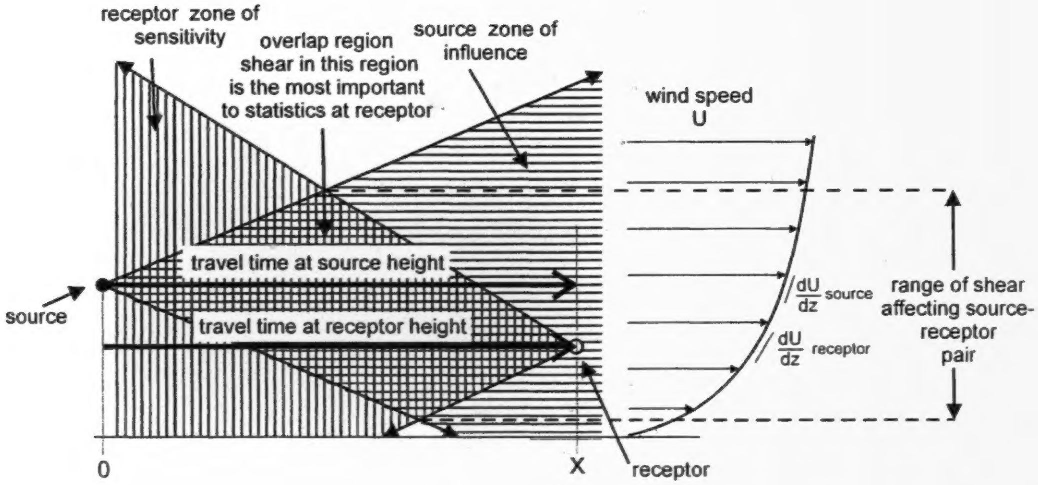
receptor zone of sensitivity
overlap region shear in this region is the most important to statistics at receptor
source zone of influence
wind speed U
travel time at source height
travel time at receptor height
source
$\frac{dU}{dz}$ source
$\frac{dU}{dz}$ receptor
range of shear affecting source-receptor pair
0
X
receptor

Figure 3.10: Physical example of the effects of shear history from the source and the receptor position. The source projects a downstream zone of influence as all material measured at any receptor must come from the source. The receptor projects an upstream zone of sensitivity because the probability of a particle of the source material getting to the receptor depends on the path it follows. The overlap region is the location of the source material most likely to travel to the receptor and the shear in this region is the cause of the shear distortion at the receptor.

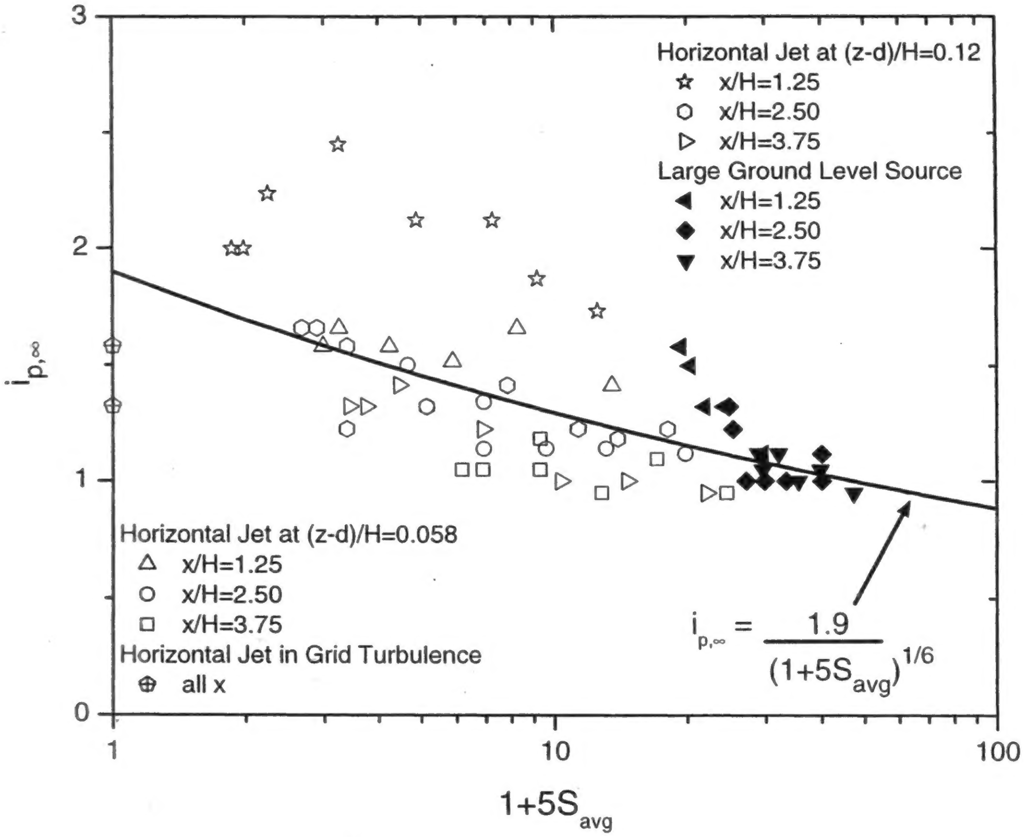

Figure 3.11: Asymptotic conditional concentration fluctuation intensity $i_{p,\infty}$ deduced from data fit to Equation (3.26) versus universal shear parameter for a range of source conditions and downstream distances including the zero-shear grid turbulence limit. Shear affects the non-zero concentration plume structure described by i_p as well as the total intermittent fluctuations described by the total concentration fluctuation intensity i, but i_p is much less sensitive to shear changes.

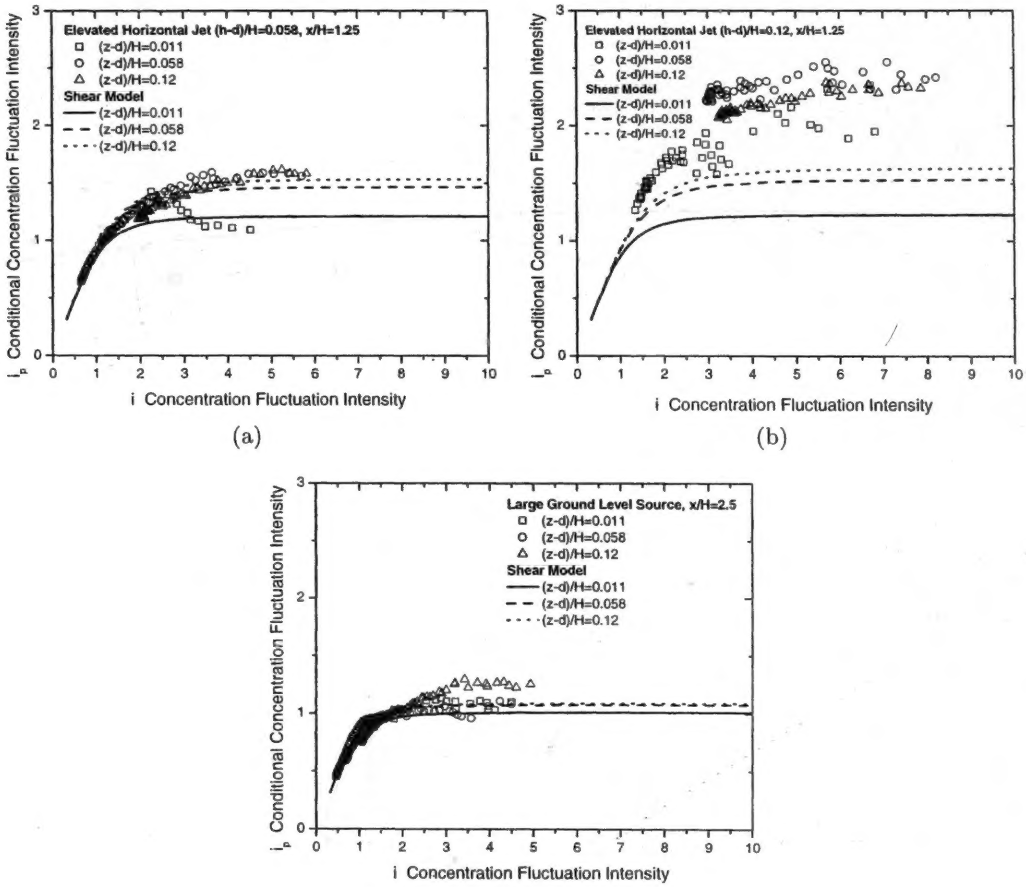

(a)

(b)

(c)

Figure 3.12: Samples of the best, worst and typical agreement with shear scaling of conditional concentration fluctuation intensity i_p versus total concentration fluctuation intensity i. (a) best agreement low elevated horizontal jet source $(h-d)/H = 0.058$ at $x/H = 1.25$ (b) worst agreement high elevated horizontal jet source, close to the source, $(h-d)/H = 0.12$ at $x/H = 1.25$ (c) typical agreement large ground level source at $x/H = 2.50$

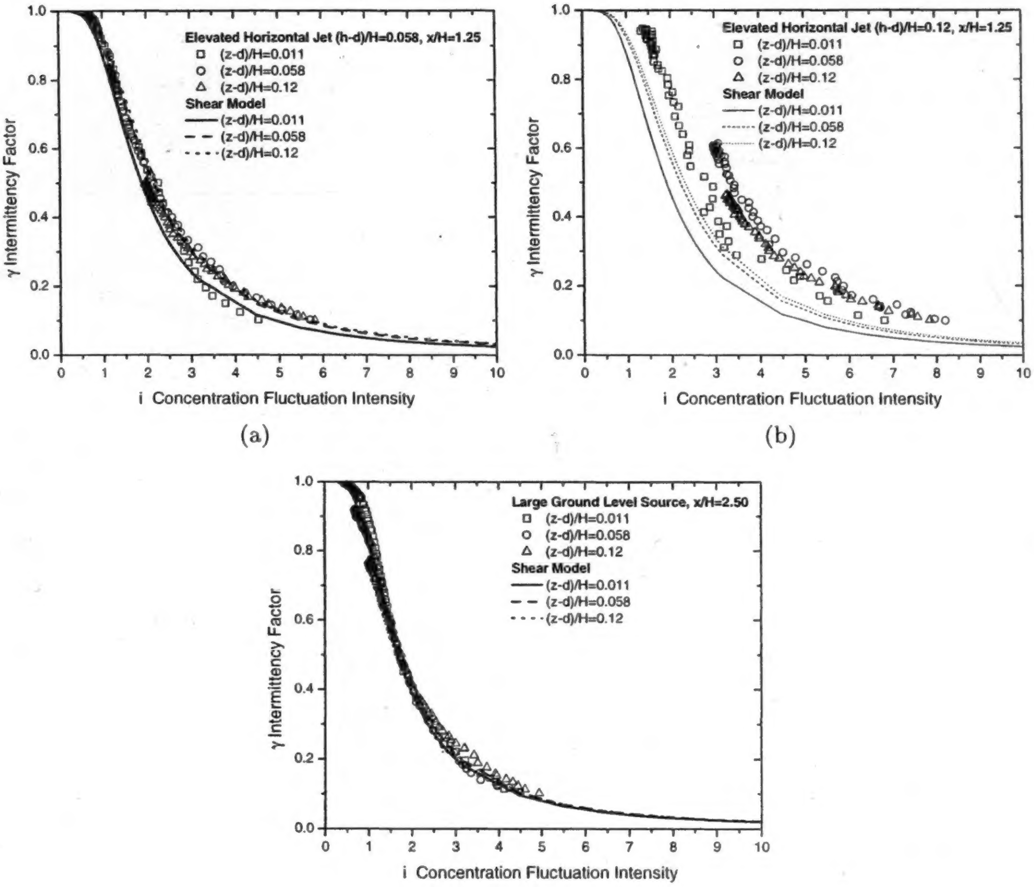

(a)

(b)

(c)

Figure 3.13: Samples of the best, worst and typical agreement with shear scaling of intermittency factor γ versus total concentration fluctuation intensity i. (a) best agreement low elevated horizontal jet source $(h-d)/H = 0.058$ at $x/H = 1.25$ (b) worst agreement high elevated horizontal jet source, close to the source $(h-d)/H = 0.12$ at $x/H = 1.25$ (c) typical agreement large ground level source at $x/H = 2.50$

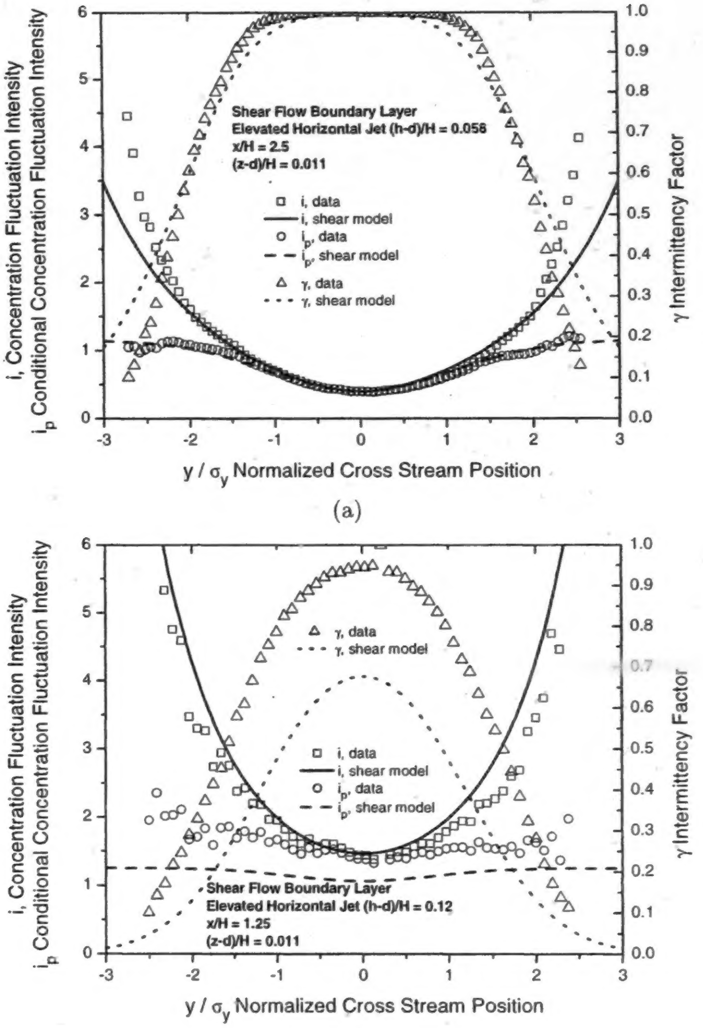

(a)

(b)

Figure 3.14: Samples of the best, worst and typical agreement of measured cross-stream profiles with pseudo-meandering plume theory of total concentration fluctuation intensity i, conditional concentration fluctuation intensity i_p and intermittency factor γ. (a) best agreement low elevated horizontal jet source $(h-d)/H = 0.058$ at $x/H = 2.5$ measured near the ground at $(z-d)/H = 0.011$. (b) worst agreement high elevated horizontal jet source $(h-d)/H = 0.12$ at $x/H = 1.25$ measured near the ground at $(z-d)/H = 0.011$. (c) typical agreement large ground level source at $x/H = 2.50$ measured near the ground at $(z-d)/H = 0.011$.

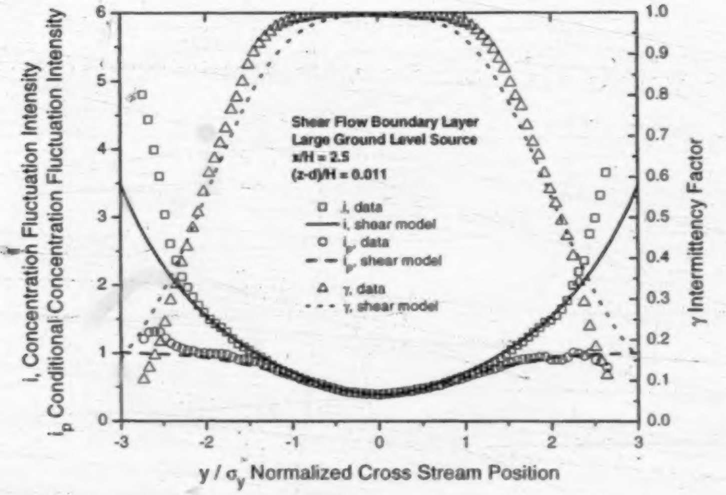

(c)

Figure 3.14: Samples of the best, worst and typical agreement of measured cross-stream profiles with pseudo-meandering plume theory of total concentration fluctuation intensity-i, conditional concentration fluctuation intensity-i_p and intermittency factor γ. (a) best agreement low elevated horizontal jet source $(h-d)/H = 0.058$ at $x/H = 2.5$ measured near the ground at $(z-d)/H = 0.011$. (b) worst agreement high elevated horizontal jet source $(h-d)/H = 0.12$ at $x/H = 1.25$ measured near the ground at $(z-d)/H = 0.011$. (c) typical agreement large ground level source at $x/H = 2.50$ measured near the ground at $(z-d)/H = 0.011$.

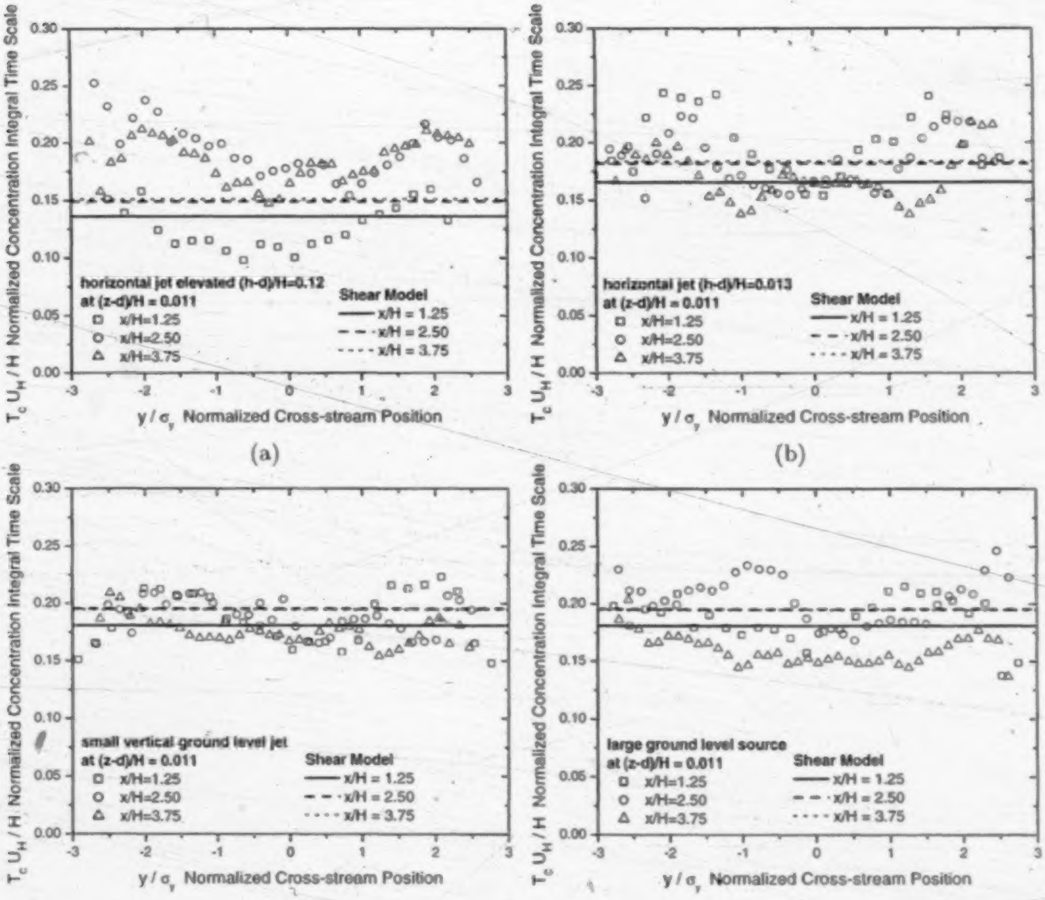

(a) (b)

(c) (d)

Figure 3.15: The concentration fluctuation integral time scale T_c is approximately constant across the plume as shown in these cross-stream profiles measured near the ground at $(z-d)/H = 0.011$. The shear model estimated time scales were calculated using Equation (3.32). Elevated measurement position show similar trends. (a) elevated iso-kinetic horizontal jet source $(h-d)/H = 0.12$ (b) horizontal ground level jet source $(h-d)/H = 0.013$ (c) small ground level vertical jet source (d) large ground level source

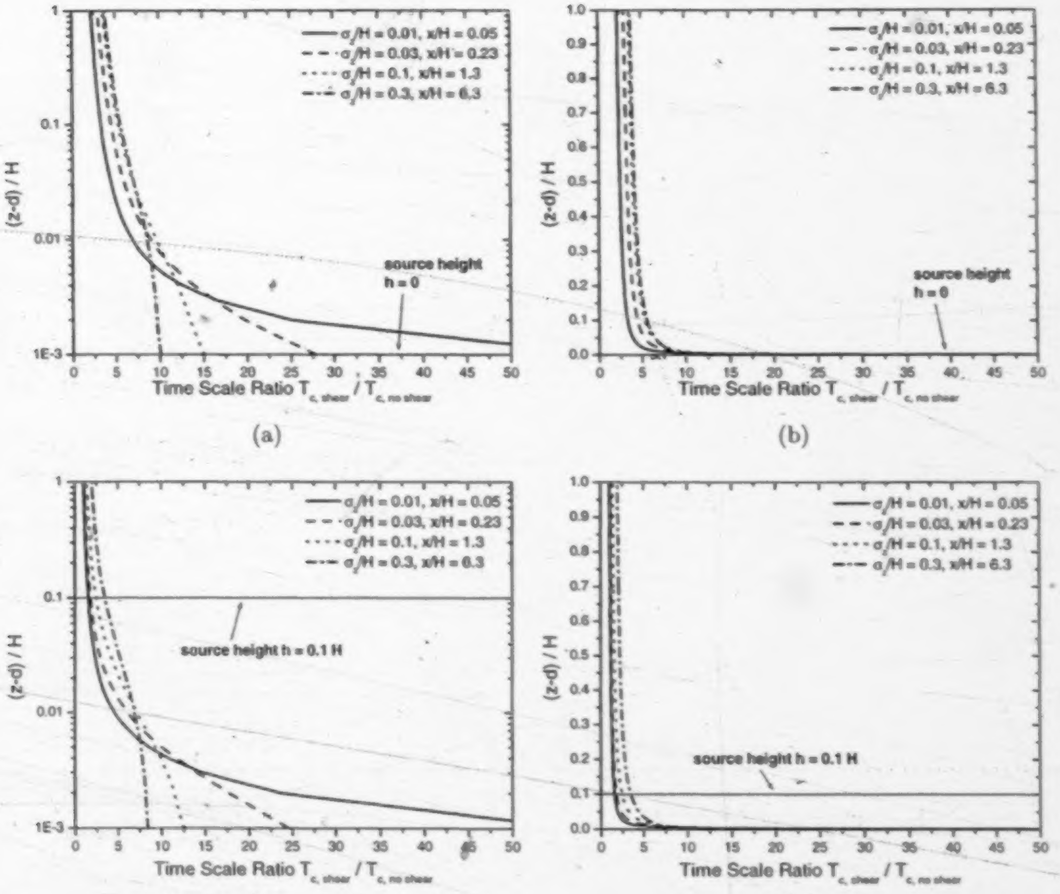

(a) (b)

(c) (d)

Figure 3.16: Case study samples of concentration fluctuation integral time scale ratios $T_{c,\text{shear}}/T_{c,\text{no-shear}}$ computed with the shear model Equation (3.32) for a neutrally stable atmosphere (high wind low heat flux). (a) ground level source with logarithmic vertical scale (b) ground level source with linear vertical scale (c) elevated source at $h = 0.1H$ logarithmic vertical scale (d) elevated source at $h = 0.1H$ linear vertical scale All curves would be constant vertical lines in zero wind shear.

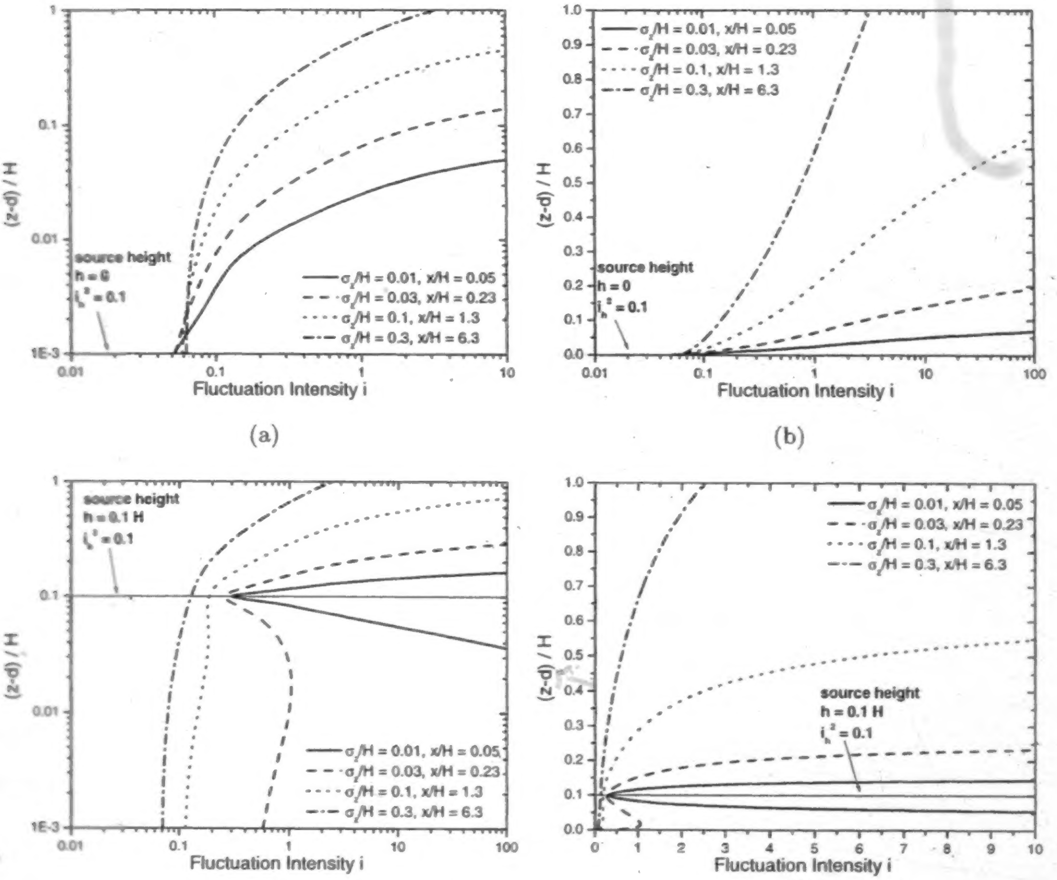

(a) (b)

(c) (d)

Figure 3.17: Case study samples of concentration fluctuation intensity i for $i_h^2 = 0.1$ computed with the shear model Equation (3.23) for a neutrally stable atmosphere (high wind low heat flux). (a) ground level source log-log plot. (b) ground level source linear plot. (c) elevated source $h = 0.1H$ log-log plot. (d) elevated source $h = 0.1H$ linear plot. Curves in (c) and (d) would be symmetric about the source height in no-shear conditions.

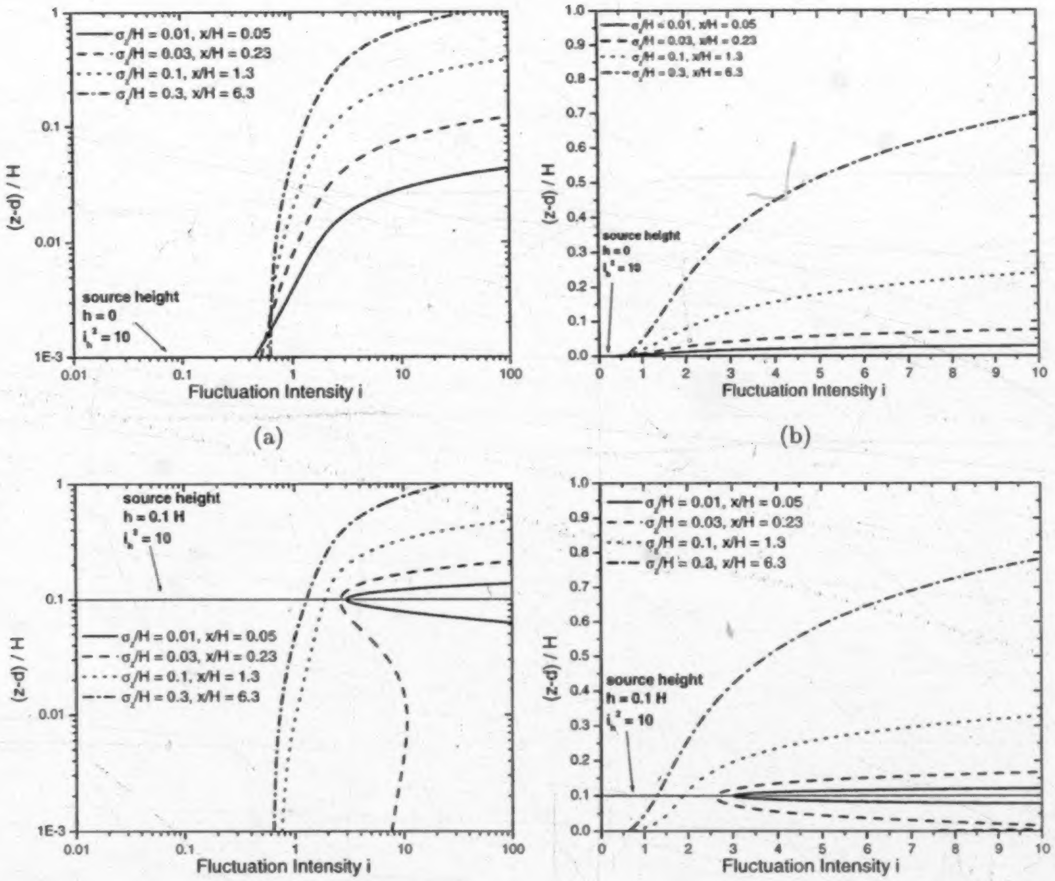

Figure 3.18: Case study samples of concentration fluctuation intensity i for $i_h^2 = 10$ computed with the shear model Equation (3.23) for a neutrally stable atmosphere (high wind low heat flux). (a) ground level source log-log plot. (b) ground level source linear plot. (c) elevated source $h = 0.1H$ log-log plot. (d) elevated source $h = 0.1H$ linear plot. Curves in (c) and (d) would be symmetric about the source height in no-shear conditions.

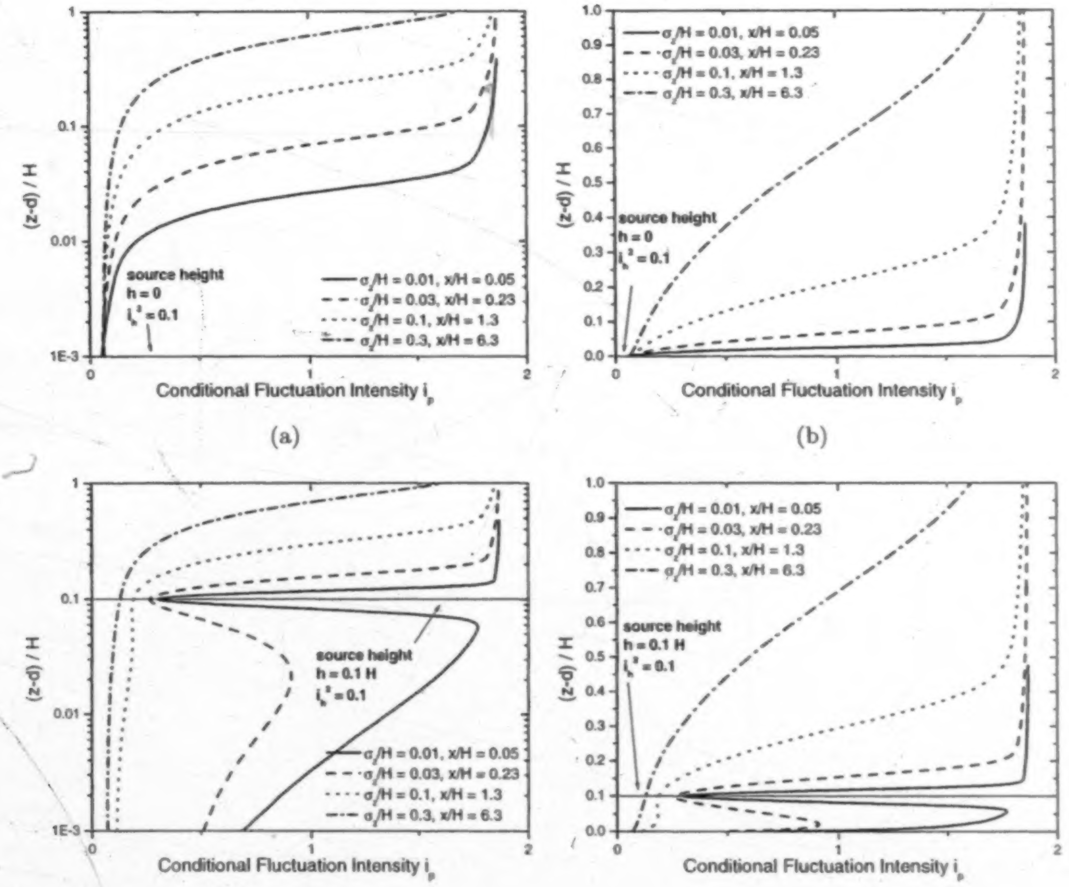

(a) (b) (c) (d)

Figure 3.19: Case study samples of conditional concentration fluctuation intensity i_p for $i_h^2 = 0.1$ computed with the shear model in Equations (3.26) and (3.27) for a neutrally stable atmosphere (high wind low heat flux). (a) ground level source log vertical scale. (b) ground level source linear vertical scale. (c) elevated source $h = 0.1H$ log vertical scale. (d) elevated source $h = 0.1H$ linear vertical scale. Curves in (c) and (d) would be symmetric about the source height in no-shear conditions.

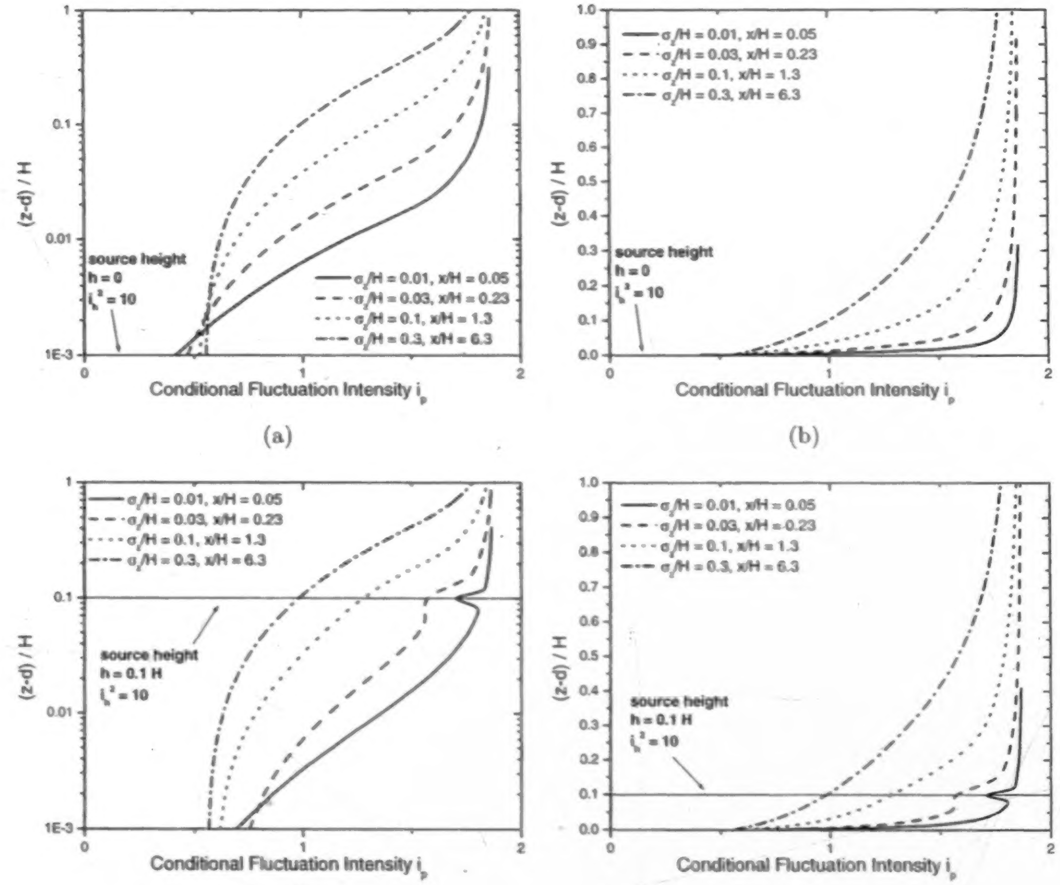

(a) (b)

(c) (d)

Figure 3.20: Case study samples of conditional concentration fluctuation intensity i_p for $i_h^2 = 10$ computed with the shear model in Equations (3.26) and (3.27) for a neutrally stable atmosphere (high wind low heat flux). (a) ground level source log vertical scale. (b) ground level source linear vertical scale. (c) elevated source $h = 0.1H$ log vertical scale. (d) elevated source $h = 0.1H$ linear vertical scale. Curves in (c) and (d) would be symmetric about the source height in no-shear conditions.

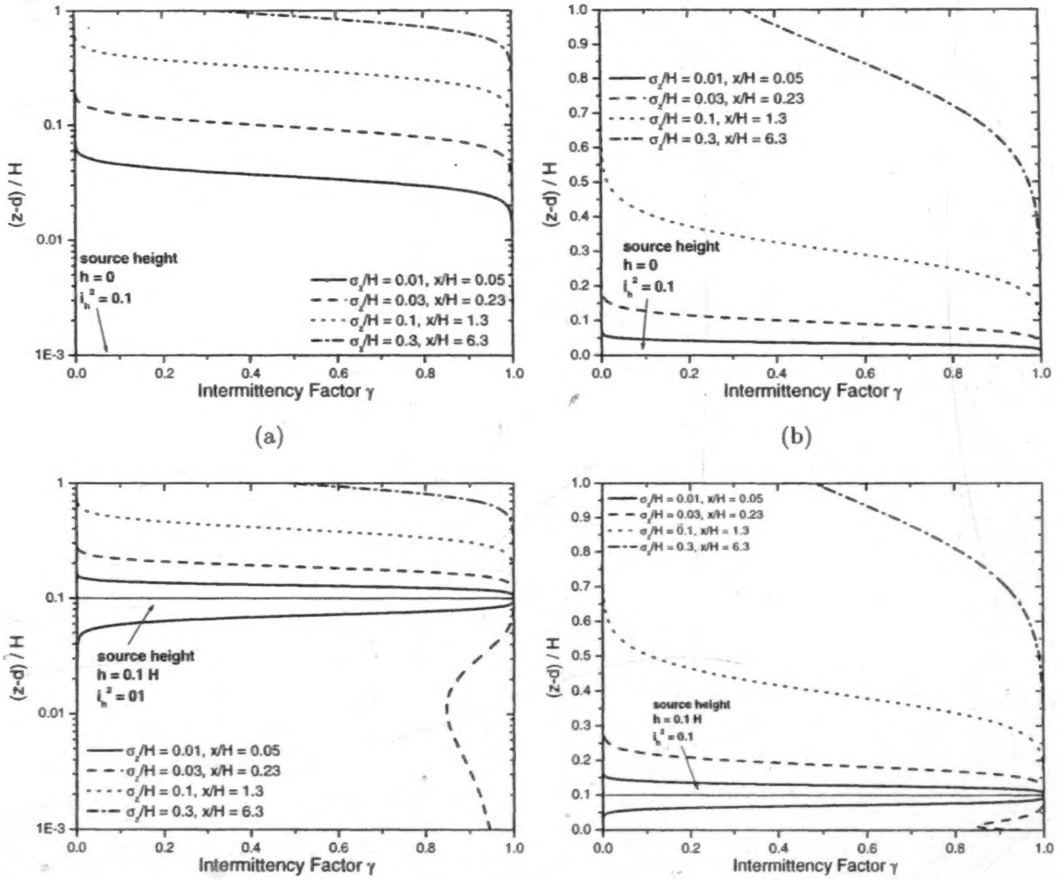

(a) (b)

(c) (d)

Figure 3.21: Case study samples of intermittency factor γ for $i_h^2 = 0.1$ computed from the i and i_p values given in Figures 3.17 and 3.19 using the definition in Equation (3.3) for a neutrally stable atmosphere (high wind low heat flux). (a) ground level source log vertical scale. (b) ground level source linear vertical scale. (c) elevated source $h = 0.1H$ log vertical scale. (d) elevated source $h = 0.1H$ linear vertical scale. Curves in (c) and (d) would be symmetric about the source height in no-shear conditions.

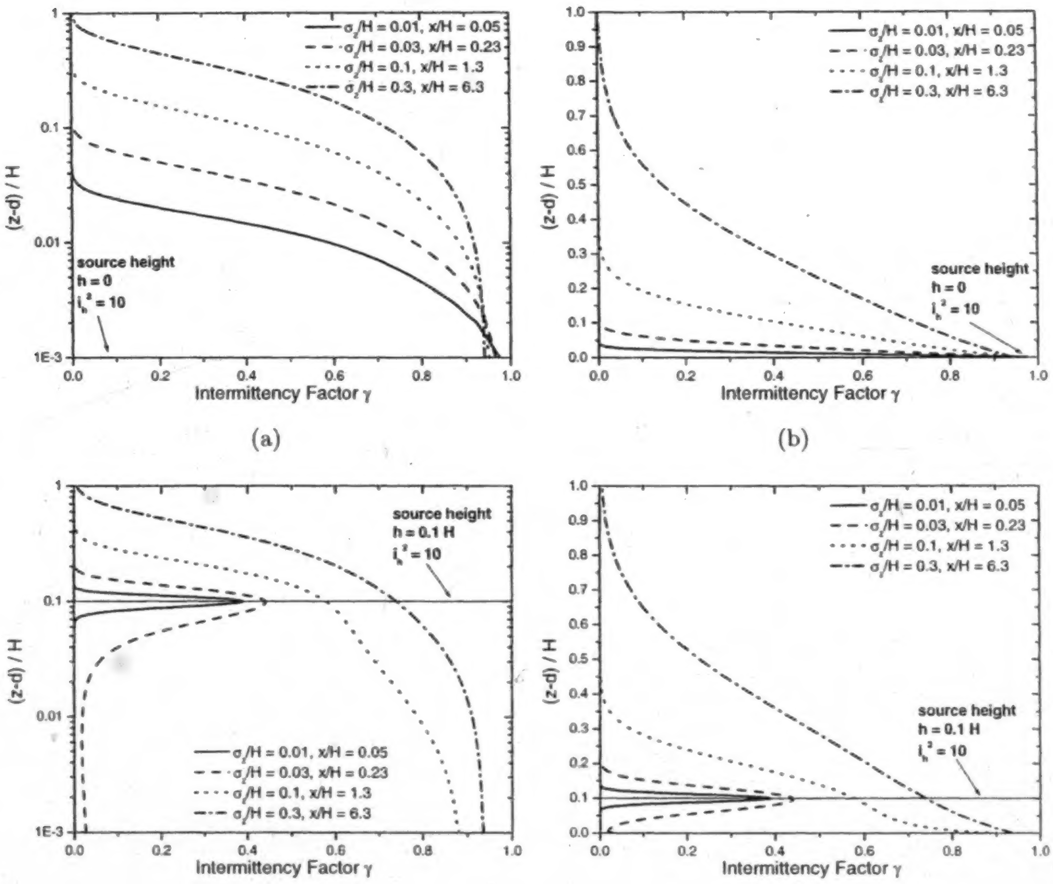

(a) (b)

(c) (d)

Figure 3.22: Case study samples of intermittency factor γ for $i_h^2 = 10$ computed from the i and i_p values given in Figures 3.18 and 3.20 using the definition in Equation (3.3) for a neutrally stable atmosphere (high wind low heat flux). (a) ground level source log vertical scale. (b) ground level source linear vertical scale. (c) elevated source $h = 0.1H$ log vertical scale. (d) elevated source $h = 0.1H$ linear vertical scale. Curves in (c) and (d) would be symmetric about the source height in no-shear conditions.

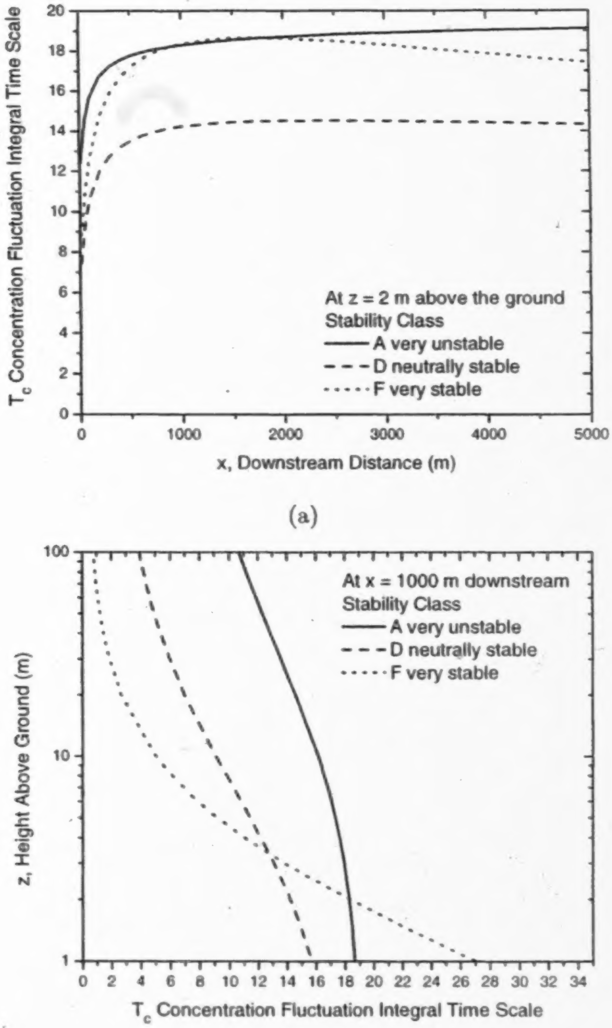

(a)

(b)

Figure 3.23: Estimated concentration fluctuation integral time scale in full-scale atmospheric conditions calculated with Equation (3.32) for stability classes A (very unstable, light wind, sunny clear day), D (neutrally stable, strong wind, low heat flux), and F (very stable, light wind, clear night sky). For all cases $U_{\text{met}} = 3$ m/s at a meteorological reference height $z_{\text{met}} = 10$ m above the ground and roughness $z_0 = 0.1$ m for a point source emission at ground level. (a) At $z = 2$ m as a function of downstream distance x. (b) At $x = 1000$ m as a function of height z above the ground. Strong variation in T_c near the ground in class F conditions suggests large uncertainties might occur when estimating near-surface time scales in stable atmospheres.

Chapter 4

Stochastic Modelling of Cross-Stream Correlated Concentration Fluctuations in a Dispersing Plume for Simultaneous Cross-Stream Hazard Evaluation

Abstract

A plume dispersing in the wind shear of the lower atmosphere produces intermittent concentration fluctuations that are an important factor in the hazardous outcome of the release. The objective of this study is to validate a stochastic simulation technique for generating realistic intermittent concentration time series at a fixed receptor point anywhere in a plume. The stochastic model is validated with a water channel experimental data set of high resolution, high frequency concentration measurements from a variety of sources in both a rough surface boundary layer and in shear-free grid turbulence. A clipped lognormal probability distribution is shown to be an excellent fit to the data and was used to describe the overall statistics of the concentration fluctuations that were simulated with the stochastic model. The stochastic model performance is tested by comparing simulated distributions of bursts of concentration above a threshold level and gaps below the threshold to the experimental data. A model for stochastic simulation of the spatial cross-wind correlation of concentration fluctuations is proposed and found to be in very good agreement with the water channel data.

4.1 Introduction

This study presents a comprehensive experimental validation of the concentration fluctuation time series stochastic simulation originally presented in Hilderman and Wilson (1999). The results of stochastic simulations of concentration time series at fixed receptor points in a dispersing plume are compared against a new, more detailed data set measured using linescan laser-induced fluorescence (LIF) as described in Chapter 2.

The main goal of this stochastic simulation is to use known or predicted mean concentration, fluctuation variance, and intermittency factors to generate ensembles of realistic random time series of concentration fluctuations for application to hazard assessment of short term acutely toxic chemicals released into the atmosphere. However, there is potential to apply this type of stochastic model to any turbulent mixing process.

Two examples of typical time series of concentration fluctuation are shown in Figure 4.1. Instantaneous concentrations can range from zero (background) concentration to more than 20 times the mean concentration C with a standard deviation c'_{rms} often several times larger than the mean. It is important to be able to model these fluctuations to predict any effect that is dependent on instantaneous concentration levels.

Toxicity, flammability, and odour are some examples of atmospheric dispersion hazards that can have a strong non-linear dependence on high frequency concentration fluctuations. For example, ten Berge et al. (1986) analyzed animal experiments for 20 different acutely toxic gases and found that fatalities are a non-linear function of toxic load, which is the product of concentration C^n and exposure time t where n ranges from 1.0 to 5.0. Many hazardous gases have exponents, n, in the range of 2.0 to 3.0. The Center for Chemical Process Safety of the American Institute of Chemical Engineers (CCPS, 1989) recommends similar non-linear models for predicting acute toxicity from common industrial chemicals. If $n > 1$, as it is for many substances, then concentration fluctuations increase the toxicity of the exposure because the high peak concentrations become much more important than low concentrations. Hilderman et al. (1999) is an example of the application of stochastic time series generation to prediction of toxicity from a hydrogen sulphide release.

Wilson (1995) reviewed the state of the art in concentration fluctuation models and recommended a combination of theoretical and empirical models to predict fluctuation intensities, time scales, and averaging time effects. Work by Yee et al. (1993a, 1994, 1995) recognized that the evaluation of toxic hazards from a release requires information on concentration level recurrence time intervals, intermittency, and level-crossing statistics in addition to the probability distributions and higher order concentration moments.

More recently, the need to have concentration fluctuation time series in addition to overall statistics has been recognized. Venkatram (2002) used a very simple time series model with randomly spaced zero and peak concentration periods to examine the effects of averaging time. Yamartino et al. (1996) and Yamartino and Strimaitis (2000) developed the Kinematic-Simulation-Particle (KSP) dispersion model that uses a computationally-intensive large and small eddy transport model to predict second-by-second concentration fluctuations. However, the published material for KSP says little about this part of the model beyond some evaluation of peak concentrations and a few probability distributions compared with experimental data. Possibly the lack of detailed experimental data has limited their ability to test this part of the KSP model.

In the present study, a time series of simulated intermittent concentration fluctuations is generated directly as a first order "inertialess" Markov process. At the most basic level, the stochastic model simply generates time series that conform to an input probability distribution and time scale. The process is computationally efficient; typically, it takes approximately 30 seconds on a 1 GHz Pentium PC to simulate a single point exposure in a 15 minute long full-scale release. Large ensembles of hundreds of exposures events at several receptor points in a dispersing plume can be generated in a few hours of computational time.

To match the stochastic simulation to an experimental time series two items must be specified:

1. $p(c)$, the probability density function (pdf) of concentration. As discussed later in this study, the recommended shape of the pdf is a shifted and clipped log-normal distribution. The mean, variance, and intermittency factor necessary to specify the pdf must come from a separate atmospheric dispersion model or from an experimental data set.

2. T_c, the integral timescale of concentration fluctuation. The stochastic simulation approximates an inertialess Markov process that inherently produces an exponential time autocorrelation and a $1/f^2$ spectrum roll-off. The integral time scale defines the time correlation of the concentration fluctuations and its value must also be determined from a separate model or experimental data set.

From these inputs, the stochastic model produces realistic random time series of concentration fluctuations with the correct time correlations. This enables complex hazard models for the effects of varying concentration to be tested.

In this study, the stochastic simulation technique is compared to concentration fluctuations from a jet source in a highly sheared rough surface turbulent boundary layer as well as shear-free grid turbulence. The data set tested in Hilderman and Wilson (1999) only included an elevated source and elevated measurement positions in relatively homogeneous turbulence.

The stochastic model will also be extended by the development of a method to introduce a realistic cross-stream correlation between two positions. This property is needed to be able to predict the risk to a row of receptors located across the plume and exposed simultaneously during a single event. During a single exposure event, the instantaneous concentrations at nearby cross-wind positions are correlated, so the hazard from this event can not be accurately determined by simulating two statistically independent stochastic time series. Instead, highly correlated time series are generated at the two positions and then de-correlated by a time delay proportional to the distance between the two points. This simple transformation will be shown to give very good agreement with measured spatial correlations.

4.2 Concentration Fluctuation Measurements

4.2.1 LIF Data

All of the data discussed in this study were obtained with digital video linescan camera laser-induced fluorescence (LIF) measurements in the recirculating water channel in the Mechanical Engineering Department at the University of Alberta, as shown in Figure 4.2. Disodium fluorescein ($C_{20}H_{10}Na_2O_5$) dye solutions were injected into either a rough surface boundary-layer shear flow or a shear-free grid turbulent flow in the 5240 mm long by 680 mm wide by 470 mm deep test section of the channel. High spatial and temporal resolution concentration measurements were made with a Dalsa model CLC6-2048T 12-bit gray-scale CCD linescan camera along a line illuminated by an argon-ion laser. Each of the 1024 pixels saw a measurement volume of approximately 0.5mm x 1mm x 1mm and was sampled at 500 samples per second. Three different dye sources were used as shown in Figure 4.3 and will be discussed in more detail in Section 4.2.3. The experimental technique and apparatus are discussed in more detail in Chapter 2.

4.2.2 Flow Fields

Rough Surface Turbulent Boundary Layer Shear Flow

A well-developed rough surface turbulent boundary layer shear flow as shown in Figure 4.2 was used for most of the experiments. This flow was similar to what would be observed in the full scale atmosphere under neutrally stable conditions. The water channel's rough bottom surface was made of 1/2" x 18 gauge raised surface stainless steel expanded metal which is about 4 mm thick. All z coordinate measurements are made from the bottom of the roughness (i.e. the top of the expanded metal is at $z = 4$ mm.)

To accelerate the boundary-layer development, an array of 4 horizontal and 4 vertical 19 mm (nominal 3/4") stainless steel square bars and a 70 mm high trip fence with 40 mm high by 60 mm wide triangular "teeth" were used to redistribute the flow and generate some mid to large scale turbulence.

Velocity components were measured with a two-component TSI Inc. Laser Doppler Velocimeter (LDV). The cross-stream uniformity of the mean velocity U was ±5%

across the channel. The vertical profile of the velocity U fit a log-law

$$U = \frac{u_*}{\kappa} \ln\left(\frac{z-d}{z_0}\right) \tag{4.1}$$

where $u_* = 14$ mm/s is the friction velocity, $\kappa = 0.4$ is the Von Karman constant, $d = 1.7$ mm is the zero-plane displacement height, and $z_0 = 0.52$ mm is the roughness height. The log-law mixing layer depth $H = 400$ mm was the entire depth of the channel and the velocity at H was $U_H = 232$ mm/s. The mixing layer depth H and velocity U_H will be used to normalize the experimental data.

For a neutrally-stable atmosphere at high Reynolds number, the transformation between the water channel and full-scale is kinematic. The flow velocity in the water channel can represent any full-scale wind speed. Only the length scale needs to be chosen, with a limitation on the plume averaging time to account for the suppression of large cross-wind turbulent scales by the side walls of the water channel. At 1:1000 scale the flow in the channel corresponds to a full-scale roughness length of $z_0 = 0.5$ m (between the typical rural roughness length of 0.1 m and urban roughness length of 1.0 m). Downstream measurements were made at $x = 500$ mm, 1000 mm and 1500 mm corresponding to full scale positions $x = 500$ m, 1000 m and 1500 m. The equivalent full-scale boundary layer depth was $H = 400$ m.

In the log-law profile the velocity goes to zero at $(z-d) = z_0$ at which point there is still a finite velocity gradient $\mathrm{d}U/\mathrm{d}z = u_*/\kappa z_0$. The velocity profiles in equation (4.1) should only be used down to the zero velocity point $z_{\min} = z_0 + d$. In the water channel, the lowest point at which measurement were taken was $z = 6$ mm, well above $z_{\min} = 2.2$ mm.

Additional shear flow turbulence statistics and graphs can be found in Appendix A of the thesis.

Grid Turbulence as a Zero Shear Reference

For comparison purposes, measurements were also made in a shear-free grid generated turbulent flow. The grid was made of flat stainless steel bars 19.2 mm wide by 5 mm thick in the flow direction with a centre to centre mesh spacing $G = 76.2$ mm and a total open area of 56%. It was positioned at $x/G = 4.5$ from the channel inlet and the flow was run 405 mm deep with an average flow velocity $U = 200$ mm/s.

The cross-stream variation of the mean velocity U was at most ±5% if the wall boundary layers were neglected. The vertical fluctuations w'_{rms} were approximately 95% of u'_{rms} indicating some small anisotropy in the flow. As expected for grid turbulence, the turbulence intensity decays with downstream distance and follows a power law decay using Saffman's invariant (Hinze, 1975, pp.265-267) to give the exponent -0.6

$$\frac{u'_{\mathrm{rms}}}{U} = 0.3\left(\frac{x}{G} - 2.3\right)^{-0.6} \tag{4.2}$$

See Hinze (1975, pp. 268-273 for more details). The constants 0.3 and 2.3 were simply fit to the data. The dye source was placed at $x/G = 23.6$ where the turbulence intensity was about 5% and decayed to about 3% at the farthest downstream measurement position $x/G = 43.3$.

4.2.3 Tracer Sources

The three tracer sources used in the experiments are illustrated in Figure 4.3.

1. **Horizontal Jet** 4.3 mm OD and 3.25 mm ID stainless steel tube, 38 mm long suspended from above the channel by a streamlined support. In normalized units the source diameter $d_s \approx 6z_0 \approx 0.008H$ in the shear flow and $d_s \approx 0.04G$ in grid turbulence. In grid turbulence, the source was placed in the centre of the channel at $z = 200$ mm $= 2.6G$ above the channel bottom, and in the shear flow the source was placed at height h between 7 and 50 mm ($(h-d)/H = 0.013$ to 0.12 or $(h-d)/z_0 = 10$ to 93) above the surface depending on the experiment. The source flow rate was iso-kinetic in grid turbulence and for $(h-d)/H = 0.12$ above the ground in the shear flow. With the small diameter and low flow rates the jets from the source were laminar ($\mathrm{Re} = U_{\mathrm{source}} d_s/\nu \approx 600$).
2. **Vertical Jet at Ground Level** 3.25 mm ID flush with ground ($d_s \approx 6z_0 \approx 0.008H$). To prevent dye from becoming trapped in the roughness elements the expanded metal was removed from an area 25 mm on either side and 100 mm downstream of the source. The source flow rate was the same as for the horizontal jets and produced a laminar jet with a mean velocity equal to the cross flow velocity at $(z-d)/H = 0.12$, $\mathrm{Re} \approx 600$.
3. **Large Ground Level Source** 11 mm ID flush with ground. ($d_s \approx 21z_0 \approx 0.028H$). As with the vertical ground level jet the expanded metal was trimmed away 25 mm on either side and 100 mm downstream of the source. The source flow rate was the same as the other 2 sources ($\mathrm{Re} \approx 175$ based on source diameter).

The sources were placed 2750 mm ($x/H = 6.9$) downstream of the channel inlet in the shear flow and 1800 mm ($x/G = 23.6$) downstream of the grid in the no-shear experiments.

For the elevated sources and grid turbulence measurements the average source flow rates were iso-kinetic with the surrounding flow. The vertical ground level sources had very low momentum with insignificant plume rise. If modelled at 1:1000 scale the full-scale equivalent source sizes were 3 to 11 m at the source and effectively 2 to 3 times larger than this after entraining sufficient fluid to take on the turbulent structure of the flow field. Measurements were taken at $x/d_s > 150$ for the jet sources and $x/d_s > 50$ for the large ground level source. At this downwind point the dilution was at least 100:1 which allowed the tracer-marked fluid to take on the turbulent structure of the cross flow. There was little measurable effect of source size or release rate. Appendix B lists all of the parameters of the data sets that were collected and used in this study.

4.3 Probability Distributions of Intermittent Time Series

The probability distribution of concentration constrains the stochastically generated fluctuating concentrations to ensure the correct mean, variance, and intermittency in the simulated time series. The stochastic model presented in Hilderman and Wilson (1999) and discussed further in Section 4.5 produces concentration time series with a probability distribution that fits the input distribution.

The complete specification of the pdf includes the following parameters:

- mean concentration C
- standard deviation c'_{rms}
- fluctuation intensity $i = c'_{\text{rms}}/C$,
- intermittency factor γ, the fraction of the total event time during which the concentration is above the zero (background) level.
- conditional (in-plume) mean concentration $C_p = C/\gamma$ which excludes all of the zero-concentration intermittent periods.
- conditional (in-plume) mean concentration fluctuation intensity which by definition is $i_p = (\gamma(1+i^2)-1)^{0.5}$.

Traditionally, probability distributions of intermittent concentrations have focused on only the measurable in-plume concentrations with the addition of a delta function at zero to describe the intermittent periods. For example, Wilson (1995, chap. 5) examined several different distributions and recommended the lognormal as the best fit to a wide variety of data. The choice of the lognormal is supported by water channel experimental data analyzed by Yee et al. (1993b), although Yee et al. (1995) and Yee and Chan (1997) analyzed full scale atmospheric data and concluded that the gamma distribution provided a better fit than the lognormal. Du et al. (1999) used both the gamma and the lognormal distribution in a stochastic model for the conditional concentration upcrossing rate and found that there was little difference between the distributions.

Hilderman and Wilson (1999) found that probability distributions with the intermittent periods simulated using a delta function with area $(1-\gamma)$ at zero concentration cannot be used directly in the stochastic time series model. With a separate delta function at zero concentration, the stochastically generated time series becomes mathematically trapped in the delta function and can never again go above zero. The solution to this problem was to run the simulation as a non-intermittent process in pseudo-concentration c_+ coordinates (the subscript "+" denotes non-intermittent pseudo-concentration parameters). Then the distribution is shifted to produce time series with both positive and negative concentrations $\tilde{c}$ (the tilde denotes a time series with both positive and negative concentrations).

Figure 4.4 shows a physical interpretation of the shifted probability distribution. The negative concentrations represent the intermittent clean air eddies in the plume. The larger the negative concentration, the larger the clear air eddy and the more likely the next time step will also be clean air. In the final analysis, all the negative concentrations are replaced by zero concentration intermittent periods. This novel interpretation of a shifted concentration probability distribution has many benefits to understanding and simulating intermittent concentration fluctuations. It implies that the zero concentration eddies are part of the same mixing process that produces the measurable non-zero concentrations.

Clipped distributions have been used by others to describe concentration fluctuations, but never with the interpretation of the shifted and clipped distribution as described above. For example, Lewellen and Sykes (1986) used a clipped normal pdf to describe intermittent plumes from a power plant, but their interpretation did not attach any significance to the missing negative concentrations and was simply a fit to the available data. Other distributions such as the clipped gamma or more complicated distributions such as Yee's (1990) g and h distribution can be made to fit the data as well as the clipped lognormal, but the shifted and clipped lognormal has the advantage of relative mathematical simplicity.

There has been no rigorous derivation of the clipped lognormal for intermittent time series, but dilution of a plume is a result of a random multiplicative process that would tend to produce lognormal distributions in at least the non-intermittent case. The clipped lognormal has also been successfully applied to describe other intermittent parameters of a dispersing plume such as the distribution of instantaneous plume spreads measured on a line across the plume, see Chapter 2.

4.3.1 Implementing a Shifted then Clipped Lognormal Distribution

Figure 4.5 shows how the time series is first simulated as a non-intermittent time series, then shifted and clipped to generate the necessary zero concentration intermittent periods:

- Step 1 in Figure 4.5 shows the pseudo-concentration c_+ time series and pdf. (the subscript "+" is used to indicate concentration parameters before they are shifted to produce positive and negative concentrations $\tilde{c}$, and clipped to produce the correct concentration values c.) In c_+ coordinates, the concentration fluctuations are represented by a complete lognormal distribution with only positive concentrations and an intermittency factor $\gamma_+ = 1.0$. There are no intermittent periods in c_+.

- In step 2 of Figure 4.5, after a simulated time series is generated, the pseudo-concentrations are shifted by a value of c_{base} to give positive and negative concentrations $\tilde{c} = c_+ - c_{\text{base}}$. In $\tilde{c}$ coordinates, the probability of obtaining a positive concentration is equal to the intermittency factor γ and the probability of obtaining a negative concentration is $(1-\gamma)$. The magnitude of the negative concentration is interpreted as inversely proportional to the likelihood of obtaining a positive concentration in the next time step.

- Negative concentrations are clearly unrealistic in the final analysis of the concentration fluctuation time series, so step 3 in Figure 4.5 is to clip all of the negative concentrations and replace them with a delta function at zero. The result is a clipped lognormal that has only real concentrations $c \geq 0$.

4.4 Experimental Validation of the Clipped Lognormal Probability Density

To demonstrate that the choice of a clipped lognormal distribution is reasonable, the experimental water channel concentration probability distributions were compared to the clipped lognormal pdf as shown in Figures 4.6 to 4.9. For this comparison only non-zero concentrations were considered, so all concentrations were normalized by the conditional mean concentration C_p that excludes the zero concentration intermittent periods. The theoretical clipped lognormal distributions were given the same intermittency factor γ and conditional fluctuation intensity i_p as the experimental data sets.

Several different forms of the probability distribution of concentration were examined:

- The probability density function (pdf) $p(c)$ is defined as the function that when integrated between two concentration values c_1 and c_2 gives the probability of obtaining a concentration between c_1 and c_2.

  $$\text{Prob}(c_1 < c < c_2) = \int_{c_1}^{c_2} p(c)\,\mathrm{d}c \tag{4.3}$$

  The probability density function is the form of the distribution used directly in the stochastic simulation.

- The cumulative probability distribution function (cdf) $P(c)$ is the probability of the concentration being less than some level c_1.

  $$P(c_1) = \int_{0}^{c_1} p(c)\,\mathrm{d}c \tag{4.4}$$

- The exceedance probability distribution function (edf) $E(c)$ is the probability of the concentration being greater than some level c_1

$$E(c_1) = \int_{c_1}^{\infty} p(c)\, \mathrm{d}c \tag{4.5}$$

Plots of all of these forms of the probability distribution are contained in Appendix I. Only the probability density (pdf) and exceedance (edf) plots are presented in this paper.

Figures 4.6 and 4.7 show pdfs for three sources in shear flow and one source in grid turbulence with measurements at the source height. Figure 4.6(a) is a iso-kinetic jet in grid turbulence, Figure 4.6(b) is a ground level source in shear flow, Figure 4.7(a) is an elevated iso-kinetic jet in shear flow and Figure 4.7(b) is a ground level horizontal jet in shear flow. These samples cover a range of positions from the source centreline up to $3\sigma_y$ off-centre, intermittency factors from $\gamma = 0.04$ to 1.0 and conditional fluctuation intensities from $i_p = 0.4$ to 1.75. The clipped lognormal fits very well under all these conditions.

In full-scale hazardous releases, high concentrations are the most important, so the exceedance (edf) plots shown in Figures 4.8 and 4.9 are more directly relevant to hazard assessment than the pdf plots. The edf (probability of exceeding a given concentration) plots cover the same range of conditions as the previous pdf plots and show very good fit to the data for all sources and receptor locations. The largest deviations from the clipped lognormal exceedances occur at the very low probability, high peak level concentrations. As an example for an exceedance probability of 0.001 at a receptor position where the intermittency factor $\gamma = 0.1$, there are only 25 points in the total data series of 250,000 points that exceed that level. The linescan LIF data sets of 250,000 points over 2000 integral time scales T_c are still not large enough to evaluate accurately these high concentration, low probability events.

4.5 Stochastic Model for Fluctuations

With the shifted and clipped lognormal probability distribution discussed in Section 4.3, the details of the stochastic model using this probability distribution can be developed. Hilderman and Wilson (1999) extended a stochastic model developed by Du et al. (1999) to produce intermittent time series of concentration using the clipped lognormal distribution. The basic assumptions of the model are that:

- the functional form of the probability distribution of concentration (i.e. the clipped lognormal) is independent of spatial position (and therefore travel time) in the plume.
- Eulerian concentration fluctuations are produced by a first order Markov process that can be described by a stochastic differential equation, and by the equivalent Fokker-Planck equation for the time dependent evolution of the concentration probability distribution.

- the derivative of concentration is dependent on the current instantaneous concentration.

- concentration fluctuations are statistically stationary.

As previously discussed, the stochastic model can only generate non-intermittent time series that are then shifted and clipped to produce the intermittent periods. All concentration values discussed in the stochastic model have the subscript "+" to denote that the simulation only works in these non-intermittent pseudo-concentration coordinates.

4.5.1 Stochastic Differential Equation

Experimental evidence from full-scale atmospheric measurements of Yee et al. (1993a) and water channel data discussed in Hilderman and Wilson (1999) showed that the root mean square concentration derivative $\dot{c}'$ increased with the concentration level at which it was measured. This requires a stochastic model for the time series of concentration fluctuations to have a deterministic component that changes dc_+/dt as concentration c_+ increases, along with the usual random component. The fluctuation process can be described as a first-order Markov (inertialess) process which is not influenced by any events before time $t-dt$. The derivative of concentration is random and the direction of the derivative is not influenced by any past events in the time series. This first-order Markov (inertialess) concentration fluctuation process at a fixed location in a dispersing plume can be described by the one dimensional stochastic differential Langevin equation:

$$\frac{dc_+}{dt} = a(c_+, t) + b(c_+, t)\frac{\delta\zeta}{\delta t} \tag{4.6}$$

where $a(c_+, t)$ is the deterministic portion of the time derivative dependent on the concentration c_+ and time t and $b(c_+, t)d\zeta$ is a random forcing function where $d\zeta$ is a Gaussian random number with a mean of zero and variance dt.

The Langevin equation, discussed in detail by Gardiner (1983, pp. 80-83) and Durbin (1983), is used to describe a wide variety of continuous stochastic processes. Originally, the equation was developed to describe the position of Brownian particles in a fluid, see Gardiner (1983, chap. 1). It has also been applied to the modelling of concentration fluctuations in the Lagrangian sense by tracking the random flights of particles emanating from a point, see for example Wilson and Sawford (1996). Here, we apply the Langevin equation in an Eulerian sense by assuming that the measured concentration at a single point can be modelled as a continuous Markov process.

4.5.2 Fokker-Planck Constraint

The Fokker-Planck equation constrains the evolution of the probability distribution of concentration with the relationship between the a and b terms in equation (4.6).

Hilderman and Wilson (1999) provides some additional detail on the derivation for the time evolution of the pdf of a Markov process as it is discussed in Durbin (1983). The one-dimensional Fokker-Planck equation describing the time evolution of $p(c_+)$ is as given in Du et al. (1999) and Hilderman and Wilson (1999)

$$\frac{\partial p}{\partial t} = -\frac{\partial(ap)}{\partial c_+} + \frac{1}{2}\frac{\partial^2(b^2p)}{\partial c_+^2} \tag{4.7}$$

Additional discussion can be found in Gardiner (1983, chap. 5).

It is assumed that the pdf of concentration $p(c_+)$ is stationary which by definition requires that a, b and the pdf p do not change with time. With this assumption $\partial p/\partial t = 0$ and equation (4.7) can be integrated once to yield:

$$\frac{d(b^2p)}{dc_+} = 2ap \tag{4.8}$$

Integrating (4.8) to solve for b^2 in terms of a produces

$$b^2 = \frac{2}{p}\int_{c_+}^{\infty} -ap\ dc_+ \tag{4.9}$$

Equation (4.9) is a deterministic relationship between the pseudo concentration time series generation parameters a and b in Equation (4.6) and the probability density function p that is specified by the user.

4.5.3 Functional Relations for a and b

The a term in equation (4.6) governs the deterministic part of the fluctuation process. As Hilderman and Wilson (1999) and Yee et al. (1993a) found, the first derivative of concentration with respect to time is strongly dependent on the current concentration. That is, large derivatives are observed at extreme concentrations relative to the mean, while small derivatives generally occur near the mean. Here, it is assumed that in the absence of random fluctuations the instantaneous concentration c_+ will return to the well mixed mean concentration C_+ at a rate dependent upon the magnitude of the current difference between c_+ and C_+.

The model proposed by Du et al. (1999) for the non-zero (conditional) part of the concentration time series assumed a non-linear relationship for the deterministic a term and found that the results were not too sensitive to the non-linearity. Hilderman and Wilson (1999) used the simplest linear form of the a term that continues to be an adequate model based on the most recent evidence.

$$a = \frac{C_+ - c_+}{T_{c+}} \tag{4.10}$$

Calculation of the integral time scale from the time series that are generated by the model confirms that the input time scale T_{c+} is the integral time scale of the pseudo-concentration fluctuation process. The fluctuating time series produced by the simulation is inertialess, so T_{c+} may be rescaled to any value without changing the physical basis of the time series. The exact T_{c+} value used for simulation is not important and it is nominally set to unity.

The lognormal pdf $p(c_+)$ completes the specification of the model. The c_{50+} median and σ_{l+}, log standard deviation values are required parameters for the c_+ lognormal pdf:

$$p(c_+) = \frac{1}{\sqrt{2\pi}\sigma_{l+}c_+} \exp\left(- \frac{\ln^2\left(\frac{c_+}{c_{50+}}\right)}{2\sigma_{l+}^2} \right) \tag{4.11}$$

The specific values for c_{50+} and σ_{l+} are chosen to produce the correct conditional mean concentration C_p intermittency factor γ and fluctuation intensity i_p after clipping the distribution at c_{base} and shifting it so that $c_{\mathrm{base}} = 0$. Hilderman and Wilson (1999) has a detailed discussion of calculating the basic statistics (mean, variance, intermittency factor etc.) of the clipped lognormal distribution and the method of finding the proper σ_{l+}, c_{50+} and c_{base} values.

The b term is calculated by substituting the pdf, Equation (4.11)and the definition of a from Equation (4.10) into Equation (4.9).

$$\begin{aligned} b^2 = {} & \frac{C_+\sqrt{2\pi}\sigma_{l+}c_+}{T_c} \exp\left(\frac{\ln^2\left(\frac{c_+}{c_{50+}}\right)}{2\sigma_{l+}^2} \right) \\ & \left(\mathrm{erf}\left(\frac{\ln\left(\frac{c_+}{c_{50+}}\right)}{\sqrt{2}\sigma_{l+}} \right) - \mathrm{erf}\left(\frac{\ln\left(\frac{c_+}{c_{50+}}\right) - \sigma_{l+}^2}{\sqrt{2}\sigma_{l+}} \right) \right) \end{aligned} \tag{4.12}$$

For a highly intermittent time series ($\gamma \ll 1$), the pseudo-mean C_+ can be a negative concentration after the shifting necessary to produce the intermittent periods. With this in mind, C_+ should be interpreted as a representative concentration that includes the effects of both the intermittent zero periods and the non-zero fluctuations. If C_+ is less than zero concentration after shifting, it implies that the clean air eddies dominate the fluctuation process.

4.6 Generating Stochastic Time Series

The stochastic differential equation (4.6) is solved numerically by using a forward difference:

$$c_{+(n+1)} = c_{+(n)} + a_n\Delta t + b_n\sqrt{\Delta t}N_n \tag{4.13}$$

where $c_{+(n+1)}$ is the instantaneous c_+ concentration at time t_{n+1}, $c_{+(n)}$ is the instantaneous concentration at time t_n, Δt is the time increment, and N_n is a Gaussian random number with zero mean and unity variance.

A uniform distribution of random numbers was generated with a shift register sequence generator as discussed by Maier (1991) and Carter (1994). This particular generator was used because it has a period of approximately 9×10^{74} before repeating. A large period generator is required to avoid repetition in the random numbers that would cause invalid stochastic simulation results. The Box-Muller (1958) transformation was used to obtain a Gaussian distributed random number N_n from the uniform distribution.

The conditional mean C_{p+} and time scale T_{c+} were arbitrarily set to unity to generate fully normalized time series. Because the simulation is an inertialess Markov process there is no sensitivity to the length of the time step (i.e. to the "acceleration" $\partial^2 c_+/\partial t^2$) and the output of the simulation can be scaled to match the time scale and mean concentration of any desired time series. The Δt time step was set to $0.01T_{c+}$ giving one hundred time steps per concentration integral time scale. Each run of the simulation was started at the median concentration c_{50+} and then allowed to run for $10T_{c+}$ to eliminate the effects of picking the same starting point for each simulation.

4.6.1 Time Scales of Intermittent and Non-Intermittent Time Series

The time scale of the non-intermittent pseudo-concentration fluctuations was set to $T_{c+} = 1.0$ for the stochastic simulation. After clipping, the time scale T_c of the remaining intermittent fluctuations concentration c is less than 1.0. The clipping process removes all of the fluctuations below c_{base} and replaces them with zero periods. The intermittent periods do little to affect the time scale (as discussed in Chapter 3), but because the level dependent derivative of the stochastic simulation is level dependent, as the intermittency factor γ decreases, the remaining non-zero concentration fluctuations tend to have higher frequencies and therefore the overall time scale is somewhat lower. As Hilderman and Wilson (1999) found, an empirical relationship between the concentration integral time scale T_{c+} before clipping and the T_c after clipping is approximately $T_c/T_{c+} = 0.78 + 0.23\gamma$. In practice, the real time scale of the simulated intermittent time series is simply calculated and the time series is rescaled to match the time scale of the process being simulated. The inertialess nature of the Markov simulation means that this rescaling has no adverse effects on the character of the time series.

4.6.2 Frequency Spectrum of Experimental Data Compared to the Simulation

Both the fluorescent dye tracer in the present study and the saline solution tracer used by Hilderman and Wilson (1999) have a major deficiency when the experimental water channel data is compared to the stochastic Markov process simulation. The molecular diffusivity of fluorescein is $D = 5.2 \times 10^{-6}$ cm^2/s. The Schmidt number, $\text{Sc} = \nu/D$, for fluorescein in water is approximately $\text{Sc} = 1930$ given that the kinematic viscosity of water is 1×10^{-6} m^2/s at 20 °C (for comparison Sc = 850 for salt into water as in Hilderman and Wilson (1999)). The effect of this large Schmidt number is that velocity-driven straining of the concentration field is dissipated by viscosity before molecular diffusion smears out the concentration fluctuations. This can be seen in the spectrum of concentration fluctuations shown in Figure 4.10 where the water channel data follows the viscous-convective Batchelor spectrum with $F_c \propto f^{-1}$ until the roll-off due to the pixel resolution. The shape of the concentration spectrum of the stochastic simulation is determined by the assumption of a first order Markov (inertialess) process which produces $F_c \propto f^{-2}$ at high frequencies. Not shown in Figure 4.10 is the spectrum of concentration fluctuations for gases dispersing in the atmosphere where $D \approx \nu$ so $\mathrm{Sc} \approx 1$ and at high frequencies $F_c \propto f^{-5/3}$, see Wilson (1995, pp. 143-146).

The important implication of this spectral mismatch between the stochastic simulation and the experimental data is that there might be some difference expected in the higher order statistics due to different distributions of fluctuation frequencies. As a possible mitigating factor, over the majority of the spectral range the differences are only a factor of 2 in spectral density. It is possible to perform some filtering to attempt to correct this mismatch, but judging from the data discussed in the following sections the effect of the mismatch appears to be small enough that this is not really necessary. If the stochastic model is used for atmospheric gas dispersion concentration fluctuations, the effect should be even smaller as the first order Markov spectrum $F_c \propto f^{-2}$ provides a much closer match to the $F_c \propto f^{-5/3}$ spectrum expected in the atmosphere.

4.7 Stochastic Model Performance - Burst Duration and Gap Duration Probability Distributions

Hilderman and Wilson (1999) examined upcrossing rates and concentration derivatives at a range of concentration levels as tests of the stochastic model. In this study, we will examine the burst and gap durations, which are closely related to upcrossings, but are a much more stringent test of the ability of the stochastic simulation to reproduce realistic time series. Burst and gap durations are also more directly applicable to hazard assessment of a toxic release.

Figure 4.11 shows the difference between a burst and a gap. A burst is a series of consecutive concentration samples that exceed a specified threshold level. A burst begins when the concentration exceeds the threshold from below ($c < c_{\mathrm{thresh}}$) and ends when the concentration drops below that threshold. A gap is the opposite of a burst, tracking a series of consecutive concentration samples below a threshold level. If the burst/gap threshold is set at zero concentration then gaps are the intermittent zero concentration clean air periods and the bursts are the non-zero conditional in-plume concentration periods.

Distributions of burst and gap durations include the information contained in upcrossing rates because the inverse of the upcrossing rate is the duration of the average burst period plus the average gap period. However, burst durations also provide information about the distribution of the time between upcrossings. In practical terms, this information is useful for considering something like toxicity to an atmospheric release where the time above a threshold level might be the important factor in determining toxicity.

There are two ways to calculate probability distributions of bursts and gaps. For simplicity, only bursts above the threshold will be discussed. Gap duration probability distribution are calculated in exactly the same way:

1. Count each burst, measure its duration and determine the probability distribution of burst duration based on the number of bursts measured. For example, if there are 100 bursts in a given event and 10 of those bursts are $10T_c$ in duration, then the probability of a burst being $10T_c$ is 0.1.

2. Determine the total event time occupied by bursts above the threshold level and then determine the probability distribution of burst duration based on the total time above the threshold. Using a similar example to the above, assume that a release event is 1000 T_c. There are 100 bursts over the course of the event that take up 50% of the total event time (the other 50% or $500T_c$ of the event time is taken up by gap periods.) If there are 10 bursts of duration $10T_c$ then a total of $100T_c$ out of $500T_c$ of burst time is spent in a burst of duration $10T_c$ so the probability is 0.2.

In both cases, we consider only conditional statistics (where the condition is that we are in a burst) so that all probabilities are scaled between zero and one. The second method allows for easier interpretation because the probability of getting a burst of a particular duration during an event can be read directly off the graph. The second method is used in this paper. If the first method is used, an additional piece of information, namely the number of bursts in the event(or equivalently the number of upcrossings in the event) must be known in order to determine the probability of a particular burst duration in the event.

Figures 4.12 through 4.17 are examples of the distribution of burst and gap durations of the linescan LIF data compared to the bursts and gaps predicted by the stochastic model. These particular examples were chosen to cover the widest range of conditions to demonstrate that the stochastic model works well under all of these conditions. Both probability density function (pdf) and exceedance probability function (edf) plots are shown for all cases. The pdf gives an indication of the overall distribution of burst and gap durations. The edf is a more rigorous test because cumulative or exceedance distributions are influenced by the extremely small or extremely large gaps and bursts. Small errors at either extreme lead to larger errors in the edf (or cdf) than one would expect from examining the pdf plots.

- Figures 4.12 and 4.13 show the results for an horizontal jet near ground level which produces a time series with a high intermittency factor $\gamma = 0.996$ and low fluctuation intensity $i_p = 0.46$. The bursts and gaps are shown for threshold levels of 0 and 2 times the conditional mean concentration. The low fluctuation intensity means that there are few excursions to very high concentrations so the upper threshold level tested was only double the conditional mean concentration. Note that with the intermittency factor near unity there is only 0.4% of the total time in intermittent periods, but this is still sufficient to resolve burst and gap distributions at a threshold concentration of zero.

- Figures 4.14 and 4.15 are the results for the large ground level source measured well off-centre in the fringes of the plume where the intermittency factor is only $\gamma = 0.039$ and the fluctuation intensity is a mid range of $i_p = 0.90$. With non-zero concentration occurring only 4% of the time, this is a very sparse data set. This example is a demanding test of the stochastic simulation because all of the concentration fluctuations are concentrated in the upper end of the lognormal concentration probability distribution with most of the body of the distribution clipped off after simulation. Even under these extreme cases the agreement between the model and the data is acceptable.

- Figure 4.16 and 4.17 show the worst case results for comparison between the stochastic model and the data. This case is an elevated horizontal iso-kinetic jet source with a mid level intermittency factor $\gamma = 0.74$ and relatively high fluctuation intensity $i_p = 1.27$. The two threshold levels shown are 0 and 10 times the conditional mean concentration C_p. This is a very extreme test of the model and the agreement is much poorer. This is a concern, but it is mitigated by the fact that the elevated source and measurement position is quite unrealistic for a typical hazardous atmospheric release. These elevated positions with the iso-kinetic jet source have consistently poor correspondence with the ground level measurement positions so these errors are not a surprise, see Chapters 2 and 3 for other examples. Fortunately, most receptors of interest are on the ground not floating in the air. A second mitigating factor is that the fit is much better for more moderate concentrations in the range of 1 to 5 times the conditions mean C_p (not shown in the Figure).

Overall, the stochastic model produces a good simulation of burst and gap distributions; particularly near the ground in sheared flow where receptors are most likely to be located. In most cases, as shown in Appendix I, the agreement is similar to that observed in Figures 4.12 to 4.17. The spectral mismatch discussed in Section 4.6.2 likely contributes to some of the simulation errors. The fit could probably be improved by creative frequency filtering to change the simulated concentration variance spectrum from its f^{-2} Markov shape to one that more closely matched the experimental measurements in the high Schmidt number plume. This was ~~not~~ done here, in part because complicated filtering for evaluating a real atmospheric exposure would require more detailed knowledge of the real concentration fluctuation time series than is available. The examples here demonstrate that even without any filtering to match spectra the results are quite acceptable for a wide range of conditions.

4.8 A Physical Model for Generating Correct Cross-Stream Event Correlation

The practical problem to be addressed by the stochastic simulation is the accurate assessment of the hazard posed by real full-scale atmospheric releases. This requires the ability to evaluate the responses of many cross-stream receptors simultaneously to properly estimate the risk. For example, if two people are close enough to each other that they are exposed to the same high and low concentration periods their risk of fatality for that event will be identical. As the distance between the two people increases, their exposures become more statistically independent and the individual risk as well as the total combined risk of fatality will change. Any realistic exposure scenario will include more than one potential receptor. For a practical example consider predicting the hazard for an individual as well as all of his neighbours during the same release.

The stochastic time series simulation generates realistic time series of concentration fluctuation for a single point in the dispersing flow. Multiple points in the plume can be evaluated, but they have to be treated separately and the simulated time series at one point are forced to be statistically independent of the time series at another point. In a real dispersing plume, the concentration at one point is correlated with the concentration at another point.

The definition of the spatial correlation coefficient R between two points at cross-stream positions y_1 and y_2 is

$$R_{y_1y_2} = \frac{\overline{c_{y_1}c_{y_2}}}{\sqrt{\left(\overline{c_{y_1}c_{y_1}}\right)\left(\overline{c_{y_2}c_{y_2}}\right)}} \tag{4.14}$$

where c_{y_1} is the instantaneous concentration at position y_1, and c_{y_2} is the instantaneous concentration at position y_2. The bars over the values indicate a time average. This is the correlation of the total instantaneous concentration $c = C + c'$ where C is the mean concentration and c' is the fluctuation from the mean. It is not the same as the fluctuating concentration correlation for c' used in most turbulent analysis. By correlating the total instantaneous concentration we are able to evaluate the suitability of the stochastic model for simulation of toxic hazards for a row of receptors (e.g. houses) in a line across the plume exposed during the same event (e.g. a pipeline rupture). If there are no fluctuations of concentration, c_{y_1} and c_{y_2} are simply the mean concentration at y_1 and y_2 and the normalization would produce $R = 1.0$ for all cross-stream positions. Any decrease in R with increasing separation of y_1 and y_2 is due entirely to the decrease in correlation between the fluctuating concentration time series at the two locations.

The solution to simulating correlated concentration fluctuations lies in the way that the concentration time series are generated. The stochastic simulation is driven by a random number generator based on a deterministic algorithm. It generates only a pseudo-random sequence of numbers. For any statistical test the numbers seem to be random, but the exact sequence of numbers is completely repeatable and determined by the seed input to the random number generator. This is very convenient because it allows us to choose either different seed values for each adjacent simulated point and produce minimally correlated time series, or to chose the same seed for each adjacent point and produce stochastic time series that are highly correlated. If the same seed is used for all points there is only a small degree of de-correlation between different simulated time series as a result of the different means, fluctuation intensities and intermittencies of adjacent points.

The challenge is to produce a correlation somewhere between these two extremes where the simulated time series of concentration for a pair of cross-stream points in the dispersing plume de-correlates as the separation between y_1 and y_2 increases. One way to de-correlate a pair of random time series in a controlled manner is to simulate both time series with the same seed, but simply delay one of the time series so the two are no longer exactly "synchronized". The simplest guess for the appropriate time delay t_{delay} is:

$$t_{\text{delay}} = \frac{(y_1 - y_2)}{U} \tag{4.15}$$

where the distance between the two cross-stream points is $(y_1 - y_2)$, and U is the streamwise velocity. It may seem counter-intuitive to scale a cross-stream delay time with a streamwise velocity, but the turbulent components u'_{rms}, v'_{rms} and w'_{rms} scale with U which in turn drive the mixing scales. This is also a frozen turbulence assumption that says that events de-correlate at the same rate in the cross-stream direction as they do in the streamwise direction. It is not obvious that this should be true, but Figures 4.18 to 4.21 demonstrate that it does produce very good comparisons between the experimental water channel data and the stochastic simulations.

4.8.1 Velocity U for Cross-Stream De-correlation in a Boundary Layer

In a shear flow boundary layer where the velocity changes with height z it is not clear which velocity U should be used in the delay calculation, Equation (4.15). In Chapter 3 it was found that the best location to evaluate the non-dimensional shear effect was at the height of interest z plus a small offset of $0.1\sigma_z$. This offset prevents the velocity from going to zero as z gets small and accounts for some spatial averaging caused by vertical mixing around the height of interest. When the receptor and the source are at different heights, an average of the receptor and source position is used to calculate the appropriate velocity U to scale receptor position statistics. The logic behind this assumption is that all material observed at the receptor must come from the source and therefore encounters the entire range of velocities and shear effects between the source and the receptor.

The same approach was used here where the velocity U in Equation (4.15) was calculated for a height z_{avg} equal to the average of the source reference position h_{ref} and the receptor reference position z_{ref}

$$h_{ref} = h + 0.1\sigma_z \tag{4.16}$$

$$z_{ref} = z + 0.1\sigma_z \tag{4.17}$$

$$z_{avg} = \frac{z_{ref} + h_{ref}}{2} \tag{4.18}$$

Some additional variations on this approach were tried including using Wilson's (1981, Equation (12)) recommendation for the appropriate height to evaluate the convection velocity for a ground level source at $z = h + 0.17\sigma_z$. The correlation results were insensitive to small changes in the velocity reference position.

4.8.2 Comparison of Cross-Stream Time Delay De-Correlation with Experimental Data.

Figures 4.18 through 4.21 show the results of comparisons between the correlation coefficients calculated for position y_1 at the plume centroid and y_2 at cross-stream positions up to $3\sigma_y$ from the centroid. Figure 4.18 shows ground level sources and ground level receptors in shear flow while Figure 4.19 shows elevated sources with receptors at source height for both the grid turbulence and shear flow. Figure 4.20 shows examples with a ground level source, but elevated receptor positions. Figure 4.21 is an elevated source with the receptor at ground level. It is interesting that the correlation is much stronger between cross-stream positions near ground level (Figures 4.18 and 4.20) than it is for elevated positions (Figures 4.19 and 4.21). Shear seems to smear everything near the ground and make even the cross-stream correlation more consistent. The elevated positions de-correlate more rapidly as the separation distance increases. The fit is quite good for all cases with the largest errors for the elevated receptor positions with the greatest difference between the receptor height z and the source position h as shown in Figure 4.20.

The practical application of this surprisingly easy adjustment to the stochastic simulation is that total population risk from a toxic gas release can be evaluated at a range of cross-stream positions with the proper correlation between the cross-stream points. We are thus able to predict effects on an individual as well as his neighbours during the same event and provide an estimate of the overall population hazardous effects in addition to the effects at a single point in the plume.

It is important to note that matching the cross-stream correlation coefficient does not imply an instantaneous mass flux conservation of tracer across the plume. However, a real plume also does not conserve instantaneous mass flux across a 1-D line because of the random magnitudes and directions of turbulent eddies causing the dilution. Mass flux is not even instantaneously conserved across a 2-D plane in the y-z

(cross-stream and vertical direction), but the difference between the instantaneous mass flux and the average mass flux in the 2-D case will be small. Tracer mass is only conserved in the complete 3-D instantaneous plume.

4.9 Summary and Conclusions

The stochastic time series simulation model of Hilderman and Wilson (1999) was re-examined and tested against a new linescan laser-induced fluorescence data set that included high frequency measurements from a variety of source types in both a rough surface shear flow boundary layer and shear free grid turbulence in a water channel. Three important findings were made in this study:

- The shifted and clipped lognormal probability distribution of concentration is an excellent fit to intermittent concentration fluctuations in both shear flow and zero-shear grid turbulence. The stochastic simulation is modelled initially as a non-intermittent lognormal process which is then shifted so that negative concentration periods represent the zero-concentration intermittent periods in a fluctuating plume. In the final step these negative concentrations are clipped off and compressed into a delta function at zero concentration. The implication of this shifting and clipping is that the intermittent zero-concentration periods are part of the same random multiplicative process that produces the non-zero concentrations observed at a fixed spatial position in the plume. This implication has yet to be rigorously proven, and it may not be possible to prove because the zero-concentration intermittent periods, by definition, have no concentration information. However, experimental evidence demonstrates that the clipped lognormal is an excellent fit to a wide range of data.

- The stochastic model produces a good approximation of the burst and gap duration distributions that are measured in the laboratory. These statistics match despite the spectral mismatch between the inertialess first-order Markov process generated by the stochastic model (with a power spectral density proportional to frequency^{-2}) and the viscous-convective Batchelor spectrum observed for the low diffusivity fluorescein tracer used in the water channel (with a power spectral density proportional to frequency^{-1}.)

- A realistic cross-stream correlation between two points in a dispersing plume can be approximated in the stochastic model by taking advantage of the deterministic pseudo-random number sequence driving the simulation. If the same seed is used to generate time series for two different cross-stream positions in the plume, then the result will be a very high correlation. The time series can then be de-correlated in a controlled manner by delaying one of the time series for a length of time equal to the distance between the two points divided by the flow velocity. This surprisingly easy and physically realistic adjustment provides a way to use the stochastic simulation technique to evaluate the hazards posed to both an individual and his neighbours during the same exposure event.

The most significant unresolved issue with the stochastic modelling technique is the spectral mismatch between the model and the data. For most cases of interest in atmospheric dispersion, this does not appear to be a large problem, but it may be the source of errors for elevated receptor positions. Application of the stochastic model to other turbulent mixing problems may require some additional modification to the model to generate the correct power spectra. An alternative solution is to filter the Markov time series after generation to produce the correct output spectrum. This spectral mismatch is a minor flaw in what has been demonstrated to be a powerful, robust, and computationally simple technique for generating realistic exposure time series for hazard assessment.

References

Box, G. E. P. and Muller, M. F. (1958), A note on the generation of random normal deviates, *Annals of Mathematical Statistics*, 29:610–611.

Carter, E. F. (1994), The Generation and Application of Random Numbers, *Forth Dimensions*, 16(1,2):67–72.

CCPS (1989), *Guidelines for Chemical Process Quantitative Risk Analysis*, Center for Chemical Process Safety of the American Institute of Chemical Engineers.

Du, S., Wilson, D. J., and Yee, E. (1999), A Stochastic Time Series Model for Threshold Crossing Statistics of Concentration Fluctuations in Non-Intermittent Plumes, *Boundary-Layer Meteorology*, 92:229–241.

Durbin, P. A. (1983), Stochastic Differential Equations and Turbulent Dispersion, Technical report, National Aeronautics and Space Administration, NASA Reference Publication 1103.

Gardiner, C. W. (1983), *Handbook of Stochastic Methods*, Springer-Verlag.

Hilderman, T. L., Hrudey, S. E., and Wilson, D. J. (1999), A Model for Effective Toxic Load from Fluctuating Gas Concentrations, *Journal of Hazardous Materials A*, 64:115–134.

Hilderman, T. L. and Wilson, D. J. (1999), Simulating Concentration Fluctuation Time Series with Intermittent Zero Periods and Level Dependent Derivatives, *Boundary-Layer Meteorology*, 91:451–482.

Hinze, J. (1975), *Turbulence*, McGraw-Hill, second edition.

Lewellen, W. S. and Sykes, R. I. (1986), Analysis of concentration fluctuations from lidar observations of atmospheric plumes, *American Meteorolgical Society*, pages 1145–1154.

Maier, W. L. (1991), A Fast Pseudo Random Number Generator, *Dr. Dobb's Journal*, pages 152–157.

ten Berge, W. F., Zwart, A., and Appelman, L. M. (1986), Concentration-time mortality response relationship of irritant and systemically acting vapours and gases, *Journal of Hazardous Materials*, 13:301–309.

Venkatram, A. (2002), Accounting for averaging time in air pollution modeling, *Atmospheric Environment*, 36:2165–2170.

Wilson, D. (1981), Along-Wind Diffusion of Source Transients, *Atmospheric Environment*, 15:489–495.

Wilson, D. J. (1995), *Concentration Fluctuations and Averaging Time in Vapor Clouds*, Center for Chemical Process Safety of the American Institute of Chemical Engineers, New York, NY.

Wilson, J. D. and Sawford, B. L. (1996), Review of Lagrangian Stochastic Models for Trajectories in the Turbulent Atmosphere, *Boundary-Layer Meteorology*, 78:191–210.

Yamartino, R. and Strimaitis, D. (2000), Results of and Extensive Evaluation of the Kinematic Simulatioln Particle Model Using Tracer and Wind Tunnel Experiments, In *11th joint AMS/AWMA Conference on the Applications of Air Pollution Meteorology, Long Beach, CA, January 9-14,2000.*

Yamartino, R. J., Strimaitis, D. G., Scire, J. S., Insley, E. M., and Spitzak, M. J. (1996), Final Report on the Phase I Development of the Kinematic Simulation Particle (KSP) Atmospheric Dispersion Model, Technical report, Institut fuer Meteorologie, Freie Universitaet Berlin, Carl-Heinrich-Becker Weg 6-10, D-12165 Berlin, Germany and Umweltbundesamt, Document No. 1274-3.

Yee, E. (1990), The Shape of the Probability Density Function of Short-Term Concentration Fluctuations of Plumes in the Atmospheric Boundary Layer, *Boundary-Layer Meteorology*, 51:269–298.

Yee, E. and Chan, R. (1997), A Simple Model for the Probability Density Function of Concentration Fluctuations in Atmospheric Plumes, *Atmospheric Environment*, 31(7):991–1002.

Yee, E., Chan, R., Kosteniuk, P., Chandler, G., Biltoft, C., and Bowers, J. (1994), Experimental Measurements of Concentration Fluctuations and Scales in a Dispersing Plume in the Atmospheric Surface Layer Obtained Using a Very Fast Response Concentration Detector, *Journal of Applied Meteorology*, 33:996–1016.

Yee, E., Chan, R., Kosteniuk, P., Chandler, G., Biltoft, C., and Bowers, J. (1995), Measurements of Level-Crossing Statistics of Concentration Fluctuations in Plumes Dispersing in the Atmospheric Surface Layer, *Boundary-Layer Meteorology*, 73:53–90.

Yee, E., Kosteniuk, P. R., Chandler, G. M., Biltoft, C. A., and Bowers, J. F. (1993a), Recurrence Statistics of Concentration Fluctuations in Plumes within a Near-neutral Atmospheric Surface Layer, *Boundary-Layer Meteorology*, 66:127–153.

Yee, E., Wilson, D. J., and Zelt, B. W. (1993b), Probability distributions of concentration fluctuations of a weakly diffusive passive plume in a turbulent boundary layer, *Boundary-Layer Meteorology*, 64:321–354.

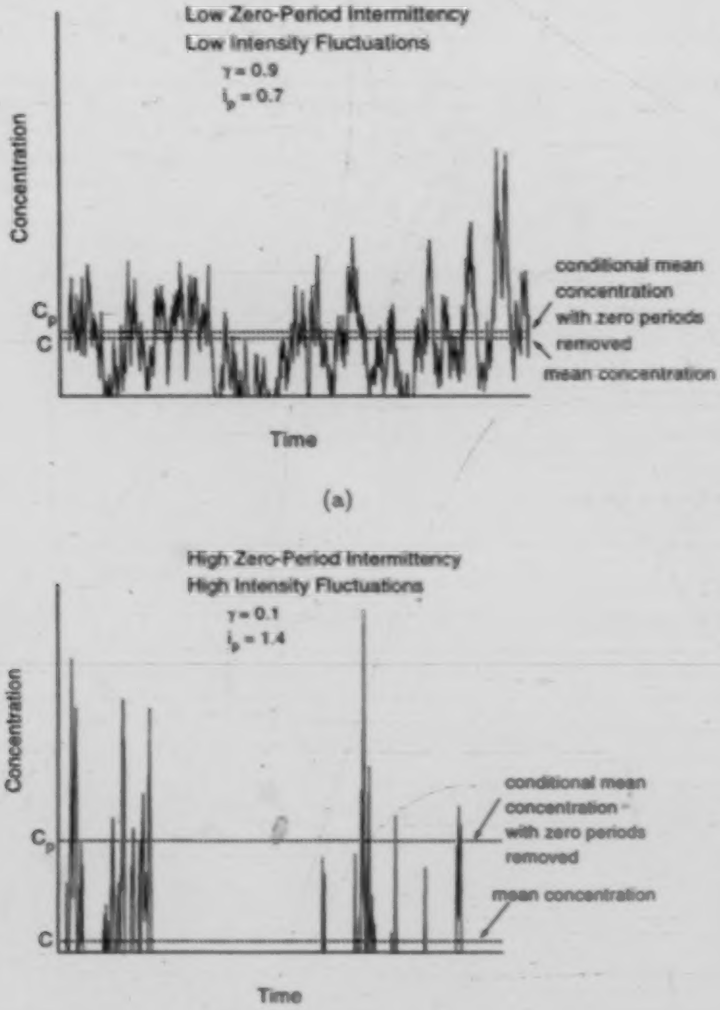

(b)

Figure 4.1: Typical intermittent concentration fluctuation time series that could be observed at a receptor positioned at a fixed point in the dispersing plume. (a) low intermittency ($\gamma = 0.9$), low fluctuation intensity ($i_p = 0.7$) (b) high intermittency ($\gamma = 0.1$), high fluctuation intensity ($i_p = 1.4$). The total mean concentration C and conditional (in-plume) mean concentration C_p which excludes the zeroes are shown as horizontal lines. The peak concentrations can be $20C$ or more.

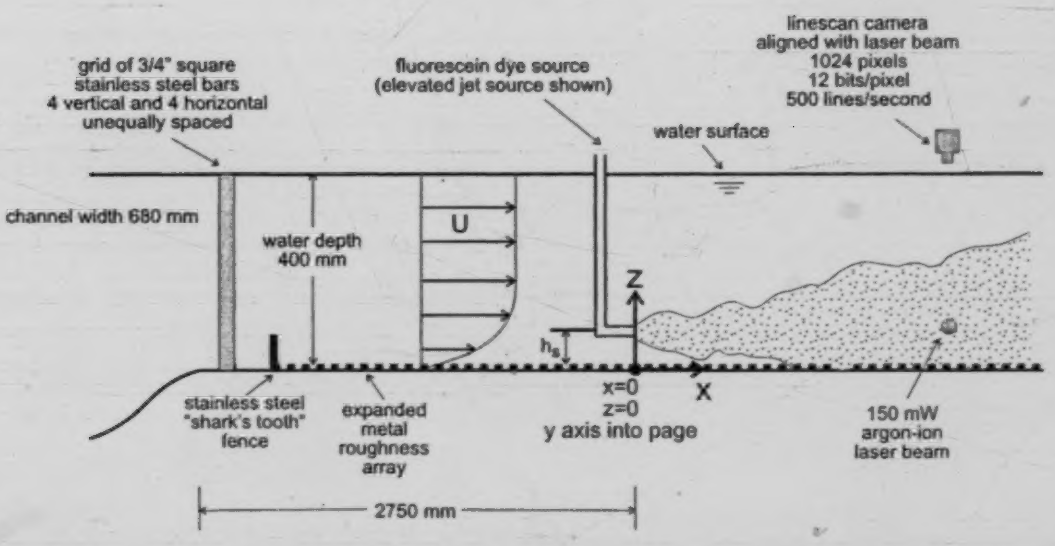
grid of 3/4" square stainless steel bars 4 vertical and 4 horizontal unequally spaced
fluorescein dye source (elevated jet source shown)
linescan camera aligned with laser beam 1024 pixels 12 bits/pixel 500 lines/second
water surface
channel width 680 mm
water depth 400 mm
U
Z
h_s
x=0
z=0
y axis into page
X
stainless steel "shark's tooth" fence
expanded metal roughness array
150 mW argon-ion laser beam
2750 mm

Figure 4.2: University of Alberta Mechanical Engineering Department water channel schematic. The recirculation piping, downstream weir gate, and inlet plenum flow straighteners are not shown. Coordinate system origin is at ground level on the channel centreline at the downstream location of the tracer source. Laser beam diameter is approximately 1 mm and projects into the page.

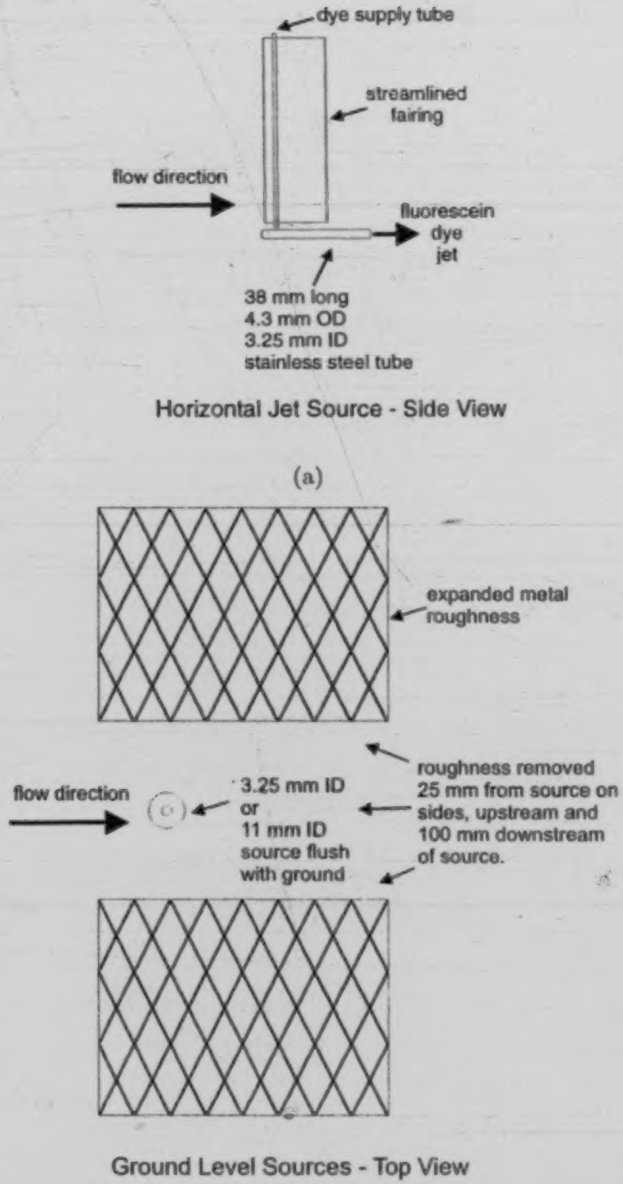
dye supply tube
streamlined fairing
flow direction
fluorescein dye jet
38 mm long
4.3 mm OD
3.25 mm ID
stainless steel tube
Horizontal Jet Source - Side View
expanded metal roughness
roughness removed 25 mm from source on sides, upstream and 100 mm downstream of source.
flow direction
3.25 mm ID or 11 mm ID source flush with ground
Ground Level Sources - Top View

(a)

(b)

Figure 4.3: Fluorescein dye sources. (a) Side view of elevated horizontal jet sources. Source was suspended from above the channel. (b) Top view of ground level sources. Expanded metal roughness was removed from the immediate area of the source and dye supply lines were underneath the acrylic panel below the roughness. The large (11 mm ID) ground level source was changed to the small ground level source by inserting a plug with a 3.25 mm ID hole for the small source.

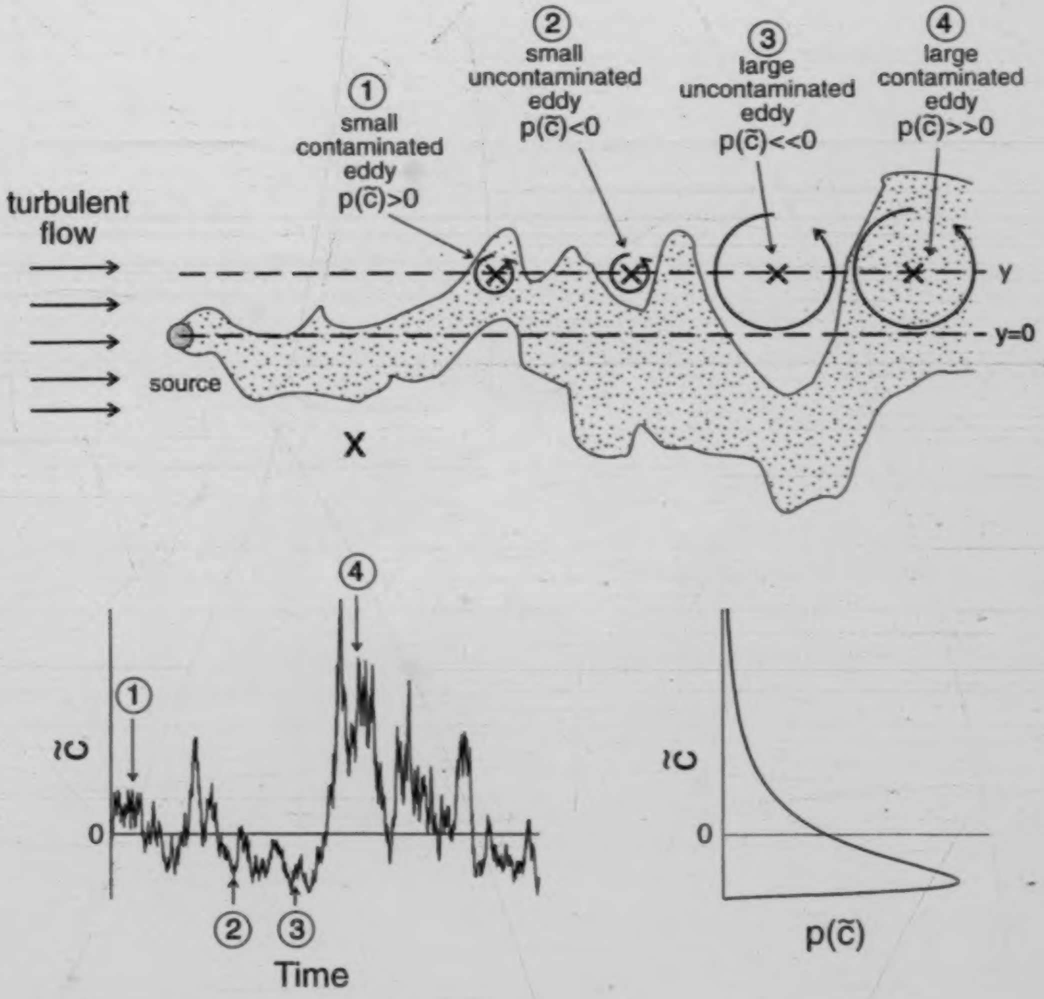
①
small
contaminated
eddy
p(c̃)>0
②
small
uncontaminated
eddy
p(c̃)<0
③
large
uncontaminated
eddy
p(c̃)<<0
④
large
contaminated
eddy
p(c̃)>>0
turbulent
flow
y
y=0
source
x
④
①
c̃
0
② ③
Time
c̃
0
p(c̃)

Figure 4.4: Physical model for interpreting the pdf of negative concentrations as intermittent periods of clean air (zero concentration). The illustration of the dispersing plume on the top of the figure shows the inhomogeneous mixing that produces the concentration fluctuations in the bottom left time series in $\tilde{c}$ coordinates which can be both positive and negative concentrations. Negative concentrations are simply the intermittent periods with the magnitude of the negative concentration inversely proportional to the probability of obtaining a non-zero concentration in the next time step. The probability distribution of the time series is shown on the bottom right.

Step 1: Simulation in c_+ coordinates, with no intermittency ($\gamma_+ = 1.00$)

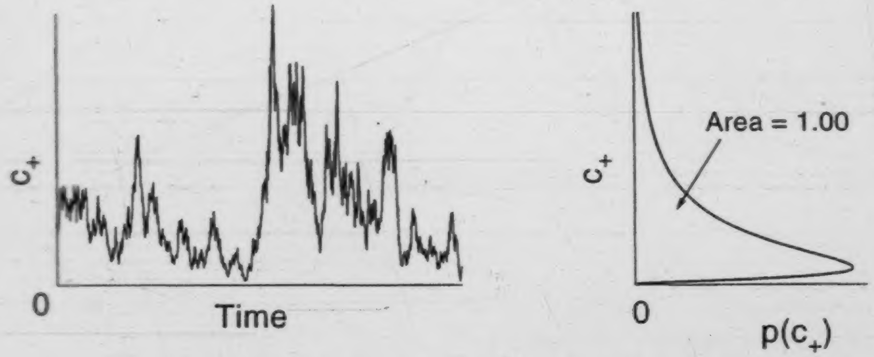

Step 2: Baseline shift by c_{base} to produce intermittency

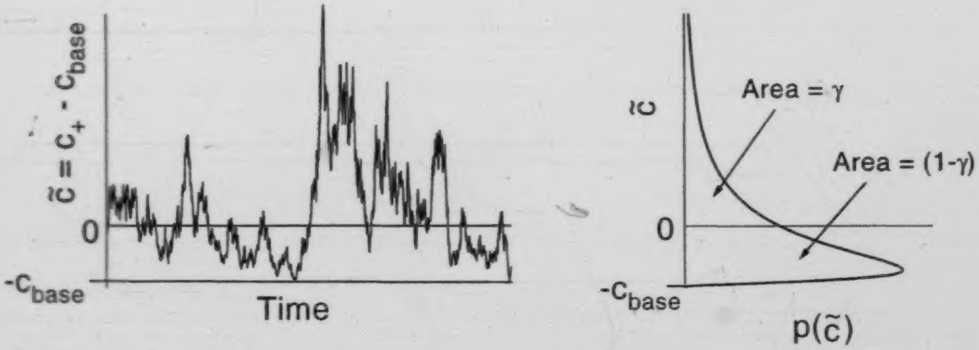

Step 3: Clipping to obtain intermittency factor γ and concentration c

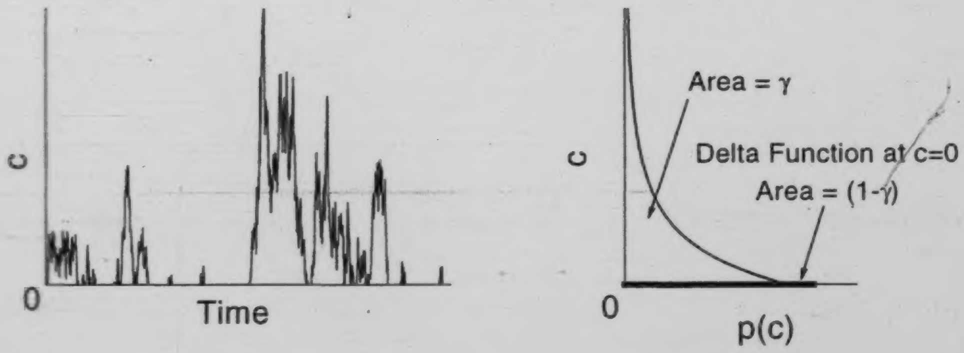

Figure 4.5: Three step shifting and clipping procedure used to produce an intermittent time series from a non-intermittent stochastic simulation.

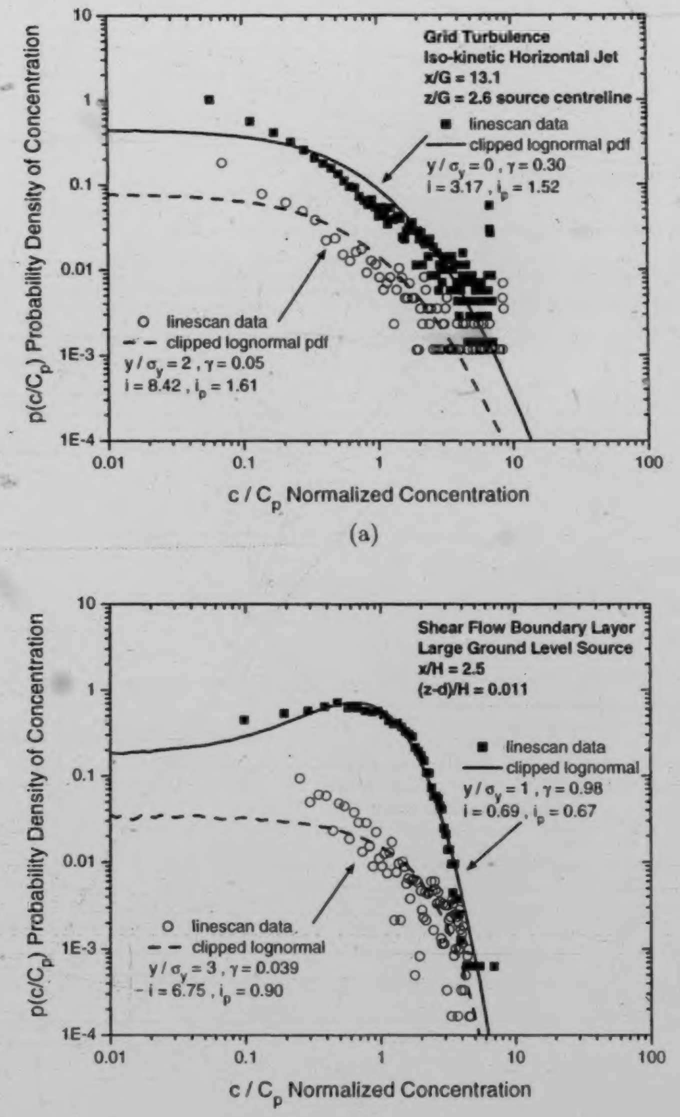

(a)

(b)

Figure 4.6: Normalized concentration probability density functions $p(c/C_p)$ of the linescan data compared to the clipped lognormal generated by the stochastic model. (a) horizontal iso-kinetic jet in grid turbulence with the receptor measurement position at source height. (b) large ground level source in shear flow with the receptor measurement position at ground level.

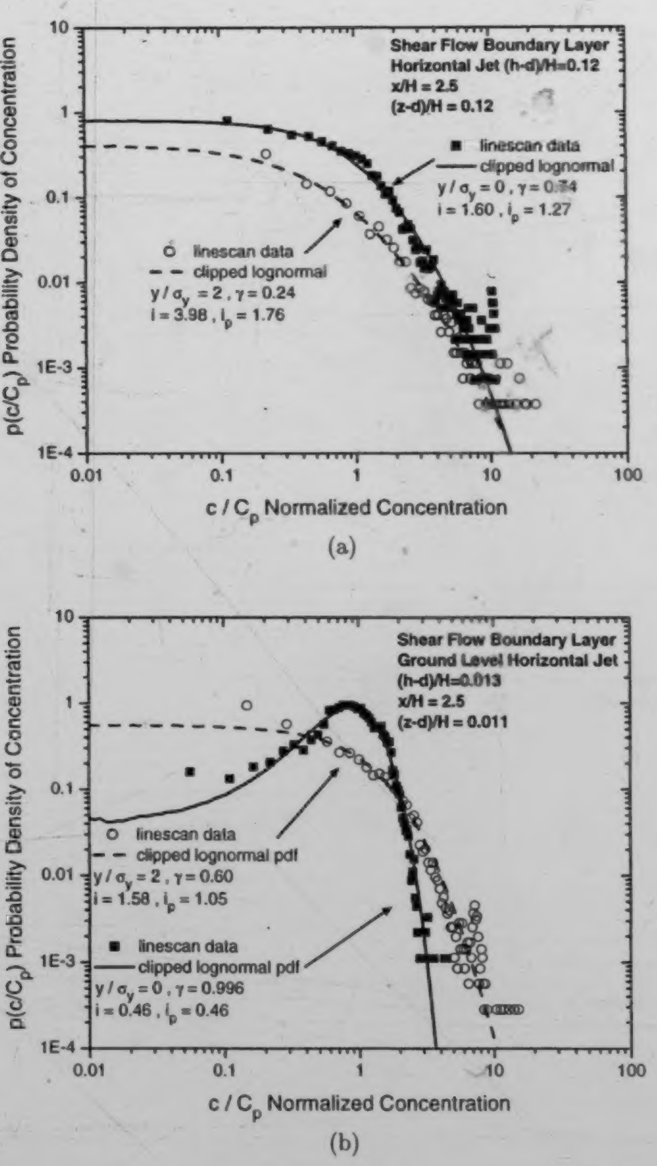

Figure 4.7: Normalized concentration probability density functions $p(C/C_p)$ of the linescan data compared to the clipped lognormal generated by the stochastic model. (a) horizontal elevated iso-kinetic jet at $(h-d)/H = 0.12$ in shear flow measured at an elevated receptor position $(z-d)/H = 0.12$. (b) horizontal jet at ground level $(h-d)/H = 0.013$ in shear flow measured at the ground level receptor position $(z-d)/H = 0.011$.

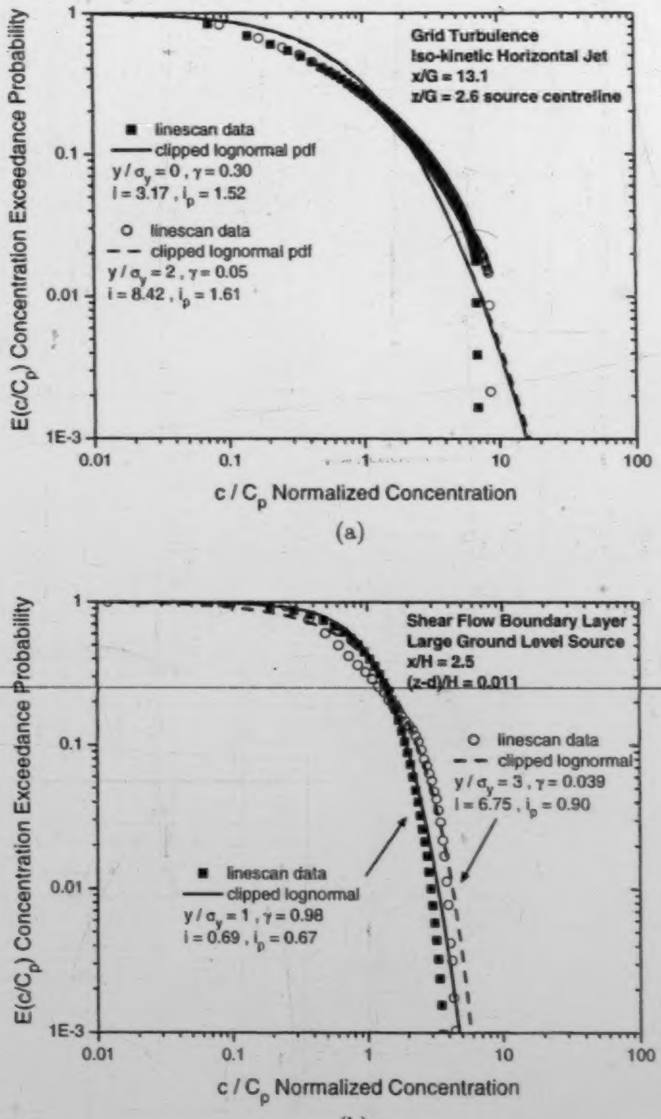

(a)

(b)

Figure 4.8: Exceedance probability functions $E(c/C_p)$ of the linescan data compared to the clipped lognormal generated by the stochastic model. (a) horizontal iso-kinetic jet in grid turbulence with the receptor measurement position at source height. (b) large ground level source in shear flow with the receptor measurement position at ground level.

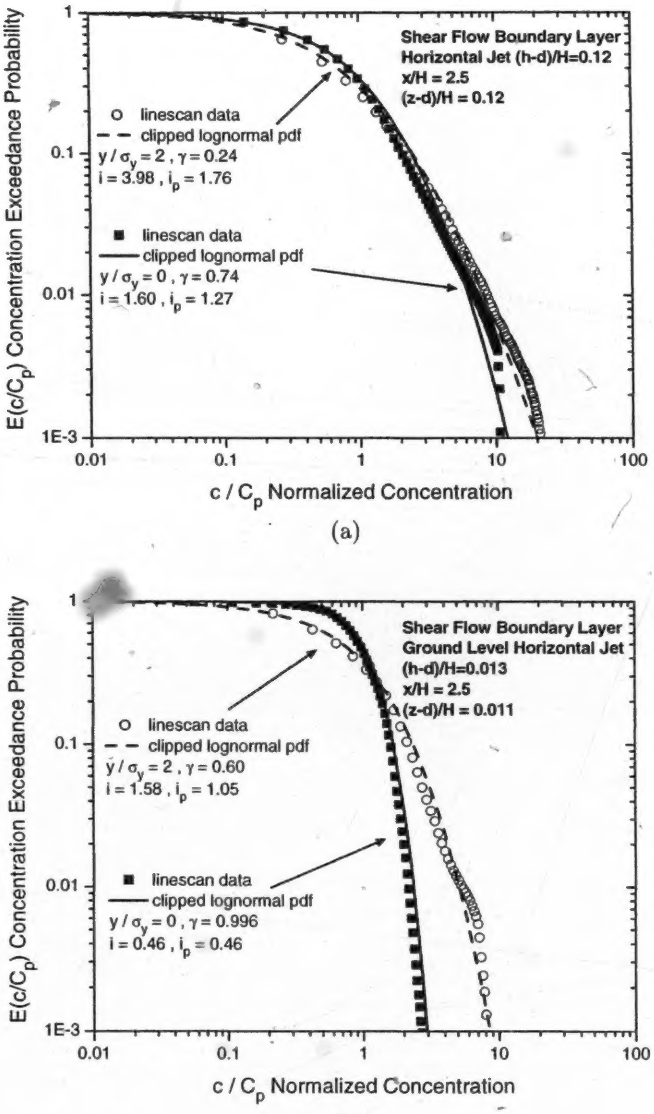

(a)

(b)

Figure 4.9: Exceedance probability functions $E(c/C_p)$ of the linescan data compared to the clipped lognormal generated by the stochastic model. (a) horizontal elevated iso-kinetic jet at $(h-d)/H = 0.12$ in shear flow measured at an elevated receptor position $(z-d)/H = 0.12$. (b) horizontal jet at ground level $(h-d)/H = 0.013$ in shear flow measured at the ground level receptor position $(z-d)/H = 0.011$. flow.

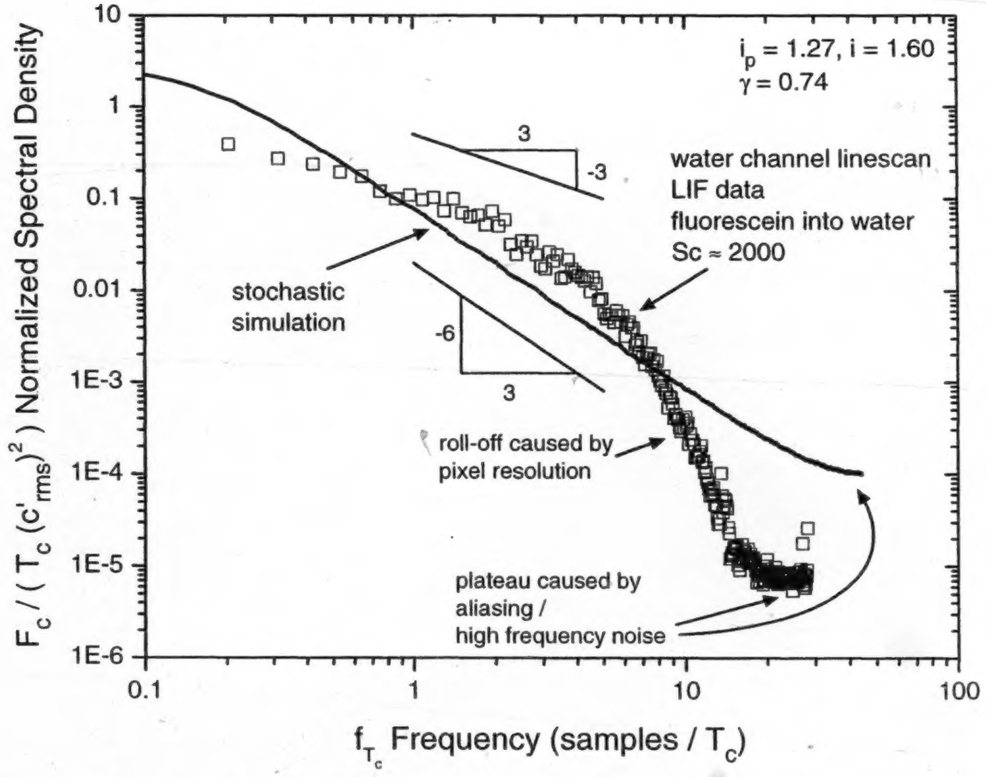

Figure 4.10: Typical normalized spectral density of the water channel linescan LIF data compared to the stochastic simulation. The slopes of the water channel data follows a Batchelor $F_c \propto f^{-1}$ slope until roll-off due to pixel resolution while the stochastic simulation follows a the Markov spectrum $F_c \propto f^{-2}$. At the highest measurable frequencies there is a small plateau caused by aliasing and random high frequency noise.

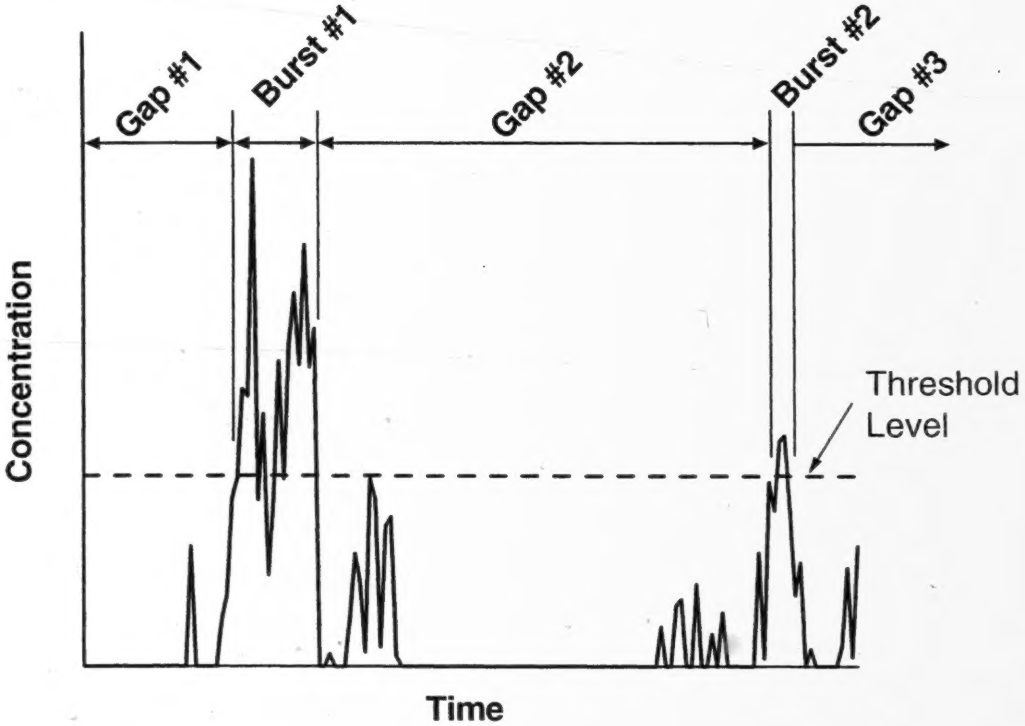

Figure 4.11: Time series example of bursts above and gaps below a threshold level in a concentration time series.

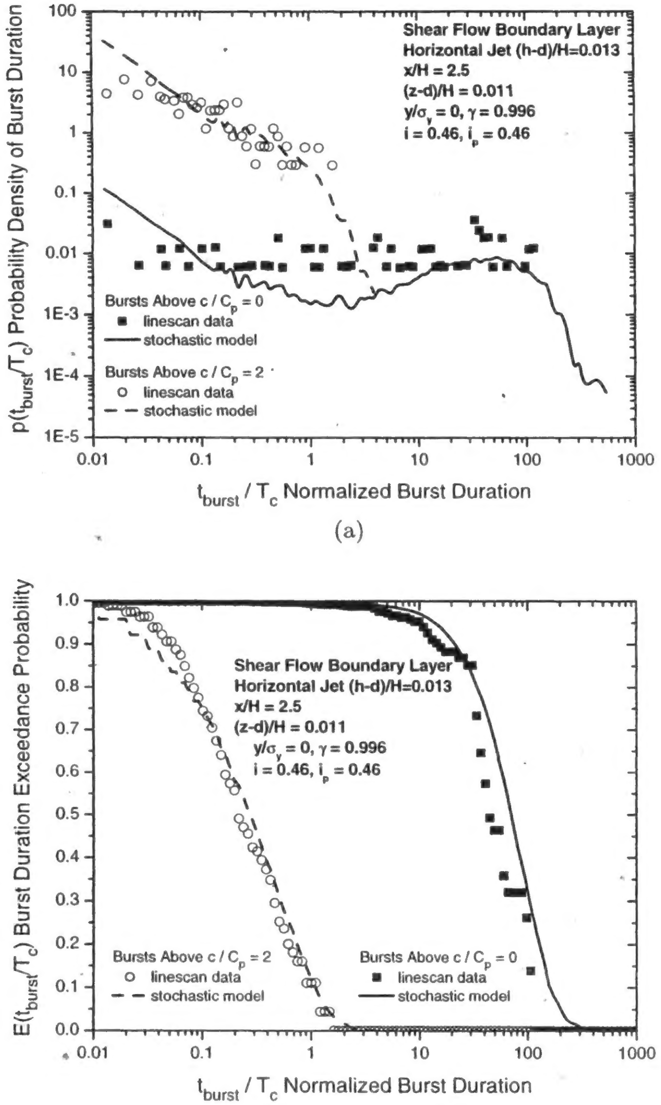

(a)

(b)

Figure 4.12: Probability distributions of bursts above $c/C_p = 0$ and $c/C_p = 2$ for a ground level horizontal jet and a ground level receptor position. This is a low zero-period intermittency $\gamma = 0.996$ and low fluctuation intensity $i_p = 0.46$ example. (a) probability density function of burst duration. (b) exceedance probability function of burst duration

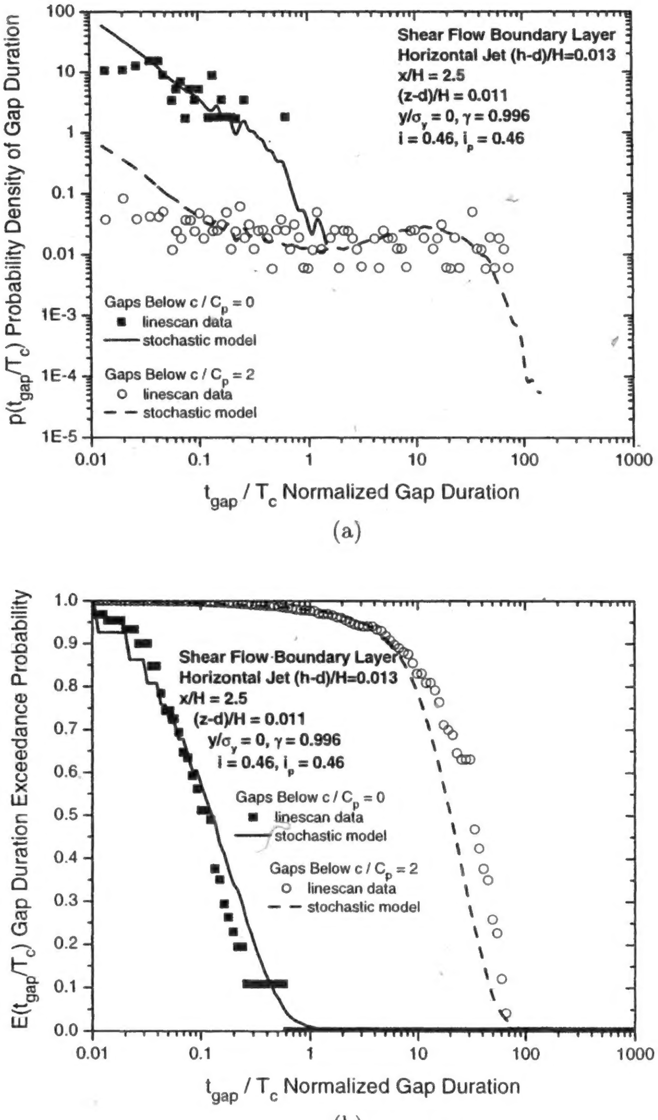

(a)

(b)

Figure 4.13: Probability distributions of gaps below above $c/C_p = 0$ and $c/C_p = 2$ for a ground level horizontal jet and a ground level receptor position. This is a low zero-period intermittency $\gamma = 0.996$ and low fluctuation intensity $i_p = 0.46$ example. (a) probability density function of gap duration. (b) exceedance probability function of gap duration

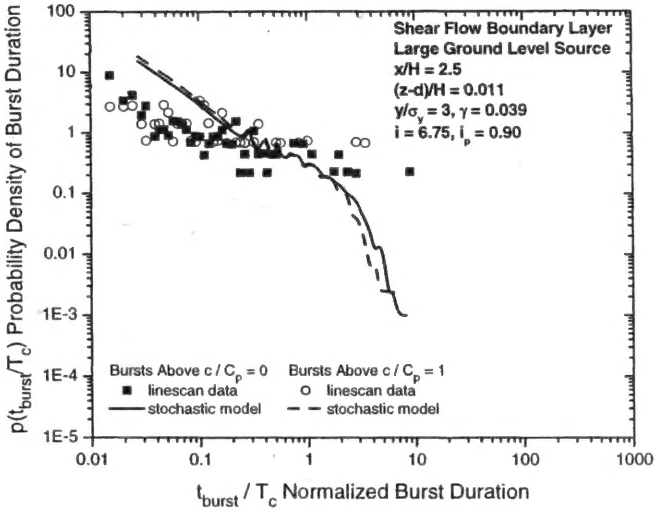

(a)

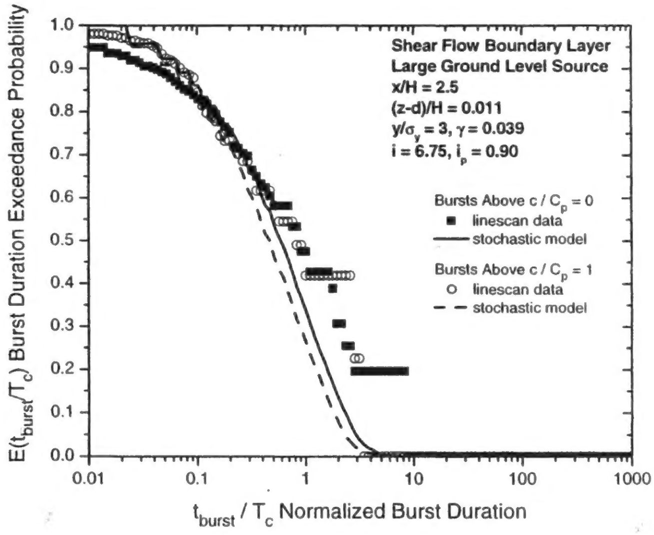

(b)

Figure 4.14: Probability distributions of bursts above $c/C_p = 0$ and $c/C_p = 1$ for a large ground level source and a ground level receptor position. This is a high zero-period intermittency $\gamma = 0.039$ and mid range fluctuation intensity $i_p = 0.90$ example. (a) probability density function of burst duration. (b) exceedance probability function of burst duration

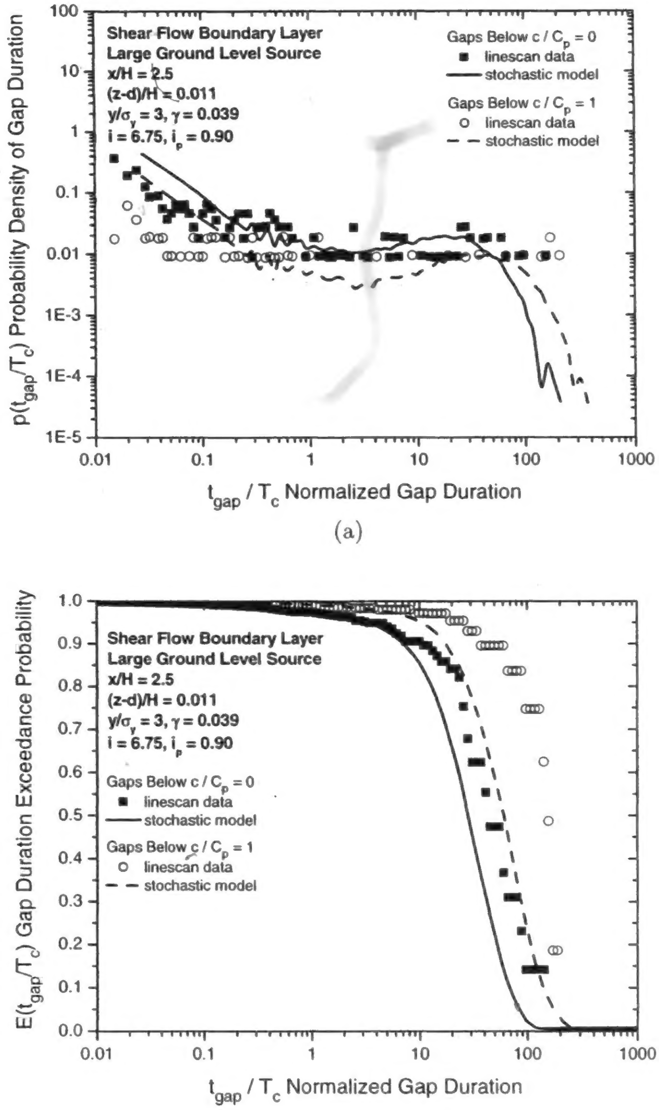

(a)

(b)

Figure 4.15: Probability distributions of gaps below above $c/C_p = 0$ and $c/C_p = 1$ for a large ground level source and a ground level receptor position. This is a high zero-period intermittency $\gamma = 0.039$ and mid range fluctuation intensity $i_p = 0.90$ example. (a) probability density function of gap duration. (b) exceedance probability function of gap duration

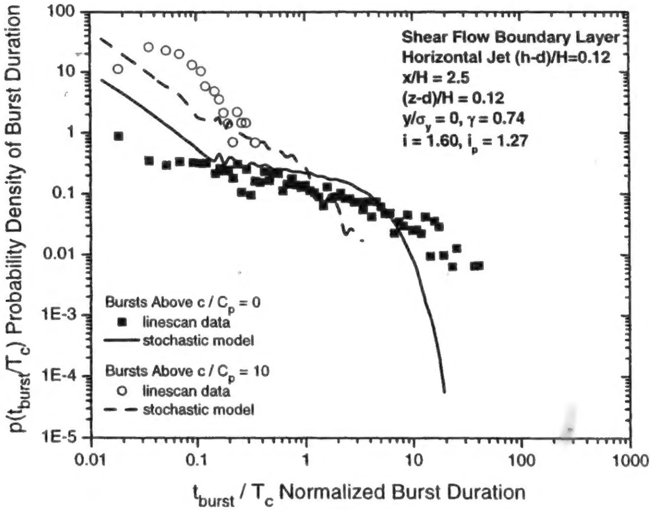

(a)

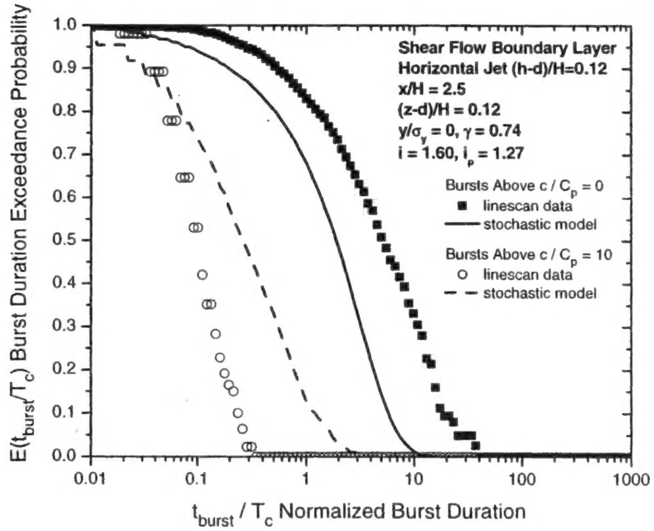

(b)

Figure 4.16: Probability distributions of bursts above $c/C_p = 0$ and $c/C_p = 10$ for an elevated iso-kinetic horizontal jet source in shear flow. This is a moderate zero-period intermittency $\gamma = 0.74$ and high fluctuation intensity $i_p = 1.27$ example. (a) probability density function of burst duration. (b) exceedance probability function of burst duration

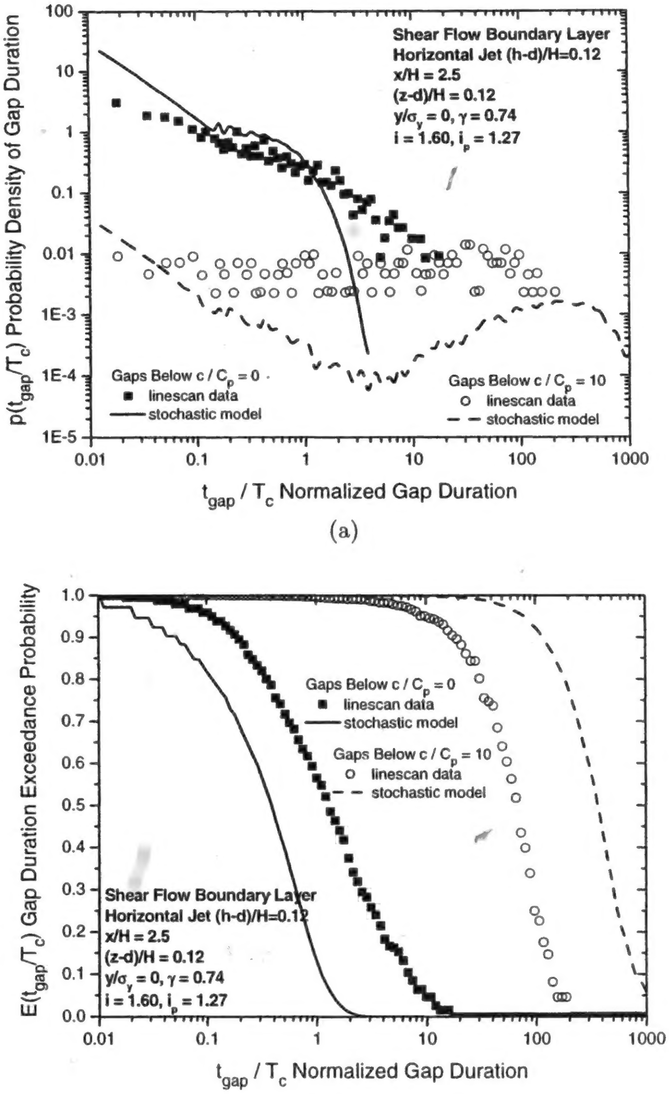

(a)

(b)

Figure 4.17: Probability distributions of gaps below above $c/C_p = 0$ and $c/C_p = 10$ for an elevated iso-kinetic horizontal jet source in shear flow. This is a moderate zero-period intermittency $\gamma = 0.74$ and high fluctuation intensity $i_p = 1.27$ example. (a) probability density function of gap duration. (b) exceedance probability function of gap duration

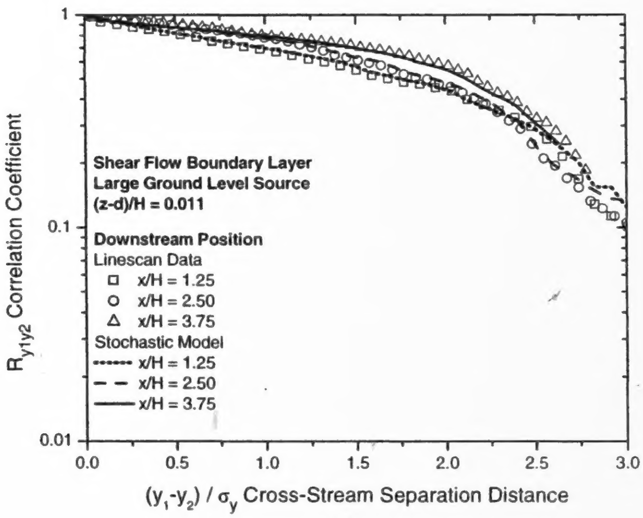

(a)

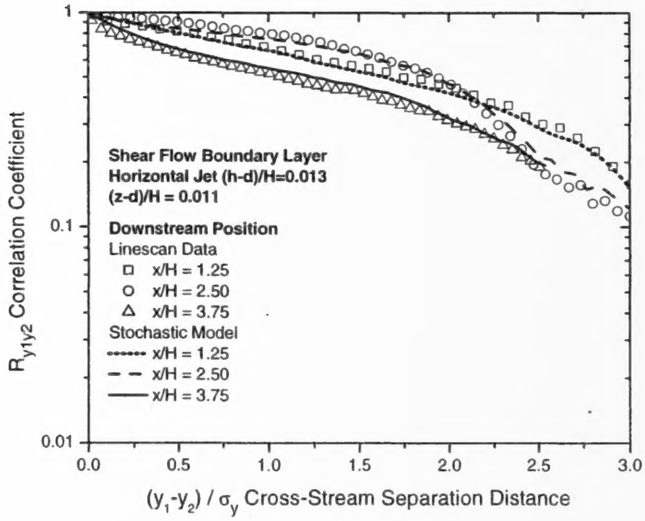

(b)

Figure 4.18: Cross-stream total concentration correlation coefficients for ground level sources and ground level receptors $(z-d)/H = 0.011$ in a boundary layer shear flow compared to the stochastic simulation (a) large ground level source. (b) horizontal jet at ground level $(h-d)/H = 0.013$.

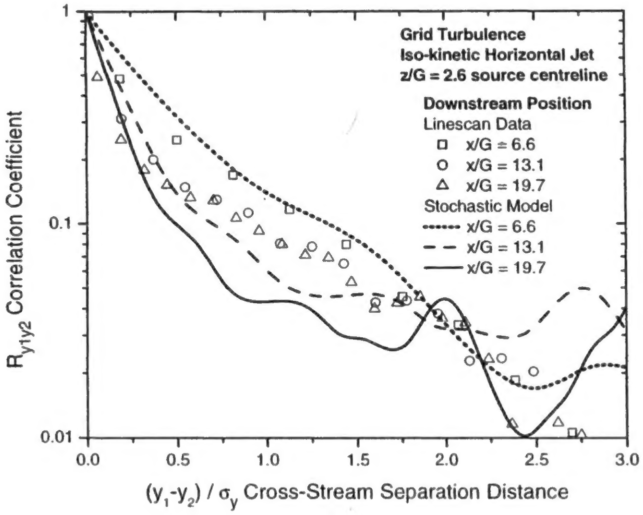

(a)

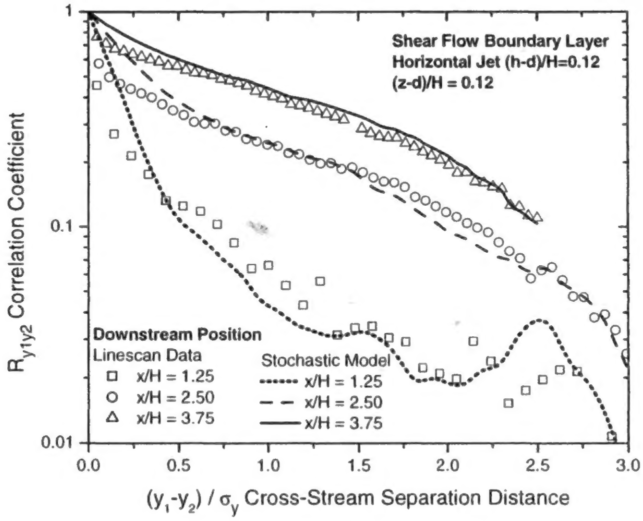

(b)

Figure 4.19: Cross-stream total concentration correlation coefficients for elevated sources with the receptor at source height compared to the stochastic simulation. (a) iso-kinetic jet in grid turbulence. (b) elevated iso-kinetic jet at $(h-d)/H = 0.12$ in shear flow.

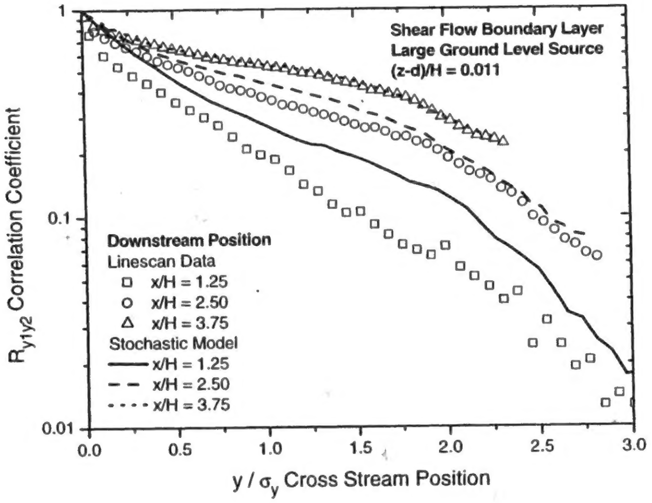

(a)

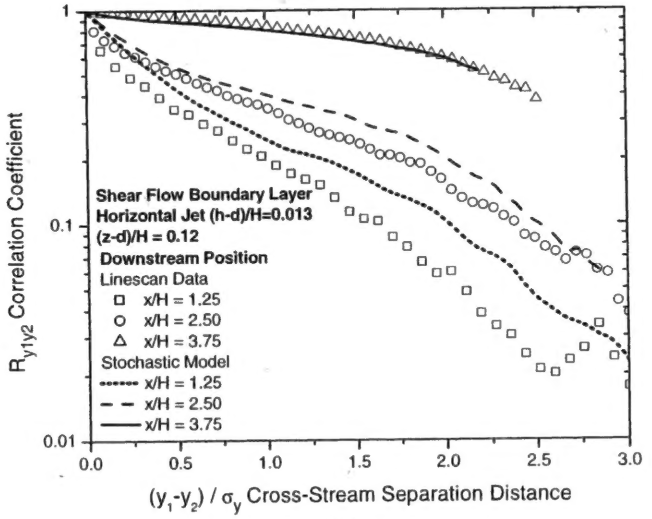

(b)

Figure 4.20: Cross-stream correlation total concentration coefficients for ground level sources with elevated receptor positions $(z-d)/H = 0.12$ in a boundary layer shear flow compared to the stochastic simulation (a) large ground level source. (b) horizontal jet at ground level $(h-d)/H = 0.013$.

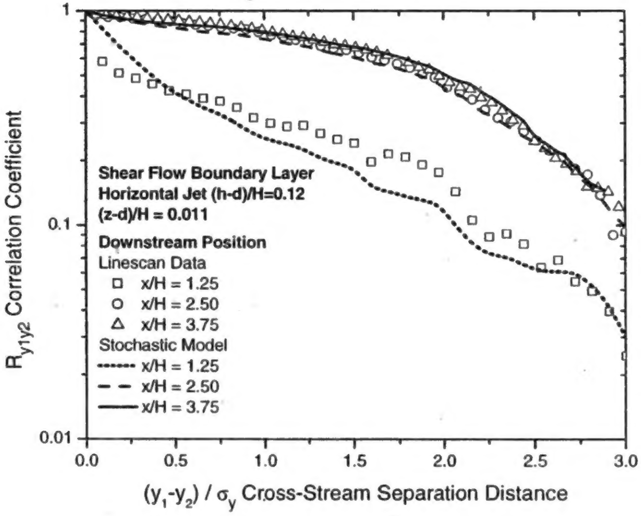

Figure 4.21: Cross-stream total concentration correlation coefficients for an elevated iso-kinetic jet source at $(h-d)/H = 0.12$ in shear flow with the receptor at ground level $(z-d)/H = 0.011$ compared to the stochastic simulation.

]

Chapter 5

Summary and Conclusions

Each of the body chapters in this thesis contributes to the development of an operational engineering model for concentration fluctuations statistics in the highly sheared flow near the ground in the atmospheric boundary layer. Chapters 2 through 4 are written as independent papers and have their own conclusions sections. This conclusion chapter will summarize the contributions of each of the chapters and discuss how the parts are put together for a complete concentration fluctuation time series generation model suitable for predicting toxicity, odour annoyance, flammability, or any other hazardous outcome of a chemical release into the atmosphere.

5.1 Complete Toxic Outcome Model

As discussed in Chapter 1, initial development of a computer-based toxic fatality outcome model called EVENTSIM was completed as part of an NSERC Strategic Research Project (see Wilson (2002) for the final report on the project). EVENTSIM was used to investigate how the toxic outcome of a pipeline blowout or well release was affected by variables such as release rate, total mass released, atmospheric stability, wind speed, pipe size, plume spread model, source density, and toxicity model.

The additional developments for modelling concentration fluctuation statistics in a shear flow as discussed in this thesis have been applied to an updated version of the program called EVENTSIM2, which takes basic meteorological and source conditions as inputs and makes the following calculations:

- predicts mean concentration using a Gaussian dispersion model
- predicts no-shear concentration fluctuation statistics using pseudo-meandering plume models from Wilson (1995)
- predicts concentration fluctuation statistics in a shear flow, using the shear models developed in Chapter 3
- adjusts the fluctuation statistics of the plume to account for averaging time using the travel time power law (TTPL) model from Chapter 2

- produces ensembles of concentration time series generated by the stochastic model discussed in Chapter 4
- applies an effective toxic load model as developed in Hilderman et al. (1999)

The output from EVENTSIM2 is a prediction of fatalities in the exposed population. However, the general method of simulating realistic exposure concentration fluctuation time series is very flexible. The initial Gaussian dispersion model can be easily replaced with any dispersion model that gives mean concentrations, plume spreads and specifies the wind velocity profile. Similarly, the final toxicity modelling step in EVENTSIM2 can be easily replaced by an odour annoyance, flammability or other hazardous outcome model.

5.2 Overview of Thesis Chapters

The key to the development of practical concentration fluctuation models in near-surface shear flows was a high quality experimental data set. The digital video linescan camera laser-induced fluorescence (LIF) measurement technique developed in Chapter 2 provided the necessary data to support the model development and verification. The high spatial and temporal resolution of the data made it possible to track the plume meander in the cross-stream direction in real time to test the averaging time effects on plume spread as discussed in Chapter 2. Detailed vertical profiles through the plumes enabled the development of the shear distortion model in Chapter 3. At present, there are no comparable laboratory or full-scale data sets available from any other source.

The shear distortion model for concentration fluctuation statistics presented in Chapter 3 uses the universal shear parameter $(1 + 5S_{\text{avg}})$ where S_{avg} is the average of the non-dimensional shear from the source and the receptor. For the cases that were tested this parameter produces the correct results, but it is uncertain how universal the shear parameter may be. It is clear that both the source position and the receptor position affect the concentration fluctuation statistics, but it is possible that the weighting factor should be more complicated than a simple average. Unfortunately, the present data set was insufficient to justify a more complicated shear distortion model. Additional laboratory and/or full-scale concentration data will be required to develop the shear model further. However, at present, the universal shear parameter presented in Chapter 3 provides a much more accurate and useful prediction of concentration fluctuations in shear flow than what has been previously available.

The stochastic model testing in Chapter 4 confirmed that it is a viable method of simulating realistic ensembles of concentration fluctuations despite the issue of poorly matched power spectra. Even for predicting relatively esoteric parameters such as gaps below and bursts above a threshold, the stochastic model produces good results. Such parameters are nearly impossible to produce analytically with simple statistical measures of concentration fluctuation moments or probability distributions. As more complicated toxicity, odour, and other outcome models are developed they can be easily applied to ensembles of simulated concentration fluctuation time series to determine probable outcomes.

The development of cross-stream correlation and de-correlation techniques in Chapter 4 has added another dimension to stochastic time series simulation and enables the simulation of realistic simultaneous correlated events. In practical terms, this enables the simultaneous hazardous exposure prediction for a receptor and his neighbours.

A final item that deserves mention is the clipped lognormal probability distribution for intermittent concentrations. From its introduction in Hilderman and Wilson (1999), it has proved to be a robust, mathematically convenient probability distribution to describe plume concentrations as demonstrated in Chapter 4. In Chapter 2 the clipped lognormal is also used to describe the distribution of instantaneous plume spreads measured across a line. The clipped lognormal is appealing because random multiplicative processes, such as dilution of concentration in a plume, are expected to be lognormal. The success of the clipped lognormal implies that the intermittent periods are an essential and inseparable part of the plume dilution process and naturally fit into the clipped-off part of the lognormal distribution.

5.3 Future Research

Future research in the area of concentration fluctuations and stochastic modelling can expand on the developments in this thesis. Some particular topics that should be addressed are the effects of other source types and sizes, buoyant or dense sources, different atmospheric stability classes, and dispersion within and around large obstacles such as houses and other buildings.

The sources used in this thesis were all small area sources with very low momentum and neutrally buoyant release. Some other source types of interest include high momentum jets from burst pipes or wells, elevated jets from stacks, evaporation from pools of spilled cryogenic material, and large area sources such as odour emissions from agricultural operations.

The effect of source density on concentration fluctuations in the shear layer is unclear, but very dense materials might be expected to suppress turbulent mixing and reduce the fluctuation level across the plume. Dense plumes would also be expected to remain close to ground level where the wind shear is very large, so shear effects will be larger than the range of effects covered by the data used to validate the present model. At present there is little dense plume concentration fluctuation data available to support model development.

In this thesis, the method of dealing with atmosphere stability was to consider the effect on the turbulent structure of the boundary layer, but otherwise there was no separate adjustment for stability. It is hoped that this method accounts for much of the effect on concentration fluctuations, but that has not been confirmed. Additional data or theory investigating the effect of atmospheric stability would help to improve the model predictions.

The experimental data and simulations in this study only address the simplified case of uniform ground level roughness over the entire extent of the plume. This type of dispersion rarely occurs in the real world where obstacles such as buildings tend to alter the local flow conditions and produce recirculation zones. Dispersion around obstacles is important for both industrial releases, which could happen near populated areas, and military defence applications for predicting the effects of dispersion of biological and chemical weapons in an urban area. At present, urban dispersion models are being developed and experimental data are being collected by a number of other institutions and agencies. The initial focus of urban dispersion modelling is mean concentration prediction, but there is little doubt that concentration fluctuations will have a significant effect on the biological outcomes predicted by urban dispersion models. Last but not least, the event-to-event variability of toxic releases can now be confidently predicted using EVENTSIM2 as an add-on to existing models.

References

Hilderman, T. L., Hrudey, S. E., and Wilson, D. J. (1999), A Model for Effective Toxic Load from Fluctuating Gas Concentrations, *Journal of Hazardous Materials A*, 64:115–134.

Hilderman, T. L. and Wilson, D. J. (1999), Simulating Concentration Fluctuation Time Series with Intermittent Zero Periods and Level Dependent Derivatives, *Boundary-Layer Meteorology*, 91:451–482.

Wilson, D. J. (1995), *Concentration Fluctuations and Averaging Time in Vapor Clouds*, Center for Chemical Process Safety of the American Institute of Chemical Engineers, New York, NY.

Wilson, D. J. (2002), Outcome-Based Risk Scaling and Uncertainty Factors for Toxic Gas Releases, Technical report, University of Alberta, Final Report for NSERC Strategic Project 215980-1998.

Appendix A

Water Channel Velocity Profiles

Chapters 2, 3, and 4 all discuss experimental dispersion measurements made in both a turbulent rough surface boundary layer shear flow and a shear free grid generated turbulent flow in the water channel. This appendix contains a complete set of all of the velocity measurements to supplement the subset of velocity information included directly in each chapter.

Note that all data in the appendix are plotted in measured laboratory units and are not normalized.

A.1 Shear Flow Boundary Layer

For most of the experiments the water channel was configured to produce a well-developed rough surface turbulent boundary layer flow similar to what would be observed in the full scale atmosphere under neutrally stable conditions. The rough bottom surface was made of standard 1/2" x 18 raised surface (i.e. not rolled flat) stainless steel expanded metal fastened to 6mm thick acrylic panels. The expanded metal has diamond shaped openings 11 mm wide in the flow direction and 24 mm wide in the cross stream direction.

Natural development of a turbulent boundary layer would require a much longer water channel, so additional flow conditioning elements were placed at the inlet of the channel test section to accelerate the boundary-layer development. The trip fence and square bar array illustrated in A.1 were used to redistribute the flow and generate some mid to large scale turbulence. The design of these elements was initially based on flow conditioning elements used in a colleague's (Castro, 1998) wind tunnel.

A two-component TSI Inc. Laser Doppler Velocimeter (LDV) system was used to make measurements of the velocity profiles in the channel. The final positions of the square bars in Figure A.1 were determined empirically by making small adjustments and then checking the results with repeated LDV measurements of cross-stream and vertical velocity profiles at several downstream locations. The objective was to produce even cross-stream distributions and a log-law vertical velocity profile.

The result of this flow conditioning is the cross-stream uniformity shown in Figures

A.2 through A.5. The mean streamwise velocity varies by about ±5% across the channel outside of the side wall boundary layer.

In the vertical direction the log-law velocity profile is

$$U = \frac{u_*}{\kappa} \ln \left(\frac{z - d}{z_0} \right) \tag{A.1}$$

where $u_* = 1.4$ cm/s is the friction velocity, $\kappa = 0.4$ is the Von Karman constant, $d = 1.7$ mm is the zero-plane displacement height, and $z_0 = 0.52$ mm is the roughness height. This log-law extends practically the entire depth $H = 400$ mm of the channel. Vertical profiles of the mean streamwise velocity U are in Figures A.6 and A.7. Figure A.8 is vertical profiles of the rms fluctuating velocity components, u'_{rms}, v'_{rms}, and w'_{rms} with an approximating function for w'_{rms} shown in Figure A.9. Figures A.10 and A.11 are vertical profiles of the Reynolds stresses $\overline{uv}$ and $\overline{uw}$. Figure A.12 shows vertical profiles of the Eulerian integral timescale of velocity fluctuations for all three coordinate directions. Figure A.13 shows the T_{vel} overall velocity time scale defined as

$$\frac{1}{T_{\text{vel}}} = \frac{1}{T_u} + \frac{1}{T_v} + \frac{1}{T_w} \tag{A.2}$$

See Chapter 3 for additional discussion on the definition of T_{vel}.

A.2 Grid Turbulence

For comparison purposes, plume dispersion measurements were also made in a shear free grid-generated turbulent flow. The grid was made of flat stainless steel bars 19.2 mm wide by 5 mm thick with a centre to centre mesh spacing of $G = 76.2$ mm and a total open area of 56%. The bars were standard stainless steel rolled stock with slightly rounded edges rather than sharply machined edges. This was the same grid constructed and used by Wilson et al. (1991). It was positioned at $x = 325$ mm from the channel inlet and the flow was run 405 mm deep with a 20 cm/s average flow rate.

The resulting velocity profiles for the streamwise component U are shown in Figures A.14 and A.15. They vary at most by ±5% if the wall boundary layers are neglected. The rms velocity fluctuation components are shown in Figures A.16 through A.19. The vertical fluctuations w'_{rms} were approximately 95% of the streamwise fluctuations u'_{rms} indicating some slight anisotropy in the flow. As expected for grid turbulence, the turbulence intensity decays with downstream distance as shown in A.20. The dye source was placed at $x = 1800$ mm where the turbulence intensity was about 5% and intensity decays to about 3% at the farthest downstream position for the concentration measurements at $x = 3300$ mm. The Eulerian timescale of velocity fluctuation for the streamwise component is about $T_u = 0.15$ seconds and for the vertical component $T_w = 0.08$ seconds as shown in Figure A.21. The fluctuation integral time scales are $T_u = 0.15$ s, $T_v = T_w = 0.08$ s and $T_{\text{vel}} = 0.032$ s. Chapter 2 has additional discussion on fitting power law decay curves to the turbulence intensity and integral time scale measurements.

References

Castro, I. P. (1998), Personal Communication, School of Mechanical and Materials Engineering, University of Surrey.

Wilson, D. J., Zelt, B. W., and Pittman, W. E. (1991), Statistics of Turbulent Fluctuation of Scalars in a Water Channel, Technical report, Department of Mechanical Engineering, University of Alberta, Edmonton, Alberta.

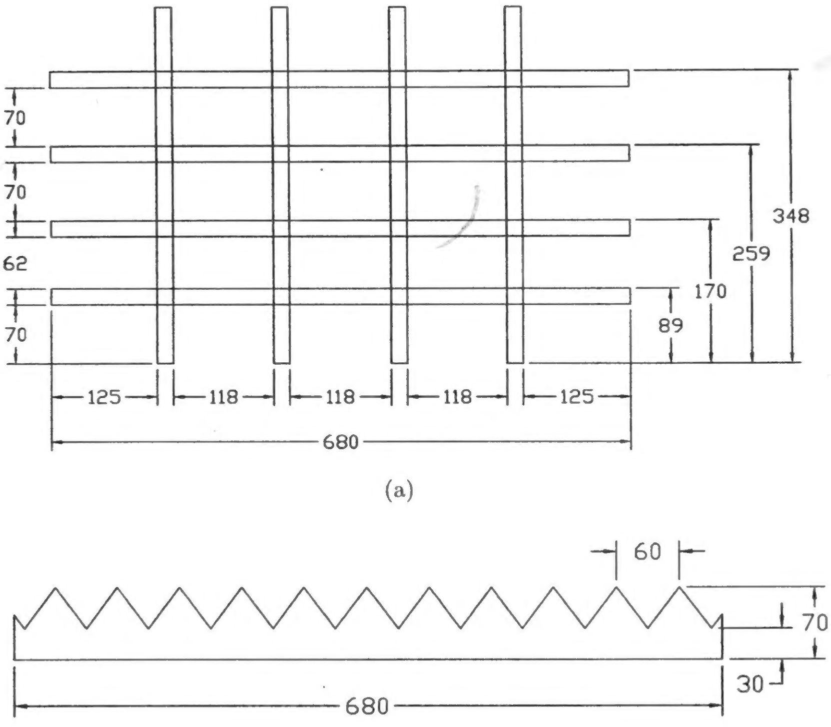
70
70
62
70
348
259
170
89
125
118
118
118
125
680
60
70
30
680

(a)

(b)

Figure A.1: (a) Square bar array. All square bars of 19mm (nominal 3/4") stainless steel hollow square tubes. (b) Trip fence made from 16 gauge stainless steel sheet metal. All dimensions are in mm.

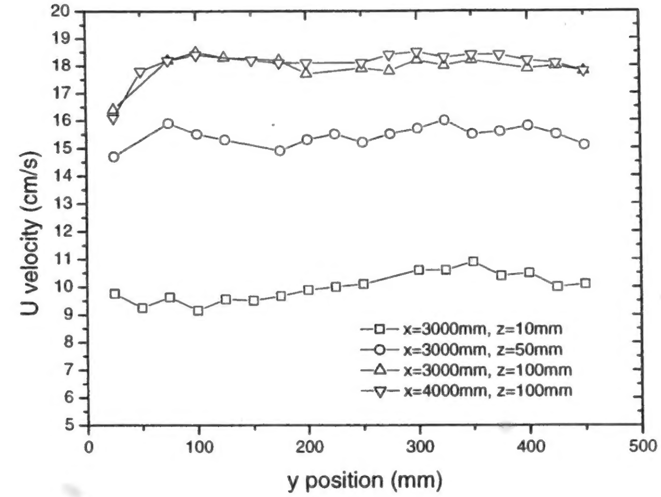

Figure A.2: Shear flow boundary layer cross-stream velocity profile of mean streamwise velocity U. The position $y = 0$ is one side wall of the channel and the total width is 680mm. Measurements are only made to $y = 450$ mm because of the limited focal length of the LDV lens.

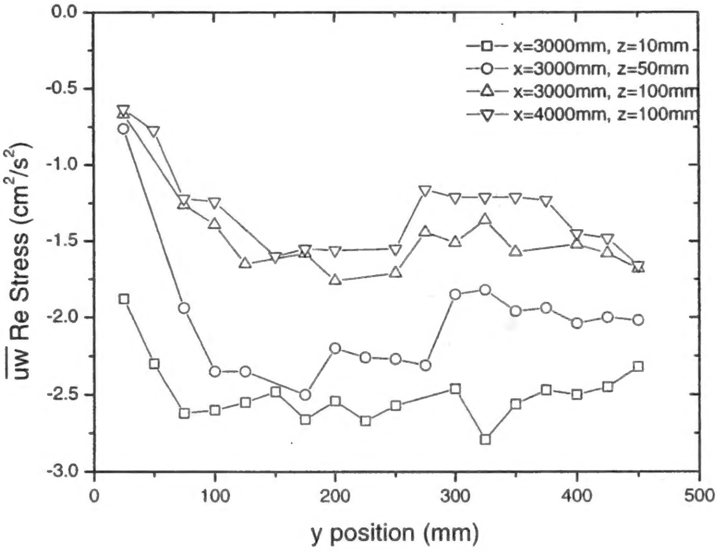

Figure A.3: Shear flow boundary layer cross-stream profiles $\overline{uw}$ Reynolds stress. The position $y = 0$ is one side wall of the channel and the total width is 680mm. Measurements are only made to $y = 450$ mm because of the limited focal length of the LDV lens.

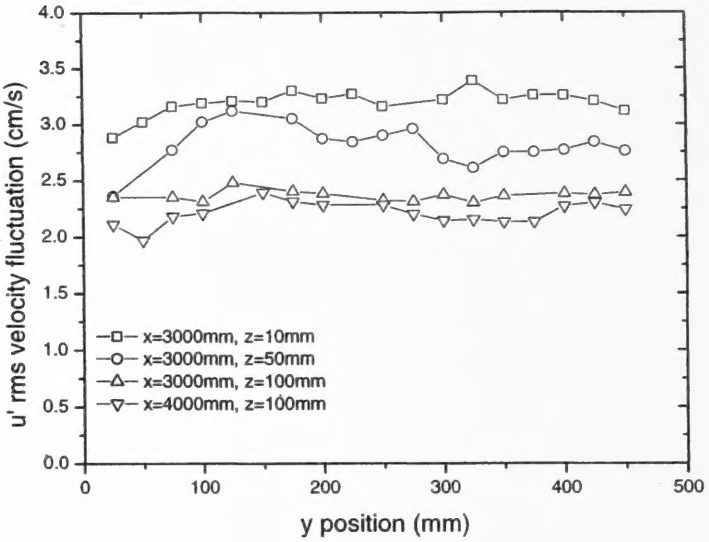

Figure A.4: Shear flow boundary layer cross-stream profiles of rms streamwise velocity fluctuation, u'_{rms}. The position $y = 0$ is one side wall of the channel and the total width is 680mm. Measurements are only made to $y = 450$ mm because of the limited focal length of the LDV lens.

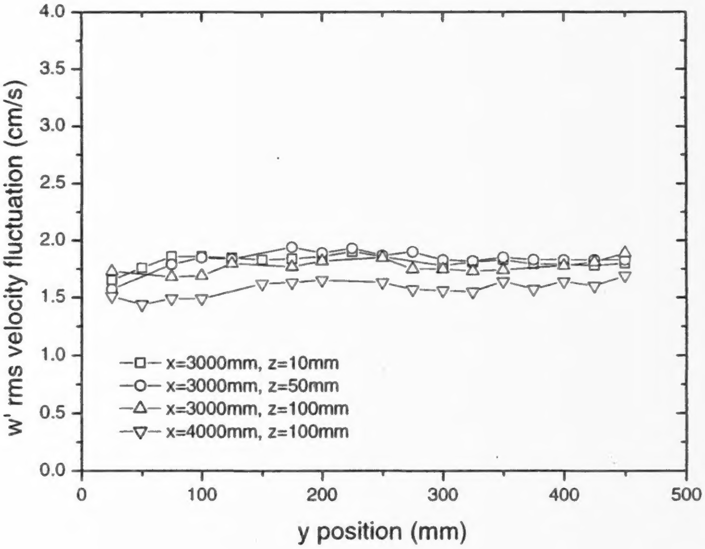

Figure A.5: Shear flow boundary layer cross-stream profiles of rms vertical velocity fluctuation, w'_{rms}. The position $y = 0$ is one side wall of the channel and the total width is 680mm. Measurements are only made to $y = 450$ mm because of the limited focal length of the LDV lens.

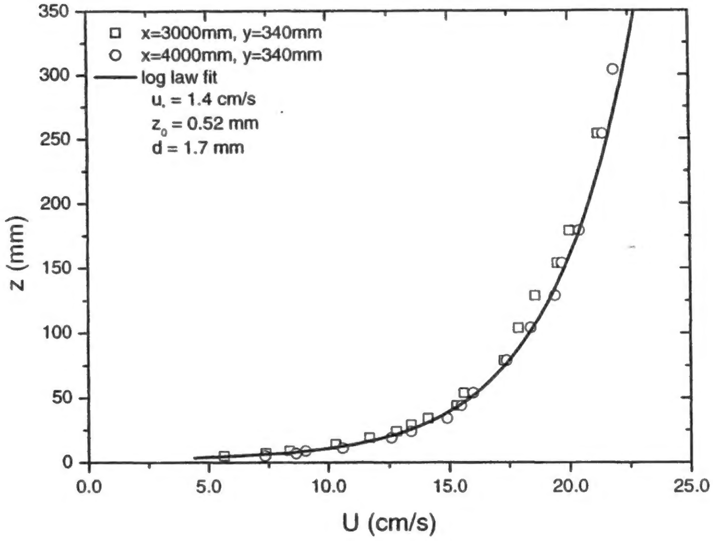

Figure A.6: Shear flow boundary layer vertical profiles of the mean velocity U on linear scales.

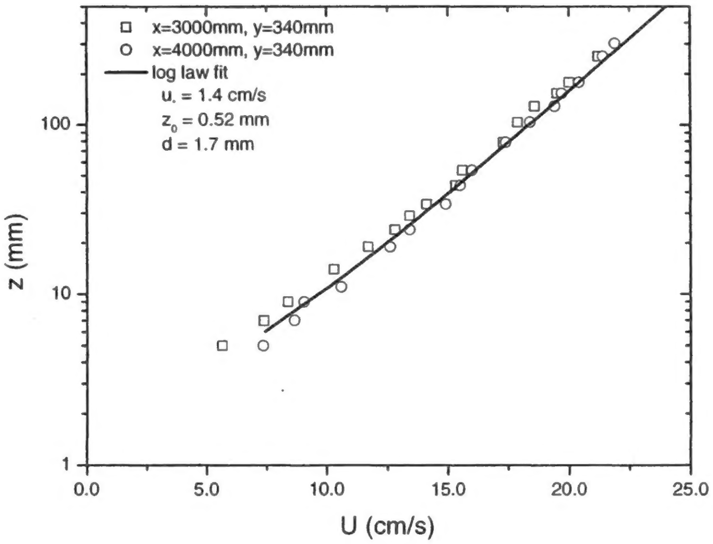

Figure A.7: Shear flow boundary layer vertical profiles of the mean velocity U on semi-logarithmic scales.

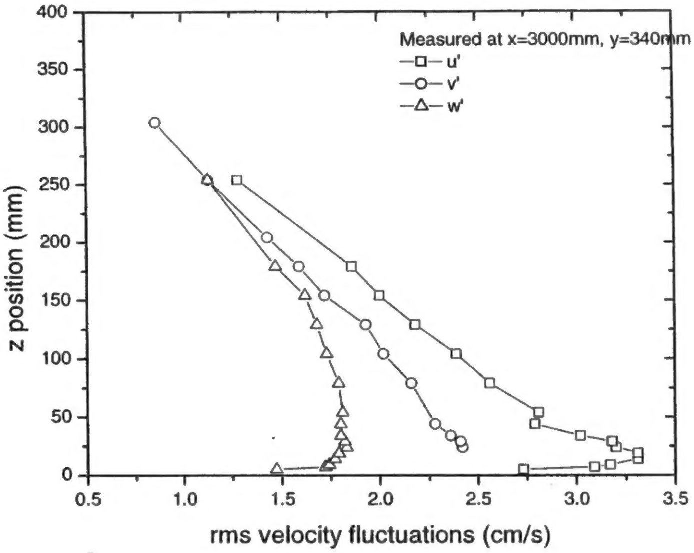

Figure A.8: Shear flow boundary layer vertical profiles of the rms fluctuating velocity components u'_{rms}, v'_{rms}, and w'_{rms}.

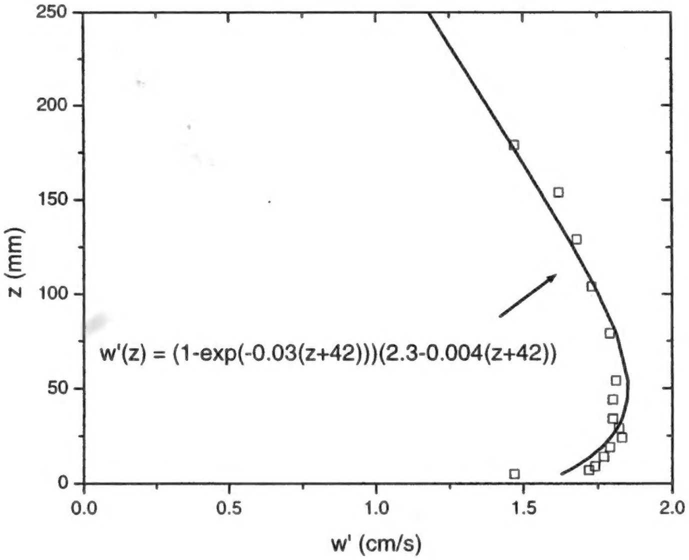

Figure A.9: Shear flow boundary layer vertical profile of rms vertical fluctuating velocity component w'_{rms} fit with an approximating function.

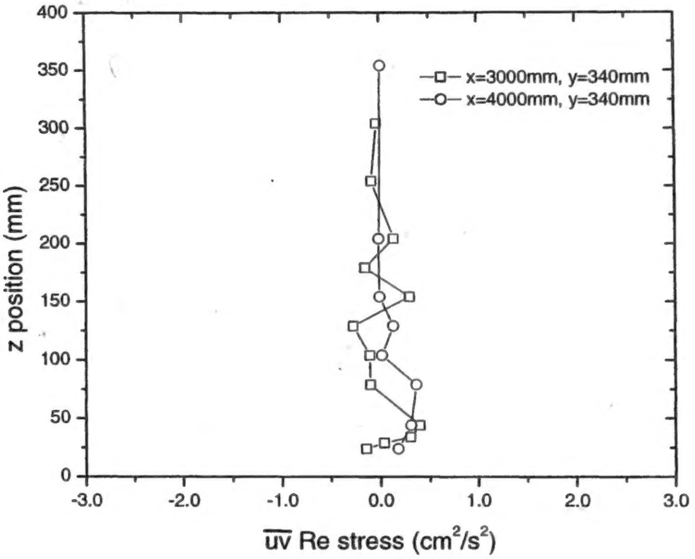

Figure A.10: Shear flow boundary layer vertical profiles of the Reynolds stresses $\overline{uv}$

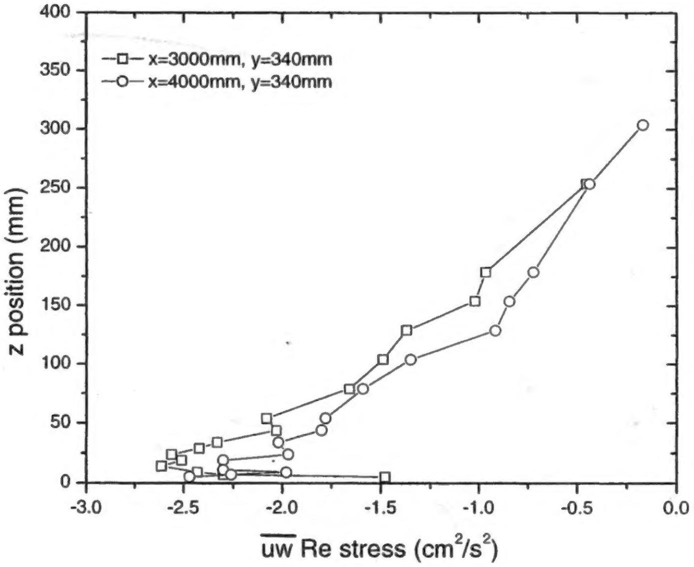

Figure A.11: Shear flow boundary layer vertical profiles of the Reynolds stresses $\overline{uw}$.

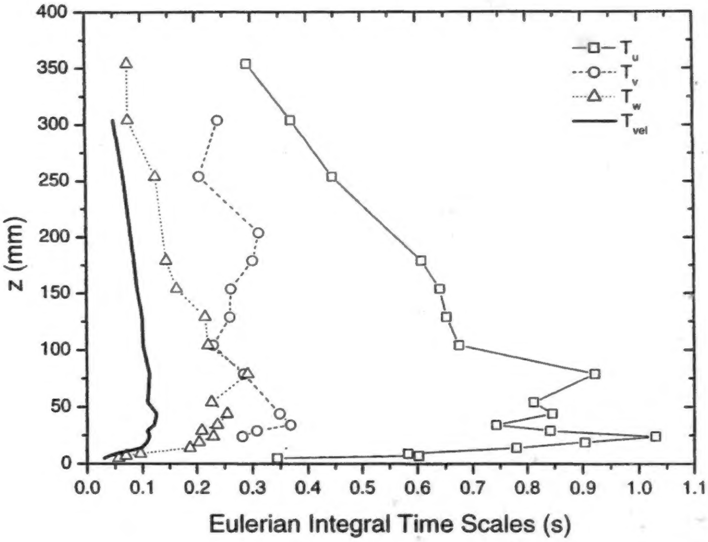

Figure A.12: Shear flow boundary layer vertical profiles of the Eulerian velocity fluctuation timescales.

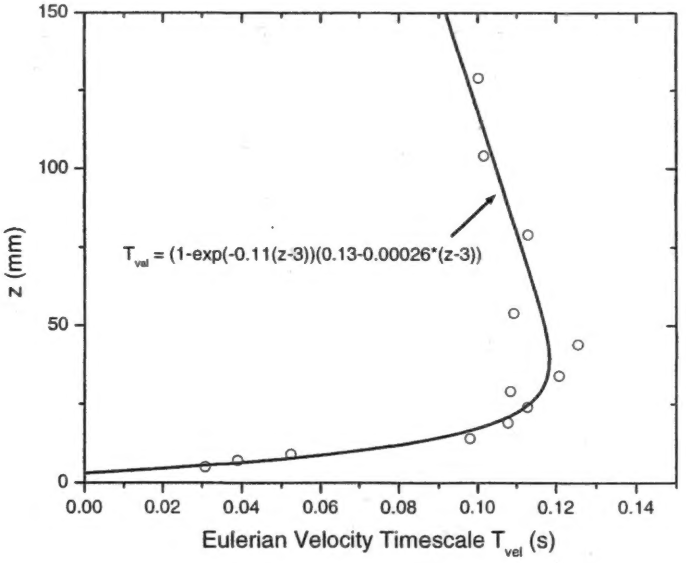

Figure A.13: Shear flow boundary layer vertical profiles of the Eulerian velocity fluctuation timescales fit with an approximating function.

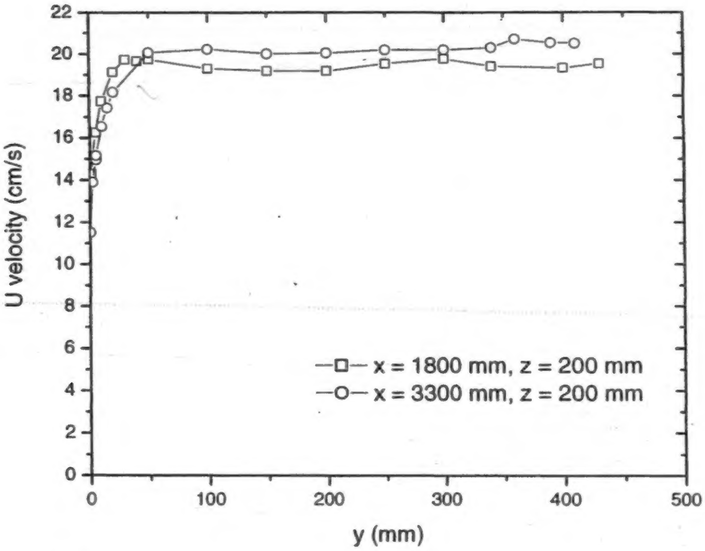

Figure A.14: Grid turbulence horizontal profile of streamwise velocity U

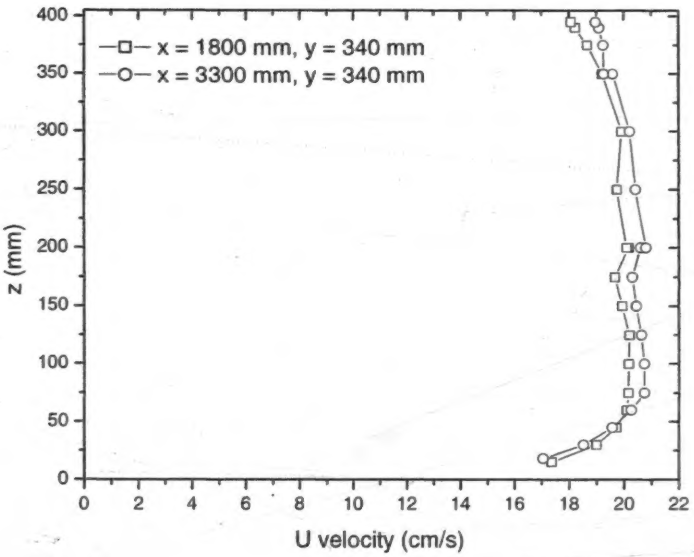

Figure A.15: Grid turbulence vertical profile of streamwise velocity U.

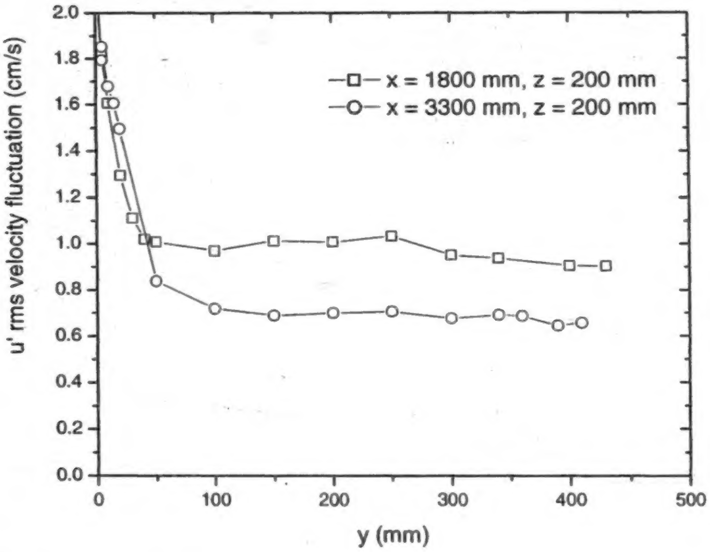

Figure A.16: Grid turbulence horizontal profile of the streamwise rms velocity fluctuation u'_{rms}

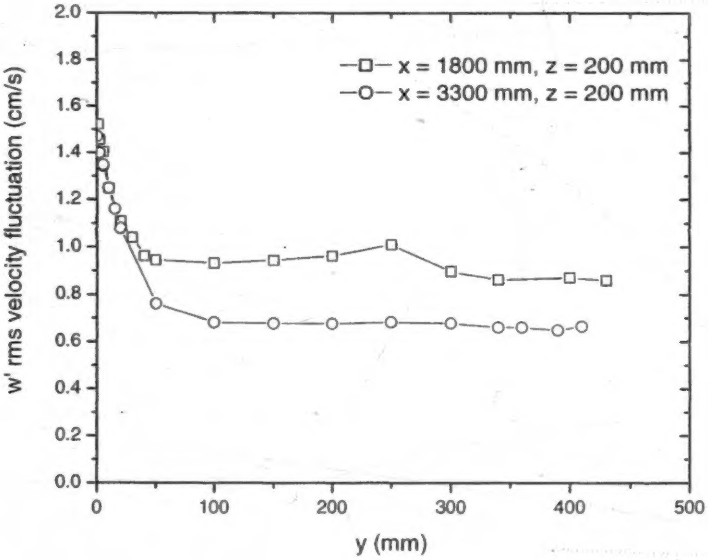

Figure A.17: Grid turbulence horizontal profile of the vertical rms velocity fluctuation w'_{rms}

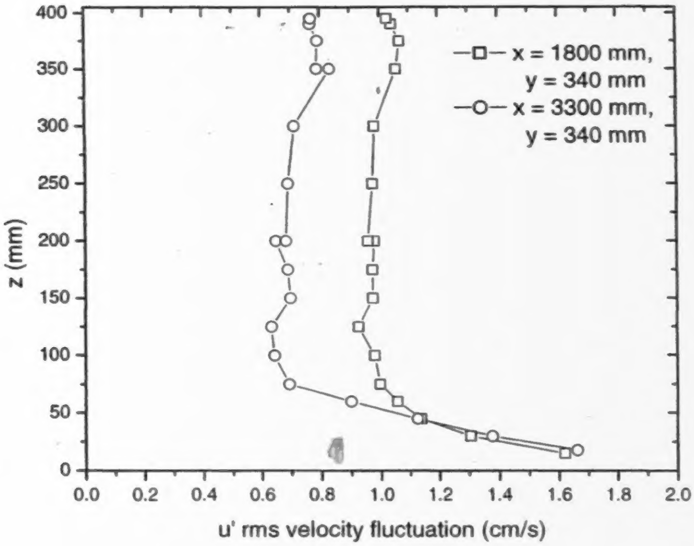

Figure A.18: Grid turbulence vertical profile of the streamwise rms velocity fluctuation u'_{rms}

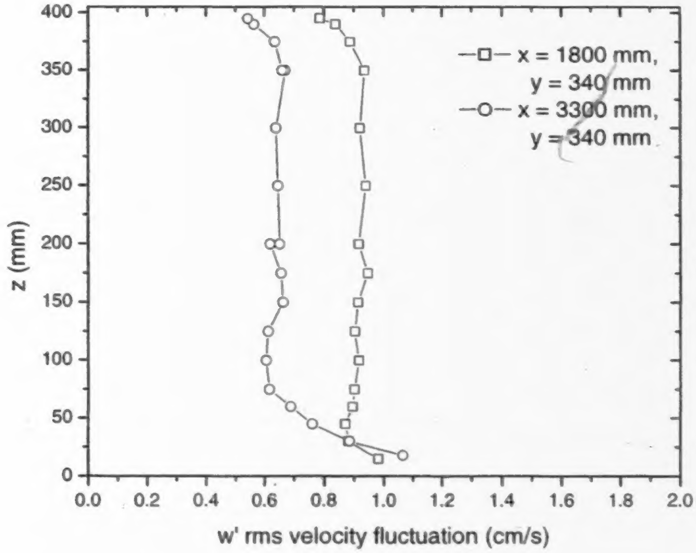

Figure A.19: Grid turbulence vertical profile of the vertical rms velocity fluctuation w'_{rms}

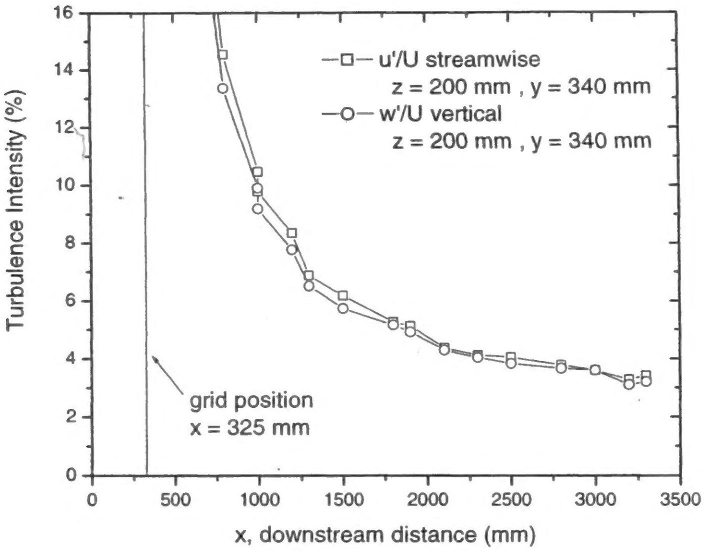

Figure A.20: Grid turbulence intensity decay with downstream distance along the centreline of the channel.

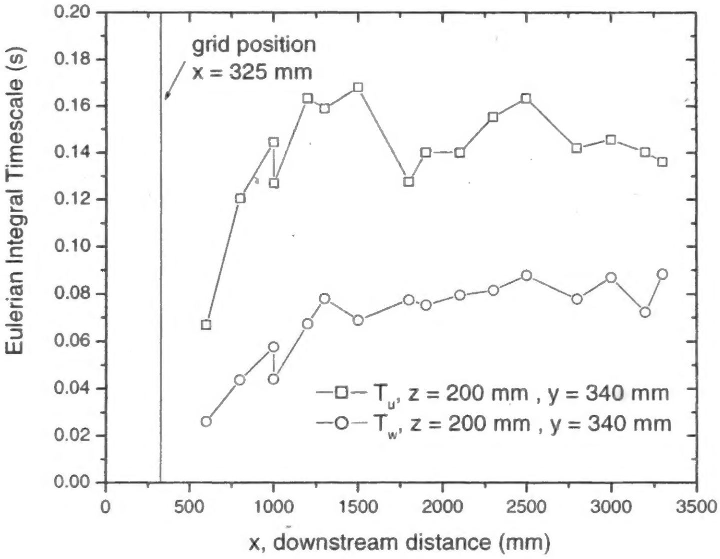

Figure A.21: Grid turbulence Eulerian integral timescales of velocity fluctuations in the streamwise T_u and vertical T_w directions along the centreline of the channel.

Appendix B

Linescan Data Summary

All concentration data used in this thesis was collected in the University of Alberta water channel using the linescan laser-induced fluorescence techniques discussed in Chapter 2. Three different dye source at various flow rates were used in the shear flow and grid turbulent flows discussed in Chapter 2 and Appendix A. Measurements were made in both horizontal and vertical line orientations in the shear flow. Only horizontal measurements were made in the grid turbulence flow based on the assumption that in grid turbulence dispersion should be the same in both the vertical and cross stream directions.

B.1 Normalization

In the body chapters of the thesis all of the experimental parameters were normalized to give non-dimensional values. In the appendices the coordinates have been left in un-normalized laboratory units of millimetres and seconds. In the few cases where normalization has been performed (cross-stream plume positions y/σ_y for example) the normalizing factors are clearly given in the plots.

For all other cases, the normalizing factors used in the body chapters depend on the flow field:

Shear Flow

- streamwise x positions are normalized by the mixing layer depth $H = 400$ mm (e.g. $x = 500$ mm is $x/H = 1.25$)
- vertical z positions are given as positions relative to the displacement height $d = 1.7$ mm of the log-law boundary layer (e.g. $z = 6$ mm is $(z-d)/H = 0.011$)
- velocities are normalized by the velocity at the top of the mixing layer $U_H = 232$ mm/s
- times are normalized by $H/U_H = 1.7$ s.

Grid Turbulence

- streamwise x and vertical z positions are normalized by the grid spacing $G = 76.2$ mm (e.g. $x = 500$ mm is $x/G = 6.6$)
- velocities are normalized by the uniform flow velocity $U_H = 200$ mm/s
- times are normalized by $G/U_H = 0.38$ s.

Conversions for common streamwise x and vertical z positions are given in Tables B.1 and B.2 for convenience.

B.2 Source Types

Three different dye sources were used. The basic configurations are illustrated in Figure B.1 and the detailed specifications are discussed below.

1. **Horizontal Jet** 4.3 mm OD and 3.25 mm ID stainless steel tube, 38 mm long suspended from above the channel by a streamlined support. In grid turbulence, the source was placed in the centre of the channel at $z = 200$ mm above the channel bottom, and in the shear flow the source was placed at height h between 7 and 50 mm above the surface depending on the experiment. The source flow rate was iso-kinetic in grid turbulence and for $h = 50$ mm above the ground in the shear flow. With the small diameter and low flow rates the jets from the source were laminar ($\mathrm{Re} = U_{\mathrm{source}} d_s/\nu \approx 600$).
2. **Vertical Jet at Ground Level** 3.25 mm ID flush with ground. To prevent dye from becoming trapped in the roughness elements, the expanded metal was removed from an area 25 mm on either side and 100 mm downstream of the source. The source flow rate was the same as for the horizontal jets and produced a laminar jet with a mean velocity equal to the cross flow velocity at $z = 50$ mm, $\mathrm{Re} \approx 600$.
3. **Large Ground Level Source** 11 mm ID flush with ground. As with the vertical ground level jet the expanded metal was trimmed away 25 mm on either side and 100 mm downstream of the source. The source flow rate was the same as the other 2 source ($\mathrm{Re} \approx 175$ based on source diameter).

For the elevated sources and grid turbulence measurements the source flow rates were iso-kinetic with the surrounding flow. The vertical sources had very low momentum with insignificant plume rise. With these laminar sources, measurements were taken at $x > 500$ mm downstream of the sources in all cases. At this downwind point the dilution was at least 100:1 which allowed the tracer-marked fluid to take on the turbulent structure of the cross flow. There was little effect of source size or release rate.

B.3 Horizontal Concentration Profiles

In the rough surface turbulent shear flow boundary layer horizontal linescan measurements at $x = 500$, 1000, and 1500 mm downstream of the source were made with the following source configurations:

1. large ground level source, flow rate $Q = 1.47$ ml/s
2. small ground level vertical jet, flow rate $Q = 1.47$ ml/s
3. small ground level vertical jet, flow rate $Q = 0.73$ ml/s
4. horizontal jet at $h = 7$ mm, flow rate $Q = 1.47$ ml/s
5. horizontal jet at $h = 7$ mm, flow rate $Q = 0.73$ ml/s
6. horizontal jet at $h = 25$ mm, flow rate $Q = 1.47$ ml/s
7. horizontal jet at $h = 50$ mm, flow rate $Q = 1.47$ ml/s

The high flow rate, $Q = 1.47$ ml/s, was chosen to produce an iso-kinetic source with the horizontal jet at $h = 50$ mm. The lower flow rate cases were simply halved to examine the effect a different flow rate.

In grid turbulence only the horizontal jet source, mounted at $z = 200$ mm in the centre of the channel with a flow rate of $Q = 1.52$ ml/s was tested.

For all of the horizontal measurements a wide range of vertical positions were tested, but only a smaller subset of data was examined in greater detail. Tables B.3 and B.4 list the smaller subset of data that was used to generate the plots that are included in the chapters and appendices. The subset was chosen to encompass the most important ranges of the experimental data:

- three downstream positions at $x = 500$,1000, and 1500 mm downstream of the source position
- three vertical positions at $z = 6$,25, and 50 mm above the ground in the shear flow
- three vertical position in the grid turbulence, $x = 500$, and $z = 200$,210 and 220 mm, $x = 1000$ and $z = 200$,220 and 240 mm and $x = 1500$, $z = 200$,225 and 250 mm

B.4 Vertical Concentration Profiles

Vertical linescan measurements in the turbulent shear flow were made with only a few of source configurations at $x = 500$ and 1500 mm downstream of the source.

1. small ground level vertical jet at a flow rate of $Q = 1.47$ ml/s

2. small ground level vertical jet at a flow rate of $Q = 0.73$ ml/s
3. horizontal jet at $h = 7$ mm at a flow rate of $Q = 1.47$ ml/s
4. horizontal jet at $h = 7$ mm at a flow rate of $Q = 0.73$ ml/s
5. horizontal jet at $h = 50$ mm at a flow rate of $Q = 1.47$ ml/s
6. horizontal jet at $h = 50$ mm at a flow rate of $Q = 0.73$ ml/s

All of these cases were used in this thesis and are listed in Table B.5.

No vertical grid turbulence profiles were measured as they would be identical to the horizontal profiles because the flow was homogeneous throughout the test section.

B.5 Additional Data Sets Collected

For future reference a number of additional horizontal linescan measurement were made, but not studied in great detail. These are listed in Tables B.6 through B.13 sorted by source type.

B.6 Data Table Description

All of the data sets listed in Tables B.3 to B.13 contain the following columns of information:

- Filename : data series base filename
- Linerate (kHz): line sampling rate for the linescan camera in (kHz)
- mm per pixel : pixel view width
- Data Time (s) : data collection time
- Source Conc. (mg/l) : source fluorescein tracer concentration
- Source Flow Rate. (ml/s) : source tracer emission rate
- Source x (mm) : downstream source position relative to channel inlet
- Source y (mm) : cross-stream source position relative to side wall of channel, $y = 340$ mm is channel centreline
- Source z (mm) : vertical source position measured from the bottom of the roughness

- Centre Pixel # or z=0 Pixel # : for horizontal linescans the centre pixel is the pixel at the y position given in column “Line y”; for vertical linescans it is the pixel at the z position given in column “Line z” (pixels are numbered from 0 to 1023)
- Line x (mm) : downstream position of linescan measurement relative to channel inlet
- Line y (mm) : cross-stream position of “Centre Pixel” for horizontal linescans; cross-stream position of vertical linescan measurement
- Line z (mm) : vertical position of horizontal linescan profile; vertical position of “z=0 Pixel” for vertical linescan profile
- x from source (mm) : downstream distance from source to measurement positon
- centroid (pixels) : plume average centroid position in terms of pixel number
- centroid (mm) : plume centroid position in mm relative to the side wall of the channel
- spread (pixels) : plume spread along measurement line in pixel units
- spread (mm) : plume spread along measurement line in mm

x (mm)	x/H	x/G
500	1.25	6.6
1000	2.5	13.1
1500	3.75	19.7

Table B.1: Streamwise, x-direction position normalization.

z (mm)	$(z-d)/H$
6	0.011
25	0.058
50	0.12

Table B.2: Vertical, z-direction position normalization.

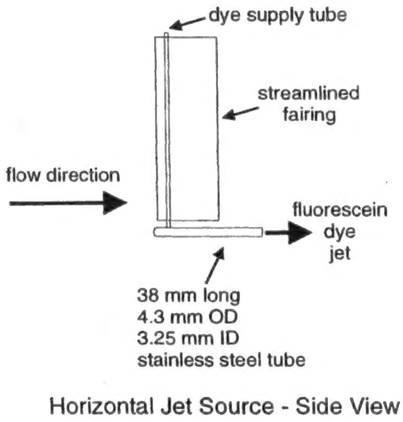
dye supply tube
streamlined fairing
flow direction
fluorescein dye jet
38 mm long
4.3 mm OD
3.25 mm ID
stainless steel tube
Horizontal Jet Source - Side View

(a)

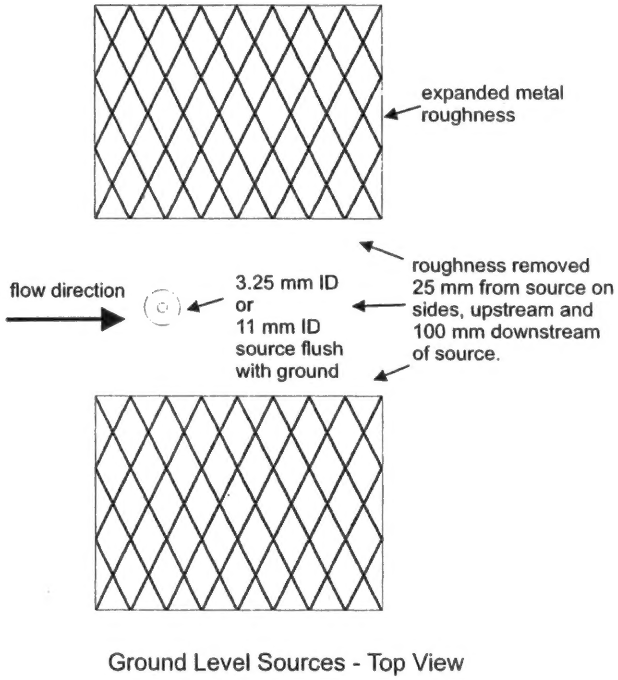
expanded metal roughness
flow direction
3.25 mm ID or 11 mm ID source flush with ground
roughness removed 25 mm from source on sides, upstream and 100 mm downstream of source.
Ground Level Sources - Top View

(b)

Figure B.1: Fluorescein dye sources. (a) Side view of elevated horizontal jet sources. Source was suspended from above the channel. (b) Top view of ground level sources. Expanded metal roughness was removed from the immediate area of the source and dye supply lines were underneath the acrylic panel below the roughness. The large (11 mm ID) ground level source was changed to the small ground level source by inserting a plug with a 3.25 mm ID hole for the small source.

Filename	Linerate (kHz)	mm per pixel	DataTime (s)	Source Conc. (mg/l)	Source Flowrate (ml/s)	Source x (mm)	Source y (mm)	Source z (mm)	Centre Pixel #	Line x (mm)	Line y (mm)	Line z (mm)	x from source (mm)	centroid (pixels)	centroid (mm)	spread (pixels)	spread (mm)
HORIZONTAL JET IN GRID TURBULENCE h = 200 mm																	
Sept10z200	0.5	0.485	500	1.5	1.52	1300	340	200	520	1800	340	200	500	527.60	343.68	31.89	15.46
Sept10z210	0.5	0.479	500	1.5	1.52	1300	340	200	520	1800	340	210	500	528.87	344.25	31.97	15.31
Sept10z220	0.5	0.472	500	1.5	1.52	1300	340	200	520	1800	340	220	500	528.39	343.96	31.90	15.06
Sept12z200b	0.5	0.485	500	4	1.52	1800	340	200	519	2800	340	200	1000	531.56	346.09	56.73	27.51
Sept12z220	0.5	0.468	500	4	1.52	1800	340	200	519	2800	340	220	1000	529.66	344.99	58.04	27.16
Sept12z240	0.5	0.457	500	4	1.52	1800	340	200	519	2800	340	240	1000	528.13	344.17	60.29	27.55
Sept6z200b	0.5	0.490	500	7	1.52	1800	340	200	543	3300	340	200	1500	532.22	334.72	78.21	38.32
Sept9z225	0.5	0.474	500	7	1.52	1800	340	200	541	3300	340	225	1500	530.06	334.81	77.02	36.51
Sept9z250	0.5	0.458	500	7	1.52	1800	340	200	541	3300	340	250	1500	527.73	333.92	81.32	37.24
LARGE GROUND LEVEL SOURCE - HIGH FLOW RATE, SHEAR FLOW																	
Idaa0192	0.5	0.519	500	10	1.47	2743	340	0	512	3243	340	6	500	519.48	343.88	113.05	58.67
Idaa0195	0.5	0.511	500	10	1.47	2743	340	0	512	3243	340	25	500	509.84	338.90	116.65	59.61
Idaa0196	0.5	0.494	500	10	1.47	2743	340	0	512	3243	340	50	500	514.01	340.99	128.12	63.29
Idaa0247	0.5	0.523	500	20	1.47	2742	340	0	512	3742	340	6	1000	514.55	341.33	154.58	80.84
Idaa0250	0.5	0.511	500	20	1.47	2742	340	0	512	3742	340	25	1000	510.87	339.42	154.15	78.77
Idaa0251	0.5	0.494	500	20	1.47	2742	340	0	512	3742	340	50	1000	502.47	335.29	174.74	86.32
Idaa0206	0.5	0.52	500	30	1.47	2742	340	0	512	4242	340	6	1500	520.67	344.51	183.36	95.35
Idaa0209	0.5	0.51	500	30	1.47	2742	340	0	512	4242	340	25	1500	515.26	341.66	194.59	99.24
Idaa0210	0.5	0.493	500	30	1.47	2742	340	0	512	4242	340	50	1500	493.50	330.88	208.75	102.91
SMALL GROUND LEVEL VERTICAL JET SOURCE - HIGH FLOW RATE, SHEAR FLOW																	
Idaa0295	0.5	0.511	500	10	1.47	2745	340	0	512	3245	340	25	500	520.35	344.27	116.59	59.58
Idaa0298	0.5	0.523	500	10	1.47	2745	340	0	512	3245	340	6	500	521.29	344.86	109.93	57.49
Idaa0299	0.5	0.494	500	10	1.47	2745	340	0	512	3245	340	50	500	501.08	334.61	122.45	60.49
Idaa0287	0.5	0.513	500	20	1.47	2745	340	0	512	3745	340	25	1000	504.18	335.99	163.72	83.99
Idaa0290	0.5	0.523	500	20	1.47	2745	340	0	512	3745	340	6	1000	483.78	325.24	154.86	80.99
Idaa0291	0.5	0.496	500	20	1.47	2745	340	0	512	3745	340	50	1000	492.28	330.22	176.78	87.68
Idaa0303	0.5	0.511	500	30	1.47	2745	340	0	512	4245	340	25	1500	522.78	345.51	189.02	96.59
Idaa0306	0.5	0.523	500	30	1.47	2745	340	0	512	4245	340	6	1500	491.76	329.41	181.87	95.12
Idaa0307	0.5	0.494	500	30	1.47	2745	340	0	512	4245	340	50	1500	482.95	325.65	197.16	97.39
SMALL GROUND LEVEL VERTICAL JET SOURCE - LOW FLOW RATE, SHEAR FLOW																	
Idaa0334	0.5	0.511	500	10	0.73	2745	340	0	512	3245	340	25	500	520.20	344.19	116.22	59.39
Idaa0337	0.5	0.523	500	10	0.73	2745	340	0	512	3245	340	6	500	518.24	343.26	106.30	55.59
Idaa0338	0.5	0.494	500	10	0.73	2745	340	0	512	3245	340	50	500	514.30	341.13	132.83	65.62
Idaa0342	0.5	0.513	500	30	0.73	2745	340	0	512	3745	340	25	1000	526.14	347.26	162.58	83.40
Idaa0345	0.5	0.523	500	30	0.73	2745	340	0	512	3745	340	6	1000	502.63	335.10	142.58	74.57
Idaa0346	0.5	0.495	500	30	0.73	2745	340	0	512	3745	340	50	1000	517.66	342.80	183.05	90.61
Idaa0350	0.5	0.512	500	40	0.73	2745	340	0	512	4245	340	25	1500	523.85	346.07	189.62	97.09
Idaa0353	0.5	0.523	500	40	0.73	2745	340	0	512	4245	340	6	1500	522.99	345.75	175.77	91.93
Idaa0354	0.5	0.494	500	40	0.73	2745	340	0	512	4245	340	50	1500	505.18	336.63	207.11	102.31

Table B.3: Horizontal linescan data subset used for analysis. Horizontal jet source in grid turbulence, large ground level source in shear flow and small ground level vertical jet in shear flow.

Filename	Linerate (kHz)	mm per pixel	DataTime (s)	Source Conc. (mg/l)	Source Flowrate (ml/s)	Source x (mm)	Source y (mm)	Source z (mm)	Centre Pixel #	Line x (mm)	Line y (mm)	Line z (mm)	x from source (mm)	centroid (pixels)	centroid (mm)	spread (pixels)	spread (mm)
HORIZONTAL JET SOURCE - GROUND LEVEL AT h=7 mm HIGH FLOW RATE, SHEAR FLOW																	
Idaa0185	0.5	0.519	500	10	1.47	2730	340	7	512	3230	340	6	500	542.26	355.71	103.38	53.653
Idaa0188	0.5	0.509	500	10	1.47	2730	340	7	512	3230	340	25	500	542.95	355.75	110.18	56.083
Idaa0189	0.5	0.494	500	10	1.47	2730	340	7	512	3230	340	50	500	541.52	354.58	123.20	60.86
Idaa0172	0.5	0.494	500	20	1.47	2730	340	7	512	3730	340	50	1000	567.18	367.26	175.71	86.80
Idaa0173	0.5	0.511	500	20	1.47	2730	340	7	512	3730	340	25	1000	562.42	365.76	162.81	83.20
Idaa0175	0.5	0.52	500	20	1.47	2730	340	7	512	3730	340	6	1000	545.17	357.25	151.61	78.84
Idaa0232	0.5	0.494	500	30	1.47	2742	340	7	512	4242	340	50	1500	561.71	364.56	192.95	95.32
Idaa0233	0.5	0.511	500	30	1.47	2742	340	7	512	4242	340	25	1500	540.01	354.31	180.56	92.27
Idaa0236	0.5	0.522	500	30	1.47	2742	340	7	512	4242	340	6	1500	543.67	356.53	173.74	90.69
HORIZONTAL JET SOURCE - GROUND LEVEL AT h=7 mm LOW FLOW RATE, SHEAR FLOW																	
Idaa0326	0.5	0.511	500	10	0.73	2745	340	7	512	3245	340	25	500	538.40	353.49	114.67	58.60
Idaa0329	0.5	0.523	500	10	0.73	2745	340	7	512	3245	340	6	500	548.19	358.93	104.75	54.79
Idaa0330	0.5	0.496	500	10	0.73	2745	340	7	512	3245	340	50	500	545.88	356.80	120.63	59.83
Idaa0318	0.5	0.512	500	30	0.73	2745	340	7	512	3745	340	25	1000	514.64	341.35	163.57	83.75
Idaa0321	0.5	0.523	500	30	0.73	2745	340	7	512	3745	340	6	1000	511.79	339.89	152.60	79.81
Idaa0322	0.5	0.495	500	30	0.73	2745	340	7	512	3745	340	50	1000	527.99	347.92	169.22	83.77
Idaa0311	0.5	0.523	500	30	0.74	2745	340	7	512	4245	340	6	1500	552.53	361.20	173.99	91.00
Idaa0313	0.5	0.512	500	40	0.74	2745	340	7	512	4245	340	25	1500	545.43	357.12	187.16	95.83
Idaa0314	0.5	0.495	500	40	0.74	2745	340	7	512	4245	340	50	1500	532.11	349.95	201.88	99.93
HORIZONTAL JET SOURCE - ELEVATED AT h=25 mm HIGH FLOW RATE, SHEAR FLOW																	
Idaa0263	0.5	0.513	500	10	1.47	2742	340	25	512	3242	340	25	500	516.25	342.18	105.84	54.30
Idaa0266	0.5	0.523	500	10	1.47	2742	340	25	512	3242	340	6	500	523.39	345.96	103.80	54.29
Idaa0267	0.5	0.496	500	10	1.47	2742	340	25	512	3242	340	50	500	519.23	343.59	116.74	57.90
Idaa0255	0.5	0.511	500	20	1.47	2742	340	25	512	3742	340	25	1000	518.23	343.19	160.79	82.17
Idaa0258	0.5	0.523	500	20	1.47	2742	340	25	512	3742	340	6	1000	513.91	341.00	153.82	80.45
Idaa0259	0.5	0.495	500	20	1.47	2742	340	25	512	3742	340	50	1000	531.31	349.56	175.64	86.94
Idaa0271	0.5	0.511	500	30	1.47	2742	340	25	512	4242	340	25	1500	509.40	338.67	190.64	97.42
Idaa0274	0.5	0.523	500	30	1.47	2742	340	25	512	4242	340	6	1500	501.32	334.41	176.53	92.33
Idaa0275	0.5	0.495	500	30	1.47	2742	340	25	512	4242	340	50	1500	504.36	336.22	197.37	97.70
HORIZONTAL JET SOURCE - ELEVATED AT h=50 mm HIGH FLOW RATE, SHEAR FLOW																	
Idaa0147	0.5	0.496	500	5	1.47	2730	340	50	512	3230	340	50	500	520.34	344.14	104.80	51.98
Idaa0148	0.5	0.511	500	5	1.47	2730	340	50	512	3230	340	25	500	532.28	350.36	100.12	51.16
Idaa0150	0.5	0.52	500	10	1.47	2730	340	50	512	3230	340	6	500	521.62	345.00	106.52	55.39
Idaa0137	0.5	0.495	500	20	1.47	2730	340	50	512	3730	340	50	1000	520.84	344.38	170.49	84.39
Idaa0138	0.5	0.51	500	20	1.47	2730	340	50	512	3730	340	25	1000	522.57	345.39	157.84	80.50
Idaa0140	0.5	0.519	500	20	1.47	2730	340	50	512	3730	340	6	1000	515.41	341.77	142.55	73.98
Idaa0222	0.5	0.494	500	30	1.47	2742	340	50	512	4242	340	50	1500	535.02	351.37	204.12	100.83
Idaa0223	0.5	0.511	500	30	1.47	2742	340	50	512	4242	340	25	1500	529.59	348.99	184.93	94.50
Idaa0225	0.5	0.522	500	30	1.47	2742	340	50	512	4242	340	6	1500	531.70	350.29	172.06	89.82

Table B.4: Horizontal linescan data subset used for analysis. Horizontal jet source in shear flow at $h = 7$ mm, $h = 25$ mm and $h = 50$ mm.

Filename	Linerate (kHz)	mm per pixel	DataTime (s)	Source Conc. (mg/l)	Source Flowrate (ml/s)	Source x (mm)	Source y (mm)	Source z (mm)	z=0 Pixel #	Line x (mm)	Line y (mm)	Line z (mm)	x from source (mm)	centroid (pixels)	centroid (mm)	spread (pixels)	spread (mm)
SMALL GROUND LEVEL VERTICAL JET SOURCE																	
ldac0002	0.5	0.468	500	10	1.47	0	340	0	714	500	340	0	500	35.60	16.66	82.69	38.7
ldac0003	0.5	0.468	500	10	0.73	0	340	0	714	500	340	0	500	34.90	16.33	81.84	38.3
ldac0017	0.5	0.48	500	30	1.47	0	340	0	723	1500	340	0	1500	55.88	26.82	134.17	64.4
ldac0018	0.5	0.48	500	30	0.73	0	340	0	723	1500	340	0	1500	55.84	26.80	133.54	64.1
HORIZONTAL JET SOURCE - GROUND LEVEL AT h=7 mm																	
ldac0021	0.5	0.48	500	30	1.47	0	340	7	723	1500	340	0	1500	58.34	28.00	142.29	68.3
ldac0022	0.5	0.48	500	30	0.73	0	340	7	723	1500	340	0	1500	56.41	27.08	137.29	65.9
ldac0006	0.5	0.468	500	10	1.47	0	340	7	714	500	340	0	500	32.01	14.98	72.01	33.7
ldac0007	0.5	0.468	500	10	0.73	0	340	7	714	500	340	0	500	32.70	15.31	72.86	34.1
HORIZONTAL JET SOURCE - ELEVATED AT h=50 mm																	
ldac0004	0.5	0.468	500	10	0.73	0	340	50	714	500	340	0	500	52.45	24.55	83.97	39.3
ldac0005	0.5	0.468	500	10	1.47	0	340	50	714	500	340	0	500	51.77	24.23	88.03	41.2
ldac0019	0.5	0.48	500	30	0.73	0	340	50	723	1500	340	0	1500	70.76	33.97	129.79	62.3
ldac0020	0.5	0.48	500	30	1.47	0	340	50	723	1500	340	0	1500	67.69	32.49	122.71	58.9

Table B.5: Vertical linescan data set used for analysis. Small ground level vertical jet, horizontal jet source at $h = 7$ mm and $h = 50$ mm.

Filename	Linerate (kHz)	mm per pixel	DataTime (s)	Source Conc. (mg/l)	Source Flowrate (ml/s)	Source x (mm)	Source y (mm)	Source z (mm)	Centre Pixel #	Line x (mm)	Line y (mm)	Line z (mm)	x from source (mm)	centroid (pixels)	centroid (mm)	spread (pixels)	spread (mm)
HORIZONTAL JET IN GRID TURBULENCE																	
Sept10z200	0.5	0.485	500	1.5	1.52	1300	340	200	520	1800	340	200	500	527.60	343.68	31.89	15.46
Sept10z210	0.5	0.479	500	1.5	1.52	1300	340	200	520	1800	340	210	500	528.87	344.25	31.97	15.31
Sept10z220	0.5	0.472	500	1.5	1.52	1300	340	200	520	1800	340	220	500	528.39	343.96	31.90	15.06
Sept12z200b	0.5	0.485	500	4	1.52	1800	340	200	519	2800	340	200	1000	531.56	346.09	56.73	27.51
Sept12z220	0.5	0.468	500	4	1.52	1800	340	200	519	2800	340	220	1000	529.66	344.99	58.04	27.16
Sept12z240	0.5	0.457	500	4	1.52	1800	340	200	519	2800	340	240	1000	528.13	344.17	60.29	27.55
Sept6z200b	0.5	0.490	500	7	1.52	1800	340	200	543	3300	340	200	1500	532.22	334.72	78.21	38.32
Sept9z225	0.5	0.474	500	7	1.52	1800	340	200	541	3300	340	225	1500	530.06	334.81	77.02	36.51
Sept9z250	0.5	0.458	500	7	1.52	1800	340	200	541	3300	340	250	1500	527.73	333.92	81.32	37.24

Table B.6: Horizontal linescan measurement for the horizontal iso-kinetic jet in grid turbulence.

Filename	Linerate (kHz)	mm per pixel	DataTime (s)	Source Conc. (mg/l)	Source Flowrate (ml/s)	Source x (mm)	Source y (mm)	Source z (mm)	Centre Pixel #	Line x (mm)	Line y (mm)	Line z (mm)	x from source (mm)	centroid (pixels)	centroid (mm)	spread (pixels)	spread (mm)
HORIZONTAL JET SOURCE - GROUND LEVEL AT h=7 mm HIGH FLOW RATE, SHEAR FLOW																	
Idaa0183	calibration																
Idaa0185	0.5	0.519	500	10	1.47	2730	340	7	512	3230	340	6	500	542.26	355.71	103.38	53.653
Idaa0186	0.5	0.52	500	10	1.47	2730	340	7	512	3230	340	10	500	538.09	353.56	105.57	54.90
Idaa0187	0.5	0.518	500	10	1.47	2730	340	7	512	3230	340	15	500	541.16	355.11	103.39	53.56
Idaa0188	0.5	0.509	500	10	1.47	2730	340	7	512	3230	340	25	500	542.95	355.75	110.18	56.083
Idaa0189	0.5	0.494	500	10	1.47	2730	340	7	512	3230	340	50	500	541.52	354.58	123.20	60.86
Idaa0190	0.5	0.52	500	10	1.47	2730	340	7	512	3230	340	6	500	540.81	354.98	105.52	54.869
Idaa0171	calibration																
Idaa0172	0.5	0.494	500	20	1.47	2730	340	7	512	3730	340	50	1000	567.18	367.26	175.71	86.80
Idaa0173	0.5	0.511	500	20	1.47	2730	340	7	512	3730	340	25	1000	562.42	365.76	162.81	83.20
Idaa0174	0.5	0.52	500	20	1.47	2730	340	7	512	3730	340	10	1000	561.36	365.67	147.01	76.45
Idaa0175	0.5	0.52	500	20	1.47	2730	340	7	512	3730	340	6	1000	545.17	357.25	151.61	78.84
Idaa0231	calibration																
Idaa0232	0.5	0.494	500	30	1.47	2742	340	7	512	4242	340	50	1500	561.71	364.56	192.95	95.32
Idaa0233	0.5	0.511	500	30	1.47	2742	340	7	512	4242	340	25	1500	540.01	354.31	180.56	92.27
Idaa0234	0.5	0.517	500	30	1.47	2742	340	7	512	4242	340	15	1500	539.70	354.32	176.03	91.01
Idaa0235	0.5	0.52	500	30	1.47	2742	340	7	512	4242	340	10	1500	542.20	355.70	179.15	93.16
Idaa0236	0.5	0.522	500	30	1.47	2742	340	7	512	4242	340	6	1500	543.67	356.53	173.74	90.69
Idaa0237	0.5	0.494	500	30	1.47	2742	340	7	512	4242	340	50	1500	537.28	352.49	198.53	98.07

Table B.7: Horizontal linescan measurement for the large ground level source in shear flow at the high flow rate.

Filename	Linerate (kHz)	mm per pixel	DataTime (s)	Source Conc. (mg/l)	Source Flowrate (ml/s)	Source x (mm)	Source y (mm)	Source z (mm)	Centre Pixel #	Line x (mm)	Line y (mm)	Line z (mm)	x from source (mm)	centroid (pixels)	centroid (mm)	spread (pixels)	spread (mm)
SMALL GROUND LEVEL VERTICAL JET SOURCE - HIGH FLOW RATE, SHEAR FLOW																	
Idaa0294	calibration																
Idaa0295	0.5	0.511	500	10	1.47	2745	340	0	512	3245	340	25	500	520.35	344.27	116.59	59.58
Idaa0296	0.5	0.517	500	10	1.47	2745	340	0	512	3245	340	15	500	518.23	343.22	113.94	58.91
Idaa0297	0.5	0.519	500	10	1.47	2745	340	0	512	3245	340	10	500	508.27	338.06	110.24	57.21
Idaa0298	0.5	0.523	500	10	1.47	2745	340	0	512	3245	340	6	500	521.29	344.86	109.93	57.49
Idaa0299	0.5	0.494	500	10	1.47	2745	340	0	512	3245	340	50	500	501.08	334.61	122.45	60.49
Idaa0300	0.5	0.478	500	10	1.47	2745	340	0	512	3245	340	75	500	505.25	336.77	138.81	66.35
Idaa0301	0.5	0.511	500	10	1.47	2745	340	0	512	3245	340	25	500	516.56	342.33	120.94	61.80
Idaa0278	calibration																
Idaa0279	0.5	0.512	500	20	1.47	2745	340	0	512	3745	340	25	1000	498.90	333.29	162.52	83.21
Idaa0280	0.5	0.519	500	20	1.47	2745	340	0	512	3745	340	15	1000	509.77	338.84	160.96	83.54
Idaa0281	0.5	0.521	500	20	1.47	2745	340	0	512	3745	340	10	1000	503.54	335.59	151.01	78.68
Idaa0282	0.5	0.523	500	20	1.47	2745	340	0	512	3745	340	6	1000	491.52	329.29	154.32	80.71
Idaa0283	0.5	0.495	500	20	1.47	2745	340	0	512	3745	340	50	1000	506.61	337.33	174.69	86.47
Idaa0284	0.5	0.48	500	20	1.47	2745	340	0	512	3745	340	75	1000	503.92	336.12	190.32	91.36
Idaa0285	0.5	0.511	500	20	1.47	2745	340	0	512	3745	340	75	1000	499.74	333.74	167.74	85.72
Idaa0286	calibration																
Idaa0287	0.5	0.513	500	20	1.47	2745	340	0	512	3745	340	25	1000	504.18	335.99	163.72	83.99
Idaa0288	0.5	0.519	500	20	1.47	2745	340	0	512	3745	340	15	1000	501.61	334.61	159.04	82.54
Idaa0289	0.5	0.52	500	20	1.47	2745	340	0	512	3745	340	10	1000	491.00	329.08	150.63	78.33
Idaa0290	0.5	0.523	500	20	1.47	2745	340	0	512	3745	340	6	1000	483.78	325.24	154.86	80.99
Idaa0291	0.5	0.496	500	20	1.47	2745	340	0	512	3745	340	50	1000	492.28	330.22	176.78	87.68
Idaa0292	0.5	0.479	500	20	1.47	2745	340	0	512	3745	340	75	1000	480.40	324.86	186.42	89.30
Idaa0293	0.5	0.512	500	20	1.47	2745	340	0	512	3745	340	25	1000	497.75	332.71	165.44	84.71
Idaa0302	calibration																
Idaa0303	0.5	0.511	500	30	1.47	2745	340	0	512	4245	340	25	1500	522.78	345.51	189.02	96.59
Idaa0304	0.5	0.517	500	30	1.47	2745	340	0	512	4245	340	15	1500	516.25	342.20	183.57	94.91
Idaa0305	0.5	0.519	500	30	1.47	2745	340	0	512	4245	340	10	1500	503.49	335.58	176.24	91.47
Idaa0306	0.5	0.523	500	30	1.47	2745	340	0	512	4245	340	6	1500	491.76	329.41	181.87	95.12
Idaa0307	0.5	0.494	500	30	1.47	2745	340	0	512	4245	340	50	1500	482.95	325.65	197.16	97.39
Idaa0308	0.5	0.479	500	30	1.47	2745	340	0	512	4245	340	75	1500	486.85	327.95	219.43	105.11
Idaa0309	0.5	0.511	500	30	1.47	2745	340	0	512	4245	340	25	1500	507.76	337.83	185.81	94.95

Table B.8: Horizontal linescan measurement for the small ground level vertical jet source in shear flow at the high flow rate.

Filename	Linerate (kHz)	mm per pixel	DataTime (s)	Source Conc. (mg/l)	Source Flowrate (ml/s)	Source x (mm)	Source y (mm)	Source z (mm)	Centre Pixel #	Line x (mm)	Line y (mm)	Line z (mm)	x from source (mm)	centroid (pixels)	centroid (mm)	spread (pixels)	spread (mm)
SMALL GROUND LEVEL VERTICAL JET SOURCE - HIGH FLOW RATE, SHEAR FLOW																	
Idaa0294	calibration																
Idaa0295	0.5	0.511	500	10	1.47	2745	340	0	512	3245	340	25	500	520.35	344.27	116.59	59.58
Idaa0296	0.5	0.517	500	10	1.47	2745	340	0	512	3245	340	15	500	518.23	343.22	113.94	58.91
Idaa0297	0.5	0.519	500	10	1.47	2745	340	0	512	3245	340	10	500	508.27	338.06	110.24	57.21
Idaa0298	0.5	0.523	500	10	1.47	2745	340	0	512	3245	340	6	500	521.29	344.86	109.93	57.49
Idaa0299	0.5	0.494	500	10	1.47	2745	340	0	512	3245	340	50	500	501.08	334.61	122.45	60.49
Idaa0300	0.5	0.478	500	10	1.47	2745	340	0	512	3245	340	75	500	505.25	336.77	138.81	66.35
Idaa0301	0.5	0.511	500	10	1.47	2745	340	0	512	3245	340	25	500	516.56	342.33	120.94	61.80
Idaa0278	calibration																
Idaa0279	0.5	0.512	500	20	1.47	2745	340	0	512	3745	340	25	1000	498.90	333.29	162.52	83.21
Idaa0280	0.5	0.519	500	20	1.47	2745	340	0	512	3745	340	15	1000	509.77	338.84	160.96	83.54
Idaa0281	0.5	0.521	500	20	1.47	2745	340	0	512	3745	340	10	1000	503.54	335.59	151.01	78.68
Idaa0282	0.5	0.523	500	20	1.47	2745	340	0	512	3745	340	6	1000	491.52	329.29	154.32	80.71
Idaa0283	0.5	0.495	500	20	1.47	2745	340	0	512	3745	340	50	1000	506.61	337.33	174.69	86.47
Idaa0284	0.5	0.48	500	20	1.47	2745	340	0	512	3745	340	75	1000	503.92	336.12	190.32	91.36
Idaa0285	0.5	0.511	500	20	1.47	2745	340	0	512	3745	340	75	1000	499.74	333.74	167.74	85.72
Idaa0286	calibration																
Idaa0287	0.5	0.513	500	20	1.47	2745	340	0	512	3745	340	25	1000	504.18	335.99	163.72	83.99
Idaa0288	0.5	0.519	500	20	1.47	2745	340	0	512	3745	340	15	1000	501.61	334.61	159.04	82.54
Idaa0289	0.5	0.52	500	20	1.47	2745	340	0	512	3745	340	10	1000	491.00	329.08	150.63	78.33
Idaa0290	0.5	0.523	500	20	1.47	2745	340	0	512	3745	340	6	1000	483.78	325.24	154.86	80.99
Idaa0291	0.5	0.496	500	20	1.47	2745	340	0	512	3745	340	50	1000	492.28	330.22	176.78	87.68
Idaa0292	0.5	0.479	500	20	1.47	2745	340	0	512	3745	340	75	1000	480.40	324.86	186.42	89.30
Idaa0293	0.5	0.512	500	20	1.47	2745	340	0	512	3745	340	25	1000	497.75	332.71	165.44	84.71
Idaa0302	calibration																
Idaa0303	0.5	0.511	500	30	1.47	2745	340	0	512	4245	340	25	1500	522.78	345.51	189.02	96.59
Idaa0304	0.5	0.517	500	30	1.47	2745	340	0	512	4245	340	15	1500	516.25	342.20	183.57	94.91
Idaa0305	0.5	0.519	500	30	1.47	2745	340	0	512	4245	340	10	1500	503.49	335.58	176.24	91.47
Idaa0306	0.5	0.523	500	30	1.47	2745	340	0	512	4245	340	6	1500	491.76	329.41	181.87	95.12
Idaa0307	0.5	0.494	500	30	1.47	2745	340	0	512	4245	340	50	1500	482.95	325.65	197.16	97.39
Idaa0308	0.5	0.479	500	30	1.47	2745	340	0	512	4245	340	75	1500	486.85	327.95	219.43	105.11
Idaa0309	0.5	0.511	500	30	1.47	2745	340	0	512	4245	340	25	1500	507.76	337.83	185.81	94.95

Table B.9: Horizontal linescan measurement for the small ground level vertical jet source in shear flow at the low flow rate.

Filename	Linerate (kHz)	mm per pixel	DataTime (s)	Source Conc. (mg/l)	Source Flowrate (ml/s)	Source x (mm)	Source y (mm)	Source z (mm)	Centre Pixel #	Line x (mm)	Line y (mm)	Line z (mm)	x from source (mm)	centroid (pixels)	centroid (mm)	spread (pixels)	spread (mm)
HORIZONTAL JET SOURCE - GROUND LEVEL AT h=7 mm HIGH FLOW RATE, SHEAR FLOW																	
ldaa0183	calibration																
ldaa0185	0.5	0.519	500	10	1.47	2730	340	7	512	3230	340	6	500	542.26	355.71	103.38	53.653
ldaa0186	0.5	0.52	500	10	1.47	2730	340	7	512	3230	340	10	500	538.09	353.56	105.57	54.90
ldaa0187	0.5	0.518	500	10	1.47	2730	340	7	512	3230	340	15	500	541.16	355.11	103.39	53.56
ldaa0188	0.5	0.509	500	10	1.47	2730	340	7	512	3230	340	25	500	542.95	355.75	110.18	56.083
ldaa0189	0.5	0.494	500	10	1.47	2730	340	7	512	3230	340	50	500	541.52	354.58	123.20	60.86
ldaa0190	0.5	0.52	500	10	1.47	2730	340	7	512	3230	340	6	500	540.81	354.98	105.52	54.869
ldaa0171	calibration																
ldaa0172	0.5	0.494	500	20	1.47	2730	340	7	512	3730	340	50	1000	567.18	367.28	175.71	86.80
ldaa0173	0.5	0.511	500	20	1.47	2730	340	7	512	3730	340	25	1000	562.42	365.76	162.81	83.20
ldaa0174	0.5	0.52	500	20	1.47	2730	340	7	512	3730	340	10	1000	561.36	365.67	147.01	76.45
ldaa0175	0.5	0.52	500	20	1.47	2730	340	7	512	3730	340	6	1000	545.17	357.25	151.61	78.84
ldaa0231	calibration																
ldaa0232	0.5	0.494	500	30	1.47	2742	340	7	512	4242	340	50	1500	561.71	364.56	192.95	95.32
ldaa0233	0.5	0.511	500	30	1.47	2742	340	7	512	4242	340	25	1500	540.01	354.31	180.56	92.27
ldaa0234	0.5	0.517	500	30	1.47	2742	340	7	512	4242	340	15	1500	539.70	354.32	176.03	91.01
ldaa0235	0.5	0.52	500	30	1.47	2742	340	7	512	4242	340	10	1500	542.20	355.70	179.15	93.16
ldaa0236	0.5	0.522	500	30	1.47	2742	340	7	512	4242	340	6	1500	543.67	356.53	173.74	90.69
ldaa0237	0.5	0.494	500	30	1.47	2742	340	7	512	4242	340	50	1500	537.28	352.49	198.53	98.07

Table B.10: Horizontal linescan measurement for the horizontal jet source $h = 7$ mm in shear flow at the high flow rate.

Filename	Linerate (kHz)	mm per pixel	DataTime (s)	Source Conc. (mg/l)	Source Flowrate (ml/s)	Source x (mm)	Source y (mm)	Source z (mm)	Centre Pixel #	Line x (mm)	Line y (mm)	Line z (mm)	x from source (mm)	centroid (pixels)	centroid (mm)	spread (pixels)	spread (mm)
HORIZONTAL JET SOURCE - GROUND LEVEL AT h=7 mm HIGH FLOW RATE, SHEAR FLOW																	
ldaa0183	calibration																
ldaa0185	0.5	0.519	500	10	1.47	2730	340	7	512	3230	340	6	500	542.26	355.71	103.38	53.653
ldaa0186	0.5	0.52	500	10	1.47	2730	340	7	512	3230	340	10	500	538.09	353.56	105.57	54.90
ldaa0187	0.5	0.518	500	10	1.47	2730	340	7	512	3230	340	15	500	541.16	355.11	103.39	53.56
ldaa0188	0.5	0.509	500	10	1.47	2730	340	7	512	3230	340	25	500	542.95	355.75	110.18	56.083
ldaa0189	0.5	0.494	500	10	1.47	2730	340	7	512	3230	340	50	500	541.52	354.58	123.20	60.86
ldaa0190	0.5	0.52	500	10	1.47	2730	340	7	512	3230	340	6	500	540.81	354.98	105.52	54.869
ldaa0171	calibration																
ldaa0172	0.5	0.494	500	20	1.47	2730	340	7	512	3730	340	50	1000	567.18	367.28	175.71	86.80
ldaa0173	0.5	0.511	500	20	1.47	2730	340	7	512	3730	340	25	1000	562.42	365.76	162.81	83.20
ldaa0174	0.5	0.52	500	20	1.47	2730	340	7	512	3730	340	10	1000	561.36	365.67	147.01	76.45
ldaa0175	0.5	0.52	500	20	1.47	2730	340	7	512	3730	340	6	1000	545.17	357.25	151.61	78.84
ldaa0231	calibration																
ldaa0232	0.5	0.494	500	30	1.47	2742	340	7	512	4242	340	50	1500	561.71	364.56	192.95	95.32
ldaa0233	0.5	0.511	500	30	1.47	2742	340	7	512	4242	340	25	1500	540.01	354.31	180.56	92.27
ldaa0234	0.5	0.517	500	30	1.47	2742	340	7	512	4242	340	15	1500	539.70	354.32	176.03	91.01
ldaa0235	0.5	0.52	500	30	1.47	2742	340	7	512	4242	340	10	1500	542.20	355.70	179.15	93.16
ldaa0236	0.5	0.522	500	30	1.47	2742	340	7	512	4242	340	6	1500	543.67	356.53	173.74	90.69
ldaa0237	0.5	0.494	500	30	1.47	2742	340	7	512	4242	340	50	1500	537.28	352.49	198.53	98.07

Table B.11: Horizontal linescan measurement for the horizontal jet source $h = 7$ mm in shear flow at the low flow rate.

Filename	Linerate (kHz)	mm per pixel	DataTime (s)	Source Conc. (mg/l)	Source Flowrate (ml/s)	Source x (mm)	Source y (mm)	Source z (mm)	Centre Pixel #	Line x (mm)	Line y (mm)	Line z (mm)	x from source (mm)	centroid (pixels)	centroid (mm)	spread (pixels)	spread (mm)
HORIZONTAL JET SOURCE - GROUND LEVEL AT h=7 mm HIGH FLOW RATE, SHEAR FLOW																	
ldaa0183	calibration																
ldaa0185	0.5	0.519	500	10	1.47	2730	340	7	512	3230	340	6	500	542.26	355.71	103.38	53.653
ldaa0186	0.5	0.52	500	10	1.47	2730	340	7	512	3230	340	10	500	538.09	353.56	105.57	54.90
ldaa0187	0.5	0.518	500	10	1.47	2730	340	7	512	3230	340	15	500	541.16	355.11	103.39	53.56
ldaa0188	0.5	0.509	500	10	1.47	2730	340	7	512	3230	340	25	500	542.95	355.75	110.18	56.083
ldaa0189	0.5	0.494	500	10	1.47	2730	340	7	512	3230	340	50	500	541.52	354.58	123.20	60.86
ldaa0190	0.5	0.52	500	10	1.47	2730	340	7	512	3230	340	6	500	540.81	354.98	105.52	54.869
ldaa0171	calibration																
ldaa0172	0.5	0.494	500	20	1.47	2730	340	7	512	3730	340	50	1000	567.18	367.26	175.71	86.80
ldaa0173	0.5	0.511	500	20	1.47	2730	340	7	512	3730	340	25	1000	562.42	365.76	162.81	83.20
ldaa0174	0.5	0.52	500	20	1.47	2730	340	7	512	3730	340	10	1000	561.36	365.67	147.01	76.45
ldaa0175	0.5	0.52	500	20	1.47	2730	340	7	512	3730	340	6	1000	545.17	357.25	151.61	78.84
ldaa0231	calibration																
ldaa0232	0.5	0.494	500	30	1.47	2742	340	7	512	4242	340	50	1500	561.71	364.56	192.95	95.32
ldaa0233	0.5	0.511	500	30	1.47	2742	340	7	512	4242	340	25	1500	540.01	354.31	180.56	92.27
ldaa0234	0.5	0.517	500	30	1.47	2742	340	7	512	4242	340	15	1500	539.70	354.32	176.03	91.01
ldaa0235	0.5	0.52	500	30	1.47	2742	340	7	512	4242	340	10	1500	542.20	355.70	179.15	93.16
ldaa0236	0.5	0.522	500	30	1.47	2742	340	7	512	4242	340	6	1500	543.67	356.53	173.74	90.69
ldaa0237	0.5	0.494	500	30	1.47	2742	340	7	512	4242	340	50	1500	537.28	352.49	198.53	98.07

Table B.12: Horizontal linescan measurement for the horizontal elevated source $h =$ 25 mm in shear flow at the high flow rate.

Filename	Linerate (kHz)	mm per pixel	DataTime (s)	Source Conc. (mg/l)	Source Flowrate (ml/s)	Source x (mm)	Source y (mm)	Source z (mm)	Centre Pixel #	Line x (mm)	Line y (mm)	Line z (mm)	x from source (mm)	centroid (pixels)	centroid (mm)	spread (pixels)	spread (mm)
HORIZONTAL JET SOURCE - ELEVATED AT h=50 mm HIGH FLOW RATE, SHEAR FLOW																	
ldaa0146	calibration																
ldaa0147	0.5	0.496	500	5	1.47	2730	340	50	512	3230	340	50	500	520.34	344.14	104.80	51.98
ldaa0148	0.5	0.511	500	5	1.47	2730	340	50	512	3230	340	25	500	532.28	350.36	100.12	51.16
ldaa0149	0.5	0.52	500	10	1.47	2730	340	50	512	3230	340	10	500	522.96	345.70	98.46	51.20
ldaa0150	0.5	0.52	500	10	1.47	2730	340	50	512	3230	340	6	500	521.62	345.00	106.52	55.39
ldaa0151	0.5	0.52	500	10	1.47	2730	340	50	512	3230	340	8	500	516.00	342.08	98.55	51.25
ldaa0152	0.5	0.518	500	5	1.47	2730	340	50	512	3230	340	15	500	519.00	343.63	98.77	51.17
ldaa0153	0.5	0.495	500	5	1.47	2730	340	50	512	3230	340	50	500	518.14	343.04	106.17	52.55
ldaa0154	0.5	0.478	500	5	1.47	2730	340	50	512	3230	340	75	500	525.72	346.56	115.41	55.17
ldaa0155	0.5	0.464	500	5	1.47	2730	340	50	512	3230	340	100	500	525.16	346.11	123.01	57.08
ldaa0136	calibration																
ldaa0137	0.5	0.495	500	20	1.47	2730	340	50	512	3730	340	50	1000	520.84	344.38	170.49	84.39
ldaa0138	0.5	0.51	500	20	1.47	2730	340	50	512	3730	340	25	1000	522.57	345.39	157.84	80.50
ldaa0139	0.5	0.519	500	20	1.47	2730	340	50	512	3730	340	10	1000	523.20	345.82	152.56	79.18
ldaa0140	0.5	0.519	500	20	1.47	2730	340	50	512	3730	340	6	1000	515.41	341.77	142.55	73.98
ldaa0141	0.5	0.519	500	20	1.47	2730	340	50	512	3730	340	8	1000	521.16	344.75	151.54	78.65
ldaa0142	0.5	0.517	500	20	1.47	2730	340	50	512	3730	340	15	1000	517.80	343.00	153.91	79.57
ldaa0143	0.5	0.494	500	20	1.47	2730	340	50	512	3730	340	50	1000	515.98	341.97	175.22	86.56
ldaa0144	0.5	0.479	500	20	1.47	2730	340	50	512	3730	340	75	1000	515.16	341.51	184.81	88.52
ldaa0145	0.5	0.462	500	20	1.47	2730	340	50	512	3730	340	100	1000	523.78	345.44	196.96	91.00
ldaa0221	calibration																
ldaa0222	0.5	0.494	500	30	1.47	2742	340	50	512	4242	340	50	1500	535.02	351.37	204.12	100.83
ldaa0223	0.5	0.511	500	30	1.47	2742	340	50	512	4242	340	25	1500	529.59	348.99	184.93	94.50
ldaa0224	0.5	0.52	500	30	1.47	2742	340	50	512	4242	340	10	1500	523.18	345.81	174.47	90.72
ldaa0225	0.5	0.522	500	30	1.47	2742	340	50	512	4242	340	6	1500	531.70	350.29	172.06	89.82
ldaa0226	0.5	0.517	500	30	1.47	2742	340	50	512	4242	340	15	1500	522.84	345.61	189.65	98.05
ldaa0227	0.5	0.494	500	30	1.47	2742	340	50	512	4242	340	50	1500	517.56	342.75	203.68	100.62
ldaa0228	0.5	0.477	500	30	1.47	2742	340	50	512	4242	340	75	1500	518.14	342.93	215.26	102.68
ldaa0229	0.5	0.458	500	30	1.47	2742	340	50	512	4242	340	100	1500	518.75	343.09	223.07	102.16
ldaa0230	0.5	0.494	500	30	1.47	2742	340	50	512	4242	340	50	1500	522.99	345.43	198.95	98.28

Table B.13: Horizontal linescan measurement for the horizontal iso-kinetic elevated source $h = 50$ mm in shear flow at the high flow rate.

Appendix C

Meander Parameters M_{spread} and $M_{\text{intensity}}$

Chapter 2 discusses the differences between the meander parameter M_{spread} based on the plume spread and the pseudo-meander parameter $M_{\text{intensity}}$ based on the concentration fluctuation intensity. Selected examples of the comparison between M_{spread} and $M_{\text{intensity}}$ as a function of averaging time t_{avg} were given in Section 2.4.2 and additional examples are presented in this Appendix. Chapter 2 has additional discussion of averaging time definitions are how to calculate time averaged plume properties by following the centroid of the plume.

C.1 Meander Definitions

The meandering plume model first proposed by Gifford (1959) leads to closed form solutions for concentration fluctuation parameters such as those given in Wilson (1995). Gifford's idea was to model a dispersing plume as a narrow instantaneous Gaussian plume with spread $\sigma_{y,i}$ and no internal concentration fluctuations, which is meandered by larger scale eddies in the flow to produce a wider time-averaged Gaussian plume. If we consider just one-dimensional meandering, in the y-direction, then the total plume spread, σ_y is the sum of the spread of the instantaneous plume, $\sigma_{y,i}$ and the spread caused by the meandering of this instantaneous plume, $\sigma_{y,M}$

$$\sigma_y^2 = \sigma_{y,i}^2 + \sigma_{y,M}^2 \tag{C.1}$$

The meander parameter M_{spread} is defined as the ratio of the squares of the meandering spread to the instantaneous spread.

$$M_{\text{spread}} = \frac{\sigma_{y,M}^2}{\sigma_{y,i}^2} \tag{C.2}$$

The subscript "spread" is necessary because there is another meander parameter, $M_{\text{intensity}}$ which is the meander required to produce the correct concentration fluctuations in the plume. Wilson (1995) implicitly included the internal instantaneous fluctuations by defining a pseudo-meander $M_{\text{intensity}}$ to account for the increased fluctuation intensity. Instead of measuring meandering directly using the ratio of spreads as in Equation (2.12), the pseudo-meander $M_{\text{intensity}}$ is the meander necessary to produce the fluctuation level that is observed. This is discussed in Wilson (1995) and Bara et al. (1992) working from the Sawford and Stapountzis (1986) meandering plume formulation for two dimensional meandering and the result is

$$M_{\text{intensity}} = i_h^2 + (i_h^4 + i_h^2)^{0.5} \tag{C.3}$$

where i_h is the fluctuation intensity on the plume horizontal and vertical centreline.

C.2 Measuring Plume Spreads and Meander

The linescan LIF measurement technique allows the one-dimensional, y-direction, meandering to be investigated because the entire cross-wind extent of the plume is sampled at 1024 points simultaneously at a high enough data rate (500 samples per second) that $\sigma_{y,i}$ can be measured directly. The high frequency data can be time averaged to determine σ_y, and the centroid movement can be tracked to measure $\sigma_{y,M}$ and thus M_{spread} calculated using Equation (C.2). The high frequency measurements also allow pseudo-meander $M_{\text{intensity}}$ to be determined by measuring the concentration fluctuation intensity i_h on the time averaged plume centreline at the effective source height h, which includes any jet momentum rise, and applying Equation (C.3).

The plume spread σ_y can be calculated directly from the data by taking the second moment of the concentration distribution about the centroid $\overline{y}$.

$$\overline{y} = \frac{\sum_{j=1}^{N} y_j c_j}{\sum_{j=1}^{N} c_j} \tag{C.4}$$

and

$$\sigma_y^2 = \frac{\sum_{j=1}^{N} (y_j - \overline{y})^2 c_j}{\sum_{j=1}^{N} c_j} \tag{C.5}$$

where j is the pixel number from 1 to $N = 1024$, c_j is the concentration measured at the pixel j, and σ_y is the cross-stream plume spread. It is assumed that the sample rate of 500 Hz is fast enough to be considered an instantaneous sample for these experiments. Time averaging is done by taking block averages of length t_{avg} from the plume data set, computing the average centroid position $\overline{y}$ and the average spread σ_y for that block of data.

There are two ways to measure the meander using the linescan data.

1. measure the time averaged plume spreads directly. With the definition of M_{spread} from Equation (C.2) and meandering spread $\sigma_{y,m}$ from Equation (C.1)

$$M_{\text{spread}} = \left(\frac{\sigma_{y,t_{\text{avg}}}}{\sigma_{y,i}}\right)^2 - 1 \tag{C.6}$$

2. directly measure $\sigma_{y,m}$, which is the variance of the position of the centroid of the plume over the averaging time. The instantaneous plume spread $\sigma_{y,i}$ is calculated as in Equation (C.5) and the result plugged into Equation (C.2).

In general, higher order moments, like plume spreads, are more difficult to measure accurately than lower order moments, like centroids. In these experiments, the most reliable method for measuring meander was to use method 2 with the instantaneous plume spread $\sigma_{y,i}$ the variance in the position of the centroid. Both calculation methods gave similar results, but using time averaged plume spreads led to more variation between data points due to the sensitivity of equation (C.6) to small changes in $\sigma_{y,t_{\text{avg}}}$.

C.3 Ensemble Averaging

There are two methods for ensemble averaging plume statistics:

1. find the ensemble average concentration distribution by taking an ensemble of samples of length t_{avg} and calculate the statistics of this ensemble average plume
2. calculate the statistics of individual t_{avg} samples and then ensemble average the results.

In a stationary ergodic system where centroid position, plume spread and concentration are uncorrelated, both methods should give the same answer. In the shear flow measurements there was very little difference between the two methods of ensemble averaging, but the grid turbulence measurements showed an order of magnitude difference between the two averaging methods.

The important difference between the flows is that the vertical meandering is very limited in shear flow cases, but not in grid turbulence. In grid turbulence, vertical and horizontal meandering are equal. This vertical meandering problem became evident because the one dimensional spread of an ensemble average concentration distribution in grid turbulence is actually equivalent to a weighted ensemble average spread of instantaneous plumes. The weighting factor is the mass (or integrated concentration) of the dye tracer material in each one-dimensional line of concentration that was measured. The vertical position of the plume in grid turbulence is highly variable, so the mass of material across the measurement line can be used as a surrogate measure of the position of the vertical plume centroid to weight the horizontal plume statistics. An ensemble average concentration distribution automatically includes this weighting factor since small total masses will contribute less to the ensemble average than larger masses.

C.4 Plots of M_{spread} versus $M_{\text{intensity}}$

Figures C.1 through C.8 compare the M_{spread} and $M_{\text{intensity}}$ values from the water channel data set. The pseudo-meander $M_{\text{intensity}}$ is typically an order of magnitude or more greater than the real meander of the plume centroid M_{spread}. This indicates that real plumes have a great deal of internal concentration fluctuation and large scale meander contributes only a small part to the overall concentration fluctuation level.

References

Bara, B. M., Wilson, D. J., and Zelt, B. W. (1992), Concentration Fluctuation Profiles from a Water Channel Simulation of a Ground-Level Release, *Atmospheric Environment*, 26A(6):1053–1062.

Gifford, F. (1959), Statistical Properties of a Fluctuating Plume Dispersion Model, In *Proceedings of Symposium on Atmospheric Diffusion and Air Pollution*, pages 117–137, New York. Academic Press.

Sawford, B. L. and Stapountzis, H. (1986), Concentration Fluctuations According to Fluctuating Plume Models in One and Two Dimensions, *Boundary-Layer Meteorology*, 37:89–105.

Wilson, D. J. (1995), *Concentration Fluctuations and Averaging Time in Vapor Clouds*, Center for Chemical Process Safety of the American Institute of Chemical Engineers, New York, NY.

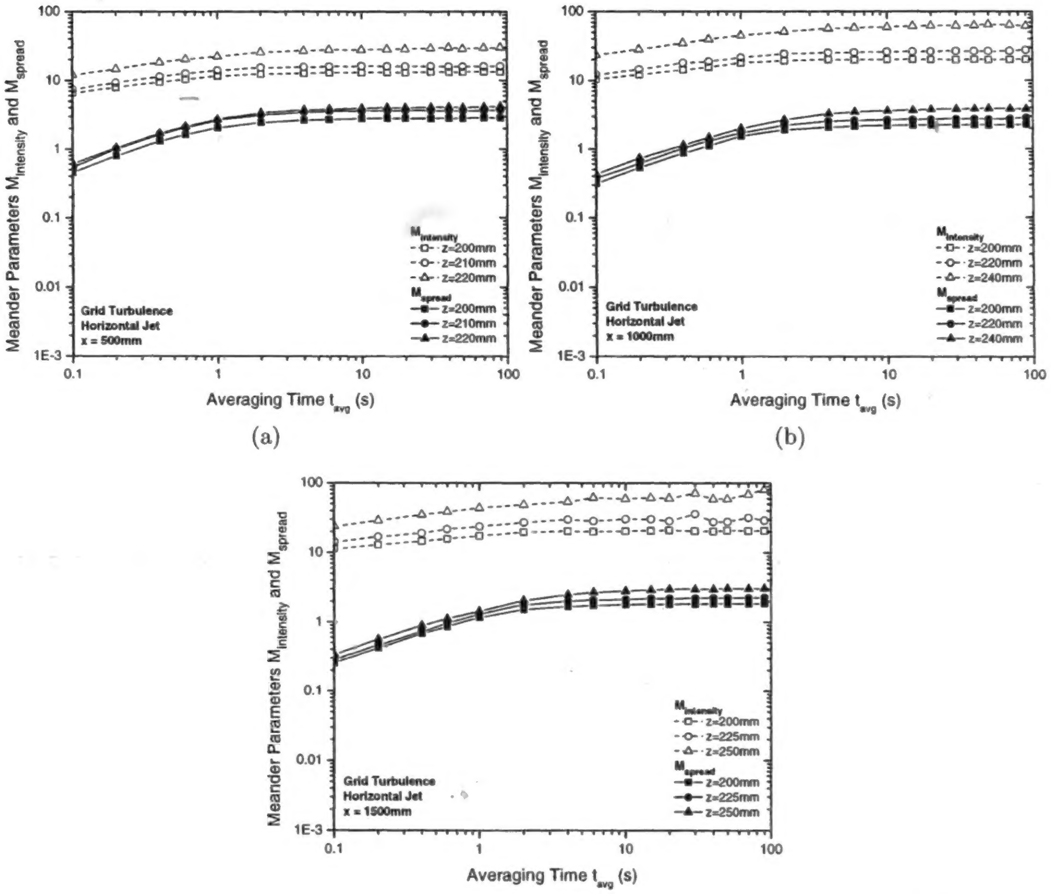

(a) (b)

(c)

Figure C.1: Meander parameter $M_{\text{intensity}}$ and M_{spread} values for the iso-kinetic horizontal jet source in grid turbulence (a) $x = 500$ mm and $z = 200, 210, 220$ mm (b) $x = 1000$ mm and $z = 200, 220, 240$ mm (c) $x = 1500$ mm and $z = 200, 225, 250$ mm

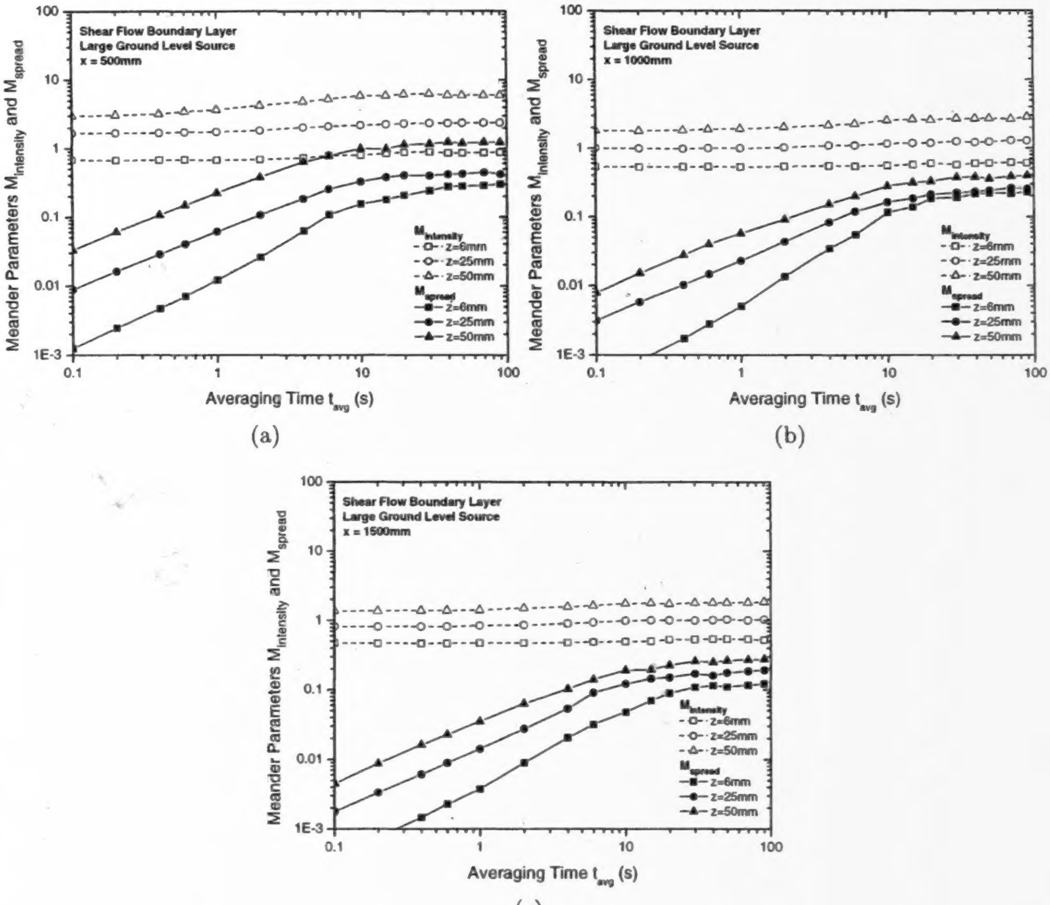

(a) (b)

(c)

Figure C.2: Meander parameter $M_{\text{intensity}}$ and M_{spread} values for the large ground level source at a flow rate $Q = 1.47$ ml/s and $z = 6,25$, and 50 mm above the ground for (a) $x = 500$ mm (b) $x = 1000$ mm (c) $x = 1500$ mm

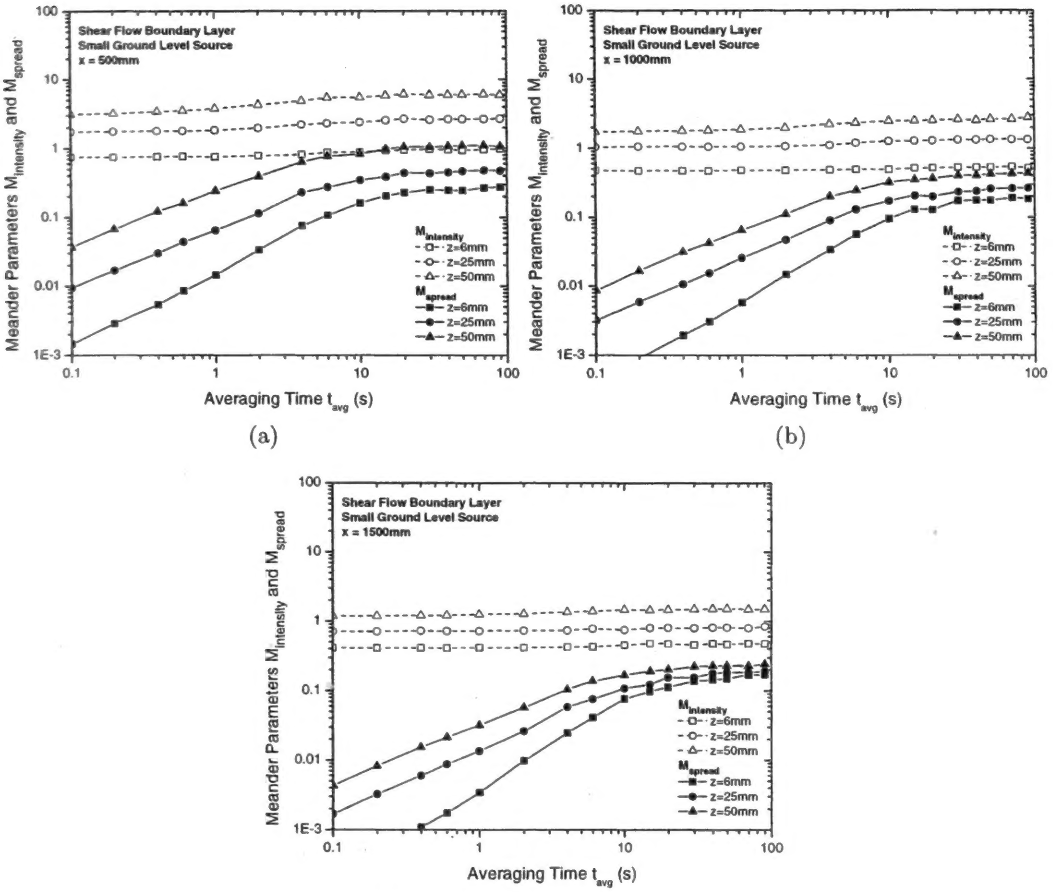

(a) (b)

(c)

Figure C.3: Meander parameter $M_{\text{intensity}}$ and M_{spread} values for the small ground level vertical jet source at a flow rate $Q = 1.47$ ml/s and $z = 6{,}25$, and 50 mm above the ground for (a) $x = 500$ mm (b) $x = 1000$ mm (c) $x = 1500$ mm

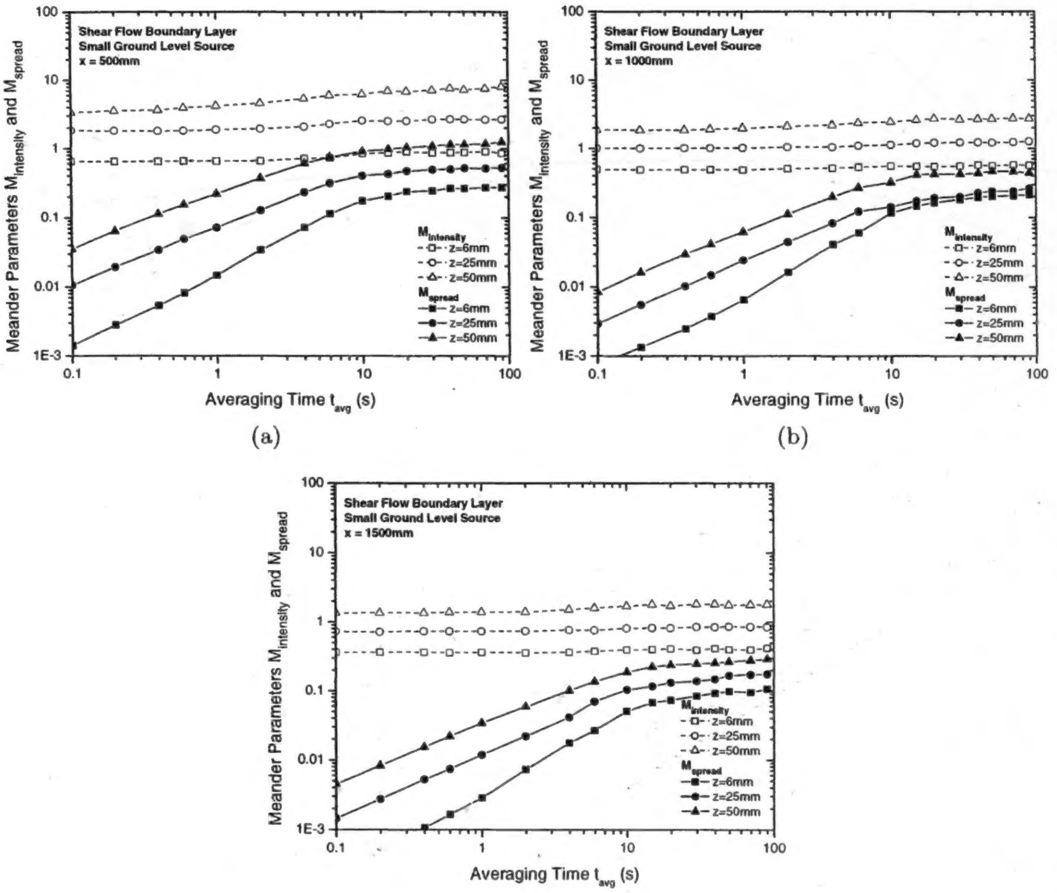

(a) (b) (c)

Figure C.4: Meander parameter $M_{\text{intensity}}$ and M_{spread} values for the small ground level vertical jet source at a flow rate $Q = 0.73$ ml/s and $z = 6{,}25$, and 50 mm above the ground for (a) $x = 500$ mm (b) $x = 1000$ mm (c) $x = 1500$ mm

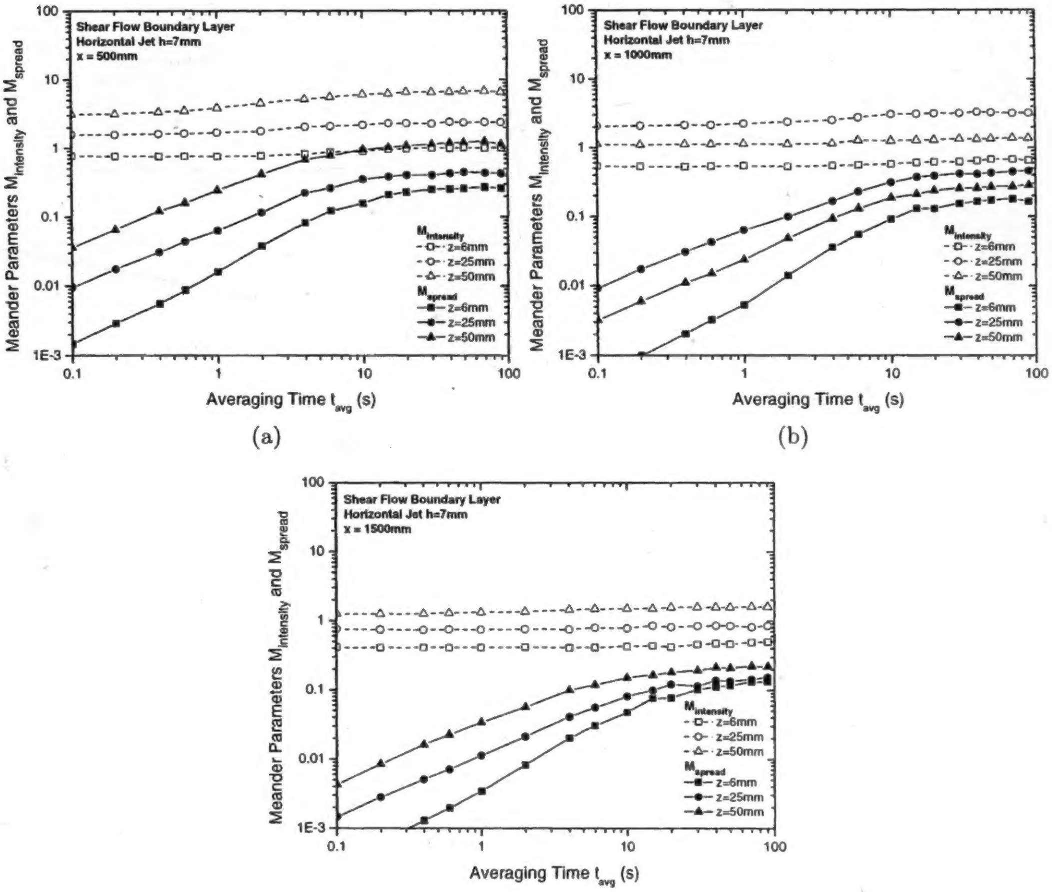

(a)

(b)

(c)

Figure C.5: Meander parameter $M_{\text{intensity}}$ and M_{spread} values for the horizontal jet source at $h = 7$ mm at a flow rate $Q = 1.47$ ml/s and measured at $z = 6{,}25$, and 50 mm above the ground for (a) $x = 500$ mm (b) $x = 1000$ mm (c) $x = 1500$ mm

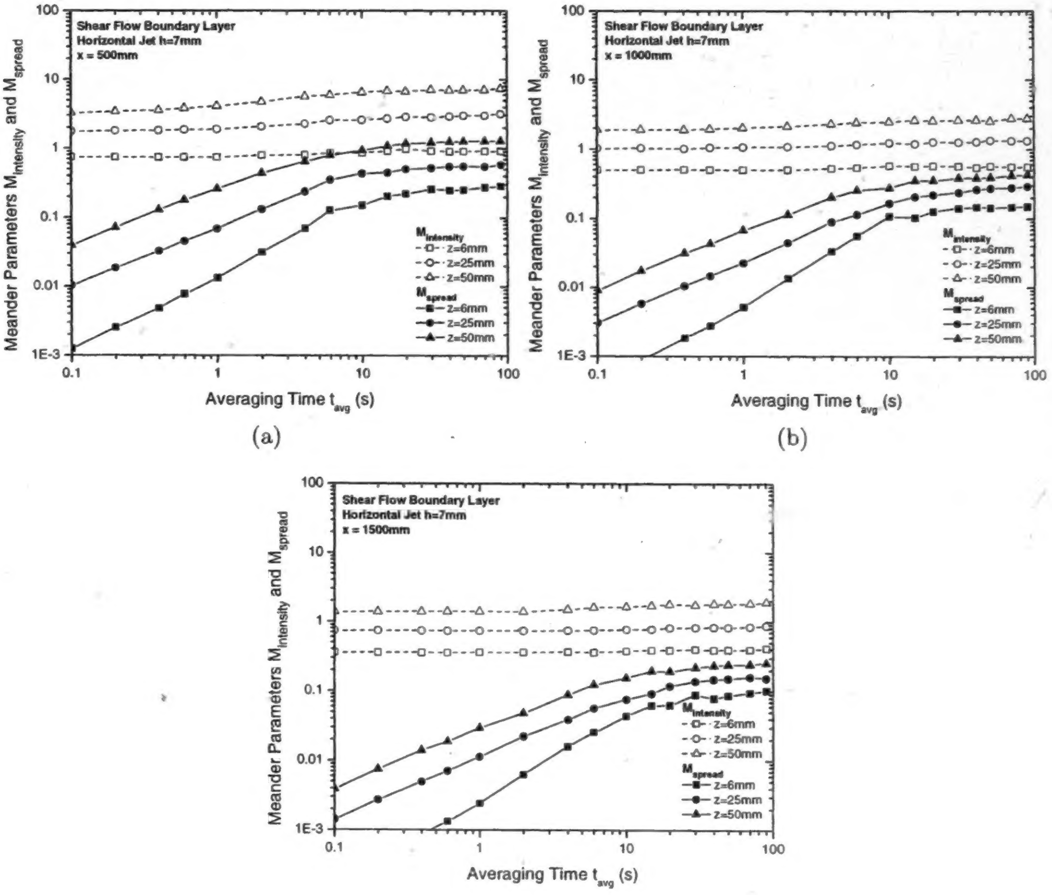

(a)

(b)

(c)

Figure C.6: Meander parameter $M_{\text{intensity}}$ and M_{spread} values for the horizontal jet source at $h = 7$ mm at a flow rate $Q = 0.73$ ml/s and measured at $z = 6,25$, and 50 mm above the ground for (a) $x = 500$ mm (b) $x = 1000$ mm (c) $x = 1500$ mm

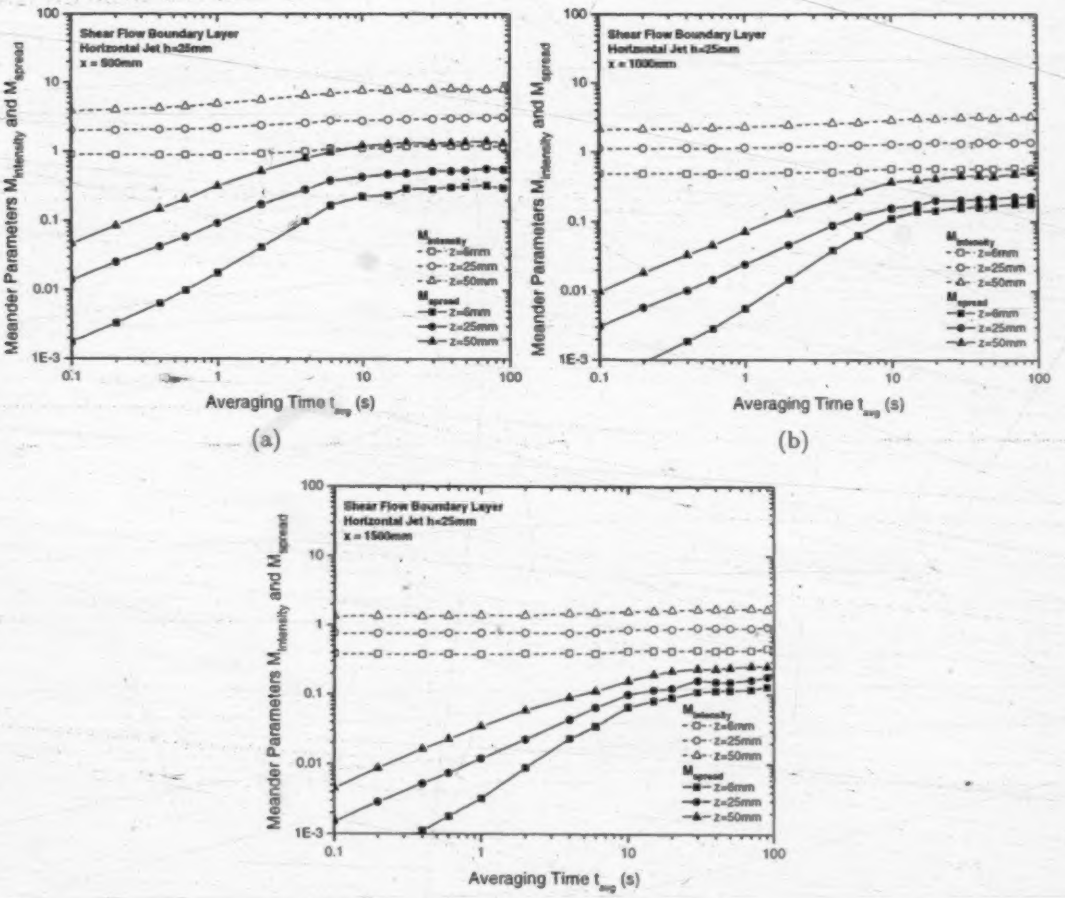

(a) (b)

(c)

Figure C.7: Meander parameter $M_{\text{intensity}}$ and M_{spread} values for the horizontal jet source at $h = 25$ mm at a flow rate $Q = 1.47$ ml/s and measured at $z = 6{,}25$, and 50 mm above the ground for (a) $x = 500$ mm (b) $x = 1000$ mm (c) $x = 1500$ mm

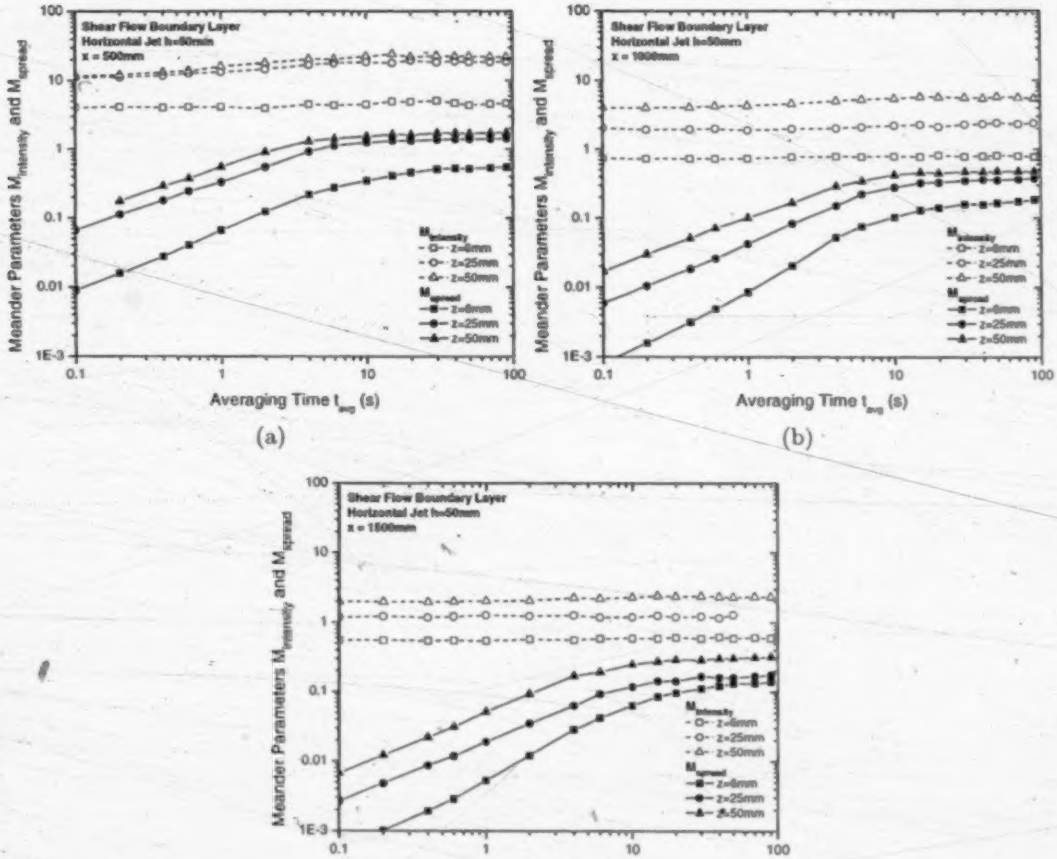

(a) (b)

(c)

Figure C.8: Meander parameter $M_{\text{intensity}}$ and M_{spread} values for the horizontal jet source at $h = 50$ mm at a flow rate $Q = 1.47$ ml/s and measured at $z = 6,25$, and 50 mm above the ground for (a) $x = 500$ mm (b) $x = 1000$ mm (c) $x = 1500$ mm

Appendix D

Averaging Time Effects on i_h and σ_y

Chapter 2 Section 2.4.3 contains examples of the comparison between the plume centreline fluctuation intensity i_h and σ_y. This appendix contains supplemental results that cover all of the source types that were tested.

In the Wilson (1995) meandering plume model it is recommended that the centreline fluctuation intensity i_h be adjusted for averaging time t_{avg} in parallel with changes in plume spread σ_y with averaging time. Wilson (1995, equation (6.9))

$$\frac{i^2_{h,t_{\text{avg}}} + 1}{i^2_{h,\text{ref}} + 1} \simeq \frac{\sigma_{y,t_{\text{avg}}}}{\sigma_{y,\text{ref}}} \tag{D.1}$$

Figures D.1 to Figures D.8 show these two ratios as determined from the water channel data with $t_{\text{ref}} = t_\infty \simeq t_{\text{avg}} = 500$ seconds.

References

Wilson, D. J. (1995), *Concentration Fluctuations and Averaging Time in Vapor Clouds*, Center for Chemical Process Safety of the American Institute of Chemical Engineers, New York, NY.

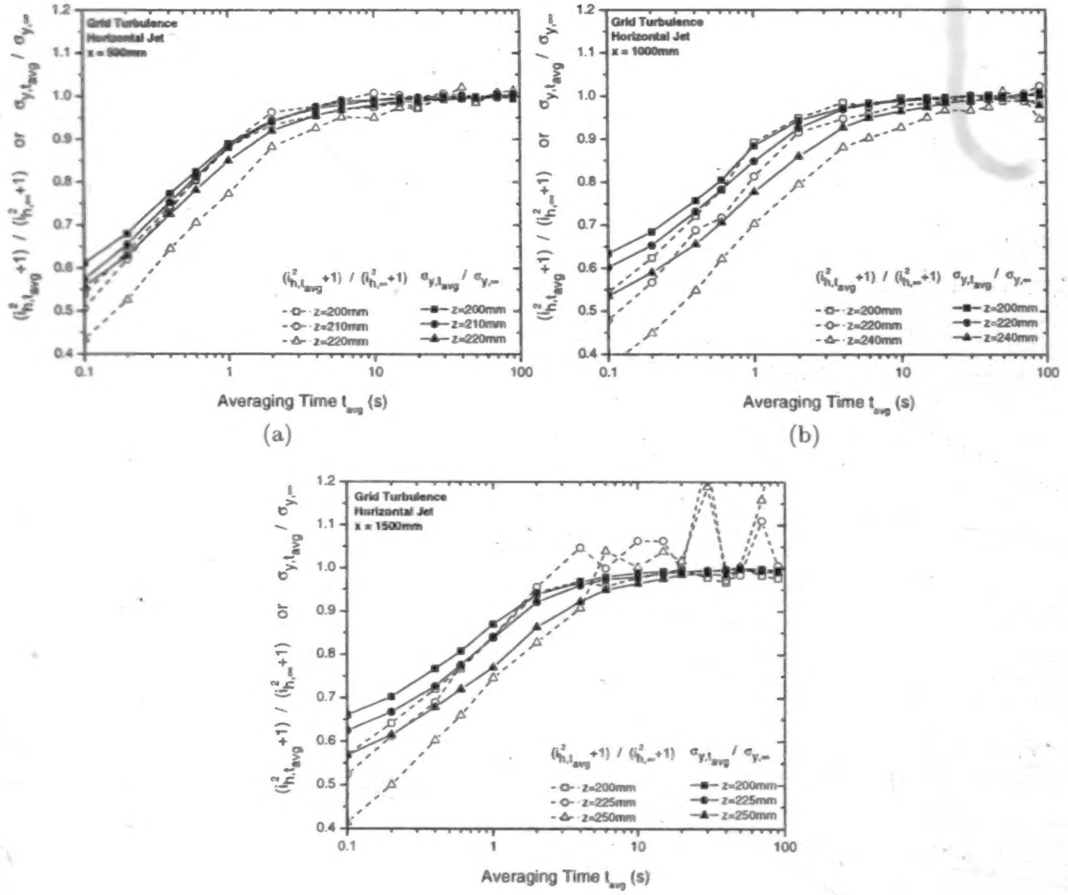

(a)

(b)

(c)

Figure D.1: Ratios of plume centreline fluctuation intensity $(i^2_{h,t_{\text{avg}}}+1)/(i^2_{h,\infty}+1)$ compared to the plume spread ratio $\sigma_{y,t_{\text{avg}}}/\sigma_{y,\infty}$ as a function of averaging time t_{avg} for the iso-kinetic horizontal jet source in grid turbulence (a) $x = 500$ mm and $z = 200$, 210, 220 mm (b) $x = 1000$ mm and $z = 200$, 220, 240 mm (c) $x = 1500$ mm and $z = 200$, 225, 250 mm

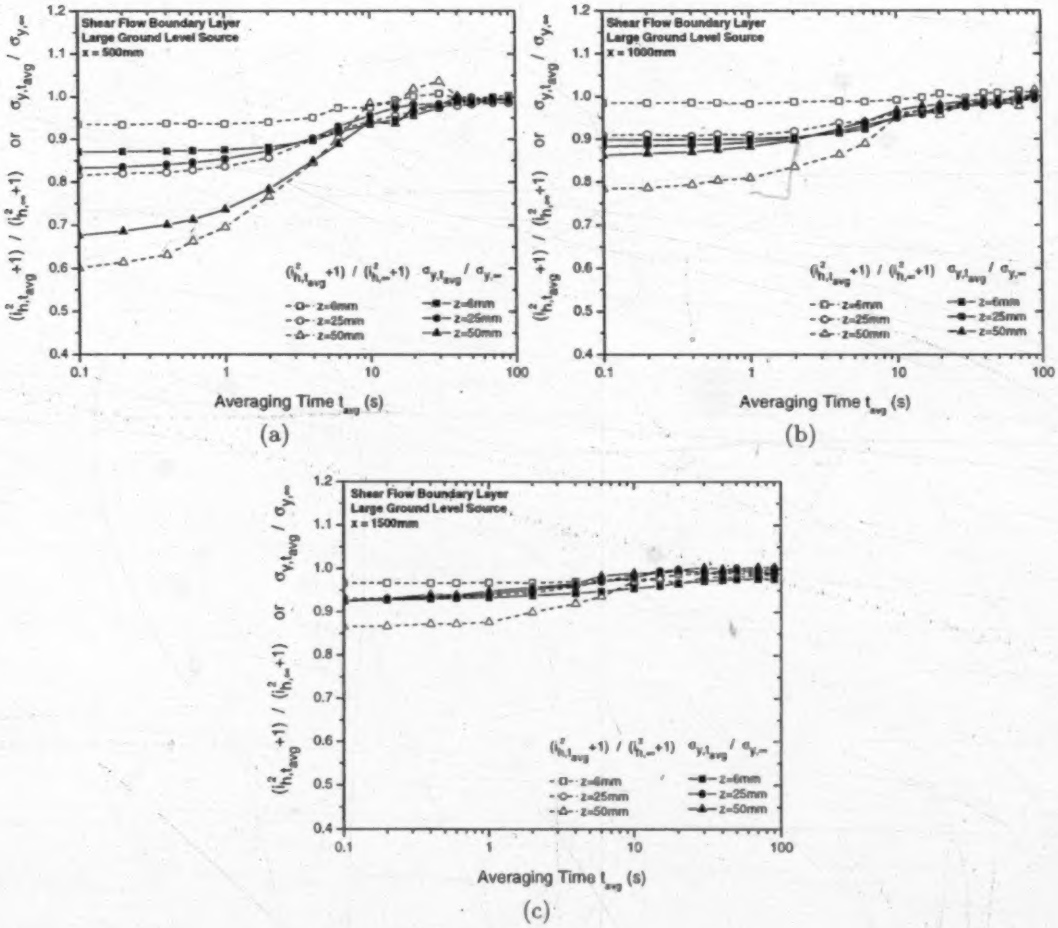

(a) (b) (c)

Figure D.2: Ratios of plume centreline fluctuation intensity $(i^2_{h,t_{\rm avg}} + 1)/(i^2_{h,\infty} + 1)$ compared to the plume spread ratio $\sigma_{y,t_{\rm avg}}/\sigma_{y,\infty}$ as a function of averaging time $t_{\rm avg}$ for the large ground level source with a flow rate $Q = 1.47$ ml/s in the boundary layer shear flow at $z = 6,25$, and 50 mm above the ground for (a) $x = 500$ mm (b) $x = 1000$ mm (c) $x = 1500$ mm

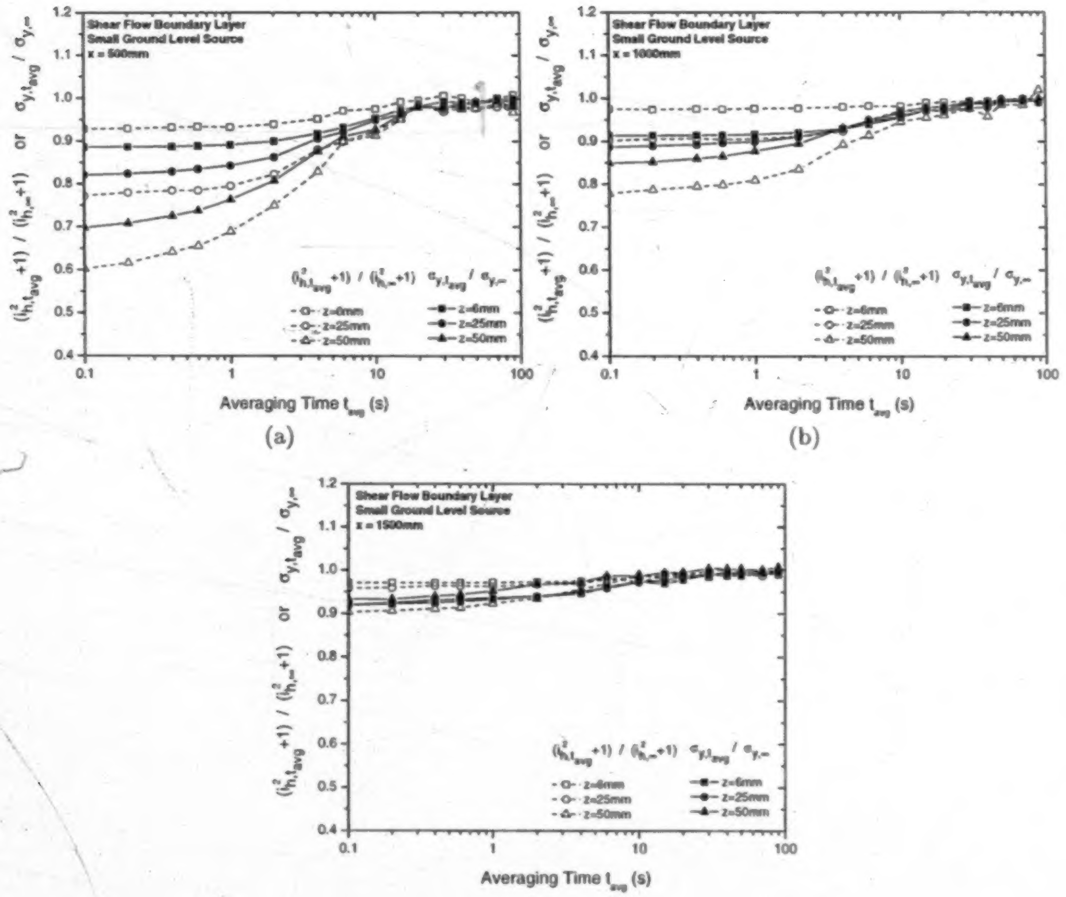

(a) (b)

(c)

Figure D.3: Ratios of plume centreline fluctuation intensity $(i^2_{h,t_{\text{avg}}} + 1)/(i^2_{h,\infty} + 1)$ compared to the plume spread ratio $\sigma_{y,t_{\text{avg}}}/\sigma_{y,\infty}$ as a function of averaging time t_{avg} for the small ground level vertical jet source at a flow rate $Q = 1.47$ ml/s in the boundary layer shear flow at $z = 6$,25, and 50 mm above the ground for (a) $x = 500$ mm (b) $x = 1000$ mm (c) $x = 1500$ mm

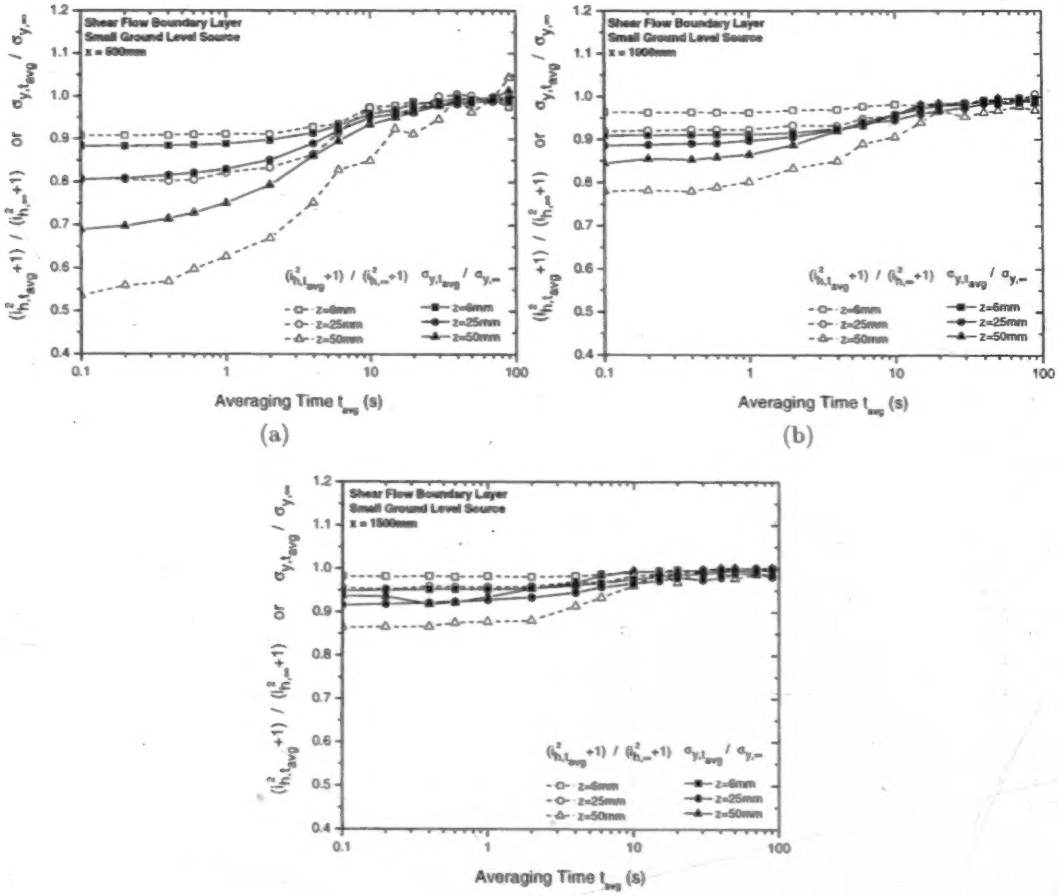

(a)

(b)

(c)

Figure D.4: Ratios of plume centreline fluctuation intensity $(i^2_{h,t_{avg}} + 1)/(i^2_{h,\infty} + 1)$ compared to the plume spread ratio $\sigma_{y,t_{avg}}/\sigma_{y,\infty}$ as a function of averaging time t_{avg} for the small ground level vertical jet source at a flow rate $Q = 0.73$ ml/s in the boundary layer shear flow at $z = 6$,25, and 50 mm above the ground for (a) $x = 500$ mm (b) $x = 1000$ mm (c) $x = 1500$ mm

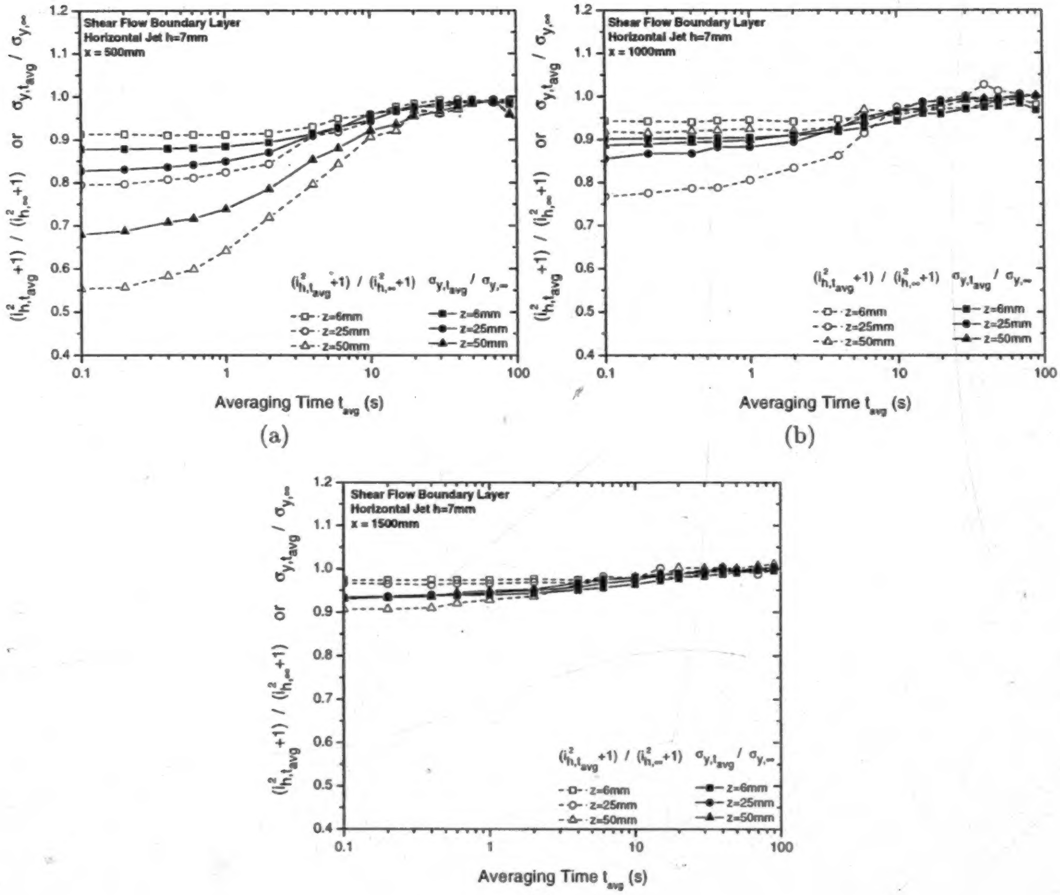

(a) (b) (c)

Figure D.5: Ratios of plume centreline fluctuation intensity $(i^2_{h,t_{\text{avg}}} + 1)/(i^2_{h,\infty} + 1)$ compared to the plume spread ratio $\sigma_{y,t_{\text{avg}}}/\sigma_{y,\infty}$ as a function of averaging time t_{avg} for the horizontal jet source at $h = 6$ mm at a flow rate $Q = 1.47$ ml/s in the boundary layer shear flow at $z = 6{,}25$, and 50 mm above the ground for (a) $x = 500$ mm (b) $x = 1000$ mm (c) $x = 1500$ mm

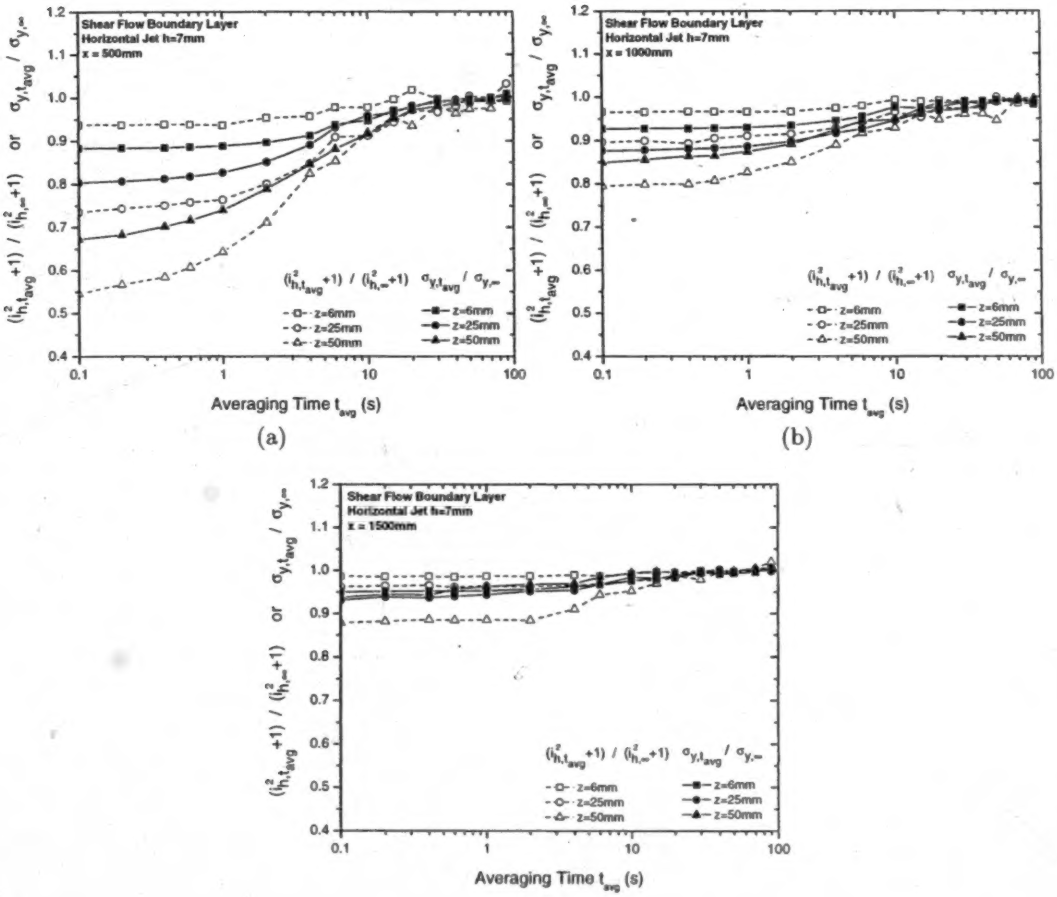

(a) (b)

(c)

Figure D.6: Ratios of plume centreline fluctuation intensity $(i^2_{h,t_{\text{avg}}} + 1)/(i^2_{h,\infty} + 1)$ compared to the plume spread ratio $\sigma_{y,t_{\text{avg}}}/\sigma_{y,\infty}$ as a function of averaging time t_{avg} for the horizontal jet source at $h = 6$ mm at a flow rate $Q = 0.73$ ml/s in the boundary layer shear flow at $z = 6$,25, and 50 mm above the ground for (a) $x = 500$ mm (b) $x = 1000$ mm (c) $x = 1500$ mm

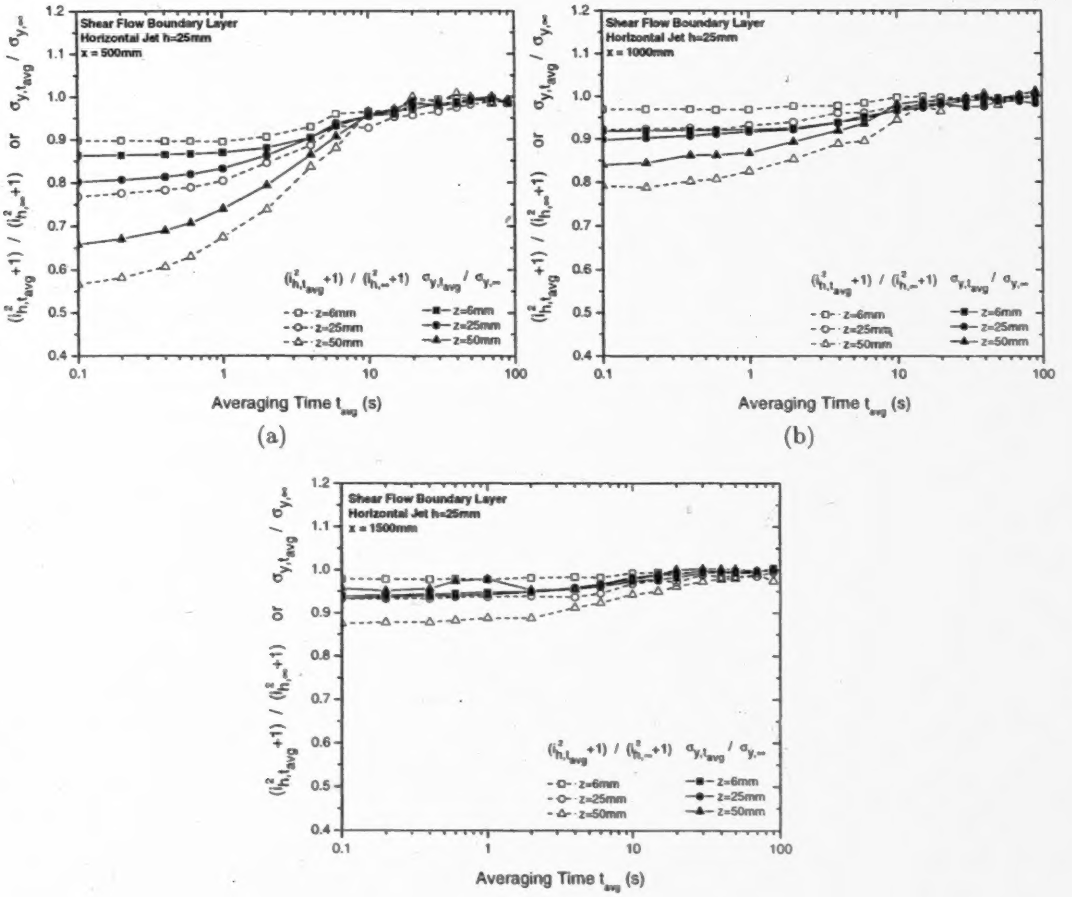

(a) (b)

(c)

Figure D.7: Ratios of plume centreline fluctuation intensity $(i^2_{h,t_{\text{avg}}}+1)/(i^2_{h,\infty}+1)$ compared to the plume spread ratio $\sigma_{y,t_{\text{avg}}}/\sigma_{y,\infty}$ as a function of averaging time t_{avg} for the horizontal jet source at $h = 25$ mm at a flow rate $Q = 1.47$ ml/s in the boundary layer shear flow at $z = 6{,}25$, and 50 mm above the ground for (a) $x = 500$ mm (b) $x = 1000$ mm (c) $x = 1500$ mm

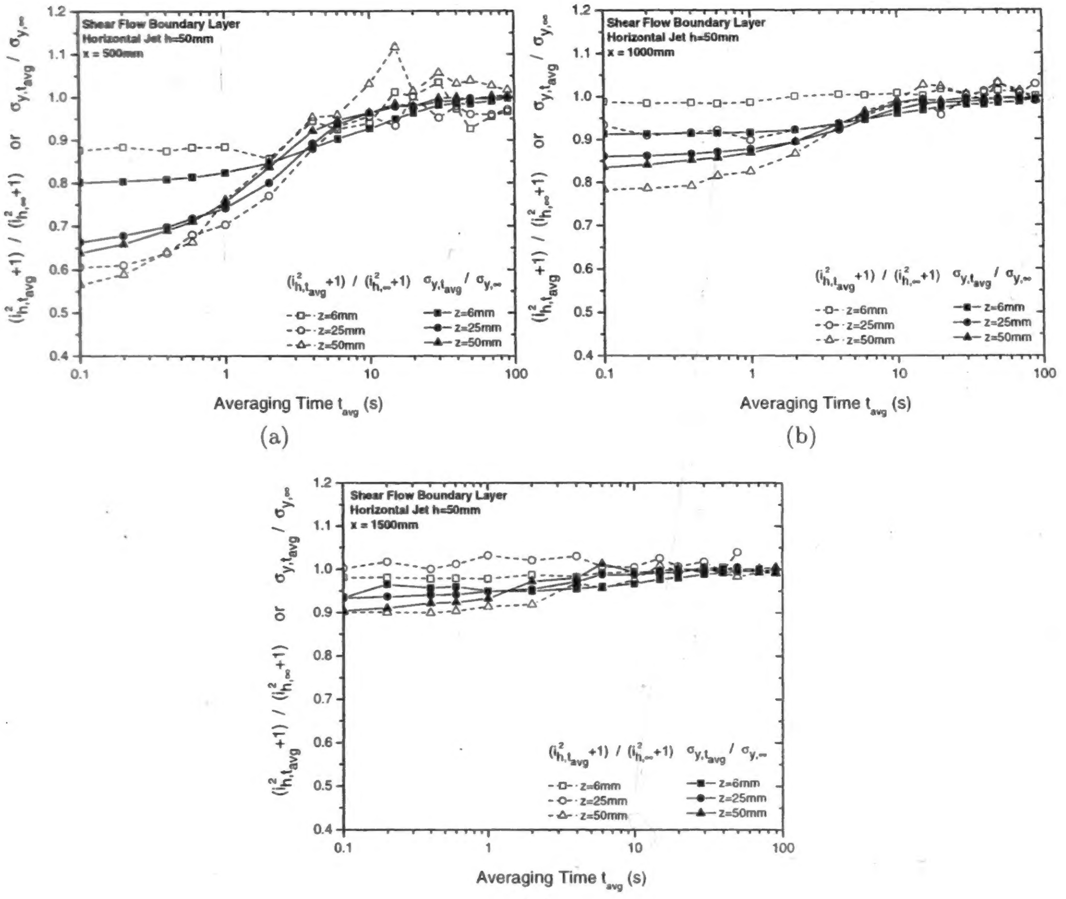

(a)

(b)

(c)

Figure D.8: Ratios of plume centreline fluctuation intensity $(i^2_{h,t_{\mathrm{avg}}}+1)/(i^2_{h,\infty}+1)$ compared to the plume spread ratio $\sigma_{y,t_{\mathrm{avg}}}/\sigma_{y,\infty}$ as a function of averaging time t_{avg} for the horizontal jet source at $h = 50$ mm at a flow rate $Q = 1.47$ ml/s in the boundary layer shear flow at $z = 6{,}25$, and 50 mm above the ground for (a) $x = 500$ mm (b) $x = 1000$ mm (c) $x = 1500$ mm

Appendix E

Cross-Stream Profiles of Concentration Fluctuation Intensity i

This appendix provides additional plots of cross-stream fluctuation intensity profiles to complement the examples given in Chapter 2 Section 2.4.4. The Wilson (1995) pseudo-meandering plume operational model for off-axis fluctuation intensity values is Wilson (1995, equation (6.8)) also given as Equation (2.15) in this thesis.

$$i^2 + 1 = (i_h^2 + 1)\left[\exp\left(\frac{(z-h)^2}{2\sigma_z^2} + \frac{y^2}{2\sigma_y^2}\right)\right]^{\frac{2M_{\text{intensity}}}{1+2M_{\text{intensity}}}} \tag{E.1}$$

The shear flow distorts this profile near the ground, and therefore using the source height intensity value i_h does not give very good results.

As demonstrated in Chapter 3, the shear distortion of concentration fluctuations is a highly localized effect. The cross-stream profile of i is much better characterized by the local cross-stream plume centreline intensity $i_{y=0}$ at the appropriate z position instead of i_h. Equation (E.1) therefore reduces to

$$i^2 + 1 = (i_{y=0}^2 + 1)\left[\exp\left(\frac{y^2}{2\sigma_y^2}\right)\right]^{\frac{2M_{\text{intensity}}}{1+2M_{\text{intensity}}}} \tag{E.2}$$

with meander $M_{\text{intensity}}$ calculated using $i_{y=0}$ instead of i_h:

$$M_{\text{intensity}} = i_{y=0}^2 + (i_{y=0}^4 + i_{y=0}^2)^{0.5} \tag{E.3}$$

Figures E.1 to E.8 show the data cross stream fluctuation intensity values i compared to Equation (E.2).

References

Wilson, D. J. (1995), *Concentration Fluctuations and Averaging Time in Vapor Clouds*, Center for Chemical Process Safety of the American Institute of Chemical Engineers, New York, NY.

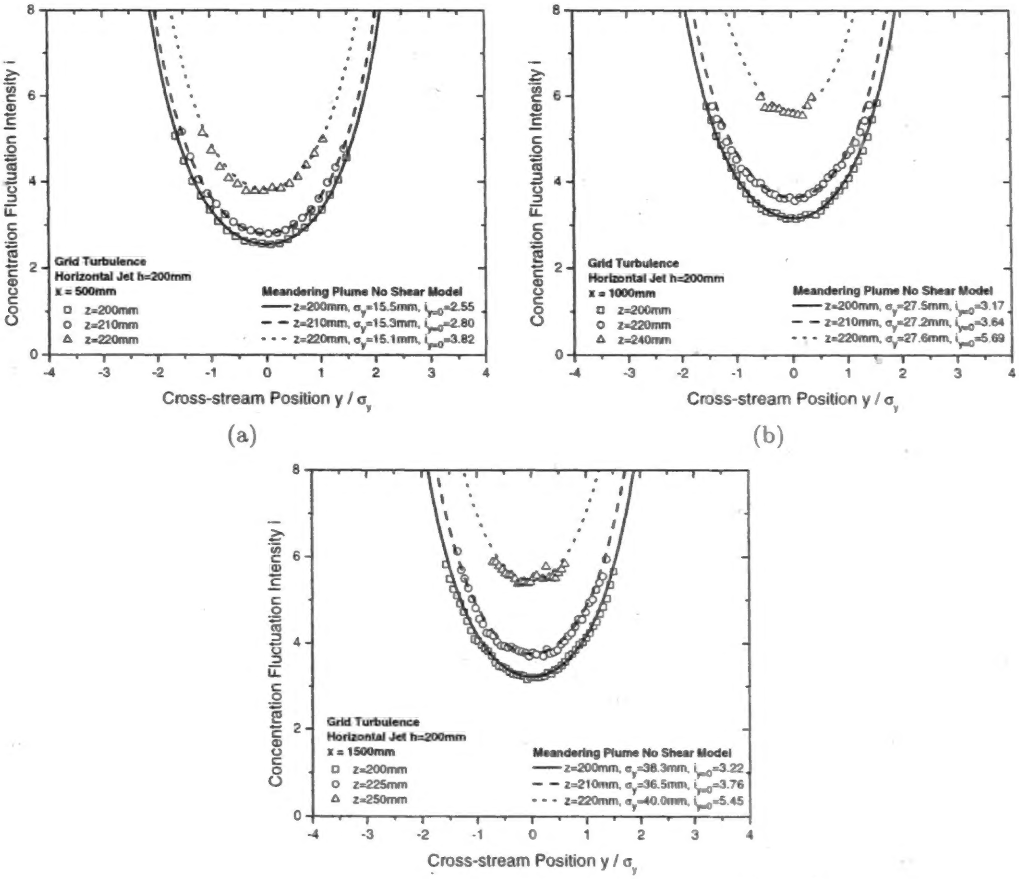

(a)

(b)

(c)

Figure E.1: Cross-stream profiles of concentration fluctuation intensity i compared to equation (E.2) for the iso-kinetic horizontal jet source in grid turbulence (a) x = 500 mm and z = 200, 210, 220 mm (b) x = 1000 mm and z = 200, 220, 240 mm (c) x = 1500 mm and z = 200, 220, 240 mm

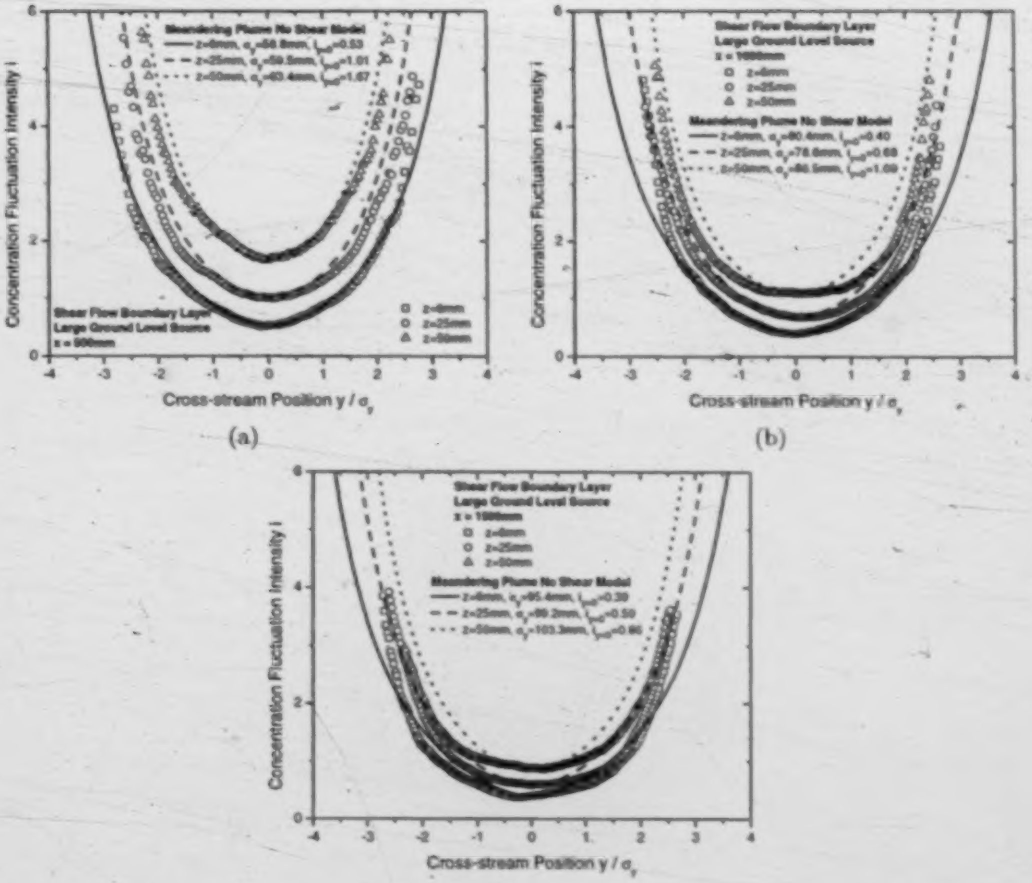

(a) (b)

(c)

Figure E.2: Cross-stream profiles of concentration fluctuation intensity i compared to equation (E.2) for the large ground level source at a flow rate $Q = 1.47$ ml/s in the boundary layer shear flow at $z = 6{,}25$, and 50 mm above the ground (a) $x = 500$ mm (b) $x = 1000$ mm (c) $x = 1500$ mm

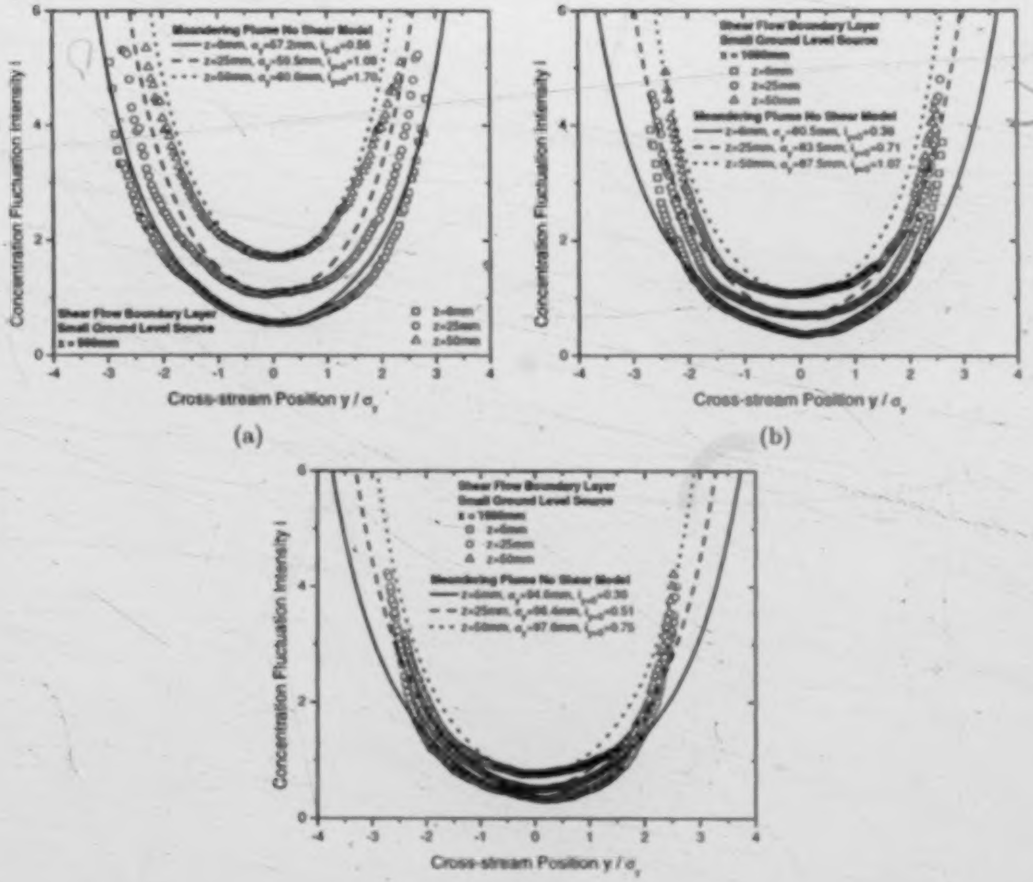

(a) (b)

(c)

Figure E.3: Cross-stream profiles of concentration fluctuation intensity i compared to equation (E.2) for the small ground level vertical jet source at a flow rate $Q =$ 1.47 ml/s in the boundary layer shear flow at $z = 6$,25, and 50 mm above the ground (a) $x = 500$ mm (b) $x = 1000$ mm (c) $x = 1500$ mm

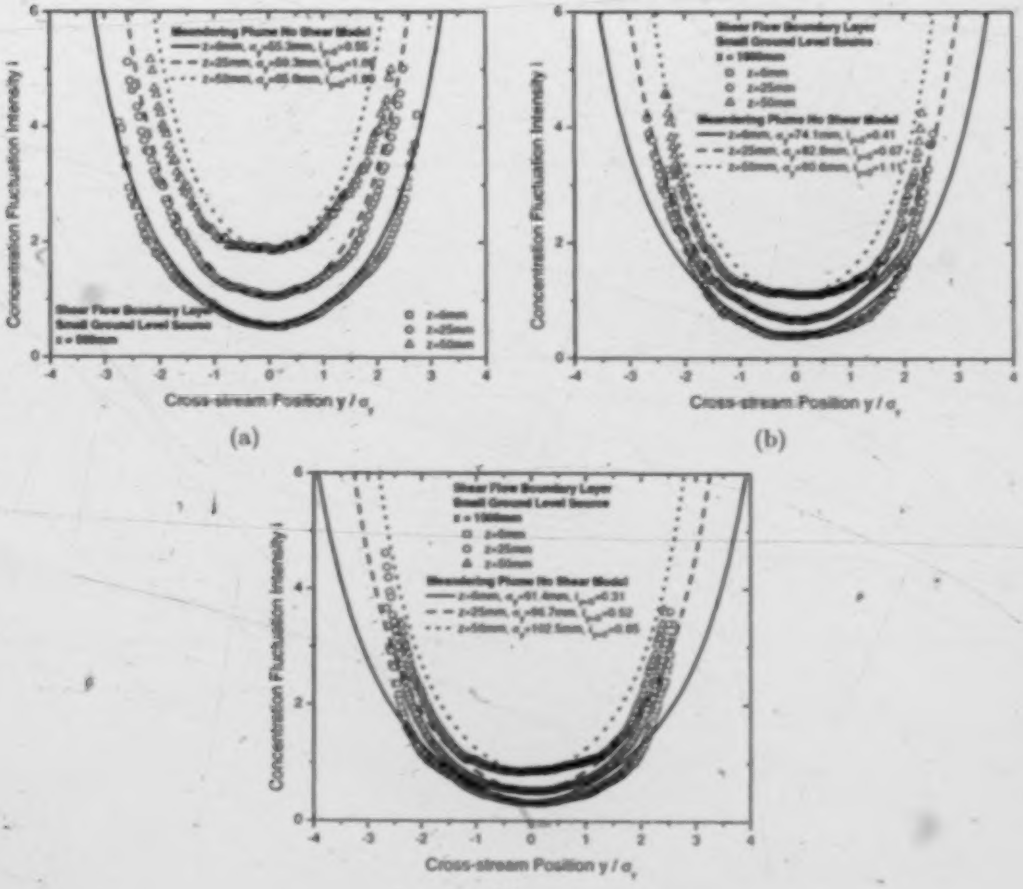

(a) (b)

(c)

Figure E.4: Cross-stream profiles of concentration fluctuation intensity i compared to equation (E.2) for the small ground level vertical jet source at a flow rate $Q = 0.73$ ml/s in the boundary layer shear flow at $z = 6{,}25$, and 50 mm above the ground (a) $x = 500$ mm (b) $x = 1000$ mm (c) $x = 1500$ mm

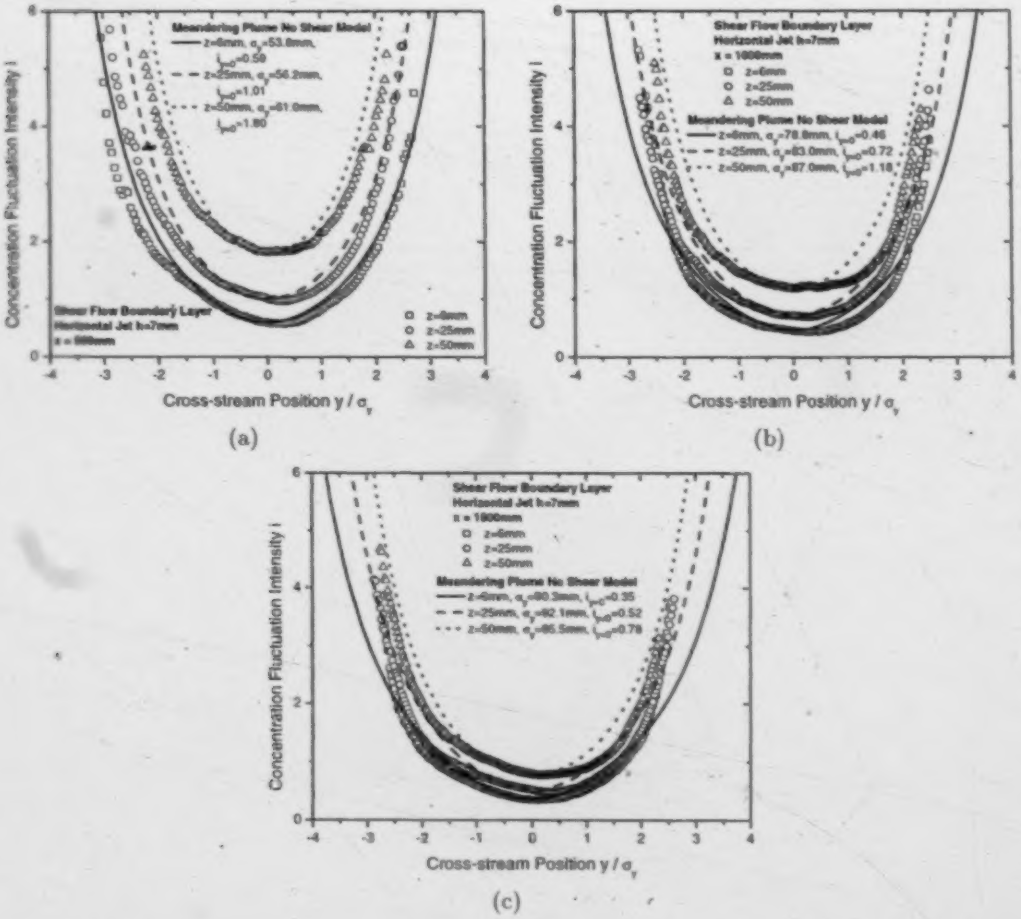

(a)

(b)

(c)

Figure E.5: Cross-stream profiles of concentration fluctuation intensity i compared to equation (E.2) for the horizontal jet source at $h = 7$ mm at a flow rate $Q = 1.47$ ml/s in the boundary layer shear flow at $z = 6$,25, and 50 mm above the ground (a) $x = 500$ mm (b) $x = 1000$ mm (c) $x = 1500$ mm

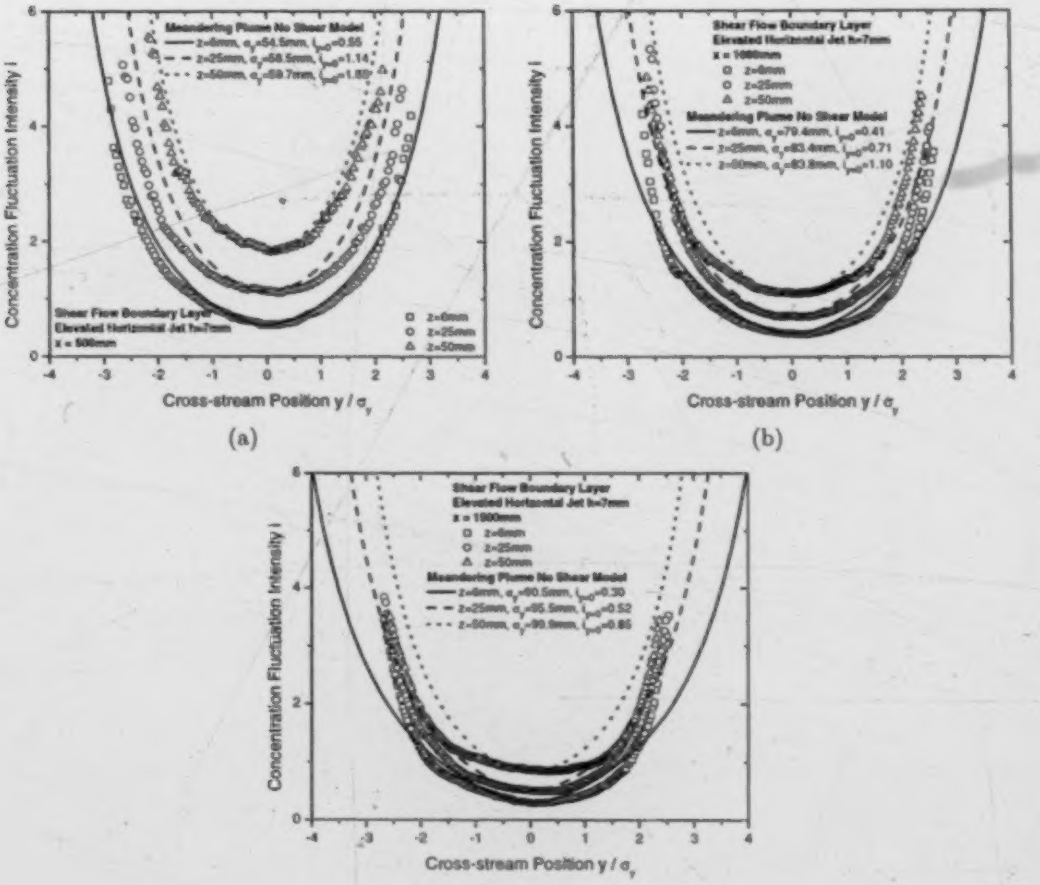

(a) (b)

(c)

Figure E.6: Cross-stream profiles of concentration fluctuation intensity i compared to equation (E.2) for the horizontal jet source at $h = 7$ mm at a flow rate $Q = 0.73$ ml/s in the boundary layer shear flow at z = 6,25, and 50 mm above the ground (a) $x = 500$ mm (b) $x = 1000$ mm (c) $x = 1500$ mm

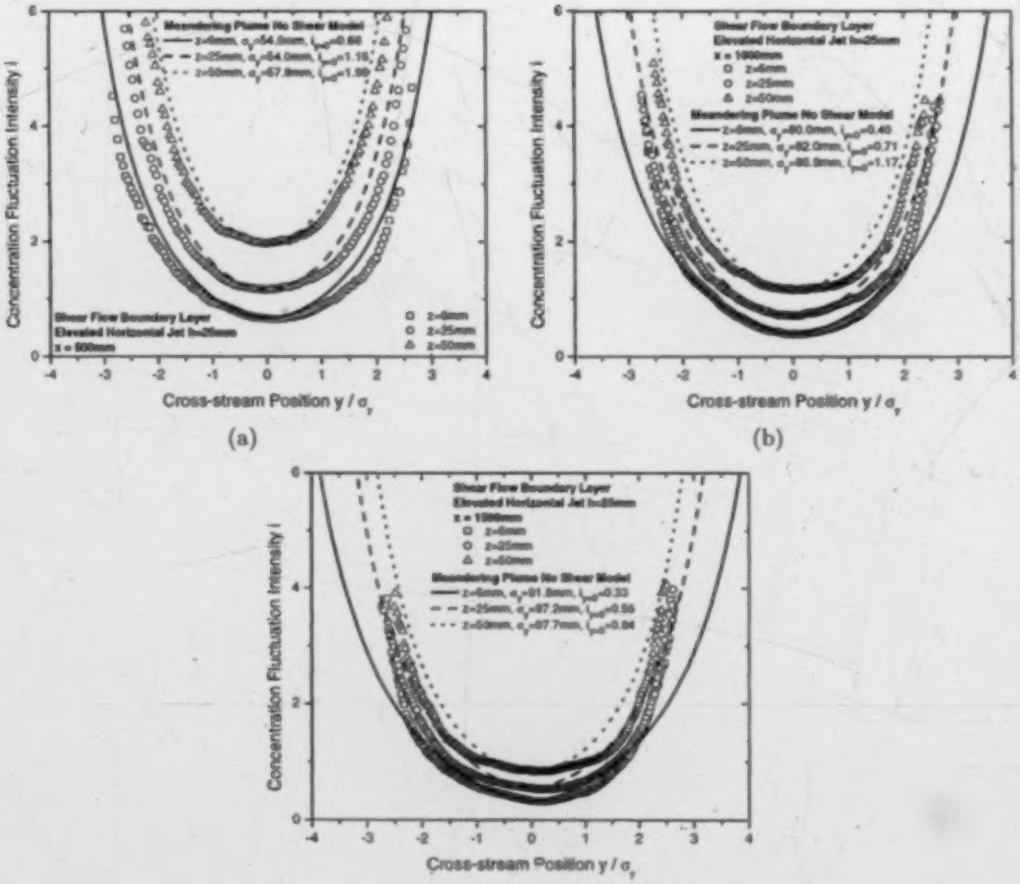

(a) (b)

(c)

Figure E.7: Cross-stream profiles of concentration fluctuation intensity i compared to equation (E.2) for the horizontal jet source at $h = 25$ mm at a flow rate $Q = 1.47$ ml/s in the boundary layer shear flow at $z = 6{,}25$, and 50 mm above the ground (a) $x = 500$ mm (b) $x = 1000$ mm (c) $x = 1500$ mm

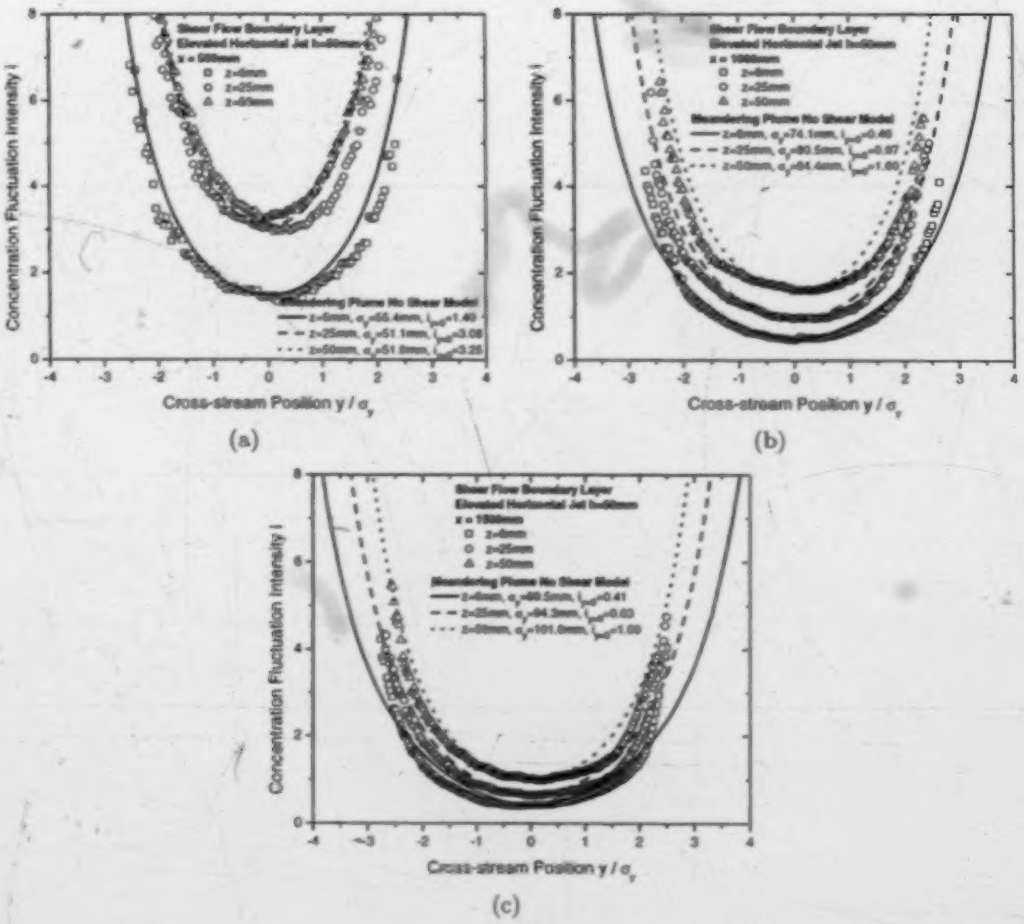

(a)

(b)

(c)

Figure E.8: Cross-stream profiles of concentration fluctuation intensity i compared to equation (E.2) for the horizontal jet source at $h = 50$ mm at a flow rate $Q = 1.47$ ml/s in the boundary layer shear flow at $z = 6{,}25$, and 50 mm above the ground (a) $x = 500$ mm (b) $x = 1000$ mm (c) $x = 1500$ mm

Appendix F

Cross-Stream Probability Distributions of Centroid Position and Plume Spread

Chapter 2 Section 2.4.5 contains selected examples of the probability distribution of centroid position $\overline{y}$ and instantaneous plume spread $\sigma_{y,ii}$. This appendix has additional plots of the centroid and spread probability distributions for all of the other sources that were tested.

F.1 Centroid Position

The probability distribution of positions of the instantaneous plume centroid $p(\overline{y})$ is expected to be Gaussian. The centroid moves as the result of a random additive process and would be expected to produce a Gaussian distribution. With a mean centroid position defined as 0 then

$$p(\overline{y}) = \frac{1}{\overline{y}'_{\mathrm{rms}}\sqrt{2\pi}} \exp\left(-\frac{\overline{y}^2}{2\overline{y}'^{\,2}_{\mathrm{rms}}}\right) \tag{F.1}$$

where $\overline{y}'_{\mathrm{rms}}$ is the standard deviation of the centroid position.

In Figures F.1 through F.16 the centroid pdfs of the data are plotted and compared to the Gaussian pdf. The Gaussian curves plotted with the data are simply Gaussian distributions with zero mean and same standard deviation $\overline{y}'_{\mathrm{rms}}$ as the data.

F.2 Plume Spread

Instantaneous plume spread $\sigma_{y,ii}$ has large variability caused by the random dilution and spreading of the plume and also by plume meandering perpendicular to the linescan measurement. In fact, in grid turbulence, there are significant periods of time during which no part of the plume is in the measurement beam even when the measurement location is on the vertical plume centreline. The intermittency factor γ_{line} is the fraction of time during which there is a measurable plume somewhere in the measurement volume. Even on the centreline of the plume, γ_{line} ranges from 87% at 500 mm from the source to 95% at x = 1500 mm. For the boundary layer shear flow some part of plume is present for 100% of the time at all position $z < 50$ mm so $\gamma_{\text{line}} = 1.0$ for all of the shear flow cases.

Figures F.17 through F.32 are the probability distributon $p(\sigma_{y,ii})$ of measured instantaneous plume spreads compared to a clipped lognormal with the same mean $\sigma_{y,ii,\text{avg}}$ and standard deviation as the data. The clipped lognormal was first used for modelling intermittent Eulerian concentration level probability distributions by Hilderman and Wilson (1999). In its application here to the instantaneous plume spread $\sigma_{y,ii}$ the pdf is

$$p(\sigma_{y,ii}) = \frac{1}{\sqrt{2\pi}\sigma_{y,ii,l}\left(\sigma_{y,ii} + \sigma_{y,ii,\text{base}}\right)} \exp\left(-\frac{\ln^2\left(\frac{\sigma_{y,ii}+\sigma_{y,ii,\text{base}}}{\sigma_{y,ii,50}}\right)}{2\sigma^2_{y,ii,l}}\right) \tag{F.2}$$

where $\sigma_{y,ii,l}$ is the log standard deviation of the plume spread, $\sigma_{y,ii,\text{base}}$ is the shift of the distribution needed to generate the correct plume intermittency, and $\sigma_{y,ii,50}$ is the median of the unclipped lognormal distribution. Essentially, this is just a lognormal distribution shifted to the left by $\sigma_{y,ii,\text{base}}$. All values less than 0 are clipped off and replaced with a delta function at zero that represents the intermittent periods where there is no measurable plume anywhere along the measurement line. The $\sigma_{y,ii,l}$ and $\sigma_{y,ii,\text{base}}$ values are chosen so that after clipping the remaining distribution has the correct mean and variance. Hilderman and Wilson (1999) give additional details on the calculations required to compute $\sigma_{y,ii,l}$ and $\sigma_{y,ii,\text{base}}$. For the non-intermittent case $\sigma_{y,ii,\text{base}} = 0$ and (2.16) reduces to the lognormal.

The clipped lognormal is a remarkably good fit to instantaneous plume spread distributions. The only discrepancies are for the extremely small plume spreads where $\sigma_{y,ii} \to 0$ such as in the grid turbulence case. These errors are not surprising as the finite camera resolution limits the ability to measure very small plume spreads with any accuracy. To date, there has been no theoretical basis developed for the clipped lognormal. A simple physical explanation is that dilution/spread is a naturally multiplicative process so a lognormal might be expected. A clipped lognormal may indicate that even zero periods are part of this same multiplicative process.

References

Hilderman, T. L. and Wilson, D. J. (1999), Simulating Concentration Fluctuation Time Series with Intermittent Zero Periods and Level Dependent Derivatives, *Boundary-Layer Meteorology*, 91:451–482.

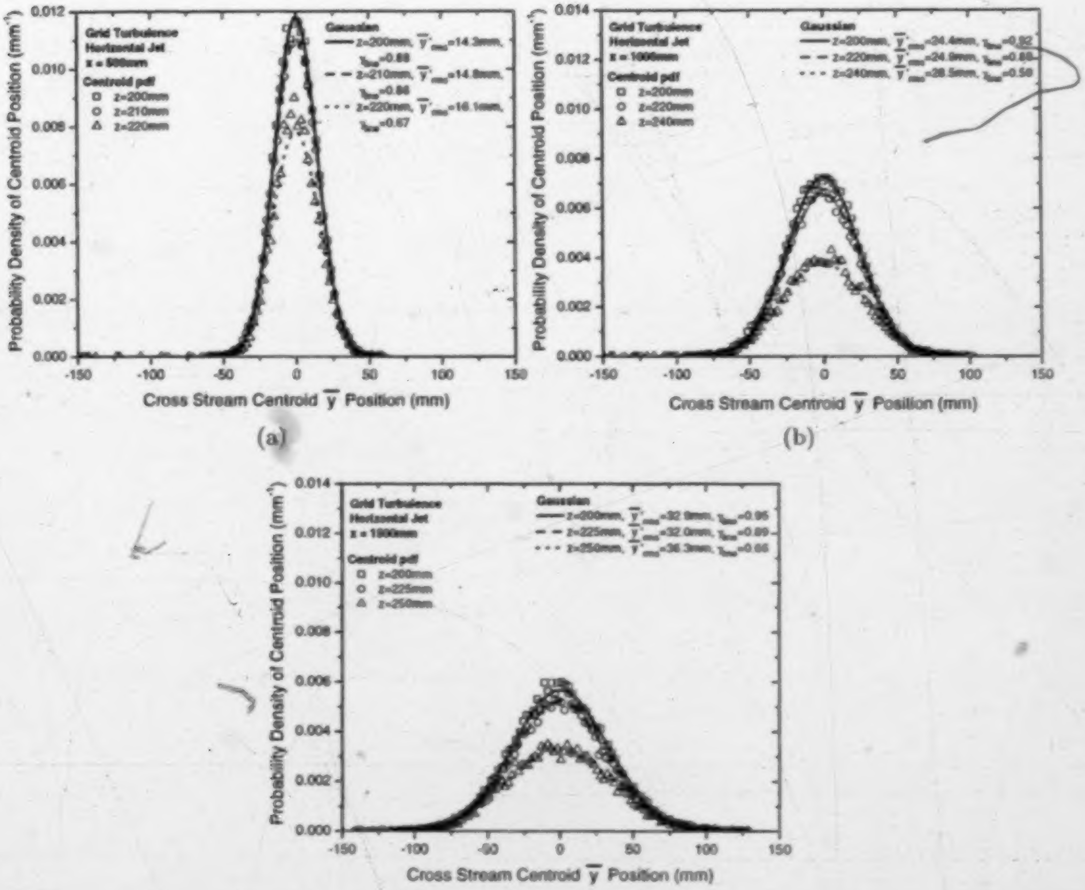

(a) (b)

(c)

Figure F.1: Probability density functions of centroid position $\overline{y}$ compared to a Gaussian for the iso-kinetic horizontal jet source in grid turbulence plotted on linear scales. (a) $x = 500$ mm and $z = 200$, 210, 220 mm (b) $x = 1000$ mm and $z = 200$, 220, 240 mm (c) $x = 1500$ mm and $z = 200$, 225, 250 mm

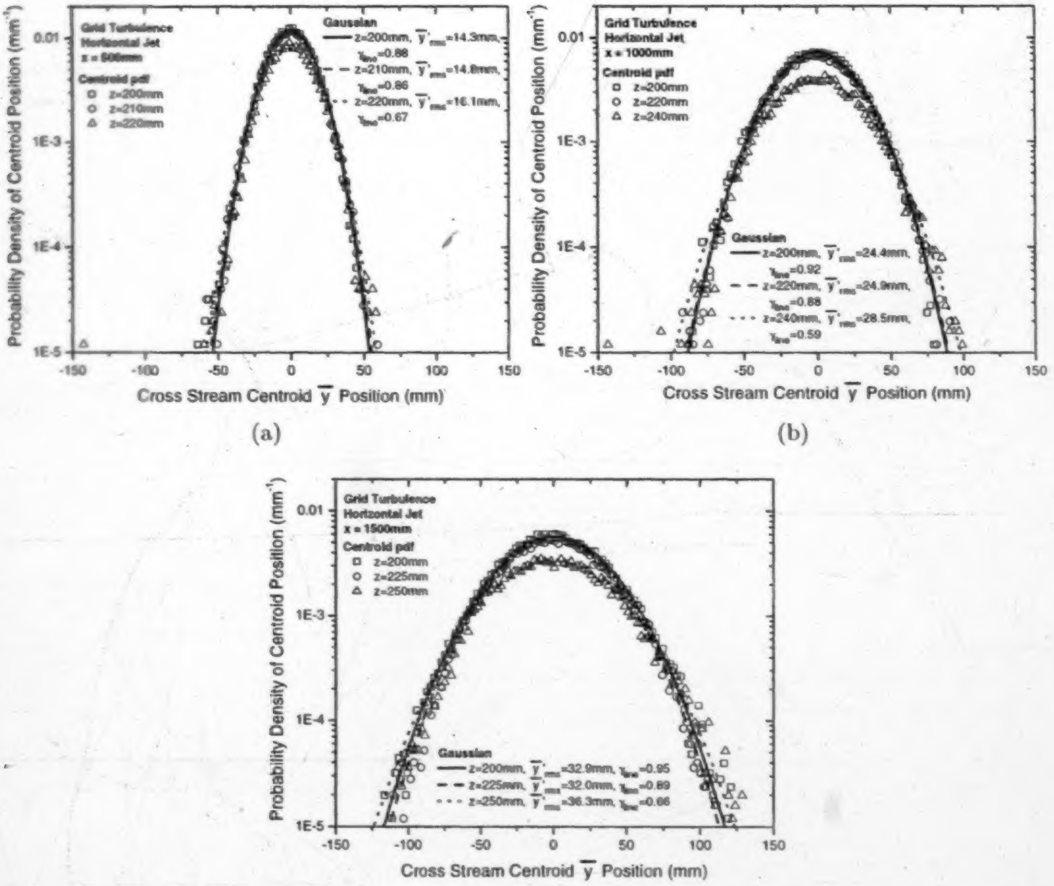

(a)

(b)

(c)

Figure F.2: Probability density functions of centroid position $\overline{y}$ compared to a Gaussian for the iso-kinetic horizontal jet source in grid turbulence plotted on linear-log scales. (a) $x = 500$ mm and $z = 200$, 210, 220 mm (b) $x = 1000$ mm and $z = 200$, 220, 240 mm (c) $x = 1500$ mm and $z = 200$, 225, 250 mm

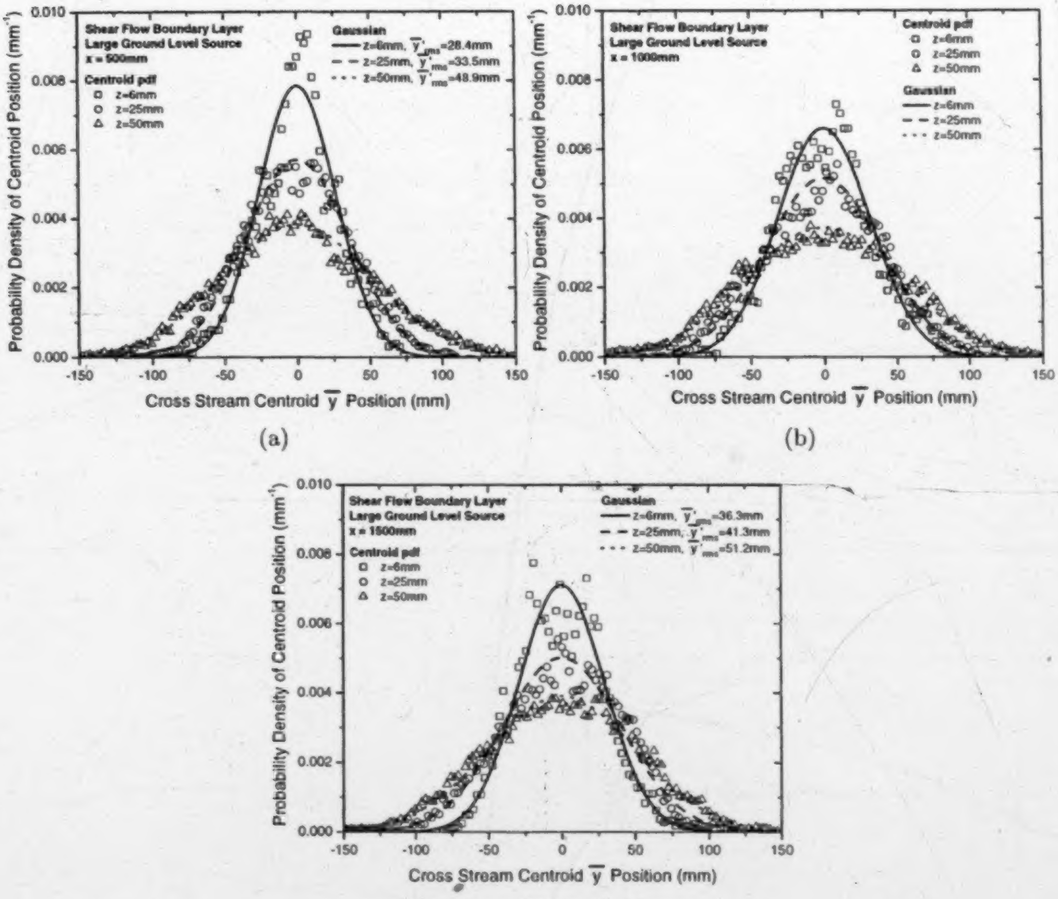

(a) (b)

(c)

Figure F.3: Probability density functions of centroid position $\overline{y}$ compared to a Gaussian for the large ground level source with a flow rate Q = 1.47 ml/s and z = 6, 25, and 50 mm above the ground plotted on linear scales. (a) x = 500 mm (b) x = 1000 mm (c) x = 1500 mm

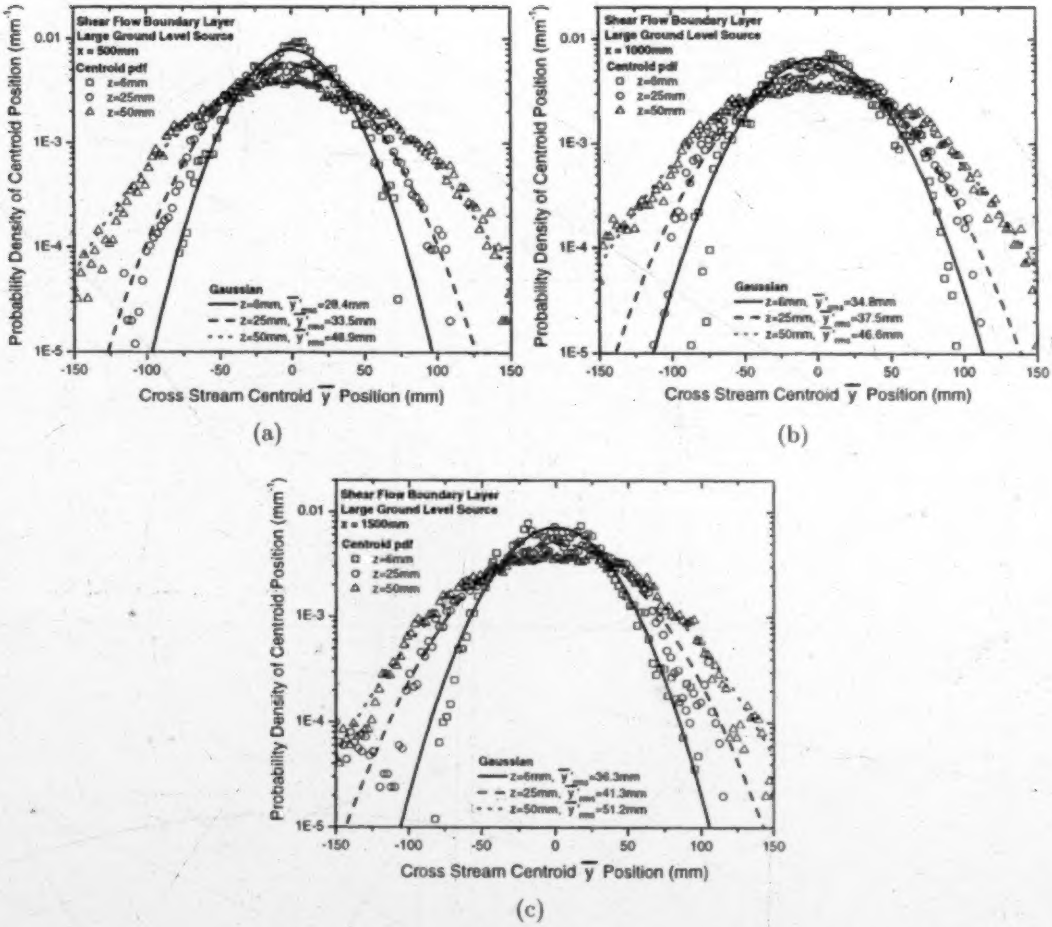

(a)

(b)

(c)

Figure F.4: Probability density functions of centroid position $\overline{y}$ compared to a Gaussian for the large ground level source with a flow rate $Q = 1.47$ ml/s and $z = 6$, 25, and 50 mm above the ground plotted on linear-log scales. (a) $x = 500$ mm (b) $x = 1000$ mm (c) $x = 1500$ mm

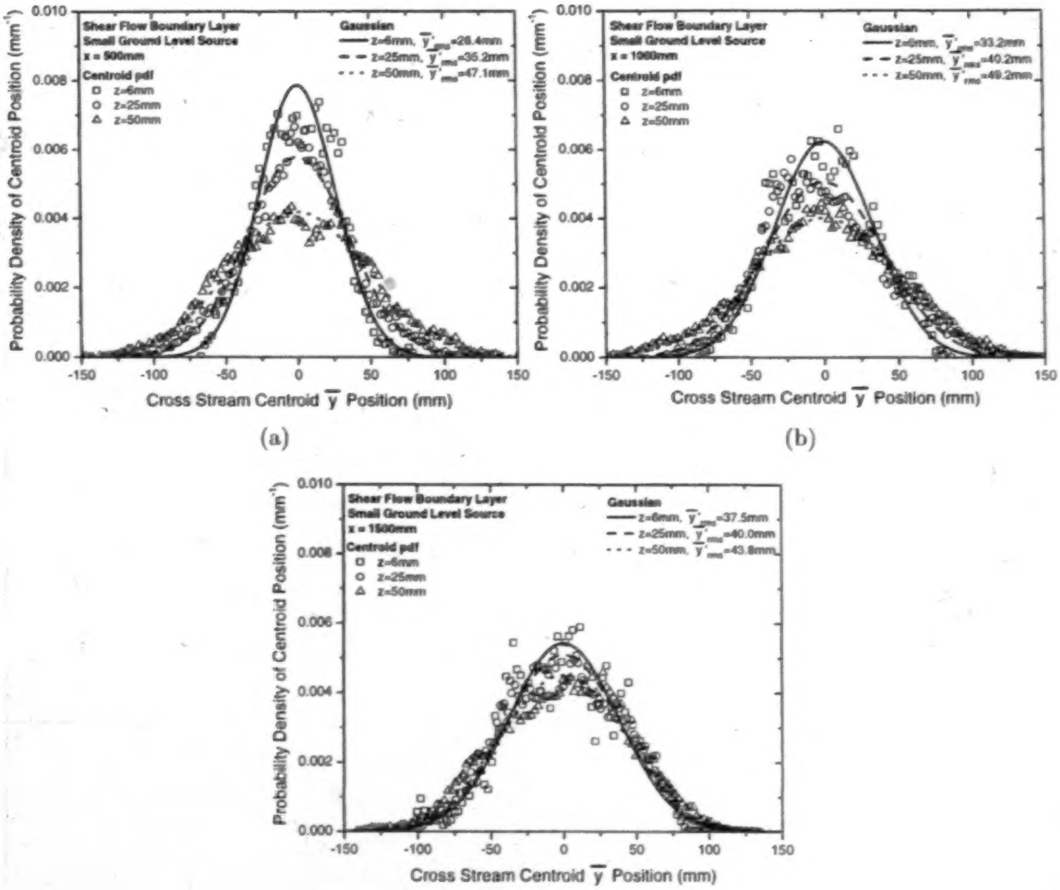

(a)

(b)

(c)

Figure F.5: Probability density functions of centroid position $\overline{y}$ compared to a Gaussian for the small ground level vertical jet source at a flow rate $Q = 1.47$ ml/s and $z = 6$, 25, and 50 mm above the ground plotted on linear scales. (a) $x = 500$ mm (b) $x = 1000$ mm (c) $x = 1500$ mm

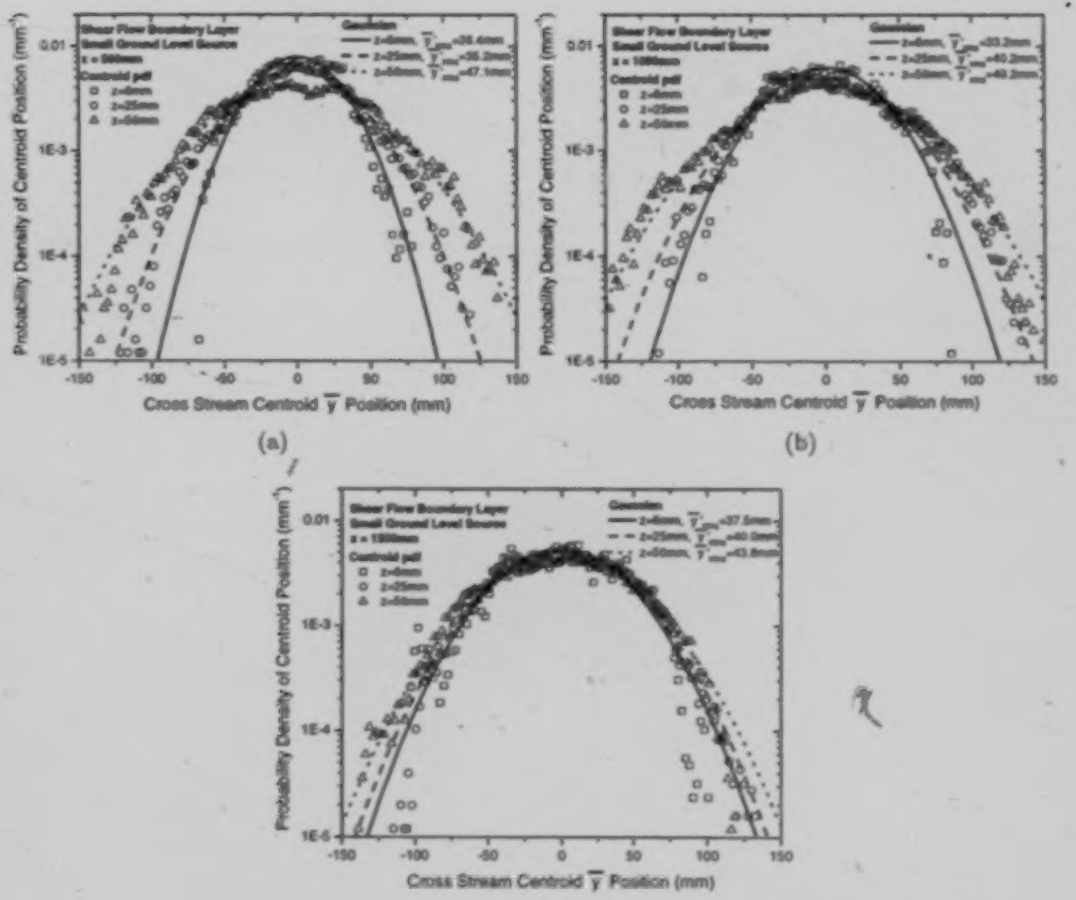

(a)

(b)

(c)

Figure F.6: Probability density functions of centroid position $\overline{y}$ compared to a Gaussian for the small ground level vertical jet source at a flow rate $Q = 1.47$ ml/s and $z = 6$, 25, and 50 mm above the ground plotted on log-linear scales. (a) $x = 500$ mm (b) $x = 1000$ mm (c) $x = 1500$ mm

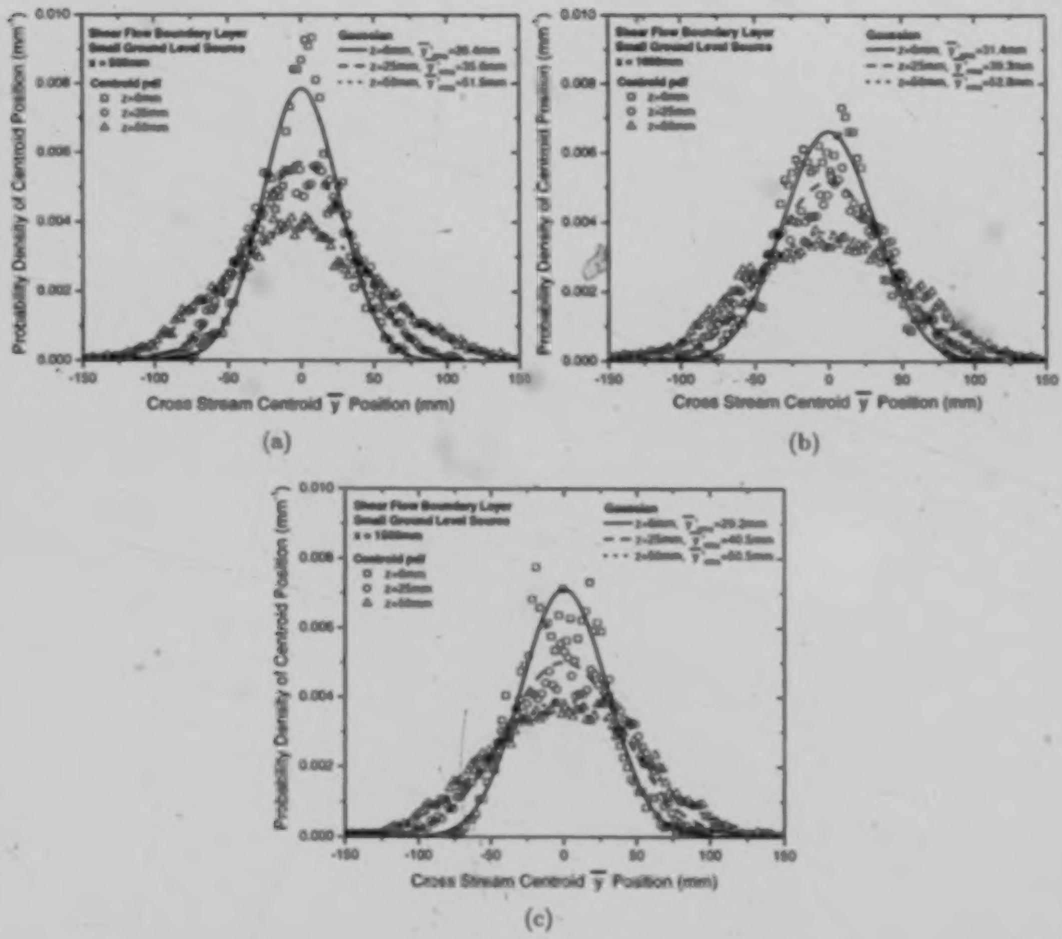

Figure F.7: Probability density functions of centroid position $\overline{y}$ compared to a Gaussian for the small ground level vertical jet source at a flow rate $Q = 0.73$ ml/s and $z = 6$, 25, and 50 mm above the ground plotted on linear scales. (a) $x = 500$ mm (b) $x = 1000$ mm (c) $x = 1500$ mm

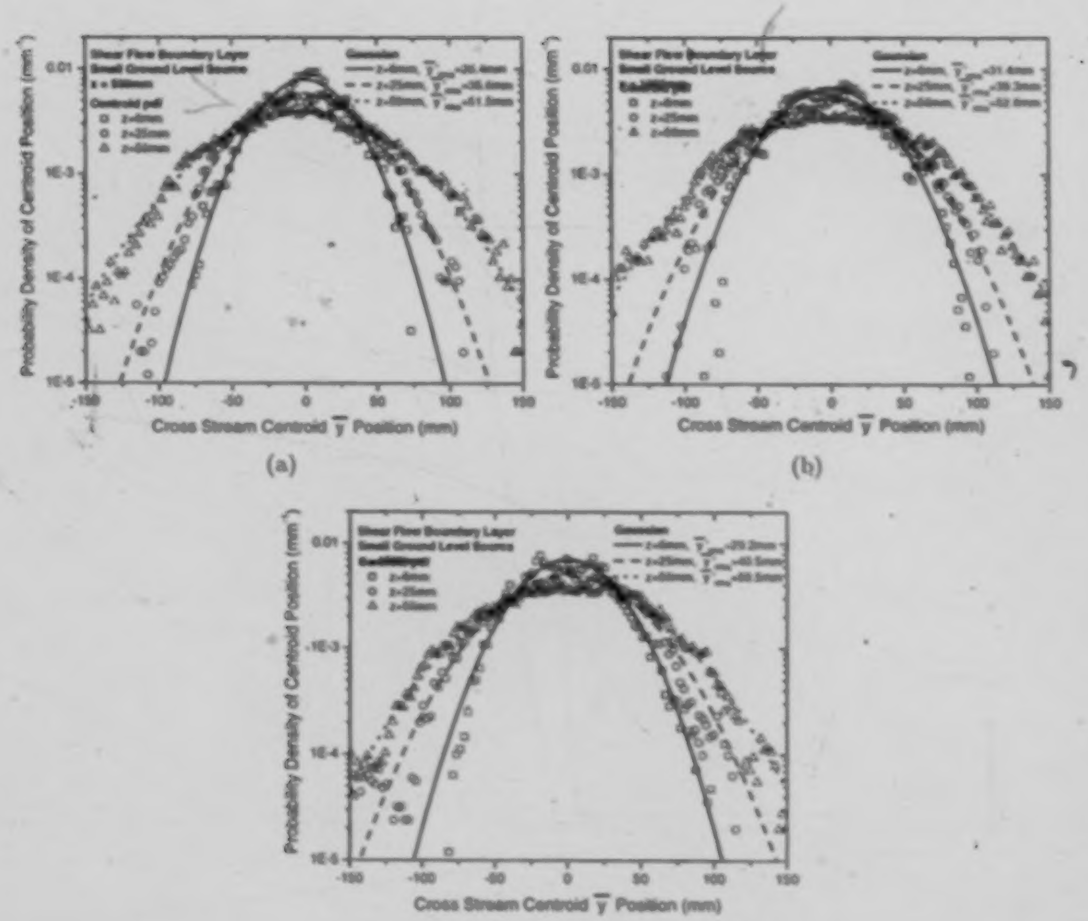

(a)

(b)

(c)

Figure F.8: Probability density functions of centroid position $\overline{y}$ compared to a Gaussian for the small ground level vertical jet source at a flow rate $Q = 1.47$ ml/s and $z = 6$, 25, and 50 mm above the ground plotted on log-linear scales. (a) $x = 500$ mm (b) $x = 1000$ mm (c) $x = 1500$ mm

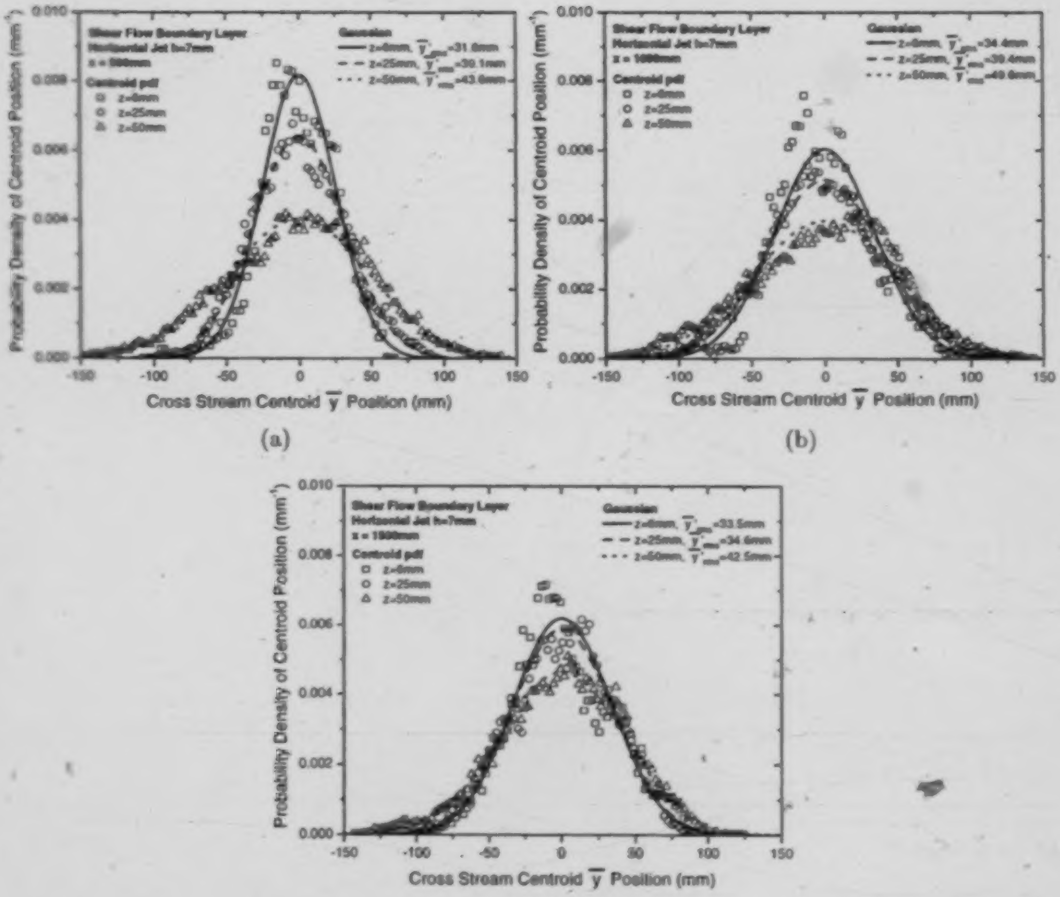

(a)

(b)

(c)

Figure F.9: Probability density functions of centroid position $\overline{y}$ compared to a Gaussian for the horizontal jet source at $h = 7$ mm at a flow rate $Q = 1.47$ ml/s and $z = 6$, 25, and 50 mm above the ground plotted on linear scales. (a) $x = 500$ mm (b) $x = 1000$ mm (c) $x = 1500$ mm

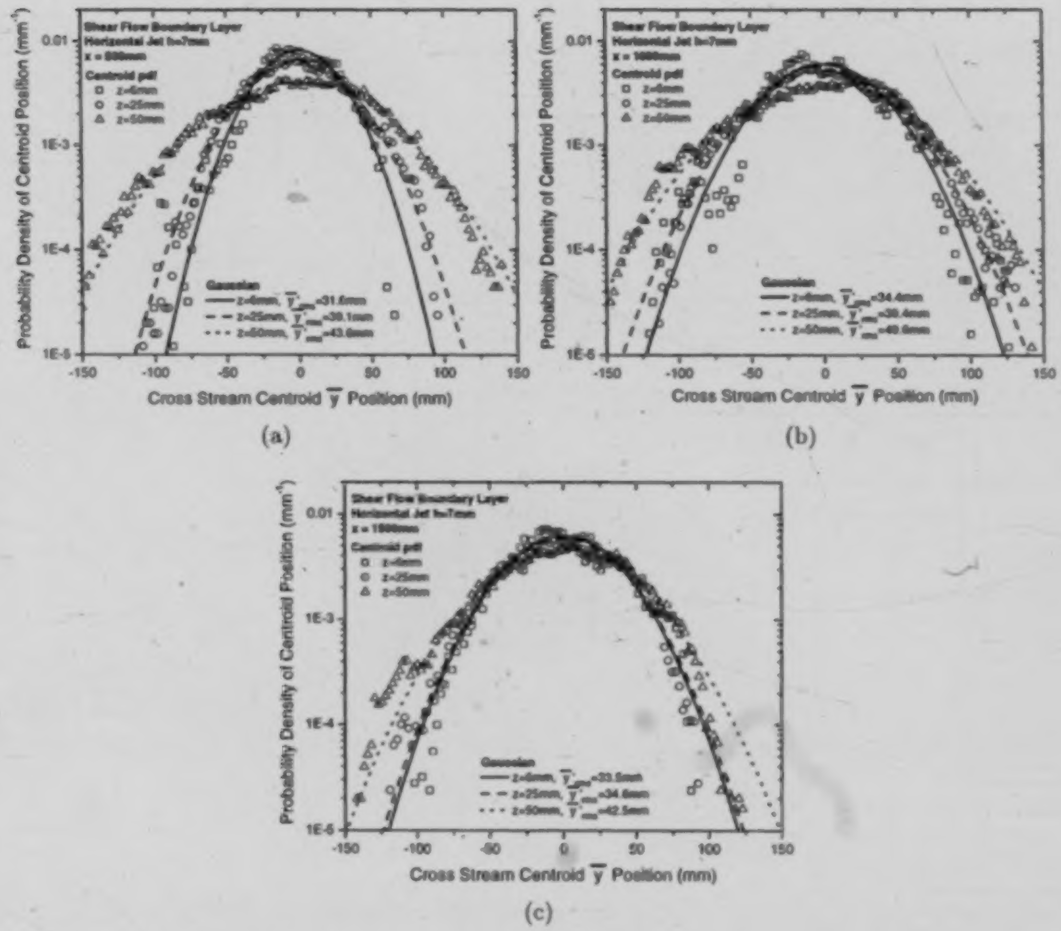

(a)

(b)

(c)

Figure F.10: Probability density functions of centroid position $\overline{y}$ compared to a Gaussian for the horizontal jet source at $h = 7$ mm at a flow rate $Q = 1.47$ ml/s and $z = 6$, 25, and 50 mm above the ground plotted on log-linear scales. (a) $x = 500$ mm (b) $x = 1000$ mm (c) $x = 1500$ mm

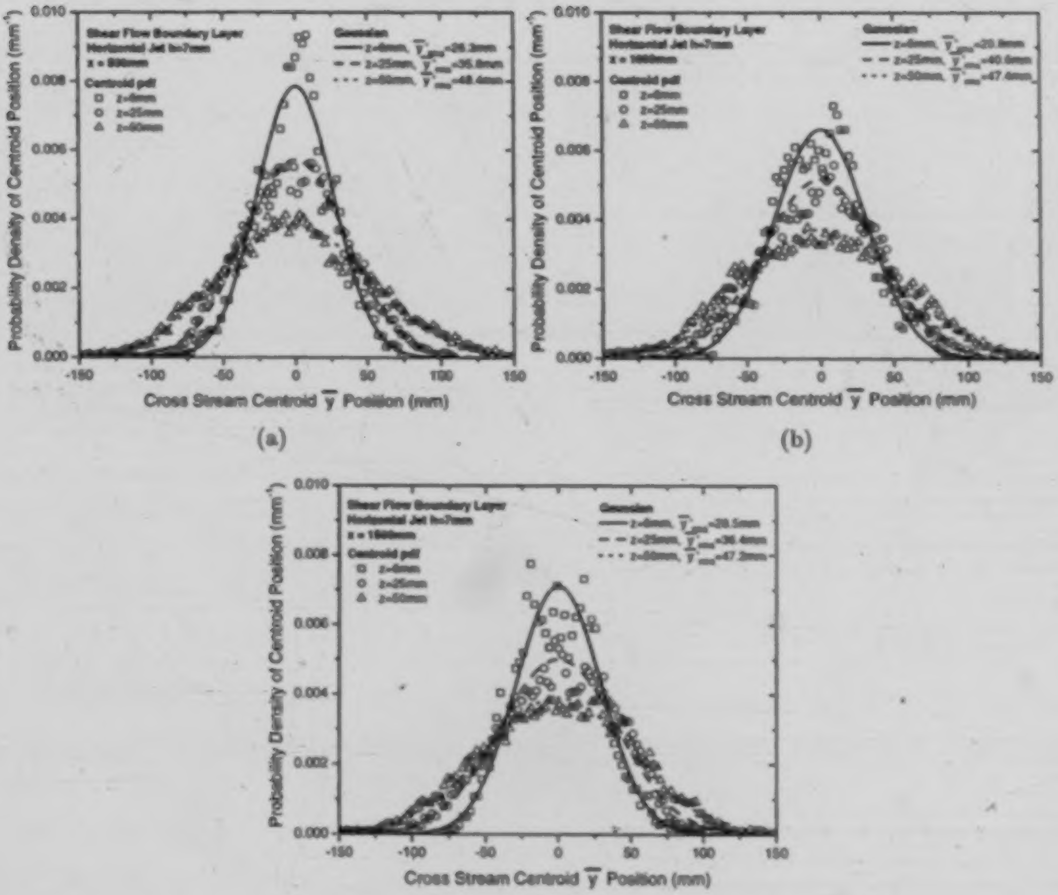

(a)

(b)

(c)

Figure F.11: Probability density functions of centroid position $\overline{y}$ compared to a Gaussian for the horizontal jet source at $h = 7$ mm at a flow rate $Q = 0.73$ ml/s and $z = 6$, 25, and 50 mm above the ground plotted on linear scales. (a) $x = 500$ mm (b) $x = 1000$ mm (c) $x = 1500$ mm

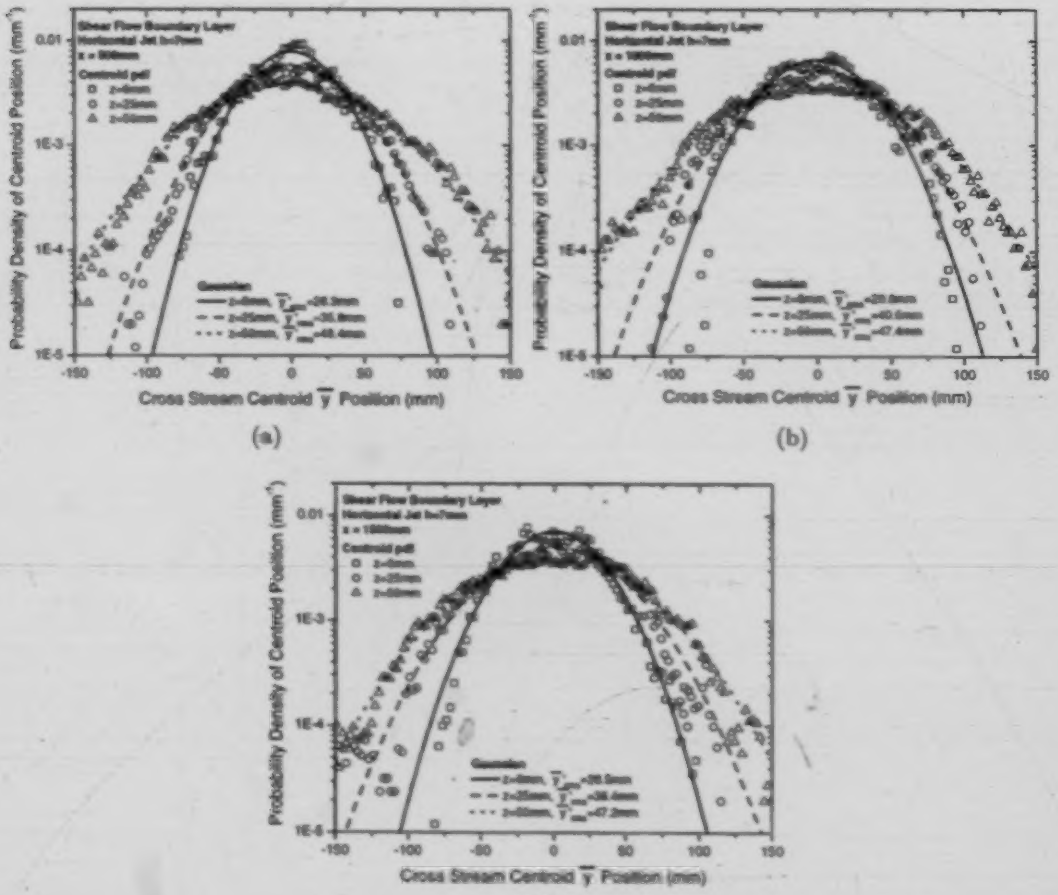

(a)

(b)

(c)

Figure F.12: Probability density functions of centroid position $\overline{y}$ compared to a Gaussian for the horizontal jet source at $h = 7$ mm at a flow rate $Q = 0.73$ ml/s and $z = 6$, 25, and 50 mm above the ground plotted on log-linear scales. (a) $x = 500$ mm (b) $x = 1000$ mm (c) $x = 1500$ mm

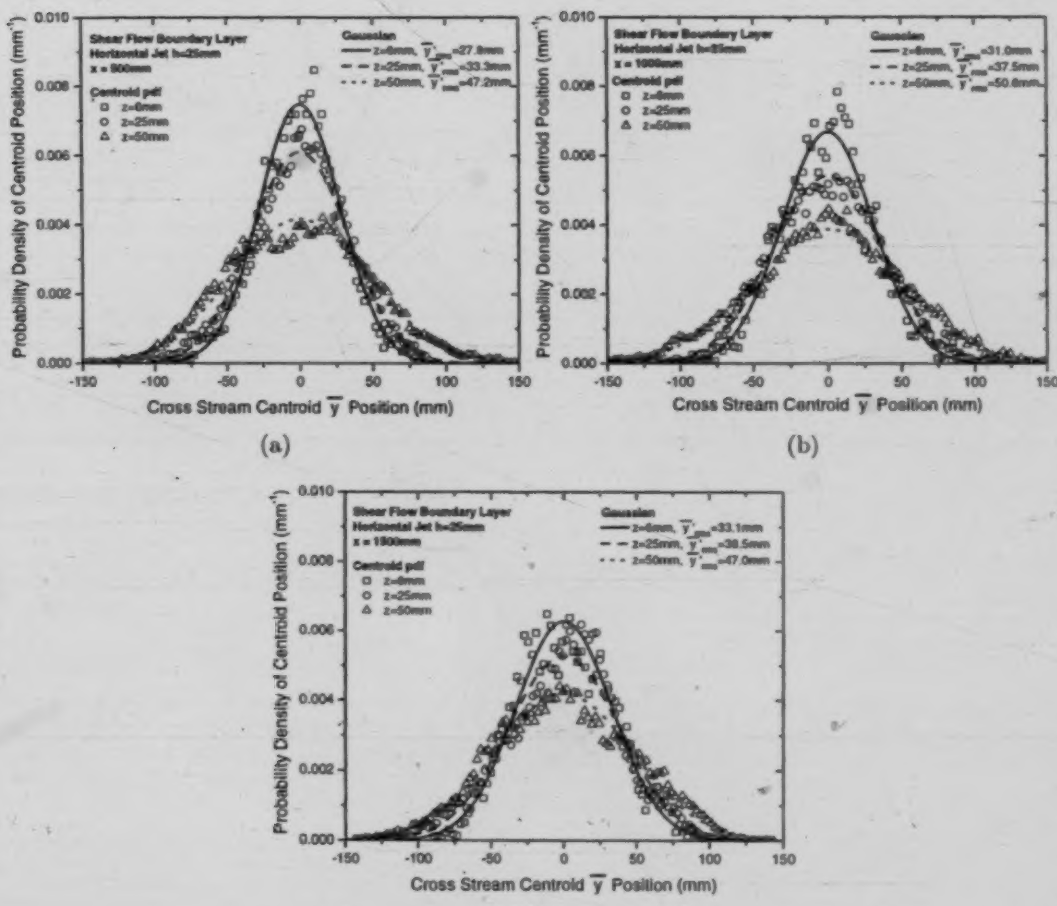

(a)

(b)

(c)

Figure F.13: Probability density functions of centroid position $\overline{y}$ compared to a Gaussian for the horizontal jet source at $h = 25$ mm at a flow rate $Q = 1.47$ ml/s and $z = 6$, 25, and 50 mm above the ground plotted on linear scales. (a) $x = 500$ mm (b) $x = 1000$ mm (c) $x = 1500$ mm

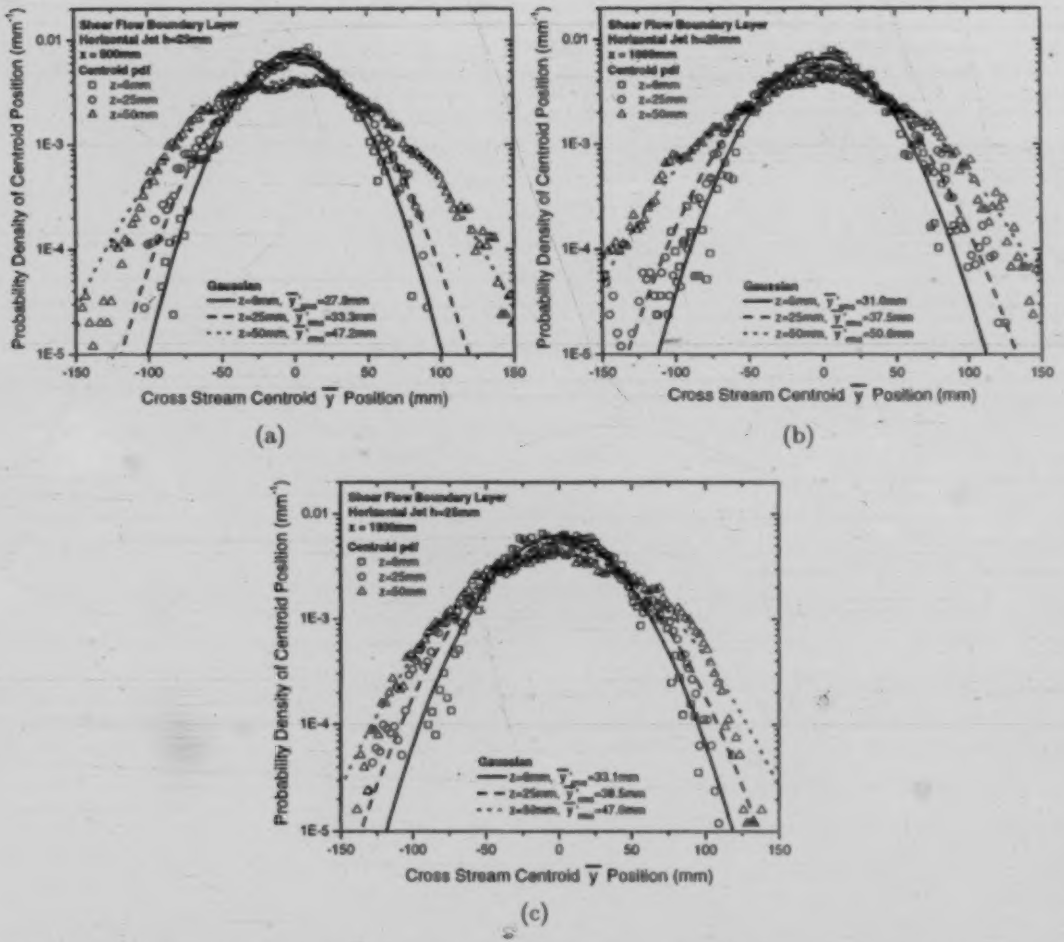

(a) (b)

(c)

Figure F.14: Probability density functions of centroid position $\overline{y}$ compared to a Gaussian for the horizontal jet source at h = 25 mm at a flow rate Q = 1.47 ml/s and z = 6, 25, and 50 mm above the ground plotted on log-linear scales. (a) x = 500 mm (b) x = 1000 mm (c) x = 1500 mm

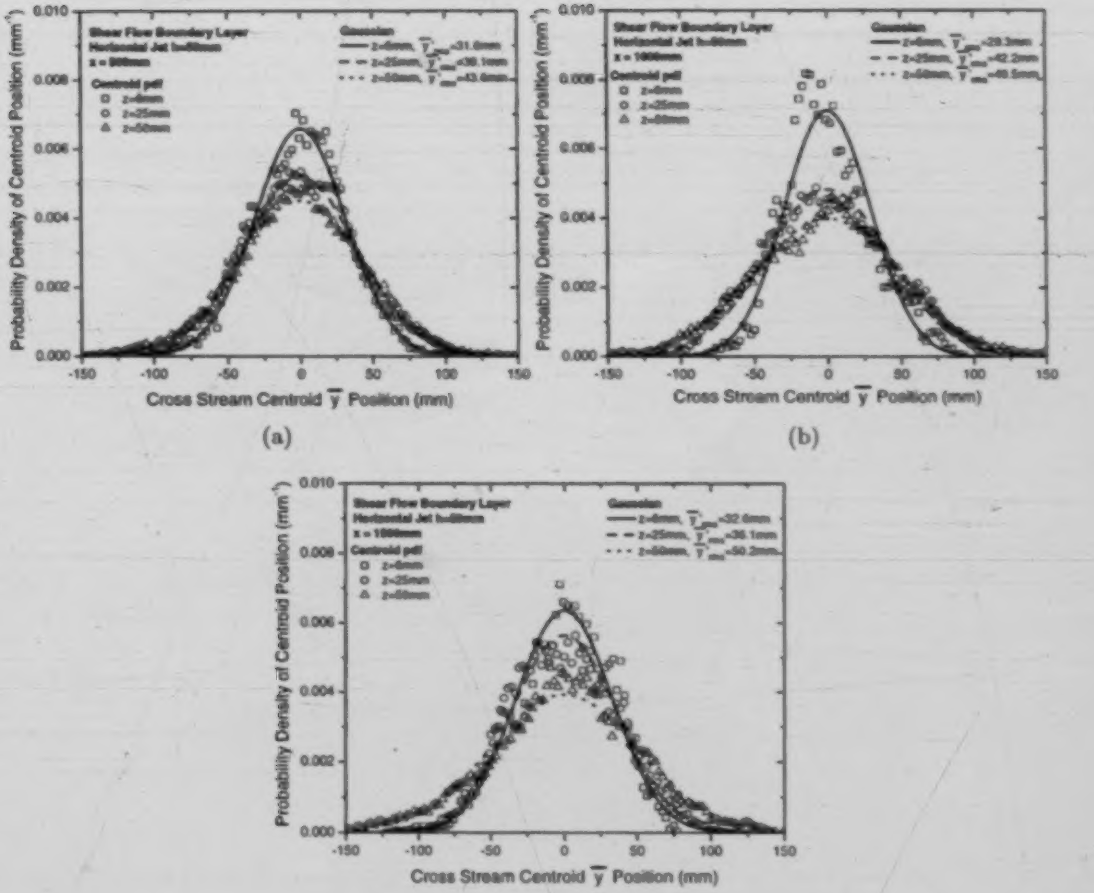

(a) (b)

(c)

Figure F.15: Probability density functions of centroid position $\overline{y}$ compared to a Gaussian for the horizontal jet source at $h = 50$ mm at a flow rate $Q = 1.47$ ml/s and $z = 6$, 25, and 50 mm above the ground plotted on linear scales. (a) $x = 500$ mm (b) $x = 1000$ mm (c) $x = 1500$ mm

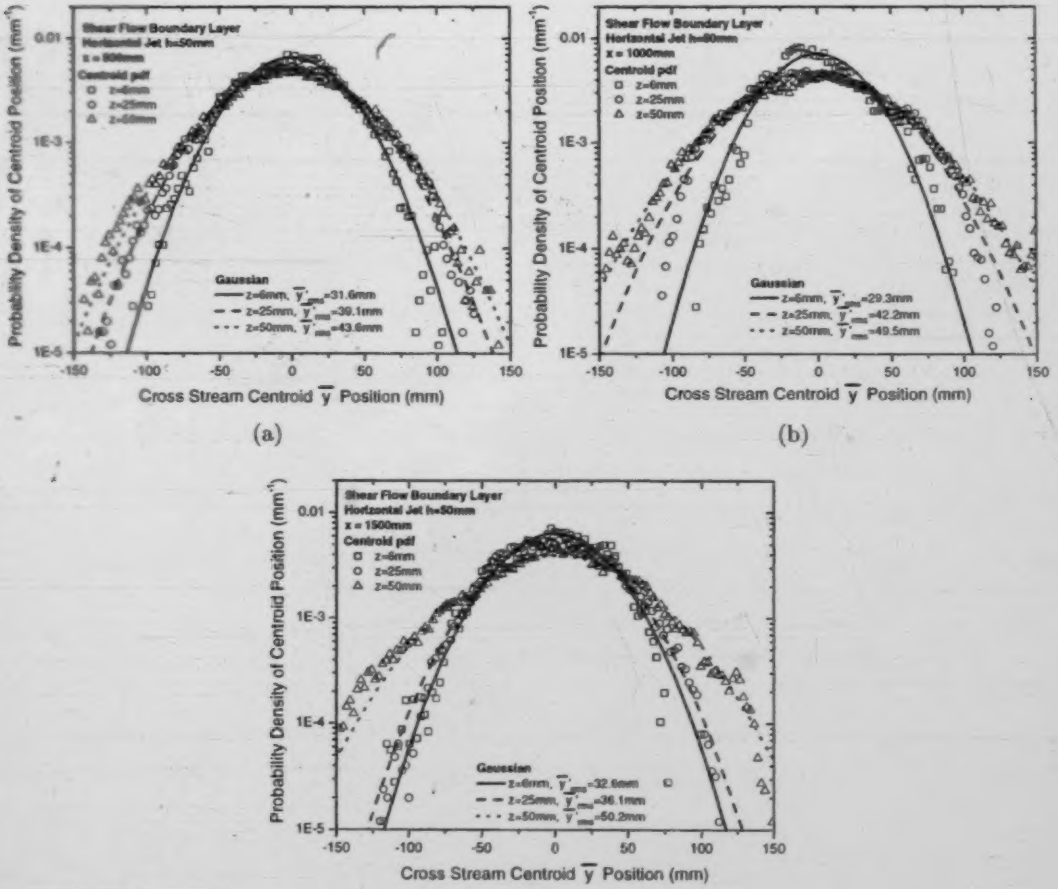

(a) (b)

(c)

Figure F.16: Probability density functions of centroid position $\overline{y}$ compared to a Gaussian for the horizontal jet source at $h = 50$ mm at a flow rate $Q = 1.47$ ml/s and $z = 6$, 25, and 50 mm above the ground plotted on log-linear scales. (a) $x = 500$ mm (b) $x = 1000$ mm (c) $x = 1500$ mm

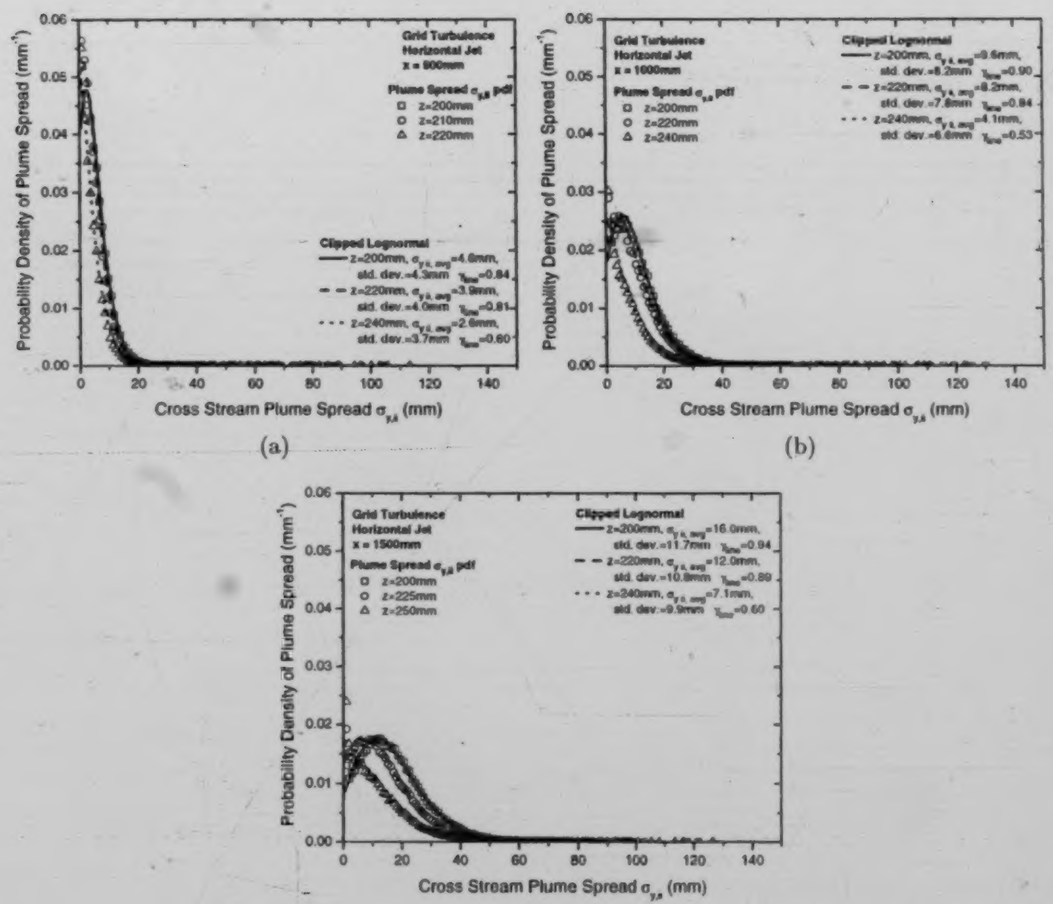

(a) (b)

(c)

Figure F.17: Probability density functions of plume spread σ_y compared to a clipped lognormal for the iso-kinetic horizontal jet source in grid turbulence plotted on linear scales. (a) $x = 500$ mm and $z = 200$, 210, 220 mm (b) $x = 1000$ mm and $z = 200$, 220, 240 mm (c) $x = 1500$ mm and $z = 200$, 225, 250 mm

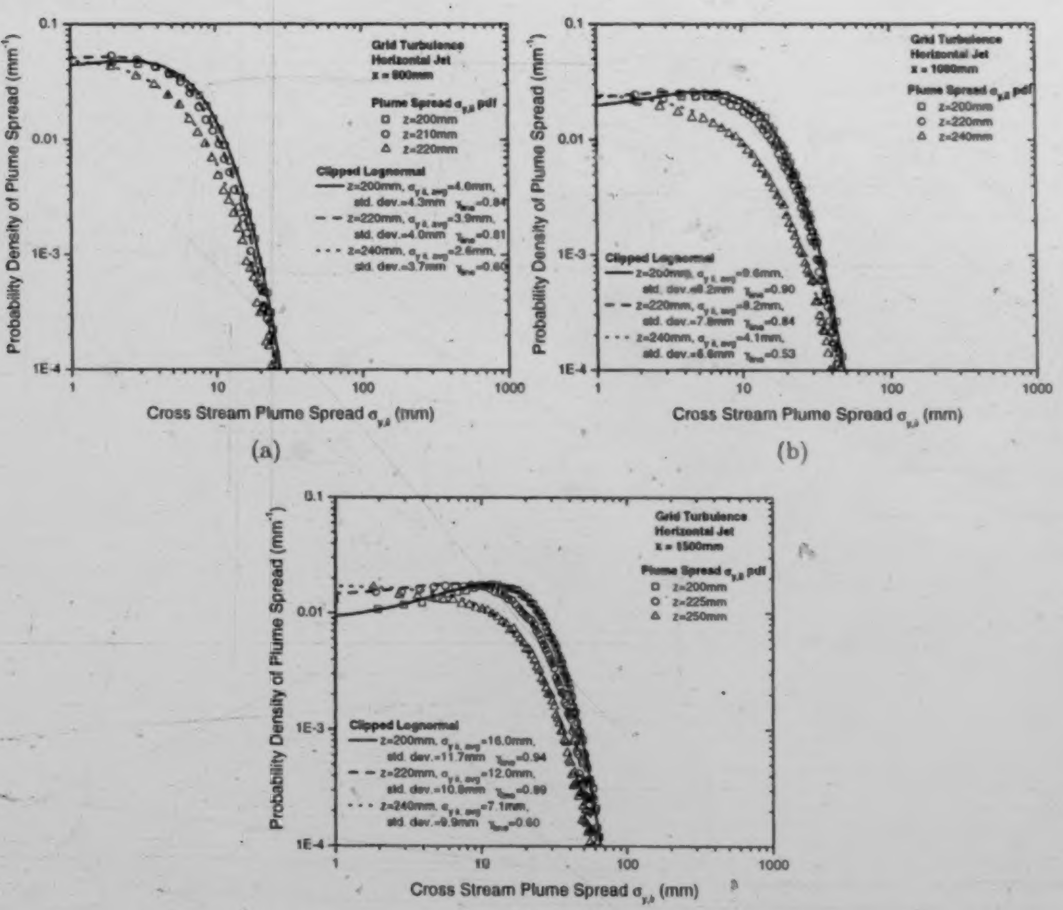

(a) (b)

(c)

Figure F.18: Probability density functions of plume spread σ_y compared to a clipped lognormal for the iso-kinetic horizontal jet source in grid turbulence plotted on logarithmic scales. (a) x = 500 mm and z = 200, 210, 220 mm (b) x = 1000 mm and z = 200, 220, 240 mm (c) x = 1500 mm and z = 200, 225, 250 mm

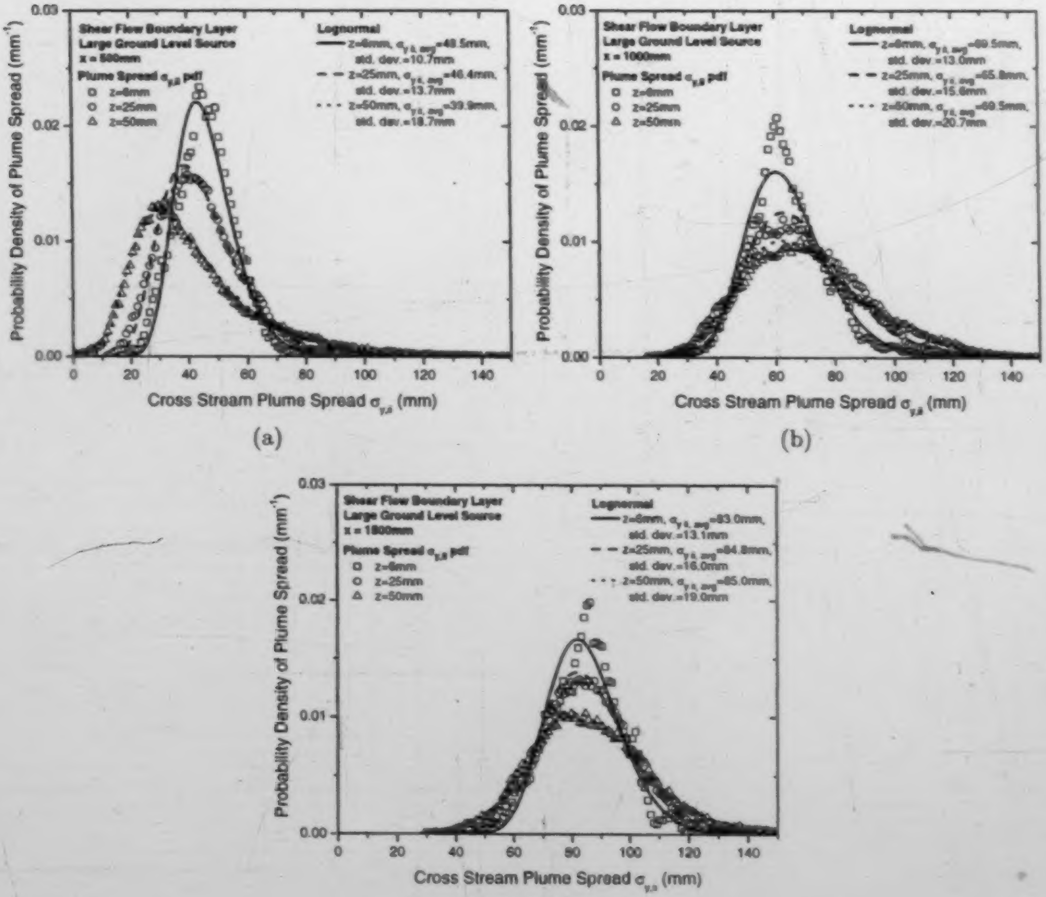

(a) (b)

(c)

Figure F.19: Probability density functions of plume spread σ_y compared to a lognormal for the large ground level source at a flow rate $Q = 1.47$ ml/s and $z = 6$, 25, and 50 mm above the ground plotted on linear scales. (a) $x = 500$ mm (b) $x = 1000$ mm (c) $x = 1500$ mm

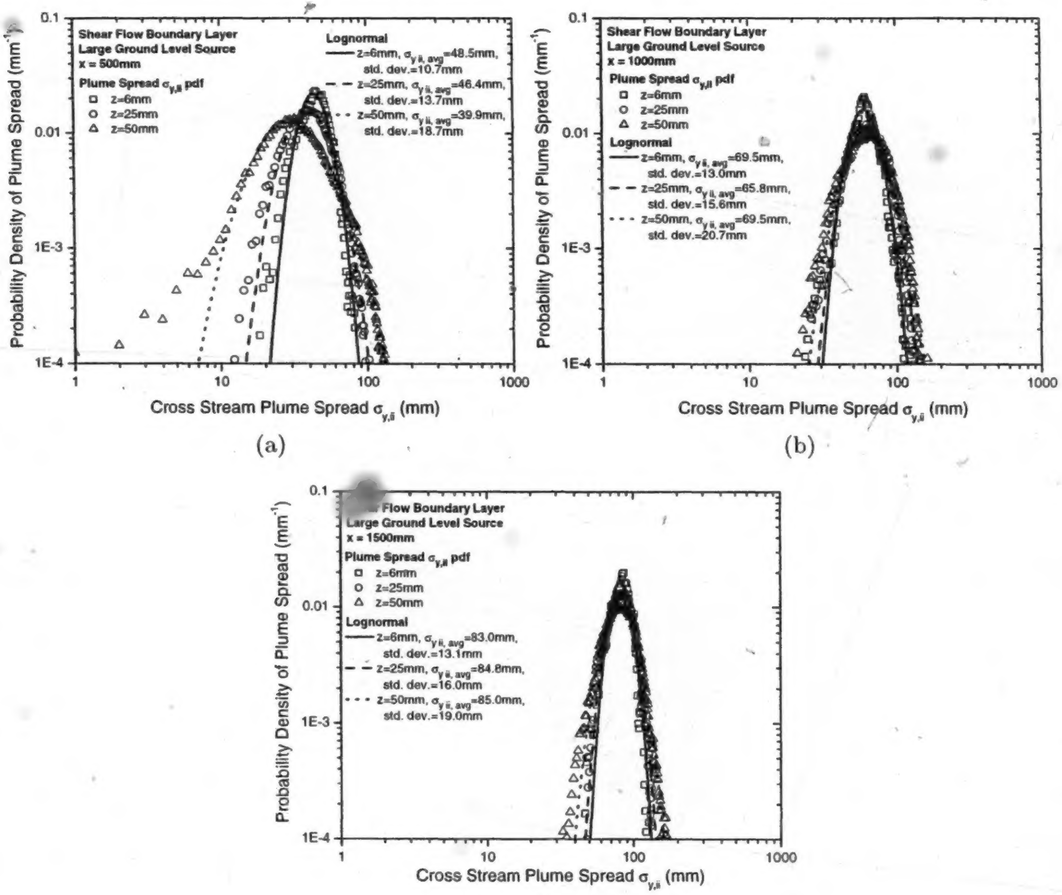

(a) (b) (c)

Figure F.20: Probability density functions of plume spread σ_y compared to a lognormal for the large ground level source at a flow rate $Q = 1.47$ ml/s and $z = 6$, 25, and 50 mm above the ground plotted on logarithmic scales. (a) $x = 500$ mm (b) $x = 1000$ mm (c) $x = 1500$ mm

7

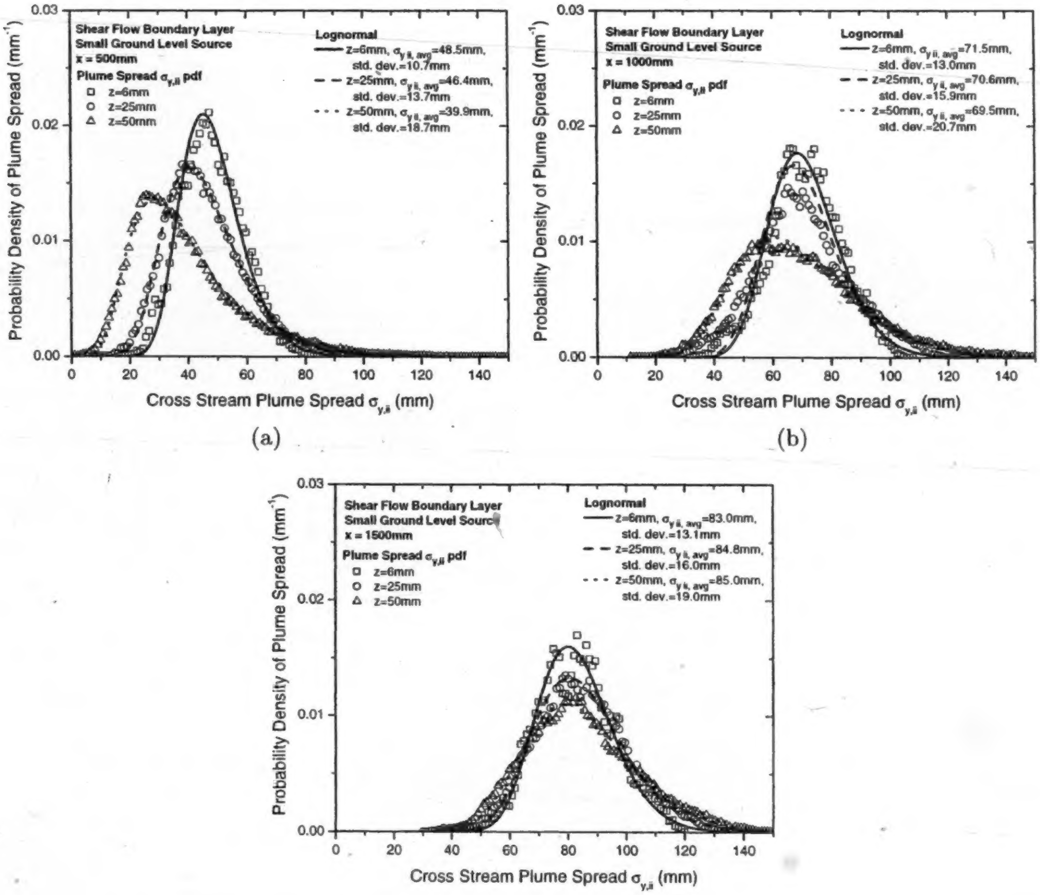

(a) (b)

(c)

Figure F.21: Probability density functions of plume spread σ_y compared to a lognormal for the small ground level vertical jet source at a flow rate $Q = 1.47$ ml/s and $z = 6$, 25, and 50 mm above the ground plotted on linear scales. (a) $x = 500$ mm (b) $x = 1000$ mm (c) $x = 1500$ mm

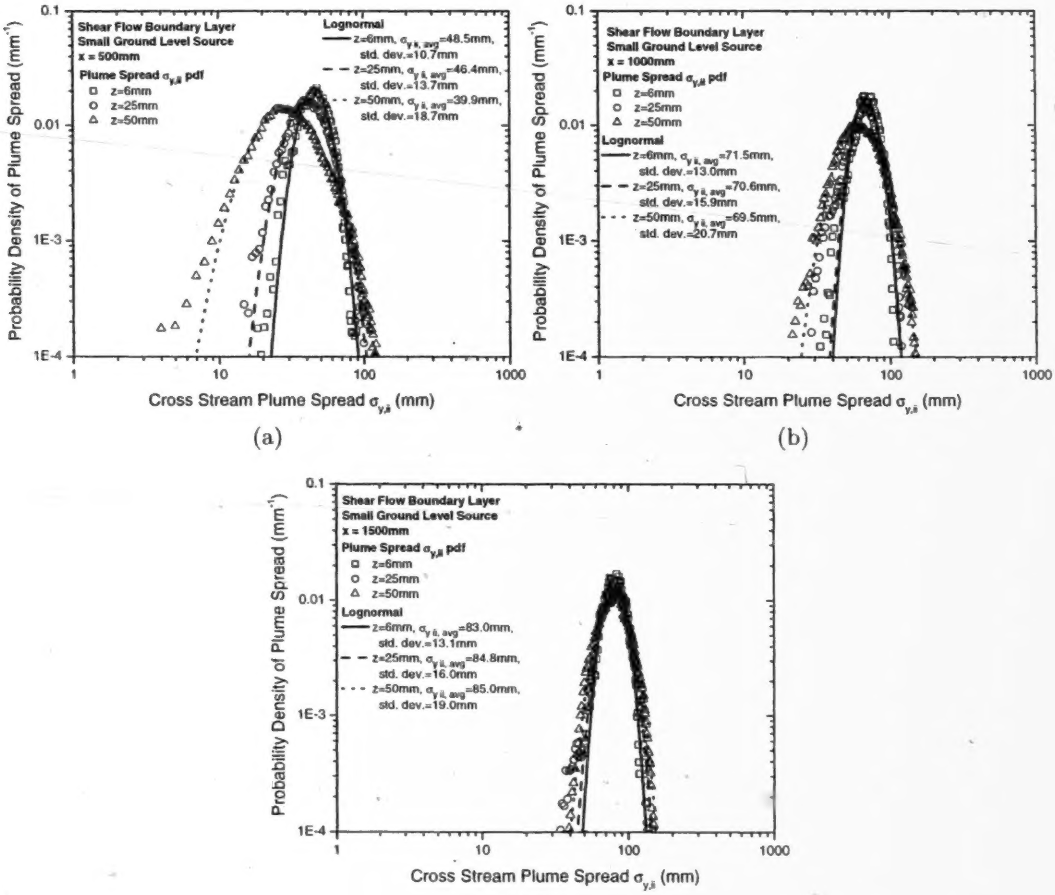

(a)

(b)

(c)

Figure F.22: Probability density functions of plume spread σ_y compared to a lognormal for the small ground level vertical jet source at a flow rate $Q = 1.47$ ml/s and $z = 6$, 25, and 50 mm above the ground plotted on logarithmic scales. (a) $x = 500$ mm (b) $x = 1000$ mm (c) $x = 1500$ mm

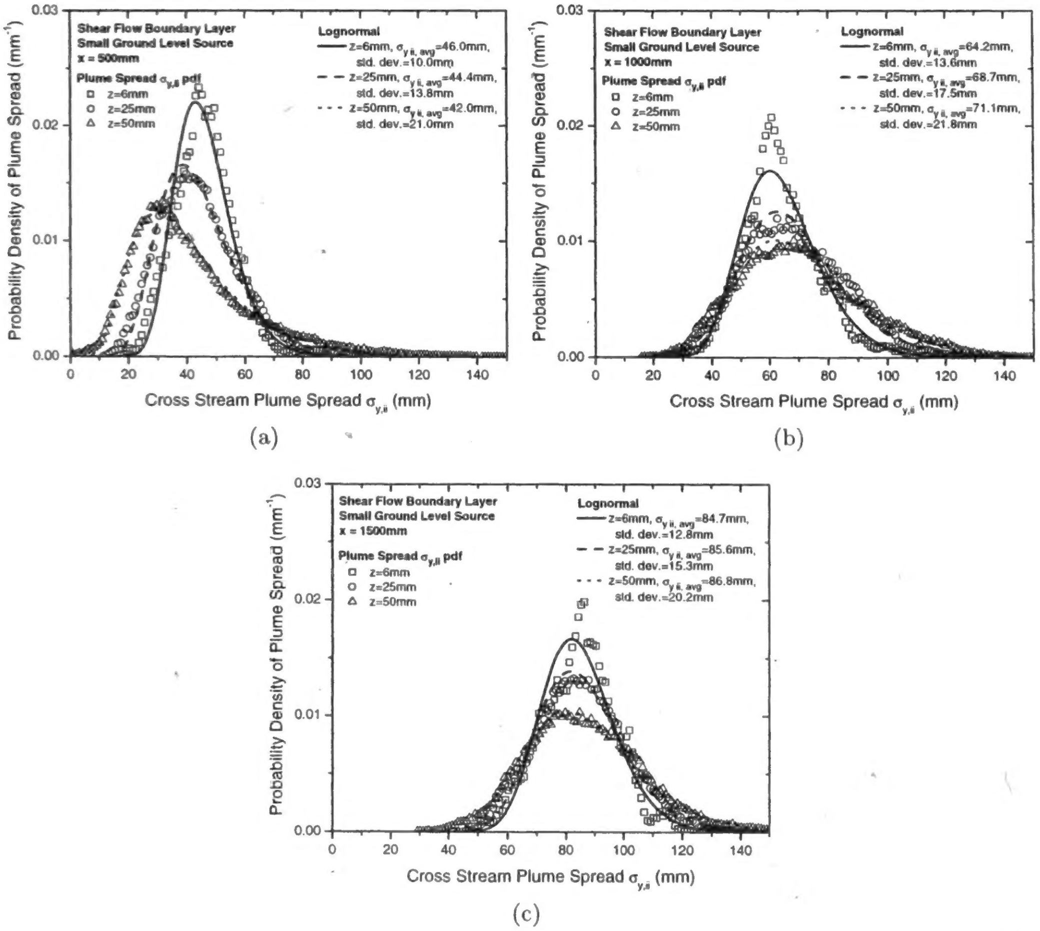

(a) (b) (c)

Figure F.23: Probability density functions of plume spread σ_y compared to a lognormal for the small ground level vertical jet source at a flow rate $Q = 0.73$ ml/s and $z = 6$, 25, and 50 mm above the ground plotted on linear scales. (a) $x = 500$ mm (b) $x = 1000$ mm (c) $x = 1500$ mm

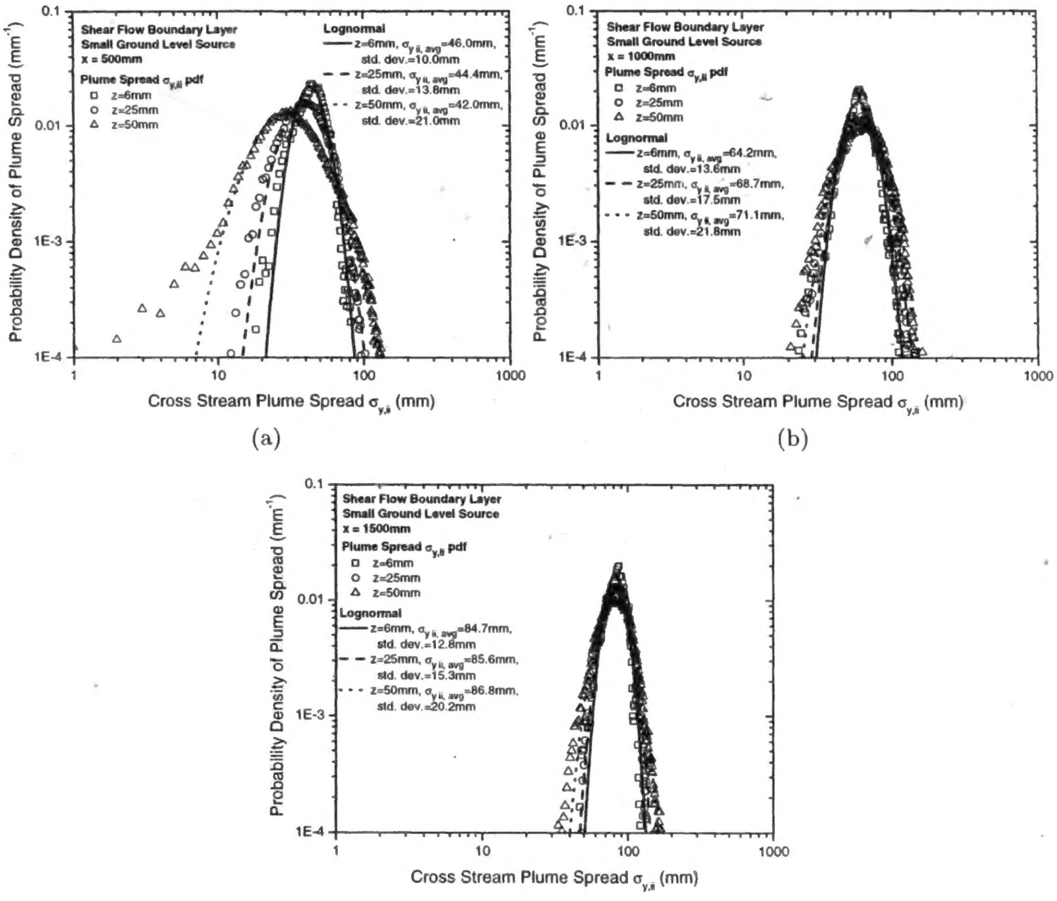

(a) (b) (c)

Figure F.24: Probability density functions of plume spread σ_y compared to a lognormal for the small ground level vertical jet source at a flow rate $Q = 0.73$ ml/s and $z = 6$, 25, and 50 mm above the ground plotted on logarithmic scales. (a) $x = 500$ mm (b) $x = 1000$ mm (c) $x = 1500$ mm

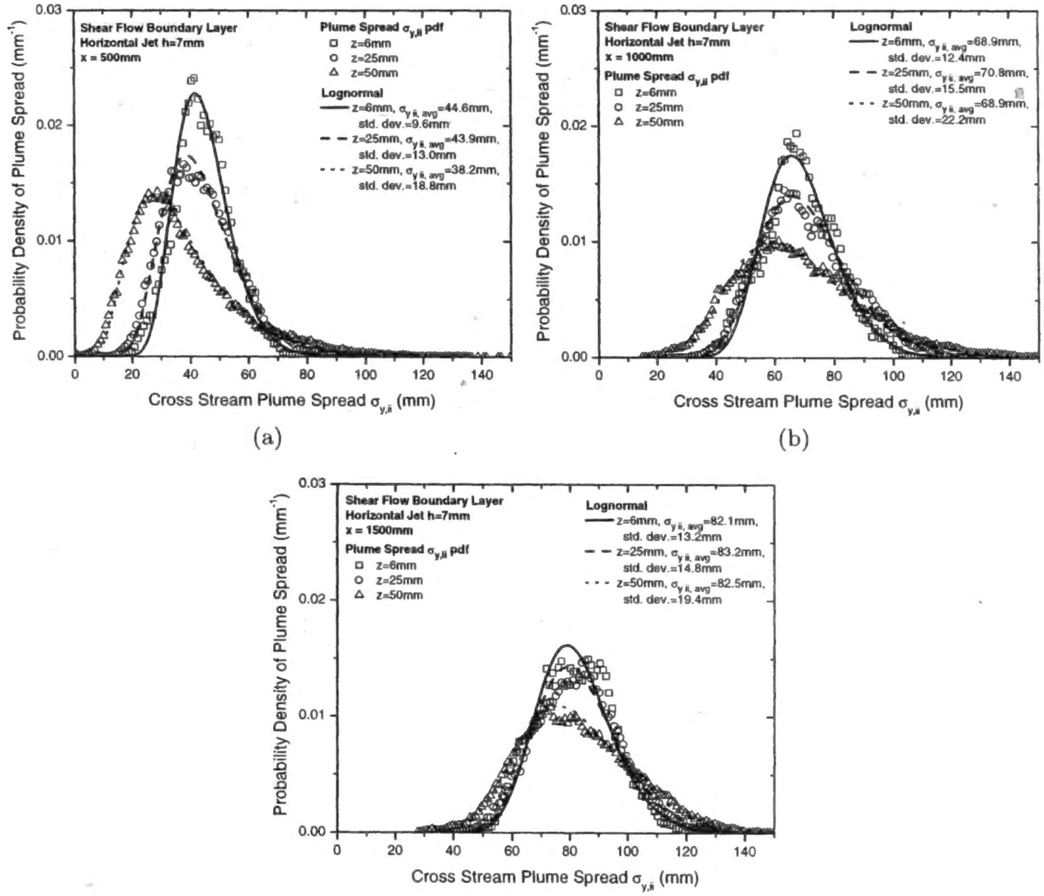

(a) (b)

(c)

Figure F.25: Probability density functions of plume spread σ_y compared to a lognormal for the horizontal jet source at $h = 7$ mm at a flow rate $Q = 1.47$ ml/s and $z = 6$, 25, and 50 mm above the ground plotted on linear scales. (a) $x = 500$ mm (b) $x = 1000$ mm (c) $x = 1500$ mm

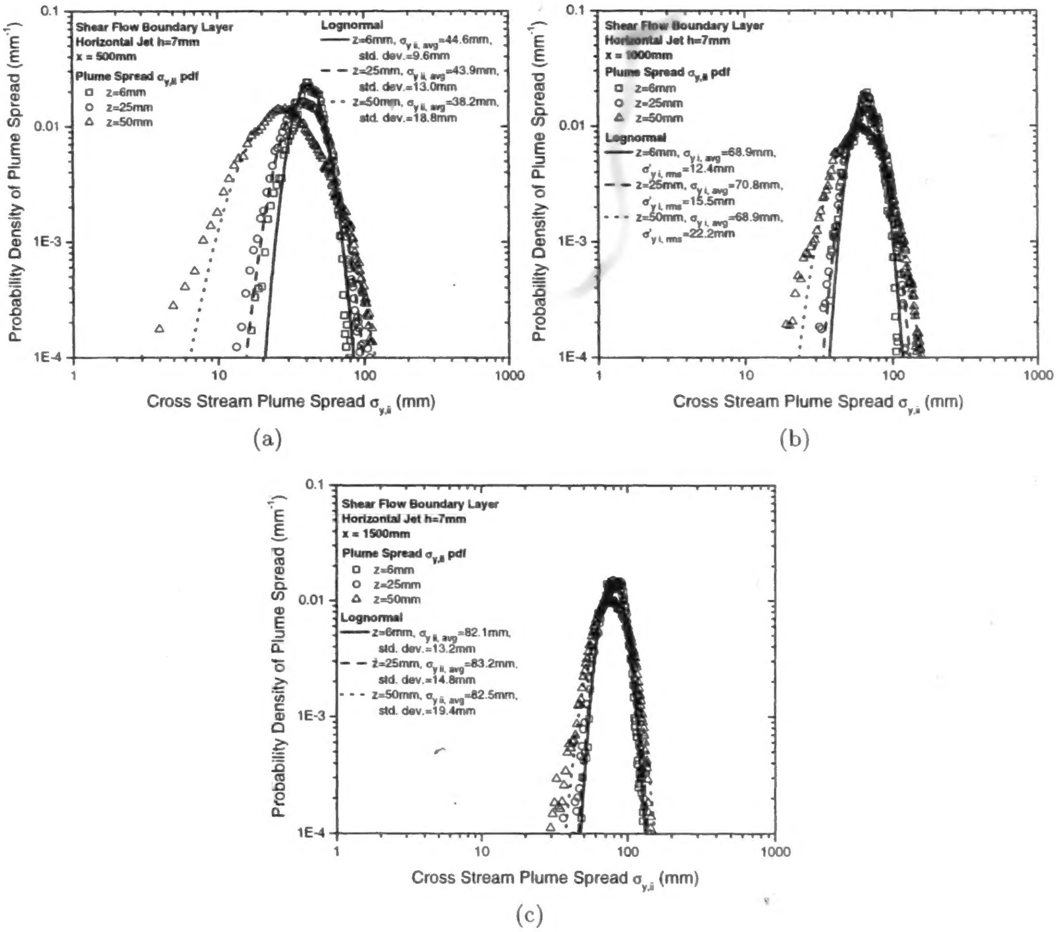

(a) (b) (c)

Figure F.26: Probability density functions of plume spread σ_y compared to a lognormal for the horizontal jet source at $h = 7$ mm at a flow rate $Q = 1.47$ ml/s and $z = 6$, 25, and 50 mm above the ground plotted on logarithmic scales. (a) $x = 500$ mm (b) $x = 1000$ mm (c) $x = 1500$ mm

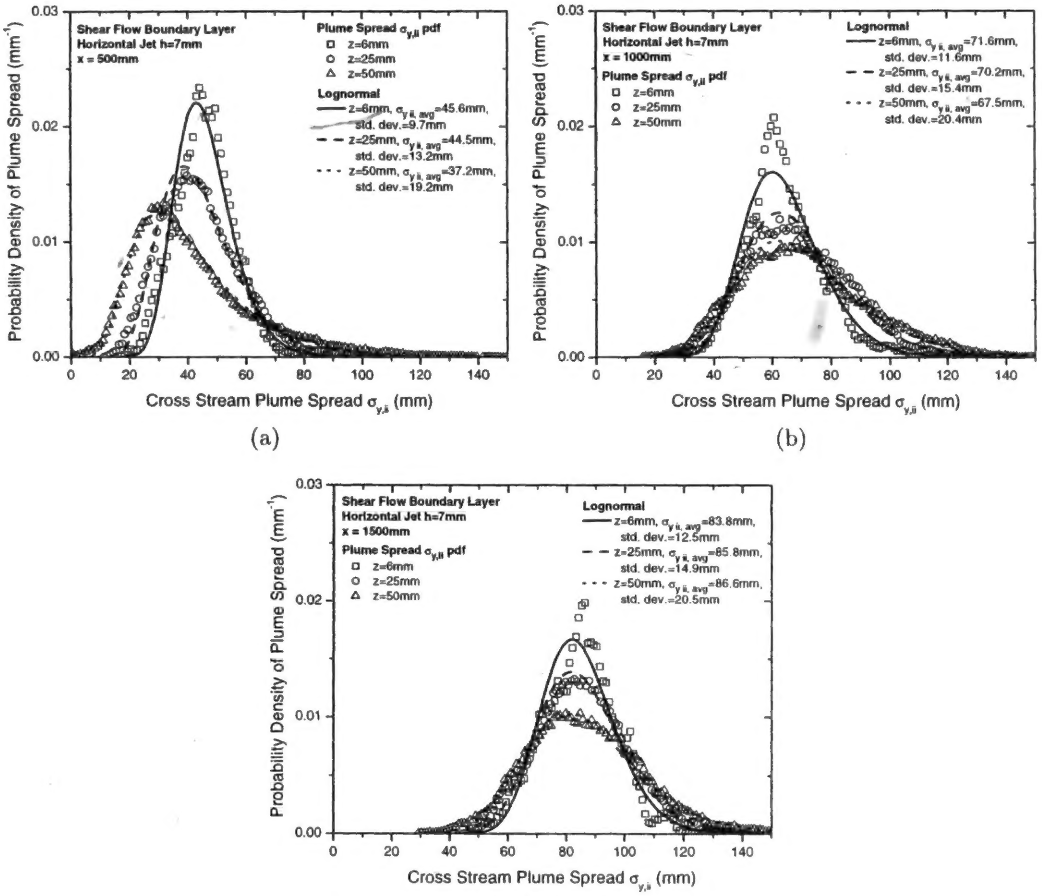

(a)

(b)

(c)

Figure F.27: Probability density functions of plume spread σ_y compared to a lognormal for the horizontal jet source at $h = 7$ mm at a flow rate $Q = 0.73$ ml/s and $z = 6$, 25, and 50 mm above the ground plotted on linear scales. (a) $x = 500$ mm (b) $x = 1000$ mm (c) $x = 1500$ mm

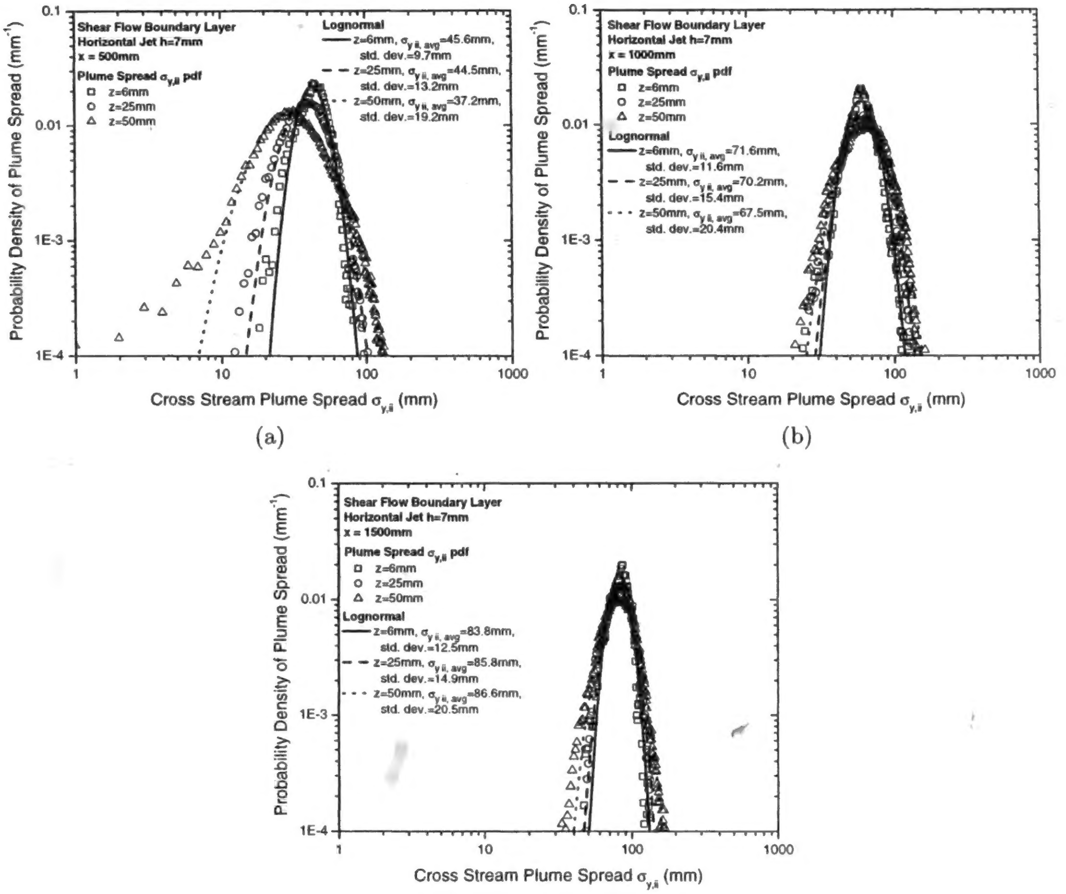

(a) (b)

(c)

Figure F.28: Probability density functions of plume spread σ_y compared to a lognormal for the horizontal jet source at $h = 7$ mm at a flow rate $Q = 0.73$ ml/s and $z = 6$, 25, and 50 mm above the ground plotted on logarithmic scales. (a) $x = 500$ mm (b) $x = 1000$ mm (c) $x = 1500$ mm

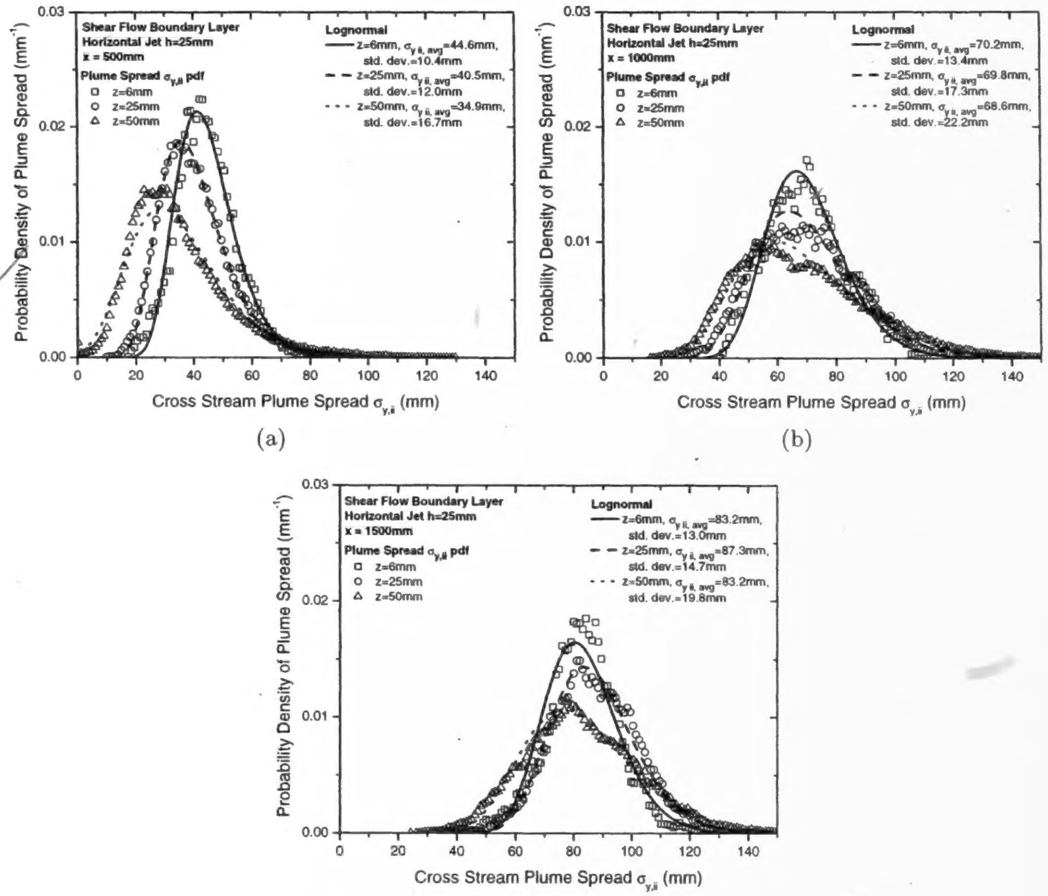

(a) (b)

(c)

Figure F.29: Probability density functions of plume spread σ_y compared to a lognormal for the horizontal jet source at $h = 25$ mm at a flow rate $Q = 1.47$ ml/s and $z = 6$, 25, and 50 mm above the ground plotted on linear scales. (a) $x = 500$ mm (b) $x = 1000$ mm (c) $x = 1500$ mm

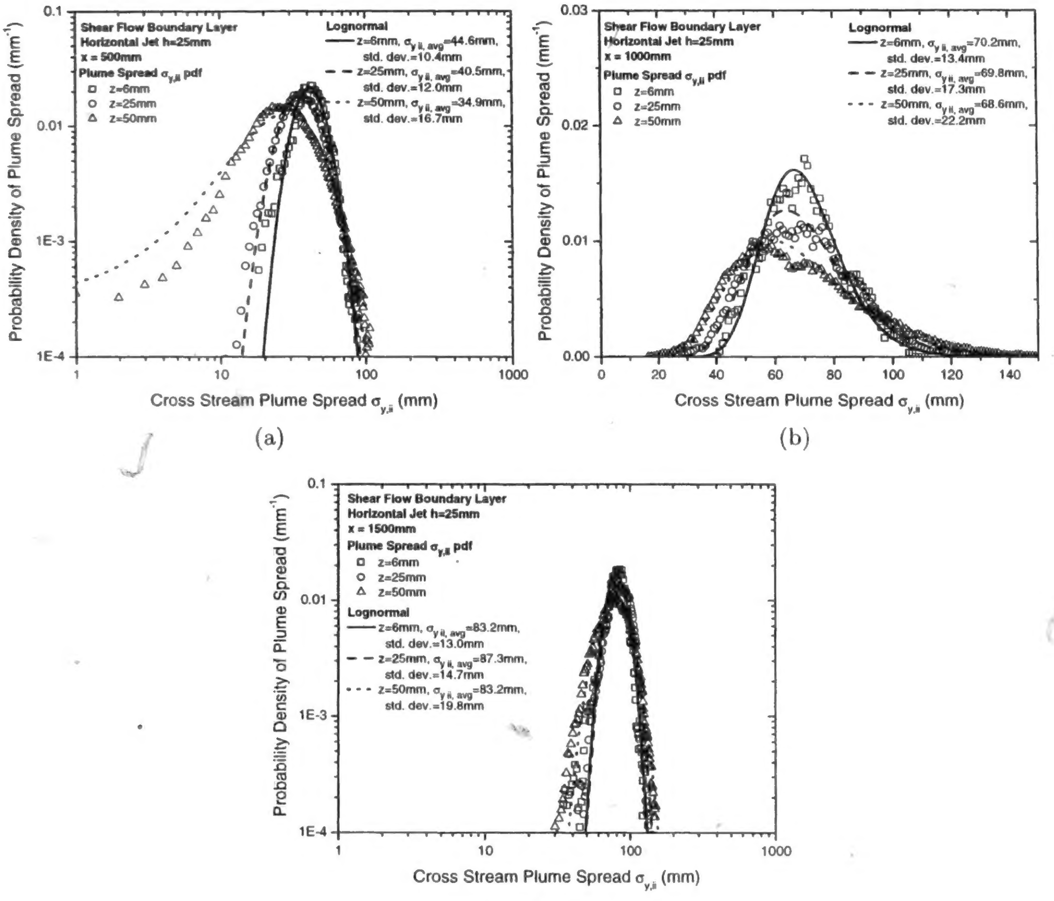

(a) (b)

(c)

Figure F.30: Probability density functions of plume spread σ_y compared to a lognormal for the horizontal jet source at $h = 25$ mm at a flow rate $Q = 0.73$ ml/s and $z = 6$, 25, and 50 mm above the ground plotted on linear scales. (a) $x = 500$ mm (b) $x = 1000$ mm (c) $x = 1500$ mm

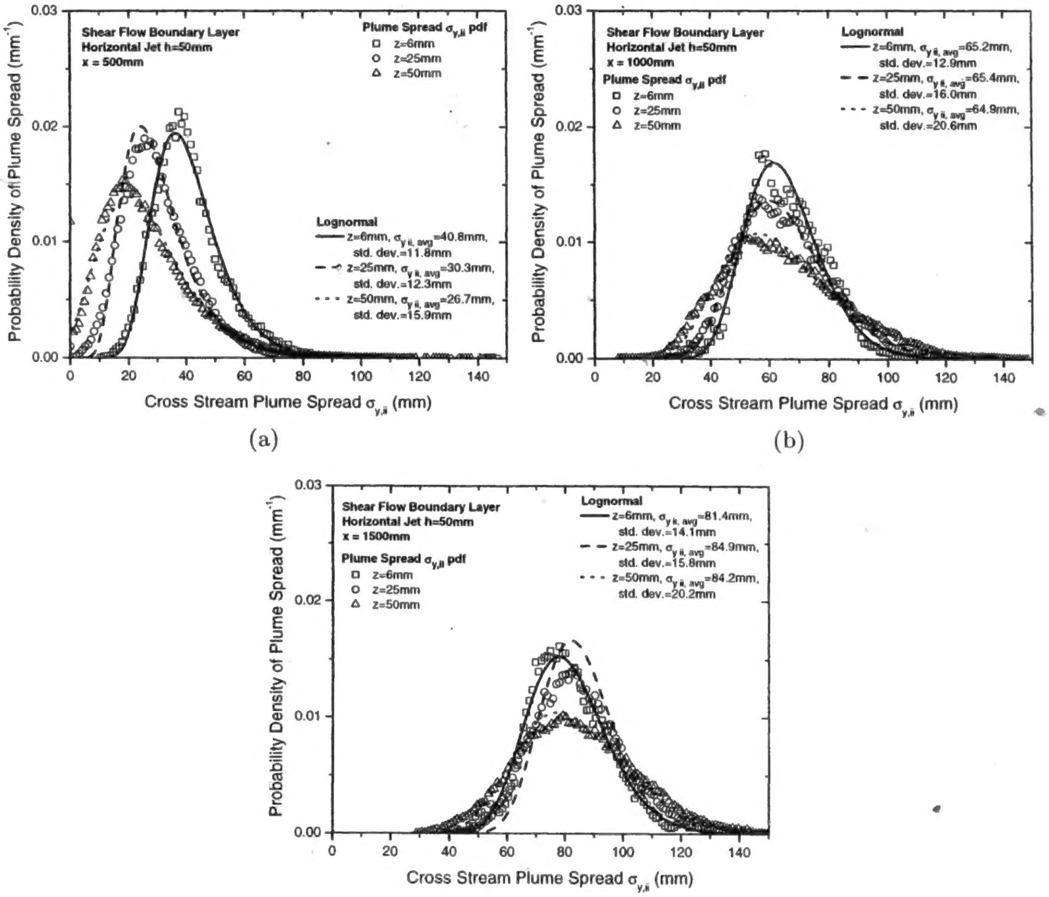

(a)

(b)

(c)

Figure F.31: Probability density functions of plume spread σ_y compared to a lognormal for the horizontal jet source at $h = 50$ mm at a flow rate $Q = 1.47$ ml/s and $z = 6$, 25, and 50 mm above the ground plotted on linear scales. (a) $x = 500$ mm (b) $x = 1000$ mm (c) $x = 1500$ mm

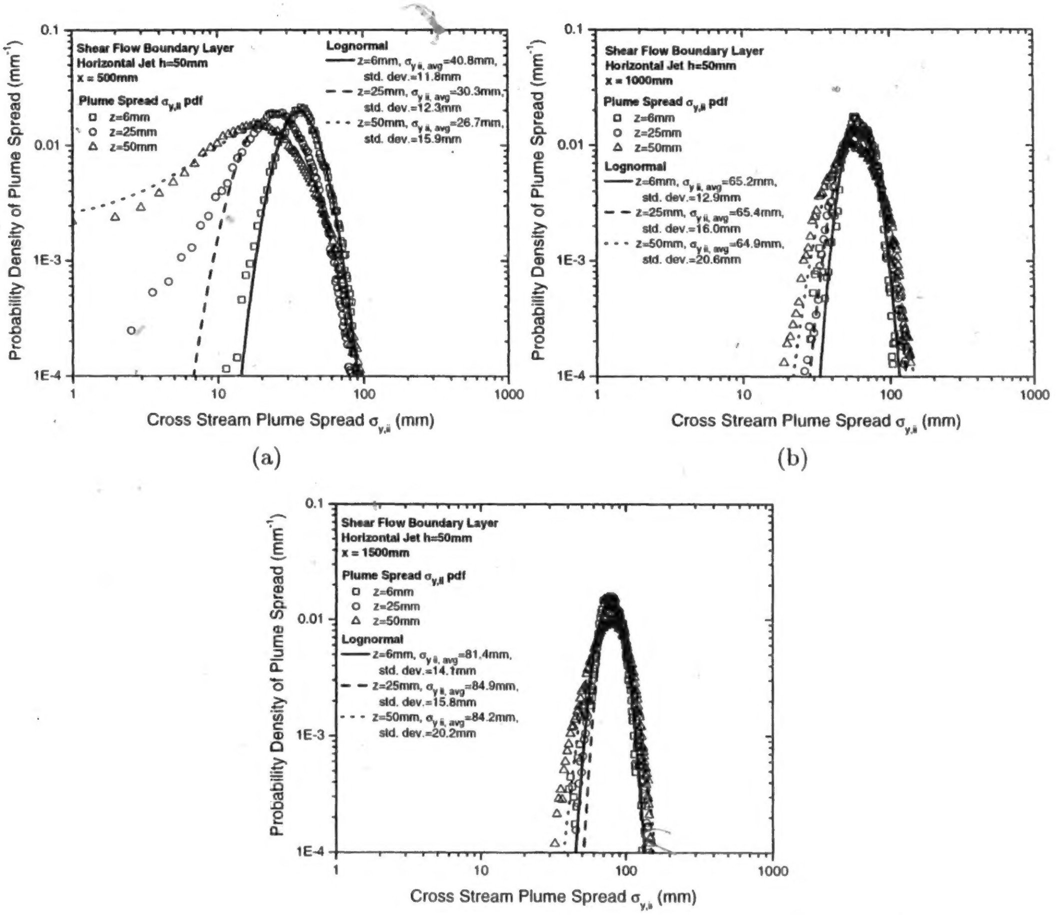

(a) (b)

(c)

Figure F.32: Probability density functions of plume spread σ_y compared to a lognormal for the horizontal jet source at $h = 50$ mm at a flow rate $Q = 1.47$ ml/s and $z = 6$, 25, and 50 mm above the ground plotted on logarithmic scales. (a) $x = 500$ mm (b) $x = 1000$ mm (c) $x = 1500$ mm

Appendix G

Travel Time Power Law Averaging Time Model compared to Water Channel Data

This appendix contains additional plots of the travel time power law averaging time adjustment model (TTPL) compared to the experimental data to supplement the examples shown in Chapter 2 Section 2.5.6. The model is discussed in more detail in Section 2.5.

As discussed in Chapter 2 the cross-stream Lagrangian time scale in shear flow is $T_{Lv} = 1.0$ s (in normalized terms $T_{Lv}U_H/H = 0.58$) and in grid turbulence $T_{Lv} = 1.2$ s ($T_{Lv}U/G = 3.1$). The Lagrangian time scale and local travel times t_t used in the TTPL model are indicated directly on the plots.

Figures G.1 to G.8 show the measured meander $M_{\text{spread}} = \sigma^2_{y,m}/\sigma^2_{y,i}$, compared to the meander predicted by the TTPL model. A representative line with the slope of the widely-used 0.2 power law averaging time adjustment from equation (2.17) is also shown on the graphs. Overall, the shape and the trends of the TTPL model are approximately correct, but the meander prediction is as much as a factor of 5 different for the shear flow cases and as much as 2 orders of magnitude underestimated in the grid turbulence. The general shape of meander M_{spread} from the TTPL is a power law with a slope of approximately 1.0 at small averaging times levelling off to a steady value as averaging time becomes large. The meander values are under-predicted by up to an order of magnitude at large averaging times. At small averaging times, meander is under-predicted for elevated measurement positions and over-predicted for ground level measurements.

Figures G.9 to G.16 compare the TTPL model for plume spread ratio $\sigma_y/\sigma_{y,t_{\text{avg}}=500}$ to the water channel data. Except for the grid turbulence, the shape and the trends of the TTPL model are approximately correct. The worst predictions with errors of up to 15% are for positions close to the source. In the grid turbulence case the slope of the main section of the TTPL seems to be approximately correct, but the absolute prediction of $\sigma_y/\sigma_{y,t_{\text{avg}}=500}$ is off by about 40%.

In all of the shear flow cases the TTPL model fits the data much better that the 0.2 power law from equation (2.17) using $\sigma_{y,t_{\text{avg}=10s}}$ as the reference spread. This reference value was chosen because it seems like the plume spread has stopped growing by $t_{\text{avg}} = 10$ s and it was necessary to create a line that would at appear on the same scales as the plots of the data and the TTPL model.

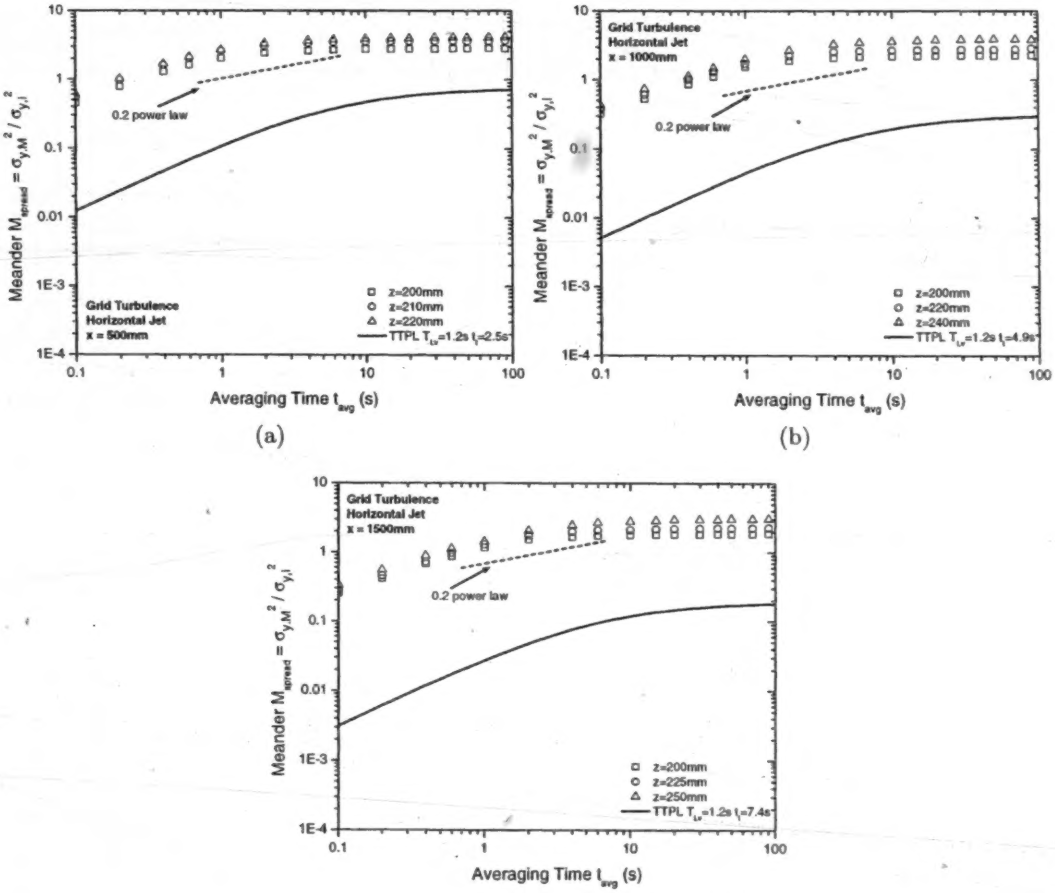

(a) (b)

(c)

Figure G.1: Measured meander M_{spread} compared to TTPL model and 0.2 power law for the iso-kinetic horizontal jet source in grid turbulence (a) $x = 500$ mm and $z = 200, 210, 220$ mm (b) $x = 1000$ mm and $z = 200, 220, 240$ mm (c) $x = 1500$ mm and $z = 200, 225, 250$ mm

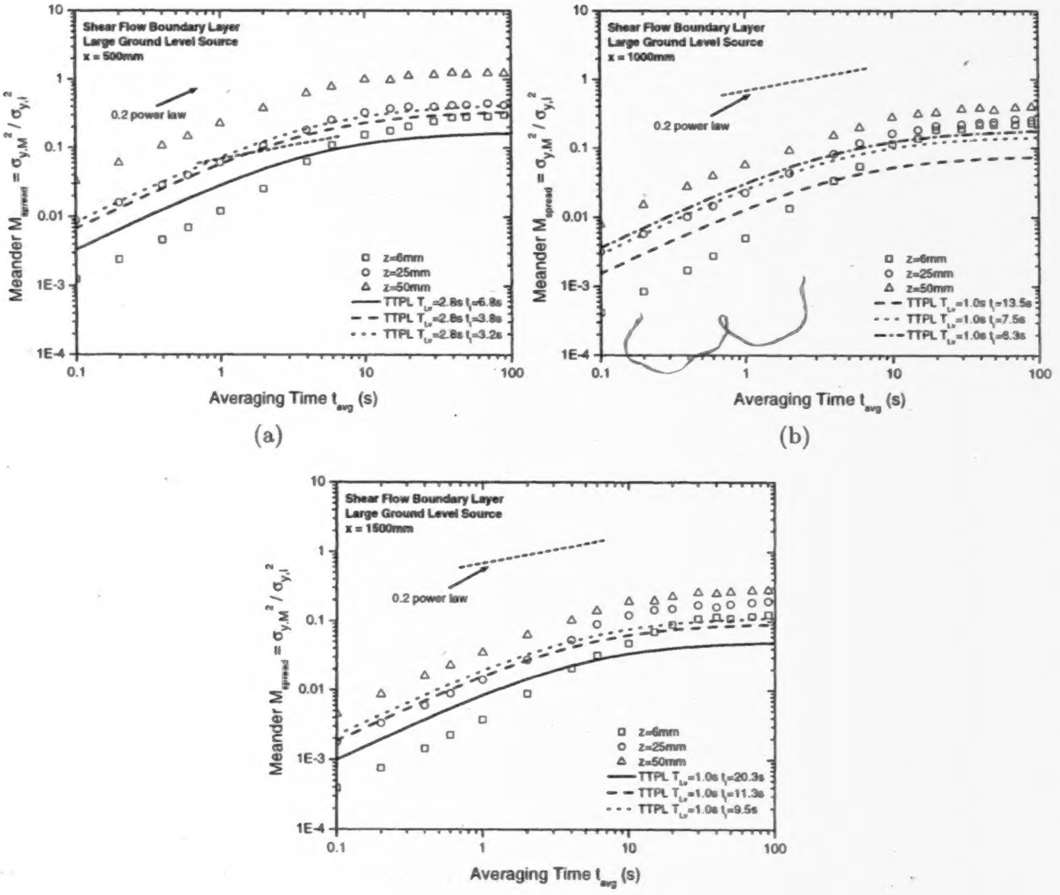

(a)

(b)

(c)

Figure G.2: Measured meander M_{spread} compared to TTPL model and 0.2 power law for the large ground level source at a flow rate $Q = 1.47$ ml/s and $z = 6$, 25, and 50 mm above the ground for (a) $x = 500$ mm (b) $x = 1000$ mm (c) $x = 1500$ mm

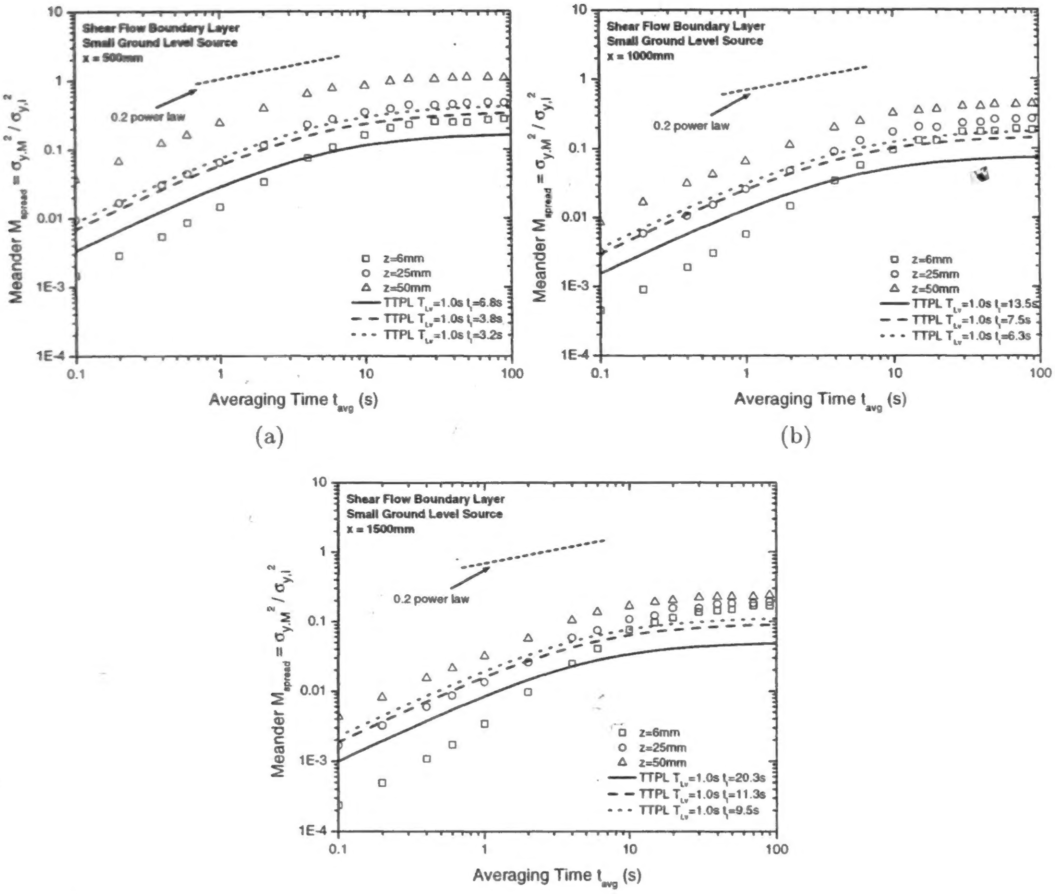

(a) (b)

(c)

Figure G.3: Measured meander M_{spread} compared to TTPL model and 0.2 power law for the small ground level vertical jet source at a flow rate $Q = 1.47$ ml/s and $z = 6$, 25, and 50 mm above the ground for (a) $x = 500$ mm (b) $x = 1000$ mm (c) $x = 1500$ mm

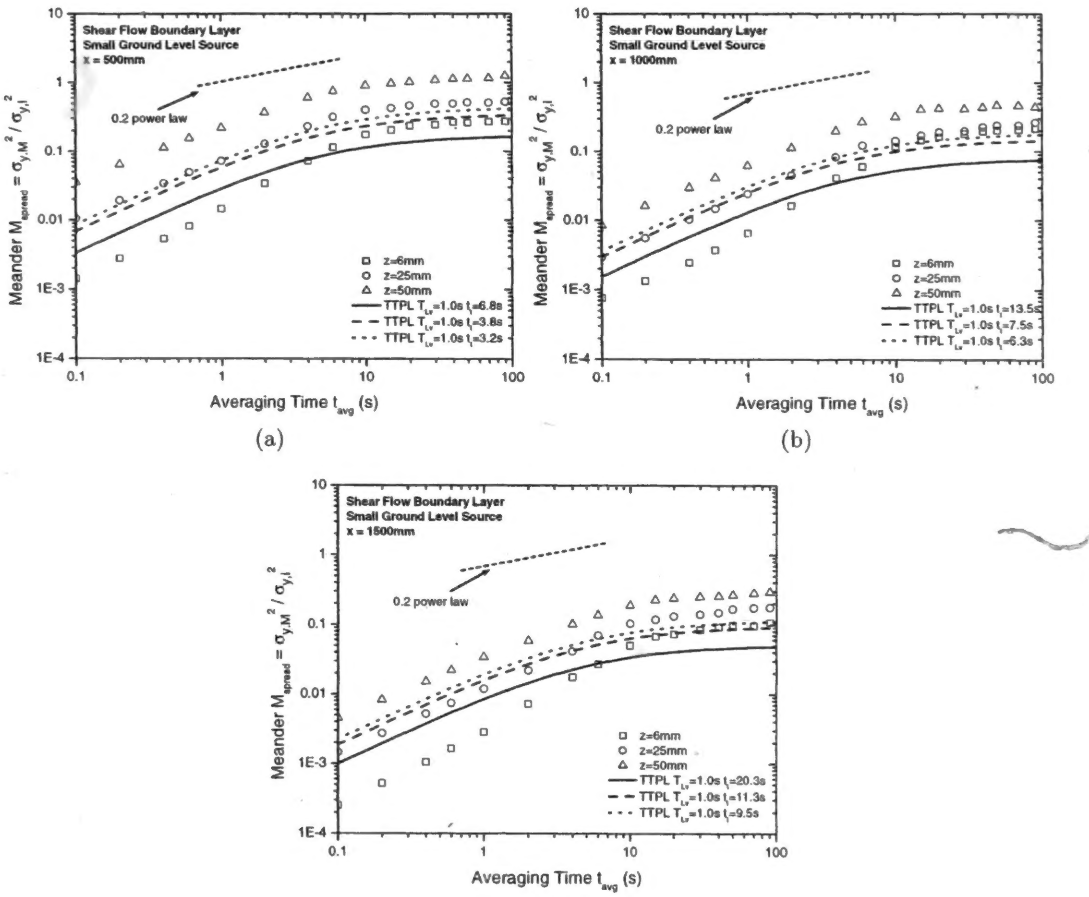

(a)

(b)

(c)

Figure G.4: Measured meander M_{spread} compared to TTPL model and 0.2 power law for the small ground level vertical jet source at a flow rate $Q = 0.73$ ml/s and $z = 6$, 25, and 50 mm above the ground for (a) $x = 500$ mm (b) $x = 1000$ mm (c) $x = 1500$ mm

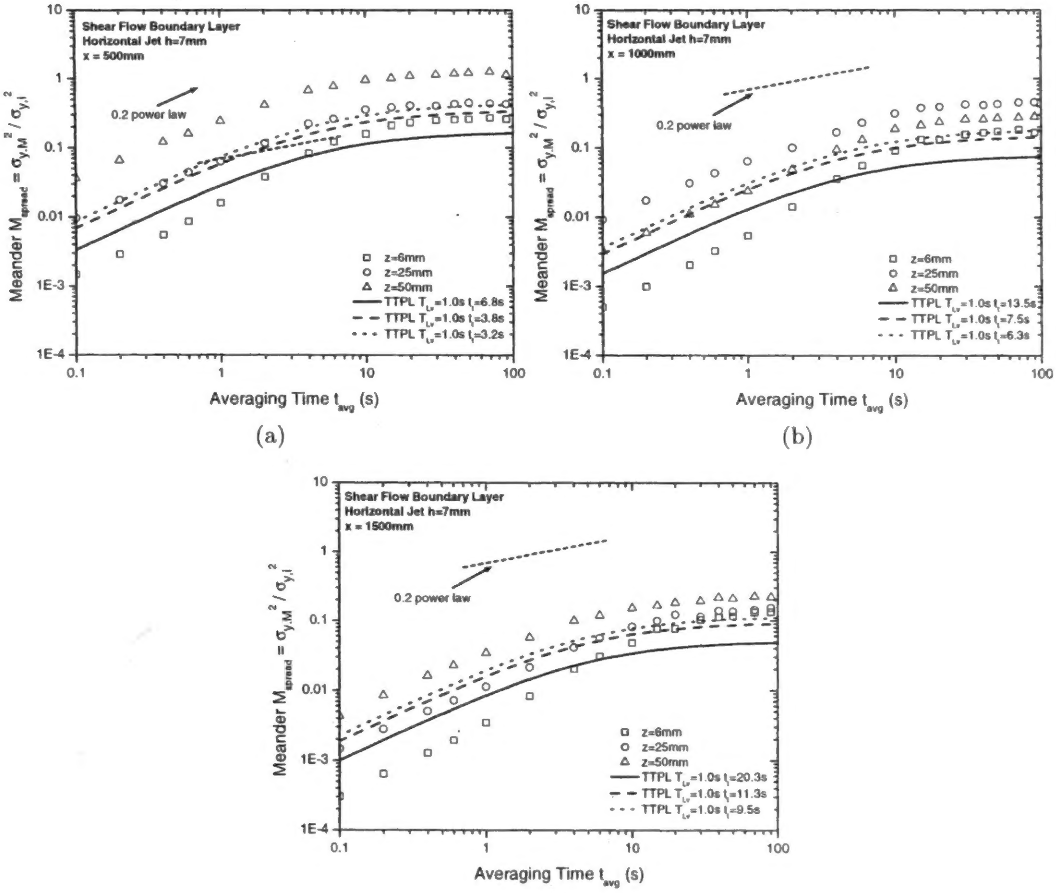

(a) (b)

(c)

Figure G.5: Measured meander M_{spread} compared to TTPL model and 0.2 power law for the horizontal jet source at $h = 7$ mm at a flow rate $Q = 1.47$ ml/s and measured at $z = 6$, 25, and 50 mm above the ground for (a) $x = 500$ mm (b) $x = 1000$ mm (c) $x = 1500$ mm

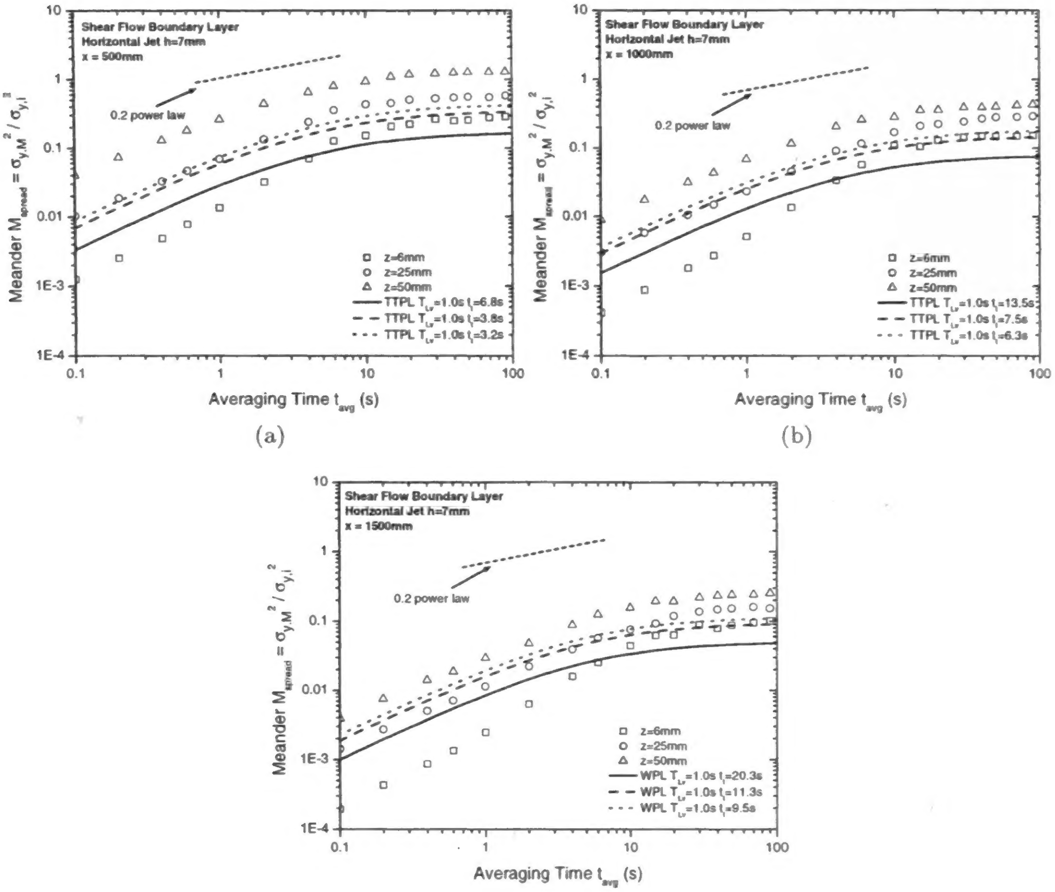

(a) (b)

(c)

Figure G.6: Measured meander M_{spread} compared to TTPL model and 0.2 power law for the horizontal jet source at $h = 7$ mm at a flow rate $Q = 1.47$ ml/s and measured at $z = 6$, 25, and 50 mm above the ground for (a) $x = 500$ mm (b) $x = 1000$ mm (c) $x = 1500$ mm

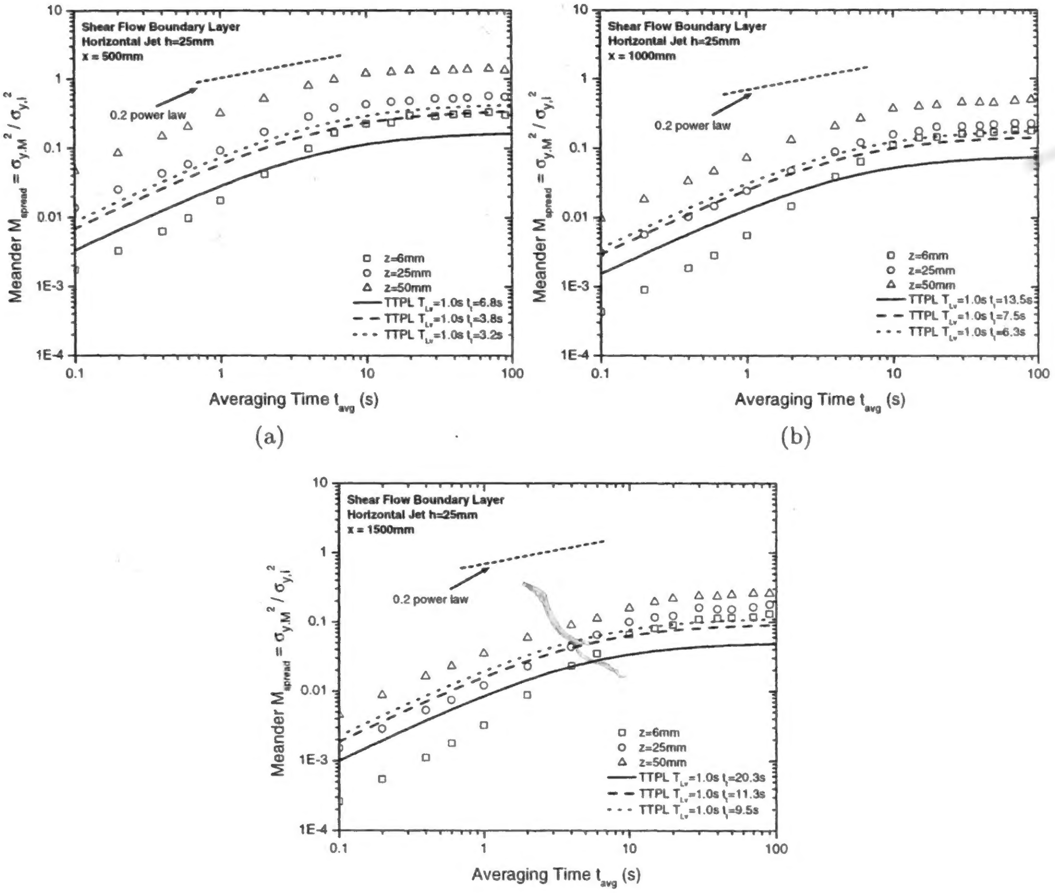

(a) (b)

(c)

Figure G.7: Measured meander M_{spread} compared to TTPL model and 0.2 power law for the horizontal jet source at $h = 25$ mm at a flow rate $Q = 1.47$ ml/s and measured at $z = 6$, 25, and 50 mm above the ground for (a) $x = 500$ mm (b) $x = 1000$ mm (c) $x = 1500$ mm

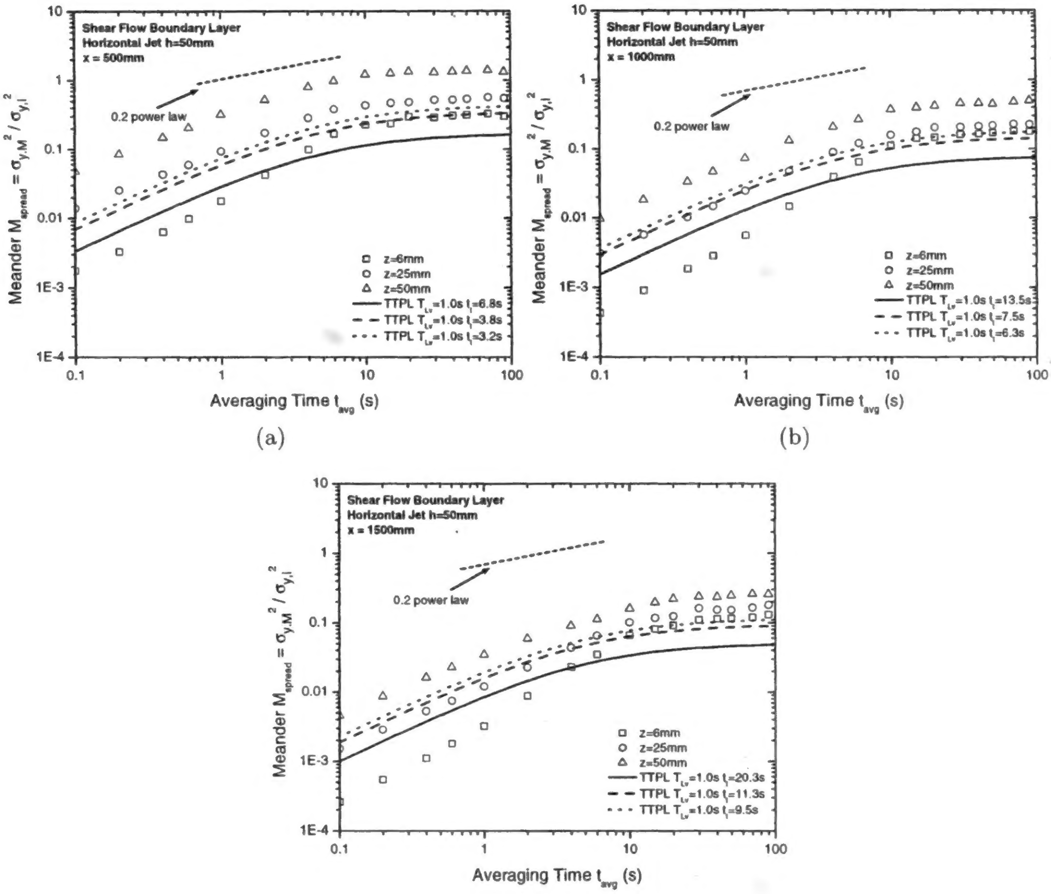

(a)

(b)

(c)

Figure G.8: Measured meander M_{spread} compared to TTPL model and 0.2 power law for the horizontal jet source at $h = 50$ mm at a flow rate $Q = 1.47$ ml/s and measured at $z = 6$, 25, and 50 mm above the ground for (a) $x = 500$ mm (b) $x = 1000$ mm (c) $x = 1500$ mm

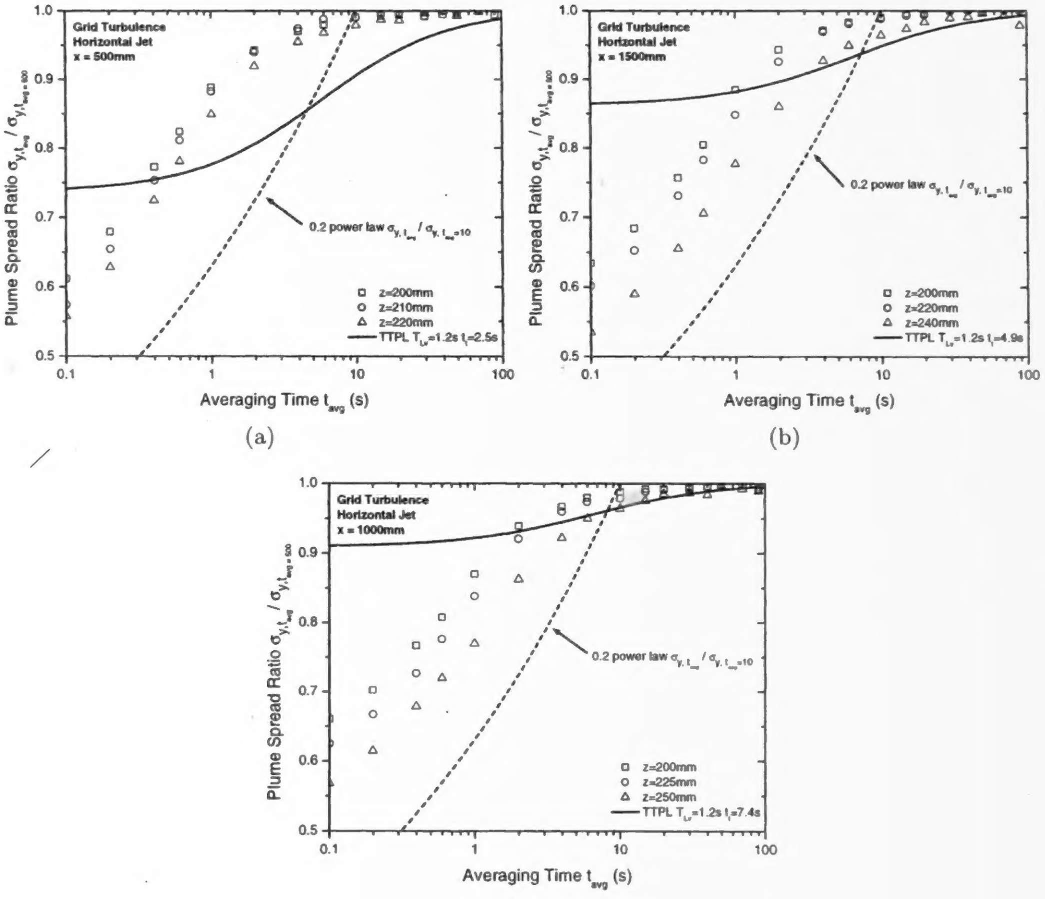

(a)

(b)

(c)

Figure G.9: Measured plume spread ratio $\sigma_{y,t_{\text{avg}}}/\sigma_{y,t_{\text{avg}\to\infty}}$ compared to TTPL model and 0.2 power law for the iso-kinetic horizontal jet source in grid turbulence (a) $x = 500$ mm and $z = 200$, 210, 220 mm (b) $x = 1000$ mm and $z = 200$, 220, 240 mm (c) $x = 1500$ mm and $z = 200$, 225, 250 mm

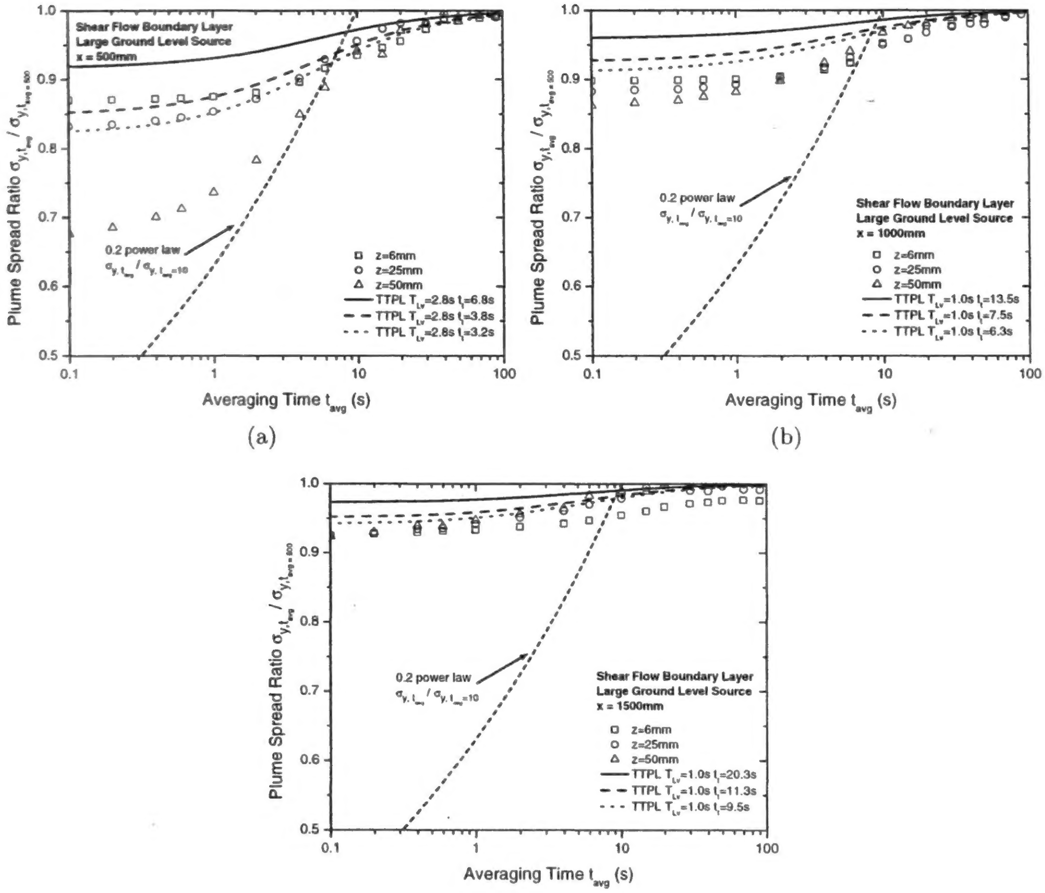

(a) (b)

(c)

Figure G.10: Measured plume spread ratio $\sigma_{y,t_{\text{avg}}}/\sigma_{y,t_{\text{avg}\to\infty}}$ compared to TTPL model and 0.2 power law for the large ground level source at a flow rate $Q = 1.47$ ml/s and $z = 6$, 25, and 50 mm above the ground for (a) $x = 500$ mm (b) $x = 1000$ mm (c) $x = 1500$ mm

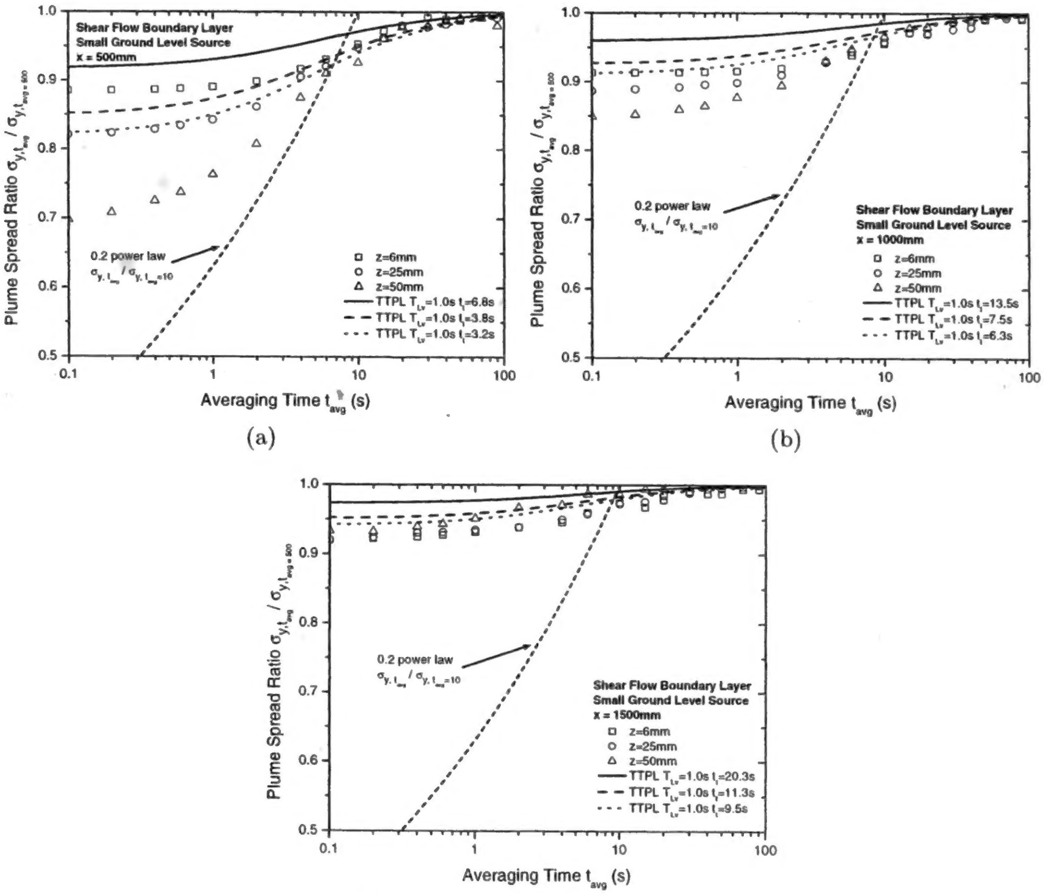

(a)

(b)

(c)

Figure G.11: Measured plume spread ratio $\sigma_{y,t_{\text{avg}}}/\sigma_{y,t_{\text{avg}\to\infty}}$ compared to TTPL model and 0.2 power law for the small ground level vertical jet source at a flow rate $Q =$ 1.47 ml/s and z = 6, 25, and 50 mm above the ground for (a) x = 500 mm (b) x = 1000 mm (c) x = 1500 mm

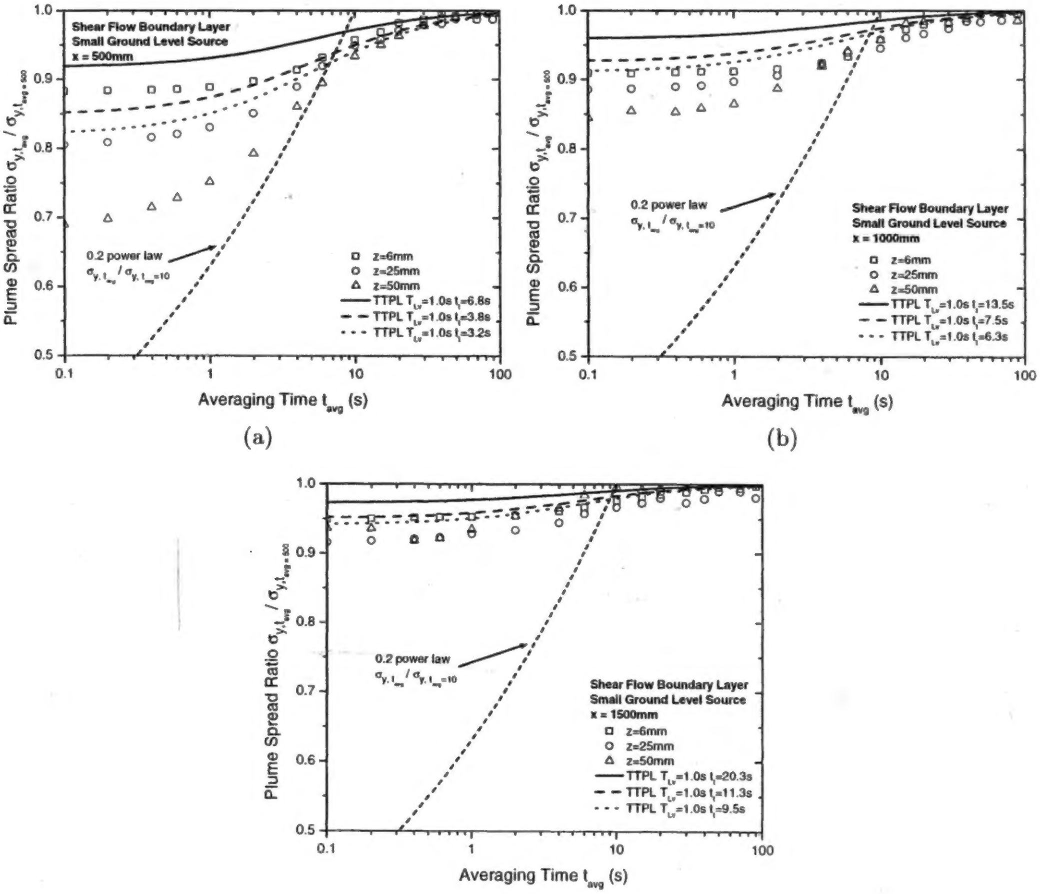

(a) (b)

(c)

Figure G.12: Measured plume spread ratio $\sigma_{y,t_{\text{avg}}}/\sigma_{y,t_{\text{avg}\to\infty}}$ compared to TTPL model and 0.2 power law for the small ground level vertical jet source at a flow rate $Q = 0.73$ ml/s and $z = 6$, 25, and 50 mm above the ground for (a) $x = 500$ mm (b) $x = 1000$ mm (c) $x = 1500$ mm

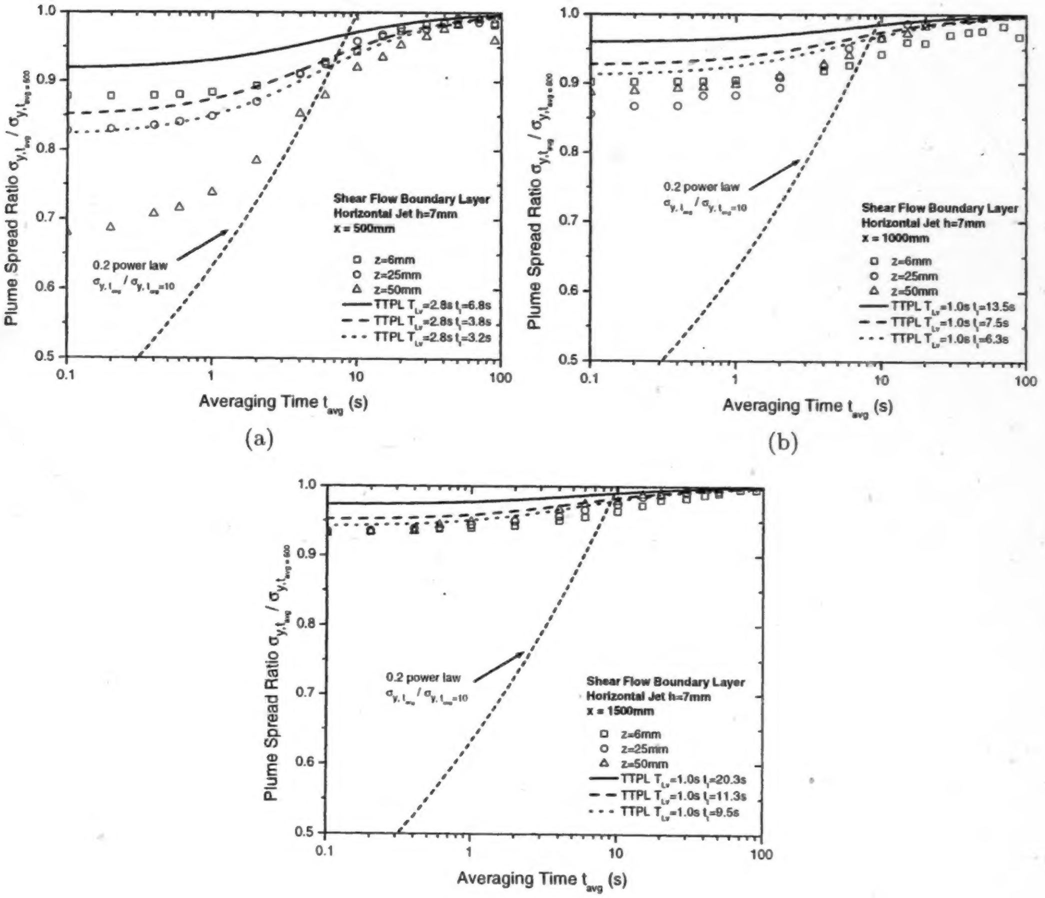

(a) (b)

(c)

Figure G.13: Measured plume spread ratio $\sigma_{y,t_{\text{avg}}}/\sigma_{y,t_{\text{avg}\to\infty}}$ compared to TTPL model and 0.2 power law for the horizontal jet source at $h = 6$ mm at a flow rate $Q = 1.47$ ml/s and measured at $z = 6$, 25, and 50 mm above the ground for (a) $x = 500$ mm (b) $x = 1000$ mm (c) $x = 1500$ mm

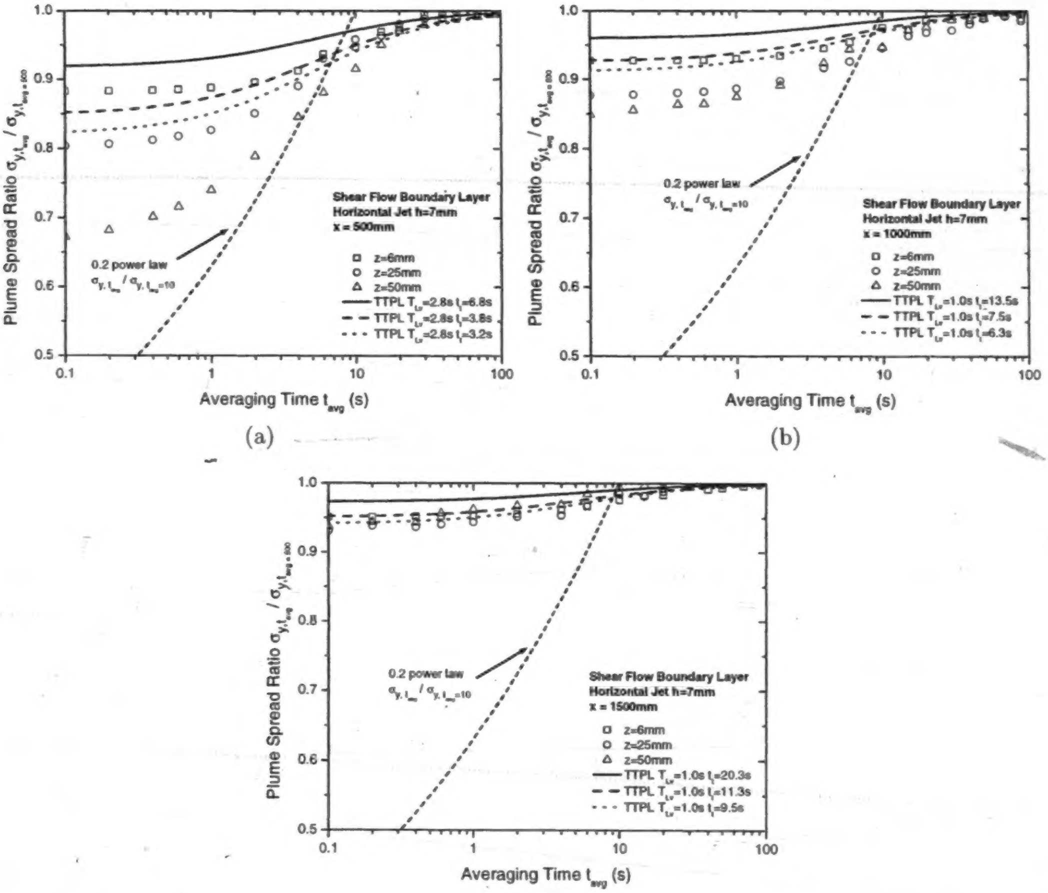

(a) (b)

(c)

Figure G.14: Measured plume spread ratio $\sigma_{y,t_{\text{avg}}}/\sigma_{y,t_{\text{avg}\to\infty}}$ compared to TTPL model and 0.2 power law for the horizontal jet source at $h = 6$ mm at a flow rate $Q = 1.47$ ml/s and measured at $z = 6$, 25, and 50 mm above the ground for (a) $x = 500$ mm (b) $x = 1000$ mm (c) $x = 1500$ mm

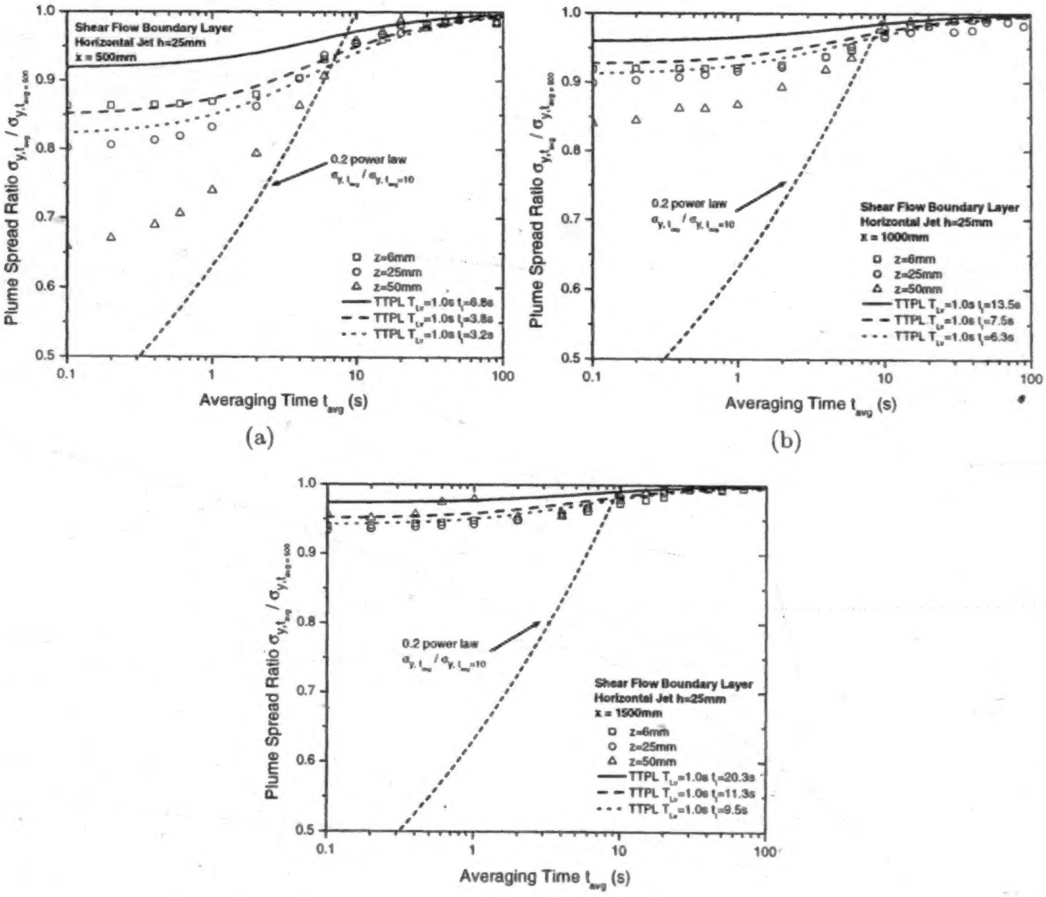

(a) (b)

(c)

Figure G.15: Measured plume spread ratio $\sigma_{y,t_{\text{avg}}}/\sigma_{y,t_{\text{avg}\to\infty}}$ compared to TTPL model and 0.2 power law for the horizontal jet source at $h = 25$ mm at a flow rate $Q = 1.47$ ml/s and measured at $z = 6$, 25, and 50 mm above the ground for (a) $x = 500$ mm (b) $x = 1000$ mm (c) $x = 1500$ mm

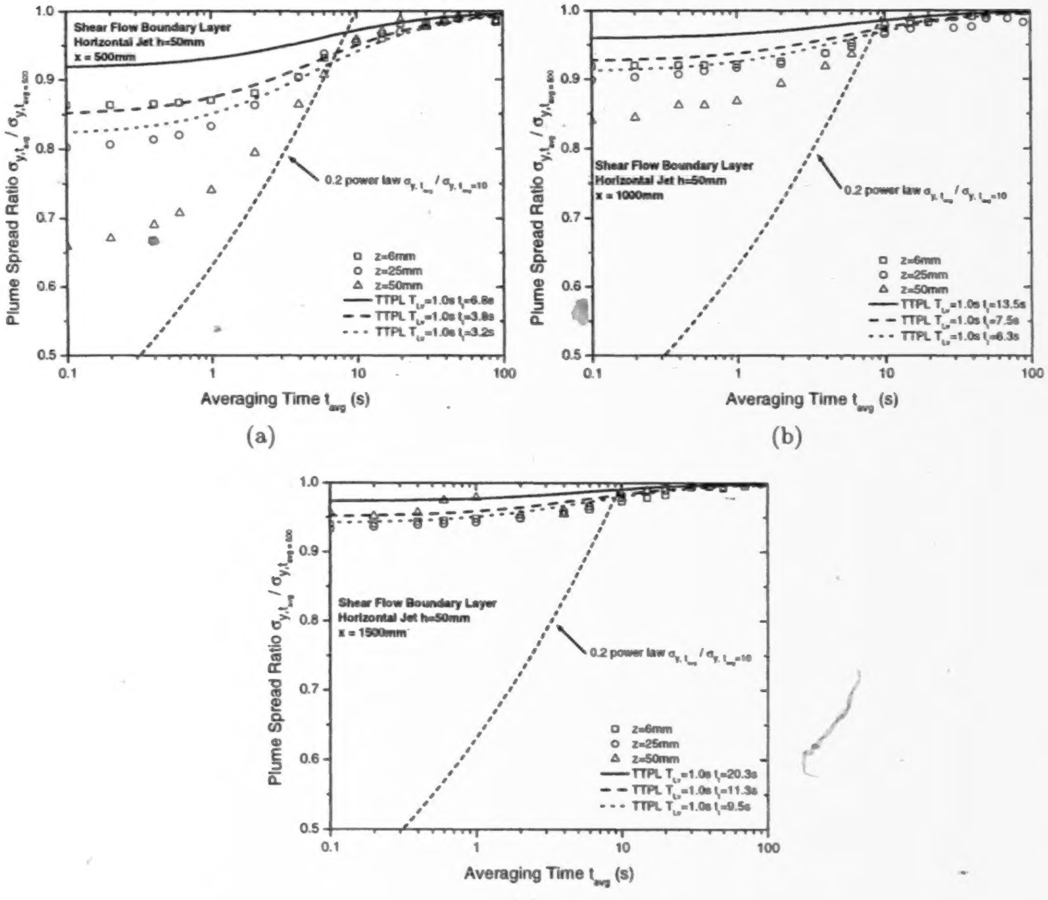

(a)

(b)

(c)

Figure G.16: Measured plume spread ratio $\sigma_{y,t_{\text{avg}}}/\sigma_{y,t_{\text{avg}\to\infty}}$ compared to TTPL model and 0.2 power law for the horizontal jet source at $h = 50$ mm at a flow rate $Q = 1.47$ ml/s and measured at $z = 6$, 25, and 50 mm above the ground for (a) $x = 500$ mm (b) $x = 1000$ mm (c) $x = 1500$ mm

Appendix H

Shear Distortion Model versus Water Channel Data

The plots in this appendix supplement the selected examples given in Chapter 3 to develop the shear distortion model for concentration fluctuation statistics. The plots in the appendix are in measured laboratory units and not normalized.

Vertical profile statistics were measured for 3 source types at 3 flow rates. The small ground level vertical jet source, the horizontal jet source at the ground level position $h = 7$ mm and the horizontal jet source elevated at $h = 50$ mm. Each of these 3 source was run at flow rates of $Q = 1.47$ ml/s and 0.73 ml/s. Vertical profiles were measured at $x = 500$ and $x = 1500$ mm downstream of the source.

Figures H.1 to H.3 show the vertical profiles of fluctuation intensity i for the 3 source types and the shear and no-shear models for i. Figures H.4 to H.9 show vertical profiles of the concentration integral time scales T_c and length scales L_c versus the shear and no shear models.

Figures H.10 through H.15 are additional examples of the relationship between the fluctuation intensity i, the conditional fluctuation intensity i_p and the intermittency factor γ for additional sources and downstream positions to supplement those shown in Chapter 3. The source conditions for these plots are the elevated horizontal jet source at $h = 25$ mm in Figures H.10 and H.11, the elevated horizontal jet source at $h = 50$ mm in Figures H.12 and H.13, and the large ground level source in Figures H.14 and H.15.

Figures H.16 through H.27 show examples of the cross-stream profiles of concentration fluctuation intensity i, conditional concentration fluctuation intensity i_p and intermittency factor γ to supplement the examples given in Chapter 3. The source conditions are the ground level horizontal jet source at $h = 7$ mm for Figures H.16 to H.18, the elevated horizontal jet source at $h = 25$ mm for Figures H.19 to H.21, the elevated horizontal jet source at $h = 50$ mm for Figures H.22 to H.24, and the large ground level source for Figures H.25 to H.27.

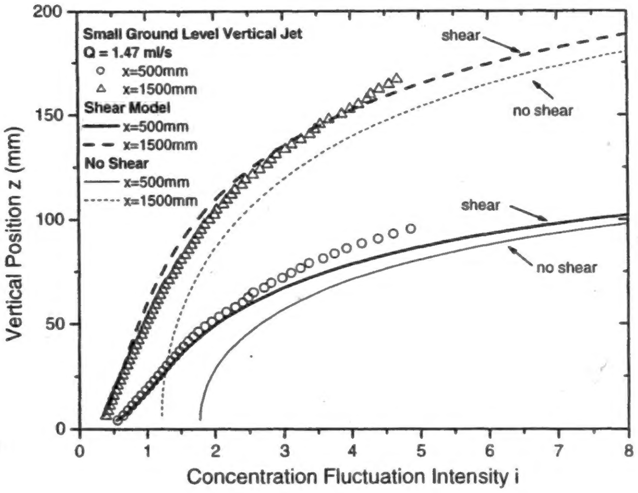

(a)

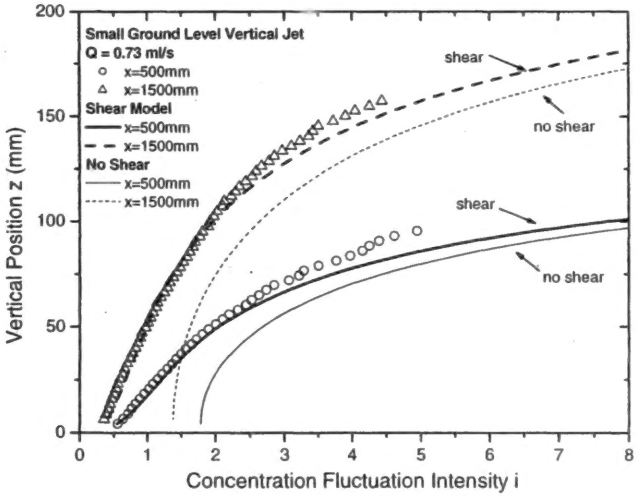

(b)

Figure H.1: Vertical profiles of the fluctuation intensity i compared to the shear model and the no shear model for the vertical ground level jet source (a) source flow rate $Q = 1.47$ ml/s (b) source flow rate $Q = 0.73$ ml/s

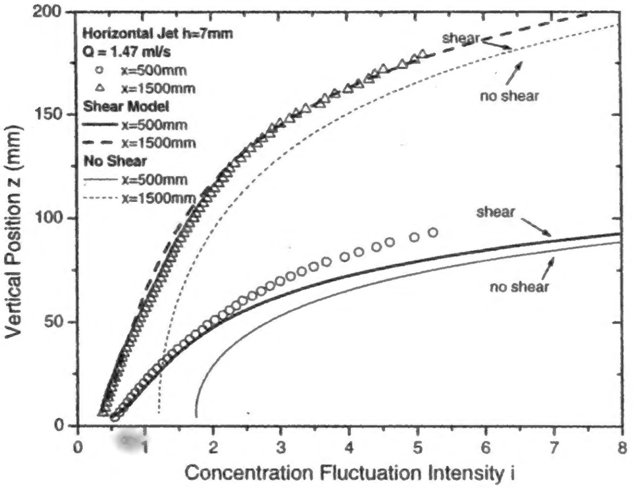

(a)

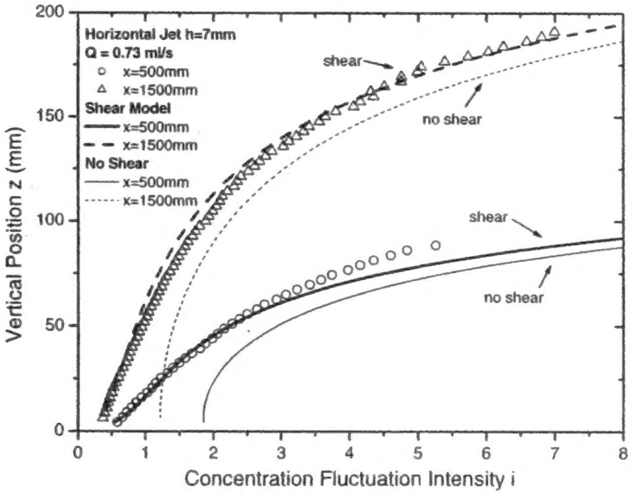

(b)

Figure H.2: Vertical profiles of the fluctuation intensity i compared to the shear model and the no shear model for the horizontal ground level jet source $h = 7$ mm. (a) source flow rate $Q = 1.47$ ml/s (b) source flow rate $Q = 0.73$ ml/s

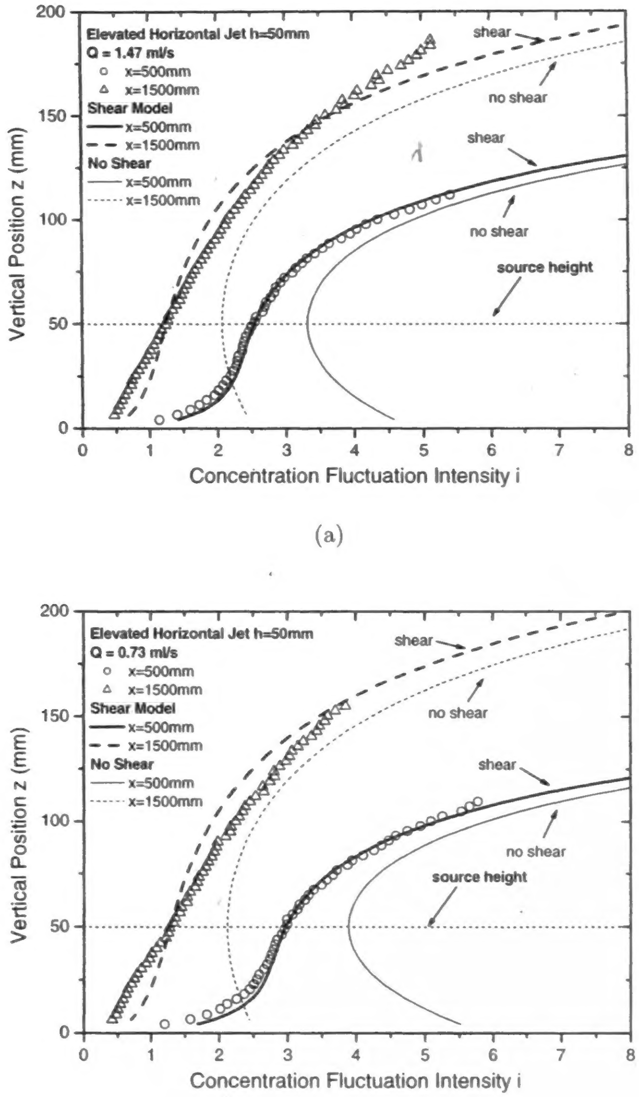

(a)

(b)

Figure H.3: Vertical profiles of the fluctuation intensity i compared to the shear model and the no shear model for the horizontal elevated jet source $h = 50$ mm. (a) source flow rate $Q = 1.47$ ml/s (b) source flow rate $Q = 0.73$ ml/s

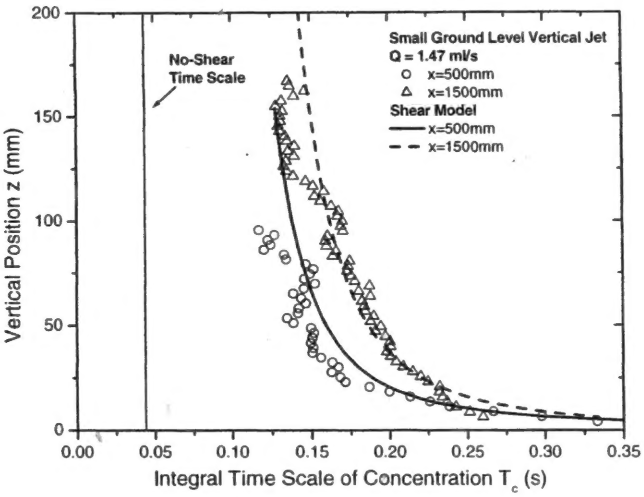

(a)

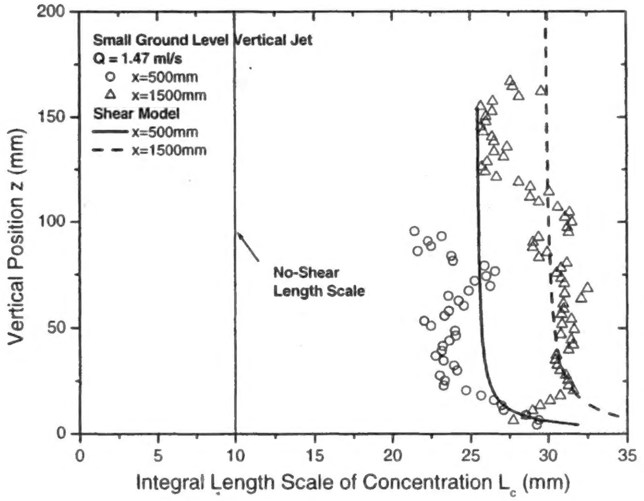

(b)

Figure H.4: Vertical profiles of the concentration fluctuation integral time scale T_c and length scale L_c for the small ground level vertical jet source at a flow rate of 1.47 ml/s compared to the shear model and the no shear model. (a) integral time scale T_c (b) integral length scale L_c.

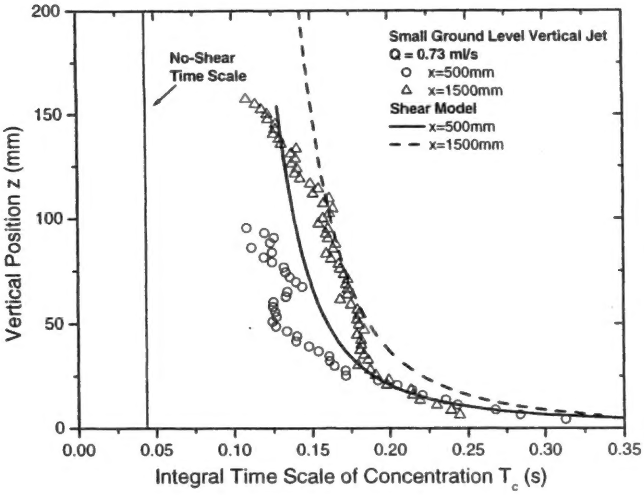

(a)

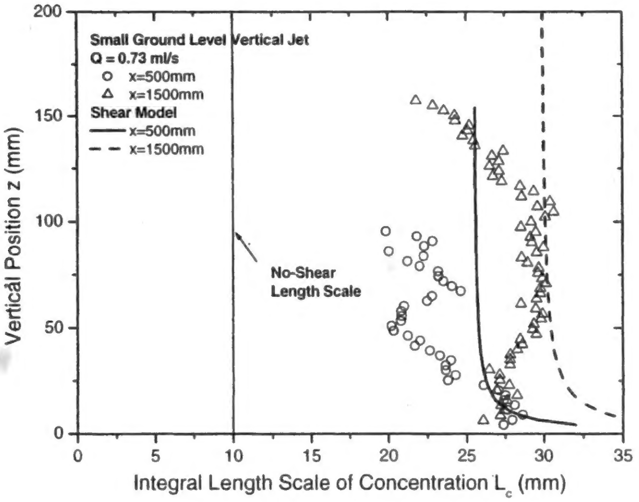

(b)

Figure H.5: Vertical profiles of the concentration fluctuation integral time scale T_c and length scale L_c for the small ground level vertical jet source at a flow rate of 0.73 ml/s compared to the shear model and the no shear model. (a) integral time scale T_c (b) integral length scale L_c.

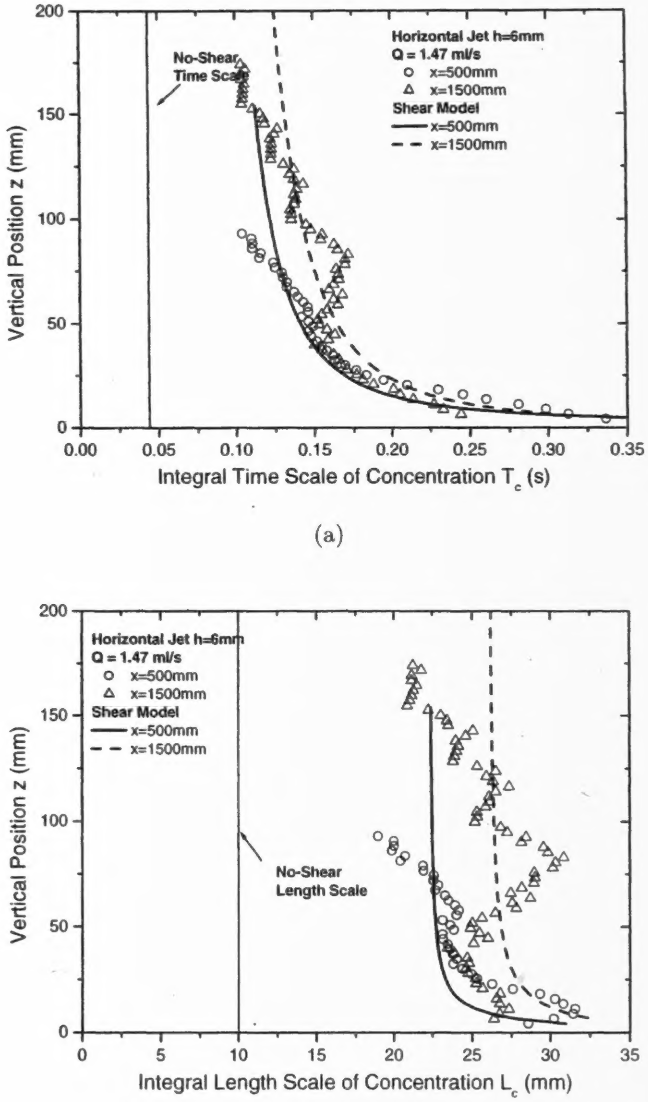

(a)

(b)

Figure H.6: Vertical profiles of the concentration fluctuation integral time scale T_c and length scale L_c for the horizontal jet source at $h = 7$ mm at a flow rate of 1.47 ml/s compared to the shear model and the no shear model. (a) integral time scale T_c (b) integral length scale L_c.

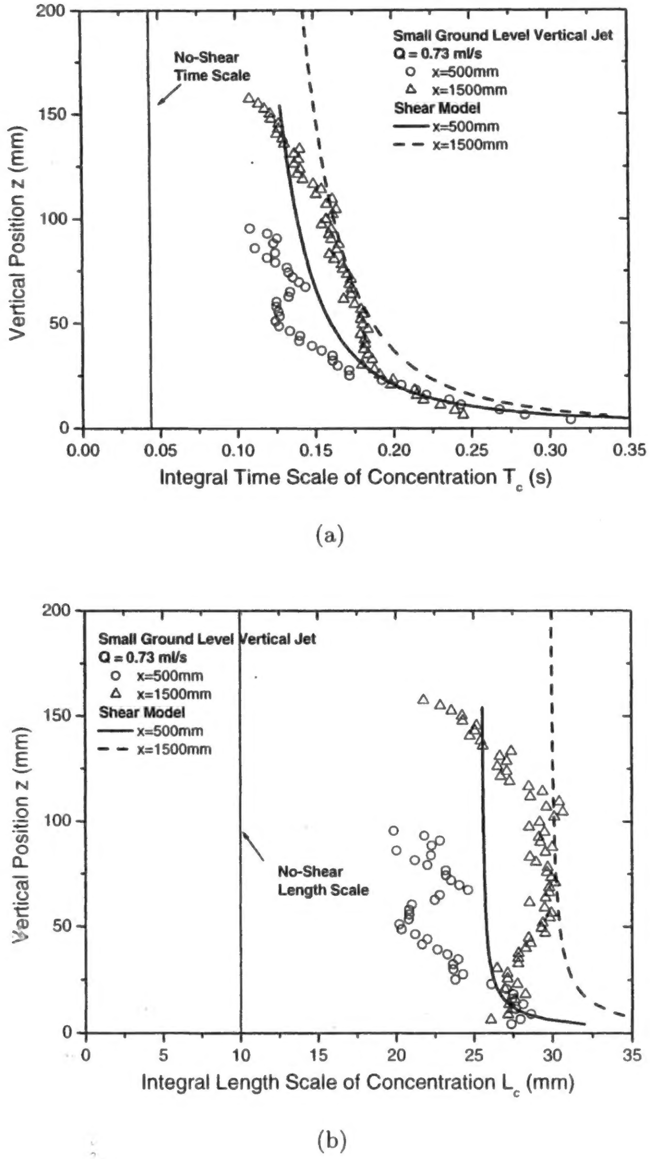

Figure H.7: Vertical profiles of the concentration fluctuation integral time scale T_c and length scale L_c for the horizontal jet source at $h = 7$ mm at a flow rate of 0.73 ml/s compared to the shear model and the no shear model. (a) integral time scale T_c (b) integral length scale L_c.

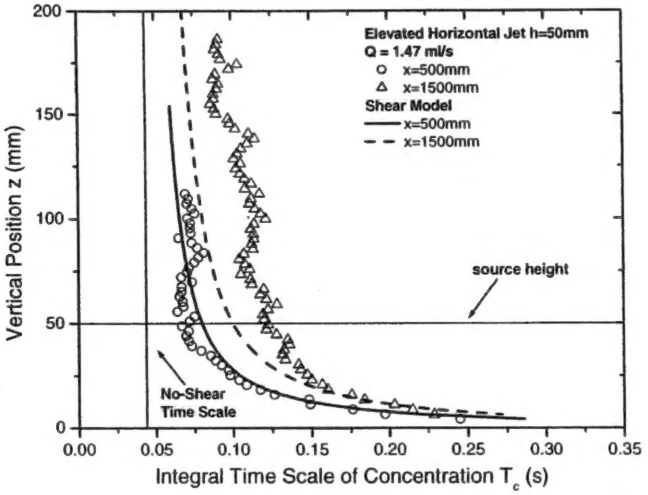

(a)

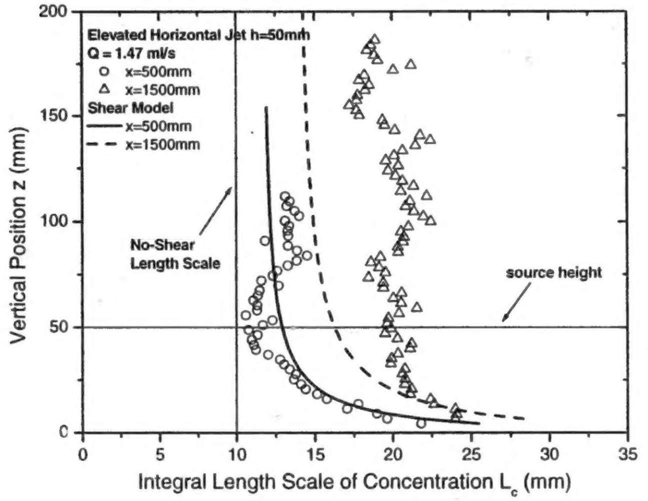

(b)

Figure H.8: Vertical profiles of the concentration fluctuation integral time scale T_c and length scale L_c for the horizontal jet source at $h = 7$ mm at a flow rate of 1.47 ml/s compared to the shear model and the no shear model. (a) integral time scale T_c (b) integral length scale L_c.

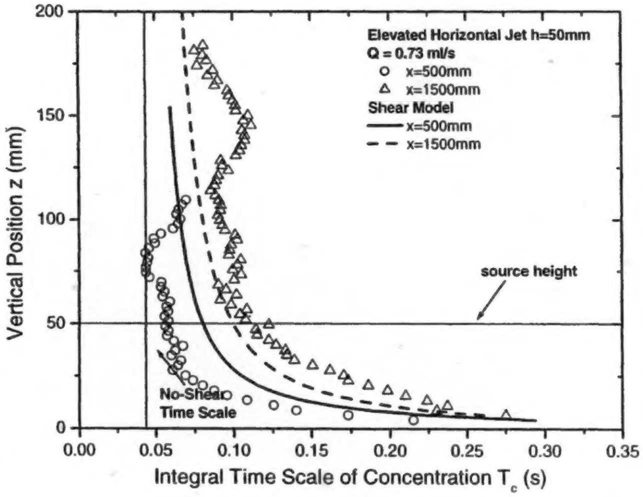

(a)

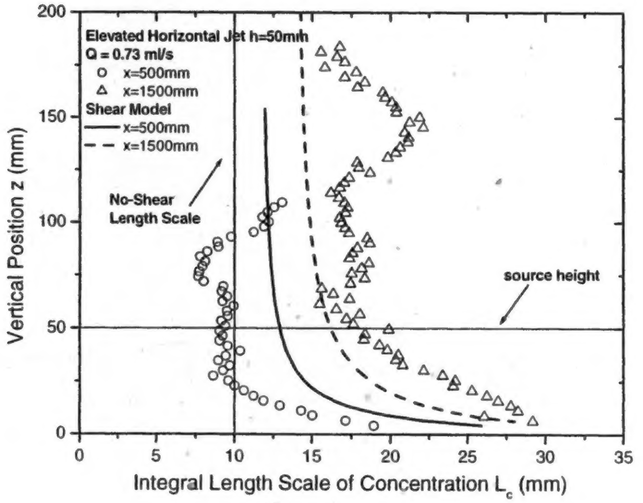

(b)

Figure H.9: Vertical profiles of the concentration fluctuation integral time scale T_c and length scale L_c for the horizontal jet source at $h = 7$ mm at a flow rate of 0.73 ml/s compared to the shear model and the no shear model. (a) integral time scale T_c (b) integral length scale L_c.

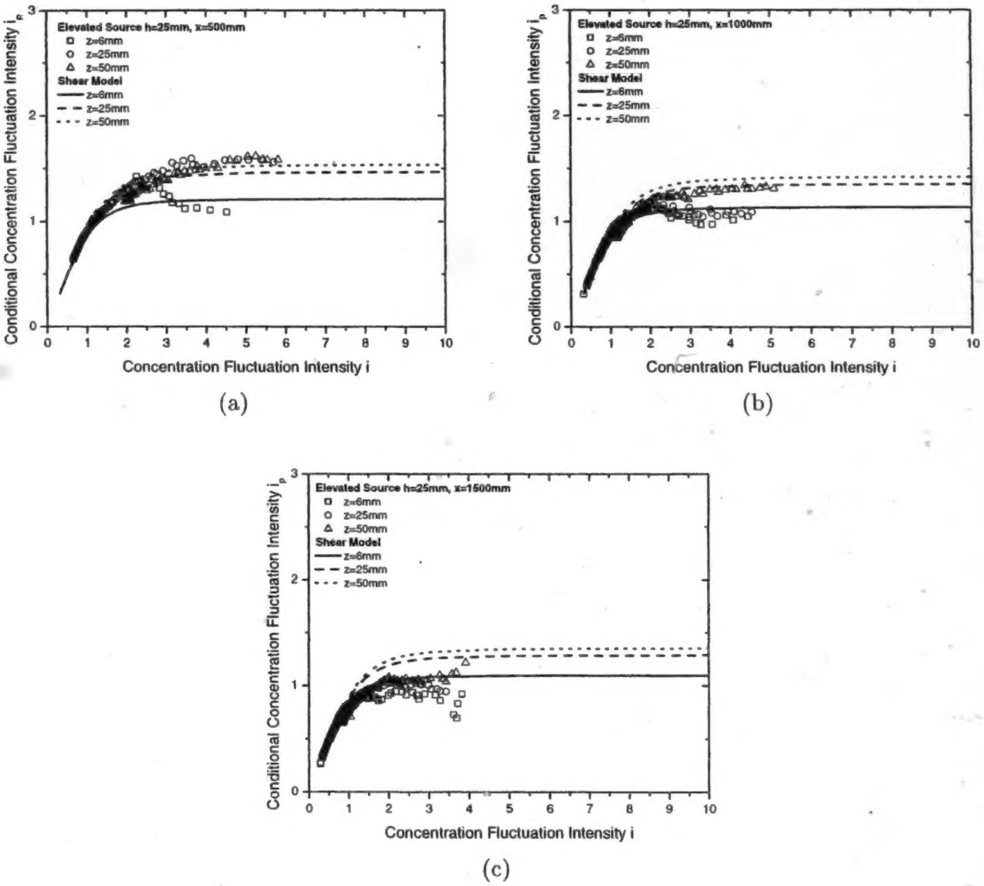

(a) (b)

(c)

Figure H.10: Conditional concentration fluctuation intensity i_p versus total concentration fluctuation intensity i for the elevated horizontal jet source $h = 25$ mm (a) $x = 500$ mm (b) $x = 1000$ mm (c) $x = 1500$ mm

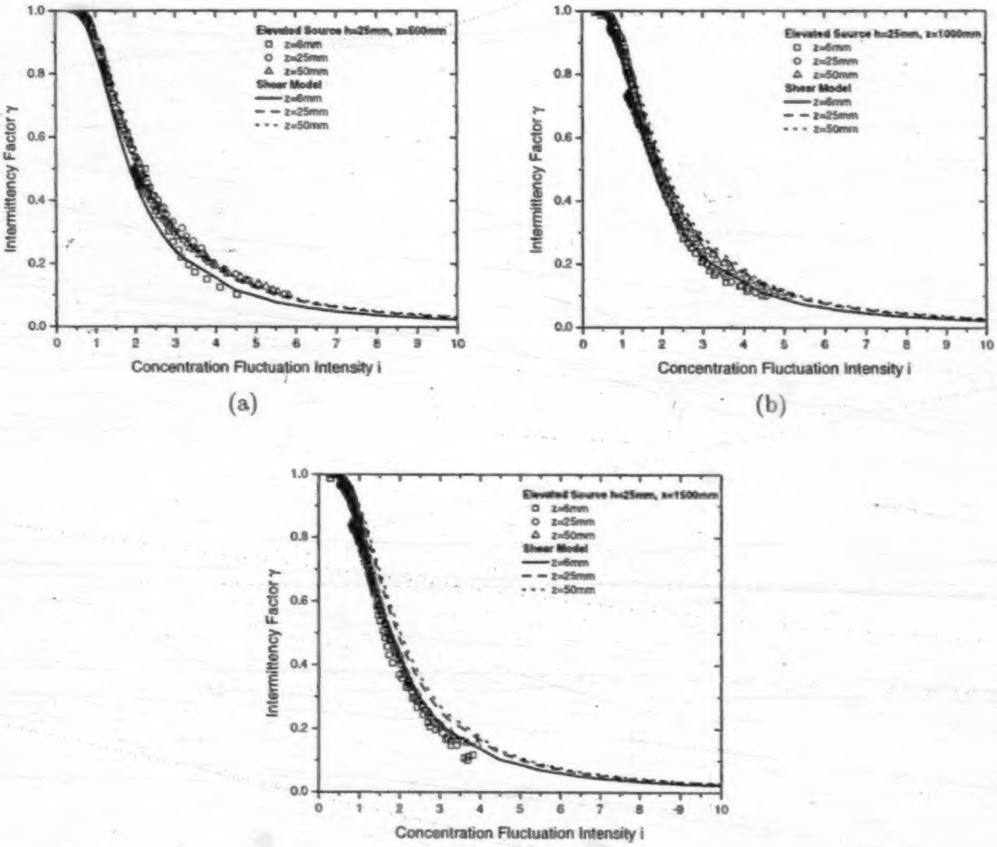

(a)

(b)

(c)

Figure H.11: Intermittency factor γ versus total concentration fluctuation intensity i for the elevated horizontal jet source h = 25 mm (a) x = 500 mm (b) x = 1000 mm (c) x = 1500 mm

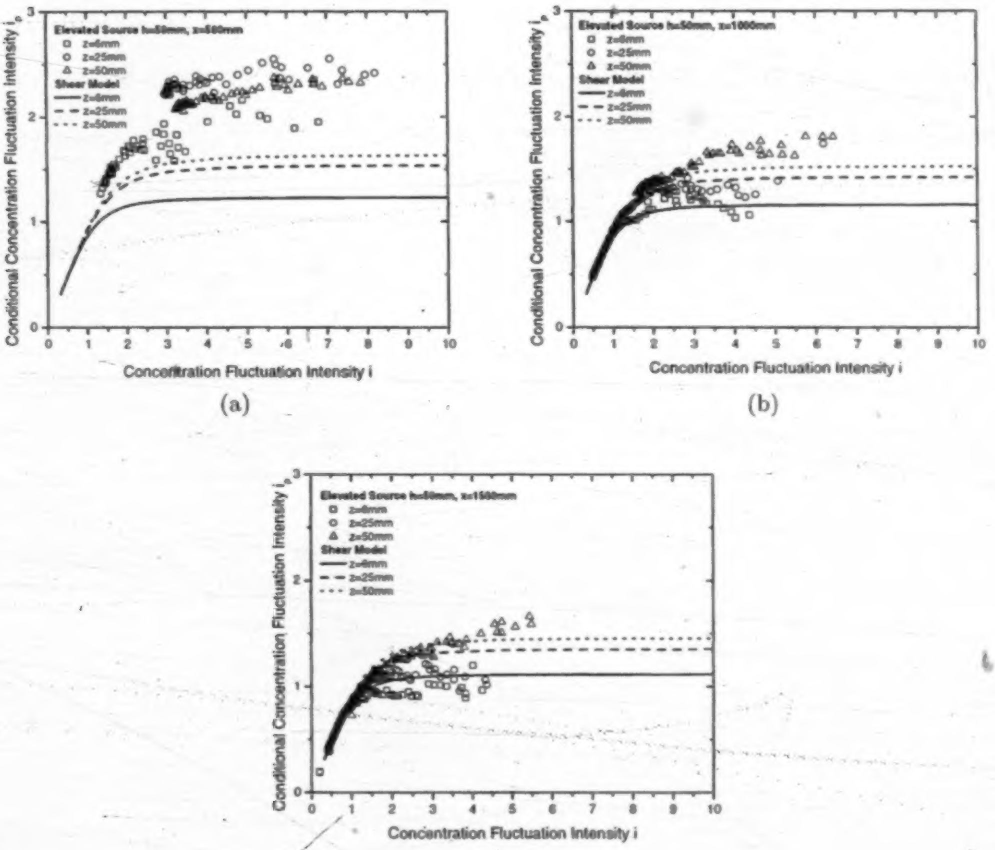

(a) (b)

(c)

Figure H.12: Conditional concentration fluctuation intensity i_p versus total concentration fluctuation intensity i for the elevated horizontal jet source $h = 50$ mm (a) $x = 500$ mm (b) $x = 1000$ mm (c) $x = 1500$ mm

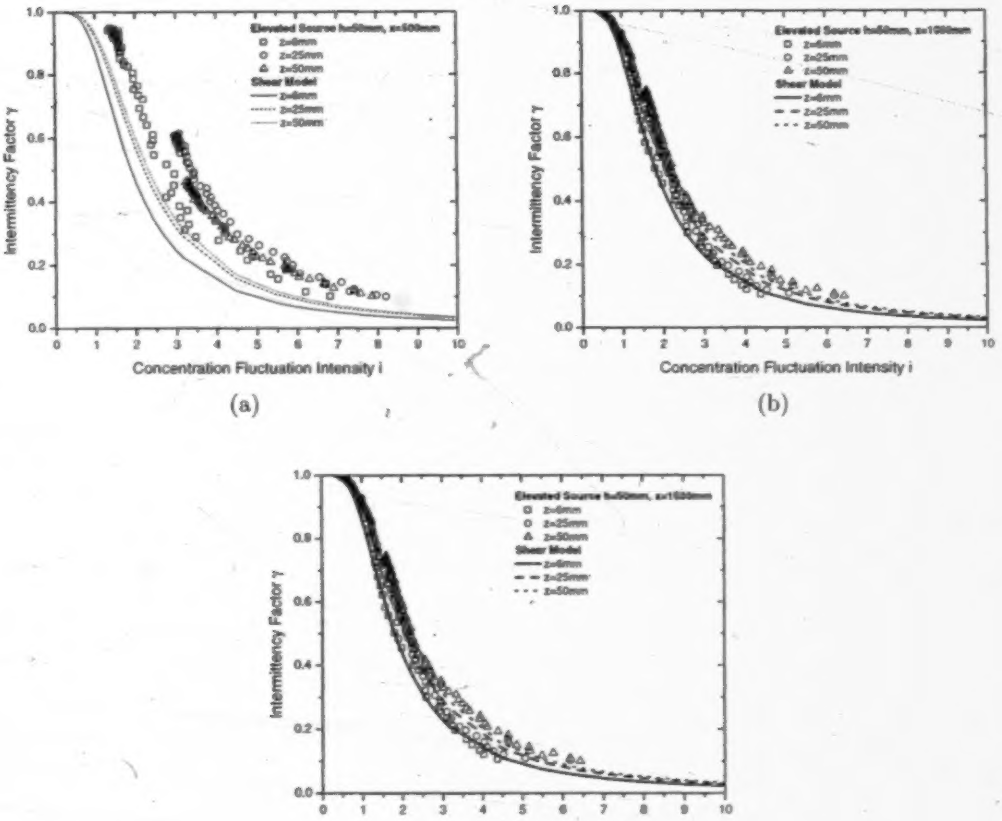

(a) (b)

(c)

Figure H.13: Intermittency factor γ versus total concentration fluctuation intensity i for the elevated horizontal jet source $h = 50$ mm (a) $x = 500$ mm (b) $x = 1000$ mm (c) $x = 1500$ mm

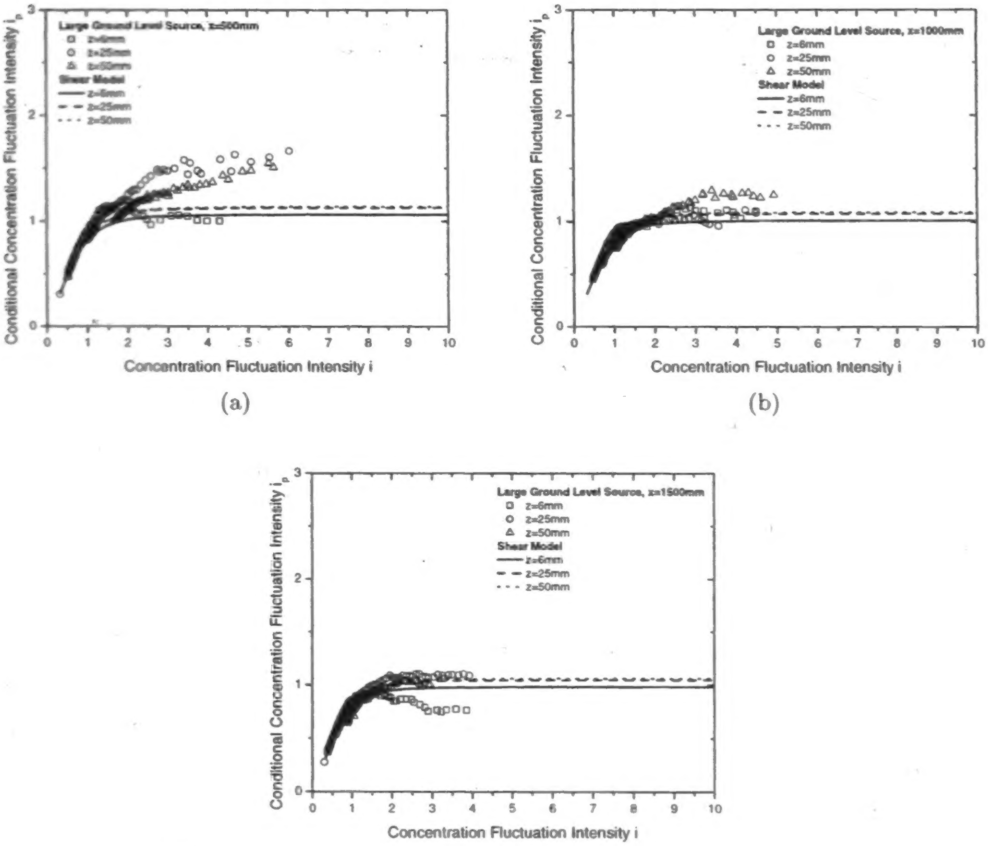

(a) (b)

(c)

Figure H.14: Conditional concentration fluctuation intensity i_p versus total concentration fluctuation intensity i for the large ground level source (a) $x = 500$ mm (b) $x = 1000$ mm (c) $x = 1500$ mm

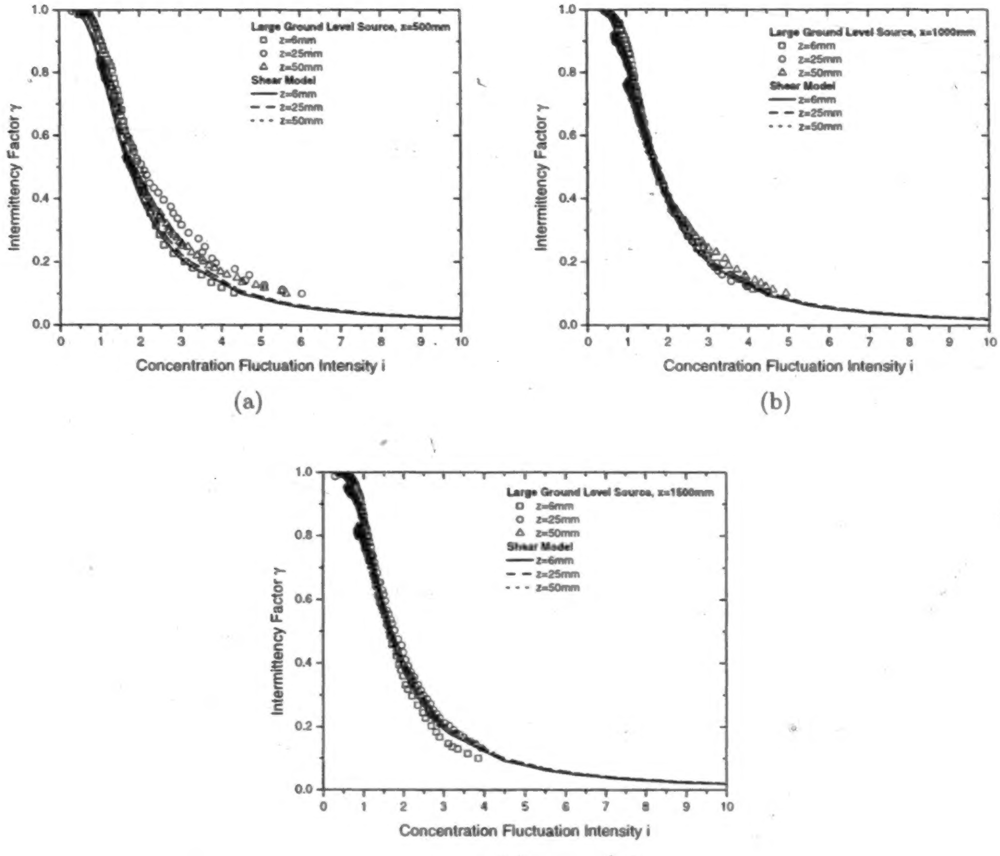

(a) (b)

(c)

Figure H.15: Intermittency factor γ versus total concentration fluctuation intensity i for the large ground level source (a) $x = 500$ mm (b) $x = 1000$ mm (c) $x = 1500$ mm

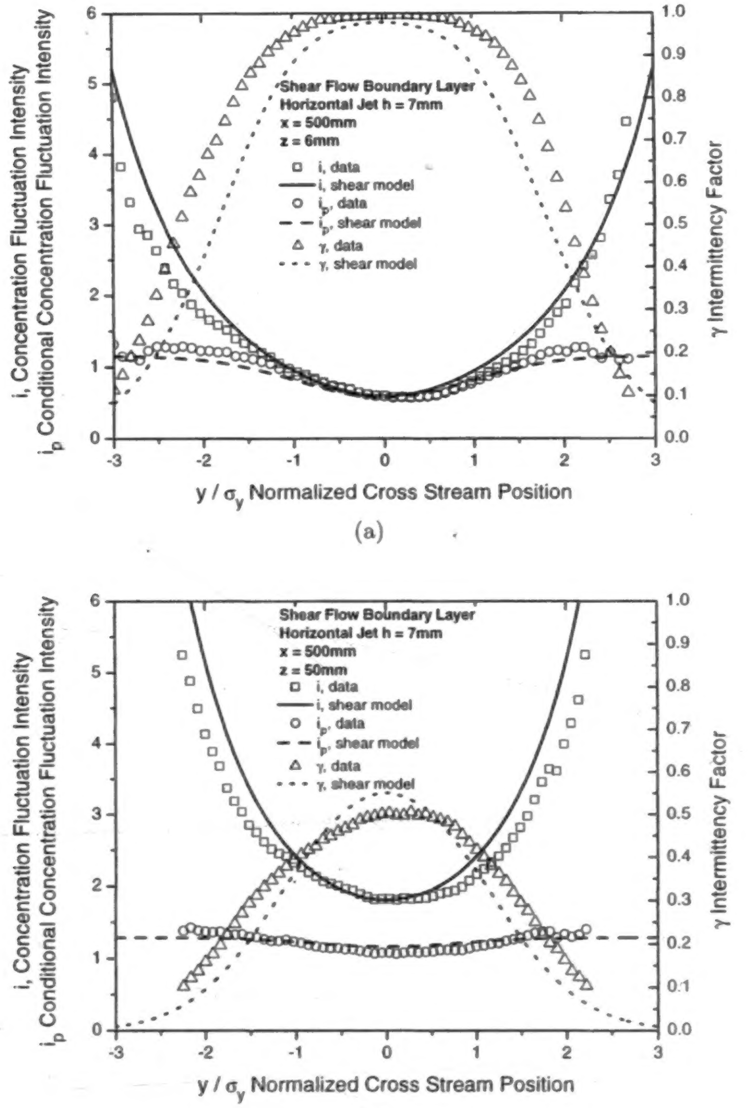

(a)

(b)

Figure H.16: Measured cross-stream profiles compared with pseudo-meandering plume theory of total concentration fluctuation intensity i, conditional concentration fluctuation intensity i_p, and intermittency factor γ for the ground level horizontal jet source $h = 7$ mm at $x = 500$ mm downstream. (a) at ground level $z = 6$ mm (b) above ground at $z = 50$ mm.

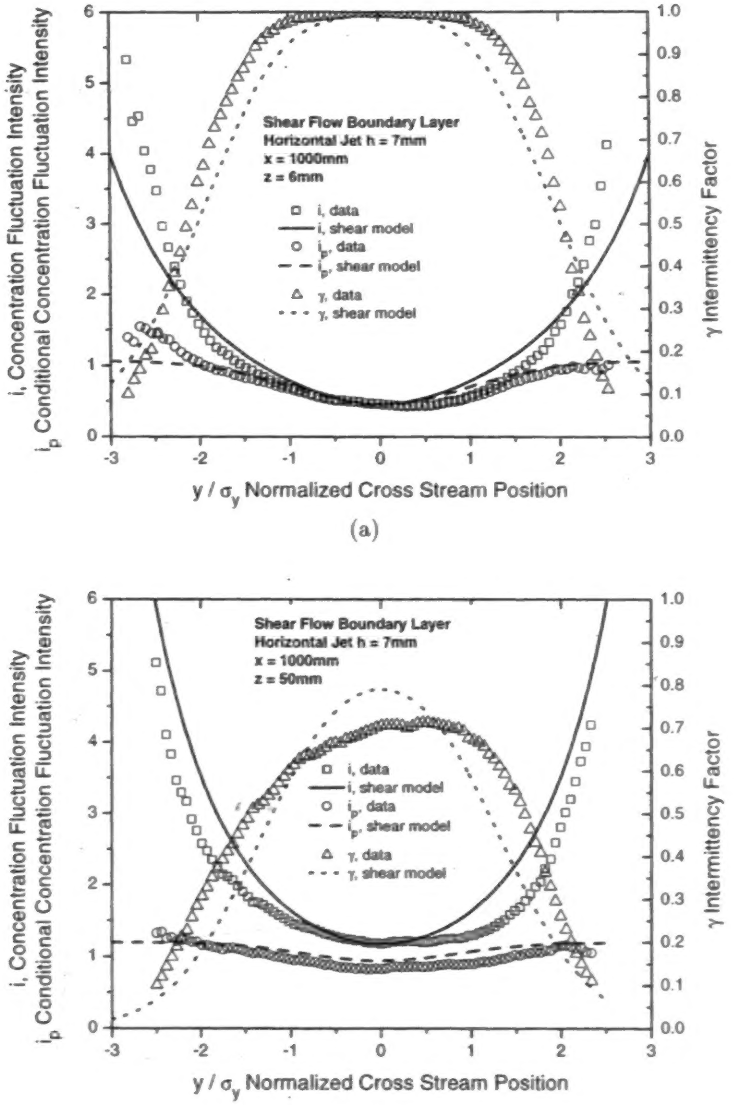

(a)

(b)

Figure H.17: Measured cross-stream profiles compared with pseudo-meandering plume theory of total concentration fluctuation intensity i, conditional concentration fluctuation intensity i_p, and intermittency factor γ for the ground level horizontal jet source $h = 7$ mm at $x = 1000$ mm downstream. (a) at ground level $z = 6$ mm (b) above ground at $z = 50$ mm.

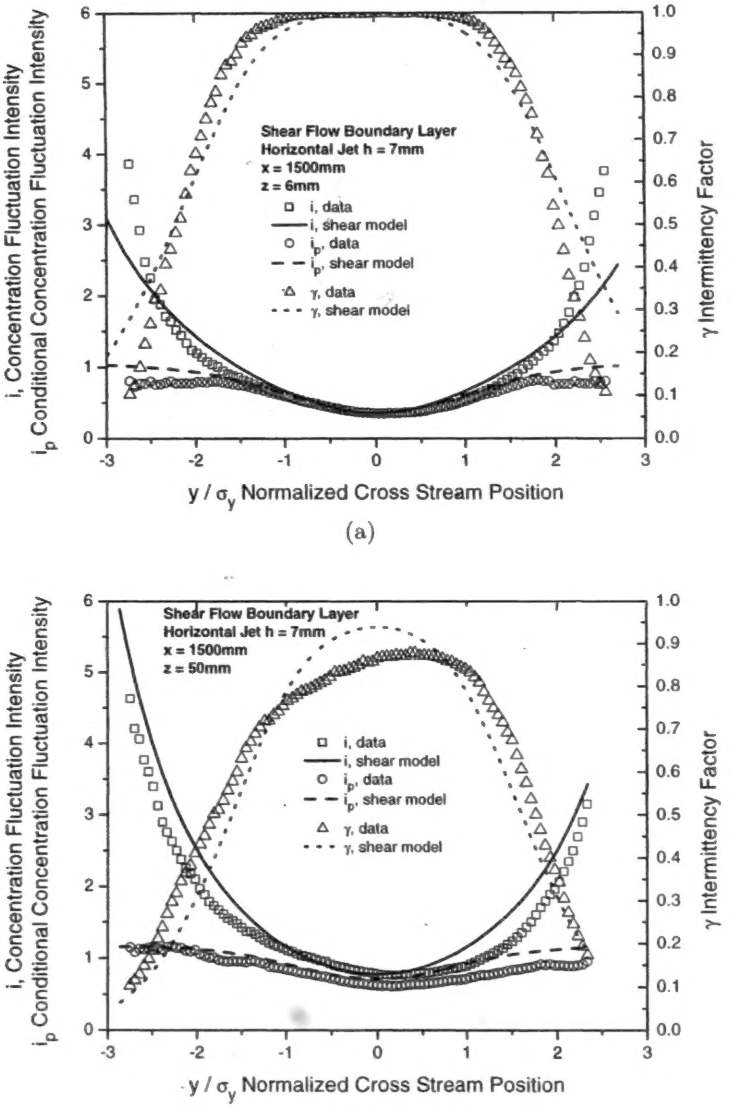

(a)

(b)

Figure H.18: Measured cross-stream profiles compared with pseudo-meandering plume theory of total concentration fluctuation intensity i, conditional concentration fluctuation intensity i_p, and intermittency factor γ for the ground level horizontal jet source $h = 7$ mm at $x = 1500$ mm downstream. (a) at ground level $z = 6$ mm (b) above ground at $z = 50$ mm.

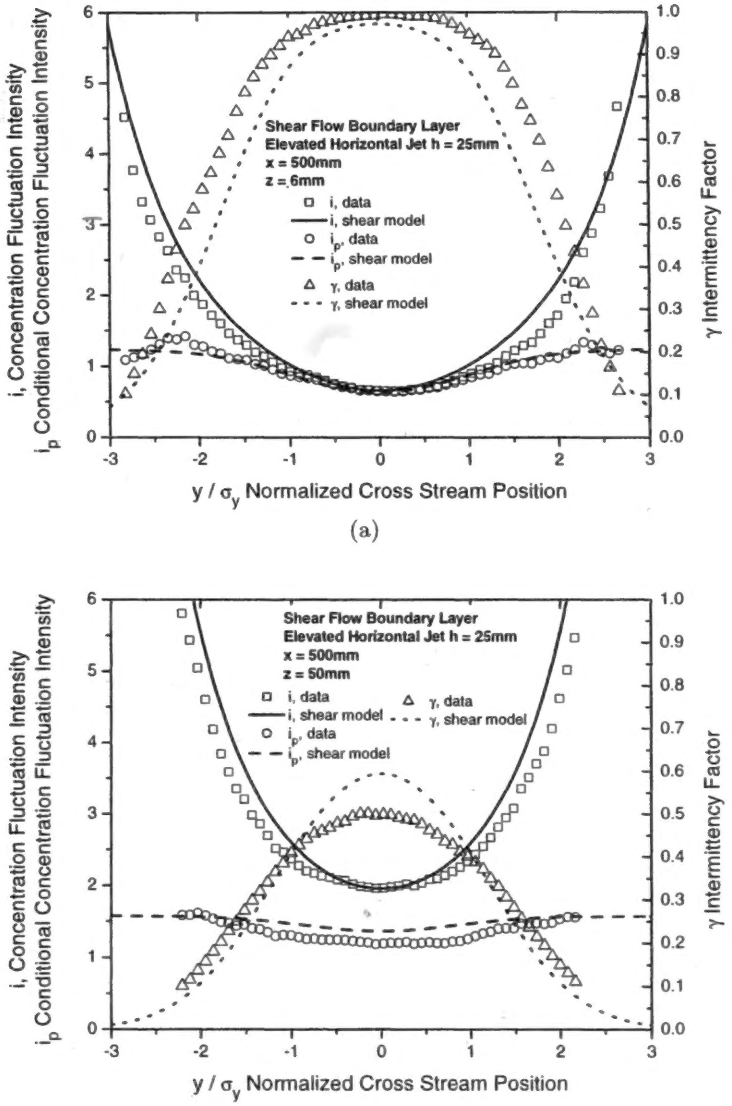

(a)

(b)

Figure H.19: Measured cross-stream profiles compared with pseudo-meandering plume theory of total concentration fluctuation intensity i, conditional concentration fluctuation intensity i_p, and intermittency factor γ for the elevated horizontal jet source $h = 25$ mm at $x = 500$ mm downstream. (a) at ground level $z = 6$ mm (b) above ground at $z = 50$ mm.

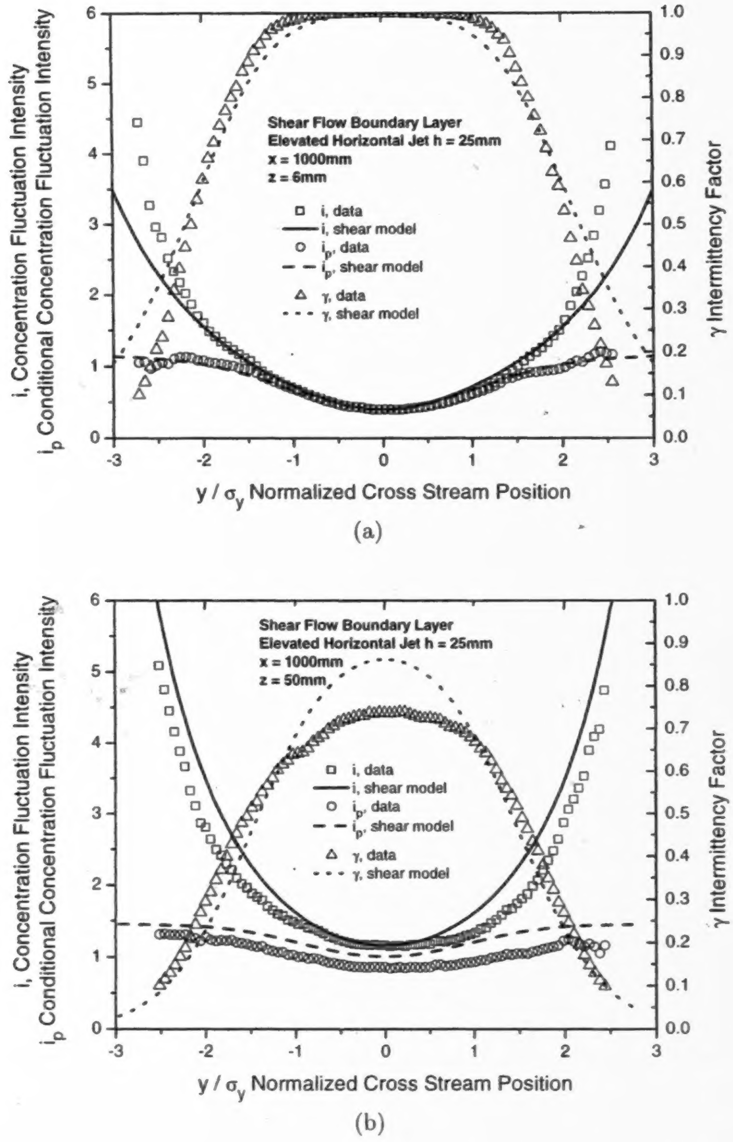

Figure H.20: Measured cross-stream profiles compared with pseudo-meandering plume theory of total concentration fluctuation intensity i, conditional concentration fluctuation intensity i_p, and intermittency factor γ for the elevated horizontal jet source $h = 25$ mm at $x = 1000$ mm downstream. (a) at ground level $z = 6$ mm (b) above ground at $z = 50$ mm.

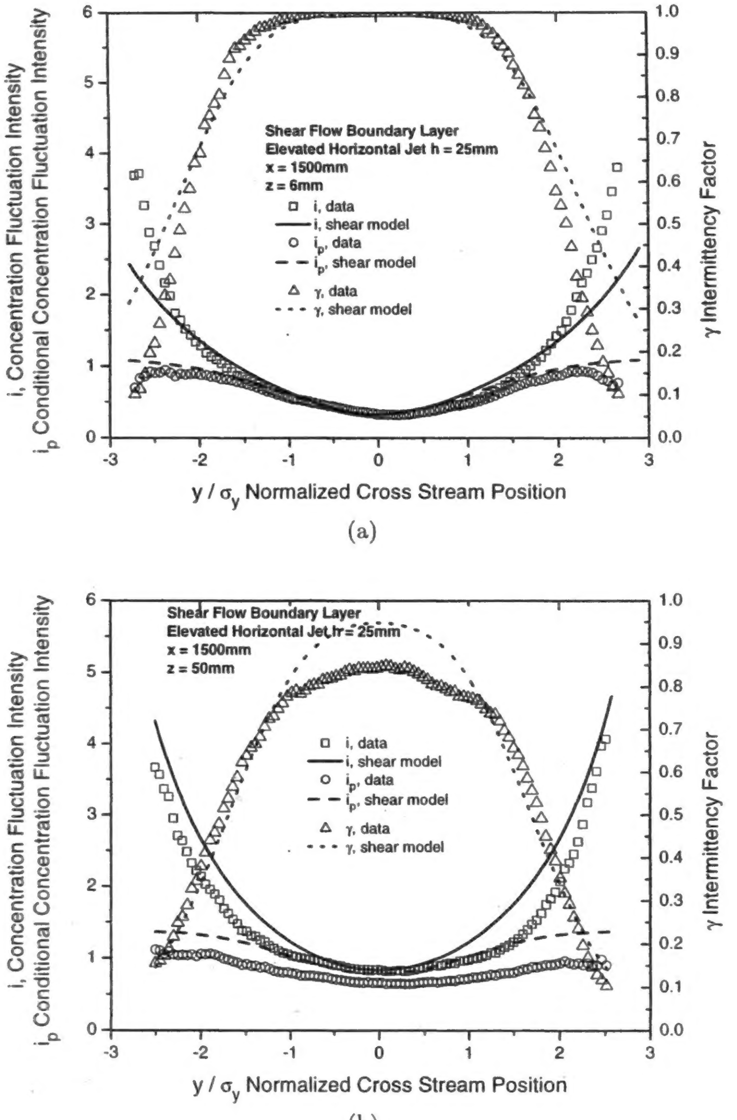

(a)

(b)

Figure H.21: Measured cross-stream profiles compared with pseudo-meandering plume theory of total concentration fluctuation intensity i, conditional concentration fluctuation intensity i_p, and intermittency factor γ for the elevated horizontal jet source $h = 25$ mm at $x = 1500$ mm downstream. (a) at ground level $z = 6$ mm (b) above ground at $z = 50$ mm.

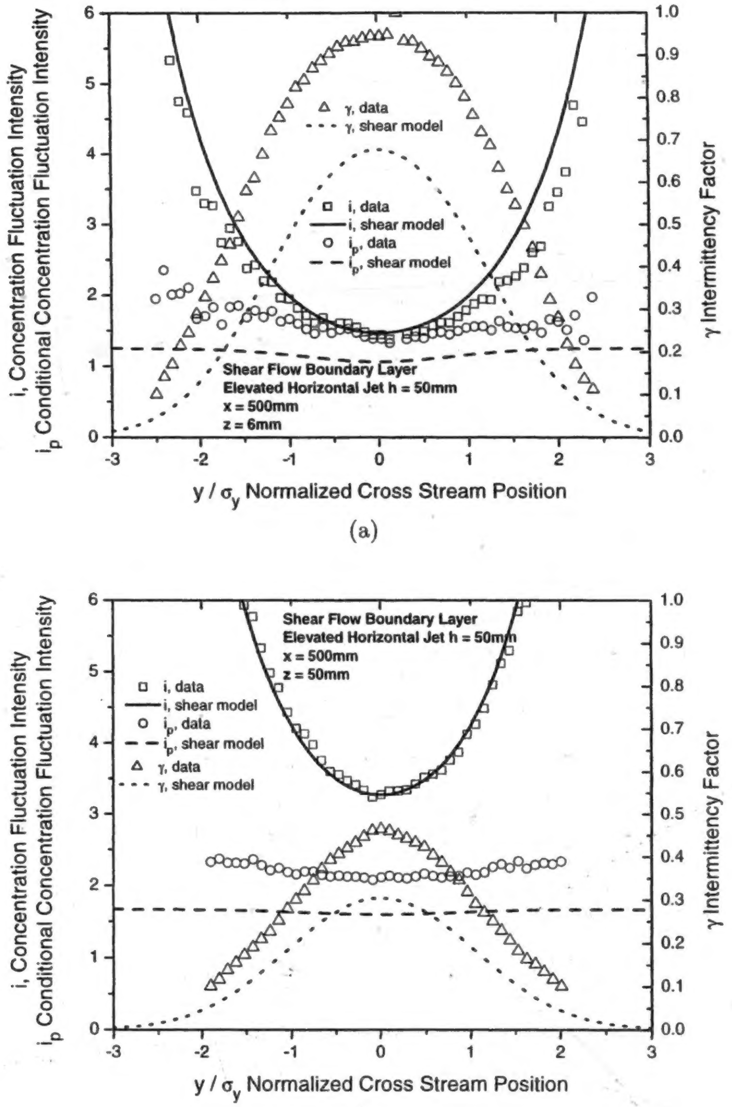

(a)

(b)

Figure H.22: Measured cross-stream profiles compared with pseudo-meandering plume theory of total concentration fluctuation intensity i, conditional concentration fluctuation intensity i_p, and intermittency factor γ for the elevated horizontal jet source $h = 50$ mm at $x = 500$ mm downstream. (a) at ground level $z = 6$ mm (b) above ground at $z = 50$ mm.

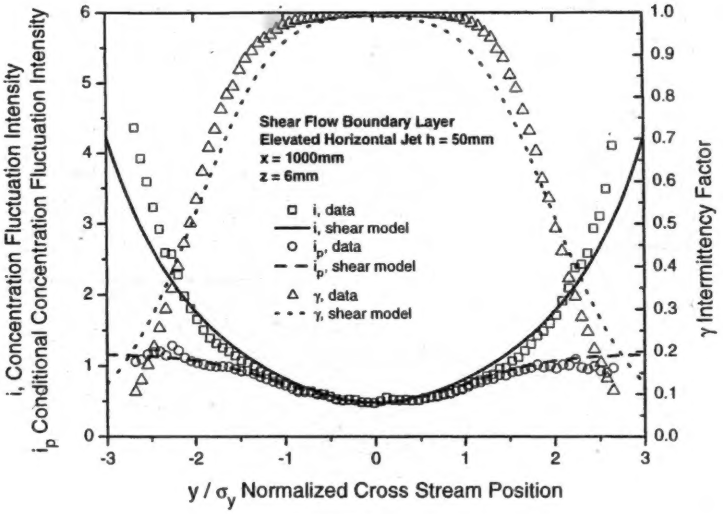

(a)

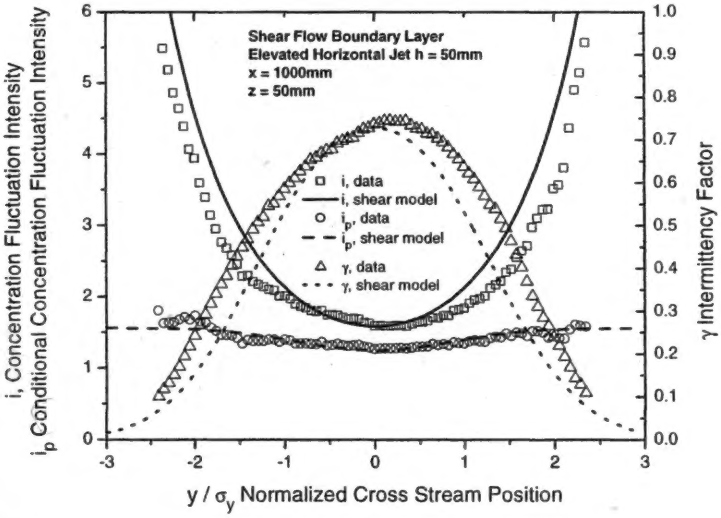

(b)

Figure H.23: Measured cross-stream profiles compared with pseudo-meandering plume theory of total concentration fluctuation intensity i, conditional concentration fluctuation intensity i_p, and intermittency factor γ for the elevated horizontal jet source $h = 50$ mm at $x = 1000$ mm downstream. (a) at ground level $z = 6$ mm (b) above ground at $z = 50$ mm.

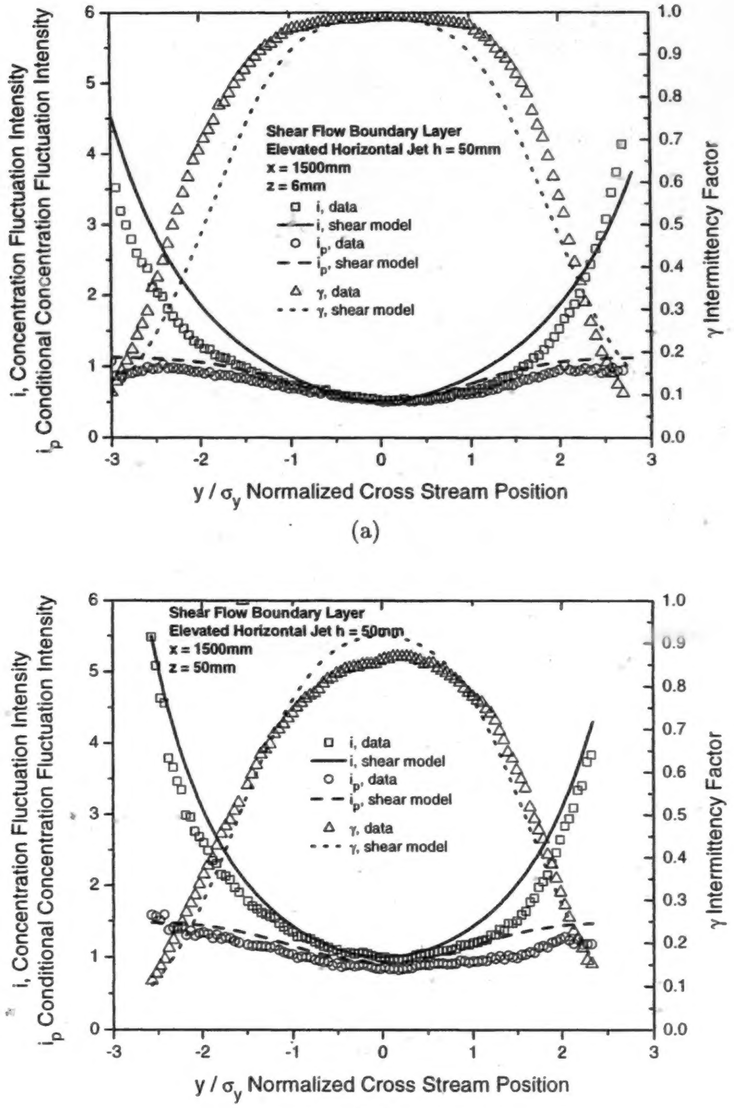

(a)

(b)

Figure H.24: Measured cross-stream profiles compared with pseudo-meandering plume theory of total concentration fluctuation intensity i, conditional concentration fluctuation intensity i_p, and intermittency factor γ for the elevated horizontal jet source $h = 50$ mm at $x = 1500$ mm downstream. (a) at ground level $z = 6$ mm (b) above ground at $z = 50$ mm.

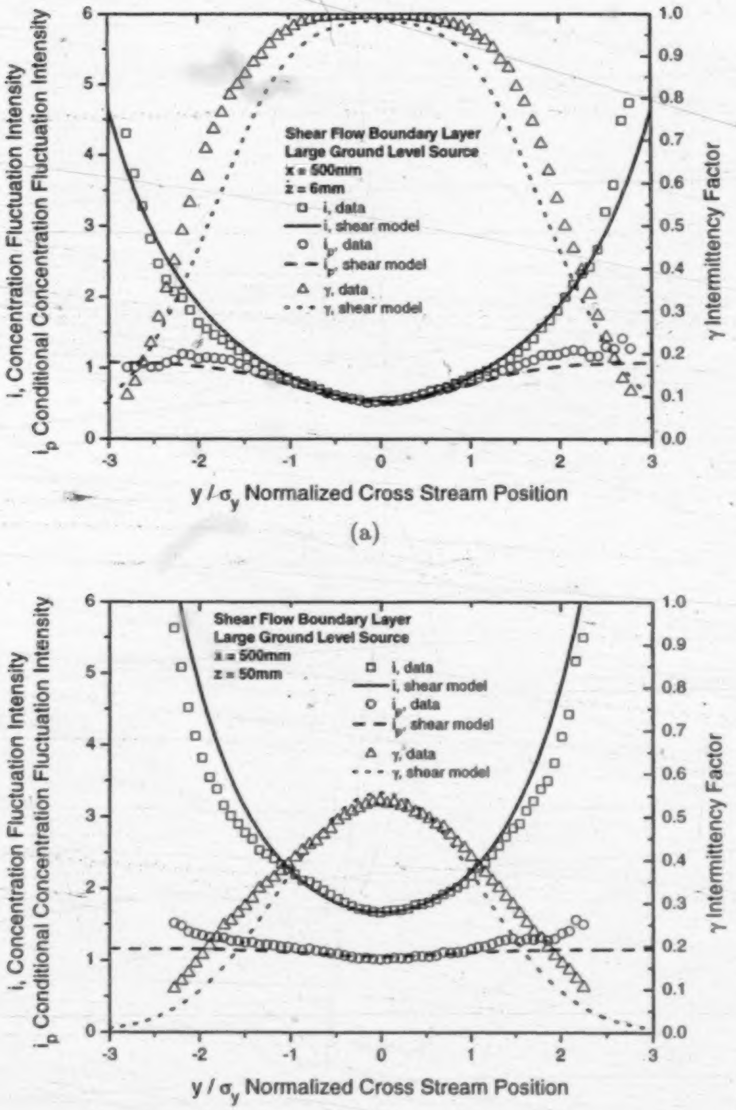

(a)

(b)

Figure H.25: Measured cross-stream profiles compared with pseudo-meandering plume theory of total concentration fluctuation intensity i, conditional concentration fluctuation intensity i_p, and intermittency factor γ for the large ground level source at $x = 500$ mm downstream. (a) at ground level $z = 6$ mm (b) above ground at $z = 50$ mm.

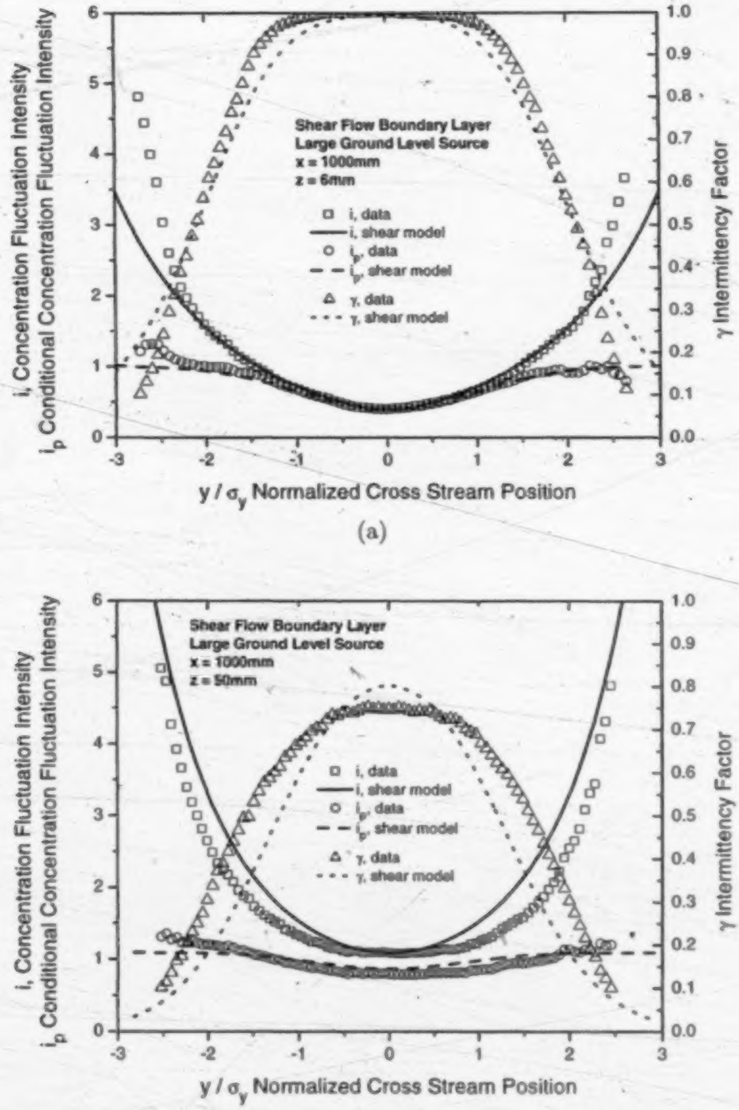

(a)

(b)

Figure H.26: Measured cross-stream profiles compared with pseudo-meandering plume theory of total concentration fluctuation intensity i, conditional concentration fluctuation intensity i_p, and intermittency factor γ for the large ground level source at $x = 1000$ mm downstream. (a) at ground level $z = 6$ mm (b) above ground at $z = 50$ mm.

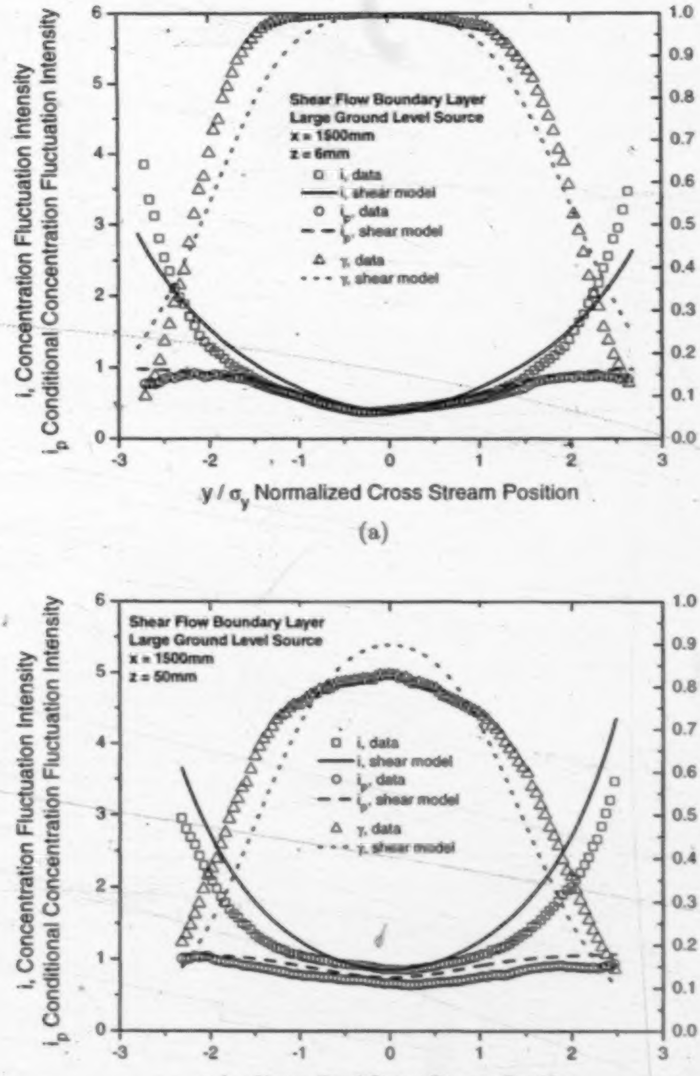

(a)

(b)

Figure H.27: Measured cross-stream profiles compared with pseudo-meandering plume theory of total concentration fluctuation intensity i, conditional concentration fluctuation intensity i_p, and intermittency factor γ for the large ground level source at $x = 1500$ mm downstream. (a) at ground level $z = 6$ mm (b) above ground at $z = 50$ mm.

Appendix I

Concentration Probability Distributions, and Burst and Gap Duration Distributions

This appendix contains additional graphs of concentration probability distributions, and burst and gap duration distributions to supplement the examples given in Chapter 4.

Figures I.1 to I.10 show examples of the concentration probability distributions of the linescan data compared to the clipped lognormal distribution. The clipped lognormal is detailed in Section 4.4. The plots show both the probability density function (pdf) and the exceedance probability distribution (edf). Figure I.1 shows an iso-kinetic jet source in grid turbulence, Figures I.2 to I.4 show the iso-kinetic horizontal elevated jet in shear flow, Figures I.5 to I.7 show the horizontal ground level jet source in shear flow, and Figures I.8 to I.10 show the large ground level source in shear flow. These examples cover a wide range of conditions and demonstrate that the clipped lognormal is an excellent fit to the data.

Figures I.11 to I.30 show additional examples of burst duration and gap duration probability distributions as discussed in Section 4.7. The plots show both the probability density function (pdf) and the exceedance probability distribution function (edf) of the burst and gap durations for a range of threshold levels normalized by the conditional mean concentration (c/C_p). The threshold levels vary for each example to cover as wide a range of thresholds as possible for each case. For each of the three sources used in these examples, bursts and gaps are shown for the cross-stream plume centreline at $y/\sigma_y = 0$ and a second off-centre position at $y/\sigma_y = 2$ or 3.

Figures I.11 to I.18 show the burst and gap statistics for the elevated horizontal iso-kinetic jet source in shear flow, Figures I.19 to I.26 show the ground level horizontal jet source in shear flow results, and Figures I.27 to I.30 show the large ground level source results. The agreement is acceptable for all cases, but the agreement between the stochastic simulation and the linescan data varies with measurement position and threshold level.

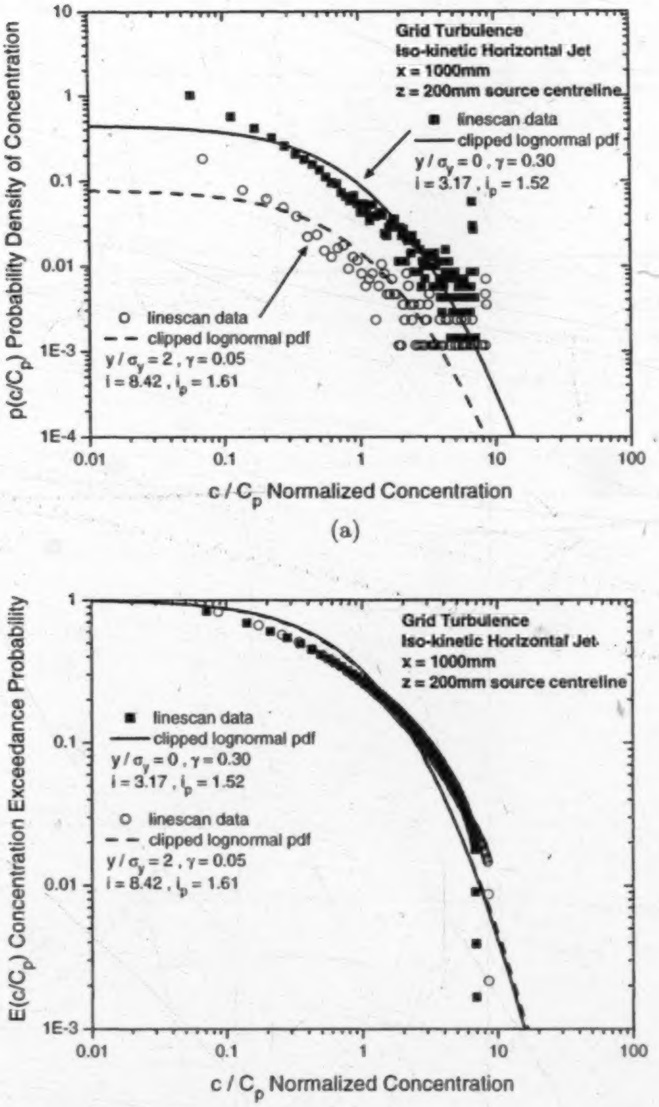

(a)

(b)

Figure I.1: Normalized concentration probability distributions for the horizontal iso-kinetic jet in grid turbulence, $h = 200$ mm (channel centreline),$x = 1000$ mm, $y/\sigma_y = 0$, measured at $z = 200$ mm compared to the clipped lognormal generated by the stochastic model (a) probability density function (pdf) (b) exceedance probability function (edf)

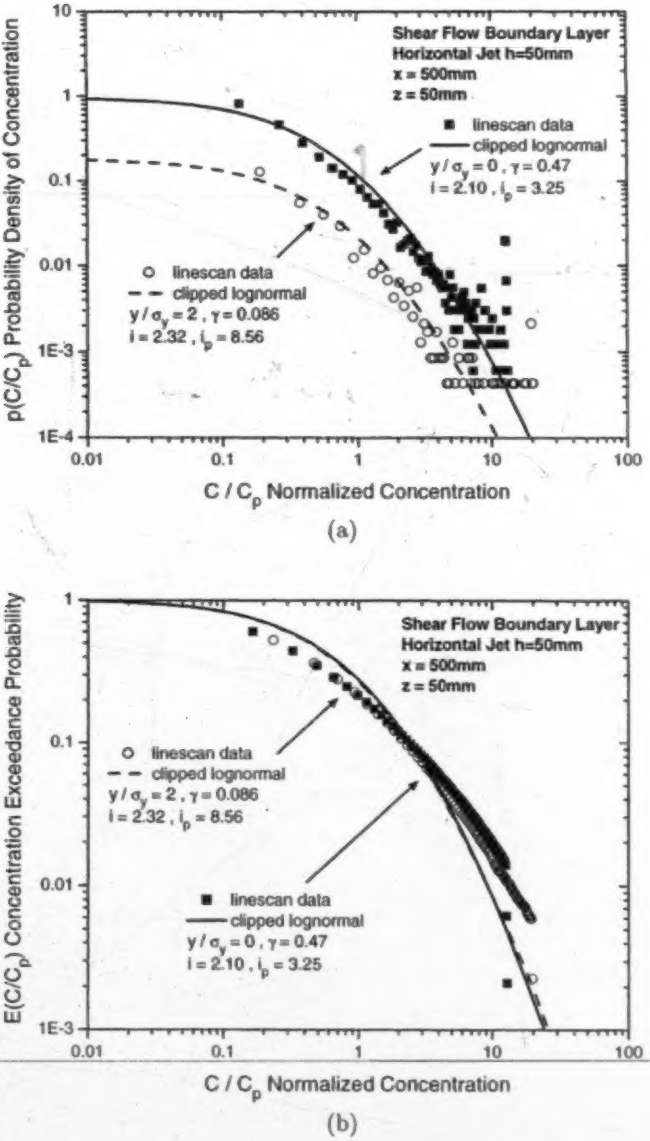

(a)

(b)

Figure I.2: Normalized concentration probability distributions for the horizontal isokinetic jet in shear flow, $h = 50$ mm, $x = 500$ mm, measured at $z = 50$ mm compared to the clipped lognormal generated by the stochastic model (a) probability density function (pdf) (b) exceedance probability function (edf)

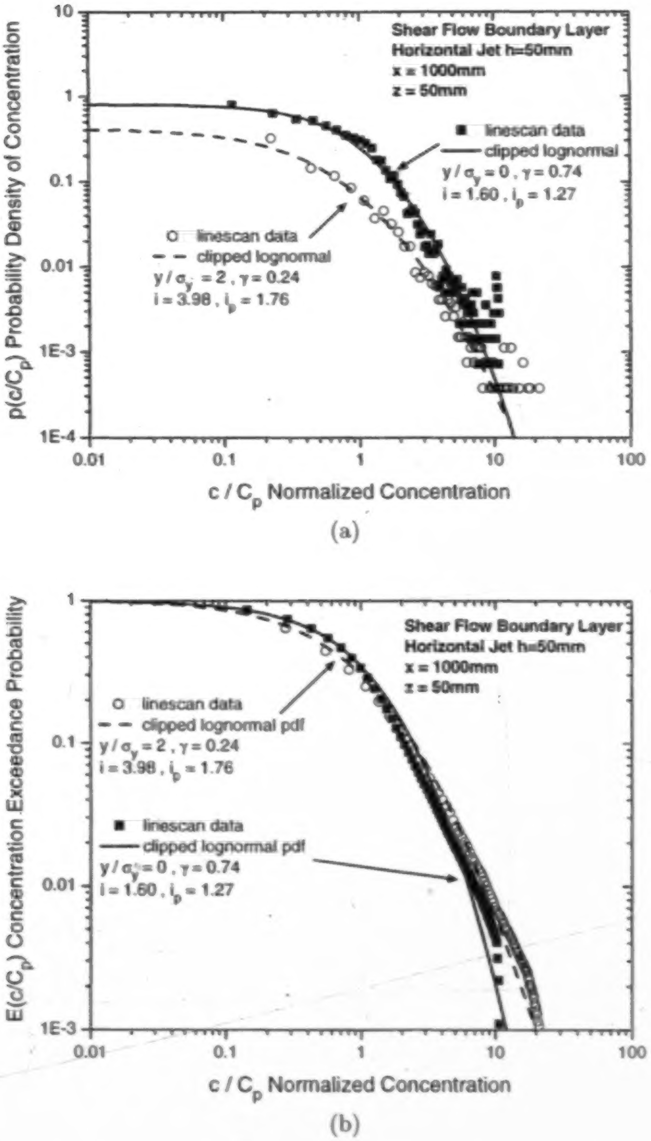

(a)

(b)

Figure I.3: Normalized concentration probability distributions for the horizontal isokinetic jet in shear flow, $h = 50$ mm, $x = 1000$ mm, measured at $z = 50$ mm compared to the clipped lognormal generated by the stochastic model (a) probability density function (pdf) (b) exceedance probability function (edf)

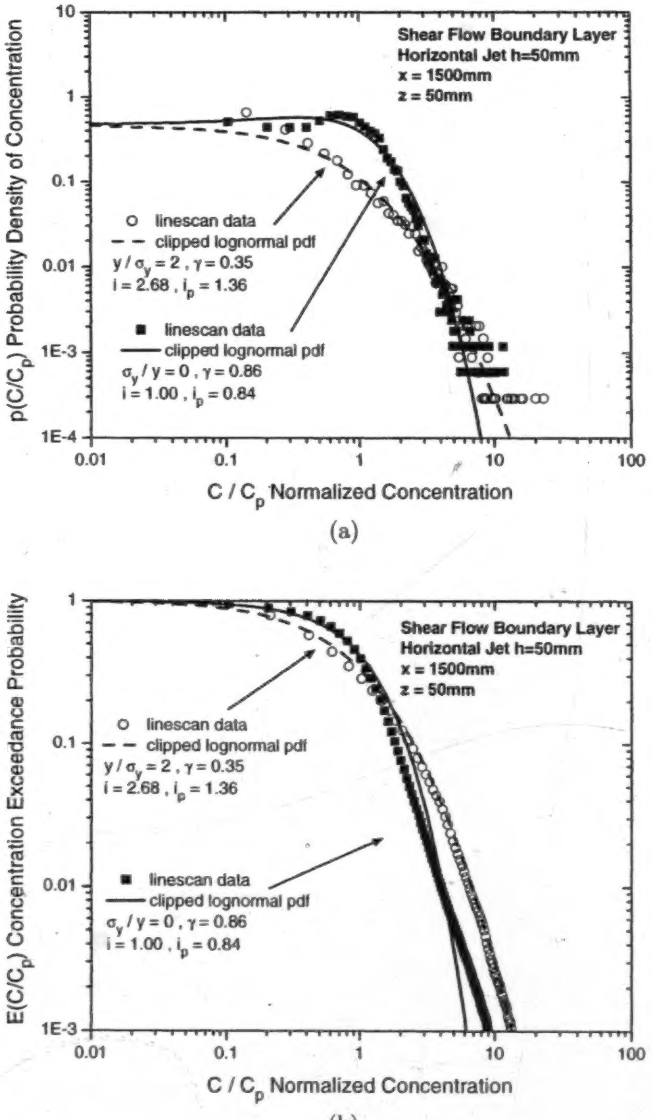

(a)

(b)

Figure I.4: Normalized concentration probability distributions for the horizontal isokinetic jet in shear flow, $h = 50$ mm, $x = 1500$ mm, measured at $z = 50$ mm compared to the clipped lognormal generated by the stochastic model (a) probability density function (pdf) (b) exceedance probability function (edf)

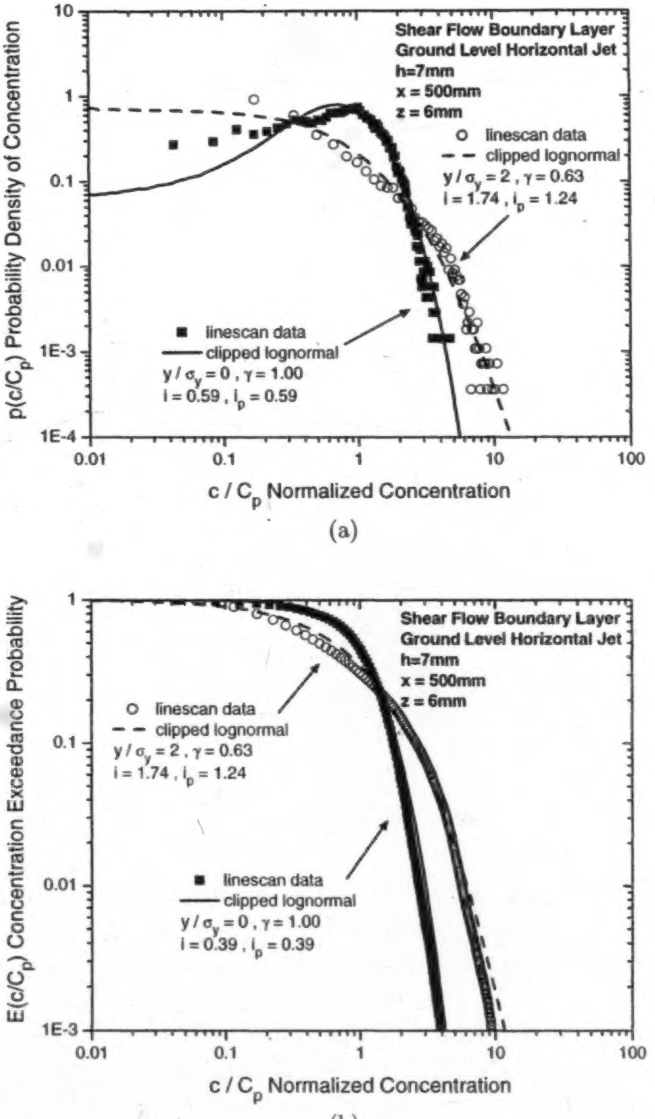

(a)

(b)

Figure I.5: Normalized concentration probability distributions for the ground level horizontal jet in shear flow, $h = 7$ mm, $x = 500$ mm, measured at $z = 6$ mm compared to the clipped lognormal generated by the stochastic model (a) probability density function (pdf) (b) exceedance probability function (edf)

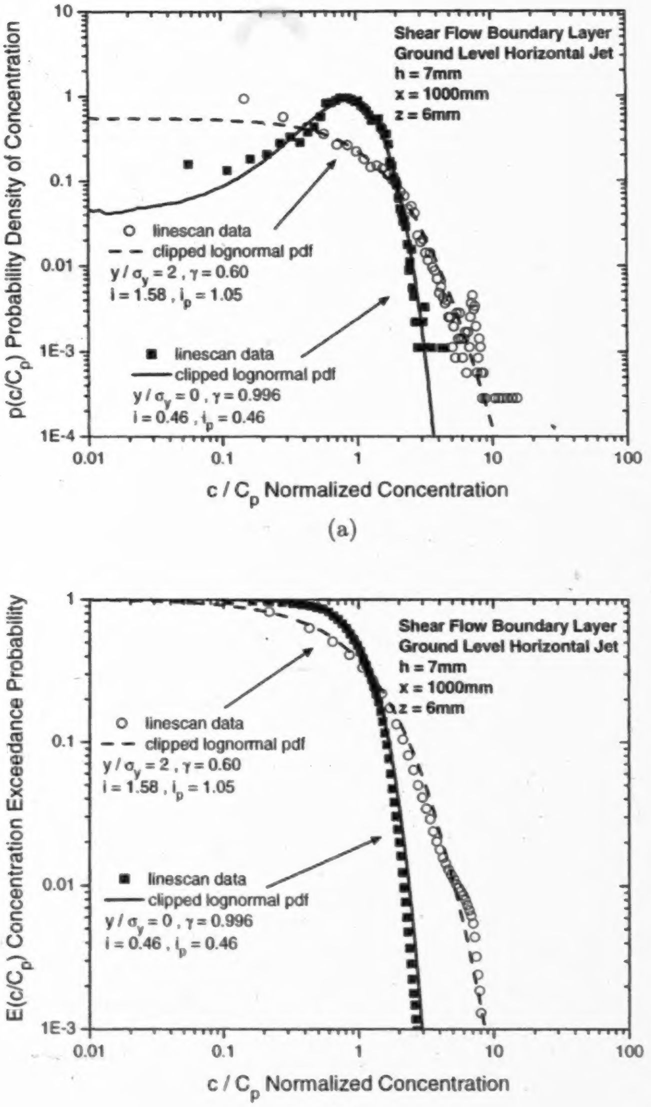

(a)

(b)

Figure I.6: Normalized concentration probability distributions for the ground level horizontal jet in shear flow, h = 7 mm, x = 1000 mm, measured at z = 6 mm compared to the clipped lognormal generated by the stochastic model (a) probability density function (pdf) (b) exceedance probability function (edf)

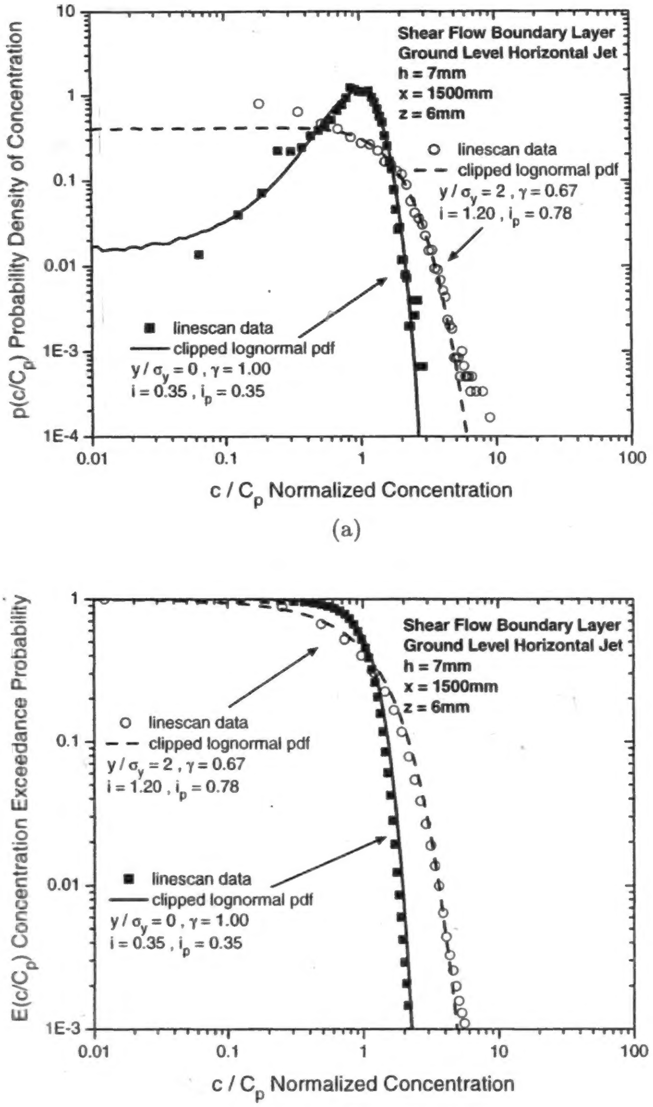

(a)

(b)

Figure I.7: Normalized concentration probability distributions for the ground level horizontal jet in shear flow, $h = 7$ mm, $x = 1500$ mm, measured at $z = 6$ mm compared to the clipped lognormal generated by the stochastic model (a) probability density function (pdf) (b) exceedance probability function (edf)

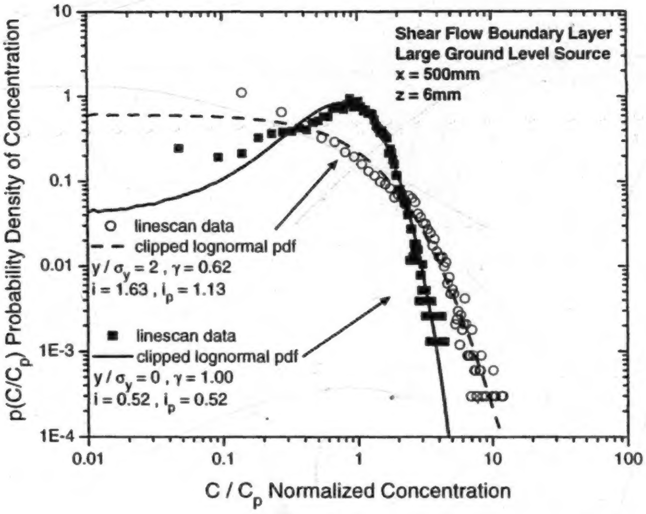

(a)

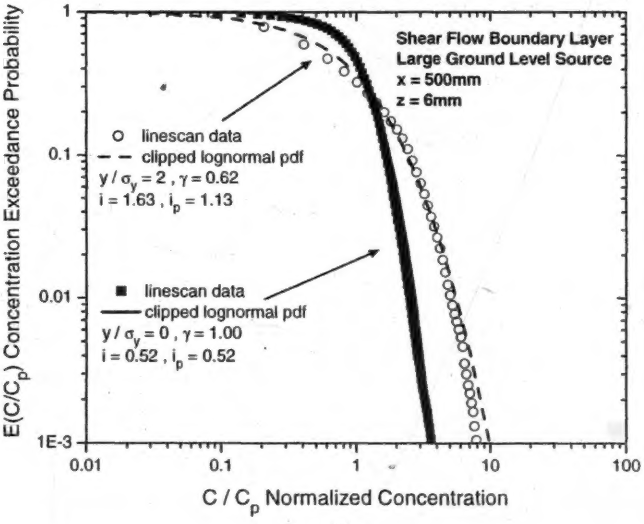

(b)

Figure I.8: Normalized concentration probability distributions for the large ground level source in shear flow, $x = 500$ mm, measured at $z = 6$ mm compared to the clipped lognormal generated by the stochastic model (a) probability density function (pdf) (b) exceedance probability function (edf)

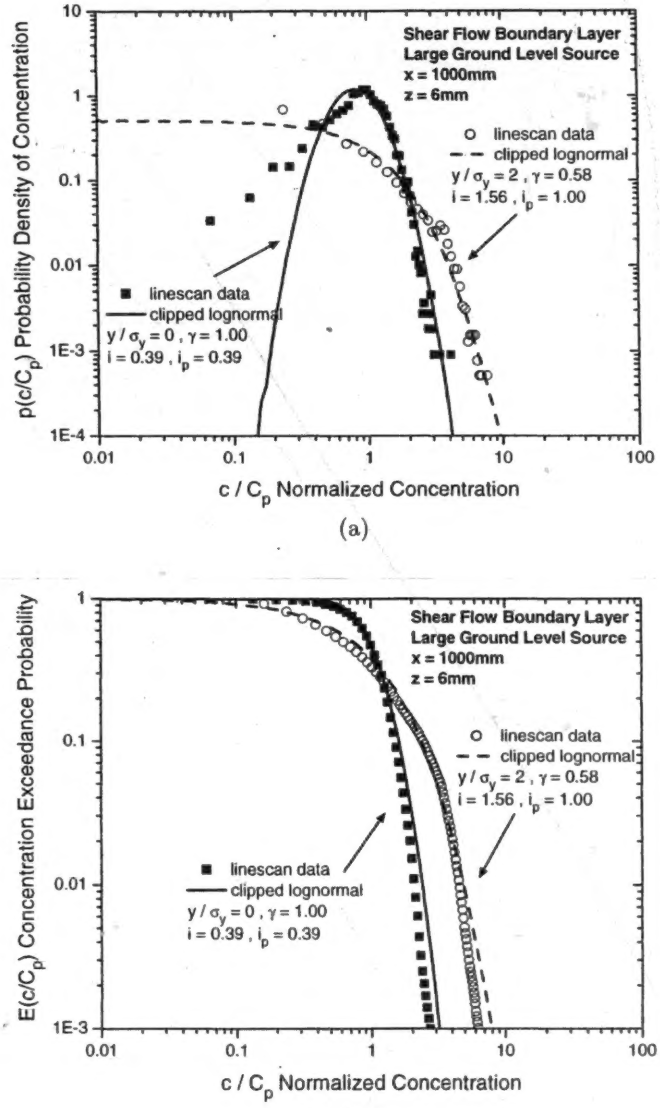

(a)

(b)

Figure I.9: Normalized concentration probability distributions for the large ground level source in shear flow, $x = 1000$ mm, measured at $z = 6$ mm compared to the clipped lognormal generated by the stochastic model (a) probability density function (pdf) (b) exceedance probability function (edf)

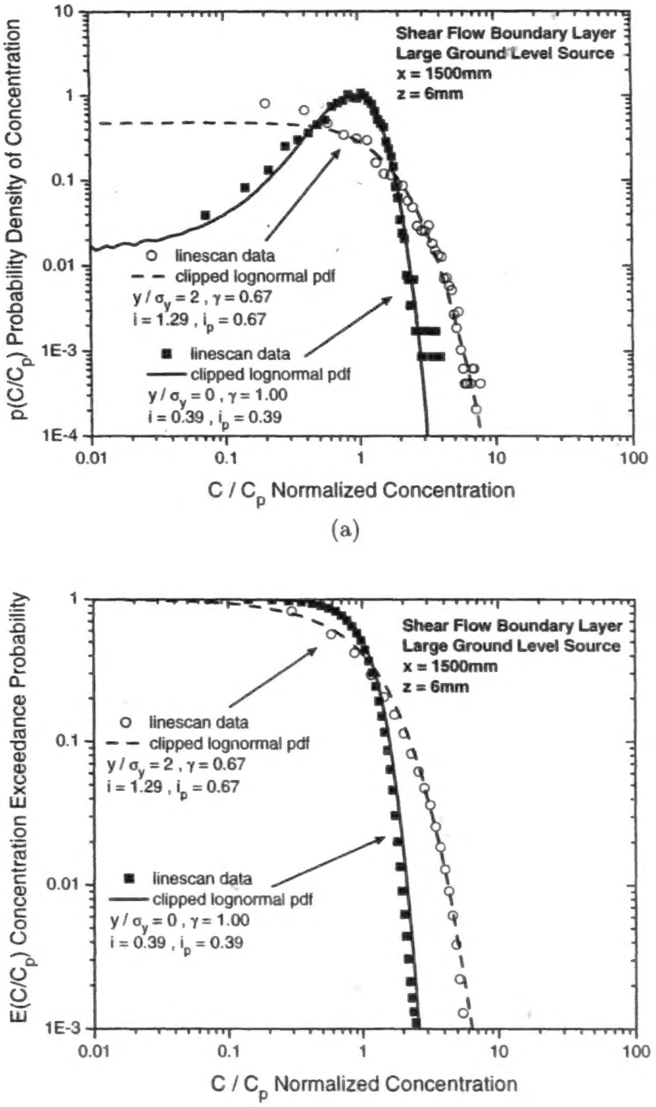

(a)

(b)

Figure I.10: Normalized concentration probability distributions for the large ground level source in shear flow, x = 1500 mm, measured at z = 6 mm compared to the clipped lognormal generated by the stochastic model (a) probability density function (pdf) (b) exceedance probability function (edf)

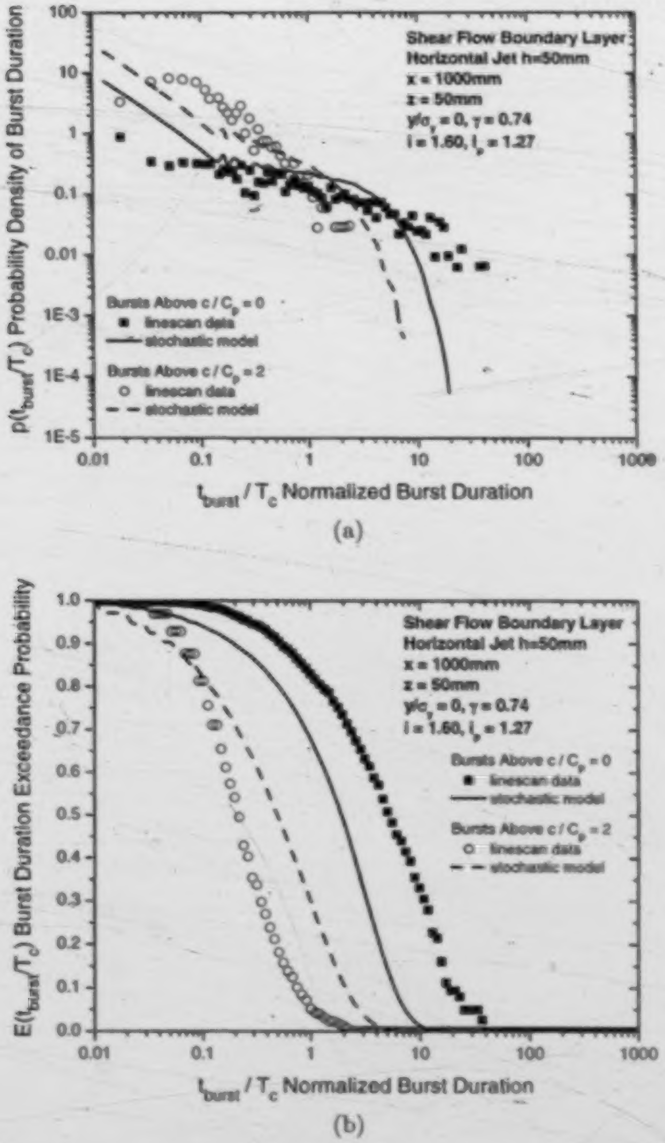

(a)

(b)

Figure I.11: Burst duration probability distributions for the horizontal iso-kinetic jet in shear flow, $h = 50$ mm, $x = 1000$ mm, measured at $z = 50$ mm, $y/\sigma_y = 0$ compared to stochastic simulation results (a) probability density function (pdf) (b) exceedance probability function (edf)

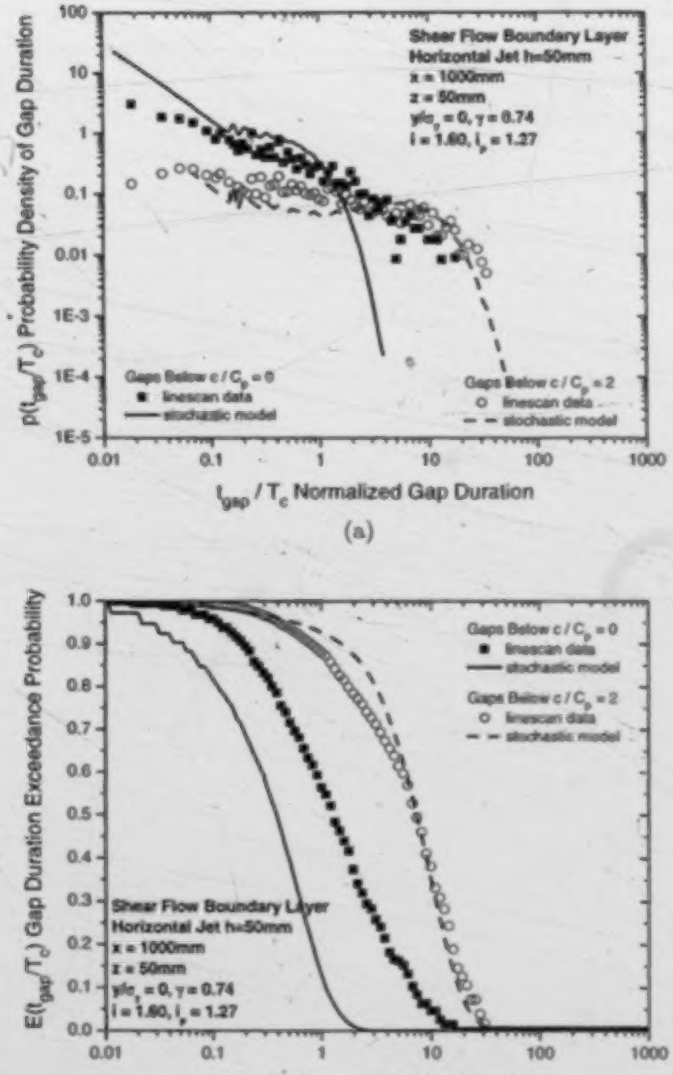

(a)

(b)

Figure I.12: Gap duration probability distributions for the horizontal iso-kinetic jet in shear flow, $h = 50$ mm, $x = 1000$ mm, measured at $z = 50$ mm, $y/\sigma_y = 0$ compared to stochastic simulation results (a) probability density function (pdf) (b) exceedance probability function (edf)

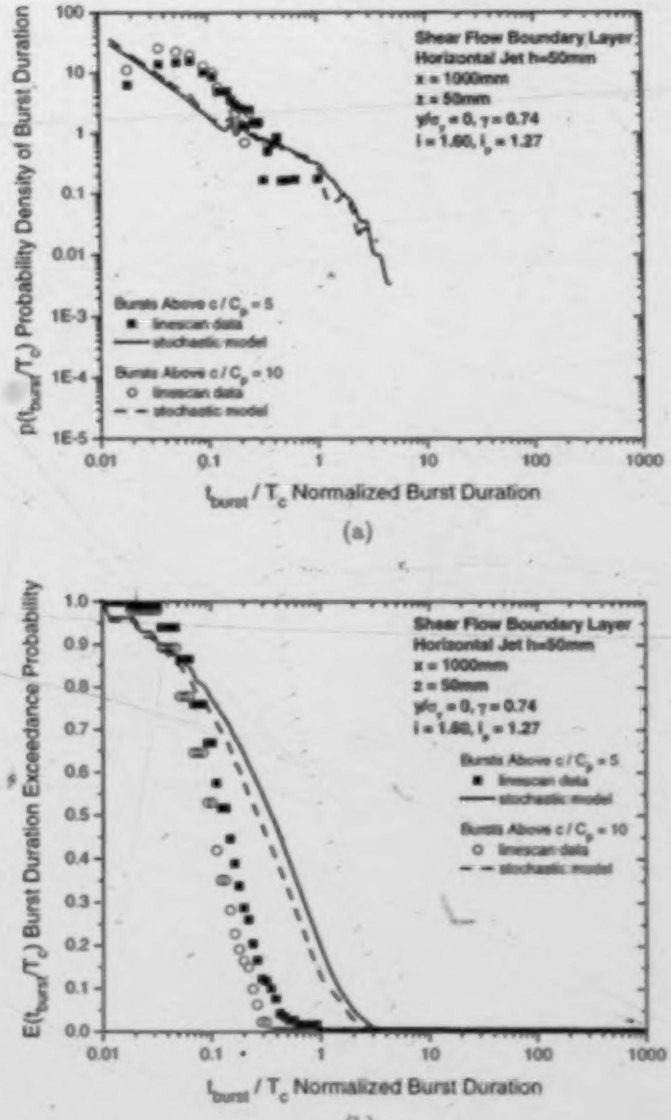

(a)

(b)

Figure I.13: Burst duration probability distributions for the horizontal iso-kinetic jet in shear flow, $h = 50$ mm, $x = 1000$ mm, measured at $z = 50$ mm, $y/\sigma_y = 0$ compared to stochastic simulation results (a) probability density function (pdf) (b) exceedance probability function (edf)

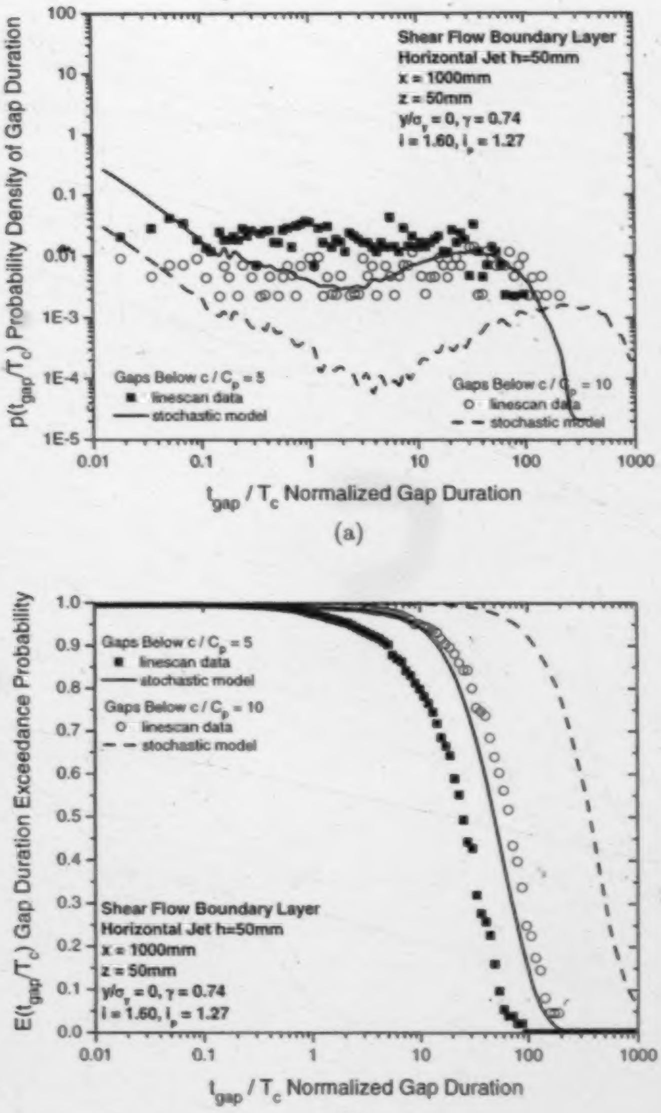

(a)

(b)

Figure I.14: Gap duration probability distributions for the horizontal iso-kinetic jet in shear flow, $h = 50$ mm, $x = 1000$ mm, measured at $z = 50$ mm, $y/\sigma_y = 0$ compared to stochastic simulation results (a) probability density function (pdf) (b) exceedance probability function (edf)

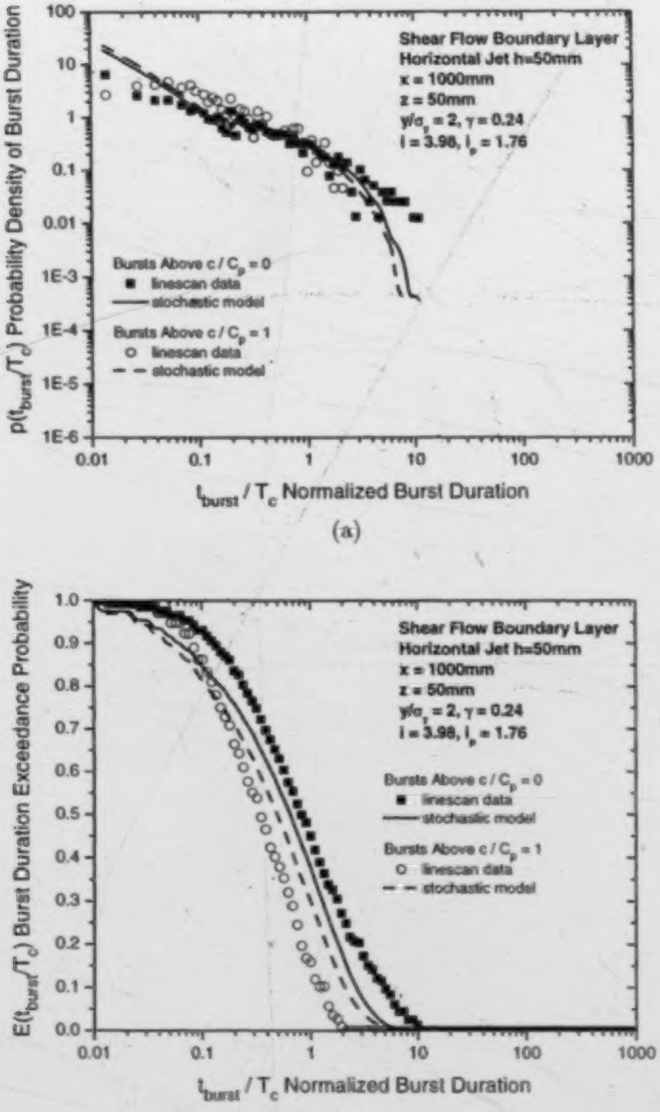

(a)

(b)

Figure I.15: Burst duration probability distributions for the horizontal iso-kinetic jet in shear flow, $h = 50$ mm, $x = 1000$ mm, measured at $z = 50$ mm, $y/\sigma_y = 2$ compared to stochastic simulation results (a) probability density function (pdf) (b) exceedance probability function (edf)

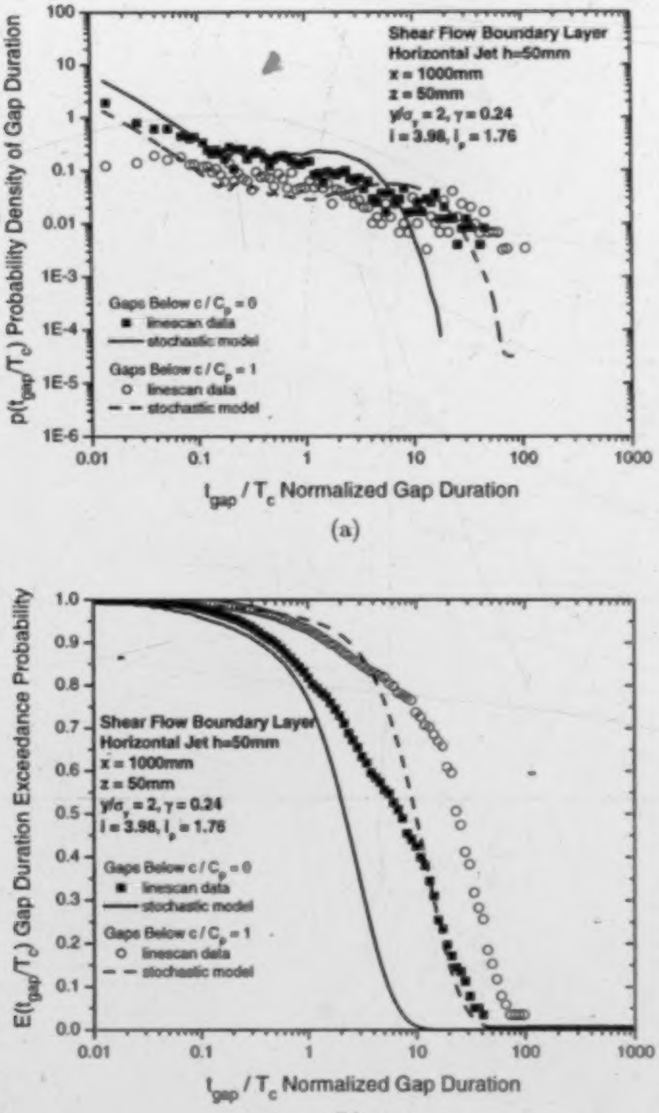

(a)

(b)

Figure I.16: Gap duration probability distributions for the horizontal iso-kinetic jet in shear flow; $h = 50$ mm, $x = 1000$ mm, measured at $z = 50$ mm, $y/\sigma_y = 2$ compared to stochastic simulation results (a) probability density function (pdf) (b) exceedance probability function (edf)

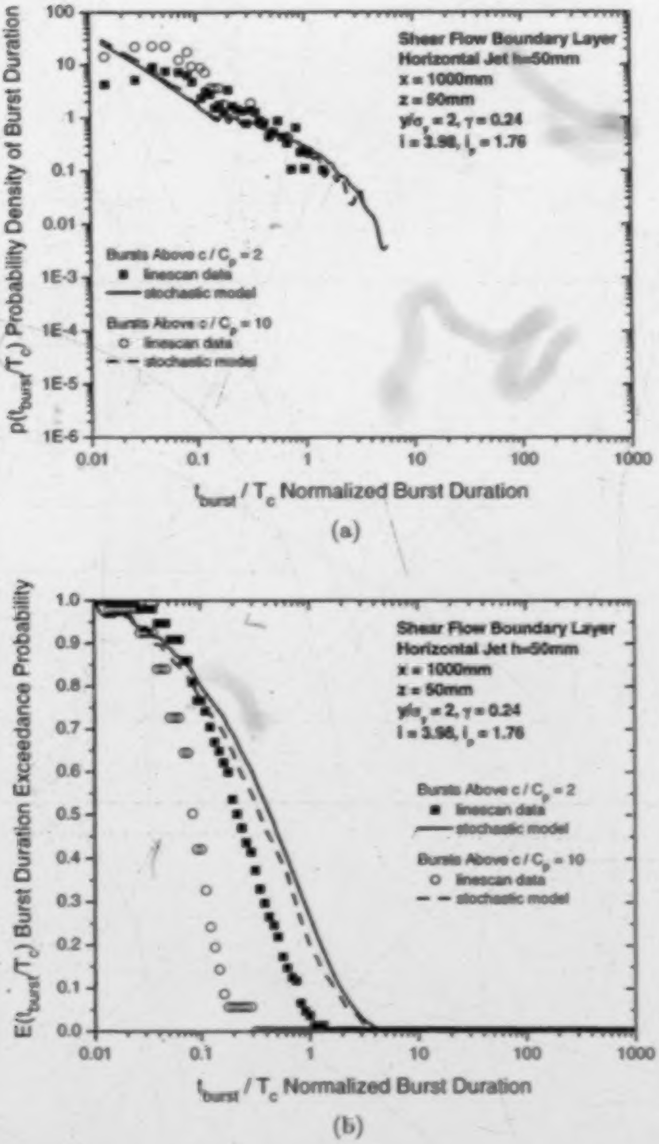

(a)

(b)

Figure I.17: Burst duration probability distributions for the horizontal iso-kinetic jet in shear flow, $h = 50$ mm, $x = 1000$ mm, measured at $z = 50$ mm, $y/\sigma_y = 2$ compared to stochastic simulation results (a) probability density function (pdf) (b) exceedance probability function (edf)

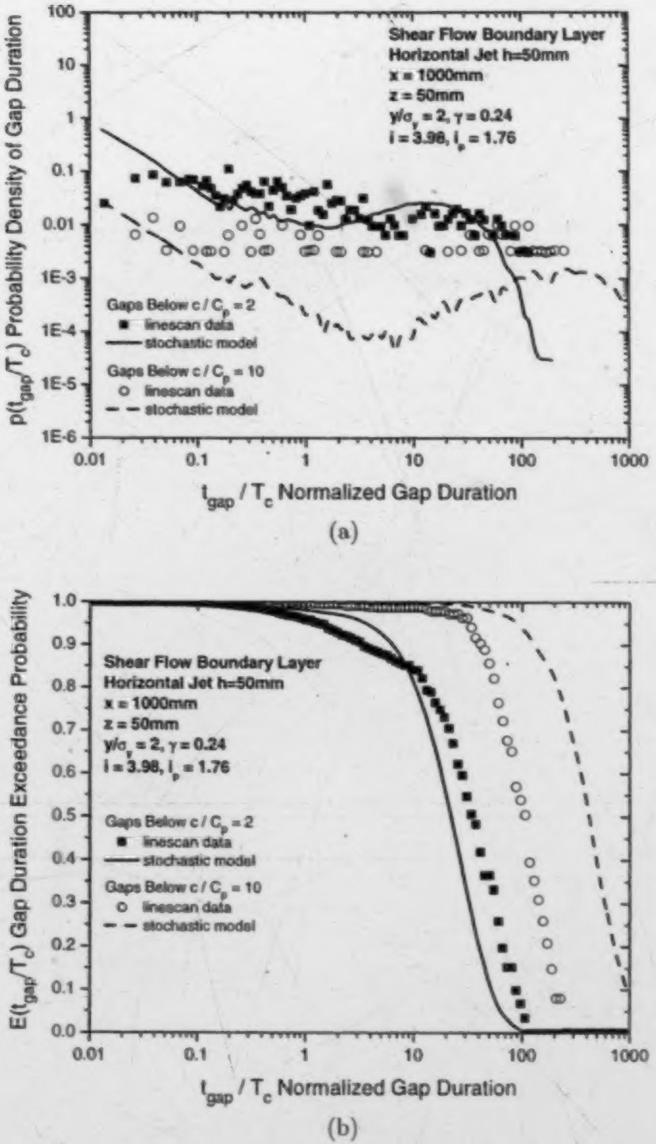

(a)

(b)

Figure I.18: Gap duration probability distributions for the horizontal iso-kinetic jet in shear flow, $h = 50$ mm, $x = 1000$ mm, measured at $z = 50$ mm, $y/\sigma_y = 2$ compared to stochastic simulation results (a) probability density function (pdf) (b) exceedance probability function (edf)

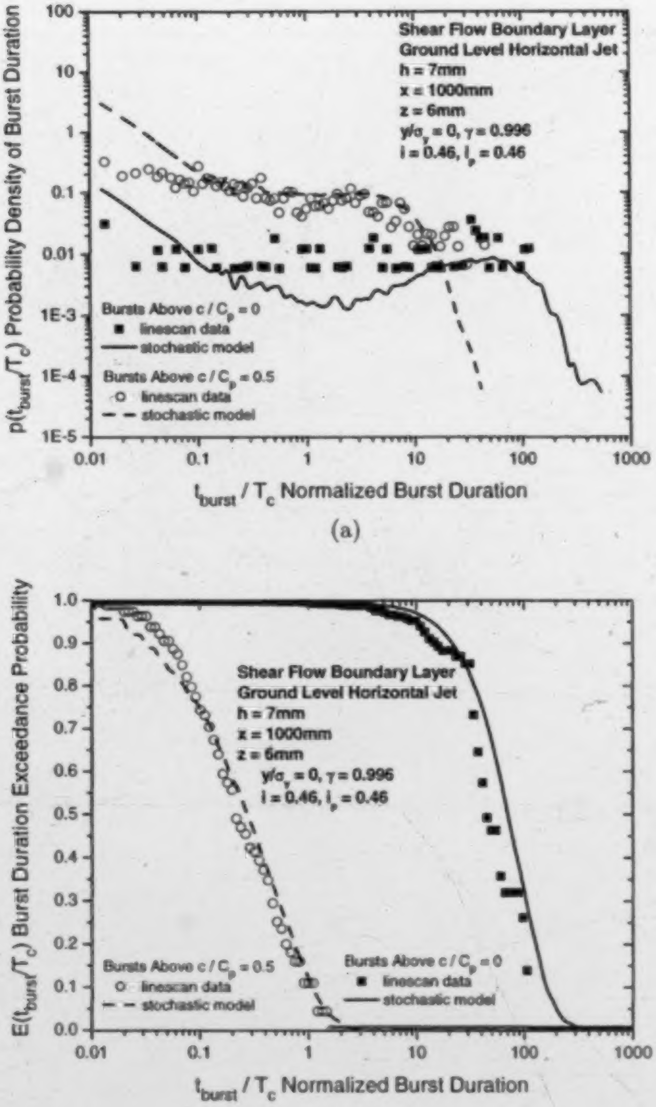

(a)

(b)

Figure I.19: Burst duration probability distributions for the ground level horizontal jet in shear flow, $h = 7$ mm, $x = 1000$ mm, measured at $z = 6$ mm, $y/\sigma_y = 0$ compared to stochastic simulation results for bursts above $(c/C_p) = 0$ and $(c/C_p) = 0.5$ (a) probability density function (pdf) (b) exceedance probability function (edf)

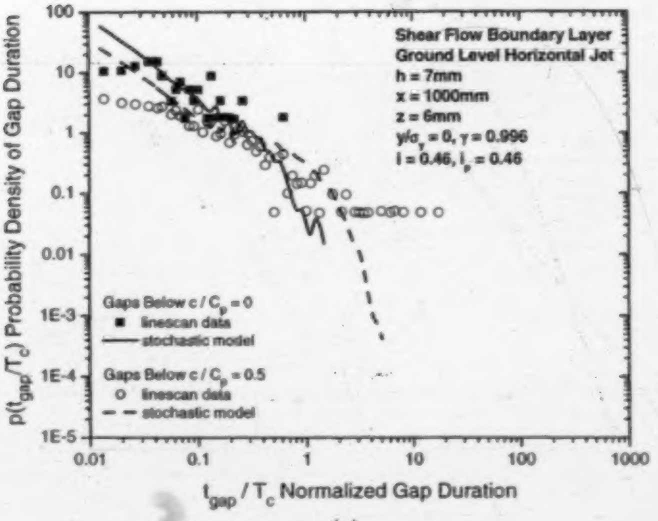

(a)

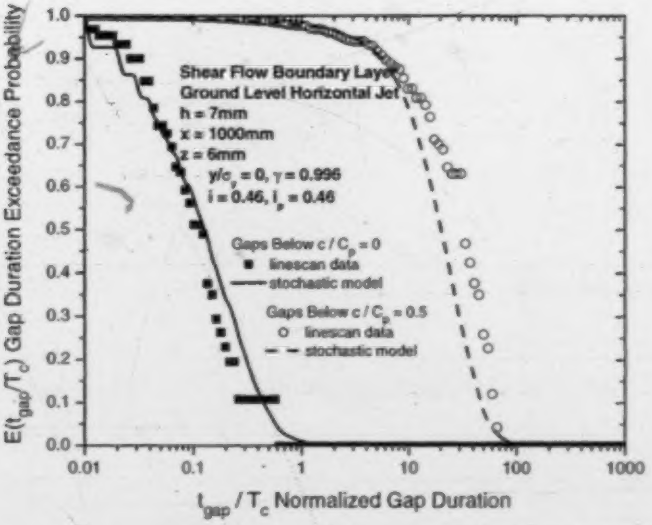

(b)

Figure I.20: Gap duration probability distributions for the ground level horizontal jet in shear flow, $h = 7$ mm, $x = 1000$ mm, measured at $z = 6$ mm, $y/\sigma_y = 0$ compared to stochastic simulation results for gaps below $(c/C_p) = 0$ and $(c/C_p) = 0.5$ (a) probability density function (pdf) (b) exceedance probability function (edf)

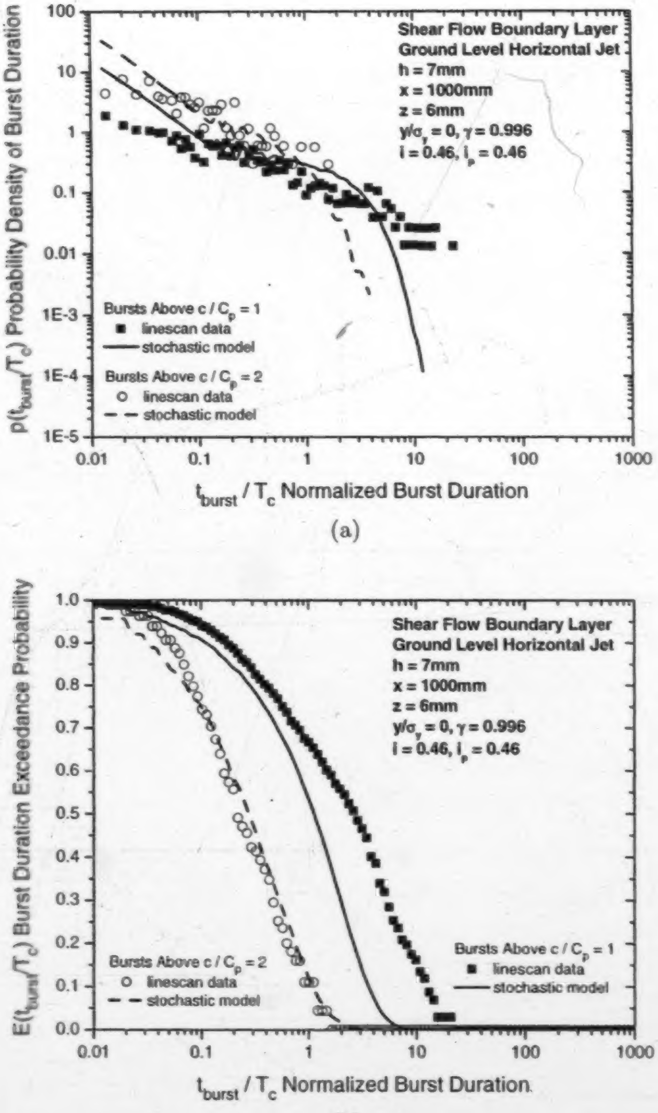

(a)

(b)

Figure I.21: Burst duration probability distributions for the ground level horizontal jet in shear flow, $h = 7$ mm, $x = 1000$ mm, measured at $z = 6$ mm, $y/\sigma_y = 0$ compared to stochastic simulation results for bursts above $(c/C_p) = 1$ and $(c/C_p) = 2$ (a) probability density function (pdf) (b) exceedance probability function (edf)

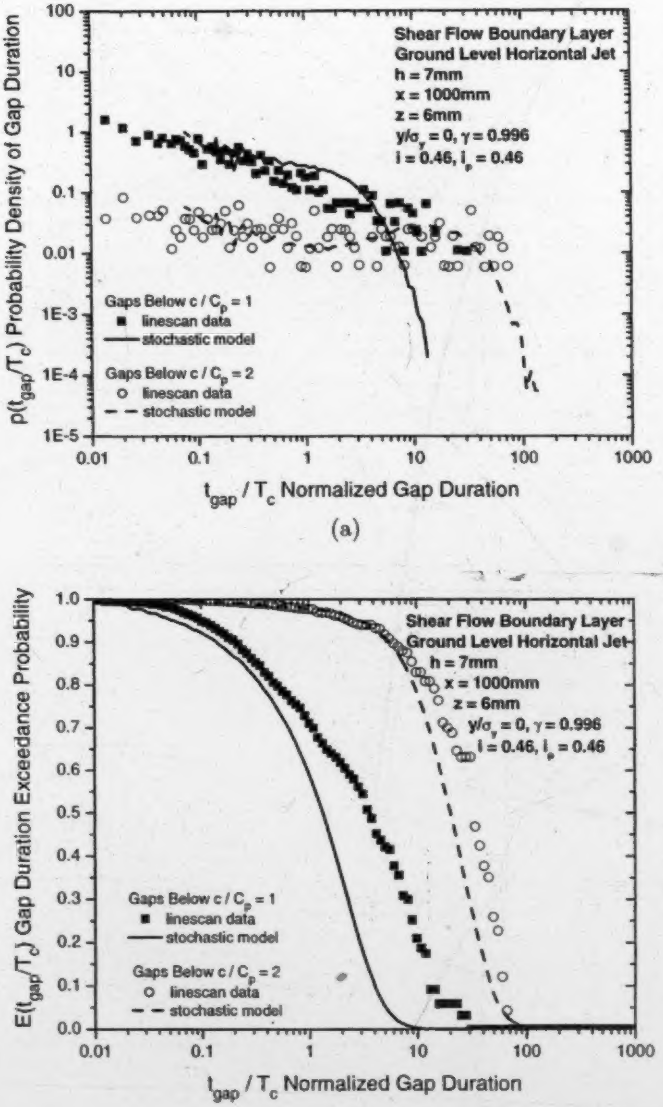

(a)

(b)

Figure I.22: Gap duration probability distributions for the ground level horizontal jet in shear flow, $h = 7$ mm, $x = 1000$ mm, measured at $z = 6$ mm, $y/\sigma_y = 0$ compared to stochastic simulation results for gaps below $(c/C_p) = 1$ and $(c/C_p) = 2$ (a) probability density function (pdf) (b) exceedance probability function (edf)

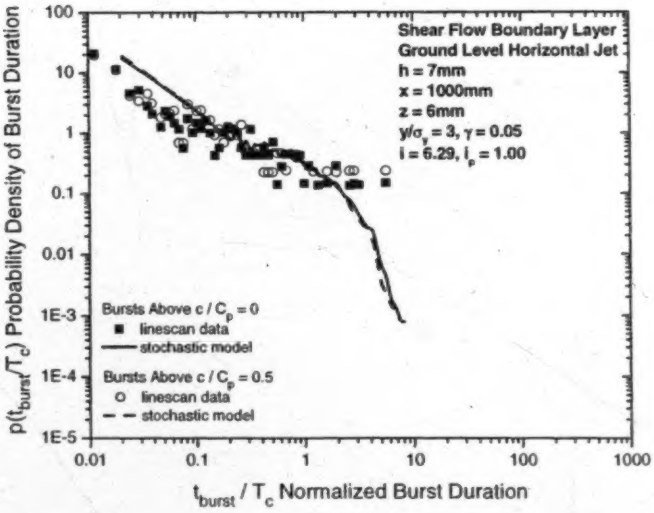

(a)

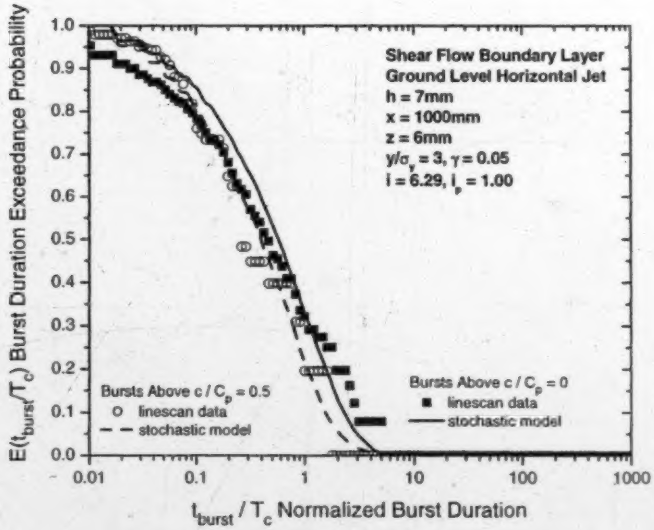

(b)

Figure I.23: Burst duration probability distributions for the ground level horizontal jet in shear flow, $h = 7$ mm, $x = 1000$ mm, measured at $z = 6$ mm, $y/\sigma_y = 3$ compared to stochastic simulation results for bursts above $(c/C_p) = 0$ and $(c/C_p) = 0.5$ (a) probability density function (pdf) (b) exceedance probability function (edf)

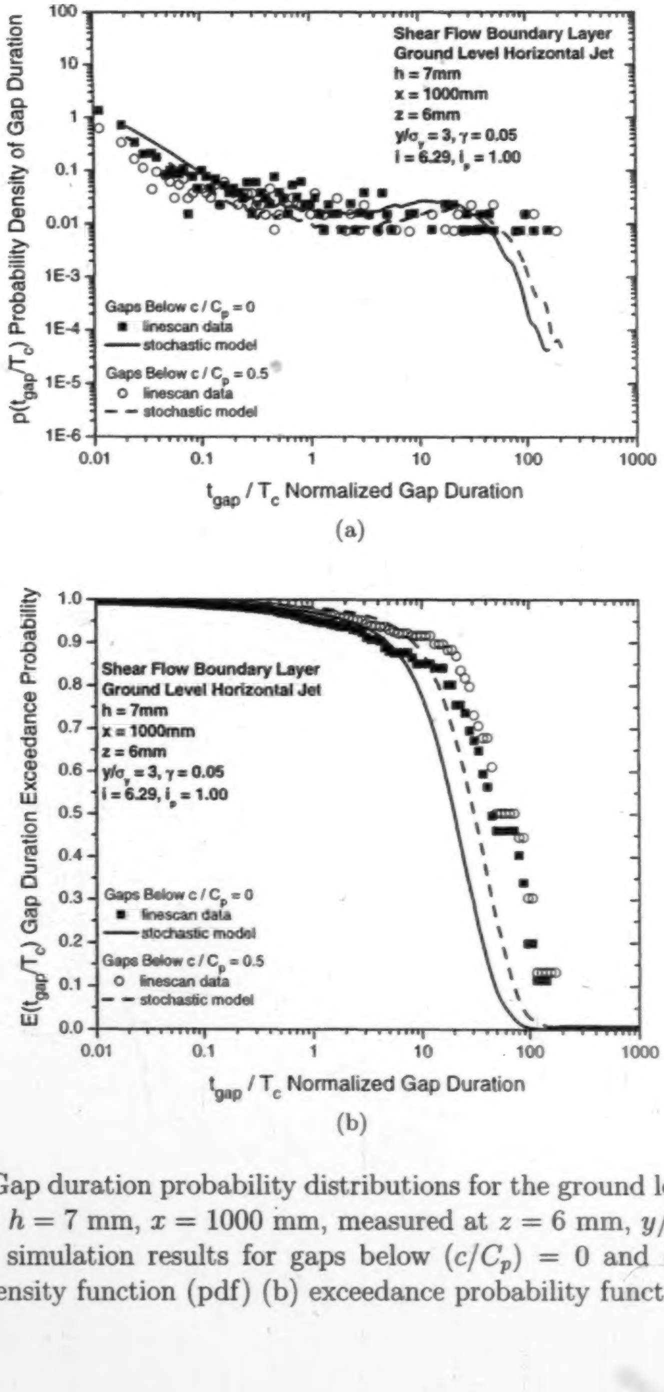

Figure I.24: Gap duration probability distributions for the ground level horizontal jet in shear flow, $h = 7$ mm, $x = 1000$ mm, measured at $z = 6$ mm, $y/\sigma_y = 3$ compared to stochastic simulation results for gaps below $(c/C_p) = 0$ and $(c/C_p) = 0.5$ (a) probability density function (pdf) (b) exceedance probability function (edf)

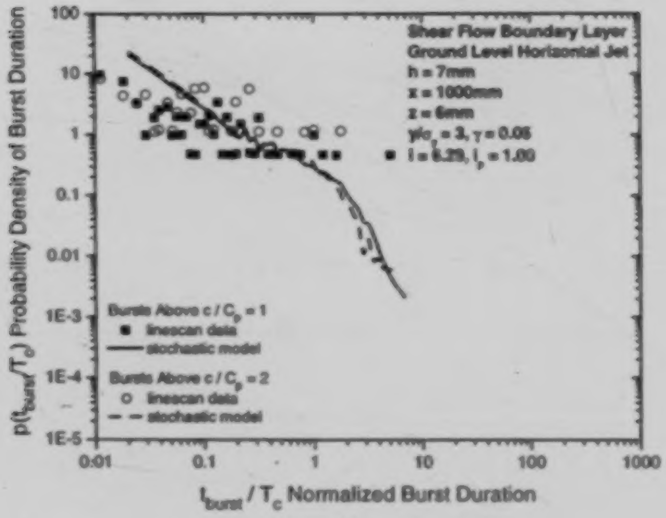

(a)

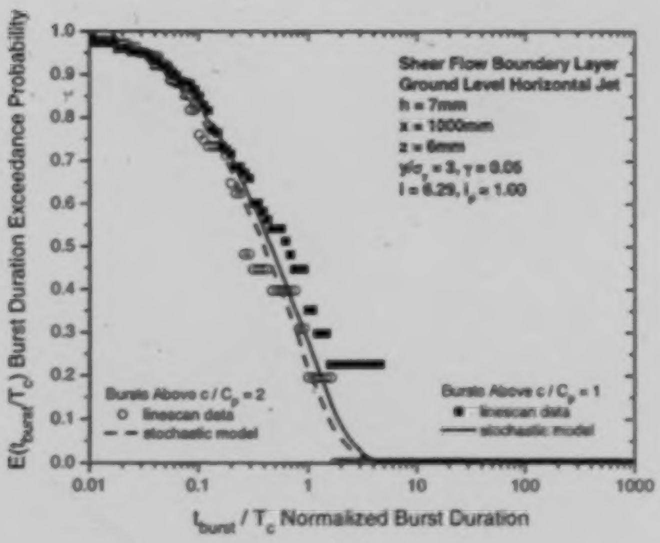

(b)

Figure I.25: Burst duration probability distributions for the ground level horizontal jet in shear flow, $h = 7$ mm, $x = 1000$ mm, measured at $z = 6$ mm, $y/\sigma_y = 3$ compared to stochastic simulation results for bursts above $(c/C_p) = 1$ and $(c/C_p) = 2$ (a) probability density function (pdf) (b) exceedance probability function (edf)

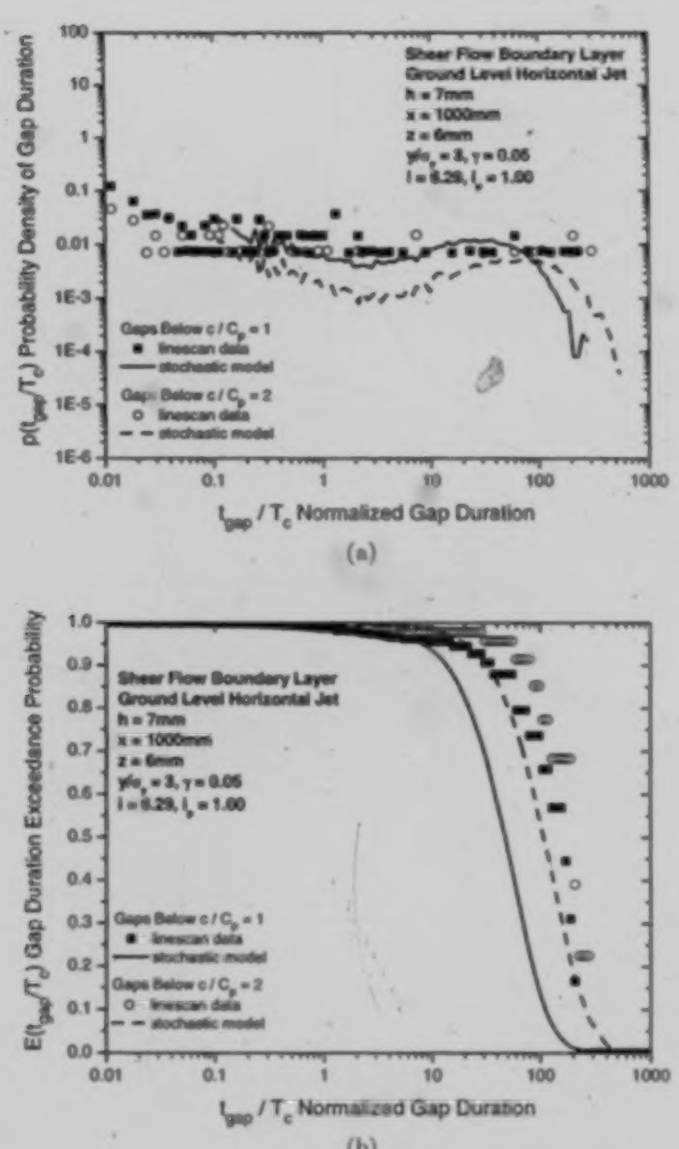

(a)

(b)

Figure I.26: Gap duration probability distributions for the ground level horizontal jet in shear flow, $h = 7$ mm, $x = 1000$ mm, measured at $z = 6$ mm, $y/\sigma_y = 3$ compared to stochastic simulation results for gaps below $(c/C_p) = 1$ and $(c/C_p) = 2$ (a) probability density function (pdf) (b) exceedance probability function (edf)

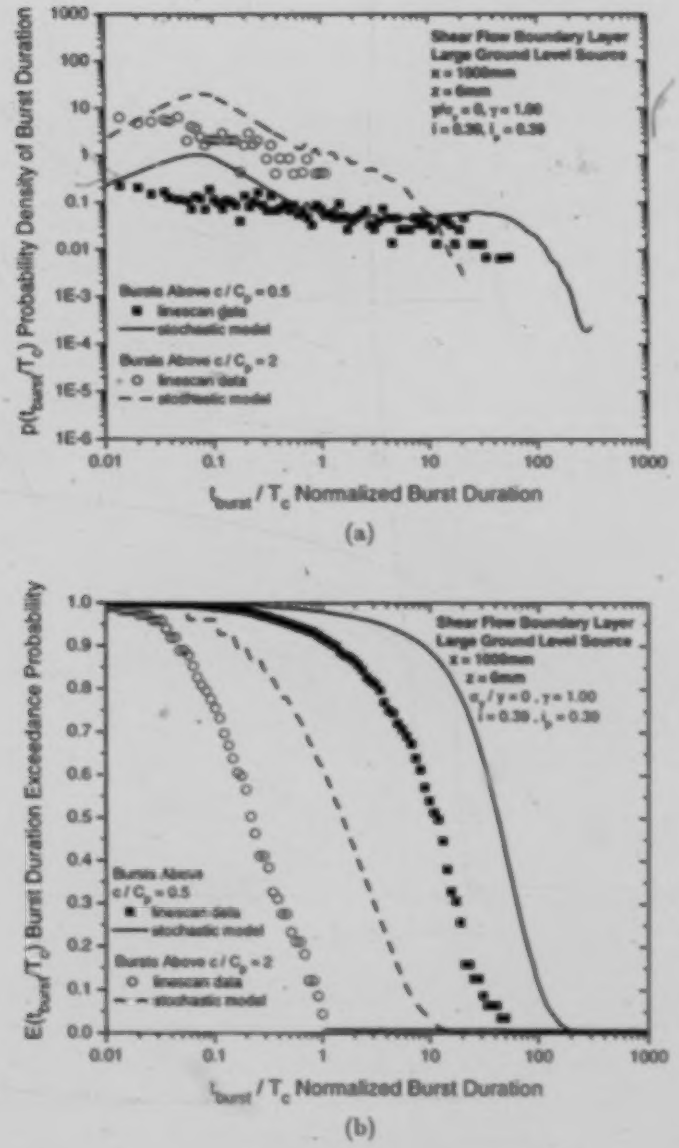

(a)

(b)

Figure I.27: Burst duration probability distributions for the large ground level source in shear flow, $h = 7$ mm, $x = 1000$ mm, measured at $z = 6$ mm, $y/\sigma_y = 0$ compared to stochastic simulation results for bursts above $(c/C_p) = 0.5$ and $(c/C_p) = 2$ (a) probability density function (pdf) (b) exceedance probability function (edf)

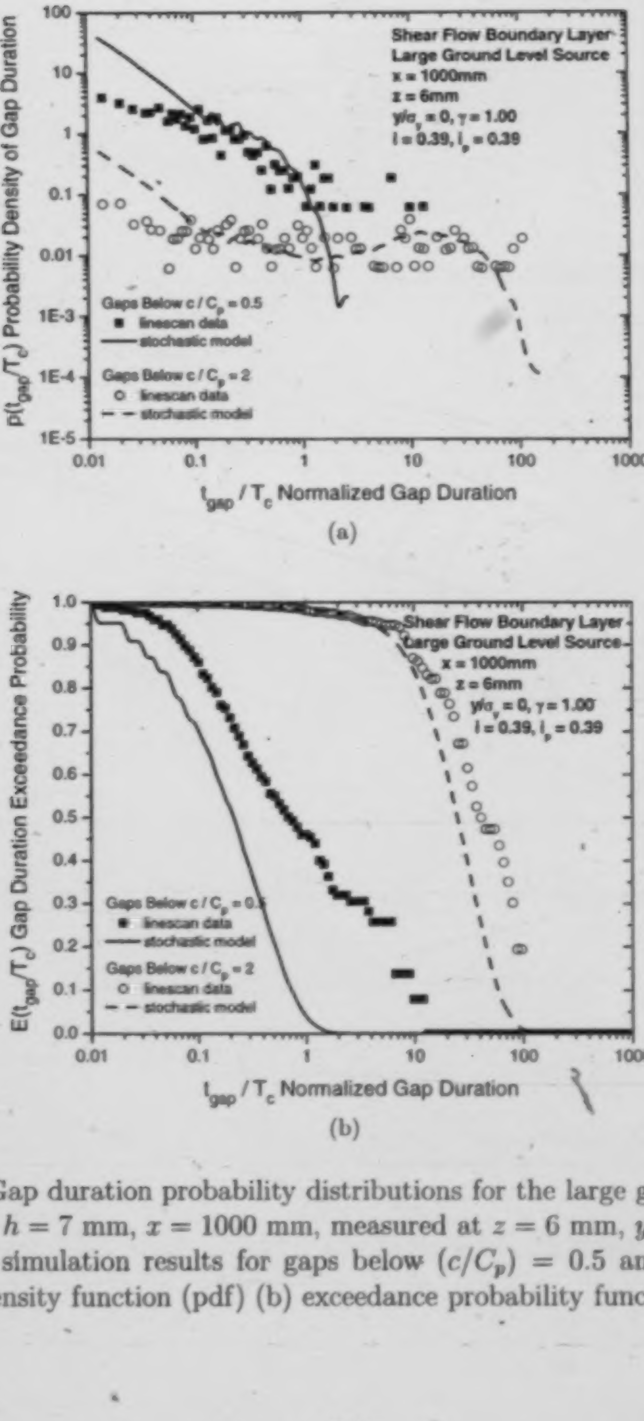

(a)

(b)

Figure I.28: Gap duration probability distributions for the large ground level source in shear flow, $h = 7$ mm, $x = 1000$ mm, measured at $z = 6$ mm, $y/\sigma_y = 0$ compared to stochastic simulation results for gaps below $(c/C_p) = 0.5$ and $(c/C_p) = 2$ (a) probability density function (pdf) (b) exceedance probability function (edf)

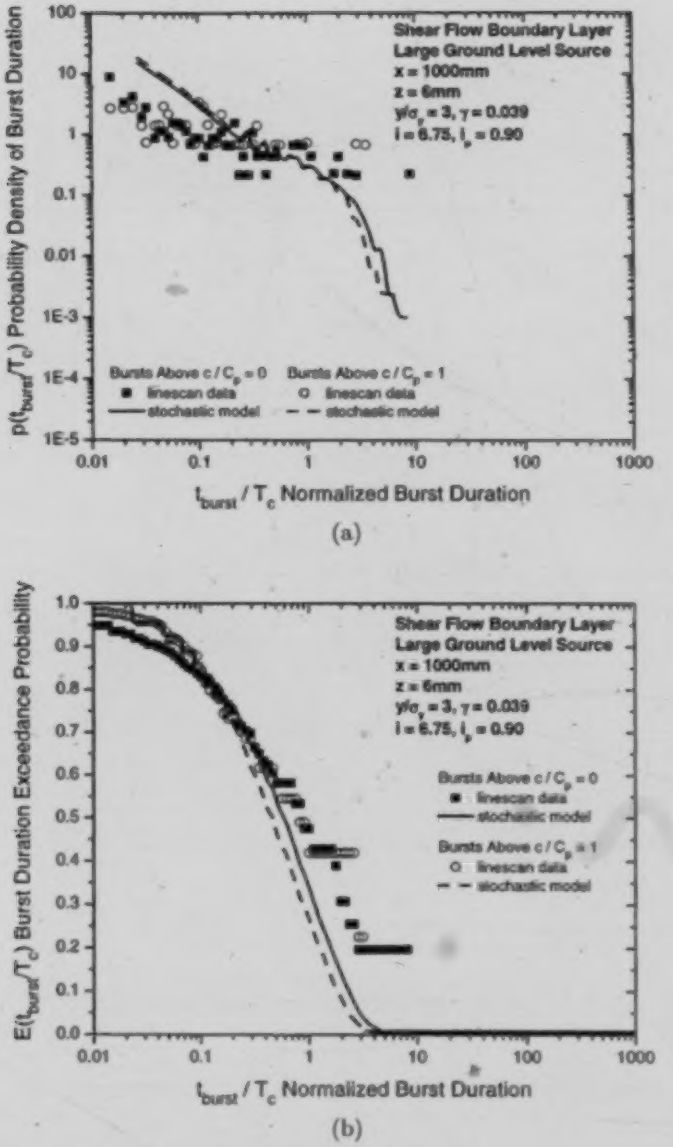

(a)

(b)

Figure I.29: Burst duration probability distributions for the large ground level source in shear flow, $h = 7$ mm, $x = 1000$ mm, measured at $z = 6$ mm, $y/\sigma_y = 3$ compared to stochastic simulation results for bursts above $(c/C_p) = 0$ and $(c/C_p) = 1$ (a) probability density function (pdf) (b) exceedance probability function (edf)

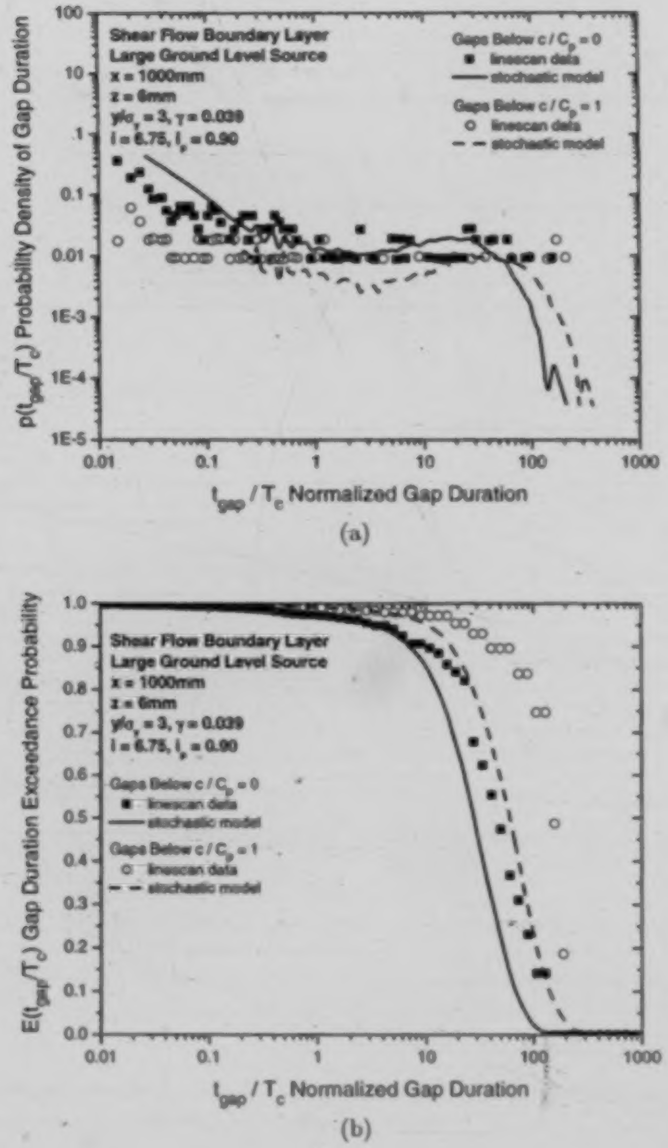

(a)

(b)

Figure I.30: Gap duration probability distributions for the large ground level source in shear flow, $h = 7$ mm, $x = 1000$ mm, measured at $z = 6$ mm, $y/\sigma_y = 3$ compared to stochastic simulation results for gaps below $(c/C_p) = 0$ and $(c/C_p) = 1$ (a) probability density function (pdf) (b) exceedance probability function (edf)